

DISS. ETH NO. 24774

**Rational Design of Inhibitors for Serine
Hydroxymethyltransferase: From Prospective Agrochemicals to
Highly Efficient Antimalarials**

A thesis submitted to attain the degree of
DOCTOR OF SCIENCES of ETH ZURICH
(Dr. sc. ETH Zurich)

presented by

Geoffrey Schwertz

M. Sc., Université de Strasbourg, France

Dipl. Ing., École Européenne de Chimie, Polymères et Matériaux, Strasbourg, France

born on 05.12.1989

citizen of France

accepted on the recommendation of
Prof. Dr. François Diederich, examiner
Prof. Dr. Donald Hilvert, co-examiner

2017

À mes parents

“A man who has no imagination has no wings”

Muhammad Ali (1942–2016)

Acknowledgements

First and foremost, I would like to express all my gratitude to *Prof. Dr. François Diederich* for allowing me to perform my doctoral studies in his group. It has been a great honor to contribute to your researches. Throughout these four years, you have been a fantastic supervisor, always supportive, passionate, inspiring, and providing great ideas. I really appreciated your trust and the freedom that I had to develop my project. It has been a rewarding experience and I learned a lot at your side. I truly believe that no other place could have been better suited to complete my PhD.

Many thanks to *Prof. Dr. Donald Hilvert* for accepting the co-examination of this Thesis.

At BASF-SE, I would like to thank *Dr. Matthias Witschel* for the exceptional collaboration. The realization of this project would not have been possible without your precious help. It has been a pleasure for me to meet you and participate with you to fruitful meetings. *Dr. Raphael Aponte*, thank you for performing excellent and accurate *in vitro* measurements.

Dr. Matthias Rottmann played a key role in the development of this Thesis, together with his technicians *Céline Freymond* and *Anja Schäfer*. Thank you for your valuable contributions, it has been a real enjoyment everytime I visited you in Basel to deliver compounds for testing, discuss science, and more.

I am grateful to *Dr. Penchit Chitnumsub*, *Dr. Ubolsree Leartsakulpanich*, *Prof. Dr. Pimchai Chaiyen*, *Aritsara Jaruwat*, and *Wanwipa Ittarat* for providing many structural data and biological results that were crucial for the development of this Thesis.

I had the pleasure to supervise four talented students during my stay at ETH: *Adrian Zwysig*, *Michele Frei*, *Kerstin Mark*, and *Marc Siggel*. All of you contributed significantly to my different projects, and it has been an enriching and refreshing experience to work with you in the lab.

Many thanks to the Medicines for Malaria Venture foundation for supporting this project for a couple of years and giving us access to their assays network that had a considerable impact on our researches. Especially, *Dr. Jeremy Burrows* and *Dr. Roger Bonnert* for the

fruitful discussions. *Dr. Karen White* and *Dr. Susan Charman* provided great insights into the metabolic degradation of the class of compounds studied herein. Additionally, *Abhijit Kundu* furnished a considerable number of synthetic intermediates that greatly boosted the progress of the project.

Many packages had to be sent out from ETH due to the numerous collaborators involved in the realization of this Thesis, who are spread all over the globe. For this reason, I am truly thankful to our administrative staff: *Irma Näf* and *Karin Puce-Schmidt*. I could not have done all this work without your help for the sendings, and also for all the paperworks related to my stay at ETH and in Zurich. *Prof. Dr. Carlo Thilgen*, thank you for organizing the practical courses OCP2 and the group in the background. A big thank goes to *Dr. Bruno Bernet* for correcting all lengthy experimental parts related to this project very thoroughly.

Performing my Thesis in the facilities of the Department of Chemistry and Applied Biosciences was priceless and I would like to thank the staff that greatly facilitate my daily work: *Dr. Marc-Olivier Ebert*, *Rainer Frankenstein*, and *René Arnold* from the NMR service; *Dr. Xiangyang Zhang*, *Louis Bertschi*, *Oswald Greter*, and *Rolf Häfliger* from the Mass-spectrometry service; *Michael Schneider* and *Peter Kälin* from the Microelemental Analysis service; and all the people working at the Shop, who were always helpful.

I am particularly thankful to *Dr. Anatol Schwab*, who gave me valuable insights into the project when I started my Thesis and provided me great assistance for all HPLC separations.

I am grateful to the Small Molecule Crystallography Center (SMoCC) of the ETH Zurich, which is composed of *Dr. Nils Trapp*, *Dr. Michael Wörle*, and *Michael Solar*, who provided me high quality crystallographic data. Additionally, I had the chance to integrate into their team for few days and learn more about crystallography, and I would like to thank them for this unique experience and for their kindness.

This Thesis was proofread by *Cornelius Gropp*. I am truly thankful to you for your careful corrections and our fruitful discussions. I had a great time sharing a writing room with you. I also need to acknowledge your enthusiastic personality in and outside the lab (especially about TLCs). Additionally, many thanks to *Dr. Nicolas Kerisit* for thoroughly proofreading the “Résumé”, but also for entertaining me with your legendary humor.

It is my honor to acknowledge the people with whom I shared the lab G312 for creating a pleasant and stimulating working atmosphere. Starting with my friend *Dr. Przemyslaw Gawel* for making my stay in Zurich unforgettable, introducing me to the delightful Polish vodka, the famous “Gawel tours”, and for your help with everything. Thank you very much *Dr. Çağatay Dengiz* for organizing a memorable trip in Turkey; *Leslie Riwar* for being the corner of piece of the lab and your help with any Swiss administrative paperwork; *Elias Halabi* for being in a great and relaxed mood on a daily basis; *Dr. Michal Tichý* for your love for exquisit meats and beers; *Dr. Manolis Tzirakis* for the rewarding discussions; and finally, *Dr. Levon Movsisyan* for all Armenian delights.

Besides my labmates, I have to thank many other group members that made my stay at ETH very enjoyable with many recreational moments includings ski weekends and apéros. Many thanks to *Dr. Oliver Dumele* for being the best ambassador of the “Deutsche Qualität”; *Dr. Christoph Hohn* for being one of the funniest guy that I know, all discussions related to chemistry or not, and the shared dinners; *Cédric Schaack* for organizing many group activities; *Raoul De Gasparo* for representing ~~Italia~~ Ticino in the group. Additionally, I will not forget all the good moments shared with: *Dr. Etienne Donckele*, *Dr. Maude Giroud*, *Dr. Jonas Thelemann*, *Dr. Michael Harder*, *Dr. Elke Persch*, *Dr. Victor García López*, and *Dr. Brendan Quigley*.

Beyond the borders of Switzerland, I would like to acknowledge my great friends *Dr. Etienne Schmitt*, *Dr. Benoit Westermann*, and *Vladimir Jovicic* for their unconditional support. I am indebted to several passionate scientists, who introduced me to chemistry and enabled me to gain professional experiences throughout internships and academical stay. In particular, *Dr. Yann Foricher* for all the discussions and advices regarding my career plan.

A mes parents, Catherine Haenggi et Patrick Schwertz, je vous remercie du fond du coeur pour vos sacrifices, votre soutien et de m’avoir encouragé pendant ces nombreuses années d’études. Je vous en suis reconnaissant à jamais !

"Last but not least", un grand merci à Cécile Zumbiehl d’avoir illuminé mes dernières années à Zurich, de m’apporter tout ce bonheur au quotidien, et aussi de me concôter tous ces bons petis plats. Je suis certain que l’avenir nous réserve pleins de bonnes surprises !

Publications and Presentations

Parts of this dissertation were published or will be submitted for publications:

G. Schwartz, M. C. Witschel, M. Rottmann, U. Leartsakulpanich, P. Chitnumsub, A. Jaruwat, W. Ittarat, A. Schäfer, R. A. Aponte, P. Chaiyen, F. Diederich. Potent Inhibitors for *Plasmodial* Serine Hydroxymethyltransferase (SHMT) Featuring a Spirocyclic Scaffold. Manuscript in preparation.

G. Schwartz, M. S. Frei, M. C. Witschel, M. Rottmann, U. Leartsakulpanich, P. Chitnumsub, A. Jaruwat, W. Ittarat, A. Schäfer, R. A. Aponte, N. Trapp, K. Mark, P. Chaiyen, F. Diederich, *Chem. Eur. J.* **2017**, *23*, 14345–14357. Conformational Aspects in the Design of Inhibitors for Serine Hydroxymethyltransferase (SHMT): Biphenyl, Aryl Sulfonamide, and Aryl Sulfone Motifs.

G. Schwartz, M. C. Witschel, M. Rottmann, R. Bonnert, U. Leartsakulpanich, P. Chitnumsub, A. Jaruwat, W. Ittarat, A. Schäfer, R. A. Aponte, S. A. Charman, K. L. White, A. Kundu, S. Sadhukhan, M. Lloyd, G. M. Freiberg, M. Srikumaran, M. Siggel, A. Zwyssig, P. Chaiyen, F. Diederich, *J. Med. Chem.* **2017**, *60*, 4840–4860. Antimalarial Inhibitors Targeting Serine Hydroxymethyltransferase (SHMT) with in Vivo Efficacy and Analysis of Their Binding Mode Based on X-Ray Cocrystal Structures. Highlighted in *Synfacts* (P. Kocienski, *Synfacts* **2017**, *13*, 0900).

M. C. Witschel, M. Rottmann, A. Schwab, U. Leartsakulpanich, P. Chitnumsub, M. Seet, S. Tonazzi, **G. Schwartz**, F. Stelzer, T. Mietzner, C. McNamara, F. Thater, C. Freymond, A. Jaruwat, C. Pinthong, P. Riangrunroj, M. Oufir, M. Hamburger, P. Mäser, L. M. Sanz-Alonso, S. Charman, S. Wittlin, Y. Yuthavong, P. Chaiyen, F. Diederich, *J. Med. Chem.* **2015**, *58*, 3117–3130. Inhibitors of Plasmodial Serine Hydroxymethyltransferase (SHMT): Cocrystal Structures of Pyrazolopyrans with Potent Blood- and Liver-stage Activities.

Publications resulting from collaboration during the doctoral studies:

A. Najer, D. Wu, M. G. Nussbaumer, **G. Schwertz**, A. Schwab, M. C. Witschel, A. Schäfer, F. Diederich, M. Rottmann, C. G. Palivan, H.-P. Beck, W. Meier, *Nanoscale* **2016**, *8*, 14858–14869. An Amphiphilic Graft Copolymer-based Nanoparticle Platform for Reduction-responsive Anticancer and Antimalarial Drug Delivery.

Publications resulting from previous research projects:

Q. Dherbassy, **G. Schwertz**, M. Chessé, C. Kumar Hazra, J. Wencel-Delord, F. Colobert, *Chem. Eur. J.* **2016**, *22*, 1735–1743. 1,1,1,3,3,3-Hexafluoroisopropanol as a Remarkable Medium for Atroposelective Sulfoxide-directed Fujiwara–Moritani Reaction with Acrylates and Styrenes.

Q. Dherbassy, **G. Schwertz**, C. Kumar Hazra, T. Wesch, J. Wencel-Delord, F. Colobert, *Phosphorus, Sulfur, and Silicon* **2015**, *190*, 1339–1351. Enantiopure Sulfoxides: Efficient Chiral Directing Group for Stereoselective C–H Bond Activation: Towards the Control of Axial Chirality.

Parts of this dissertation were presented at local or international conferences:

G. Schwertz, M. C. Witschel, M. Rottmann, R. Bonnert, P. Chaiyen, P. Chitnumsub, K. L. White, F. Diederich, *Identification of a Potent in Vivo Candidate Inhibiting SHMT, an Underexploited Antimalarial Target*. 254th ACS National Meeting, Washington DC, United-States, 20–24.08.2017 (Poster presentation).

G. Schwertz, M. C. Witschel, M. Rottmann, R. Bonnert, P. Chaiyen, P. Chitnumsub, K. L. White, F. Diederich, *Inhibition of SHMT: A Neglected Enzyme from the Folate Cycle*. Swiss Chemical Society Fall Meeting, Zurich, Switzerland, 15.09.2016 (Poster presentation).

G. Schwertz, M. C. Witschel, M. Rottmann, R. Bonnert, P. Chaiyen, P. Chitnumsub, K. L. White, F. Diederich, *SHMT Inhibition: A New Hope to Defeat Malaria*. XXIV International Symposium on Medicinal Chemistry, Manchester, United-Kingdom, 28.08.2016–01.09.2016 (Poster presentation). Awarded with a Poster Prize.

G. Schwertz, M. C. Witschel, M. Rottmann, P. Chaiyen, U. Leartsakulpanich, K. L. White, F. Diederich, *Tackling Malaria by Inhibiting the SHMT Enzyme*. Swiss Chemical Society Fall Meeting, Lausanne, Switzerland, 04.09.2015 (Poster presentation). Awarded with a Poster Prize.

G. Schwertz, M. C. Witschel, M. Rottmann, R. Bonnert, P. Chaiyen, P. Chitnumsub, K. L. White, F. Diederich, *Lead Optimization of SHMT Inhibitors: A Complex Puzzle to Solve for Defeating Malaria*. European School of Medicinal Chemistry, Urbino, Italy, 29.06.2014–04.07.2014 (Poster presentation).

G. Schwertz, M. C. Witschel, M. Rottmann, A. Schwab, P. Chaiyen, F. Diederich, *Inhibition of P. falciparum SHMT: Improvement of the Pharmacokinetic Properties to Reach In Vivo Activity*. Swiss Chemical Society Fall Meeting, Zurich, Switzerland, 11.09.2014 (Poster presentation).

Table of Contents

Abbreviations	I
Abstract.....	VII
Résumé.....	X
1. Introduction.....	2
1.1. Drug Repurposing in Medicine	4
1.1.1. Principle and General Aspects.....	4
1.1.2. Drug Repurposing in Action.....	6
1.2. The Perpetual Threat of Malaria	7
1.2.1. Key Facts of the Malaria Disease	8
1.2.2. Towards a Global Elimination of Malaria.....	10
1.2.3. Novel Treatments Currently Under Investigation.....	14
1.2.4. Drug Repurposing: An Opportunity for the Discovery of New Antimalarials?.....	19
1.3. The Folate Metabolism: A Privileged Antimalarial Target.....	22
1.3.1. General Overview.....	22
1.3.2. The Bifunctional Enzyme DHFR–TS.....	23
1.4. Serine Hydroxymethyltransferase (SHMT): An Underexploited Target	25
1.4.1. Function and Structure.....	25
1.4.2. Mechanism of the One-carbon Unit Transfer	30
1.4.3. Known Inhibitors for SHMT.....	32
1.5. Project Goal and Outline	33
2. Identification of Pyrazolopyran-based Inhibitors for SHMT and Their Primary Optimization.....	36
2.1. From Agrochemicals to Antimalarials: Identification of Pyrazolopyran-based Inhibitors for SHMT.....	36
2.2. Co-crystal Structure of (+)- 67 with PvSHMT and Ligand Design	38
2.3. Evaluation of Thienyl-containing Analogues.....	40
2.3.1. Derivatization of the Terminal Thienyl Ring.....	40
2.3.2. Alteration of the Substituents on the Pyrazolopyran Core.....	50
2.3.3. Identification of the Potential Metabolites from (±)- 129	55
2.4. Terminal Heteroalicyclic Rings as Thiophene Replacement	56
2.4.1. Design and Synthesis of Ligands (±)- 152–160 , (±)- 165–167 , and (±)- 186	56
2.4.2. In Vitro Biological Activities.....	61
2.5. Discovery of Potent Aromatic N-Heterocyclic Ligands.....	63
2.6. Summary on the Hit Identification and Primary Optimization	66

3. Conformational Aspects in the Design of Inhibitors for SHMT: Biphenyl, Aryl Sulfonamide, and Aryl Sulfone Motifs.....	68
3.1. Biphenyl Series.....	68
3.1.1. <i>Torsion Angles of Biphenyl Fragments and their Influence on Cellular Efficacy</i>	69
3.1.2. <i>Co-crystal Structures: Elucidation of Dipolar Interactions with Tyr63</i>	74
3.2. Aryl Sulfonamide/Aryl Sulfone Series.....	78
3.2.1. <i>Conformational Analysis</i>	78
3.2.2. <i>Design and Synthesis of Ligands (±)-229–237, (±)-263–265, and (±)-269,270</i>	81
3.2.3. <i>Small Molecule X-ray Crystal Structures</i>	86
3.2.4. <i>Biological Activities</i>	87
3.2.5. <i>Co-crystal Structures with C364A-PvSHMT Mutant Highlighting the Lipophilic Character of the SO₂ Moiety</i>	89
3.3. Tautomerism of the Pyrazolopyran Core.....	93
3.4. Summary on Biphenyl and Aryl Sulfonamide/Aryl Sulfone Analogues and their Conformational Preferences.....	96
4. In Vivo Validation of SHMT as a Druggable Antimalarial Target	99
4.1. Identification of an in Vivo Candidate and Animal Model.....	99
4.2. Cytotoxicity and Mutagenicity Evaluation.....	106
4.3. Co-crystal Structures of Carboxylate Analogues with PvSHMT.....	107
4.3.1. <i>Binding Mode of the Biaryl Series</i>	107
4.3.2. <i>Binding Mode of the N-Piperidine-Aryl Series</i>	111
4.3.3. <i>Spatial Location of the Carboxylate Moiety in the PvSHMT–Ligand Complexes</i>	114
4.3.4. <i>Cys364–Loop Movement</i>	115
4.4. Summary on the Discovery of a Potent in Vivo Inhibitor and Co-crystal Structures Analysis.....	117
5. Investigation of Novel Scaffolds Inhibiting SHMT.....	119
5.1. Spirocyclic Analogues Featuring a Pyrazolopyran Core.....	119
5.1.1. <i>Spiro-2-indolinone Series</i>	119
5.1.2. <i>Spiro-dihydroindene Series</i>	123
5.1.3. <i>Binding Mode of Spiro-dihydroindene Analogues</i>	130
5.2. De novo Design of Inhibitors for SHMT.....	133
5.2.1. <i>Design and Synthesis of Pyrimidine-based Ligands</i>	133
5.2.2. <i>Design and Synthesis of Triazine-based Ligands</i>	140
5.2.3. <i>Biological Activities</i>	143
5.3. Summary on the Discovery of a Novel Potent Class of SHMT Inhibitors.....	144

6. Affinity Assessment Towards Human SHMT and Metabolomics Study	147
6.1. Affinity Assessment for Human SHMT.....	147
6.2. Metabolomics Study Involving Pyrazolopyran-based Inhibitor (\pm)- 158	151
6.3. Summary on the Inhibition of Human SHMT and the Metabolomics Study.....	156
7. Conclusions and Outlook	159
7.1. General Conclusions.....	159
7.2. Outlook and Perspectives	161
8. Experimental Part.....	165
8.1. Synthetic Protocols and Characterization of Selected Ligands.....	165
8.1.1. <i>Materials and Experimental Methods</i>	165
8.1.2. <i>General Procedures</i>	167
8.1.3. <i>Synthetic Procedures and Characterizations of Selected Compounds for Chapters 2–4</i> . 169	
8.1.4. <i>Synthetic Procedures and Characterizations for Chapter 5</i>	184
8.1.5. <i>HPLC Chromatograms of (\pm)-291, (+)-291, (-)-291, (\pm)-342, (+)-342, (-)-342, (\pm)-348, (+)-348, and (-)-348</i>	237
8.2. Biological Assays and Co-crystallization with PvSHMT	241
8.2.1. <i>In Vitro Experiments</i>	241
8.2.2. <i>In Vivo Experiments</i>	244
8.2.3. <i>Co-crystallization with PvSHMT</i>	245
9. Appendix.....	248
9.1. Alignment of <i>At</i> SHMT with <i>Pf</i> - and <i>Pv</i> SHMT.....	248
9.2. Metabolites Identification from Ligands (\pm)- 69 , (\pm)- 129 , (\pm)- 130 , and (\pm)- 151	251
9.3. In Vivo Efficacy Evaluation in SCID Mouse Models.....	254
9.4. AMES Study.....	255
9.5. Small Molecule X-ray Crystal Structures	257
10. References.....	270

Abbreviations

Å	Ångström (1 Å = 10 ⁻¹⁰ m)
Ac	acetyl
ACT	Artemisinin-based combination therapy
ADMET	absorption, distribution, metabolism, excretion, and toxicity
AICAR	5-aminoimidazole-4-carboxamide-1β-ribofuranosyl-5'-monophosphate
AIDS	acquired immune deficiency syndrome
AMP	adenosine monophosphate
AMPK	AMP-activated kinase
ANOVA	analysis of variance
aq.	aqueous
Ar	Argon
ASL	adenylosuccinate lyase
<i>At</i>	<i>Arabidopsis thaliana</i>
ATIC	AICAR transformylase
ATP	adenosine triphosphate
AUC	area under the curve
ax	axial
Bn	benzyl
Boc	<i>tert</i> -butyloxycarbonyl
Boc ₂ O	di- <i>tert</i> -butyl dicarbonate
br.	broad
Bu	butyl
C	Celsius
cal	calorie (1 cal = 4.185 Joule)
calcd.	calculated
CCDC	Cambridge Crystallographic Data Centre
CDI	1,1'-carbonyldiimidazole
<i>clogP</i>	calculated logarithmic distribution constant for <i>n</i> -octanol–water
c.n.d.	could not determine
conc.	concentrated
CQ	chloroquine
CSD	Cambridge Structural Database

Abbreviations

d	doublet
Da	Dalton (1 Da = 1.66×10^{-27} kg)
dba	dibenzylidenacetone
DDT	dichlorodiphenyltrichloroethane
decomp.	decomposition
DFT	density functional theory
DHA	dihydroartemisinin
DHF	dihydrofolate
DHFR	dihydrofolate reductase
DHFS	dihydrofolate synthase
DHODH	dihydroorotate dehydrogenase
DHP	dihydropteroate
DHPS	dihydropteroate synthase
DIC	<i>N,N'</i> -diisopropylcarbodiimide
DIPEA	<i>N,N</i> -diisopropylethylamine
DMA	<i>N,N</i> -dimethylacetamide
DME	dimethoxyethane
DMF	<i>N,N</i> -dimethylformamide
DMSO	dimethylsulfoxide
DNA	deoxyribonucleic acid
dppf	1,1'-bis(diphenylphosphino)ferrocene
dTMP	deoxythymidine monophosphate
dTTP	deoxythymidine triphosphate
dUMP	deoxyuridine monophosphate
<i>E</i>	energy
<i>E. coli</i>	<i>Escherichia coli</i>
EC ₅₀	half-maximal (50%) effective concentration
<i>e.g.</i>	Latin <i>exempli gratia</i> , “for example”
EI	electron impact
eq	equivalent or equatorial (NMR)
ESI	electron spray ionization
Et	ethyl
Et ₃ N	triethylamine
Et ₂ O	diethyl ether

Abbreviations

EtOAc	ethyl acetate
EtOH	ethanol
FAICAR	5-formamidoimidazole-4-carboxamide ribotide
FDA	food and drug administration
FMN	flavin mononucleotide
g	gram(s)
<i>gem</i>	geminal
GP	general procedure
h	hour(s)
H-bond	hydrogen bond
hERG	human ether-à-go-go-related gene
H ₄ F	tetrahydrofolate
HIV	human immunodeficiency virus
HMBC	heteronuclear multiple bond correlation
HOBt	hydroxybenzotriazole
HPLC	high performance liquid chromatography
HR	high resolution
<i>Hs</i> NMT1	human NMT1
HSQC	heteronuclear single quantum coherence
HTS	high throughput screening
Hz	Hertz
IC ₅₀	half-maximal (50%) inhibitory constant
IMP	inosine monophosphate
<i>i</i> -PrOH	isopropanol
IR	infrared
IP	intellectual property
IUPAC	International Union of Pure and Applied Chemistry
i.v.	intravenous injection
<i>J</i>	coupling constant (NMR) in Hz
<i>k</i> _{cat}	enzymatic rate constant
kg	kilogram(s)
K	Kelvin
kcal	kilocalories
KOAc	potassium acetate

Abbreviations

L	liter
LC/MS	liquid chromatography coupled to mass spectrometry
LiAlH ₄	lithium aluminium hydride
LiHMDS	lithium bis(trimethylsilyl)amide
LLQ	lower limit of quantification
m	multiplet (NMR), medium (IR), meter (distance)
<i>m</i> -CPBA	<i>meta</i> -chloroperbenzoic acid
m.p.	melting point
<i>m/z</i>	mass over charge ratio
M	molar
<i>M</i>	molecular ion peak (MS)
μ	micro (10 ⁻⁶)
μ W	microwave irradiation
Me	methyl
MeCN	acetonitrile
MeOH	methanol
mg	milligram(s)
min	minute(s)
MS	mass spectrometry
MTX	methotrexate
n	nano (10 ⁻⁹)
n.d.	not determined
NADP ⁺	nicotinamide adenine dinucleotide phosphate (oxidized form)
NADPH	nicotinamide adenine dinucleotide phosphate (reduced form)
<i>n</i> -BuLi	<i>n</i> -butyllithium
NBS	<i>N</i> -bromosuccinimide
NCE	new chemical entity
NMR	nuclear magnetic resonance
NMT	<i>N</i> -myristoyltransferase
NTDs	neglected tropical diseases
ORTEP	Oak Ridge thermal ellipsoid program
p.o.	Latin <i>per os</i> , “oral administration”
<i>P.</i>	<i>Plasmodium</i>

Abbreviations

<i>p</i> ABA	<i>para</i> -aminobenzoic acid
<i>Pb</i>	<i>Plasmodium berghei</i>
PDB	Protein Data Bank
PDE5	phosphodiesterase-5
PES	potential energy scan
<i>Pf</i>	<i>Plasmodium falciparum</i>
<i>Pf</i> CRT	<i>Plasmodium falciparum</i> chloroquine resistant transporter
<i>Pf</i> K13	<i>Plasmodium falciparum</i> K13
<i>Pf</i> PI3K	<i>Plasmodium falciparum</i> phosphatidylinositol-3-kinase
pH	decimal logarithmic of the reciprocal of the hydrogen ion activity
PI	phosphatidylinositol
PI3P	phosphatidylinositol 3-phosphate
<i>Pk</i>	<i>Plasmodium knowlesi</i>
p <i>K</i> _a	logarithmic measure of the acid dissociation constant
PKM2	pyruvate kinase
PLP	pyridoxal 5'-phosphate
<i>Pm</i>	<i>Plasmodium malariae</i>
<i>Po</i>	<i>Plasmodium ovale</i>
PPh ₃	triphenylphosphine
ppm	parts per million
PRR	parasite reduction ratio
<i>p</i> TSOH	<i>para</i> -toluenesulfonic acid
<i>Pv</i>	<i>Plasmodium vivax</i>
q	quartet
quant.	quantitative
quint	quintet
<i>R</i> _f	retention factor
RBC	red blood cells
RNA	ribonucleic acid
R&D	research and development
s	singlet (NMR) or strong (IR)
SAR	structure-activity relationship
sat.	saturated
SCID	severe combined immunodeficiency

Abbreviations

SERCaP	Single Exposure Radical Cure and Prophylaxis
sept	septet
sext	sextet
SHMT	serine hydroxymethyltransferase
SHMT1	human cytosolic form of serine hydroxymethyltransferase
SHMT2	human mitochondrial form of serine hydroxymethyltransferase
SUI	stress urinary incontinence
<i>T</i>	temperature
<i>t</i>	triplet
$t_{1/2}$	half-life
TBAF	tetrabutylammonium fluoride
TdP	Torsade de Pointes
TFA	trifluoroacetic acid
THF	tetrahydrofuran
TK	thymidine kinase
TLC	thin layer chromatography
TS	thymidylate synthase
Ub	ubiquitin groups
UV	ultraviolet
X-Phos	2-dicyclohexylphosphino-2',4',6'-triisopropylbiphenyl
w	weak
W	water molecule
WHO	World Health Organization
5-FU	5-fluorouracil
5-CHO-H ₄ F	(6 <i>R</i>)-5-formyltetrahydrofolate
5,10-CH ₂ -H ₄ F	5,10-methylenetetrahydrofolate
Δ	difference
δ	chemical shift
$\tilde{\nu}$	wavenumber(s)
°	degree

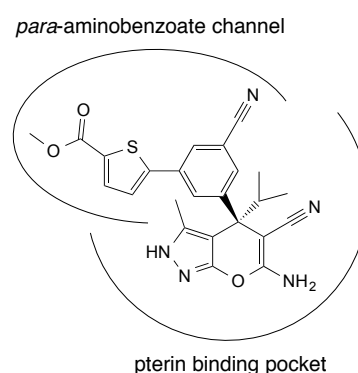
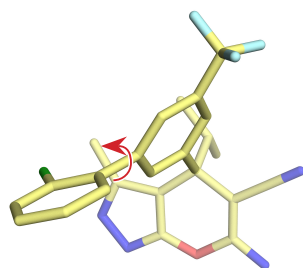
The three-letter code for amino acids is used.

Abstract

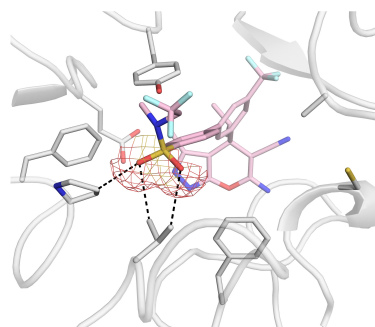
Malaria has been threatening the life of millions of people for over a century and continues to do so. Considerable progress has been made in the past decade to reduce the malaria burden by virtue of better prevention and improved access to treatments for the populations at risk. Nonetheless, millions of clinical cases and more than 400 000 deaths are still imputed to this disease every year. Eradication endeavors are seriously jeopardized by the widespread resistance to most antimalarials and the emergence of resistance against the first-line artemisinin-based combination therapy. Spurred by these concerning indicators, the scientific community is actively seeking for alternative treatments. In this context, we envisioned to take advantage of the unique vulnerability of *Plasmodium* parasites to the disruption of the *de novo* pyrimidine biosynthetic pathway by inhibiting the serine hydroxymethyltransferase (SHMT) enzyme, which is a crucial component of the folate synthesis cycle.

Screening of a BASF herbicides library yielded a potent class of pyrazolopyran-based ligands with single-digit nanomolar activity (EC_{50}), however, their poor metabolic stability ($t_{1/2} < 10$ min) precluded to reach significant *in vivo* efficacy. One of the main goals of this Thesis was therefore to unite potency and stability in order to achieve sufficient *in vivo* exposure. An X-ray co-crystal structure with *P. vivax* SHMT was solved early in this project, which enabled the use of structure-based design to guide the optimization program. The different substituents on the pyrazolopyran core were systematically altered, and particular emphasis was put on the bicyclic scaffold departing from the stereogenic center, as the terminal thienyl fragment proved to be particularly sensitive to metabolic degradation.

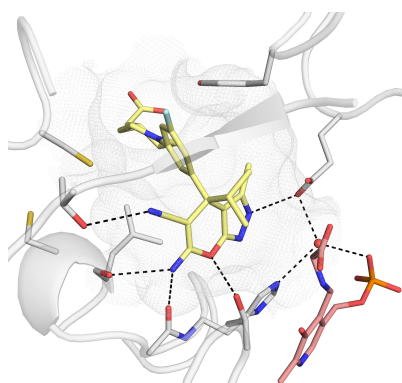
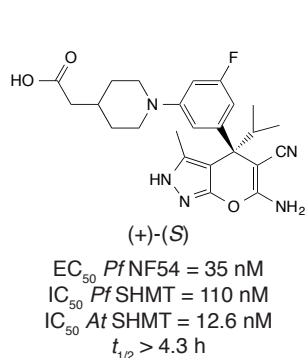
The paramount importance of the conformational aspects for drug design is highlighted in two series of inhibitors featuring either a biphenyl or an aryl sulfonamide/aryl sulfone fragment. Indeed, an unprecedented influence of the torsion angle of *ortho*-substituted biphenyl moieties on cell-based efficacy was observed with discrepancies up to 37-fold ($EC_{50} = 18\text{--}665$ nM). By databases searches, as well as by theoretical calculations, we found that the loss of cellular efficacy correlates with the increase of the biphenyl torsion angle in the ligands. Thereby, it is postulated that cell permeation is affected



by the conformation of the biphenyl fragment. The preferred conformations of aryl sulfonamides/aryl sulfones were analyzed by databases mining, theoretical calculations, and crystallographic data. Additionally, the peculiar lipophilic character of the sulfonyl moiety was underscored thanks to three protein–ligand complexes, in which the SO₂ group points to non-polarized C–H bonds of lipophilic residues.



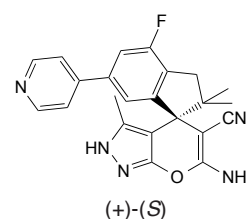
In an extensive structure-activity relationship study, a cluster of carboxylate analogues with promising metabolic stability was identified. Further refinements enabled the discovery of a potent ligand featuring a piperidine fragment that displayed a half-life in human liver microsomes exceeding 4 h. It is noteworthy that the pyrazolopyran class of molecules and SHMT exhibit a high level of chiral recognition, as the (+)-(*S*)-enantiomer proved to be substantially more active than its stereoisomer in all biological assays. The selected candidate was further studied in a *P. falciparum* severe combined immunodeficiency (SCID) mouse model. Remarkably, a compelling reduction of 73% of parasitemia (vs. untreated mice) was measured,



which constitutes the very first example of the treatment of a malaria infection by an inhibitor targeting SHMT, hence, revealing that SHMT is a druggable target for antimalarials. In addition, a comprehensive analysis of the

binding mode of this ligand, as well as the ones of other compounds from this series, with *P. vivax* SHMT showed a good match with the natural substrate of SHMT, namely tetrahydrofolate. The pyrazolopyran core occupies the pterin binding pocket, while the bicyclic scaffold extends orthogonally from the core into the *para*-aminobenzoate channel with the carboxylate protruding from the latter.

All knowledge gained in the aforementioned studies served for the design of a back-up series. The *de novo* design of pyrimidine- and triazine-based ligands remained unsuccessful, whereas several conformationally locked inhibitors featuring a pyrazolopyran core with low nanomolar activity (EC_{50}) were discovered. The binding mode of these novel active substances, which was elucidated by X-ray co-crystal structures, resembles the one of their non-spiro analogues. However, subtle



EC_{50} *Pf* NF54 = 334 nM
 IC_{50} *Pf* SHMT = 18 nM
 IC_{50} *At* SHMT = 281 nM

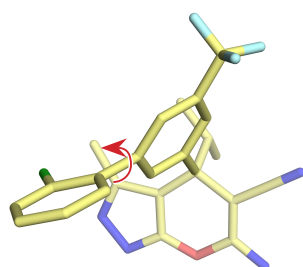
differences were pinpointed and analyzed. In particular, the filling of the small-lateral pocket lined by the Cys364-loop.

Furthermore, the affinity of selected inhibitors for human SHMT, as well as their cytotoxicity, was assessed. We found that despite their high target affinity ($IC_{50} \sim 100$ nM), none of the ligands proved to be cytotoxic ($EC_{50} > 10$ μ M). This result is presumably linked to the ability of mammals to salvage nucleotides for the pyrimidine biosynthesis, conversely to *Plasmodium* parasites. Finally, a metabolomics study confirmed the mode of action of the pyrazolopyran-based class of SHMT inhibitors, and shed light on their potential use to inhibit the proliferation of cancer cells.

Résumé

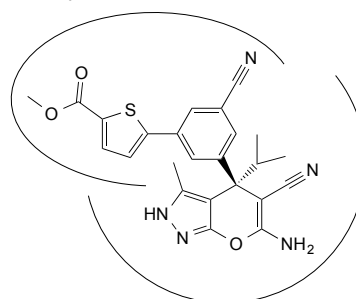
La malaria menace la vie de millions de personnes depuis plus d'un siècle et continue de le faire. Des progrès considérables ont été accompli au cours de la dernière décennie afin de réduire le fléau qu'est la malaria, notamment grâce à une meilleure prévention et à un accès amélioré aux traitements pour les populations à risque. Néanmoins, des millions de cas cliniques et plus de 400 000 décès sont toujours imputé à cette maladie chaque année. Les efforts d'éradication sont sérieusement mis en péril par la résistance généralisée à la majorité des médicaments contre la malaria et l'émergence de résistance contre les traitements de première ligne à base d'artémisinine. Compte tenu de ces signes alarmants, des traitements alternatifs sont activement recherchés par la communauté scientifique. A cet égard, nous avons envisagé de tirer profit de l'unique vulnérabilité des parasites du genre *Plasmodium* face à l'interruption de la voie de biosynthèse *de novo* de pyrimidine en inhibant l'enzyme sérine hydroxyméthyltransférase (SHMT), qui est une composante cruciale au sein du cycle de synthèse de folates.

Le criblage d'une librairie d'herbicides issue de BASF a permis d'identifier une puissante classe de ligands de la famille des pyrazolopyranes possédant une activité (EC_{50}) nanomolaire à un chiffre mais avec une stabilité métabolique insuffisante ($t_{1/2} < 10$ min), ce qui a empêché d'atteindre une efficacité *in vivo* significative. Par conséquent, un des objectifs principaux de cette thèse a été d'unifier puissance et stabilité afin d'atteindre une exposition *in vivo* suffisante. Une structure co-cristalline avec *P. vivax* SHMT, obtenue par diffraction de rayons X, a été résolue au commencement de ce projet, ce qui a permis le recours à la conception structurelle pour guider le programme d'optimisation. Les différents substituants du noyau pyrazolopyrane ont été systématiquement modifiés et une attention particulière a été portée sur la partie bicyclique partant du centre stéréogénique, car le thienyl terminal s'est avéré particulièrement sensible à la dégradation métabolique.



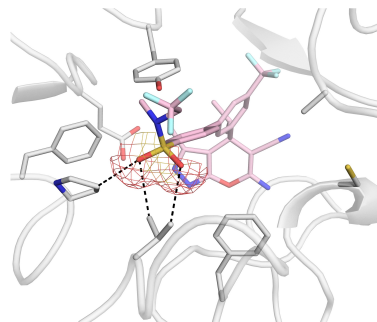
L'importance capitale des aspects conformationnels dans la conception d'un médicament est soulignée au travers de deux séries d'inhibiteurs incorporant soit un fragment biphenyle soit un fragment aryle sulfonamide/aryle sulfone. En effet, une influence sans précédent de l'angle de torsion de biphenyles *ortho*-substitués sur

canal *para*-aminobenzoate

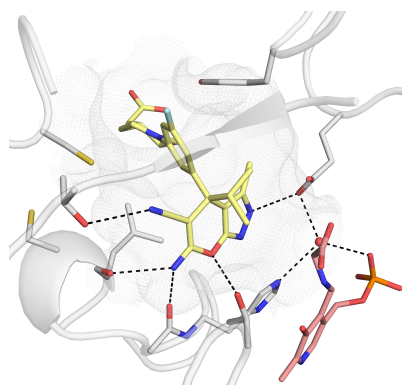
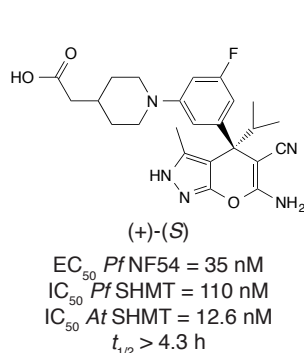


poche de liaison ptérine

l'efficacité cellulaire a été observée, avec des différences allant jusqu'à un facteur 37 ($EC_{50} = 18\text{--}665\text{ nM}$). Par des recherches au sein de bases de données, ainsi que des calculs théoriques, nous avons déterminé que la perte d'efficacité cellulaire corrèle avec l'augmentation de l'angle de torsion du groupement biphenyle au sein des ligands. Ainsi, il est postulé que la perméation cellulaire est affectée par la conformation du biphenyle. Les conformations privilégiées d'aryles sulfonamides et d'aryles sulfones ont été analysées à l'aide de recherches dans des bases de données, de calculs théoriques et de données cristallographiques. En outre, le caractère lipophile singulier du groupe fonctionnel sulfonyle a été mis en évidence grâce à trois complexes protéine–ligand, au sein desquels le groupement SO_2 pointe vers des liaisons C–H non-polarisées de résidus lipophiles.



A la suite d'une étude approfondie des relations structure-activité, plusieurs carboxylates possédant une stabilité métabolique prometteuse ont été identifiés. Des modifications supplémentaires ont permis l'identification d'un puissant ligand comprenant un fragment pipéridine, pour lequel une demi-vie excédant 4 h au sein de microsomes hépatiques humains a été mesurée. Il est à noter que la famille des pyrazolopyranes et SHMT exhibent un haut niveau de reconnaissance chirale. En effet, l'énantiomère (+)-(S) s'est avéré être considérablement plus actif que son stéréoisomère dans tous les essais biologiques. Ce candidat a été sélectionné pour une étude approfondie chez le rongeur au cours d'un essai communément appelé: "*P. falciparum* severe combined immunodeficiency (SCID) mouse model".



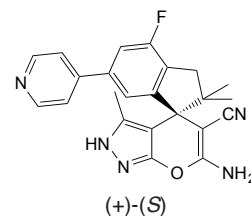
Une réduction significative de la parasitémie de 73% (comparé au groupe de souris non traitées) a été mesurée, ce qui constitue le tout premier exemple d'un traitement d'une infection de la malaria par un inhibiteur ciblant

SHMT. De ce fait, il a été révélé que SHMT est une cible thérapeutique pour le traitement de la malaria. De plus, une analyse détaillée du mode de liaison de ce ligand, ainsi que ceux d'autres composés de cette série, avec *P. vivax* SHMT a permis de souligner la bonne concordance avec le substrat naturel de SHMT, appelé tétrahydrofolate. Le noyau pyrazolopyrane occupe le site de liaison du fragment ptérine, alors que la partie bicyclique

s'étend orthogonalement par rapport au reste de la molécule dans la portion dénommée "canal *para*-aminobenzoate" et le groupement carboxylate dépasse de cette dernière.

Les connaissances acquises au cours des travaux mentionnés ci-dessus ont été utilisées pour la conception d'une série d'appoint. Le *de novo* design de ligands de la famille des pyrimidines et triazines n'a pas été concluant, en revanche plusieurs inhibiteurs conformationnellement contraints comprenant un noyau pyrazolopyrane et possédant une activité (EC_{50}) à de faibles concentrations nanomolaires ont été découverts. Le mode de liaison de ces nouvelles substances actives, élucidé à l'aide de plusieurs structures co-cristallines obtenues par diffraction de rayons X, ressemble à celui de leurs analogues non-spirocycliques. Cependant, de subtiles différences ont pu être identifiées et analysées. En particulier, l'occupation d'une petite poche latérale bordée par la boucle dénommée "Cys364-loop".

Par ailleurs, l'affinité d'une sélection d'inhibiteurs pour la SHMT humaine, ainsi que leur cytotoxicité, ont été évaluées. Nous avons trouvé que malgré leur affinité élevée ($IC_{50} \sim 100$ nM), aucun ligand n'est cytotoxique ($EC_{50} > 10 \mu\text{M}$). Ce résultat est probablement lié à la capacité des mammifères de biosynthétiser des nucléotides pyrimidiques par la voie de sauvetage des nucléotides, contrairement aux parasites du genre *Plasmodium*. Enfin, une étude métabolomique a permis de confirmer le mode d'action des inhibiteurs de la famille des pyrazolopyranes ciblant l'enzyme SHMT et a mis en lumière leur possible utilisation contre la prolifération de cellules cancéreuses.



EC_{50} PfNF54 = 334 nM
 IC_{50} Pf SHMT = 18 nM
 IC_{50} At SHMT = 281 nM

1. Introduction

In this Chapter, a brief status of the field of medicinal chemistry is given. The general aspects of drug repurposing and the advantage of this approach, over traditional drug development, are detailed. Subsequently, the malaria burden is exposed and the current treatments (marketed or in clinical trials) are introduced. The folate biosynthesis cycle is described and a particular attention is given to the enzyme serine hydroxymethyltransferase. Thereafter, the outline of this thesis is presented.

1. Introduction

In the course of the past two centuries, human life expectancy has increased significantly from about 45 years of age at the start of the twentieth century to 71.4 years in 2015 according to the World Health Organization (WHO).^[1] It ranges from 60.0 years in the WHO African Region to 76.8 years in the WHO European Region. The increase in global life expectancy has been driven by an improvement of the quality of life and by the development of modern medicine. Indeed, major breakthroughs in medicines allowed to improve health care considerably. Preeminent achievements have been made in the nineteenth century by Louis Pasteur with his discoveries of the principles of vaccination, microbial fermentation, and pasteurization. His work inspired Joseph Lister (also known as “the father of modern surgery”), who applied carbolic acid compounds as antiseptic on surgical wounds.^[2] This led to a striking decrease of mortality in hospitals and opening the way towards asepsis and sterile techniques. Later, the discoveries of numerous groundbreaking medicines have contributed to the enhancement of health care, starting with the antibiotic penicillin discovered accidentally by Alexander Fleming in 1928, which revolutionized the treatment of bacterial diseases. In the field of pain relieving medications, morphine together with aspirin (**1**) (Figure 1) have dramatically impacted the wellness of the patients.

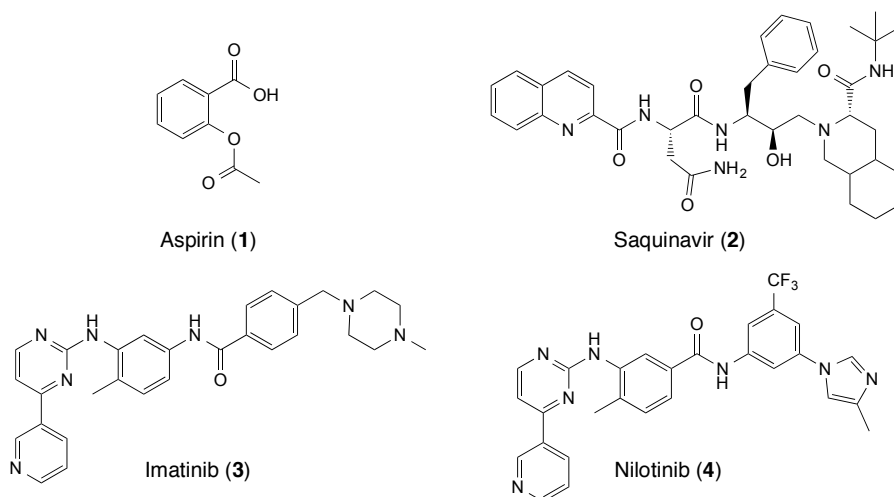


Figure 1. Molecular structures of aspirin (**1**), saquinavir (**2**), imatinib (**3**), and nilotinib (**4**).

Lately, the development of human immunodeficiency virus (HIV) protease inhibitors allowed to drop the acquired immune deficiency syndrome (AIDS)-related mortality drastically, which became a controllable and chronic disease.^[3] In 1995, the active substance saquinavir (**2**, Invirase®, developed by F. Hoffmann-La Roche) was the first HIV protease inhibitor used in the treatment of patients with AIDS (Figure 1).^[4,5] HIV-1 protease inhibitors

constitute one of the biggest successes of structure-based drug design, which was enabled by the elucidation of the three-dimensional structure of the aspartic protease of interest.^[6] Finally, the development of oncology and chemotherapy led to the diminishment of the burden of numerous type of cancers. The development of the blockbuster drug imatinib (**3**, Glivec®, developed by Novartis), a selective tyrosine-kinase inhibitor, for the treatment of chronic myelogenous leukaemia is a recent and compelling example (Figure 1).^[7] Further studies employing structure-based design led to the discovery of nilotinib (**4**, Tasigna®, developed by Novartis), a second-generation tyrosine-kinase inhibitor, which is more potent than **3** and active against resistant strains (Figure 1).^[8-10]

As illustrated above, the pharmaceutical industry, especially medicinal chemistry, had a crucial role in increasing human life expectancy and improving the life of patients. However, after decades of success, the pharmaceutical industry is facing a very delicate period with very low approval rates by the regulatory authorities. For instance, in 2002 only 17 new chemical entities (NCE) were approved by the food and drug administration (FDA) in the United States.^[11] Additionally, a dispiriting average success rate for all therapeutic areas of 11% has been reported.^[11] In other words, only 1 in 10 drugs receives the FDA approval to be sold on the market.^[12] This high attrition rate is disastrous given the resources and time (10–15 years) necessary to develop a drug. Indeed, a recent estimation of the capitalized total costs of research and development (R&D) for an approved NCE calculates to \$2558 million.^[13] In this report, the costs of abandoned NCEs were linked to the costs of the compounds that obtained approval. Several causes are at the origin of this recent slackening of approval: diseases with great complexity are targeted; the entry bar for new drugs is higher because they are often competing with enhanced standard of care; and the regulatory authorities are more demanding.^[11]

In order to lower the attrition rates, researchers tried to underlie causes of failure. In 1991, the most significant causes of attrition were attributed to poor pharmacokinetic and bioavailability results (~40%).^[11] Such failures mainly occurred in clinical Phase I. Theoretical and empirical rules such as the famous Lipinski's rule of 5 were established to help researchers to develop more "drug-like" molecules.^[14] Thereby, the number of attritions related to poor pharmacokinetic and bioavailability was decreased to only 10% in 2000. However, it seems that solving these problems has shifted the temporal failure profiles to later stages of the development process (Phases II and III in clinical trials). Lack of efficacy and

safety (accounting for approximately 30% of failures each) were found to be the main contributors of attrition in Phase II.^[11,15]

The high failure rates underscore the need to increase the likelihood of success in drug development by elaborating more efficient research approaches. Shortening of the drug development programs will also impact positively the overall R&D costs. Consequently, drug repurposing/repositioning has recently gained more interest, as it allows to accelerate the R&D process and to reduce the related costs.

1.1. Drug Repurposing in Medicine

1.1.1. Principle and General Aspects

Despite an increase of the R&D spending since the beginning of the 2000s, the drug development output remained particularly low, which kept the pharmaceutical industry under significant pressure to reduce the high attrition rates. In the past decade, researchers investigated with an increased interest existing drugs as potential therapies for other diseases in order to increase their chances of success. This approach has been referred to as drug repositioning or drug repurposing. Although those two terms are closely related, it is necessary to stress their difference. Drug repurposing refers to cases where an existing drug, approved for one disease area, is found to have activity against another disease. Whereas drug repositioning characterizes the process in which a drug, active against a specific disease, is derivatized or used as a template for the synthesis of derivatives to treat another disease.^[16]

Three key players are involved in drug repurposing.^[17] Next to pharmaceutical companies, academia and research institutes are highly active in this field. More recently, companies specialized in repurposing technologies have emerged. In the early days, drug repurposing stemmed essentially from serendipity and observation of the clinical performances of tested molecules.^[17,18] Analysis of the relevant side effects followed by the identification of their related protein targets generated new therapeutic indications. The recent years have seen the expansion of mode of action-based research efforts with a focus on identifying known chemical entities with the potential for repositioning.^[17] Several *in silico* methods that use the extensive amount of available biologicals have been developed too.^[18,19] They provide an undeniable gain in time and costs, however, they heavily depend on the quantity and quality of the data sets and remain limited in predicting the new drug–target interactions.^[19]

In general, three categories of drugs are screened: generic drugs; failed (at a clinical stage) active substances; and patented drugs.^[17] The greatest advantage of drug repurposing/repositioning is that the molecular hits can be rapidly advanced into clinical examination. Indeed, these strategies use as starting point drugs or active substances that are already in an advanced stage of development. Hence, in most of the cases a plethora of information, such as the pharmacokinetic and safety profiles, are documented for the considered substances. This constitutes two considerable advantages over more classical discovery programs. First, it allows to reduce the risk of failure due to safety concern; second, the selected candidate is usually moved to clinical studies only 4 years after the beginning of the investigations (Figure 2). Regarding the screening approaches in drug repurposing, a range of 500 to 2000 compounds are usually screened, which is a much more manageable size of library than the usual screening libraries containing thousands of molecules.^[17] This allows a broader complexity of assay types during the screening process.

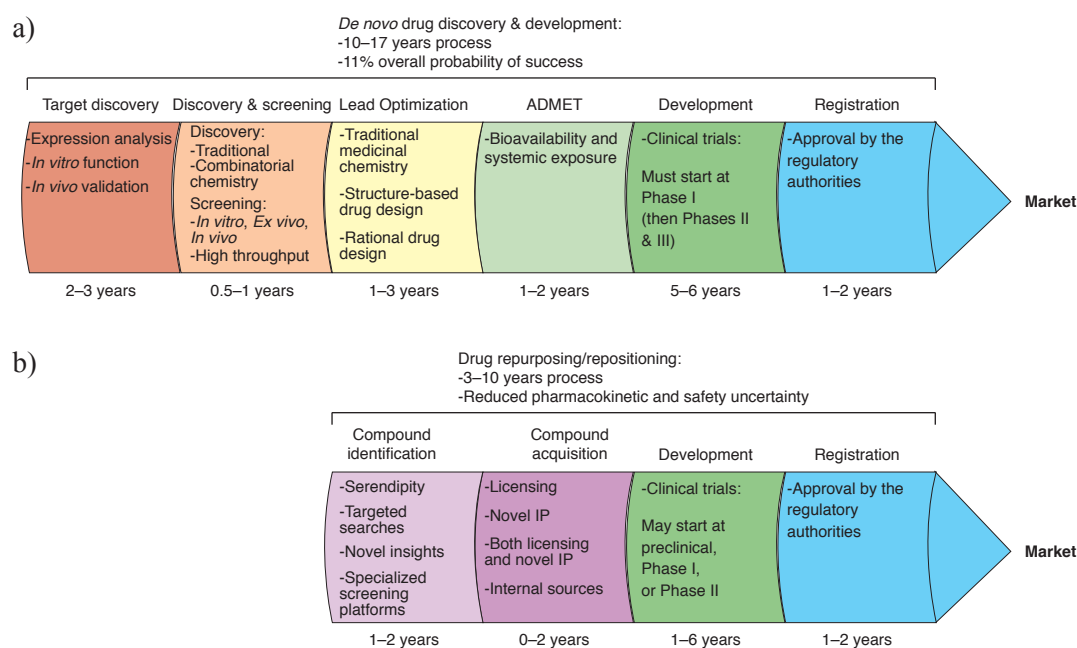


Figure 2. Simplified drug discovery processes: a) *via* the classical *de novo* pathway; b) *via* drug repurposing/repositioning. Adapted from T. T. Ashburn and K. B. Thor.^[20] IP = intellectual property.

The faster development time combined with the reduced risks of the repurposing/repositioning strategies offer a better risk-versus-reward trade-off.^[20] The reduced costs associated with it are particularly appealing, especially in the case of neglected tropical diseases (NTDs) where only limited resources and no financial incentives to develop new treatments are available.^[21] Finally, several governments are promoting drug repositioning,

such as the USA, where the National Centre for Advancing Translational Sciences has launched the Discovering New Therapeutic Uses for Existing Molecules Program.

1.1.2. Drug Repurposing in Action

The strategy of drug repurposing has been successful in a number of cases. According to a recent estimate, 25% of repurposed compounds reach the market from Phase II clinical trials and 65% from Phase III, whereas for NCEs these numbers drop significantly to 10% and 50%, respectively.^[22] Numerous examples of successful drug repurposing can be found in the literature and several reviews have compiled interesting case studies. A large number of existing drugs have been studied for an alternative use, such as anticancer.^[23] For instance, aspirin,^[23] as well as vitamin D,^[24] were investigated for their potential anticancer efficacy. Interestingly, some clinical and epidemiological research suggested that two of the most common diseases of aging, type 2 diabetes and Alzheimer disease, are linked. This relationship has been exploited to repurpose diabetes drugs to treat Alzheimer disease.^[25]

Two case studies illustrate particularly well the benefits of drug repurposing. A first example showcases the discovery of duloxetine (**5**, Duloxetine SUI®) (Figure 3), a compound developed in the late 1980s by Eli Lilly.^[20] This substance blocks the reuptake of serotonin and noradrenaline in the synaptic cleft and was intended to replace fluoxetine (Prozac®) as antidepressant. In the discovery program, the scientists of the Neuroscience Division of Eli Lilly anticipated that duloxetine (**5**) might also increase urethral sphincter tone and decrease detrusor activity *via* the same mode of action. The proof of concept was made in preclinical studies, in which it was shown that duloxetine potentiated the excitatory effects of serotonin and noradrenaline on sphincter motor neurons.^[26] Successful clinical trials motivated Eli Lilly to prescribe this treatment against stress urinary incontinence (SUI).^[27] Interestingly, it was initially thought that SUI resulted from anatomical defect and that it would not respond to any drug therapy. In 2003, duloxetine (**5**, Duloxetine SUI®) received an “approvable” letter by the FDA. In parallel, duloxetine is commercialized under the brand name Cymbalta® as antidepressant.

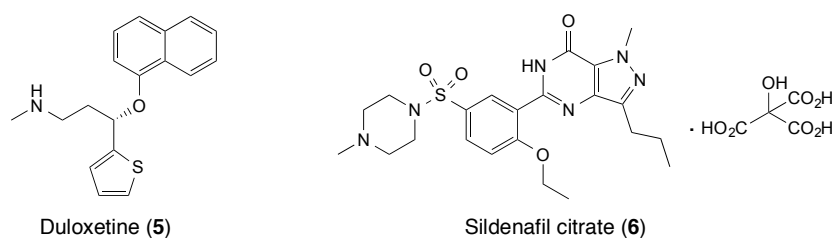


Figure 3. Molecular structures of duloxetine (**5**) and sildenafil citrate (**6**).

Secondly, the discovery of the active substance sildenafil (**6**, Viagra®) is arguably one of the most famous illustration of drug repurposing (Figure 3). Sildenafil (**6**) was originally developed in the 1980s by researchers at Pfizer to cure angina.^[20,28] This molecule inhibits selectively phosphodiesterase-5 (PDE5), and was intended to relax coronary blood arteries and to consequently allow greater coronary blood flow. Unfortunately, no cardiovascular effects were reported on healthy volunteers. However, a careful analysis of the clinical questionnaires revealed that a number of volunteers reported that they had unusually strong and persistent erections. Intrigued by this outcome, the scientists at Pfizer figured out that PDE5 is also a key enzyme in the biochemical pathway mediating erections. Subsequent large-scale clinical studies on 3700 impotent men confirmed the efficacy of sildenafil for this application. Since its launch in 1998, Viagra® (sildenafil citrate) became rapidly a blockbuster drug, as demonstrated by the annual sales of US \$1217 millions in 2016.^[29]

1.2. The Perpetual Threat of Malaria

Major progress has been made during the last decade to reduce the malaria burden. Indeed, the malaria landscape has changed considerably with a 22% decrease of the cases and a 50% decrease of the deaths attributed to malaria during the span of 2000–2015.^[30] These positive results are the fruit of increased funding and a scale-up of life-savings tools. Nevertheless, malaria continues to have a devastating global impact with 212 million estimated cases in 2015 and 429 000 deaths, mainly in sub-Saharan Africa (Figure 4).^[30]

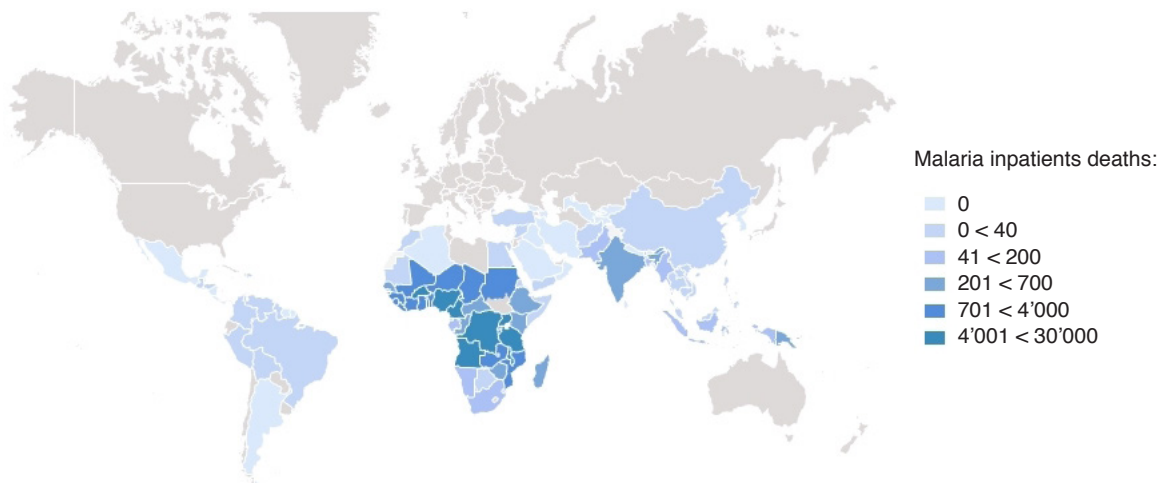


Figure 4. Global mortality caused by Malaria. The map was made using the online tool Global Malaria Mapper.

1.2.1. Key Facts of the Malaria Disease

Malaria is a mosquito-borne protozoal infection caused by the genus *Plasmodium* parasite transmitted to humans by female *Anophele* mosquitoes.^[16,31] The discovery of the malaria parasite dates back to 1880 by Alphonse Laveran, a French army surgeon, who was awarded the Nobel Prize in 1907 for his remarkable work. This disease is caused by five *Plasmodium* species that are single-celled eukaryotic organisms,^[32] namely: *P. falciparum* (Pf), *P. knowlesi* (Pk), *P. malariae* (Pm), *P. ovale* (Po), and *P. vivax* (Pv). The greatest threat, however, arises from *P. falciparum* and *P. vivax*. A large majority of the deaths (99%) are attributed to *P. falciparum*, which is the most prevalent malaria parasite in Africa (malaria tropica).^[30] *P. vivax* is the dominant malaria parasite outside Africa, and is known to form resting stages in the liver (hypnozoites). When reactivated, these dormant parasites cause a clinical relapse three weeks and up to several years after the initial event.^[33] Mixed-infection of *P. falciparum* and *P. vivax* are rare, perhaps because *P. falciparum* suppresses the development of *P. vivax*.^[33]

The life cycle of *Plasmodium* parasites is divided into a sexual part and an asexual part (Figure 5). While the sexual part happens in the mosquito, the asexual part takes place exclusively in the human body. During a blood meal of an infected mosquito, approximately 15–20 parasites in a form of sporozoites are transmitted sub-cutaneously to the human host (Figure 5). Next, the sporozoites infect liver cells, mature into schizonts, and merozoites are released in the bloodstream upon rupture of these latter. This initial phase, called the liver stage, spans for one to two weeks after which starts the so-called blood stage.

In the erythrocytic cycle, the merozoites invade red blood cells (RBC), spread into thin biconcave discs, and feed from small aliquots of haemoglobin, as well as take up other nutrients from the plasma (Figure 5). Merozoites enter into RBC through specific receptor–ligand interactions mediated by proteins on the surface of the parasite, which interact with receptors on the host erythrocyte.^[34] At the end of the ring stage, the rings grow into more rounded trophozoites stage. Most of the active feeding and growth occur during this period. Next, each parasite undergoes a series of nuclear divisions in the schizont, leading to the generation of about 16 nuclei, which migrate into merozoite buds. Finally, the RBC lyse and the newly formed merozoites are released.^[35] Afterwards, a new erythrocytic cycle starts as the majority of the fresh merozoites reinfect RBC. Overall, the cycle of invasion, intracellular growth, multiplication, and reinvasion lasts 48 hours. In parallel, few merozoites differentiate into male and female gametes (gametocytes), the sexual forms of the parasite, which concentrate in skin capillaries and are taken up by a mosquito during a second blood meal (Figure 5).

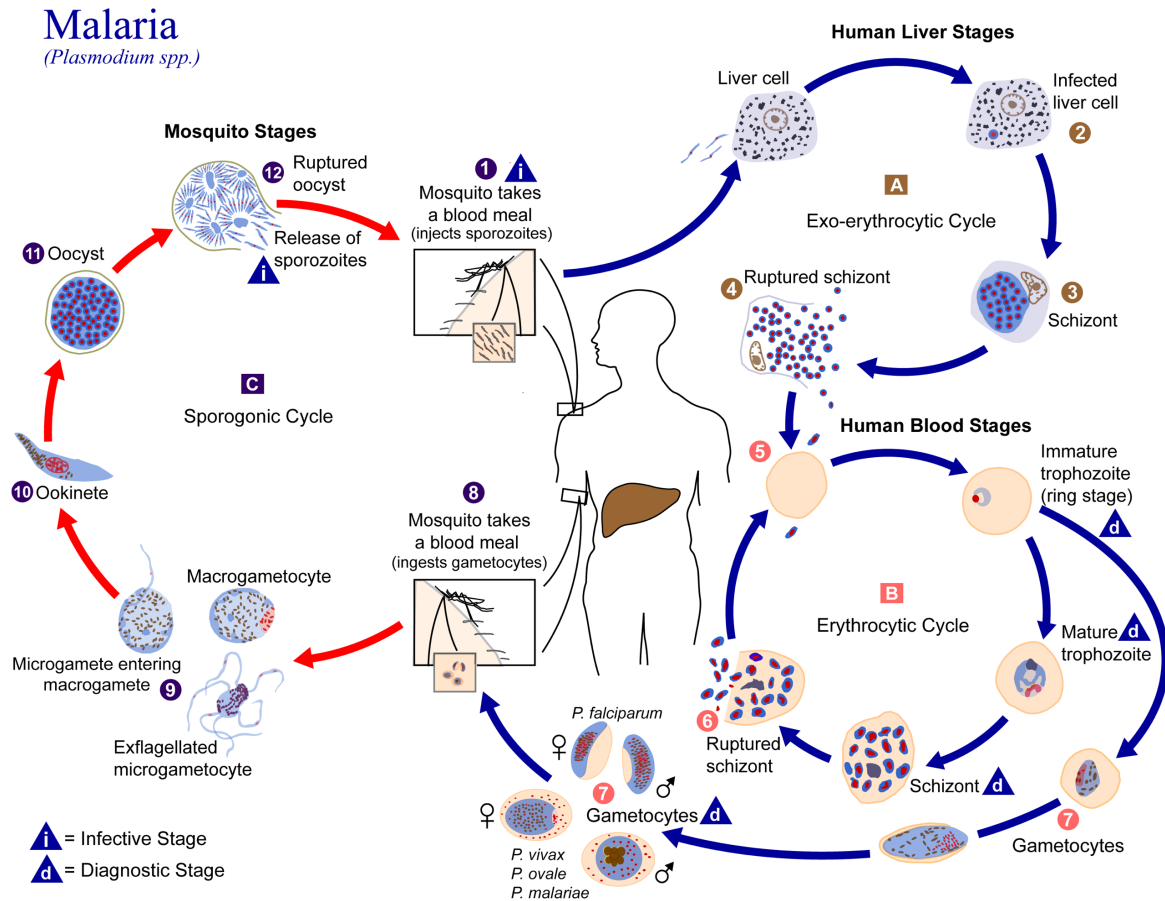


Figure 5. Life cycle of the *Plasmodium* parasite in mosquitos and in humans. The illustration was obtained free of any copyright restrictions from the Public Health Image Library.

Schizonts rupture and destruction of erythrocytes are primarily responsible for the clinical symptoms of malaria that often resemble to those of common viral infections. The onset of clinical symptoms generally occurs 7–10 days after the initial mosquito bite. Patients usually experience fever, chills, headaches, and diaphoresis.^[36] These symptoms can also be accompanied by dizziness, nausea, and dry cough. In case of severe malaria, complications such as cerebral malaria, pulmonary edema, acute renal failure, severe anemia, and/or bleeding may occur,^[37] along with metabolic complications, such as acidosis and hypoglycemia.^[36] These complications are generally due to microvascular obstruction, which results from the stiffening of infected red blood cells.^[32,37] Any of these complications are particularly aggressive and result in death within hours or days.

1.2.2. Towards a Global Elimination of Malaria

Despite the fact that malaria is known for centuries, its global elimination is far from realization. The WHO defines malaria elimination as the following: “Malaria elimination is the interruption of local transmission of specified malaria parasite species in a defined geographic area”. Several strategies are applied to stop the proliferation of the disease and cure patients.

Vector control is a crucial approach to prevent malaria and its transmission *via* mosquitoes. In this regard, insecticide-treated mosquito nets and indoor residual spraying of insecticides are the two approaches of choice.^[38] In 2015, 57% of the people at risk of malaria in sub-Saharan Africa were protected by either bed nets or indoor insecticides. Malaria vector control is based on thirteen indoor insecticides approved by the WHO, which are part of four chemical classes (Figure 6): pyrethroids (*e.g.* deltamethrin, **7**), organochlorine (*e.g.* dichlorodiphenyltrichloroethane (DDT, **8**)), carbamates (*e.g.* bendiocarb, **9**), and organophosphates (*e.g.* fenitrothion, **10**).^[39] These insecticides proceed *via* two mechanisms of action: carbamates and organophosphates inhibit acetylcholinesterase, while pyrethroids and DDT (**8**) disrupt the voltage-gated sodium channels.^[40] Treatment of mosquito nets relies solely on the pyrethroids class, as the chemical entities of this class, such as deltamethrin (**7**) (Figure 6a), are the only insecticides approved by the WHO.^[38] However, their efficacy is threatened by the emergence of worldwide resistance mainly based on target-site insensitivity and metabolic resistance mechanisms.^[38,41,42] Additionally, no new insecticide recommended by the WHO has been released in the past 30 years, which renders the situation even more critical.

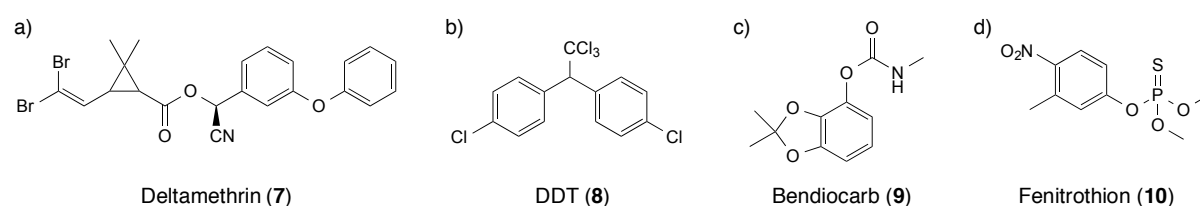


Figure 6. Examples of the WHO approved insecticides from four chemical classes: a) Pyrethroids, b) organochlorine, c) carbamates, and d) organophosphates.

Prophylactic therapies are also key measures to prevent infection, especially for the most vulnerable populations constituted by pregnant women, infants, and children under the age of five. By virtue of bed nets, indoor insecticides, and prophylaxis, the WHO estimated that 663 million cases were prevented in sub-Saharan African during the period of 2001–2015.

Bed nets alone account for 69% of the cases.^[38] These prevention campaigns also contributed to save an estimated US\$ 900 million in case management costs.

Regarding the available medicines to cure the disease, the recommended first line treatments have evolved over the decades. Historically, the first medications used were quinine (**11**) and its pseudo-enantiomer quinidine (**12**) (Figure 7), two active substances present in the powdered bark from the cinchona tree.^[43] Later, the microbiologist Paul Ehrlich noticed that methylene blue (**13**) (Figure 7), originally used as a dye, was particularly effective in staining malaria parasites. From this observation, he made the hypothesis that this dye might be selectively toxic for the parasite. Assisted by Guttman, he was able to cure two malaria patients with methylene blue (**13**) in 1891, which became the first synthetic drug ever used in therapy and set the basis for the further development of synthetic antimalarials.^[43]

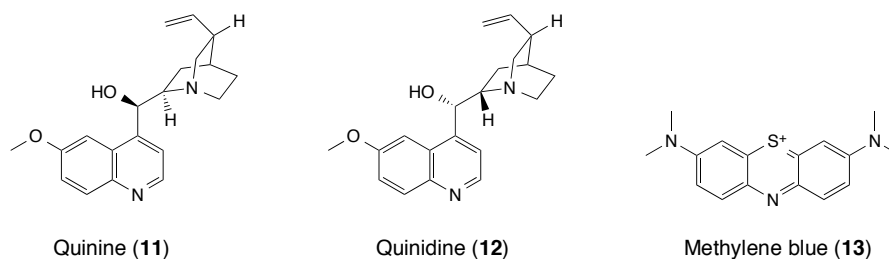


Figure 7. First active substances used to cure malaria.

These two historical discoveries paved the way towards new antimalarials, and as of today several families of active substances are available (Figure 8).^[44] First, the quinoline class takes its origin from **11** mentioned above (Figure 8a). Chloroquine (**14**) and amodiaquine (**15**) represent two important compounds of this class due to their high efficacy and very low cost. As chloroquine-resistant strains emerged, ligands such as mefloquine (**16**) were developed to counterattack resistance. Sadly, resistance also developed rapidly against this new drug. Additionally, the 8-aminoquinoline analogues, such as primaquine (**17**), have a particular importance, since radical cure of *P. vivax* malaria can only be achieved by this family of compounds.

The second key class of antimalarials is based on antifolate inhibitors, which are targeting the folate synthesis cycle (*vide infra*). Proguanil (**18**) is an early example of a ligand targeting this pathway by inhibiting the dihydrofolate reductase (DHFR) enzyme. It is a pro-drug that cyclizes *via* oxidative ring closure to its active metabolite cycloguanil (**19**) (Figure 8b).^[43] Proguanil (**18**) was successfully combined with chloroquine (**14**), however, this therapy was rivaled by another combination of antifolates.^[45] Indeed, the application of 2,4-diaminopyrimidine pyrimethamine (**20**) together with sulfadoxine (**21**) (marketed under the

brand name Fansidar® in the early 1960s) is the most compelling antifolate-based treatment against malaria (Figure 8b).^[46,47] Each ligand targets a specific enzyme of the folate pathway. Pyrimethamine (**20**) inhibits DHFR, while sulfadoxine (**21**) disrupts the activity of dihydropteroate synthase (DHPS). The synergetic effect exerted by the two drugs provides enhanced activity and a reduced propensity for resistance development. Nevertheless, resistant strains based on several point mutations in both the *dhfr* and *dhps* genes ultimately appeared, which strongly reduced the use of this combination.^[48]

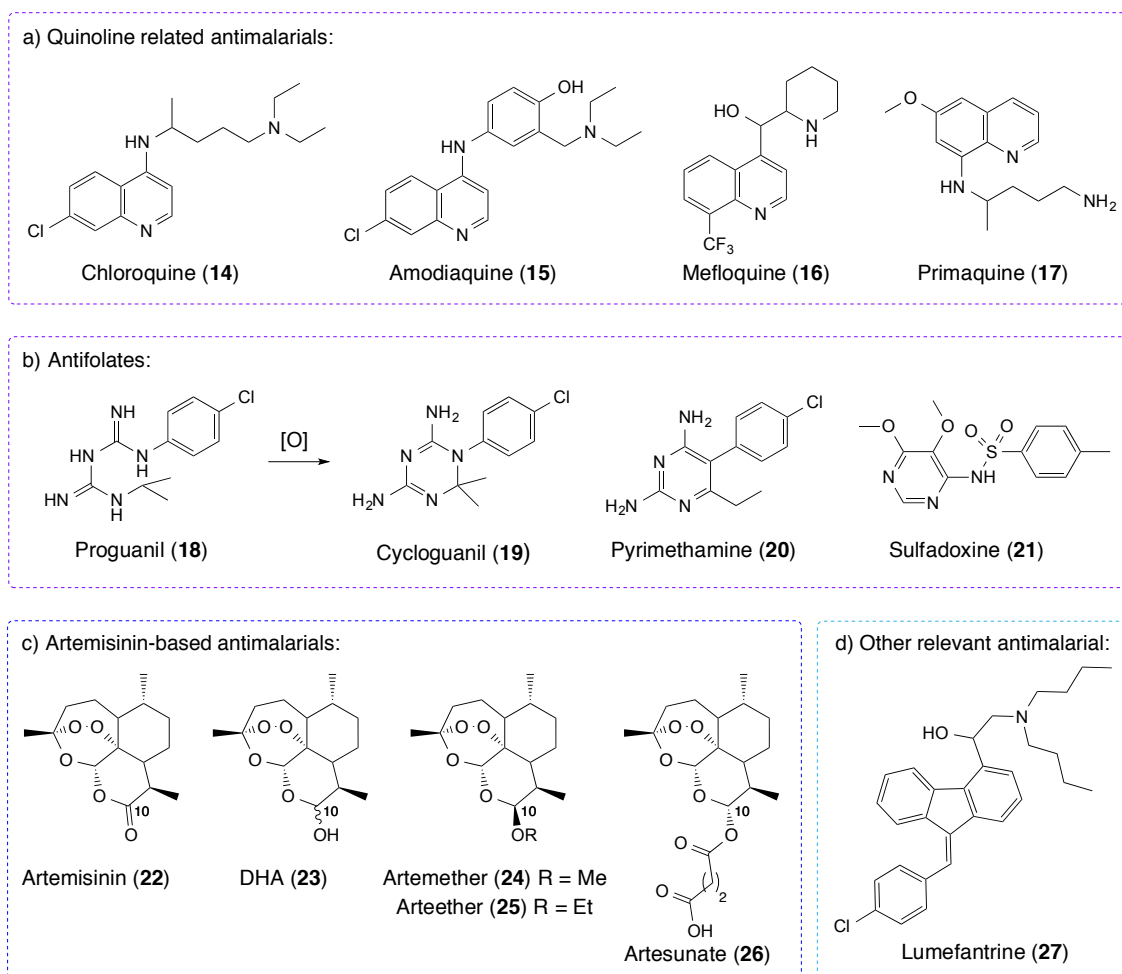


Figure 8. Most significant antimalarials on the market as of today. a) Quinoline related antimalarials. b) Antifolates. c) Artemisinin-based antimalarials. d) Lumefantrine (**27**).

The last substantial class of antimalarials relies on artemisinin (**22**) and its derivatives (Figure 8c).^[49] Artemisinin (**22**) is issued from the plant *Artemisia annua* L., which was used traditionally in the Chinese medicine to treat malaria patients. Its discovery in the 1970s, by Chinese researchers in the so-called Project 523, was arguably the main breakthrough in the battle against malaria in the past century.^[50] In light of these pioneering researches led by Dr.

Youyou Tu, she was awarded with the 2015 Nobel Prize in medicine.^[51] Artemisinin (**22**) is a sesquiterpene trioxane lactone whose endoperoxide bridge is the hallmark for antimalarial activity. Its activation is characterized by the generation of highly reactive carbon-centered radicals through endoperoxide cleavage.^[52] Two distinct theories are under debate establishing the origin of iron sources required for artemisinin (**22**) activation. It has been proposed that either free ferrous iron^[53] or haem^[54] is responsible for the activation. A recent report by Wang *et al.* laid out convincing arguments that haem is predominantly responsible for artemisinin activation.^[55] Additionally to mechanistic studies, several semisynthetic analogues of **22** were developed. Reduction of the carbonyl moiety led to dihydroartemisinin (DHA, **23**) that proved to be 4-fold more potent than **22** (Figure 8c).^[51] The alcohol functionality of **23** provided a handle for further derivatization, resulting in artemether (**24**), arteether (**25**), and artesunate (**26**) (Figure 8c), which are in fact rapidly metabolized to the main active substance DHA (**23**) in the human body.^[56] The bioactivity of artemisinin-based antimalarials reaches its peak at 1–2.6 h after administration.^[56] Hence, due to their short half-lives, 5–7 days of treatment are required for complete cure if solely these compounds are administered. To circumvent this drawback, they are mainly used together with other antimalarials in treatments known as artemisinin-based combination therapy (ACT). It is believed that the rapid clearance of the parasites by artemisinin derivatives reduces the likelihood of resistance development against the partner drug. The two major ACTs are the combinations artemether (**24**)/lumefantrine (**27**) (Figure 8d) and artesunate (**26**)/amodiaquine (**15**).^[57] To date, ACTs constitute the first-line treatment against malaria and are used in 80% of the clinical cases.^[30]

Artemisinin (**22**) and its derivatives are effective against all plasmodial stages that actively digest hemoglobin.^[49] However, their molecular target has not been clearly identified yet. Lately, Mbengue *et al.* provided compelling evidence that artemisinins effectively inhibit the *P. falciparum* phosphatidylinositol-3-kinase (*Pf*PI3K).^[58] *Pf*PI3K phosphorylates the phospholipid phosphatidylinositol (PI), resulting into the formation of phosphatidylinositol 3-phosphate (PI3P) (Figure 9). The latter is key to promote cell signaling and survival in malaria parasite. Accordingly, inhibition of *Pf*PI3K precludes the formation of PI3P, leading to a subsequent cell death. In the same year, Wang *et al.* shed light on other targets of this drug.^[55] One hundred and twenty four artemisinin covalent binding targets were identified by a chemical proteomics approach.^[55] To do so, an alkyne-tagged-clickable probe was incubated with live parasites, labelled with biotin, purified by streptavidin beads, and finally characterized by mass spectrometry. Through gene ontology analysis, the authors could show that the targets are involved in many essential biological processes of the parasite, such as the

metabolism of carboxylic acids, cellular biogenic amines and nucleosides, as well as ribonucleoside biosynthesis. The identification of numerous targets is not surprising given the promiscuous nature of the radicals. This pleiotropic mechanism of drug action also explains the high efficiency of artemisinins and the slow development of resistance against these active substances.

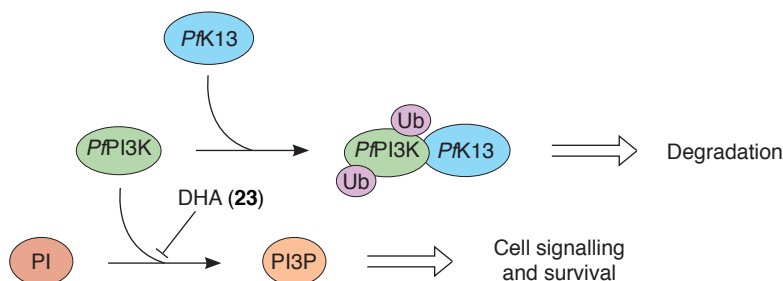


Figure 9. Function of *PfPI3K* and *PfK13* in the malaria parasite. Adapted from J. Burrows.^[59]

Nevertheless, a number of reports relate the development of resistance, especially in Southeast Asia.^[60–62] This is a major concern as resistance to artemisinin derivatives could jeopardize all eradication effort pursued so far. Determination of the resistance mechanism is highly challenging due to the multiple targets of artemisinins. Recent evidences indicated that the protein *P. falciparum* K13 (*PfK13*), which belongs to the kelch super-family of proteins, is a potential key player in the resistance mechanism^[58,59,63] and that K13-propeller mutations are at the origin of artemisinin resistance.^[64,65] This protein binds to *PfPI3K* and mediates the addition of ubiquitin groups (Ub), which leads to the formation of tagged *PfPI3K* for degradation (Figure 9). Mutations of *PfK13* prevent its binding to *PfPI3K*. By this mechanism, the levels of *PfPI3K* increase and subsequently helps parasites to overcome the effects of **23**.

1.2.3. Novel Treatments Currently Under Investigation

Despite the large panel of tools available to prevent and cure malaria discussed in Section 1.2.2, the global resistance to most insecticides and antimalarials is alarming. This phenomenon arises partly from the widespread misuse of medications and the extensive deployment of drugs that exert tremendous selection pressure on human malaria parasites to evolve mechanisms of resistance.^[66] Hence, the community is challenged to find new ways of eliminating the disease and new treatments are highly desirable in order to furnish alternative to ACTs. In this context, the term SERCaP (Single Exposure Radical Cure and Prophylaxis) has been coined to define the ultimate antimalarial medicine. Such medicine, by definition, should with a single dose

cure malaria patients, kill the hypnozoites in *P. vivax* or *P. ovale*, block transmission, and deliver post-treatment prophylaxis. Nonetheless, it is obvious that a single active substance can hardly meet these requirements, but rather a combination of several drugs can provide all needs required for the ideal medicine. A significant number of new active substances are currently investigated,^[33,67] among which the more promising are discussed in the following.

In analogy to artemisinin (**22**) and its analogues (**23–26**), inhibitors containing a pharmacophoric peroxide bond have been investigated.^[49] Artemisone (**28**) is closely related to this class of compounds (Figure 10). Its discovery was driven by the necessity to reduce the neurotoxicity associated with artemisinin derivatives.^[68] DHA (**23**) was found to be neurotoxic, therefore, a prerequisite was to block phase I metabolism to **23** and additionally reduce $\log P$. In collaboration with Bayer, researchers studied a series of 10-alkylaminoartemisins leading to the identification of **28**, which did not display any neurotoxicity.^[68] The choice of 10-alkylaminoartemisins was not aleatory since this class of compounds is known to be resistant to phase I and phase II metabolism. Gratifyingly, **28** is more active than artesunate (**26**) on resistant strains *in vitro* and *in vivo*, and has enhanced bioavailability. These remarkable results allowed to advance **28** into clinical trials.

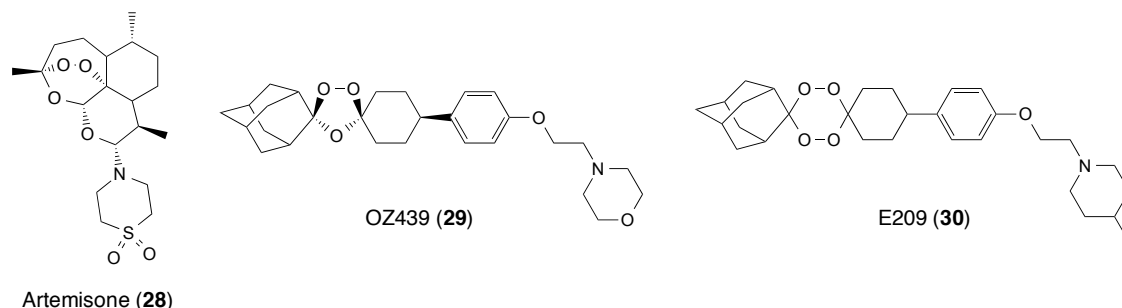


Figure 10. Molecular structures of artemisone (**28**), OZ439 (**29**), and E209 (**30**).

In contrast, the synthetic ozonide OZ439 (**29**) is based on a very different scaffold but retains the crucial endoperoxide bridge (Figure 10).^[69] This molecule contains a *cis*-phenyl substituent that confers a substantially improved stability towards Fe(II)-mediated degradation with respect to the first generation of ozonides, as the aforementioned moiety generates a greater steric interaction with the bound iron complex. Consequently, **29** has an *in vivo* half-life ($t_{1/2}$) of more than 20 h, which is substantially better than DHA (**23**) ($t_{1/2} \sim 0.5$ h). Similarly to artemisinins, OZ439 (**29**) has most certainly a pleiotropic mode of action, as 1,2,4-trioxolane-based antimalarials covalently target a broad range of proteins.^[70] Ligand **29** displayed complete *in vivo* efficacy in a *P. berghei* mouse model with a single oral dose of

20 mg/kg, a rapid onset of action against *P. berghei*, and a significant prophylactic activity. In 2015, **29** entered Phase IIb clinical trials. The latest generation of endoperoxide-based inhibitors is represented by E209 (**30**), which features a tetraoxane moiety (Figure 10).^[71] This core has the advantage to be achiral and to have a remarkable thermodynamic stability, which is believed to arise from the stereoelectronic “double anomeric effect” that stabilizes the six-membered ring system. The inhibitor **30** is unique by virtue of its potential to overcome the *PfK13* resistance faced by artemisinins (*vide supra*).

The spiroindolone NITD609 (**31**) (Figure 11) is a notable example of the fruitful collaboration between academia and the pharmaceutical industry.^[72] This inhibitor was developed by a network of academic researchers together with scientists from Novartis. The spiroazepineindole scaffold was identified in a screening of 12 000 compounds, and after an optimization program NITD609 (**31**) was selected as a clinical candidate. It meets all the SERCaP requirements, with activities in the single-digit nanomolar range against drug resistant strains and is active in all asexual blood stages. It is noteworthy that its target is particularly vulnerable in schizonts. All mice treated with a single dose of 100 mg/kg of **31** were cured in a *P. berghei* mouse model. Interestingly, application of a constant drug pressure for 4 months induced only a low level of resistance. NITD609 (**31**) successfully cleared parasitemia in adults in phase II clinical trial.^[73]

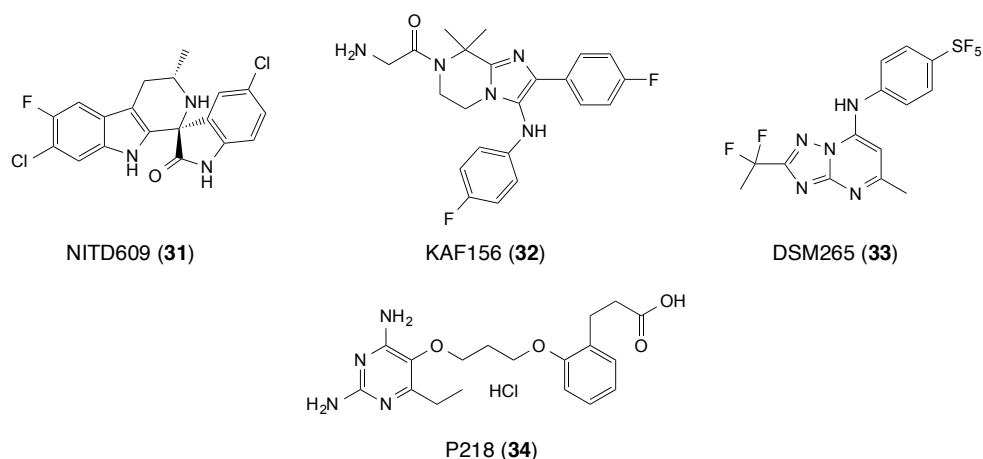


Figure 11. Molecular structures of NITD609 (**31**), KAF156 (**32**), DSM265 (**33**), and P218 (**34**).

Another collaboration between Novartis and public partners of the Swiss Tropical and Public Health Institute yielded KAF156 (**32**) (Figure 11). This active substance, based on a imidazolopiperazine core, was identified after a high throughput screening (HTS) of a library containing 2 million compounds and an extensive structure-activity relationship (SAR) study.^[74,75] KAF156 (**32**) proved to be effective *in vivo* at single doses, it also acts on all stages

of the life cycle of the parasite, blocks transmission of parasitemia, and has prophylactic activity.^[76] These encouraging results were translated into good efficacy in human, as **32** just finished phase II, open-label, two-part clinical study trials.^[77,78]

The exact targets of the advanced antimalarials presented above are so far unknown, which is problematic for anticipating and understanding resistance mechanisms. DSM265 (**33**) (Figure 11) does not display this limitation, as it was discovered through a target-based approach.^[79] Ligand **33** inhibits the enzyme dihydroorotate dehydrogenase (DHODH), which catalyzes the flavin mononucleotide (FMN)-dependent oxidation of dihydroorotate to orotic acid. This enzyme is a crucial component in the *de novo* pyrimidine biosynthetic pathway, and parasites rely on this pathway for the formation of pyrimidine nucleosides required for ribonucleic acid (RNA) and deoxyribonucleic acid (DNA) synthesis. DSM265 (**33**) was identified by a state-of-the-art structure-based design using X-ray crystallography. One of the key findings was the installation of the CF₂CH₃ moiety at the C2 position of the triazolopyrimidine ring to fill a lipophilic channel at the entry of the FMN binding site. Additionally, **33** showed activity at the liver and blood stages of the life cycle of the parasite and is currently in phase IIb clinical trials.^[80]

The last example focuses on P218 (**34**) (Figure 11), which is another rare example of target-based approach leading to the identification of a new antimalarial.^[81] This molecule inhibits DHFR, such as the marketed drugs proguanil (**18**) and pyrimethamine (**20**) (*vide supra*). P218 (**34**) stems from the optimization of a previously reported ligand based on a 2,4-diaminopyrimidine core. Yuthavong *et al.* reasoned that a potent inhibitor would be obtained by anchoring the 2,4-diaminopyrimidine core deeply into the active site of the protein and by establishing a strong charge-mediated interaction with Arg122 that is located at the exit of the pocket.^[81] Gratifyingly, this design resulted in ligand **34**, which overlaps almost perfectly with the natural substrate dihydrofolate (DHF, **35**) (Figure 12). This is a particularly important feature, as it renders **34** less susceptible to drug resistance. Indeed, possible mutations will also interfere with substrate binding, which would be deleterious to the enzyme activity. This new active substance is highly potent on wild type and on the quadruple mutant *P. falciparum* DHFR, while it shows only a poor affinity for the human DHFR homolog. Ligand **34** is currently in phase I clinical trials after successful *in vivo* efficacy determination and preclinical studies.

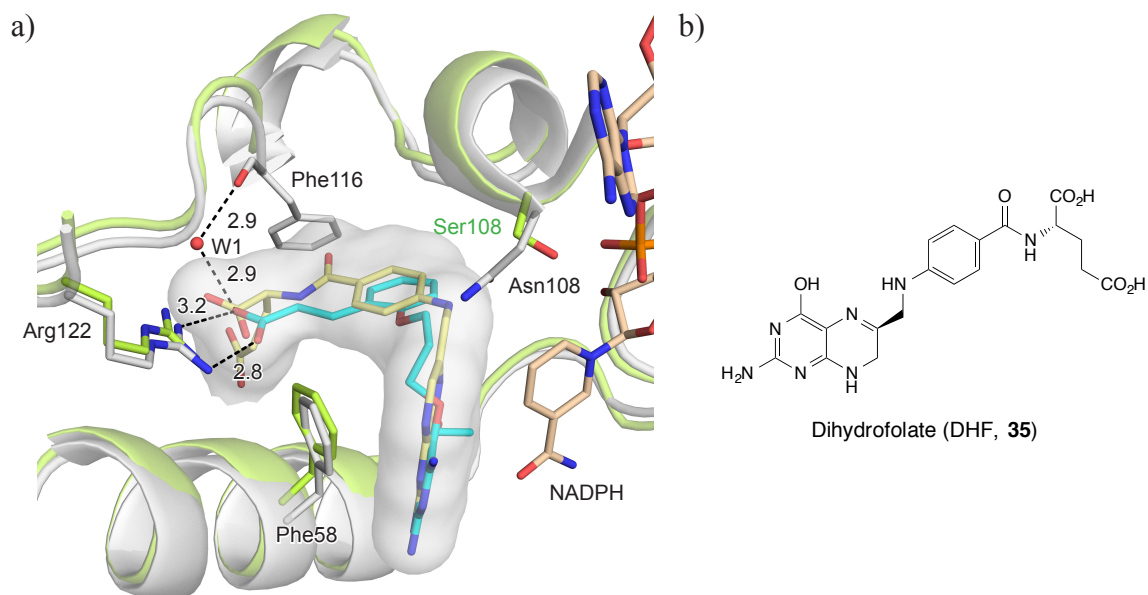


Figure 12. a) Overlap of P218 (**34**) (cyan; PDB code 4DP3, 2.4 Å) and DHF (**35**) (yellow; PDB code 4DPD, 2.5 Å) bound to quadruple mutant and wild type *PfDHFR*, respectively.^[81] The water molecule W1 is represented as a red sphere. The surface spans the volume of DHF. Distances are given in Å. Color code: $C_{\text{quad. mutant } PfDHFR}$ grey, $C_{\text{wild type } PfDHFR}$ green, C_{DHF} yellow, C_{P218} cyan, C_{NADPH} wheat, N blue, O red, P orange. All pictures of protein–ligand complexes included in this Thesis were made using the software Pymol.^[82] b) Molecular structure of DHF (**35**).

A major hope in malaria elimination resides in the development of a vaccine. Unfortunately, after several decades of endeavors no preventive vaccine could be brought to the market yet. Researchers face a tremendous challenge, as adults naturally acquire only partial immune protection against the disease.^[83] Indeed, the parasite has a sophisticated mechanism for avoiding the host immune system, which is due to the antigenic variation used by protozoan parasites.^[84] In other words, the infectious organisms are able to systematically alter their immunogenic epitopes exposed to the immune system of their host, hence, avoiding the antibody response. There is a large portfolio of vaccine candidates, however, the only vaccine in late stage phase III clinical trials is RTS,S/AS01 (RTS,S is a recombinant protein with parts of the *P. falciparum* circumsporozoite protein combined with the hepatitis B virus surface antigen, and AS01 is an adjuvant).^[32,85,86] The latter needs to be administered once a month for three months with an additional fourth dose 18 months later. Encouraging results were achieved lately, as RTS,S/AS01 prevented many cases of clinical and severe malaria in children and young infants.^[87] Consequently, three pilot runs will start in 2018 in Ghana, Kenya, and Malawi.

1.2.4. Drug Repurposing: An Opportunity for the Discovery of New Antimalarials?

The portfolio of novel antimalarials discussed in the previous section is encouraging, nonetheless, it is crucial to permanently find active substances with various mechanisms of action to prevent resistance development. In this respect, drug repurposing is an appealing approach to find new treatments against neglected diseases due to the reduced costs associated with it.^[88] This is particularly true for the leading pharmaceutical companies, which have no financial incentives to develop drugs for populations unable to afford them. Selected examples are described in the following.

Sulfur-based antibacterials were the first compounds repurposed as antimalarials.^[89] These substances target the *de novo* folate synthesis pathway, which exists in both bacteria and the malaria parasite. Researchers took advantage of this key feature and used sulfonamide drugs targeting DHPS and DHFR to treat malaria infections. This paved the way for the discovery of sulfadoxine (**21**) and its successful combination with pyrimethamine (**20**) (referred to as Fansidar) as detailed in Section 1.2.2. Co-trimoxazole® was developed in analogy to this combination.^[89] It is composed of the antibacterials sulfamethoxazole (**36**) (DHPS inhibitor) and trimethoprim (**37**) (DHFR inhibitor) (Figure 13). Unfortunately, its use was rapidly abandoned as Fansidar-resistant parasites were also resistant to co-trimoxazole.

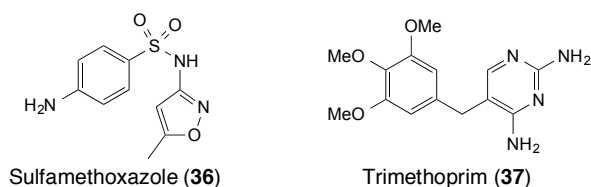


Figure 13. Molecular structures of sulfamethoxazole (**36**) and trimethoprim (**37**) initially used as antibacterials.

Interestingly, an anti-fungal *N*-myristoyltransferase (NMT) inhibitor was used as a lead in a target repurposing approach. Target repurposing has the advantage to offer the possibility of performing structure-based design and simplify mode-of-action studies. The Leatherbarrow group repurposed a benzofuran-based scaffold (**38**) initially used at Roche and subsequently developed a potent *Pf*NMT inhibitor (**39**) that showed excellent selectivity over human NMT1 (*Hs*NMT1) (Figure 14).^[90] The structural information gained by co-crystallization with *Pf*NMT allowed to identify a second generation of NMT inhibitors by a lead-hopping approach,^[91] which was further developed to the optimized lead **40** (Figure 14).^[92]

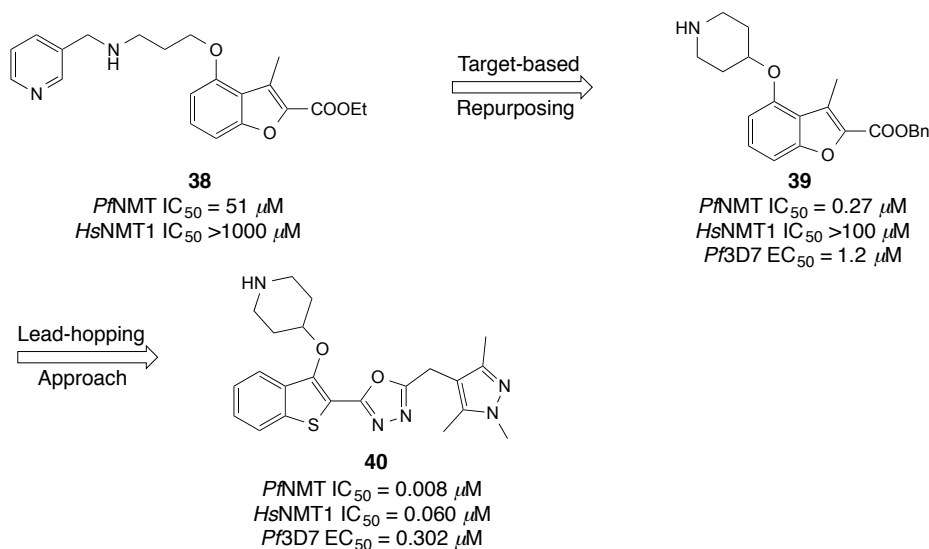


Figure 14. Repurposing of the benzofuran-based scaffold **38** and development of *Pf*NMT inhibitors **39** and **40**.

Cancer and malaria cells have in common to both be rapidly dividing cells, therefore, critical pathways controlling cell division can be targeted by the same molecules.^[93] This characteristic was exploited in the 1970s to block parasitemia growth *in vivo* with methotrexate (MTX, **41**), an anti-cancer drug that disrupts folate metabolism.^[89] At that time, major concerns regarding the safety profile of **41**, which was known to be toxic at high doses, prevented further investigations. This substance is an “old” drug synthesized during World War II, which is used, among other indications, to treat leukemia.^[94] It interrupts purine and pyrimidine synthesis by mainly inhibiting DHFR. This molecule is closely related to folic acid (**42**), which constitutes the scaffold of most co-factors involved in the folate pathway (Figure 15). MTX (**41**) recently regained interest, as clinical studies at low doses of 2.5 mg/day demonstrated that it can be effective and safe in malaria-infected patients.^[89]

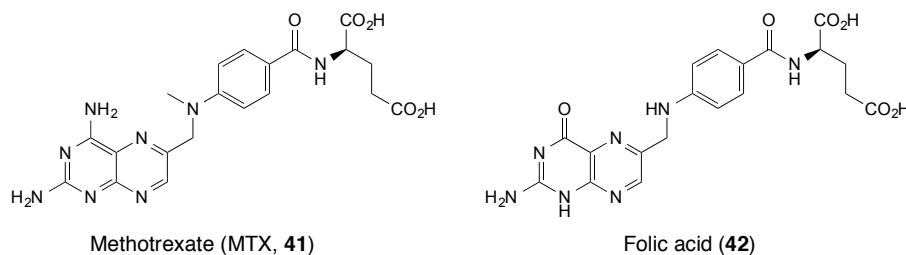


Figure 15. Molecular structures of methotrexate (MTX, **41**) and folic acid (**42**).

Agrochemicals constitute another source of lead structures for antimalarials. They usually display attractive profiles with good selectivity, broad toxicological characterization,

and low production costs. However, since few decades they are not systematically included in screening libraries for NTDs. Indeed, in the 1990s most life sciences companies split their agrochemical and pharmaceutical branches resulting in a less effective cooperation between these two research entities. Protozoan parasites and plants share some important features. *Plasmodium* parasites belong to the phylum Apicomplexa that possess a characteristic four membrane-bounded plastid known as apicoplast.^[95–97] The latter is similar to the chloroplast of plants and algae. The apicoplast is a non-photosynthetic organelle and is critical for the survival of the parasites, as it is involved in all stages of its life cycle. Several functions have been attributed to this plastid. At the liver stage, it is involved in the synthesis of fatty acids, iron-sulfur clusters, and heme. During the blood stage it produces isoprenoid precursors. The important role of the apicoplast makes it an attractive target to tackle malaria infection. Witschel *et al.* recently highlighted the potential of such agrochemical-based approaches by screening approximately 600 compounds from a BASF compound library.^[98] Remarkably, this yielded 24 substances with sub-micromolar *in vitro* activity against *P. falciparum*. For instance, fluacrypyrim (**43**) led to an impressive IC₅₀ (half maximal inhibitory constant) of 8.3 nM (Figure 16). Azoxystrobin (**44**), one of the most predominant agrochemicals on the market, inhibited *P. falciparum* with an IC₅₀ of 15 nM (Figure 16). Also, the insecticide hydramethylnon (**45**) demonstrated 53 nM activity (Figure 16). The last two molecules (**44** and **45**) showed significant *in vivo* efficacy in the *P. berghei* mouse model when administered orally at 4×100 mg/kg. Azoxystrobin (**44**) extended the survival time by 6–10.7 days compared to untreated control mice, whereas a survival time up to 16 days was achieved with **45**.

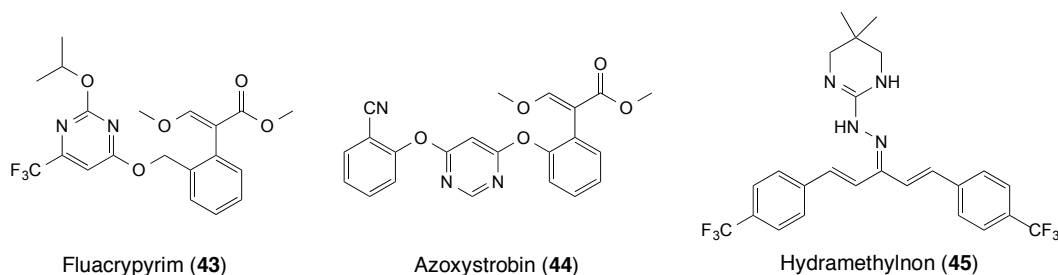


Figure 16. Molecular structures of the agrochemicals fluacrypyrim (**43**), azoxystrobin (**44**), and hydramethylnon (**45**) that showed high activity against *P. falciparum*.^[98]

As detailed in this section, it is not rare to find examples of drug repurposing approaches that generated new active substances against malaria. Additional examples were reported in recent reviews.^[16,21] Finally, it is worthwhile to mention that existing antimalarials can also be used for alternative indications. Corral *et al.* recently investigated herbicidal properties of

known antimalarials.^[99] Interestingly, the potent artemisinin derivatives exerted promising activity against a variety of cancer *in vitro*, *in vivo*, and in clinical trials.^[100]

1.3. The Folate Metabolism: A Privileged Antimalarial Target

During the intraerythrocytic growth phase, purine and pyrimidine metabolic pathways are heavily used by *Plasmodium* parasites to support their sizable needs in nucleotides for the synthesis of DNA and RNA.^[101,102] In this regard, the folate metabolism has been deeply investigated and numerous drugs target this pathway in order to restrain the proliferation of malaria parasites as discussed in the previous sections. Among these, sulfadoxine (**21**) and pyrimethamine (**20**) are probably the most prominent examples, both inhibitors target an enzyme of the folate metabolism: DHPS and DHFR, respectively. In the following, the components constituting this pathway are presented, and the enzyme serine hydroxymethyltransferase (SHMT) is introduced in more details.

1.3.1. General Overview

Parasites causing malaria depend on the *de novo* biosynthesis of nucleobases for their replication and survival. In this respect, *Plasmodium* species primarily rely on the folate metabolism for the *de novo* pyrimidine biosynthesis. The folate biosynthesis cycle is composed of three enzymes, namely DHFR, SHMT, and thymidylate synthase (TS) that interconvert essential folate co-factors (Figure 17a).^[45,103] Folates, such as tetrahydrofolate (H₄F, **46**), are part of the B9 family of vitamins and carry a critical one-carbon unit (Figure 17b). These substances, which are found in nature, comprise a pterin ring linked to a *para*-aminobenzoic acid (*p*ABA) moiety and at least one glutamate residue. In *Plasmodium*, folates are synthesized *de novo*. However, due to the high metabolic needs of rapidly proliferating cells, malaria parasites developed mechanisms to salvage folates from the hosts in order to complement the *de novo* folate pathway and meet their folates needs. *p*ABA is believed to be synthesized *via* the shikimate pathway, while pterin is issued from the transformation of guanosine-5'-triphosphate.^[103] The condensation of *p*ABA onto the pterin precursor is catalyzed by DHPS leading to dihydropteroate (DHP, **47**). The latter is then converted to DHF (**35**) by dihydrofolate synthase (DHFS) prior entering the folate synthesis cycle.

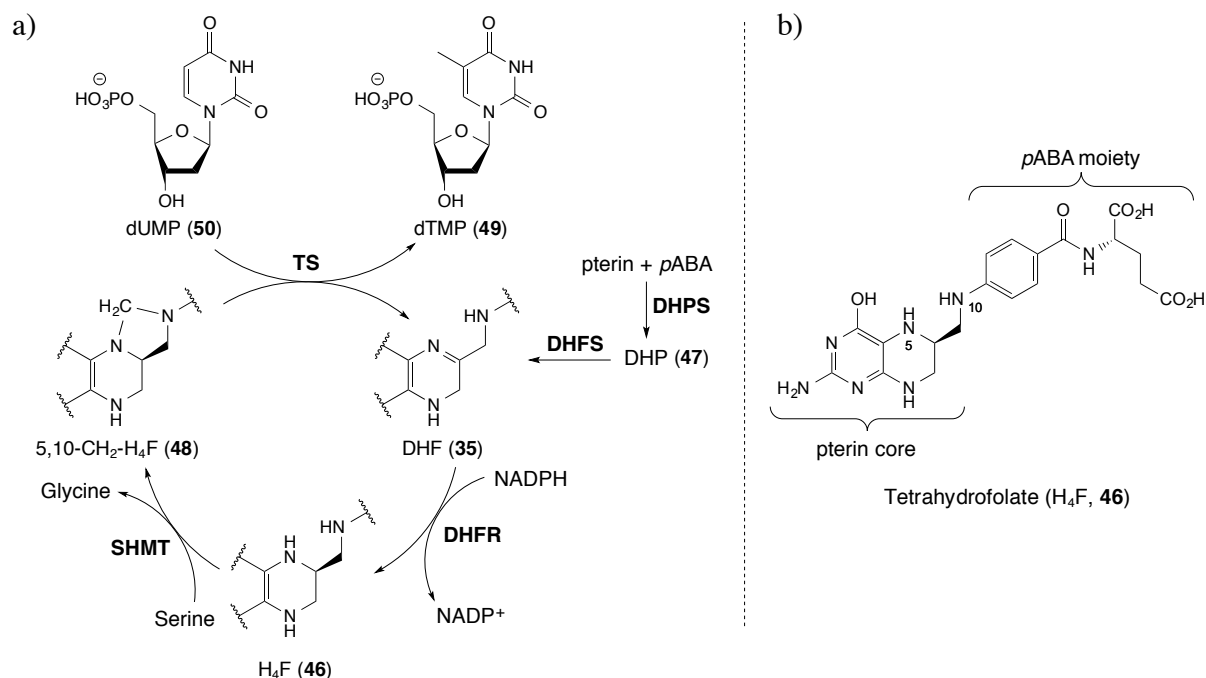


Figure 17. a) The folate synthesis cycle. b) Molecular structure of tetrahydrofolate (H₄F, 46).

Within the folate biosynthesis cycle, DHF (35) is reduced to H₄F (46) by DHFR with nicotinamide adenine dinucleotide phosphate (NADPH) as reducing agent. The one-carbon unit is transferred from serine to H₄F by SHMT upon which 5,10-methylenetetrahydrofolate (5,10-CH₂-H₄F, 48) is formed along with a release of glycine. Subsequently, the one-carbon unit is used by TS to form deoxythymidine monophosphate (dTMP, 49) by means of reductive methylation of deoxyuridine monophosphate (dUMP, 50). Through this process, DHF (35) is recovered and another catalytic cycle commences. The folate cycle includes alternative biosynthetic reactions that use 5,10-CH₂-H₄F (48) precursors for the synthesis of methionine (not discussed herein).^[103]

1.3.2. The Bifunctional Enzyme DHFR–TS

In *Plasmodia*, contrary to other organisms, DHFR and TS are both incorporated in a bifunctional enzyme that has a homodimeric structure. This arrangement may have evolved as a mechanism for the proximate generation of reduced folate in order to support the high needs of dTMP during cell proliferation. Knighton *et al.* were the first to provide compelling insights into the structure and the kinetic channeling of this bifunctional enzyme by analyzing an X-ray crystal structure of the DHFR–TS dimer from *Leishmania major*.^[104] Later, Yuvaniyama *et al.* completed this initial report by unveiling the very first co-crystal structure of wild type

*Pf*DHFR–TS with WR99210 (**51**), NADPH, and dUMP (**50**) (PDB code 1J3I, 2.3 Å) (Figure 18).^[105]

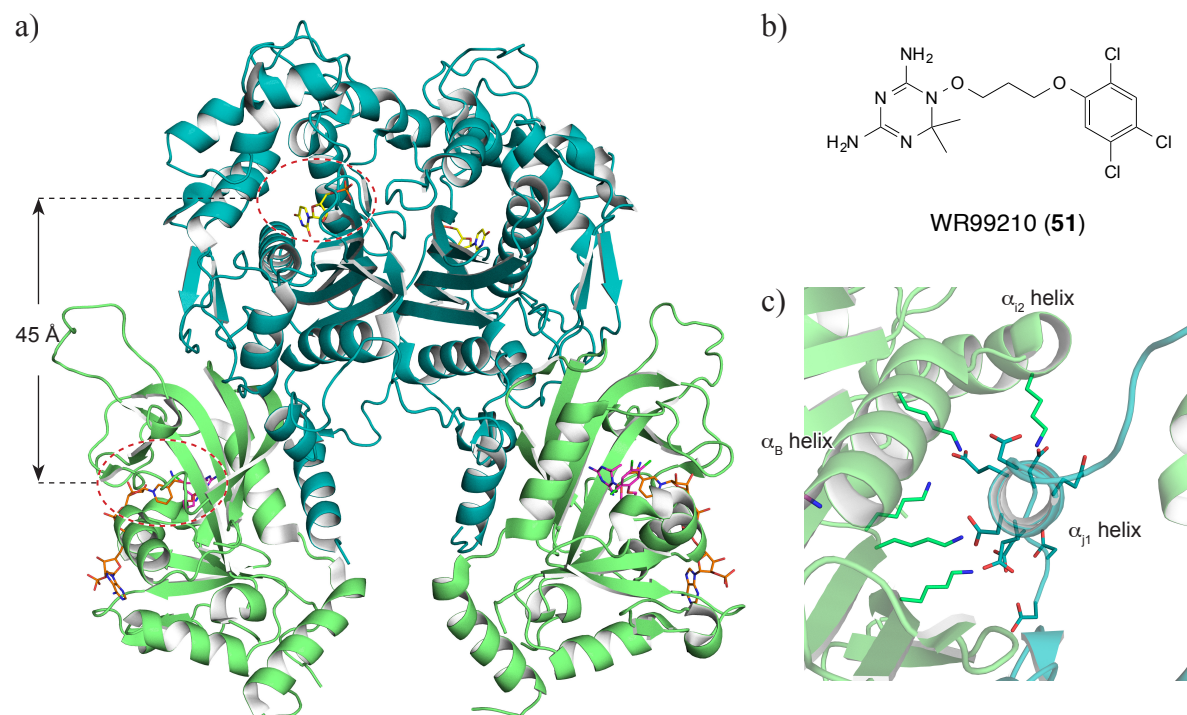


Figure 18. a) Co-crystal structure of wild type *Pf*DHFR–TS with WR99210 (**51**), NADPH, and dUMP (**50**) (PDB code 1J3I, 2.3 Å).^[105] The DHFR domains are represented as lime cartoons. The TS domains are represented as blue cartoons. b) Molecular structure of WR99210 (**51**). c) Close-up on the junction at the DHFR–TS interface and the long range electrostatic interactions.

On the one hand, the individual TS domains are involved in extensive intersubunit contacts with the two TS active sites being at a 32 Å distance to each other. On the other hand, the DHFR domains are not in contact with each other with their active sites being ~65 Å apart. DHFR and TS are primarily connected by long range electrostatic interactions that attract the negatively charged α_{j1} helix of a TS domains to the surface groove lined with positively charged amino acids from helices α_B and α_{i2} of a neighboring DHFR domain (Figure 18c). These interactions are reinforced by van der Waals and hydrogen-bonding contacts.

Given the proximity of the respective active sites of DHFR and TS, it is believed that DHF (**35**) (which is produced by TS) is immediately channeled to DHFR in order to regenerate H_4F . The mechanism of this process, defined as “substrate channeling”, is still unclear. The DHFR and TS active sites of a same subunit are separated by ~45 Å (Figure 18a), while those of different subunits are ~55 Å apart from each other. This makes it difficult to rationalize the substrate channeling solely in terms of proximity. A complementary explanation is based on

the electrostatic potential of the surface of the homodimer. The electrostatic potential is highly positive around the active sites and there are two positively charged grooves on the surface that link the folate binding sites (Figure 19). Thus, the substrate might be channeled electrostatically since folates are negatively charged molecules due to the one or more glutamate moieties.

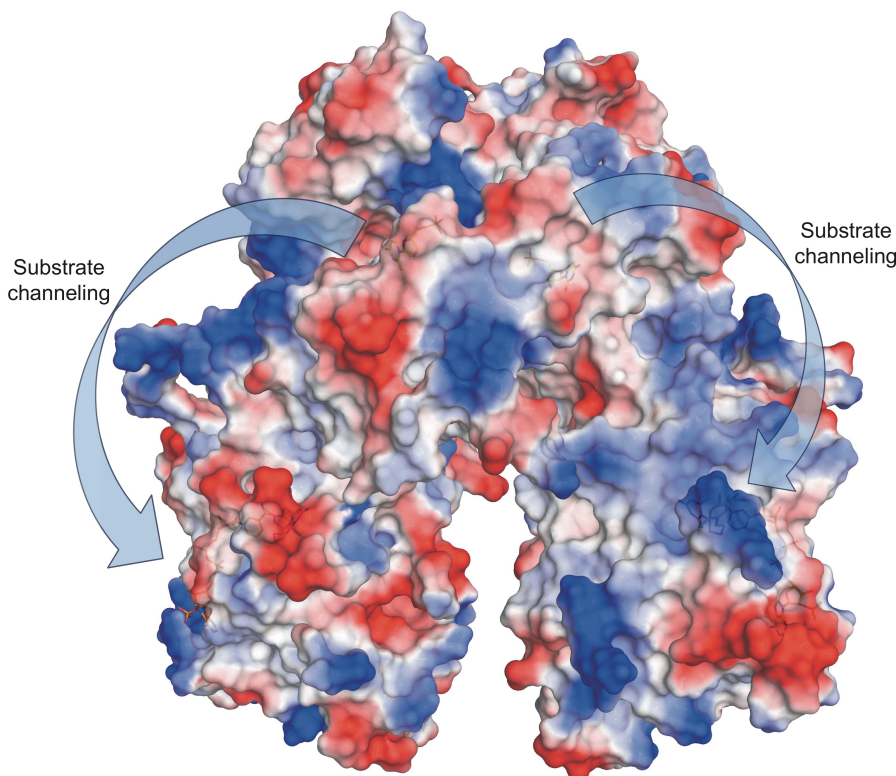


Figure 19. Surface electrostatic potential of wild type *PfDHFR*-TS (PDB code 1J3I, 2.3 Å).^[105] The surface is colored according to electrostatic potential in a gradient from negative (red) to positive (blue) values.

Inhibition of DHFR has been extensively studied and a number of potent active substances have been identified, such as pyrimethamine (**20**), P218 (**34**), and methotrexate (**41**) discussed in Sections 1.2.2, 1.2.3, and 1.2.4. Antimalarials targeting TS are rarer and the antitumor agent 5-fluorouracil remains to date the most prominent example of a TS inhibitor.

1.4. Serine Hydroxymethyltransferase (SHMT): An Underexploited Target

1.4.1. Function and Structure

Contrary to DHFR and TS, much less attention has been given to SHMT, the third enzyme of the folate cycle. SHMT is a pyridoxal 5'-phosphate (PLP, **52**)-dependent enzyme catalyzing

the reversible interconversion of serine and glycine with H₄F (**46**) that leads to the formation of the one-carbon carrier 5,10-CH₂-H₄F (**48**) (Figure 17a). This enzyme is ubiquitous in nature with more than 60 primary structures known.^[106] Evidences of significantly increased SHMT levels during cell-proliferation suggested that it has a pivotal role in supplying one-carbon units to sustain the considerable quantities of dTMP (**49**) needed.^[93,107] Indeed, malaria parasites have a high demand for DNA components, with an average increase in DNA content of approximately 14-fold per parasite per 48 h cycle. Its natural substrate, H₄F (**46**), has a K_m of $190 \pm 20 \mu\text{M}$ and $140 \pm 20 \mu\text{M}$ for *Pf*SHMT and *Pv*SHMT, respectively.^[108,109] The overall structures of *Pf*- and *Pv*SHMT are highly similar. In plasmodia, SHMT adopts a homodimeric structure with 2 active sites per homodimer (Figure 20a),^[110] which differs from the tetrameric structure found in other eukaryote organisms (Figure 20c).^[111]

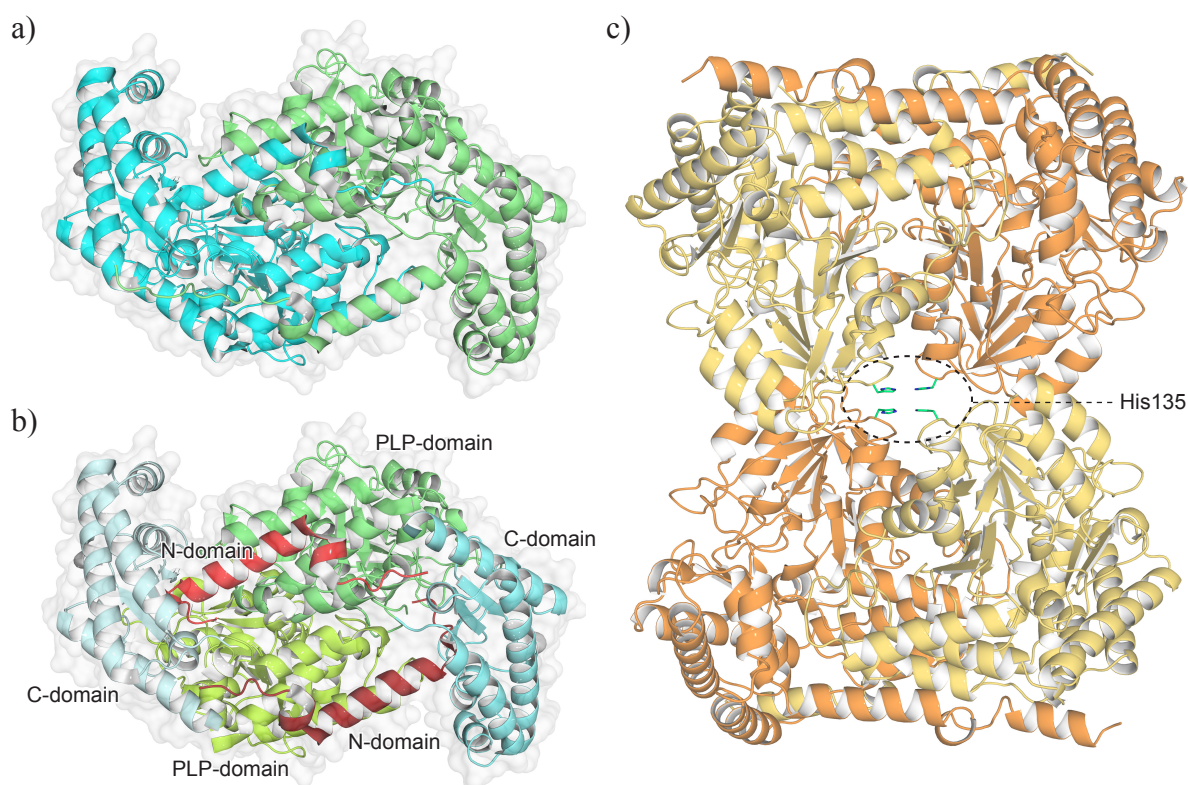


Figure 20. a) Homodimeric structure of *Pf*SHMT (PDB code 4O6Z, 3.0 Å).^[110] b) The three domains of *Pf*SHMT: N-domain (red and firebrick), PLP-domain (green and lemon), and C-domain (pale cyan and aquamarine). c) Tetrameric structure of *h*SHMT (PDB code 1BJ4, 2.7 Å) with the His135 residues highlighted.^[111]

Indeed, *Pf*- and *Pv*SHMT lack crucial histidine residues (His135) and insertions that are necessary to hold the tetrameric structure together. The mass of the dimer has been

calculated to be 81.5 kDa.^[112] Three domains are perceptible (Figure 20b): The N-terminal domain, the PLP/substrate binding domain, and the C-terminal domain.

Importantly, *Plasmodium* SHMTs possess a unique cysteine switch that regulates their activity (Figure 21).^[110] Chitnumsub *et al.* showed that the cysteines oxidation state modulates the *Pf*SHMT activity by altering the redox status of Cys125 and Cys364 with an external reducing agent (dithiothreitol).^[110] In the absence of dithiothreitol, only very low catalytic activity was measured. In other words, when a disulfide bridge is formed between Cys125 and Cys364, the enzyme becomes catalytically inactive. Upon reduction of this bond by gradual addition of dithiothreitol, the activity of SHMT can be restored to the level of *Pf*SHMT prepared in the presence of reducing agent. Similarly, the catalytic activity of *Pv*SHMT is also regulated by this redox switch.^[113]

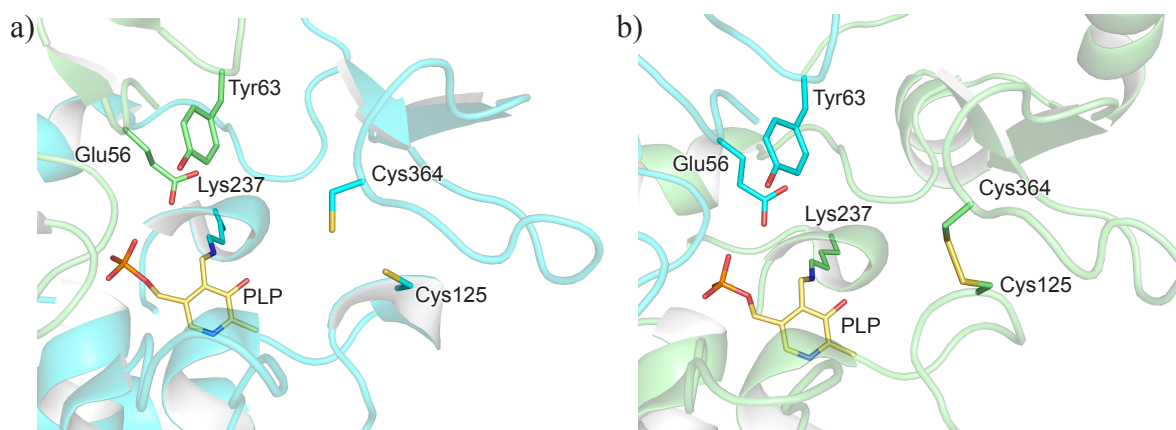


Figure 21. Cysteine bridge in the crystal structure of apo-*Pf*SHMT (PDB code 4O6Z, 3.0 Å)^[110]: a) Sulfhydryl cysteines (reduced state) and b) disulfide bond (oxidized state). Color code: C_{monomer 1} cyan, C_{monomer 2} green, C_{PLP} gold, N blue, O red, P orange, S yellow.

The disulfide bond formation presumably freezes the loops at the folate binding site essential for H₄F (**46**) binding. In addition, it has been suggested that the disulfide bond interferes with **46**, thus reducing its affinity towards the enzyme. In contrast, in human SHMT (*h*SHMT) two cysteine residues (Cys204 and Cys389) are present at similar positions but are too far apart to form the disulfide bond ($d(C^{\alpha}_{\text{Cys204}} - C^{\alpha}_{\text{Cys389}}) = 9.9 \text{ \AA}$). Thus, *h*SHMT retained its activity in the presence or absence of reducing agent.^[110]

Two other residues are critical for the catalytic activity, namely Glu56 and Lys237. Glu56 is believed to be protonated within the active site and to act as a proton donor in the retro-aldol cleavage of serine (see below).^[106,114] Lys237 binds covalently to PLP (**52**) to form an internal aldimine linkage (also referred to as Schiff base) that ensures, along with other non-covalent interactions, a tight binding of **52** (Figure 22a).^[113] Indeed, PLP (**52**) establishes

multiple hydrogen bonds (H-bonds) *via* its phosphate moiety to the side chain of Tyr54, Ser100, Ser102, and Arg243. The pyridoxal ring also participates in the binding by interacting with Thr183, Asp208, and His211, along with parallel π - π stacking with His129. Due to the presence of external serine, the covalent bond with Lys237 is cleaved and an external aldimine, between **52** and serine, is generated. The PLP-serine adduct (**53**) remains tightly bound to *Pv*SHMT and an additional salt-bridge with the nearby Arg371 is formed (Figure 22b).^[113]

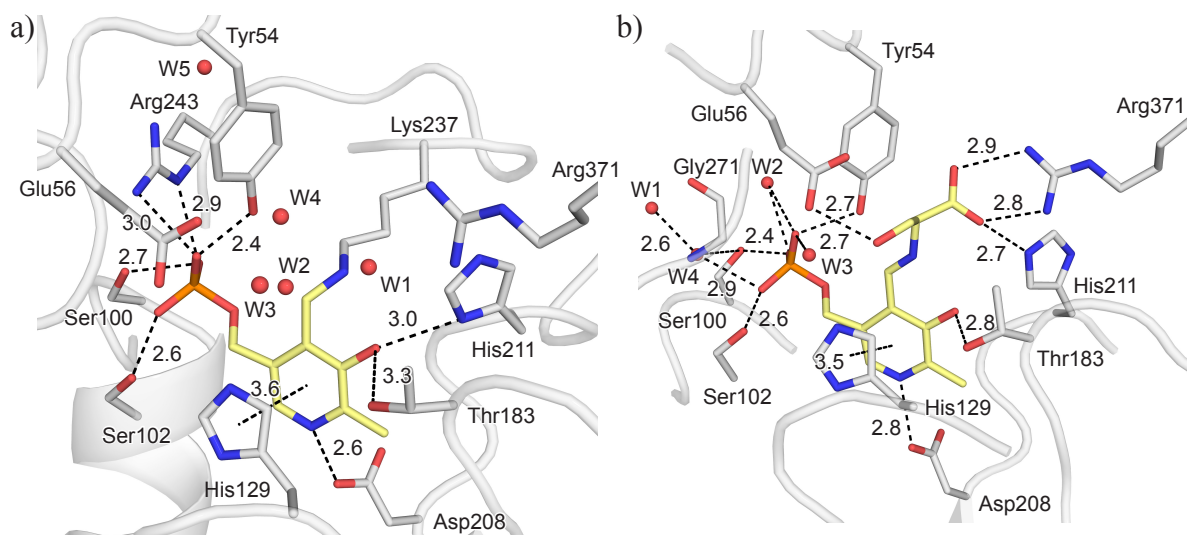


Figure 22. Comparison of the binding mode of PLP in two apo-*Pv*SHMT crystal structures.^[113] a) PLP-Lys237 Schiff base complex (PDB code 4PFF, 2.3 Å). b) PLP-L-serine complex (PDB code 4PFN, 2.5 Å). Water molecules are represented as red spheres. Distances are given in Å. Color code: C_{*Pv*SHMT} grey, C_{PLP} gold, N blue, O red, P orange.

The formation of **53** induces a notable movement of the pyridoxal ring by 18° compared to the structure in which it is covalently bound to Lys237 (Figure 23). The position of the majority of the residues of the protein in the vicinity of PLP remains unchanged between the two structures, with the exception of Arg243, which undergoes a significant repositioning. Indeed, the conformation of Arg243 changes considerably; in the PLP-Lys237 Schiff base complex it directly interacts with the phosphate moiety of PLP *via* Coulombic interactions (Figure 24a). In the PLP-L-serine complex, it rotates by almost 90° and establishes a water-mediated interaction with PLP together with direct H-bonding to the backbone carbonyls of Ser51 and Lys53 (Figure 24b).

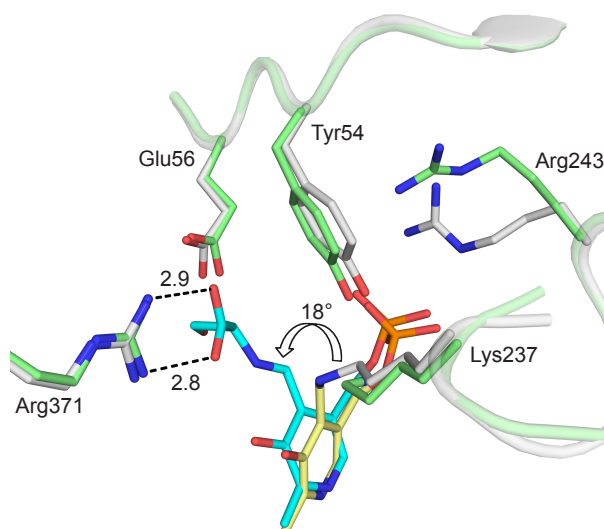


Figure 23. Overlay of two apo-*Pv*SHMT crystal structures (PDB codes 4PFF, 2.3 Å and 4PFN, 2.5 Å)^[113] showing the movement of the pyridoxal ring induced by the addition of L-serine. Distances are given in Å. Color code: C_{4PFF} grey, C_{4PFN} lime, C_{PLP-Lys237} gold, C_{PLP-L-serine} cyan, N blue, O red, P orange.

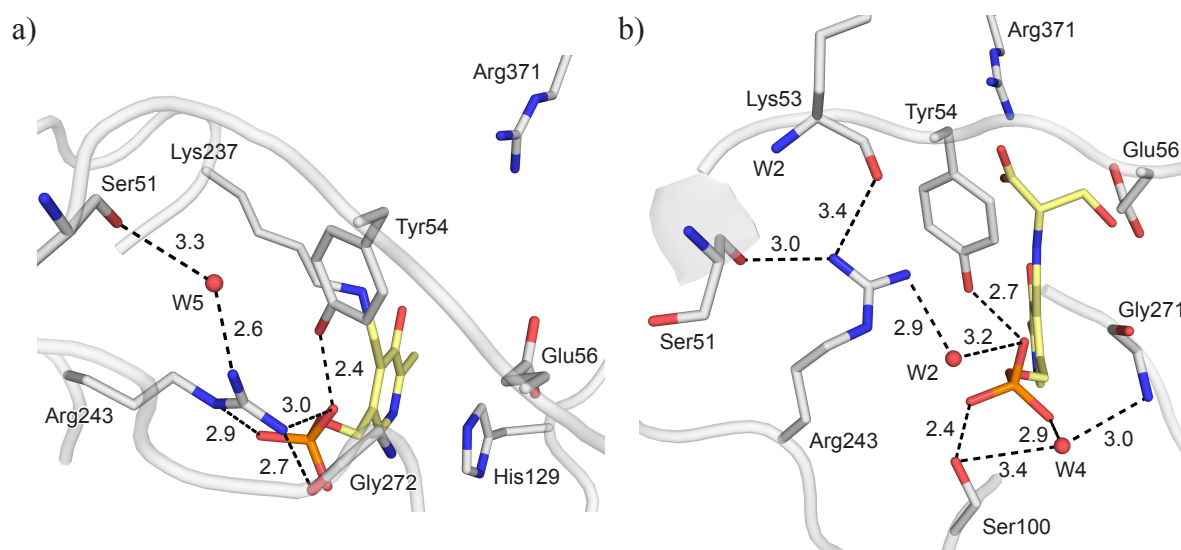


Figure 24. Comparison of the positioning of Arg243 in two apo-*Pv*SHMT crystal structures.^[113] a) PLP-Lys237 Schiff base complex (PDB code 4PFF, 2.3 Å). b) PLP-L-serine complex (PDB code 4PFN, 2.5 Å). Water molecules are represented as red spheres. Distances are given in Å. Color code: C_{*Pv*SHMT} grey, C_{PLP} gold, N blue, O red, P orange.

The natural substrate of SHMT binds in close proximity to the co-factor **52** in order to facilitate the transfer of the one-carbon unit as shown in the co-crystal structure of (6*R*)-5-formyltetrahydrofolate (5-CHO-H₄F, **54**) with *Pv*SHMT (Figure 25).^[113] The pterin ring of **54** is deeply buried in the pocket, while the *p*ABA moiety extends orthogonally from the core into

a channel lined by hydrophobic residues. An array of polar interactions with His129, the backbone carbonyl of Leu124, and the backbone carbonyl and NH of Leu130 ensure a tight binding of the pterin core with *Pv*SHMT (Figure 25b). In addition, Glu56 is at close distance to the hydroxyl group of serine and the formyl moiety of **54**. Therefore, it is likely that Glu56 is protonated in this complex, otherwise severe electrostatic repulsion would occur with the formyl moiety of **54**. Interestingly, a glycerol molecule was found to be present in the right-hand side of the binding site (Figure 25b).

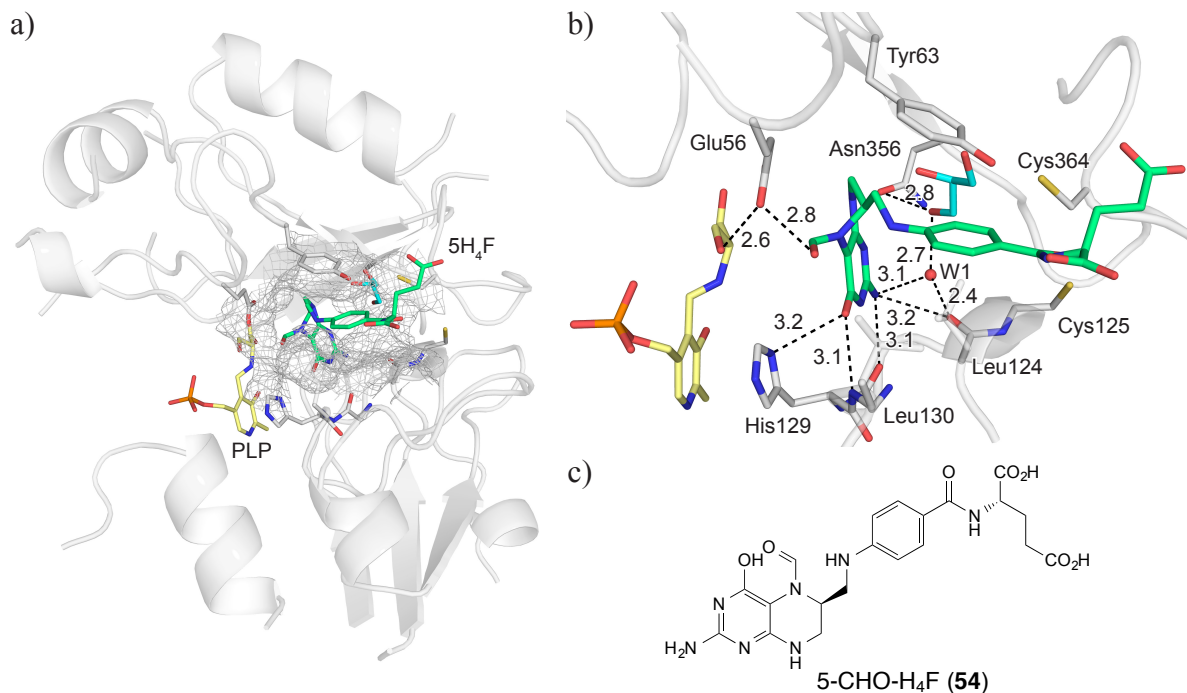
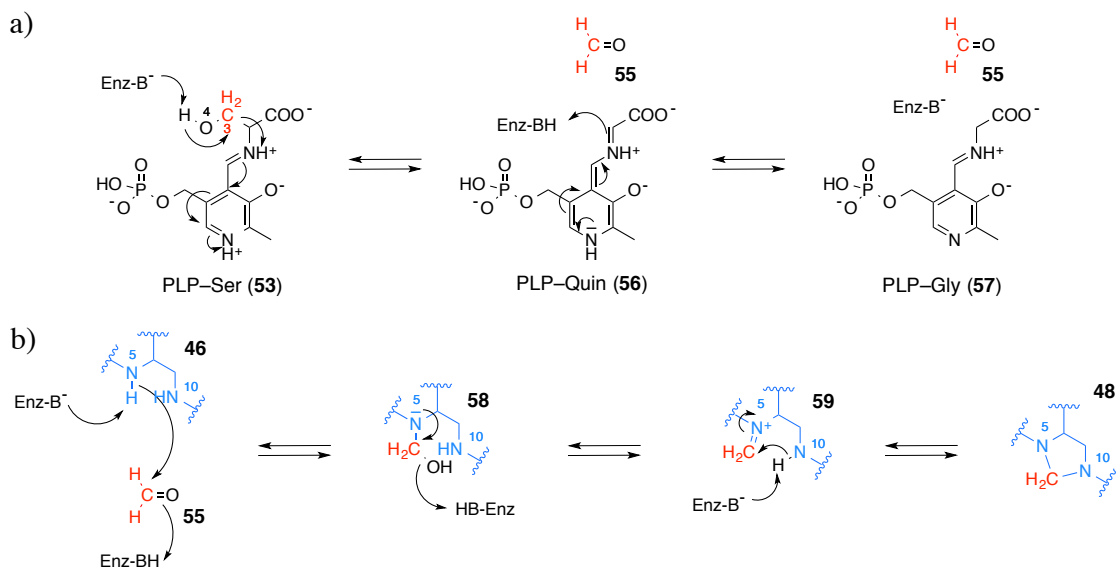


Figure 25. a) Occupancy of the binding pocket by **54** within *Pv*SHMT (PDB code 4OYT, 2.4 Å).^[113] The mesh spans the volume of the binding pocket. b) Polar interactions between **54** and the protein. c) Molecular structure of **54**. The water molecule (W1) is represented as a red sphere. Distances are given in Å. Color code: C_{PvSHMT} grey, C_{PLP} gold, $C_{5-CHO-H_4F}$ lime, $C_{glycerol}$ cyan, N blue, O red, P orange, S yellow.

1.4.2. Mechanism of the One-carbon Unit Transfer

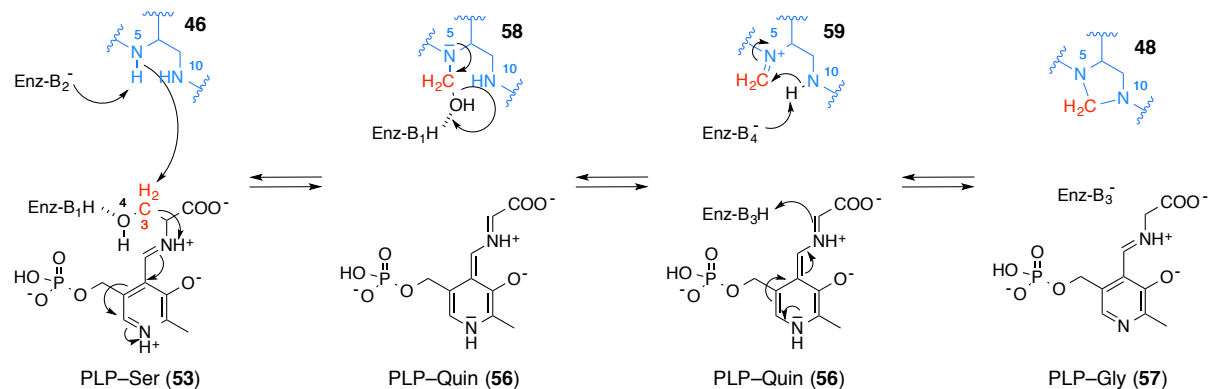
The structures and the critical amino acids of *Pv*- and *Pf*SHMT as well as the binding mode of H₄F (**46**) are well defined; conversely, the mechanism of the one-carbon unit transfer from serine to **46** is still unclear. Two possible mechanisms have been postulated: a retro-aldol cleavage of serine leading to the formation of free formaldehyde (**55**) or a direct nucleophilic attack of the N5 atom of **46** onto the C^β atom (C3) of serine.^[106,111,114] In the retro-aldol cleavage mechanism, it is proposed that a catalytic base abstracts a proton from the γ -hydroxyl

group (O4) of serine leading to the formation of **55** (Scheme 1a). Subsequently, protonation of the PLP-quinoid adduct **56** results in the PLP-glycine adduct **57**. Nucleophilic attack of the N5 atom of H₄F (**46**) onto **55** gives a carbinolamine intermediate **58** (Scheme 1b). Dehydration of the latter assisted by a catalytic acid leads to an iminium cation **59** that cyclizes to 5,10-CH₂-H₄F (**48**) upon intramolecular nucleophilic attack of the N10 atom.



Scheme 1. a) Retro-aldol cleavage leading to the formation of free formaldehyde (**55**). b) Nucleophilic attack of the N5 atom of H₄F (**46**) and formation of 5,10-CH₂-H₄F (**48**).

In the alternative mechanism, it is suggested that the carbinolamine intermediate **58** is formed after a direct attack of the N5 atom of **46** to the C^β atom (C3) of serine (Scheme 2). Structural investigations indicated that Glu56 is in close proximity to the OH moiety of **58**, hence, Glu56 is presumably the acid catalyst (Enz-B₁H) that promotes the dehydration to **59** (Scheme 2). The one-carbon carrier **48** is consequently formed *via* **59**.



Scheme 2. Direct nucleophilic attack of the N5 atom of **46** onto the C^β atom of the adduct **53**.

However, no solid ground to support the retro-aldol cleavage mechanism has been established to date; especially, no suitable base, which supports the proton abstraction in the first step of the mechanism (Scheme 1a), could be identified and the conformation of the bound serine was found to be unfavorable for the retro-aldol cleavage.^[114] Compelling structural evidences tend to support the direct nucleophilic attack by the N5 atom. The requirement for the nucleophilic displacement are the following: the serine C^β methylene group should be perpendicular to the pterin ring of **46** or align close to 180° with the p orbital of N5. By superimposing the structures of *Pv*SHMT–L-serine and *Pv*SHMT–D-serine–5-CHO-H₄F, Chitnumsub *et al.* nicely showed that the N5 atom is at close distance to the C^β of serine ($d(N\cdots C^\beta) = 3.0 \text{ \AA}$) and the C^α - C^β -N angle (171°) is optimal (Figure 26).^[110,113] Therefore, supporting the nucleophilic displacement mechanism between aldimine-bound L-serine and **46**.

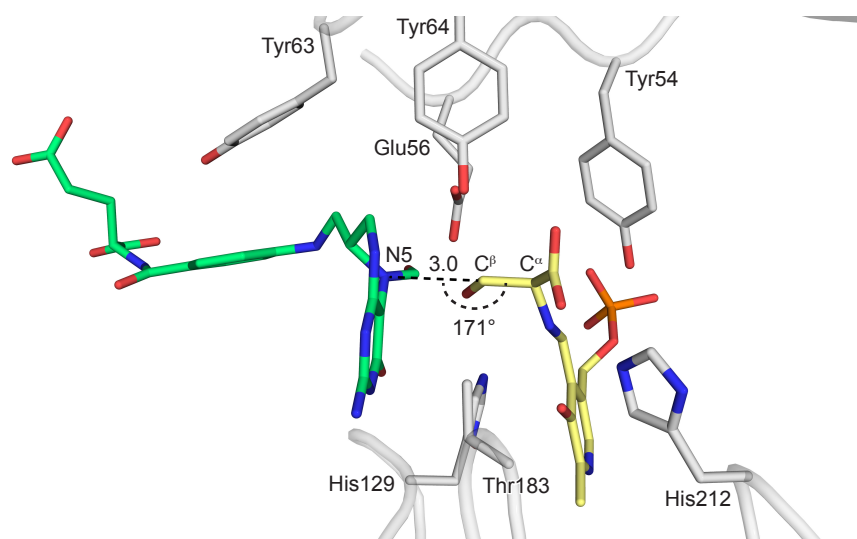


Figure 26. Superposition of the crystal structure of apo-*Pv*SHMT containing PLP–L-serine (PDB code 4PFN, 2.5 Å)^[113] with the 5-CHO-H₄F substrate (**54**) extracted from its co-crystal structure with *Pv*SHMT (PDB code 4OYT, 2.4 Å)^[113] showing the favorable conformation for the nucleophilic attack by N5. The distance is given in Å. Color code: C_{*Pv*SHMT} grey, C_{5-CHO-H₄F} lime, C_{PLP} gold, N blue, O red, P orange.

1.4.3. Known Inhibitors for SHMT

Only a limited number of active substances have been tested against *Pv*- and/or *Pf*SHMT (Figure 27).^[112,115] Small libraries of known antifolates have been screened, among which, one can find pyrimethamine (**20**), methotrexate (**41**), and the triazine-based ligand **51**, together with few related analogues **60–64**. However, these ligands only displayed IC₅₀ values in the high

micromolar range against *Pf*SHMT, which are close to the K_m value of H₄F (**46**) (K_m *Pf*SHMT = $190 \pm 20 \mu\text{M}$).^[108] Amino acids analogues, such as D-serine, D-threonine, and thiosemicarbazide, were investigated as well but no inhibition was observed either.^[115] Therefore, it appears that the use of known antifolates to disrupt the activity of *Plasmodium* SHMTs is likely to yield only poor inhibitors, making other sources of potentially active scaffolds highly desirable.

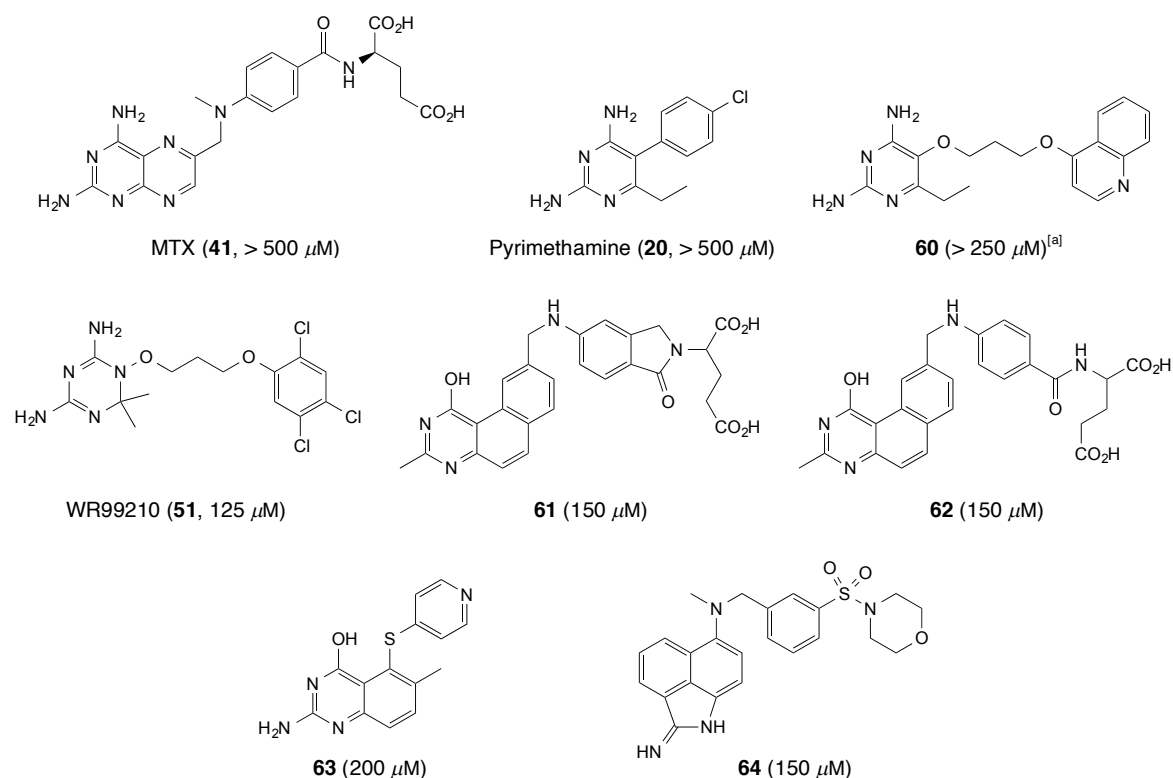


Figure 27. Molecular structures of selected antifolates **20,41,51,60–64** tested against *Pf*SHMT.^[112,115] The IC₅₀ values for each compound are given in parenthesis. [a] Tested against *Pv*SHMT.

1.5. Project Goal and Outline

This Thesis is dedicated to the rational design of inhibitors for the serine hydroxymethyltransferase enzyme and to the validation of the latter as novel and viable antimalarial target. The outline follows the structure-based optimization program that was pursued. Commencing with the identification of a promising hit, based on a pyrazolopyran core, inhibiting SHMT and the optimization of the pharmacokinetic properties of this class of compounds with a particular emphasis on the improvement of their metabolic stability, eventually leading to the discovery of an inhibitor with significant *in vivo* efficacy.

In the initial investigations, a comprehensive structure-activity relationship study was undertaken to identify positions on the pyrazolopyran core that tolerate changes without

affecting the activity considerably. The main soft spots of selected ligands were pinpointed by analysis of their metabolites in human liver microsomes. Following this approach, the key structural motifs providing good stability together with high affinity were determined with high confidence.

The conformational aspects in the design of SHMT inhibitors are highlighted with two series of ligands bearing either a biphenyl, an aryl sulfonamide, or an aryl sulfone moiety, which were designed to harvest hydrophobic contacts within the *para*-aminobenzoate channel of *Pv*SHMT. The extensive conformational study is underpinned by databases searches, theoretical calculations, and single molecule X-ray crystal structures. An unprecedented effect of the torsion angle of the biphenyl analogues, governed by their respective *ortho*-substituent, on the cell-based efficacy is detailed. The favored orientation of aryl sulfonamides/sulfones is introduced in Chapter 3. Several *Pv*SHMT–ligand complexes highlight the lipophilic character of the SO₂ group in these commonly used motifs.

Chapter 4 guides through the discovery of potent and metabolically stable pyrazolopyran-based ligands featuring a carboxylate moiety. It describes the first example of *in vivo* reduction of parasitemia by an enantiopure ligand disrupting the activity of SHMT. A total of eighteen co-crystal structures with *Pv*SHMT enabled a detailed analysis of the unique binding mode of this class of molecules and underscored the flexibility of the Cys364–loop at the entrance of the folate binding pocket.

Alternative scaffolds designed by computer-assisted modeling were investigated too. Gratifyingly, novel spirocyclic analogues displayed high affinity for *At*- and *Pf*SHMT together with promising efficacy in cell-based assays. Finally, the last Chapter describes a metabolomics study involving a potent pyrazolopyran-based inhibitor and its peculiar effects on purine biosynthesis in human cells, revealing SHMT as a potential target for chemotherapeutics.

2. Identification of Pyrazolopyran-based Inhibitors for SHMT and Their Primary Optimization

The following results were published in the *Journal of Medicinal Chemistry*.^[116,117] The HTS was initiated by Dr. Matthias C. Witschel (BASF-SE, Germany) and preliminary work on SHMT inhibitors was performed by Dr. Michael Seet, Dr. Sandro Tonazzi, and Anatol Schwab at ETH Zurich. The target-based assays on *Pf*SHMT and *At*SHMT were performed in the group of Dr. Pimchai Chaiyen by Dr. Ubolsree Leartsakulpanich and Aritsara Jaruwat (National Center for Genetic Engineering and Biotechnology, Thailand), and by Dr. Raphael Aponte (BASF-SE, Germany), respectively. The cell-based assays were performed in the group of Dr. Matthias Rottmann (Swiss Tropical and Public Health Institute, Basel) by Céline Freymond and Anja Schäfer. The co-crystal structures with *Pv*SHMT were solved by Dr. Penchit Chitnumsub and Wanwipa Ittarat (National Center for Genetic Engineering and Biotechnology, Thailand). The metabolic stability measurements were performed by Dr. Karen L. White (Monash University, Australia). Adrian Zwysig contributed with a Semester project to the synthesis of several ligands.

2. Identification of Pyrazolopyran-based Inhibitors for SHMT and Their Primary Optimization

Several active substances already take advantage of the unique vulnerability of malaria parasites to the inhibition of the folate pathway in order to stop the proliferation of the disease, however, none of these molecules target SHMT. Although, few ligands have been tested towards *Pf*SHMT (Section 1.4.3), their activity remained poor.

2.1. From Agrochemicals to Antimalarials: Identification of Pyrazolopyran-based Inhibitors for SHMT

As discussed in Section 1.2.4, screening of agrochemicals can yield highly potent antimalarial hits. Interestingly, a comparison of several eukaryotic genomes revealed that the genome of *P. falciparum* has the greater similarity with the genome of the flowering plant *Arabidopsis thaliana* (*At*) than any other non-apicomplexan taxa.^[118] The *A. thaliana* organism has been heavily studied yet, in fact, it was the first plant to have its genome sequenced.^[119] In parallel, SHMT has been found to be essential for plant survival, especially in plant specific photorespiration by restoring the Calvin cycle. This enzyme is involved in the photorespiratory decarboxylation of glycine to serine, CO₂, and NH₃.^[120] SHMT is also present in *A. thaliana* and researchers at BASF-SE developed herbicides targeting this enzyme. From an HTS of about 100 000 compounds, issued from the BASF compound collection, on the *At*SHMT enzyme overexpressed in *Escherichia coli* (*E. coli*), they could identify a cluster of novel pyrazolopyrans, such as (±)-**65**, with activities in the low micromolar range (Figure 28).^[121] An extensive optimization program enabled the identification of ligands, such as (±)-**66**, with single-digit nanomolar to sub-nanomolar activity against *At*SHMT (Figure 28).

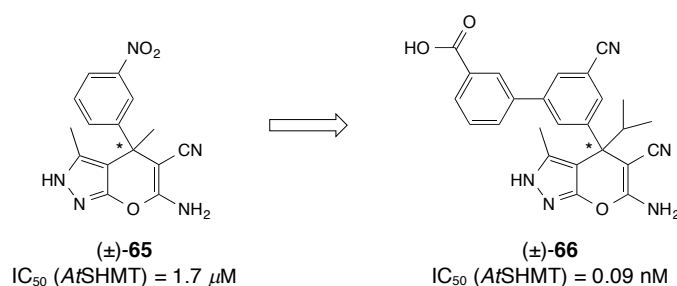


Figure 28. Hit (±)-**65** issued from the HTS and improved lead (±)-**66**.^[121]

Despite the promising *in vitro* activity of several candidates, only poor herbicidal efficacy could be measured in the greenhouse model due to the low uptake and limited

2. Identification of Pyrazolopyran-based Inhibitors for SHMT and Their Primary Optimization

translocation (phloem mobility) in the plant, together with a rapid metabolism. Phloem mobility could be improved by introduction of acidic components, however, it had a deleterious effect on greenhouse activity.^[122] After seven years of optimization, the program was stopped at BASF-SE due to the limited physicochemical and ADMET properties that prevented this class of compounds to become systemic herbicides.

Given the fact that *At*SHMT is highly similar to *Pf*- and *Pv*SHMT with 45% of sequence identity (Appendix, Section 9.1, Table 26 and Figures 107 and 108) and only very few amino acid residues differ within each active site (Figure 29), we envisioned that pyrazolopyran-based inhibitors of *At*SHMT could also effectively inhibit *Pf*SHMT. Hence, 338 inhibitors of plant SHMT were screened and, out of these, several ligands with EC₅₀ (half maximal effective concentration) values below 100 nM in *P. falciparum* cell-based assays could be identified. Remarkably, the methyl ester analogue (±)-**67** displayed an EC₅₀ of 3 nM against the *Pf*NF54 strain (Figure 30). A small number of new derivatives were synthesized and tested, for instance, a mono-glutamate fragment similar to the one found in H₄F (**46**) was grafted onto the pyrazolopyran-based inhibitor (4*R*/*S*,2''*S*)-**68** (Figure 30). Nevertheless, the activity of (±)-**67** could only be rivaled by the benzyl ester analogue (±)-**69**.

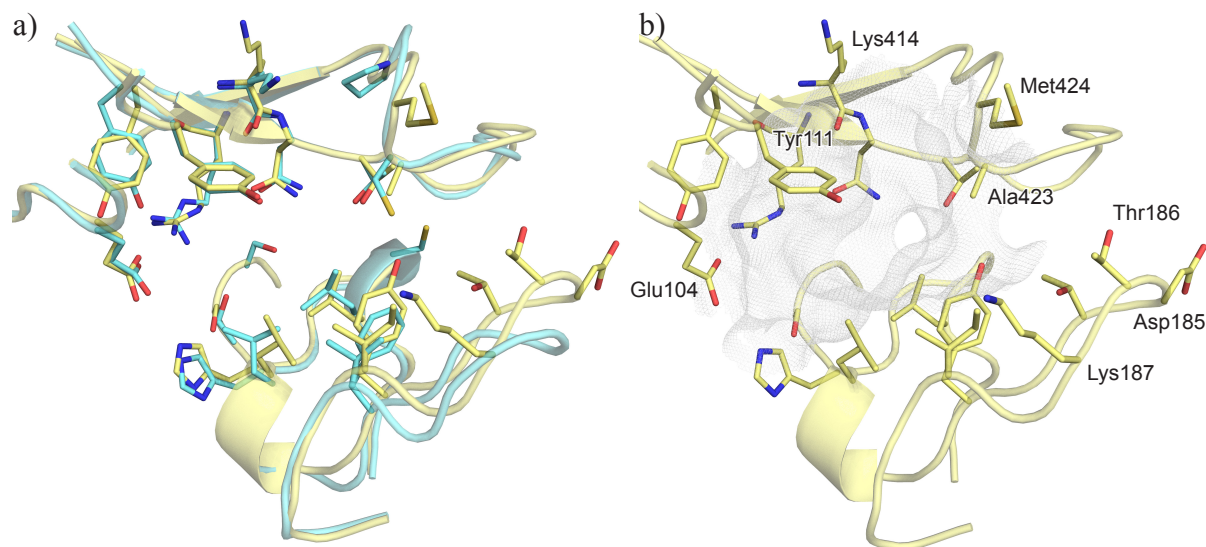


Figure 29. a) Overlay of the active site of *Pv*SHMT (PDB code 4TMR, 2.6 Å) and the active site of *At*SHMT (unpublished) showing the key residues. b) Active site of *At*SHMT and selected residues (unpublished). Proteins are represented as cartoon and selected residues as sticks. The grey mesh spans the surface of the active site. PLP is omitted for clarity. Color code: C_{*Pv*SHMT} cyan, C_{*At*SHMT} gold, N blue, O red, S yellow.

Ligand (±)-**67** inhibited *Pf*SHMT in the low nanomolar range (IC₅₀ = 370 nM) and effective chiral recognition at the active site of *Pf*SHMT was observed, as (+)-**67** was

considerably more active in both target- and cell-based assays ($IC_{50} = 60$ nM and $EC_{50} = 2$ nM, respectively) than (-)-**67** ($IC_{50} = 5420$ nM and $EC_{50} = 49$ nM, respectively).

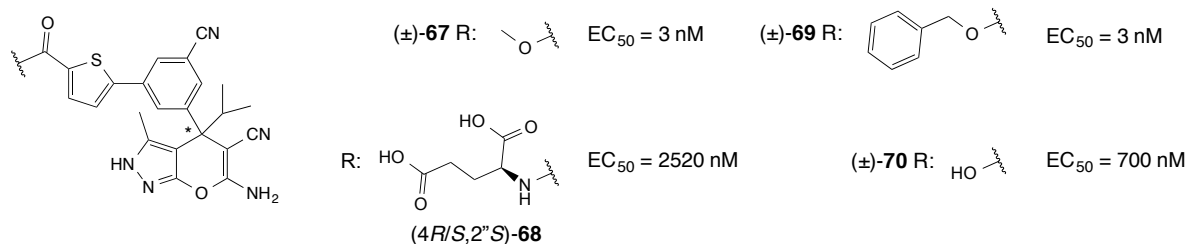


Figure 30. Molecular structures and EC_{50} values against *PfNF54* of hit (±)-**67**, mono-glutamate analogue (4*R*/*S*,2''*S*)-**68**, benzyl ester (±)-**69**, and carboxylic acid (±)-**70**.

Subsequent to the remarkable cell-based potency of (±)-**67** and (±)-**69**, their efficacy in a *P. berghei* (*Pb*) mouse model was studied, however, no significant activity could be measured for none of the two ligands. Pharmacokinetic studies with (±)-**69** were undertaken. After oral and intraperitoneal administration of (±)-**69** at 10 and 100 mg/kg, respectively, plasma levels were below the limit of detection at all tested time points (1, 4, and 24 h after treatment). Analysis of the plasma samples revealed that the ester group was cleaved to its corresponding acid (Appendix, Section 9.2, Table 28). Therefore, it is likely that the main metabolite corresponds to the poorly active carboxylic acid (±)-**70** (Figure 30), thus, possibly explaining the lack of *in vivo* activity. Additionally, the metabolic stability of (±)-**69** in human liver microsomes was assessed, resulting in a poor $t_{1/2}$ of 13 min. Taken together, these results clearly indicated that replacing the labile ester moiety for a more stable functional group, while keeping high potency, was imperative in order to achieve significant *in vivo* efficacy. Accordingly, the following criteria were set for a compound susceptible to be tested in a mouse model: $EC_{50} < 100$ nM, $t_{1/2} > 2$ h, and no cytotoxicity.

2.2. Co-crystal Structure of (+)-**67** with *Pv*SHMT and Ligand Design

A co-crystal structure of (+)-**67** with *Pv*SHMT could be solved at 2.6 Å resolution, revealing a tight binding of the ligand within the folate binding site (Figure 31). Importantly, in this binary complex, as well as in all other co-crystal structures reported in the following, both active sites were populated with a ligand (Figure 31a). From this co-crystal structure, it can be derived that (+)-**67** is (*S*)-configured at the stereogenic center. The pyrazolopyran core is deeply buried into the pterin binding pocket (Figure 31b). An array of polar interactions anchor the core into the active site. The N(2) atom of the pyrazole ring is protonated (the preferred tautomer of the

pyrazolopyran core is discussed in detail in Section 3.3) and forms a short ionic H-bond with the side chain of Glu56 (Figure 31b). While the vinylogous cyanamide interacts with Leu124, Gly128, and Ser184 through its exocyclic amino group, and the cyano moiety is in close proximity to Asn356 and Thr357. The biaryl scaffold departing from the stereogenic center extends into the channel normally occupied by the *p*ABA moiety of H₄F (**46**). The nitrile on the phenyl ring fills nicely the small lateral pocket lined by Pro367, and the S-atom of the thienyl ring establishes a S···S interaction^[123,124] with Cys364, which is in its reduced state (Figure 31b). The additional hydrophobic contacts are discussed in more details with the co-crystal structures of biologically optimized ligands in Chapter 4, Section 4.3.

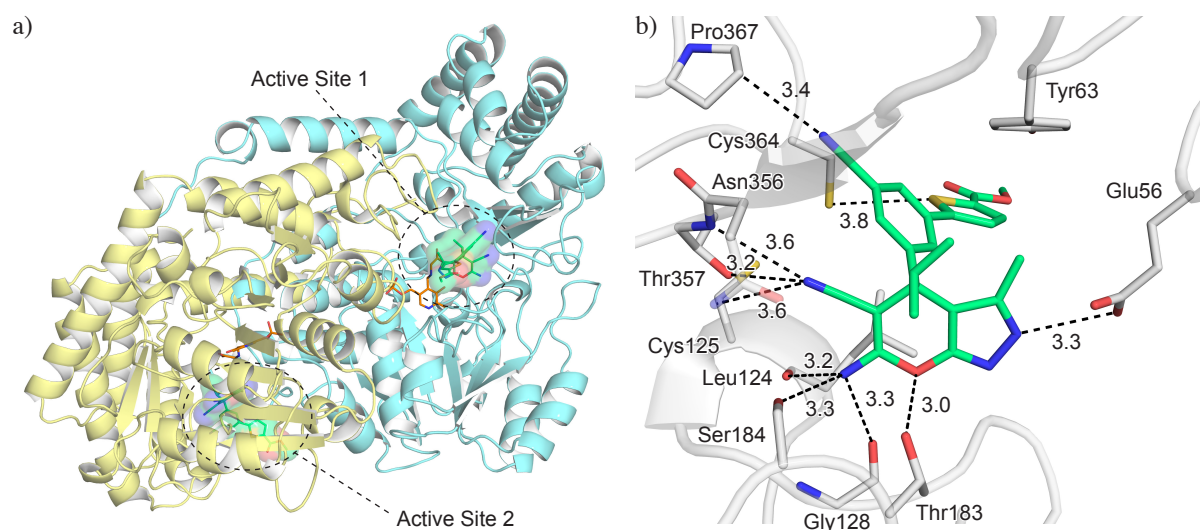


Figure 31. a) Homodimeric structure of *Pv*SHMT (PDB code 4TMR, 2.6 Å) with the two active sites occupied by ligand (+)-**67**. Each monomer is represented as cartoon. b) Binding mode of (+)-**67** within the active site of *Pv*SHMT (PDB code 4TMR, 2.6 Å). PLP is omitted for clarity in b). Distances are given in Å. Color code: C_{*Pv*SHMT} grey, C₍₊₎₋₆₇ lime, C_{PLP} orange, Monomer 1 cyan, Monomer 2 pale yellow, N blue, O red, P orange, S yellow.

The structural information gained from this co-crystal structure guided the next rounds of optimization. Molecular modeling with MOLOC^[125] was used to design ligands and prioritize ideas for synthesis. As shown in the schematic representation of the binding mode of (+)-**67** (Figure 32), two pockets are distinguishable: the pterin binding pocket hosts the pyrazolopyran core, whereas the bicyclic scaffold occupies the *p*ABA channel. During the optimization program, the core of the molecule was kept intact, while its substituents, on the stereogenic center and on the pyrazole ring, were systematically altered. These modifications are reported in the following.

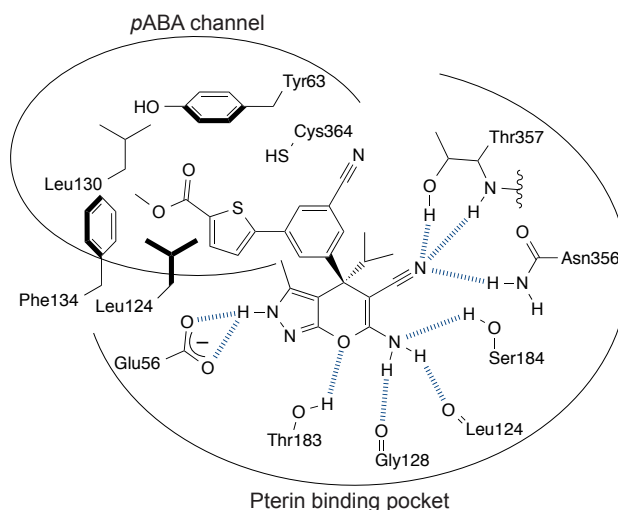


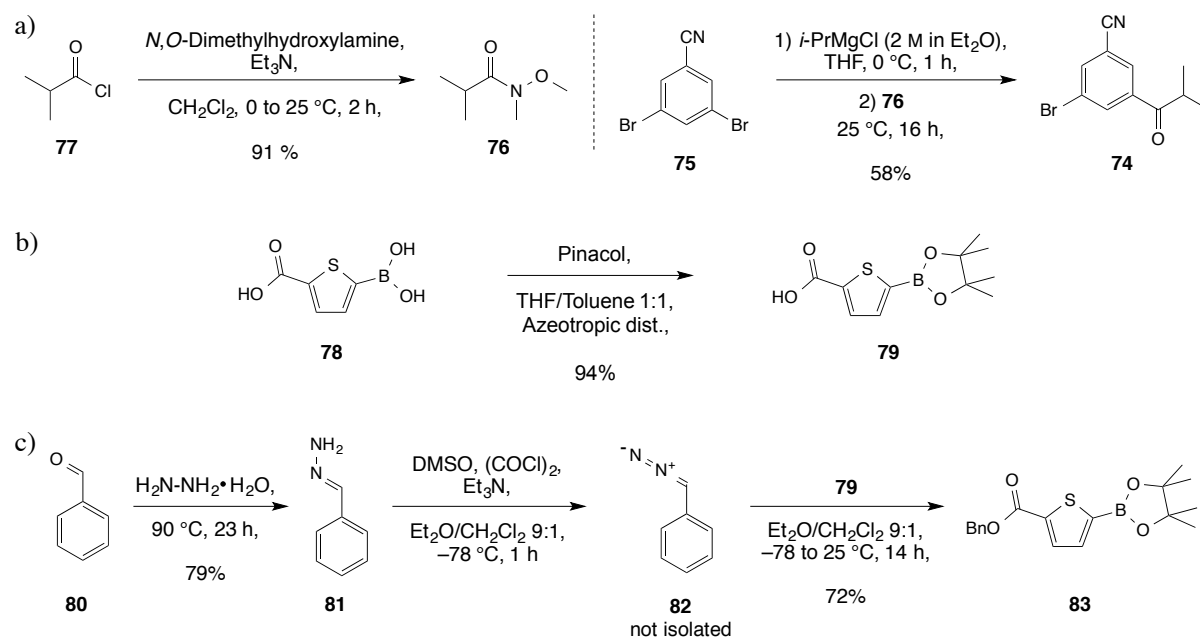
Figure 32. Schematic depiction of the binding mode of (+)-**67** as seen in the co-crystal structure with PvSHMT. Intermolecular H-bonding is indicated by blue dashed lines.

2.3. Evaluation of Thienyl-containing Analogues

2.3.1. Derivatization of the Terminal Thienyl Ring

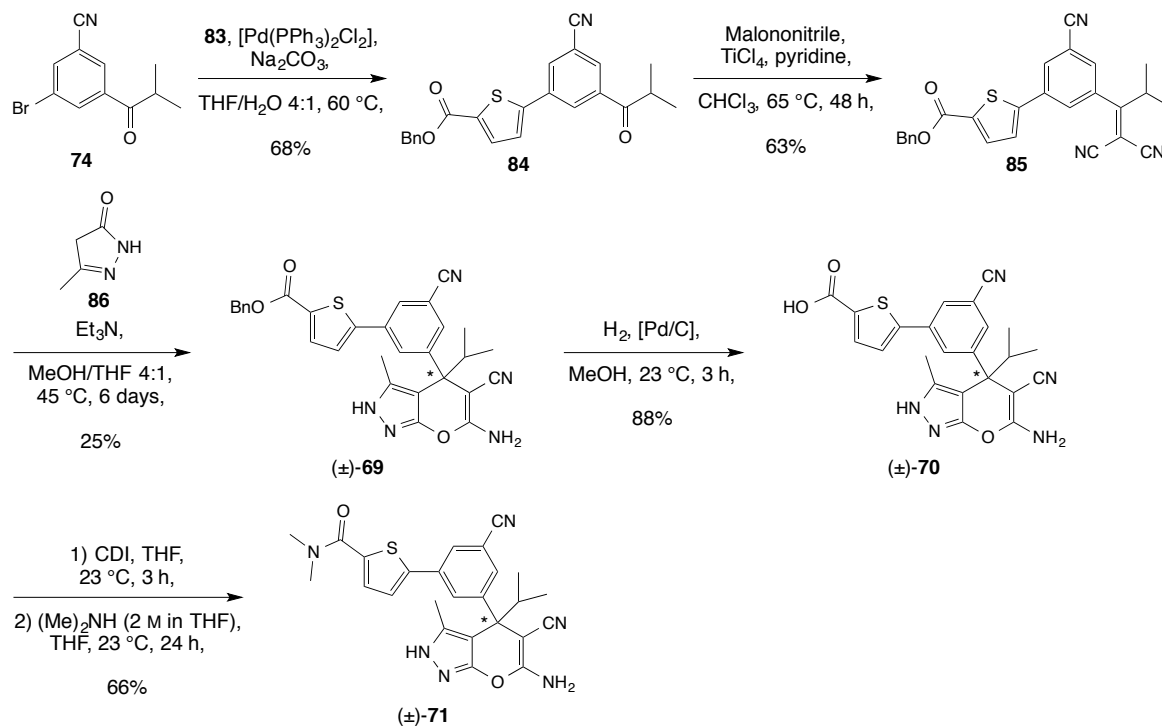
The initial goal was to find a suitable surrogate for the ester moiety that would maintain high cell-based efficacy, as there was evidence of ester cleavage in (\pm)-**69**. Accordingly, three analogues bearing a bioisosteric functional group of ester^[126] were investigated, namely an *N,N*-dimethylamide (in (\pm)-**71**), an oxadiazole (in (\pm)-**72**), and a sulfonamide (in (\pm)-**73**). The key building block in the synthesis of (\pm)-**71–73** is the arylketone **74**, which was obtained in good yield by formation of the Grignard reagent of 3,5-dibromobenzonitrile (**75**) and a subsequent addition of the Weinreb amide **76** (Scheme 3a). The latter was easily synthesized in one step from isobutyryl chloride (**77**). For the preparation of (\pm)-**71**, it was decided to introduce the amide functional group at the very last step *via* an amide coupling. Therefore, a benzyl protected acid was used throughout the multi-step synthesis. First, the commercially available boronic acid **78** was converted almost quantitatively to its pinacolato protected derivative **79** (Scheme 3b). In parallel, hydrazine was condensed on benzaldehyde (**80**) to give the hydrazone **81**, which was converted to phenyl diazomethane (**82**) under Swern-like conditions^[127] prior to addition of **79** to form **83** in 72% yield (Scheme 3c).

2. Identification of Pyrazolopyran-based Inhibitors for SHMT and Their Primary Optimization



Scheme 3. a) Synthesis of the key building block **74** and Weinreb amide **76**. b) Synthesis of pinacol boronate **79**. c) Esterification of **79** using phenyldiazomethane (**82**).

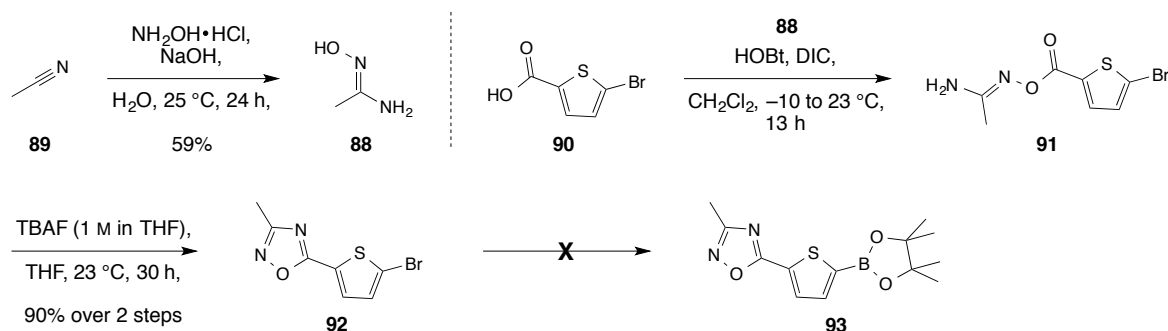
Next, the pinacol boronate ester **83** was coupled with **74** *via* a Suzuki-Miyaura cross-coupling^[128] to give the biaryl **84** in good yield (Scheme 4). A Knoevenagel condensation^[129] of malononitrile onto the ketone moiety of **84** was used to obtain the dinitrile **85**.



Scheme 4. Multi-steps synthesis of *N,N*-dimethylamide analogue (±)-**71**.

The pyrazolopyran core was formed by reaction of 3-methyl-1*H*-pyrazol-5(4*H*)-one (**86**) with **85** in presence of triethylamine (Et₃N). The transformation corresponds to a Michael addition of **86** onto the dinitrile **85**, followed by an intramolecular cyclization that gives the desired molecule (±)-**69** as a racemic mixture.^[130,131] The free carboxylic acid (±)-**70** was obtained in high yield by a palladium-catalyzed hydrogenation. Finally, ligand (±)-**71** was prepared by formation of an active ester using 1,1'-carbonyldiimidazole (CDI) prior to addition of *N,N*-dimethylamine (Scheme 4).

Towards the synthesis of oxadiazole (±)-**72**, it was decided to install the 1,2,4-oxadiazole moiety onto a thiophene building block prior to cross-coupling to obtain the biaryl **87** (see Scheme 6). First, *N*-hydroxyacetamide (**88**) was synthesized by reaction of acetonitrile (**89**) with hydroxylamine in presence of a base (NaOH) (Scheme 5).^[132] Secondly, **88** was coupled with the readily available carboxylic acid **90** using hydroxybenzotriazole (HOBt) and *N,N'*-diisopropylcarbodiimide (DIC)^[133] to give **91** that was directly treated with tetrabutylammonium fluoride (TBAF) to obtain the 1,2,4-oxadiazole derivative **92** (Scheme 5).

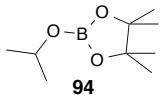
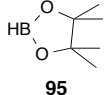
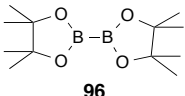
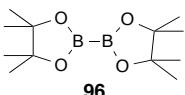


Scheme 5. Synthesis of *N*-hydroxyacetamide **88** and the bromothiophene-1,2,4-oxadiazole **92**.

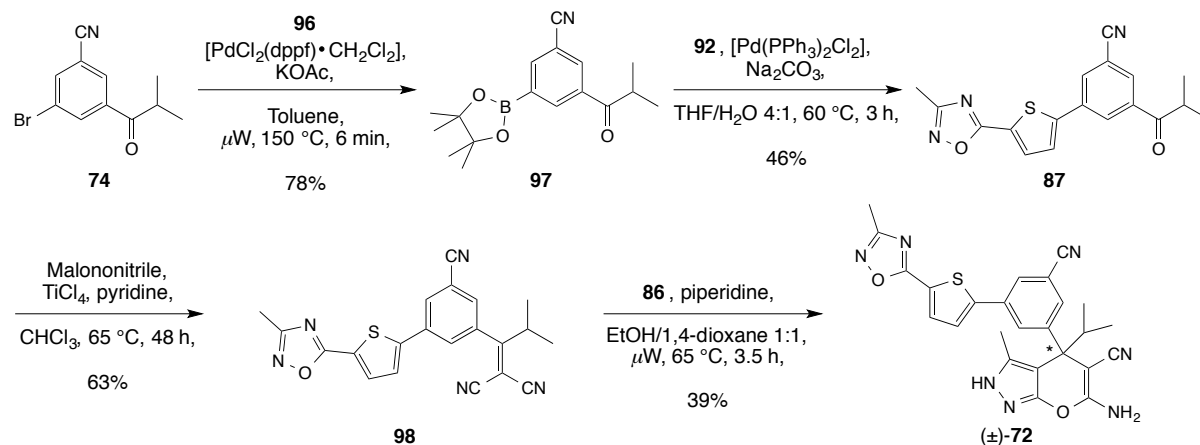
Attempts to convert the bromothiophene-1,2,4-oxadiazole **92** to its corresponding pinacol boronate derivative **93** (Scheme 5), either by lithiation or cross-coupling and with different boronate sources (**94–96**), remained unsuccessful (Table 1).

2. Identification of Pyrazolopyran-based Inhibitors for SHMT and Their Primary Optimization

Table 1. Screening of the reaction conditions towards the formation of the pinacol boronate **93**.

Entry	Boronate source	Conditions	Yield
1		<i>n</i> -BuLi, THF, -78 to 23 °C, 4 h	0%
2		Mg, THF, 23 °C, 12 h	0%
3		KOAc, [PdCl ₂ (dppf)•CH ₂ Cl ₂], 1,4-dioxane, 75 °C, 12 h	0%
4		KOAc, [PdCl ₂ (dppf)•CH ₂ Cl ₂], dimethoxyethane (DME), 90 °C, 1 h	0%

Instead, the building block **74** was easily transformed to the boronate **97** under microwave irradiation (μ W) (Scheme 6), which allowed to perform a cross-coupling between the latter and **92** to give biaryl **87** in a moderate yield. Reaction of 3-methyl-1*H*-pyrazol-5(4*H*)-one (**86**) with dinitrile **98** afforded ligand (\pm)-**72** in 39% yield (Scheme 6). In contrast to the transformation reported in Scheme 4, piperidine was used as base and microwave irradiation was employed, which allowed to perform the reaction in only 3.5 h.

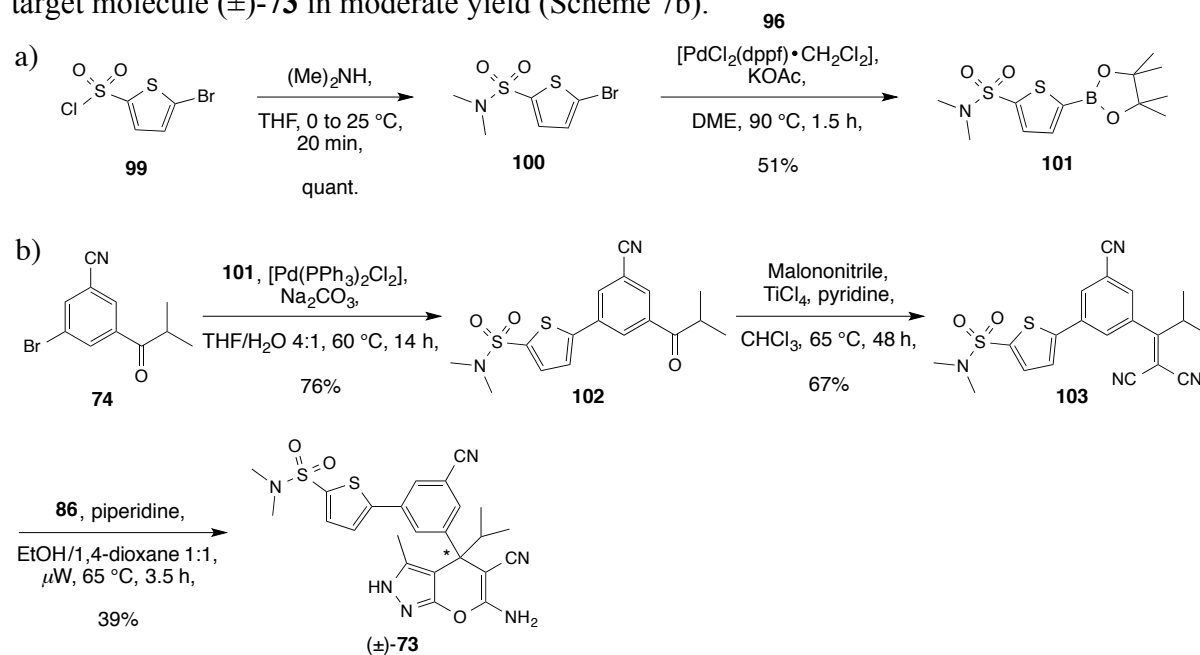


Scheme 6. Conversion of **74** to the pinacol boronate **97** and synthesis of 1,2,4-oxadiazole analogue (\pm)-**72**.

Ligand (\pm)-**73** was synthesized in a straightforward manner (Scheme 7). The thienylsulfonyl chloride **99** was first reacted with *N,N*-dimethylamine to obtain quantitatively sulfonamide **100**, which was directly converted to the pinacol boronate **101** via a palladium catalyzed cross-coupling (Scheme 7a). Afterwards, the biaryl **102** was isolated in good yield

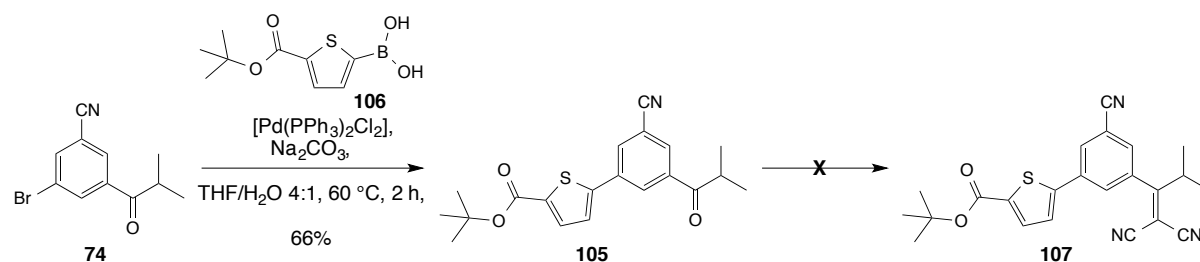
2. Identification of Pyrazolopyran-based Inhibitors for SHMT and Their Primary Optimization

and reacted with malononitrile to give **103**, which was subsequently used to synthesize the target molecule (\pm)-**73** in moderate yield (Scheme 7b).



Scheme 7. a) Synthesis of the *N,N*-dimethylamide precursor **100**. b) Preparation of ligand (\pm)-**73**.

Synthesis of a ligand bearing a bulky *tert*-butylester ((\pm)-**104**) was attempted. In this regard, the biaryl scaffold **105** was synthesized by coupling brominated **74** with boronic acid **106** (Scheme 8). However, the dinitrile **107** could not be obtained, despite the use of different reaction conditions (Table 2). By using TiCl_4 (entry 1), a complete decomposition of the starting material **105** was observed, which presumably corresponded to the cleavage of the *tert*-butylester moiety. Milder reaction conditions using either titanium (IV) isopropoxide ($\text{Ti}(i\text{-PrO})_4$)^[134] (entries 2 and 3) or with an excess of pyridine (entry 4) did not lead to any conversion of **105**.

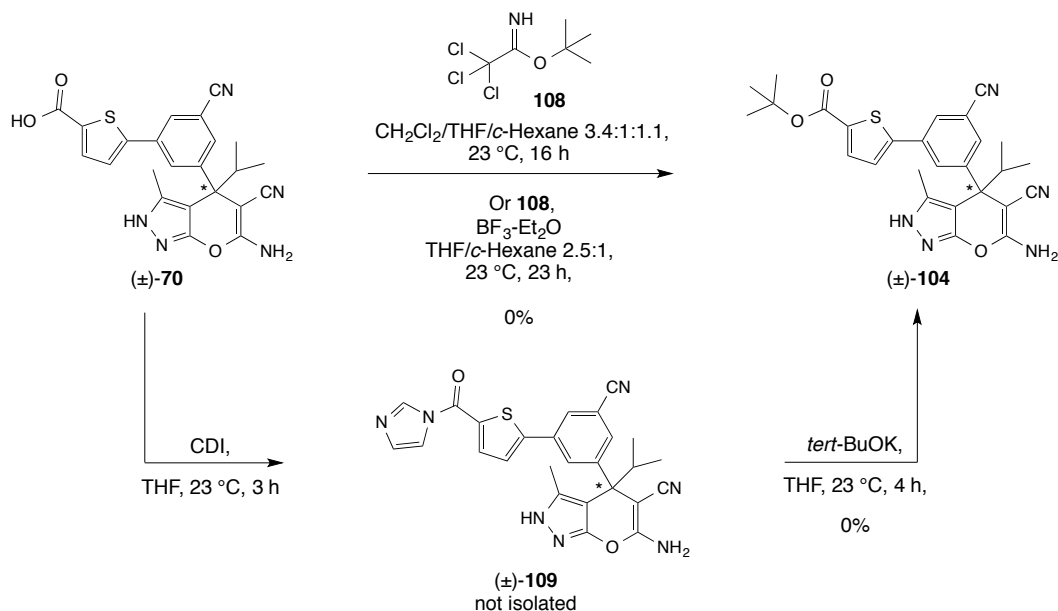


Scheme 8. Attempt to synthesize the dinitrile **107**.

Table 2. Screening of the reaction conditions for the formation of dinitrile **107**.

Entry	Conditions	Result
1	Malononitrile (5.0 eq), TiCl ₄ (1.3 eq), pyridine (4.0 eq), CHCl ₃ , 65 °C, 8 h	Decomposition of 107
2	Malononitrile (1.0 eq), Ti(<i>i</i> -PrO) ₄ (3.0 eq), pyridine (2.0 eq), THF, 23 °C, 3 h	No conversion
3	Malononitrile (1.0 eq), Ti(<i>i</i> -PrO) ₄ (3.0 eq), pyridine (2.0 eq), THF, 50 °C, 40 h	No conversion
4	Malononitrile (1.4 eq), pyridine (excess), 50 °C, 24 h	No conversion

Alternatively, it was attempted to esterify carboxylic acid (\pm)-**70**, which would provide directly the target molecule (\pm)-**104**. Unfortunately, direct esterification by using *tert*-butyltrichloroacetamide (**108**)^[135] did not yield any product (Scheme 9). Addition of a catalytic amount of boron trifluoride etherate (BF₃–Et₂O)^[136] did not have any influence on the outcome of the reaction. Formation of the activated ester (\pm)-**109** followed by treatment with potassium *tert*-butoxide (*tert*-BuOK) did not yield (\pm)-**104** either (Scheme 9). Consequently, the work towards this target molecule was put on a halt.

**Scheme 9.** Attempt to synthesize (\pm)-**104** by esterification of (\pm)-**70**.

In addition to ligands (\pm)-**71**–**73**, four other analogues bearing a 5-substituted thienyl ring were designed and successfully synthesized. The following functional groups were introduced on the 5-position: a CF₃ (in (\pm)-**110**), a methoxy group (in (\pm)-**111**), a

2. Identification of Pyrazolopyran-based Inhibitors for SHMT and Their Primary Optimization

methoxymethyl ether moiety (in (\pm)-**112**), and a chloride (in (\pm)-**113**). To complement this list, a ligand containing a benzothiophene moiety ((\pm)-**114**) was designed with the intention of maintaining the S \cdots S interaction to Cys364 and improving the hydrophobic interactions with the surrounding residues, such as Tyr63 and Phe266 (Figure 33).

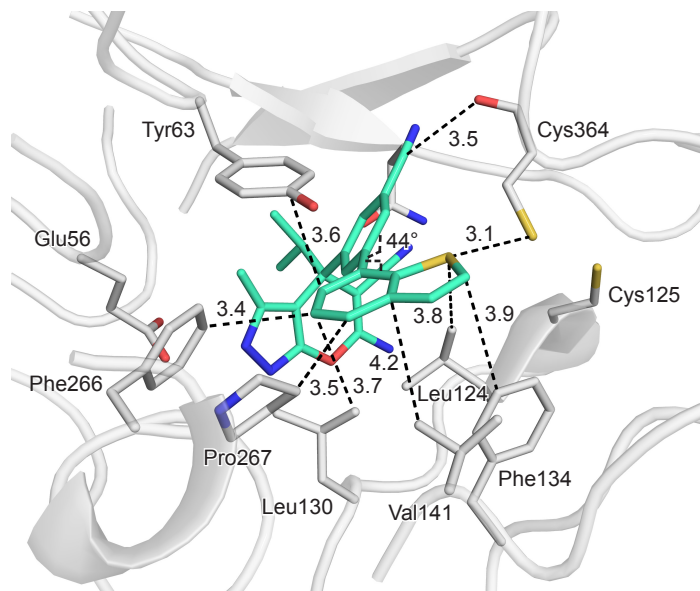
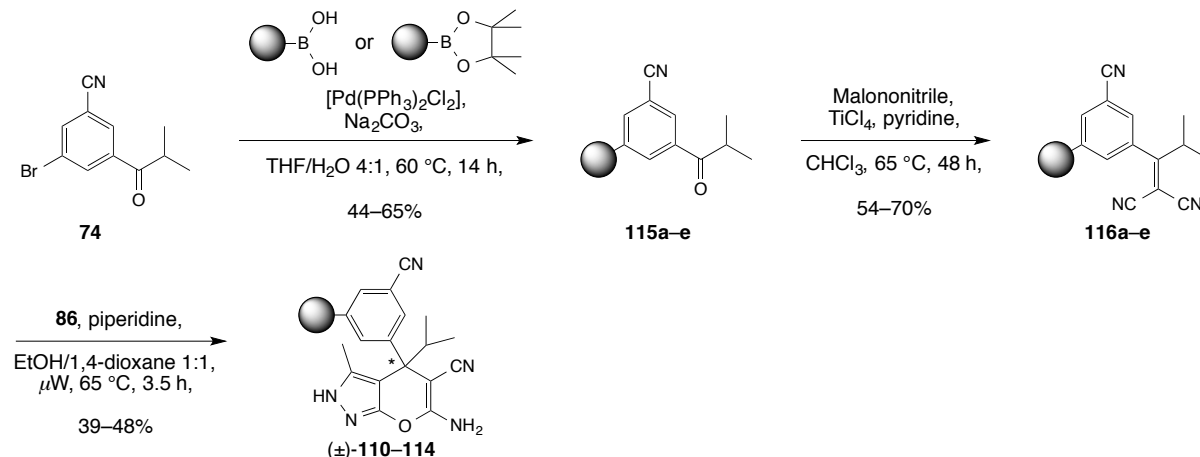


Figure 33. Proposed binding mode of benzothiophene analogue (\pm)-**114** in the active of *Pv*SHMT (PDB code 4TMR, 2.6 Å) as modeled with MOLOC. The torsion angle between the phenyl ring and the benzothiophene was measured to be 44°, no similar structure could be found in the CSD for comparison. PLP is omitted for clarity. Distances are given in Å. Color code: C_{PvSHMT} grey, $C_{(\pm)-114}$ cyan, N blue, O red, S yellow.

These five ligands were synthesized following a three steps synthetic sequence involving a Suzuki-Miyaura cross-coupling^[128] to **115a–e**, a Knoevenagel condensation^[129] to **116a–e**, and a Michael addition of 3-methyl-1*H*-pyrazol-5(4*H*)-one (**86**), followed by an intramolecular cyclization to provide (\pm)-**110–114** (Scheme 10).^[130,131]

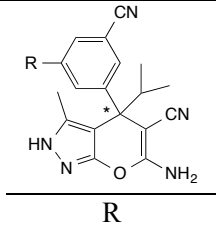
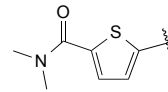
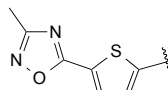
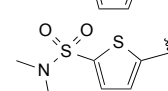
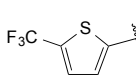
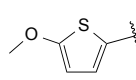
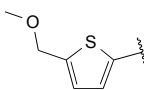
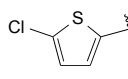
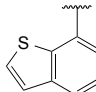


Scheme 10. Representative synthesis of ligands (\pm)-**110–114**.

2. Identification of Pyrazolopyran-based Inhibitors for SHMT and Their Primary Optimization

Following their successful synthesis, ligands (\pm)-**71–73** and (\pm)-**110–114** were tested in a target-based assay towards *Pf*SHMT and in a cell-based assay against the *Pf*NF54 strain (Table 3). Moderate inhibition of *Pf*SHMT was obtained with ligands (\pm)-**71**, (\pm)-**110**, (\pm)-**111**, and (\pm)-**113**, while oxadiazole (\pm)-**72** and sulfonamide (\pm)-**73** analogues displayed better affinities for *Pf*SHMT with IC_{50} values in the low three digit nanomolar range. The methoxymethyl ether (\pm)-**112** inhibited strongly the activity of the enzyme with an IC_{50} of 42 nM (Table 3). Remarkably, the predicted interactions of the benzothiophene analogue (\pm)-**114** within the *p*ABA channel led to a low IC_{50} value of 60 nM.

Table 3. Biological activities of thienyl derivatives (\pm)-**71–73** and (\pm)-**110–114**.

Cpd.		EC_{50} <i>Pf</i> NF54 [nM]	IC_{50} <i>Pf</i> SHMT \pm SD [nM] ^[a]
	R		
(\pm)- 71		59	270 \pm 9
(\pm)- 72		212	133 \pm 6
(\pm)- 73		151	99 \pm 2
(\pm)- 110		594	388 \pm 5
(\pm)- 111		410	323 \pm 43
(\pm)- 112		228	42 \pm 1
(\pm)- 113		501	202 \pm 9
(\pm)- 114		197	60 \pm 1

[a] Standard deviations are given.

Co-crystal structures of (\pm)-**73** and (\pm)-**112** with *Pv*SHMT were obtained and confirmed the binding mode seen with (+)-**67** (Figures 34 and 35). Despite using a racemic mixture of ligands in each case, only the (+)-enantiomer was found to be bound to *Pv*SHMT, which

corroborated the large affinity discrepancies between both enantiomers. Unfortunately, no clear explanation became apparent for the improved target affinity of these two ligands compared to (\pm)-**71** or (\pm)-**111**, for example. The sulfonamide moiety of (+)-**73** adopted the preferred staggered conformation with the N-lone pair bisecting the SO₂ angle^[137] (Figure 34) (conformations of sulfonamides are discussed in detail in Chapter 3). It is too far away from Tyr63 ($d(\text{S}=\text{O}\cdots\text{O}_{\text{Tyr63}}) = 3.7 \text{ \AA}$) to establish a strong polar interaction (Figure 34b). One S=O moiety points to the hydrophobic side chain of Val141 and Pro267, whereas one of the *N*-methyl groups is at close distance to the edge of Phe134 ($d(\text{N}-\text{C}\cdots\text{C}_{\text{Phe134}}) = 3.1 \text{ \AA}$) leading to a rather repulsive C–H $\cdots\pi$ contact.^[138]

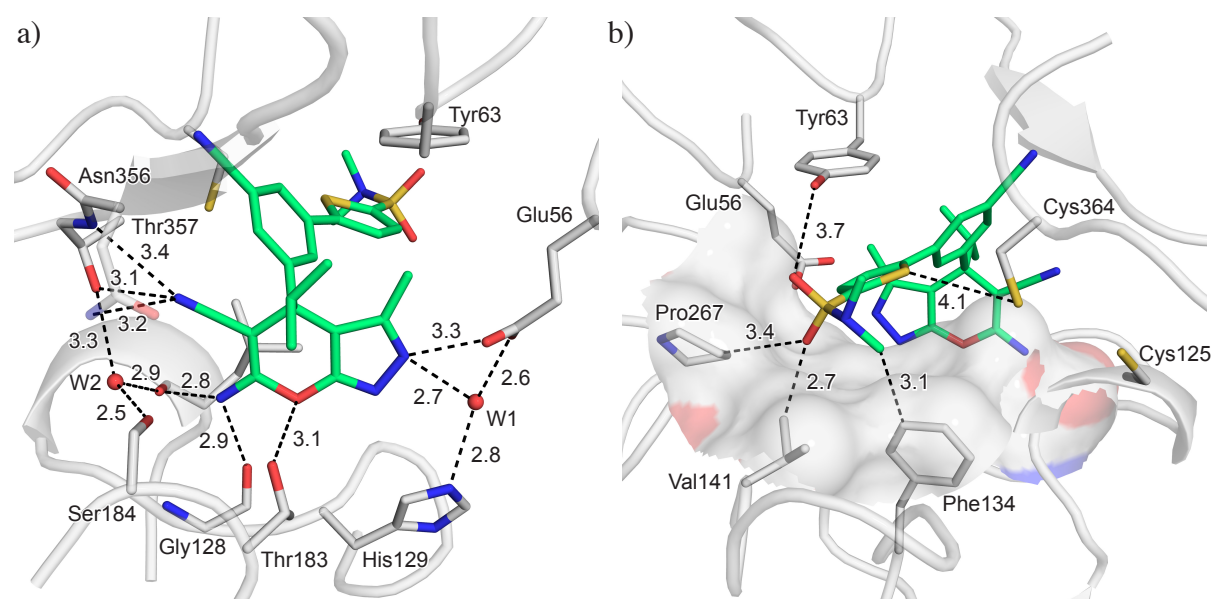


Figure 34. Co-crystal structure of (+)-**73** with *Pv*SHMT (PDB code 5GVK, 2.3 Å). a) Polar protein–ligand interactions. b) Selected hydrophobic protein–ligand interactions. The surface spans the volume of the *p*ABA channel. PLP is omitted for clarity. Water molecules (W1 and W2) are represented as red spheres. Distances are given in Å. Color code: C_{PvSHMT} grey, $C_{(+)-73}$ lime, N blue, O red, S yellow.

Concerning (\pm)-**112**, its methoxymethyl ether moiety is located at the exit of the *p*ABA channel at the periphery of the protein (Figure 35), it is turned out of the plan compared to the ester group in (+)-**67** ($\text{C}-\text{C}-\text{C}-\text{O}$ torsion angle = 69°) and does not directly interact with any protein residue.

2. Identification of Pyrazolopyran-based Inhibitors for SHMT and Their Primary Optimization

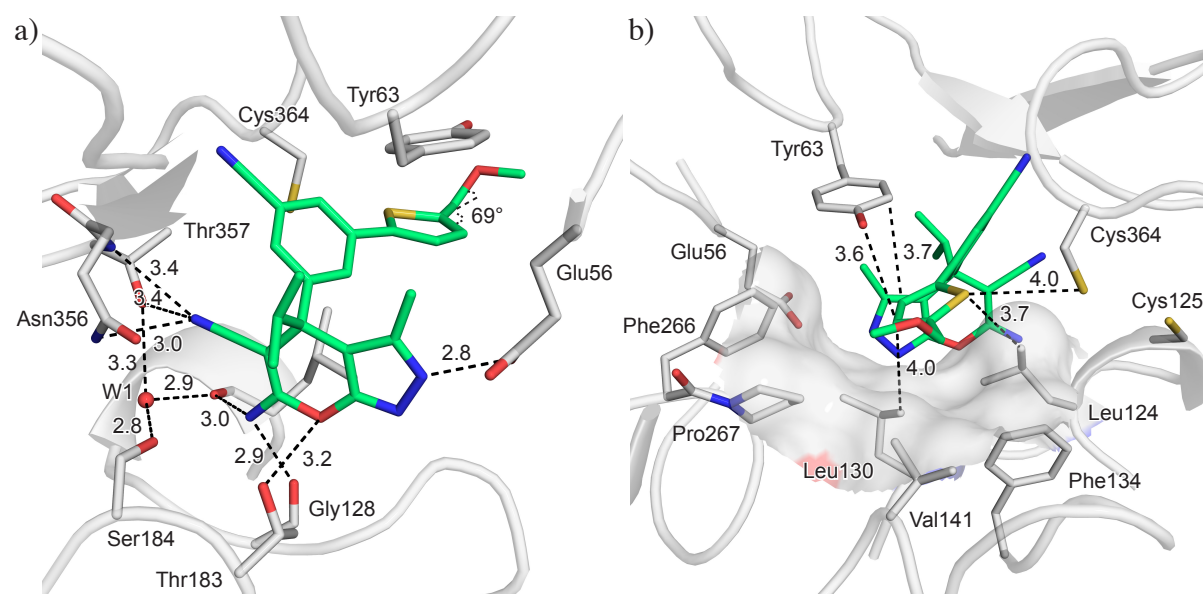


Figure 35. Co-crystal structure of (+)-**112** with *Pv*SHMT (PDB code 5GVL, 2.6 Å). a) Polar protein–ligand interactions. b) Selected hydrophobic protein–ligand interactions. The surface spans the volume of the *p*A_{BA} channel. PLP is omitted for clarity. The water molecule (W1) is represented as a red sphere. Distances are given in Å. Color code: *C_{PvSHMT}* grey, *C₍₊₎₋₁₁₂* lime, N blue, O red, S yellow.

In the *Pf*NF54 cell-based assay, (±)-**71** was the best inhibitor of this series (Table 3). The efficacy of all other ligands was two orders of magnitude lower than the one of (±)-**67** ($EC_{50} = 3$ nM). The microsomal stability of (±)-**71** remained poor with a half-life of only 4 min, in both, human and rat liver microsomes. Hence, it was not surprising to observe only 38% of parasitemia reduction in a 4-day-test severe combined immunodeficiency (SCID) mice model^[139] with *P. falciparum* 3D7 infected SCID mice upon administration of (±)-**71** at 4×30 mg/kg (p.o).

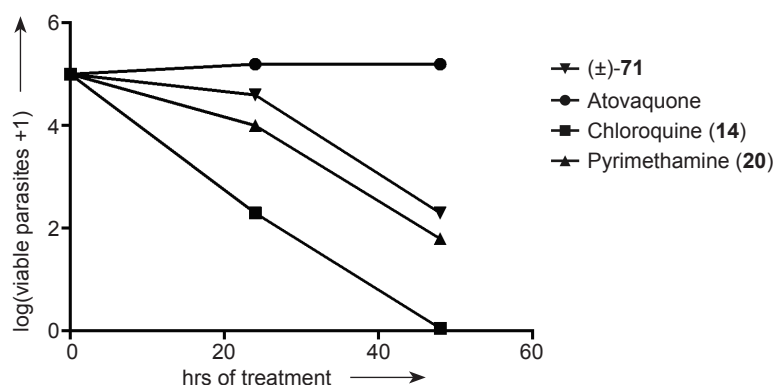


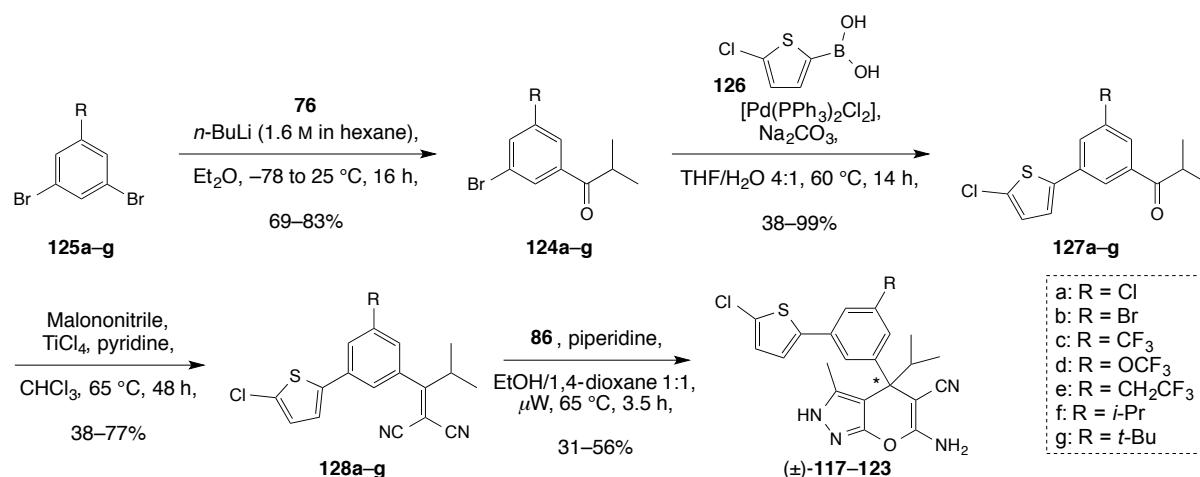
Figure 36. PRR chart: the number of viable parasites is plotted against the time after treatment with either (±)-**71**, atovaquone, chloroquine (**14**), or pyrimethamine (**20**).

2. Identification of Pyrazolopyran-based Inhibitors for SHMT and Their Primary Optimization

Compound (\pm)-**71** was also investigated in an *in vitro* parasite reduction ratio (PRR) assay to determine the onset of drug action and the rate of killing (Figure 36).^[140] A lag phase of 24 h was observed, after which the number of parasites decreased significantly. The profile of ligand (\pm)-**71** is similar to the DHFR inhibitor pyrimethamine (**20**) and is characteristic of the antifolate class of active substances.

2.3.2. Alteration of the Substituents on the Pyrazolopyran Core

Since the cell-based affinity of the series of ligands presented in the previous section remained at least 20-fold lower than the one of (\pm)-**67**, modification at other positions of the molecule were evaluated to enhance biological activity. First, the *meta* substituent on the phenyl ring was systematically changed. The chlorothieryl analogue (\pm)-**113** was chosen as reference compound as it displayed intermediate cell-based efficacy. A series of seven ligands ((\pm)-**117**–**123**) (Table 4) was prepared by first isolating the corresponding bromoaryl building blocks **124a–g** synthesized by lithiation of the commercially available 3,5-dibromoaryls **125a–g** followed by the addition of Weinreb amide **76** (Scheme 11). Intermediates **124a–g** were reacted with chlorothiophene boronic acid (**126**) to give **127a–g** in excellent yields at the exception of the bromo analogue **127b**. Indeed, a non-negligible amount of diarylated bi-product was formed and several consecutive purifications were required to isolate **127b** pure. Subsequently, **127a–g** were converted to the dinitriles **128a–g** prior to formation of the pyrazolopyran core in (\pm)-**117**–**123** (Scheme 11).



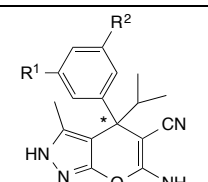
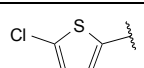
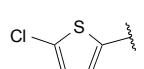
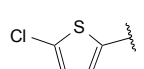
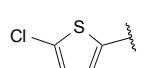
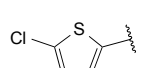
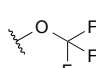
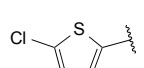
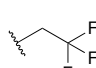
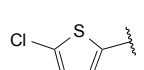
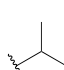
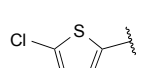
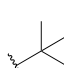
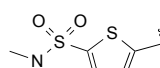
Scheme 11. Synthesis of chlorothieryl analogues (\pm)-**117**–**123**.

In this series of compounds, target affinities remained in the same range as for the cyano analogue (\pm)-**113** (Table 4), except for ligands bearing a CH₂CF₃ ((\pm)-**121**) or a *tert*-butyl

2. Identification of Pyrazolopyran-based Inhibitors for SHMT and Their Primary Optimization

moiety ((±)-**123**), which were less effective. More significant discrepancies were measured against the *Pf*NF54 strain. A chloride ((±)-**117**) or bromide ((±)-**118**) had minor effects on the *in vitro* potency, while substitution of the nitrile in (±)-**113** for a CF₃ in (±)-**119** resulted in an appreciable 2-fold improvement of efficacy (EC₅₀ = 226 nM, Table 4). Introduction of bulkier substituents in (±)-**120–123** were deleterious to cell-based efficacy with EC₅₀ values in the micromolar range. The larger groups interfere with the conformationally flexible Cys364-loop, which was only discovered later and is discussed in Chapter 4 based on several new co-crystal structures. Substitution of the nitrile moiety for a CF₃ group was applied to the potent *N,N*-dimethylsulfonamide analogue (±)-**73**. Hence, ligand (±)-**129** was synthesized following the approach described in Scheme 7b, the sole difference was the use of the fluorinated aryl building block **124c** instead of **74**. Remarkably, (±)-**129** displayed a low nanomolar cell-based efficacy (EC₅₀ = 18 nM, Table 4) that was 10-fold better than the one of (±)-**73**.

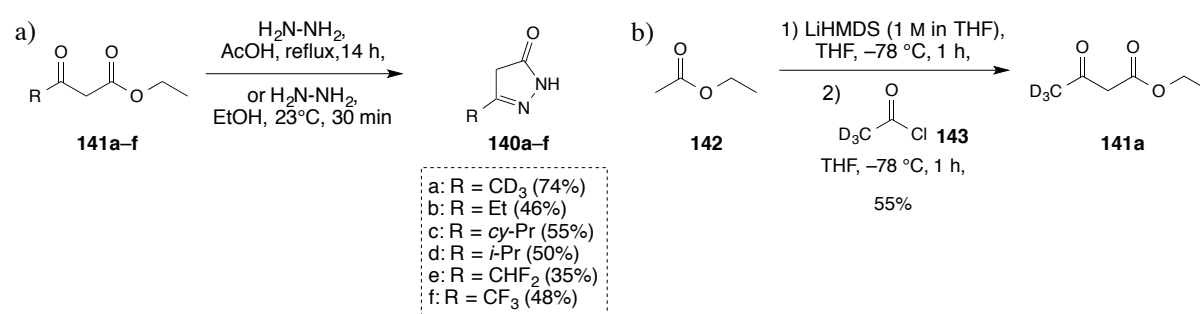
Table 4. SAR for the *meta* position (R²) on the phenyl ring.

Cpd.			EC ₅₀ <i>Pf</i> NF54 [nM]	IC ₅₀ <i>Pf</i> SHMT ± SD [nM] ^[a]
	R ¹	R ²		
(±)- 113		CN	501	202 ± 9
(±)- 117		Cl	485	255 ± 16
(±)- 118		Br	892	339 ± 11
(±)- 119		CF ₃	226	279 ± 10
(±)- 120			3760	291 ± 4
(±)- 121			7106	744 ± 30
(±)- 122			4511	280 ± 5
(±)- 123			5501	953 ± 21
(±)- 129		CF ₃	18	375 ± 20

[a] Standard deviations are given.

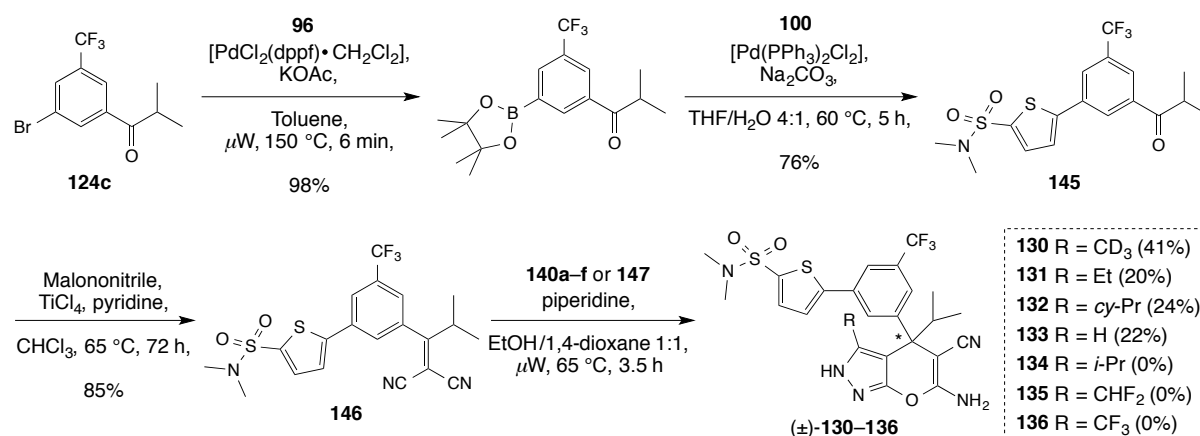
2. Identification of Pyrazolopyran-based Inhibitors for SHMT and Their Primary Optimization

Following these encouraging results, different substituents on the pyrazolopyran core were also investigated. The terminal *N,N*-dimethylsulfonamide moiety and the *meta*-CF₃ were kept intact, while the substituent on the pyrazole ring and on the stereogenic center were systematically altered in ligands (±)-**130**–**136** and (±)-**137**–**139**, respectively (Scheme 13 and Table 5). Six distinct pyrazolones **140a**–**f** were synthesized in one-step by reacting their corresponding β-ketoester **141a**–**f** with hydrazine in ethanol (for **140a**) or in refluxing acetic acid (for **140b**–**f**) (Scheme 12a). The deuterated β-ketoester **141a** was not commercially available and was synthesized in moderate yield by reacting ethyl acetate (**142**) with lithium bis(trimethylsilyl)amide (LiHMDS) followed by addition of the deuterated acyl chloride **143** (Scheme 12b).



Scheme 12. a) Synthesis of pyrazolones **140a**–**f**. b) Synthesis of the deuterated β-ketoester **141a**.

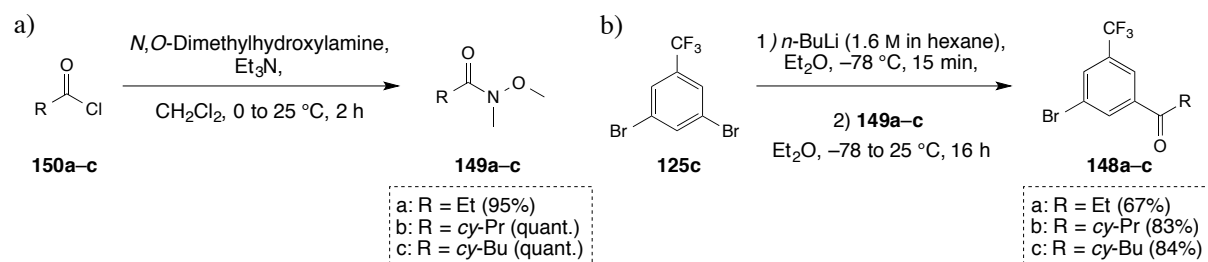
The aryl ketone **124c** was converted almost quantitatively to the pinacol boronate **144** (Scheme 13) prior to a cross-coupling with brominated sulfonamide **100** leading to **145**. Next, a Knoevenagel condensation was performed onto **145** to obtain **146** in high yield. Finally, pyrazolones **140a**–**f** and commercially available 1*H*-pyrazol-5(4*H*)-one (**147**) were used to synthesize ligands (±)-**130**–**136** (Scheme 13). However, only traces of product were formed when **146** was reacted with pyrazolones **140d**–**f** and ligands (±)-**134**–**136** could not be prepared.



Scheme 13. Synthesis of ligands (±)-**130**–**133** and attempt to synthesize ligands (±)-**134**–**136**.

2. Identification of Pyrazolopyran-based Inhibitors for SHMT and Their Primary Optimization

Regarding ligands (\pm)-**137–139** bearing different lipophilic moieties on their stereogenic center, they were synthesized following the same synthetic route as the one depicted in Scheme 13. The respective aryl ketones **148a–c** were prepared by lithiation of 1,3-dibromo-5(trifluoromethyl)benzene (**125c**) followed by the addition of the corresponding Weinreb amide **149a–c** (Scheme 14). The latter were readily prepared by nucleophilic addition of *N,O*-dimethylhydroxylamine onto the commercially available acyl chlorides **150a–c** (Scheme 14a).



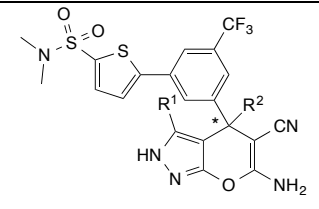
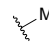
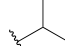
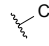
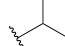

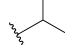

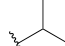
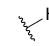
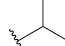
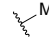
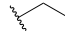
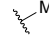

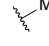
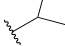
Scheme 14. a) Preparation of the Weinreb amides **149a–c**. b) Synthesis of aryl ketones **148a–c**.

The biological activities of ligands (\pm)-**129–133** and (\pm)-**137–139** are summarized in Table 5. The IC_{50} values in the *Pf*SHMT target assay were all very similar, in the triple-digit nanomolar range, possibly due to a limited dynamic range of the assay in particular at higher binding affinity. To refine the SAR, IC_{50} values of selected compounds were measured against *At*SHMT, which correlate much better with the EC_{50} data. The cell-based inhibition values varied more than a factor of 600. On the one hand, the methyl substituent on the pyrazole ring (position R^1) was optimal, and its potency could only be matched by a CD_3 - (EC_{50} (\pm)-**130** = 11 nM) or a H-substituent (EC_{50} (\pm)-**133** = 29 nM). Ethyl and cyclopropyl substituents in this position were detrimental to activity. On the other hand, the SAR involving the substituent at the stereogenic center revealed that this position was not amenable to broad changes either. The isopropyl moiety was required for high cell-based efficacy (EC_{50} (\pm)-**129** = 18 nM), any other substituent ((\pm)-**137–139**) led to markedly reduced potency (Table 5).

The promising antiparasitic activity of (\pm)-**129** was diminished by its poor liver microsomal stability with a measured half-life of 3 min. Hence, the major metabolites of this molecule were determined in order to guide the next round of optimization.

2. Identification of Pyrazolopyran-based Inhibitors for SHMT and Their Primary Optimization

Table 5. SAR for the positions on the pyrazole ring (R^1) and on the stereogenic center (R^2).

Cpd.			EC_{50} <i>Pf</i> NF54 [nM]	IC_{50} <i>Pf</i> SHMT \pm SD [nM] ^[a]	IC_{50} <i>At</i> SHMT [nM]
	R^1	R^2			
(±)- 129			18	375 \pm 20	25.2
(±)- 130			11	374 \pm 6	16.2
(±)- 131			172	185 \pm 2	n.d. ^[b]
(±)- 132			576	437 \pm 13	n.d.
(±)- 133			29	340 \pm 18	n.d.
(±)- 137			340	153 \pm 4	n.d.
(±)- 138			1202	350 \pm 15	n.d.
(±)- 139			498	439 \pm 4	n.d.

[a] Standard deviations are given. [b] n.d. = not determined.

2.3.3. Identification of the Potential Metabolites from (\pm)-**129**

Metabolite identification performed on (\pm)-**129** in NADPH-supplemented human liver microsomes revealed major degradation pathways *via* thiophene oxidation and *N*-demethylation accounting for approximately 50 and 33% of total metabolites, respectively (Figure 37) (more details about the metabolites identification are reported in Appendix, Section 9.2). The same metabolites were detected in an isotopic labelling experiment with (\pm)-**130**, which enabled to exclude potential metabolism on the methyl substituent of the pyrazole ring.

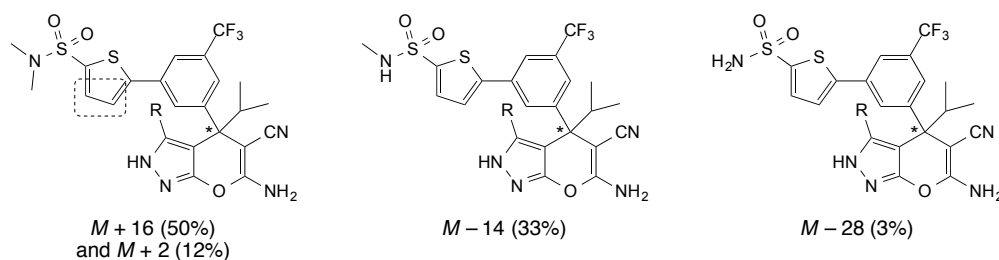


Figure 37. Proposed metabolites structures for (\pm)-**129** and (\pm)-**130**. R = CH₃ or CD₃. The dotted line indicates proposed site(s) of metabolism. $M + 16$ = oxygenation; $M + 2$ = reduction. The numbers in parenthesis correspond to the relative peak area as % of total metabolite peak area formed after 60 min.

Distinct metabolites were obtained by incubating compound (\pm)-**151**, which is issued from the initial screening library and features a 3,5-dichlorophenyl substituent at the stereogenic center. For this molecule, the main metabolite arises from oxidation on the pyrazolopyran core, possibly by oxidation of the vinylogous cyanamide (Figure 38). Taken together, these results suggested that metabolism is compound-specific and that the vinylogous cyanamide moiety might be a liability. Nevertheless, the further optimization focused on the replacement of the substituted-thiophene peripheral part to prepare more stable ligands.

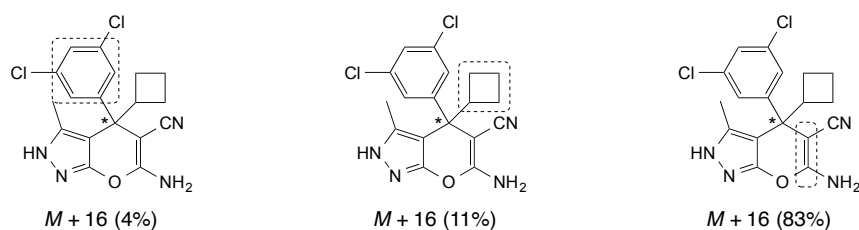


Figure 38. Proposed metabolites structures for (\pm)-**151**. The dotted line indicates proposed site(s) of metabolism. $M + 16$ = oxygenation. The numbers in parenthesis correspond to the relative peak area as % of total metabolite peak area formed after 60 min.

2.4. Terminal Heteroalicyclic Rings as Thiophene Replacement

Subsequent to the metabolites identification discussed above, the first priority was to replace the metabolizable thienyl moiety, while maintaining high *in vitro* potency. In this regard, 13 inhibitors featuring *N*-heteroalicycles of various sizes and different nature were designed and synthesized.

2.4.1. Design and Synthesis of Ligands (\pm)-152–160, (\pm)-165–167, and (\pm)-186

The peripheral moieties in (\pm)-152–160 (Table 6) were chosen to preserve the hydrophobic interactions within the *p*ABA channel and to reduce the overall lipophilicity of the ligand. An example is shown with the modeling of (+)-153 within the active site of *Pv*SHMT (Figure 39), in which a fluoride from the azetidine moiety nicely points to the hydrophobic side chains of Leu130, Phe134, and Val141.

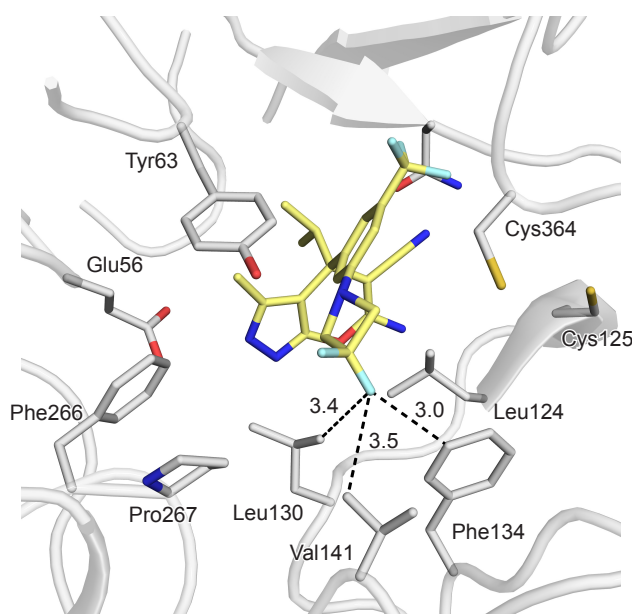
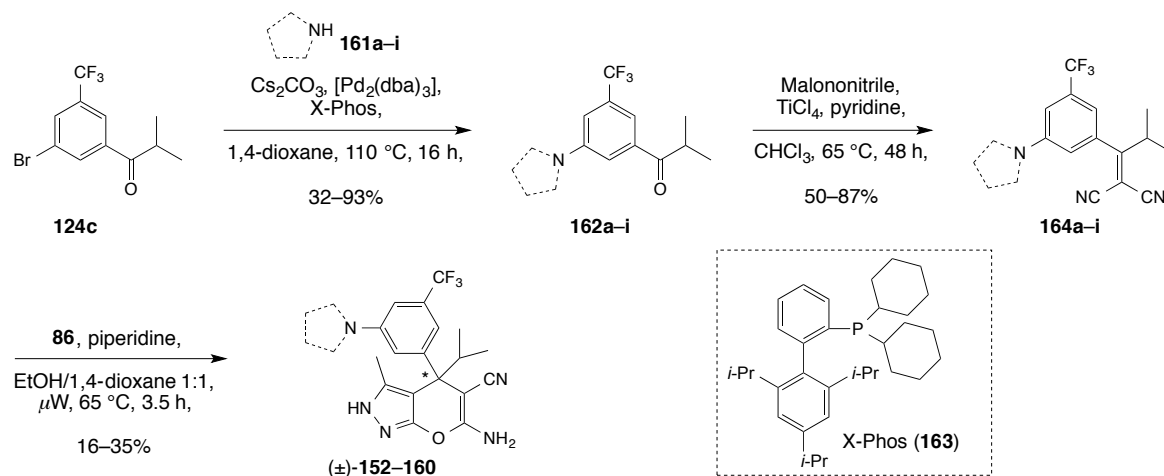


Figure 39. Proposed binding mode of fluoroazetidine analogue (+)-153 within the active of *Pv*SHMT (PDB code 4TMR, 2.6 Å) as modeled with MOLOC. PLP is omitted for clarity. Distances are given in Å. Color code: C_{PvSHMT} grey, $C_{(+)-153}$ gold, F cyan, N blue, O red, S yellow.

A Buchwald-Hartwig amination^[141] was employed between the bromoaryl **124c** and the desired cyclic secondary amine **161a–i** in order to synthesize the corresponding bicyclic scaffolds **162a–i** in moderate to high yields (Scheme 15). In this reaction, a highly reactive palladium complex was generated *in situ* by mixing palladium dibenzylidenacetone ($[Pd_2(dba)_3]$) with 2-dicyclohexylphosphino-2',4',6'-triisopropylbiphenyl (X-Phos, **163**).^[142] Afterwards, the synthesis remained identical as for other derivatives presented above, the

2. Identification of Pyrazolopyran-based Inhibitors for SHMT and Their Primary Optimization

dinitriles **164a–i** were first prepared in good yields prior to the formation of the pyrazolopyran core in ligands (\pm)-**152–160** (Scheme 15).



Scheme 15. Synthesis of ligands (\pm)-**152–160** involving a Buchwald-Hartwig amination.

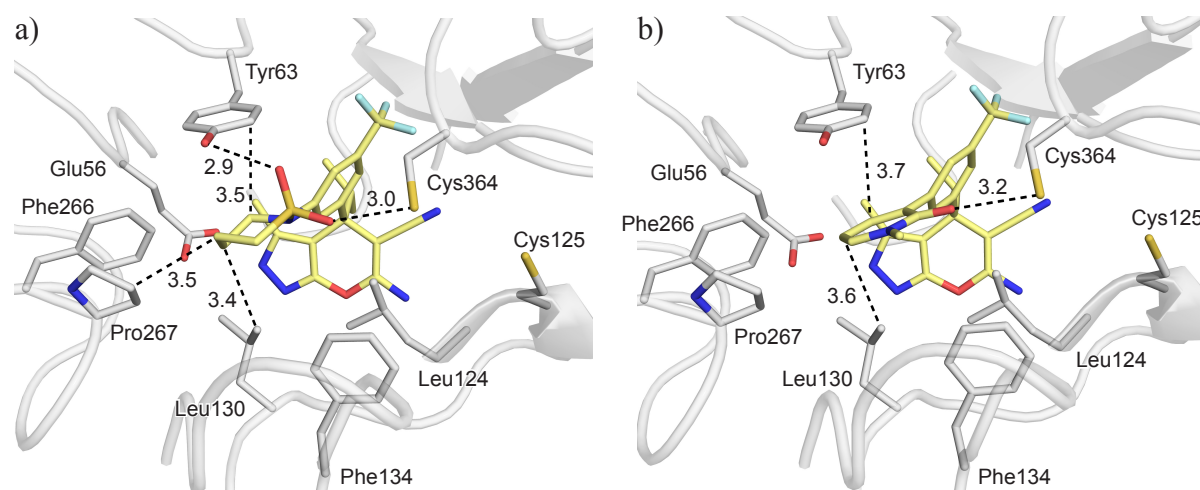


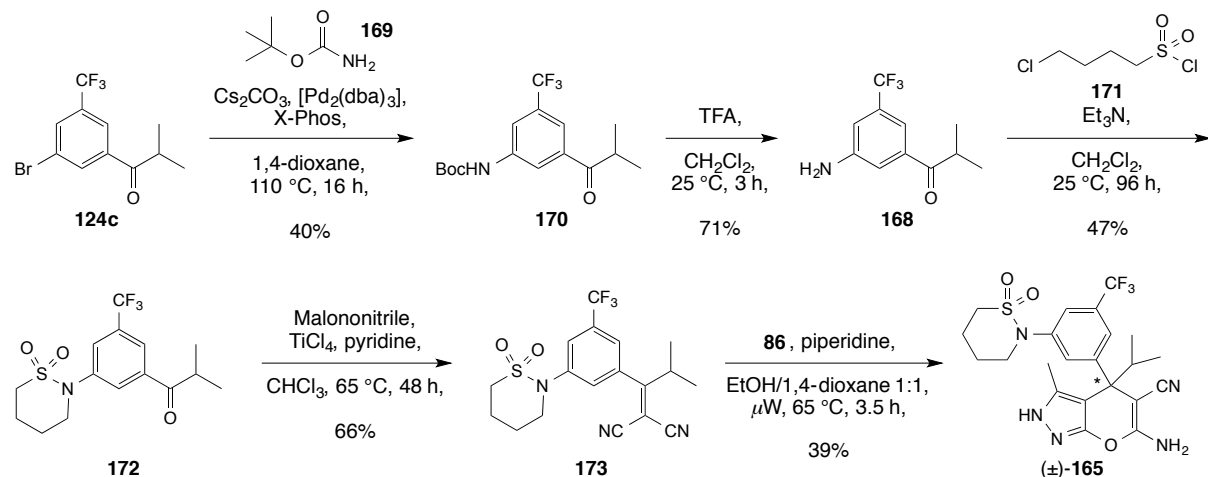
Figure 40. Proposed binding mode of a) sultam (+)-**165** and b) *N*-methylpyridone analogue (+)-**167** within the active of *Pv*SHMT (PDB code 4TMR, 2.6 Å) as modeled with MOLOC. PLP is omitted for clarity. Distances are given in Å. Color code: C_{PvSHMT} grey, $C_{Ligands}$ gold, F cyan, N blue, O red, S yellow.

Functional groups able to interact with Cys364 *via* chalcogen interactions ($S\cdots O$)^[123] were incorporated in sultam (\pm)-**165**, in thiadiazinane (\pm)-**166** (a more polar derivative of (\pm)-**165**), and in the *N*-methylpyridone analogue (\pm)-**167**. The proposed binding modes of (+)-**165** and (+)-**167** are depicted in Figure 40. In both complexes, the exocyclic oxygen is in the vicinity of Cys364 and the terminal ring is nicely lined by Tyr63 and Leu130.

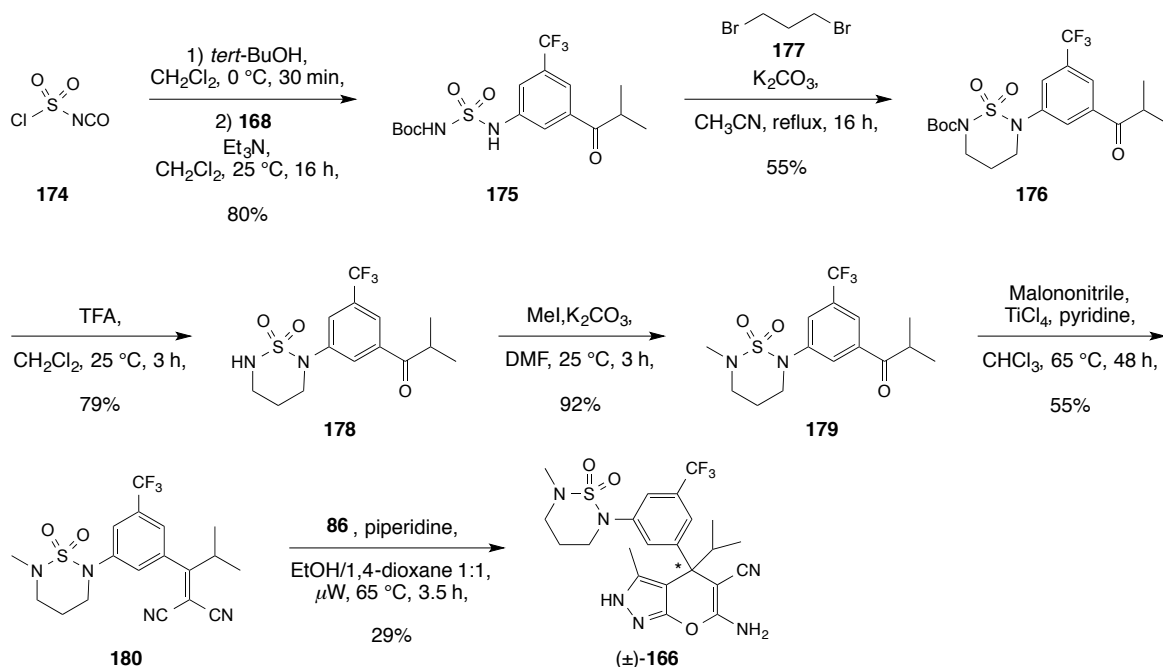
In contrast to the series of ligands discussed above, the sultam moiety could not be directly attached to **124c** *via* a Buchwald-Hartwig amination.^[141] Instead, aniline **168** was

2. Identification of Pyrazolopyran-based Inhibitors for SHMT and Their Primary Optimization

synthesized in two-steps from **124c** (Scheme 16), which was reacted with *tert*-butyl carbamate (**169**) to give Boc-protected intermediate **170** in 40% yield. A subsequent cleavage of the Boc-group using trifluoroacetic acid (TFA) yielded **168**. The sultam moiety was generated by reaction of aniline **168** with 4-chloro-butane-1-sulfonyl chloride (**171**) in presence of Et₃N. A sizable reaction time was required for a complete conversion of **168**, and **172** was isolated in 47% yield. The latter underwent Knoevenagel condensation to **173** and core formation, yielding (±)-**165** (Scheme 16).



Scheme 16. Synthesis of sultam (±)-**165**.

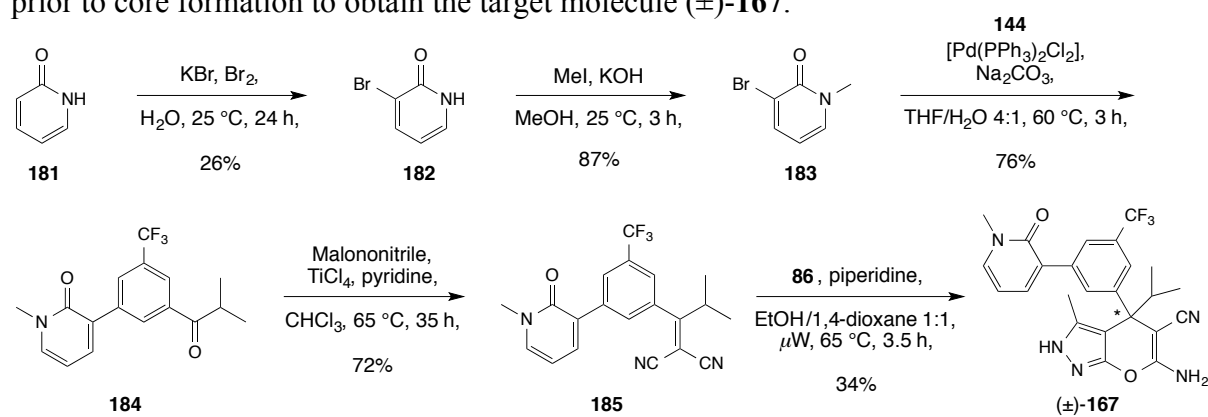


Scheme 17. Synthesis of thiadiazinane (±)-**166**.

2. Identification of Pyrazolopyran-based Inhibitors for SHMT and Their Primary Optimization

The synthesis of thiadiazinane (\pm)-**166** started with the addition of *tert*-butanol onto the isocyanate **174** followed by the nucleophilic attack of aniline **168** onto the sulfonyl chloride moiety leading to sulfamoyl **175** in good yield (Scheme 17). The thiadiazinane scaffold in **176** was formed by a di-N-alkylation of **175** with 1,3-dibromopropane (**177**)/K₂CO₃. Boc-cleavage gave **178** that was N-methylated to **179**, which was transformed *via* **180** to (\pm)-**166**.

The synthesis of *N*-methylpyridone (\pm)-**167** is straightforward. First, 2-pyridone (**181**) was selectively brominated at the 3-position^[143] in a modest yield, then *N*-methylation of **182** led to **183** in 87% yield (Scheme 18). Afterwards, a Suzuki-Miyaura cross-coupling between pinacol boronate **144** and pyridone **183** gave **184** that was readily transformed to dinitrile **185** prior to core formation to obtain the target molecule (\pm)-**167**.



Scheme 18. Synthesis of *N*-methylpyridone (\pm)-**167**.

The last ligand (\pm)-**186** of the series was designed to interact with Tyr63 *via* its sulfonamide moiety. This latter was installed on an azetidine so that it was finely oriented and in close proximity to Tyr63 (Figure 41).

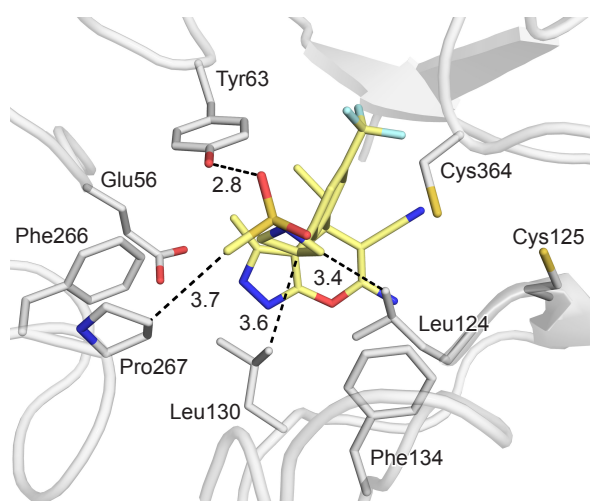
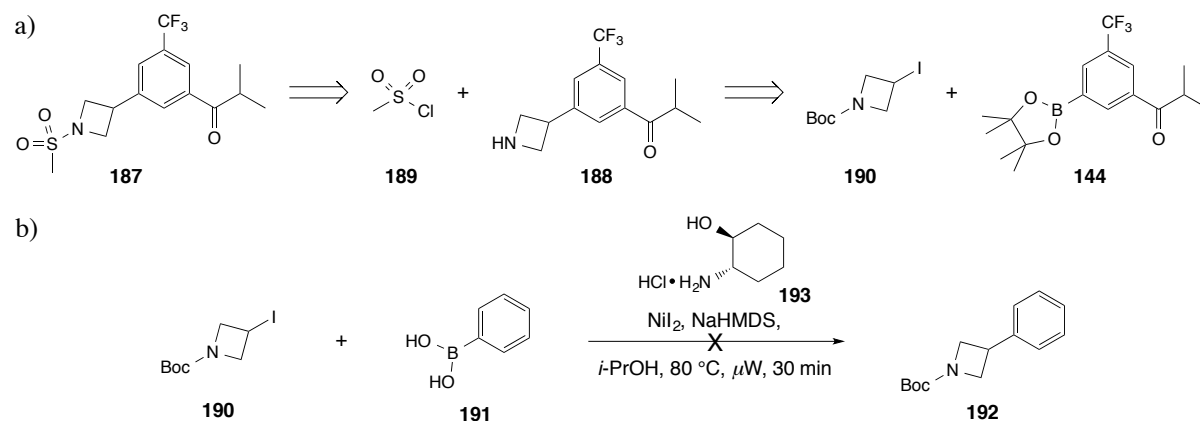


Figure 41. Proposed binding mode of ligand (+)-**186** within the active of *Pv*SHMT (PDB code 4TMR, 2.6 Å) as modeled with MOLOC. PLP is omitted for clarity. Distances are given in Å. Color code: C_{*Pv*SHMT} grey, C₍₊₎₋₁₈₆ gold, F cyan, N blue, O red, S yellow.

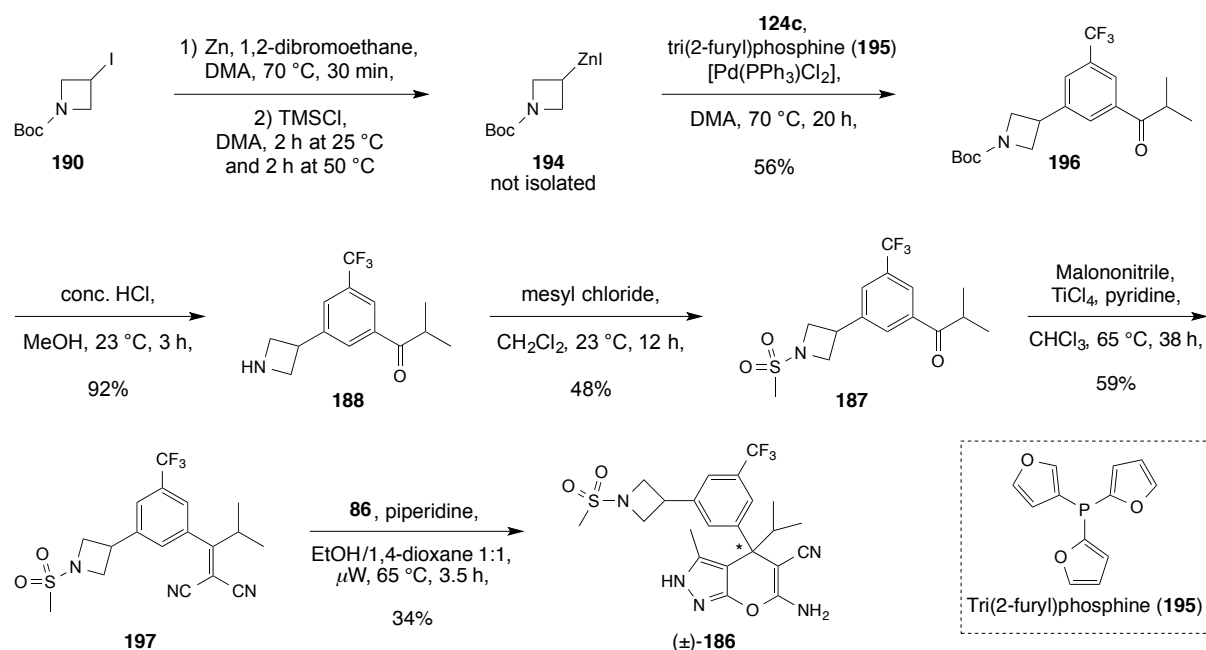
In the retrosynthetic analysis (Scheme 19a), it was envisioned that the bicyclic scaffold **187** could be obtained by reacting the azetidine moiety of **188** with mesyl chloride (**189**). The crucial step in this synthesis was the formation of the C_{sp2}–C_{sp3} bond between the aryl ring and the terminal azetidine. This can potentially be achieved *via* a Suzuki-type cross-coupling between the commercially available Boc-protected iodoazetidine **190** and the borylated building block **144**. Duncton *et al.* reported in 2008 the successful coupling of **190** with phenylboronic acid (**191**) and could isolate **192** in 51% yield (Scheme 19b).^[144] In this approach, the authors employed an active catalyst that is furnished by mixing NiI₂ and *trans*-2-aminocyclohexanol (**193**), previously reported by González-Bobes and Fu.^[145] However, it was not possible to reproduce the exact same reaction despite several attempts. Therefore, a different approach was pursued to realize the cross-coupling (Scheme 20).



Scheme 19. a) Retrosynthesis of bicyclic scaffold **187**. b) Attempt to reproduce the result reported by Duncton *et al.*^[144]

Gratifyingly, the alkyl–aryl coupling was successfully performed by employing a Negishi-type reaction (Scheme 20).^[146,147] Iodoazetidine **190** was converted to its organozinc derivative **194**, which was directly reacted with bromoaryl **124c** in presence of [Pd(PPh)₃Cl₂] and an additional phosphine-based ligand **195** (Scheme 20). That way, **196** was obtained in good yield, deprotected to **188** and reacted with mesyl chloride (**189**) to install the SO₂Me moiety onto the azetidine ring in **187**. The desired ligand (±)-**186** was subsequently obtained *via* dinitrile **197**.

2. Identification of Pyrazolopyran-based Inhibitors for SHMT and Their Primary Optimization



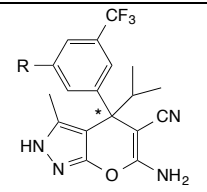
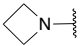
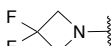
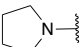
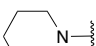
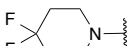
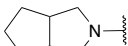
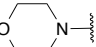
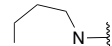
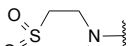
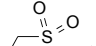
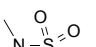
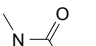
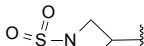
Scheme 20. Successful alkyl–aryl coupling and subsequent synthesis of (±)-**186**.

2.4.2. In Vitro Biological Activities

Among the thirteen ligands of the series, eight displayed cell-based activity below 100 nM (Table 6). The fluoropiperidine ((±)-**156**) and morpholine ((±)-**158**) analogues were the most effective with EC_{50} values of 25 and 26 nM, respectively. Furthermore, the high cellular potency of the fused *N*-heterocyclic derivatives (±)-**153–158** suggest the establishment of good hydrophobic interactions with the apolar surface at the exit of the *p*A_{BA} channel, formed by Leu124, Leu130, Phe134, and Val141 within the active site as anticipated by modeling (*vide supra*). Overall, good inhibition of *Pf*SHMT was observed with this series of ligands (IC_{50} = 84–398 nM). However, IC_{50} values measured against *At*SHMT correlated much better with the data from the cell-based assay (Table 6). Attempts to gain affinity by interacting with Cys364 apparently remained unsuccessful ((±)-**165–167**) according to both EC_{50} and IC_{50} values. Whereas, sulfone (±)-**160** and sulfonamide (±)-**186** gave both promising EC_{50} (65 nM) and IC_{50} values (*Pf*SHMT: 127 and 84 nM; *At*SHMT: 43.3 and 31.5 nM, respectively), which is presumably the result of favorable H-bonding interactions with Tyr63 as suggested by modeling (Figure 41). Despite the replacement of the thienyl ring that was incorporated in the previous series of ligands, the microsomal stability of these *N*-heteroalicyclic analogues still remained poor (Table 6).

2. Identification of Pyrazolopyran-based Inhibitors for SHMT and Their Primary Optimization

Table 6. Biological activities and microsomal half-lives of ligands (±)-152–160, (±)-165–167, and (±)-186.

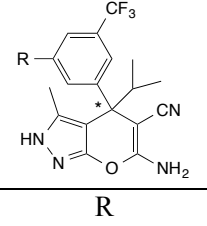
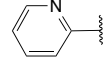
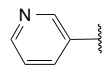
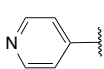
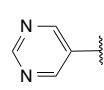
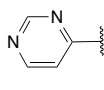
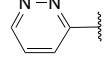
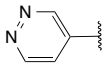
Cpd.		EC ₅₀ <i>Pf</i> NF54 [nM]	IC ₅₀ <i>Pf</i> SHMT ± SD [nM] ^[a]	IC ₅₀ <i>At</i> SHMT [nM]	t _{1/2} [min] ^[b]
	R				
(±)-152		350	192 ± 5	37.6	3
(±)-153		44	160 ± 6	33.2	n.d. ^[c]
(±)-154		56	85 ± 4	30.5	n.d.
(±)-155		59	142 ± 1	25.4	2
(±)-156		25	307 ± 14	17.7	3
(±)-157		49	246 ± 8	n.d.	2
(±)-158		26	179 ± 9	n.d.	3
(±)-159		193	137 ± 8	37.6	n.d.
(±)-160		65	127 ± 8	43.3	3
(±)-165		454	n.d.	21.5	n.d.
(±)-166		523	229 ± 6	n.d.	n.d.
(±)-167		610	398 ± 31	n.d.	4
(±)-186		65	84 ± 1	31.5	n.d.

[a] Standard deviations are given. [b] *In vitro* metabolic stability measured in human liver microsomes. [c] n.d. = not determined.

2.5. Discovery of Potent Aromatic *N*-Heterocyclic Ligands

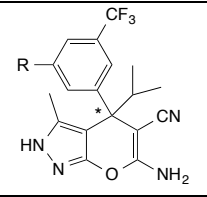
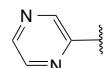
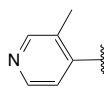
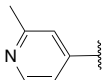
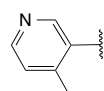
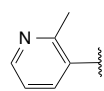
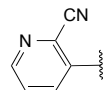
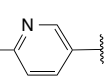
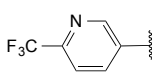
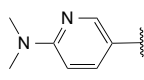
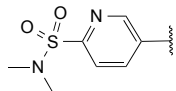
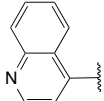
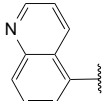
In parallel to the set of ligands discussed in the previous section, an extended series of inhibitors bearing a variety of aromatic *N*-heterocycle ((±)-**198–216**) were synthesized according to the route described in Scheme 10. The SAR against *Pf*SHMT was rather flat, on the contrary, most of the ligands inhibited the *Pf*NF54 strain in the low nanomolar range (Table 7). While the 2-pyridyl (±)-**198** displayed an acceptable EC₅₀, 3- and 4-pyridyl ligands ((±)-**199** and (±)-**200**) provided a dramatic potency improvement, down to desired EC₅₀ values in the single-digit nanomolar range (4.8 and 3.2 nM, respectively), and reached a similar efficacy level as the initial hit (±)-**67**. Methylation at various position of the pyridyl ring was well tolerated and high efficacy could be retained with ligands (±)-**206–208** (Table 7). On the other hand, larger substituents as in (±)-**210** and (±)-**212–214** were detrimental to activity. Finally, low nanomolar efficacy was also observed with quinoline moieties in (±)-**215** and (±)-**216**. Target assays towards *At*SHMT supported well the cell-based data, with affinities in the single-digit nanomolar range too (Table 7).

Table 7. Biological activities and microsomal half-lives of ligands (±)-**198–216**.

Cpd.		EC ₅₀ <i>Pf</i> NF54 [nM]	IC ₅₀ <i>Pf</i> SHMT ± SD [nM] ^[a]	IC ₅₀ <i>At</i> SHMT [nM]	<i>t</i> _{1/2} [min] ^[b]
(±)- 198		115	188 ± 5	n.d. ^[c]	5
(±)- 199		4.8	262 ± 6	8.1	7
(±)- 200		3.2	243 ± 14	n.d.	3
(±)- 201		10	547 ± 5	n.d.	n.d.
(±)- 202		27	n.d.	n.d.	n.d.
(±)- 203		125	132 ± 5	n.d.	n.d.
(±)- 204		18	249 ± 3	n.d.	n.d.

2. Identification of Pyrazolopyran-based Inhibitors for SHMT and Their Primary Optimization

Table 7 continued.

Cpd.		EC ₅₀ <i>Pf</i> NF54 [nM]	IC ₅₀ <i>Pf</i> SHMT ± SD [nM] ^[a]	IC ₅₀ <i>At</i> SHMT [nM]	t _{1/2} [min] ^[b]
R					
(±)-205		52	201 ± 9	n.d.	n.d.
(±)-206		4.2	163 ± 3	4.2	n.d.
(±)-207		5.1	129 ± 5	12.6	< 2
(±)-208		6.4	n.d.	1640 ^[d]	n.d.
(±)-209		14	196 ± 9	28.5	n.d.
(±)-210		288	226 ± 6	n.d.	4
(±)-211		66	130 ± 2	8.2	n.d.
(±)-212		386	192 ± 2	n.d.	n.d.
(±)-213		709	129 ± 10	n.d.	n.d.
(±)-214		214	340 ± 3	n.d.	n.d.
(±)-215		10	160 ± 2	n.d.	n.d.
(±)-216		18	143 ± 2	n.d.	n.d.

[a] Standard deviations are given. [b] *In vitro* metabolic stability measured in human liver microsomes. [c] n.d. = not determined. [d] Outlier value.

The cytotoxicity of (±)-**199** and (±)-**200** was assessed on human HepG2 cell line (human liver carcinoma) (IC₂₀ (±)-**199** = 18.9 μM) and rat myoblast cell line (L6) (IC₅₀ (±)-**200** = 16.7 μM), respectively. No adverse effects were measured with inhibition values in the high micromolar range. Additionally, the potential inhibition of the human ether-à-go-go-

related gene (hERG) by (\pm)-**199** was investigated. Disruption of hERG has been defined as a marker of potential cardiotoxicity.^[148,149] This gene codes for a cardiac potassium ion channel that is part of an ensemble of ion channels that creates the cardiac action potential at the cellular level. Upon blockage of this channel, a mechanism that essentially corresponds to an elongation of the QT interval (often referred to as Torsade de Pointes (TdP)) (Figure 42) is initiated and can lead to cardiac arrhythmia. Regarding (\pm)-**199**, an IC₅₀ value of 29 μ M was measured, which enabled to exclude cardiotoxicity associated with the pyrazolopyran class of inhibitors.

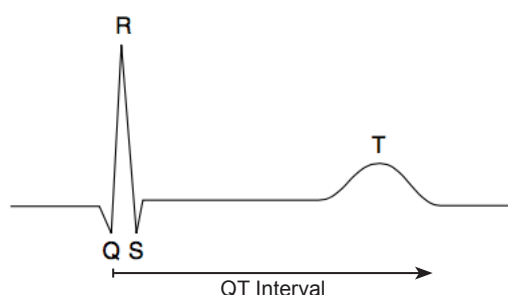


Figure 42. Representation of an electrocardiogram on the surface of the heart. The time from point Q to point T is called QT interval (from depolarization to repolarization).

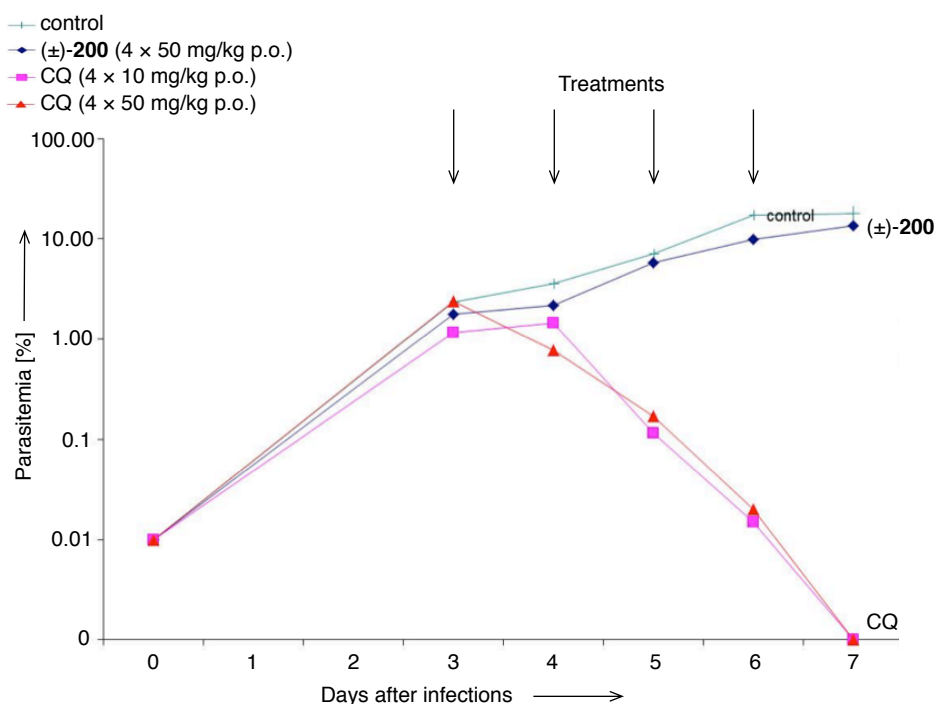


Figure 43. Therapeutic efficacy of (\pm)-**200** against *P. falciparum* Pf3D7^{0087/N9}. The arrows indicate the days of treatment in the 4-day test by Peters.^[139] Values are the level of parasitemia in peripheral blood of n = 2 mice/group. CQ = chloroquine (**14**).

The potential of these ligands, however, was greatly diminished by their very short half-life when incubated with human liver microsomes (< 10 min) (Table 7). Despite this liability, the antiplasmodial activity of (±)-**200** was further studied in a *P. falciparum* SCID mouse model at 4 × 50 mg/kg (p.o.). The rather low 25% parasitemia reduction is presumably the result of poor exposure due to high metabolic instability of (±)-**200** (Figure 43 and Appendix, Section 9.3, Tables 35 and 36).

2.6. Summary on the Hit Identification and Primary Optimization

An HTS, using a BASF compounds library, enabled to identify *A. thaliana* SHMT inhibitors with remarkably high efficacy against the *Pf*NF54 strain. A primary optimization of these pyrazolopyran-based ligands was undertaken in order to identify compounds with improved metabolic stability. Accordingly, three distinct series of ligands were designed, synthesized, and tested in target- and cell-based assays.

The labile ester moiety in (±)-**67** and (±)-**69** was replaced by selected bioisosteres, however, the measured activities remained in the two-digit nanomolar range at best. An extensive SAR study looking at the substituents of the pyrazolopyran core confirmed that the combination methyl/*iso*-propyl on the pyrazole ring and on the stereogenic center, respectively, gave the best results *in vitro*. A major step forward was made by replacing the nitrile moiety on the phenyl ring departing from the core by a CF₃ group, which provided up to 10-fold potency improvement.

A series of *N*-heteroalicyclic analogues displayed high cellular potency, suggesting the establishment of good hydrophobic interactions with the apolar surface at the exit of the *p*ABA channel. Importantly, single-digit nanomolar efficacy was measured for five ligands bearing distinct pyridyl moieties. No cytotoxicity, neither cardiotoxicity, was detected for this class of molecules. The potent ligand (±)-**200** was studied in a *Pf*SCID mouse model at 4 × 50 mg/kg (p.o.), however, only 25% of parasitemia reduction was recorded, which is possibly the result of poor exposure due to high metabolic instability.

3. Conformational Aspects in the Design of Inhibitors for SHMT: Biphenyl, Aryl Sulfonamide, and Aryl Sulfone Motifs

The following results were published in *Chemistry – A European Journal*.^[150] The target-based assays on *Pf*SHMT and *At*SHMT were performed in the group of Dr. Pimchai Chaiyen by Dr. Ubolsree Leartsakulpanich and Aritsara Jaruwat (National Center for Genetic Engineering and Biotechnology, Thailand), and by Dr. Raphael Aponte (BASF-SE), respectively. The cell-based assays were performed in the group of Dr. Matthias Rottmann (Swiss Tropical and Public Health Institute, Basel) by Anja Schäfer. The co-crystal structures with *Pv*SHMT were solved by Dr. Penchit Chitnumsub and Wanwipa Ittarat (National Center for Genetic Engineering and Biotechnology, Thailand). The metabolic stability measurements were performed by Dr. Karen L. White (Monash University, Australia). Single molecule X-ray crystal structures were resolved by Dr. Nils Trapp. Kerstin Mark and Michelle Frei contributed with a Semester project and her Master thesis, respectively, to the synthesis of most of the aryl sulfonamide ligands.

3. Conformational Aspects in the Design of Inhibitors for SHMT: Biphenyl, Aryl Sulfonamide, and Aryl Sulfone Motifs

A large repertoire of tools is available to assist medicinal chemists in their drug development efforts. It covers a broad range of predictions, from pK_a or $\log D$ calculations to more intricate predictions of preferential ligand docking modes by molecular modeling or protein–ligand binding energies by free energy calculations.^[151–153] In order to minimize the entropic penalty caused by the change in conformation of a given ligand when it binds to a receptor, it is crucial that the preferred conformations of bound and unbound ligands are closely related.^[154,155] Indeed, a difference in conformational energy between free and bound state of $\Delta\Delta G_{\text{unbound}\rightarrow\text{bound}} \approx 1.4 \text{ kcal mol}^{-1}$ already translates into a 10-fold decrease in Gibbs binding energy.^[137,156] Conformational preferences of small molecules are best retrieved by databases mining. In this respect, the Cambridge Structural Database (CSD), reaching more than 875 000 entries in 2017,^[157–162] together with the Protein Data Bank (PDB)^[163,164] constitute absolute gold mines. Conformational analysis based on crystallographic information was nicely illustrated by Brameld *et al.*,^[137] who reported a reference study on motifs commonly used in medicinal chemistry. Lately Cottrell *et al.* completed this search by looking at saturated rings.^[165]

Over the course of the optimization program of SHMT inhibitors, two series of ligands bearing either a biphenyl or aryl sulfonamide/aryl sulfone motif were designed with the intention to maximize the hydrophobic interactions within the *p*ABA channel, such as the *N*-heteroalicyclic analogues discussed in Section 2.4. The profound effect of their molecular conformations on the binding geometry and biological activity is discussed in the following.

3.1. Biphenyl Series

Biphenyl corresponds to the motif the most frequently used in drug design and its substitution pattern governs its preferred conformation. In other words, the geometry of a biphenyl motif can be tuned by intramolecular interactions. Alteration of the substitution pattern can lead to enhanced protein–ligand interaction by adjusting the two rings and the attached exit vectors in a definite way. Additionally, the overall conformation of a molecule can be drastically influenced by incorporation of heteroatoms into its backbone, for instance by sulfur–lone pair interaction (chalcogen bonding).^[166]

3. Conformational Aspects in the Design of Inhibitors for SHMT: Biphenyl, Aryl Sulfonamide, and Aryl Sulfone Motifs

3.1.1. Torsion Angles of Biphenyl Fragments and their Influence on Cellular Efficacy

Seven *ortho*-substituted biphenyls ((\pm)-**217**–**223**) were prepared according to Scheme 10 to enhance the hydrophobic interactions with the apolar residues lining the *p*ABA channel. In the proposed binding pose of ligand (+)-**223** within the *Pv*SHMT active site, the terminal phenyl ring is in close proximity to Leu124, Leu130, and Phe134, and the CF₃ moiety is nicely surrounded by the side chain of Tyr63, Leu130, Phe266, and Pro267 (Figure 44).

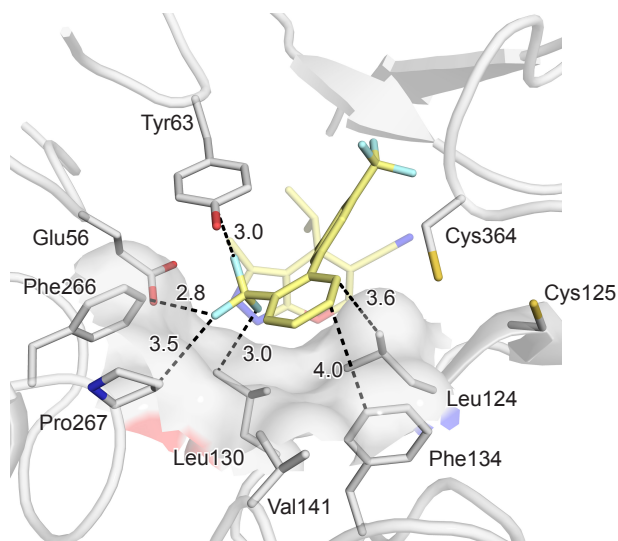
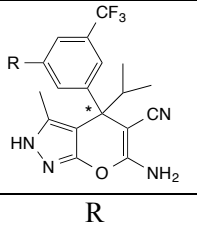
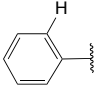
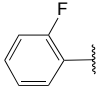
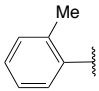
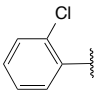
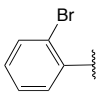
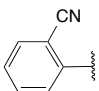
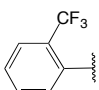


Figure 44. Proposed binding mode of ligand (+)-**223** within the active of *Pv*SHMT (PDB code 4TMR, 2.6 Å) as modeled with MOLOC. PLP is omitted for clarity. Distances are given in Å. Color code: C_{*Pv*SHMT} grey, C₍₊₎₋₂₂₃ gold, F cyan, N blue, O red, S yellow.

Nevertheless, the binding affinities for *Pf*SHMT were in disagreement with the modeling (Table 8). In this assay, the unsubstituted analogue (\pm)-**217** displayed the best affinity of the series (IC₅₀ = 111 nM), whereas a moderate activity was measured for (\pm)-**221** (IC₅₀ = 471 nM). Stronger inhibitions were measured on *At*SHMT (Table 8). In this assay, (\pm)-**218** gave the best result with a significant IC₅₀ value of 7.3 nM, and (\pm)-**221** was again the weakest binder of the series (IC₅₀ = 32.0 nM). Overall, a rather flat SAR was obtained in both enzymatic assays.

3. Conformational Aspects in the Design of Inhibitors for SHMT: Biphenyl, Aryl Sulfonamide, and Aryl Sulfone Motifs

Table 8. Biological activities of biphenyl analogues (\pm)-**217**–**223**.

Cpd.		EC ₅₀ <i>Pf</i> NF54 [nM]	IC ₅₀ <i>Pf</i> SHMT \pm SD [nM] ^[a]	IC ₅₀ <i>At</i> SHMT [nM]	clog <i>P</i> ^[b]	Biphenyl Median τ [°] ^[c]
	R					
(\pm)- 217		18	111 \pm 5	18.6	5.2	30.3
(\pm)- 218		20	144 \pm 0	7.3	4.9	43.2
(\pm)- 219		27	263 \pm 11	30.9	5.3	55.5
(\pm)- 220		51	165 \pm 4	20.9	5.5	51.3
(\pm)- 221		81	471 \pm 8	32.0	5.5	56.8
(\pm)- 222		356	289 \pm 13	26.2	4.7	46.1
(\pm)- 223		665	330 \pm 22	18.5	6.0	71.8

[a] Standard deviations are given. [b] Calculated with ACD/Percepta (GALAS prediction model) from ACD/Labs, release 2016.2. [c] Derived from the CSD searches in CSD 5.38 (February 2017).

The cell-based data contrast with these results (Table 8). Differences up to 37-fold were measured between the best ligand of the series (EC₅₀ (\pm)-**217** = 18 nM) and the weakest one (EC₅₀ (\pm)-**223** = 665 nM). No direct correlation between lipophilicity (clog*P*) and efficacy is distinguishable. However, the nature of the *ortho*-substituent exerted a significant influence on cellular potency, as an increase of its size led to considerable decrease in antiparasitic efficacy. The torsion angle (τ) of biphenyl motifs in the CSD and the PDB were examined^[167] in order to rationalize these observations. As foreseen, the smallest torsion angles retrieved belong to unsubstituted biphenyls (Table 8 and Figure 45a), while introduction of any substituent onto one *ortho*-position of the biphenyl motif results into a significant increase of the torsion angle (Figure 45b). It is noteworthy to point out that differences may exist between the solid and solution phase, and biphenyls without any *ortho*-substituent are particularly sensitive to crystal packing effect.^[168] As shown in Figure 45a, the torsion angles for unsubstituted biphenyl converge towards 35°, a value that is lower than the average torsion

3. Conformational Aspects in the Design of Inhibitors for SHMT: Biphenyl, Aryl Sulfonamide, and Aryl Sulfone Motifs

angle (44°) in the gas phase.^[168] Introduction of any substituent leads to values above 50° (Figures 45b and 46), with the higher torsion angle retrieved for *ortho*-CF₃ biphenyl (71.8°), although some caution is advised as only 6 structures were found in the CSD. Additionally, a small molecule X-ray crystal structure recorded for (\pm)-**221** displayed a torsion angle of 57.5° (Figure 47) that is in good agreement with the CSD search.

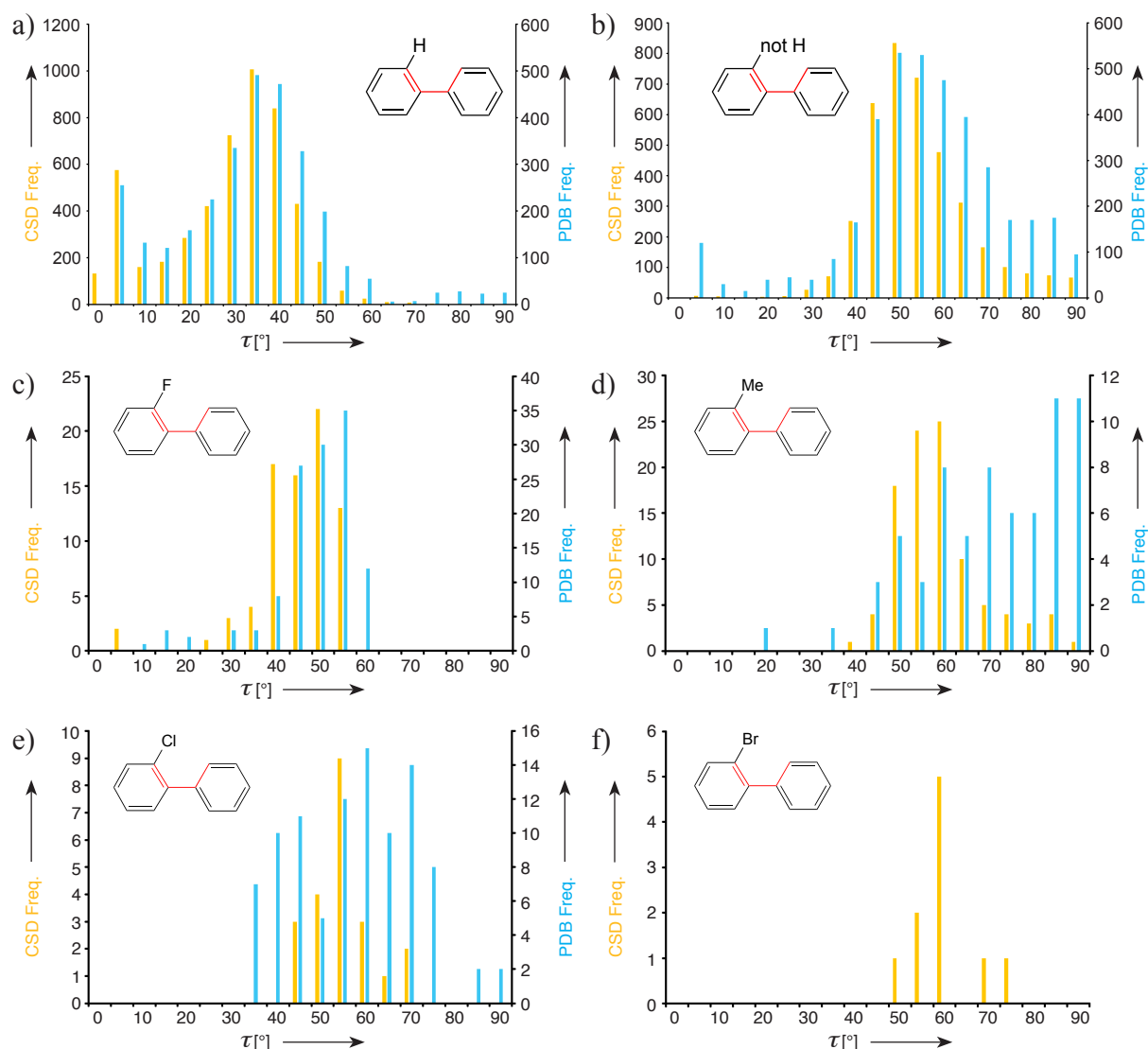


Figure 45. Torsion angle histogram derived from the CSD ligands (yellow) and bound ligands in the PDB (blue). a) Biphenyls without any *ortho*-substituent; b) *ortho*-Substituted biphenyls; c) *ortho*-F substituted biphenyls; d) *ortho*-Me substituted biphenyls; e) *ortho*-Cl substituted biphenyls; f) *ortho*-Br substituted biphenyls (no structure found in the PDB).

3. Conformational Aspects in the Design of Inhibitors for SHMT: Biphenyl, Aryl Sulfonamide, and Aryl Sulfone Motifs

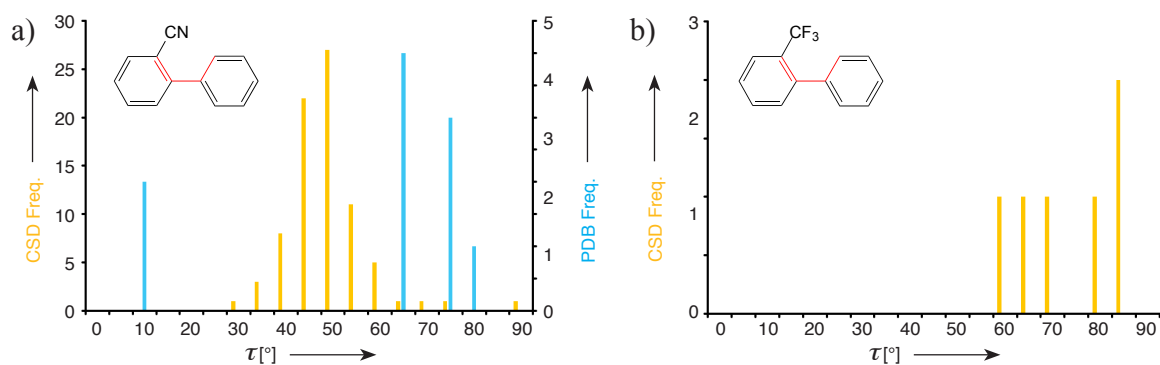


Figure 46. Torsion angle histogram derived from the CSD ligands (yellow) and bound ligands in the PDB (blue). a) *ortho*-CN substituted biphenyls and b) *ortho*-CF₃ substituted biphenyls (no structure found in the PDB).

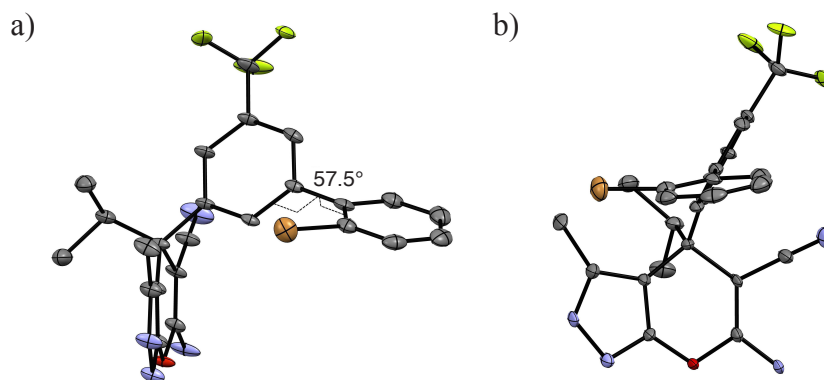


Figure 47. a) Biaryl torsion angle in (±)-**221**. b) Front view of (±)-**221**. H-atoms and disorder are omitted for clarity.

A potential energy scan (PES) was performed at the B3LYP/cc-pVDZ level of theory (in water with polarizable continuum solvent model) using Gaussian 09^[169] (Figure 48a) to complement the database searches. The most favorable biphenyl torsion angles for all compounds range from 36.5° to 62.0°, in agreement with the CSD search results. Additionally, the energy gap between the least stable, co-planar structure, and the most stable conformations increases with the size of the *ortho*-substituent. For example, for (±)-**217** without an *ortho*-substituent, the energy difference between these two conformations is 2.4 kcal mol⁻¹, whereas it is calculated as 9.4 kcal mol⁻¹ for the CF₃ derivative (±)-**223**. Furthermore, the computed rotational barriers correlate with the efficacy values (Figure 48b).

3. Conformational Aspects in the Design of Inhibitors for SHMT: Biphenyl, Aryl Sulfonamide, and Aryl Sulfone Motifs

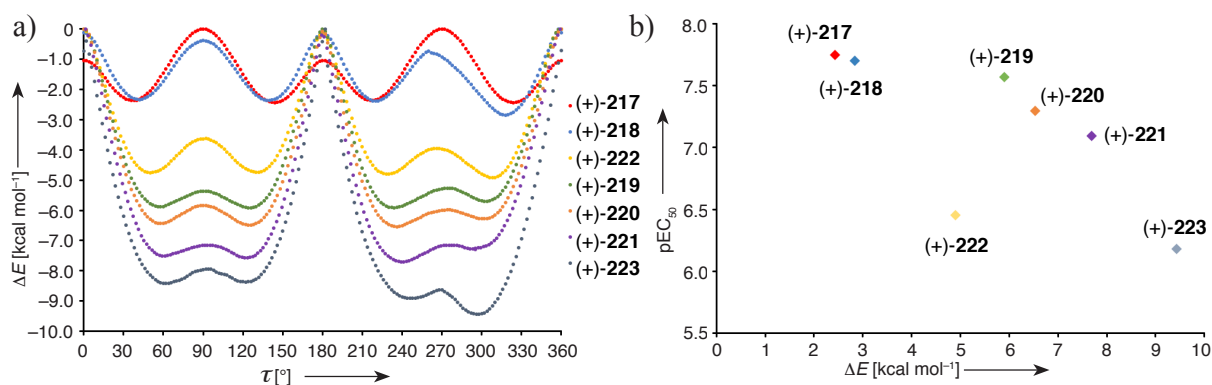


Figure 48. a) Energy profile at the B3LYP/cc-pVDZ level of theory in H₂O plotted against the dihedral angle of the biphenyl moiety for (+)-217–223. b) pEC₅₀ of (±)-217–223 plotted against their respective torsion barrier. pEC₅₀ = $-\log(\text{EC}_{50})$.

It is likely that the cell-permeation of the ligands was influenced by the conformation at the biphenyl motif, resulting in discrepancies in cell-based efficacy. Permeability is defined as the velocity of drug passage through a biological membrane barrier.^[170] It occurs *via* passive diffusion through the lipid bilayer of a cell membrane, carrier proteins (transporters), and channel proteins.^[171,172] Passive diffusion is the main contributor to permeation and is poorly sensitive (or not sensitive at all) to the stereochemistry of a drug, in contrast, configuration and conformation matters with transporters.^[171] Due to their complexity, the number of transporters in *P. falciparum* has not been precisely defined yet. A first estimation was made by Gardner *et al.*, who reported around 50 transporters.^[118] Later, Martin *et al.* exploited a bioinformatics analysis to refine this number to more than 100 transport proteins.^[173] Interestingly, transporters can be involved in the resistance mechanism towards a drug.^[174] For instance, the *P. falciparum* chloroquine resistant transporter (*PfCRT*) is responsible for the resistance developed towards chloroquine (**14**).^[175,176] Concerning ligands (±)-217–223, it is conceivable that their biphenyl motif need to adopt a co-planar conformation to facilitate the penetration into the cell. Hence, ligands with a small moiety at the *ortho*-position lead to better efficacy. In a study involving inhibitors of the ABCC2/MRP2 transporters, it was reported that the affinity for the transporter was enhanced by increasing the torsion angle of the considered biphenyl moiety.^[177] However, such an influence of the torsion angle on cell-based efficacy has not been disclosed so far. It is also possible that difference in serum albumin binding occurred across this series of inhibitors, nonetheless, only 0.5% of ALBUMAX® II was implemented in the assay and it is therefore rather unlikely that the discrepancies in efficacy arose from protein binding. To conclude, it is important to emphasize that a number of factors

3. Conformational Aspects in the Design of Inhibitors for SHMT: Biphenyl, Aryl Sulfonamide, and Aryl Sulfone Motifs

affect cell-permeation and that the measured cellular efficacy is certainly not solely governed by the torsion angle of the biphenyl motif.

3.1.2. Co-crystal Structures: Elucidation of Dipolar Interactions with Tyr63

Four co-crystal structures of either (\pm)-**218**, (\pm)-**219**, (\pm)-**220**, or (\pm)-**222** with *Pv*SHMT were solved at 2.5, 2.4, 2.2, and 2.6 Å resolution, respectively, and belong to the *C*2 space group (Figure 49).

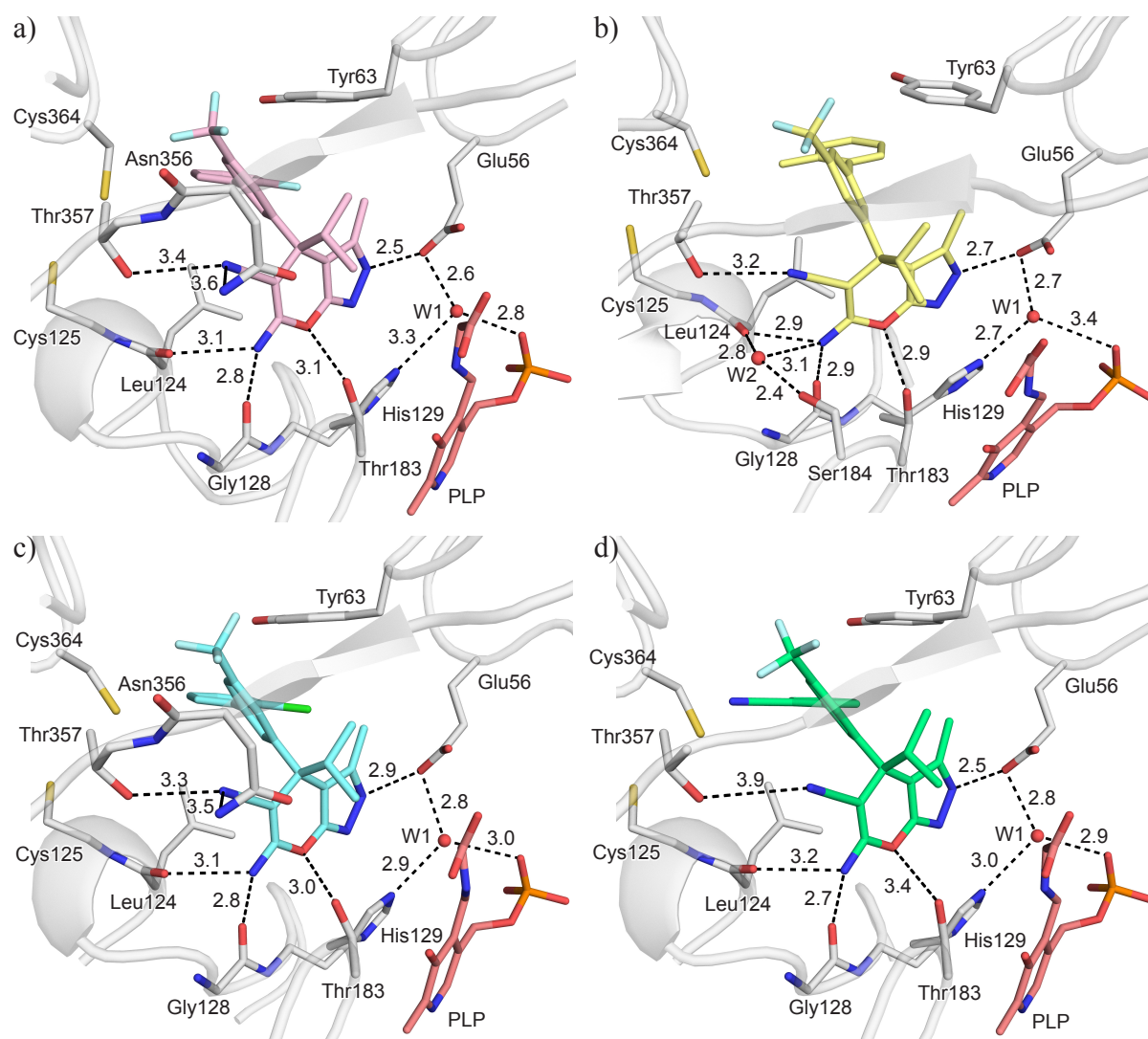


Figure 49. Co-crystal structures showing the polar protein–ligand interactions of *Pv*SHMT (grey) and pyrazolopyran: a) (+)-**218** (pink; PDB code 5XMS, 2.5 Å); b) (+)-**219** (gold; PDB code 5XMU, 2.4 Å); c) (+)-**220** (cyan; PDB code 5XMV, 2.2 Å); d) (+)-**222** (lime; PDB code 5XMT, 2.6 Å). Water molecules (W1 and W2) are represented as red spheres. Distances are given in Å. Color code: C_{protein} grey, $C_{(+)-218}$ pink, $C_{(+)-219}$ gold, $C_{(+)-220}$ cyan, $C_{(+)-222}$ lime, C_{PLP} salmon, Cl green, F light cyan, N blue, O red, P orange, S yellow.

3. Conformational Aspects in the Design of Inhibitors for SHMT: Biphenyl, Aryl Sulfonamide, and Aryl Sulfone Motifs

The binding mode of these inhibitors remained unchanged compared with previous PvSHMT–ligand complexes (*vide supra*). A H-bonding network maintains the pyrazolopyran core strongly attached into the pterin binding pocket through interactions with residues Glu56, Leu124, Gly128, and Thr357. The measured torsion angles at the biphenyl motifs (47–62°) are in good agreement with the CSD searches (Table 8) and the optimized structures at the B3LYP/cc-pVDZ level of theory (Figure 50). Although, it is important to note that the optimized structure of (+)-**220** exhibits a dihedral of 58°, which is substantially different than the 49° measured in the complex with PvSHMT.

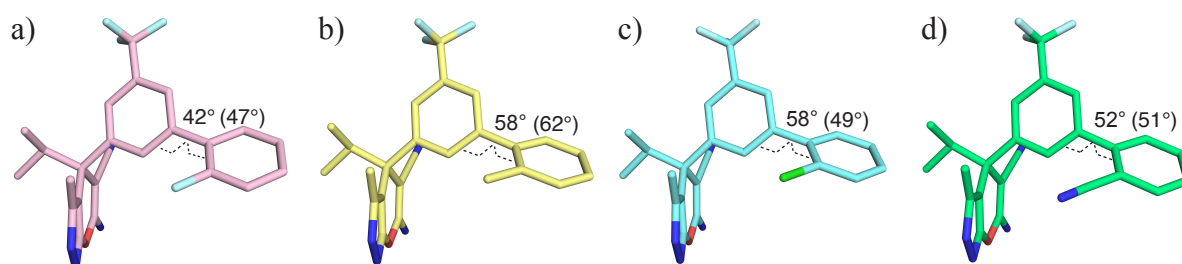


Figure 50. Optimized structures performed with Gaussian 09 using the B3LYP/cc-pVDZ basis set in H₂O of: a) (+)-**218**; b) (+)-**219**; c) (+)-**220**; d) (+)-**222**. The values in parenthesis correspond to the dihedral measured in the respective co-crystal structures.

The striking difference between those four complexes lies in the location of the *ortho*-substituent of the peripheral phenyl ring (Figure 51). The C–F/C–Cl dipoles in (+)-**218** and (+)-**220**, respectively, are aligned in an anti-parallel fashion with respect to the C–O dipole of Tyr63 (Figures 51a and 51c). The fluoride and chloride of (+)-**218** and (+)-**220**, respectively, are in close proximity to Tyr63 and establish local direct interactions. Those *ortho*-substituents are involved in electrostatic interactions of the local dipole associated with the substituent with the nearby local C–H dipole of Tyr63, as in the model championed by Wheeler and Houk.^[178–180] A model, which was further underpinned by quantum-mechanical calculations by Sherill and Parrish,^[181] as well as experimentally.^[182,183] Conversely, the respective methyl and cyano moiety of (+)-**219** and (+)-**222** point towards Cys364 (Figures 51b and 51d). The biphenyl in (+)-**219** adopts a torsion of 62° that precludes the methyl group to lie below Tyr63, otherwise, this exocyclic moiety would be at sub-van der Waals distance to the phenolic ring of Tyr63. Instead of adopting a slightly different conformation to avoid a steric clash, it preferred to flip over to the other side to address apolar interactions with Leu124 and Cys364 (Figure 51b). Similarly, in order to avoid any repulsion of the C≡N triple bond with the arene of Tyr63, the nitrile of (+)-**222** points to Cys364 and lies almost orthogonally to one CH₃ group of Leu124

3. Conformational Aspects in the Design of Inhibitors for SHMT: Biphenyl, Aryl Sulfonamide, and Aryl Sulfone Motifs

(Figure 51d). Those structural distinctions had only minor impact onto target affinities (Table 8). Finally, two water molecules (W1 and W2) solvating Tyr63 can be seen in the co-crystal structures with (+)-**219** and (±)-**220**, respectively (Figures 51b and 51c). W2 is in the vicinity of the chloro-arene of and establishes a weak O–H··· π interaction.^[138]

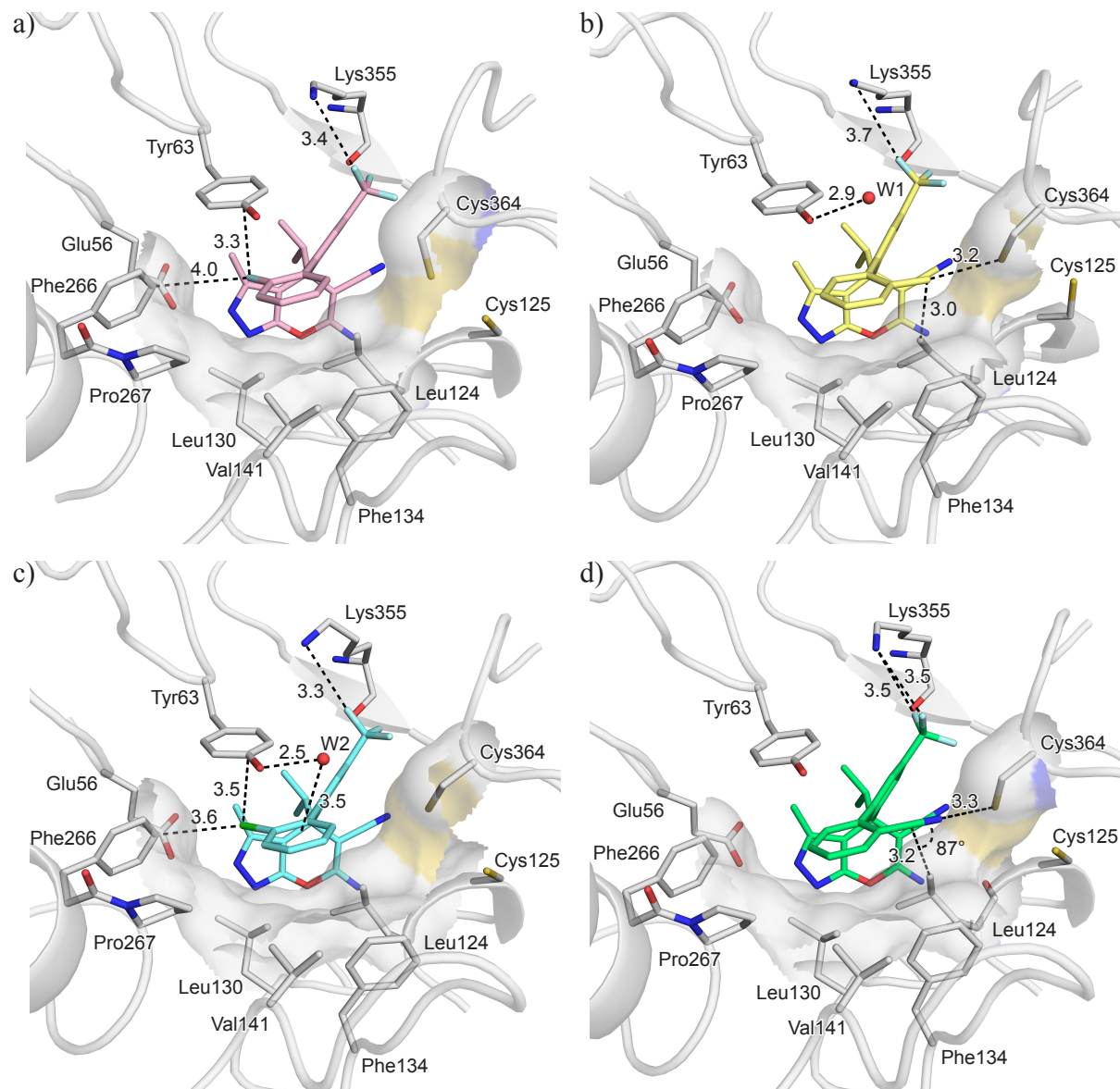


Figure 51. Co-crystal structures showing the hydrophobic protein–ligand interactions of *Pv*SHMT (grey) and pyrazolopyran: a) (+)-**218** (pink; PDB code 5XMS, 2.5 Å); b) (+)-**219** (gold; PDB code 5XMU, 2.4 Å); c) (+)-**220** (cyan; PDB code 5XMV, 2.2 Å); d) (+)-**222** (lime; PDB code 5XMT, 2.6 Å). The surface spans the volume of the *p*ABA channel. Water molecules (W1 and W2) are represented as red spheres. PLP is omitted for clarity. Distances are given in Å. Color code: C_{protein} grey, C₍₊₎₋₂₁₈ pink, C₍₊₎₋₂₁₉ gold, C₍₊₎₋₂₂₀ cyan, C₍₊₎₋₂₂₂ lime, C_{PLP} salmon, Cl green, F light cyan, N blue, O red, S yellow.

3. Conformational Aspects in the Design of Inhibitors for SHMT: Biphenyl, Aryl Sulfonamide, and Aryl Sulfone Motifs

Interestingly, in the second active site of the complex with (+)-**222**, Cys125 and Cys364 were found in their oxidized state (Figure 52). The S–S bond formed presumably after binding of the ligand and most likely results from a prolonged seeding period. Nevertheless, the observed binding mode remains identical to the one with the cysteines in their sulfhydryl state (Figure 49).

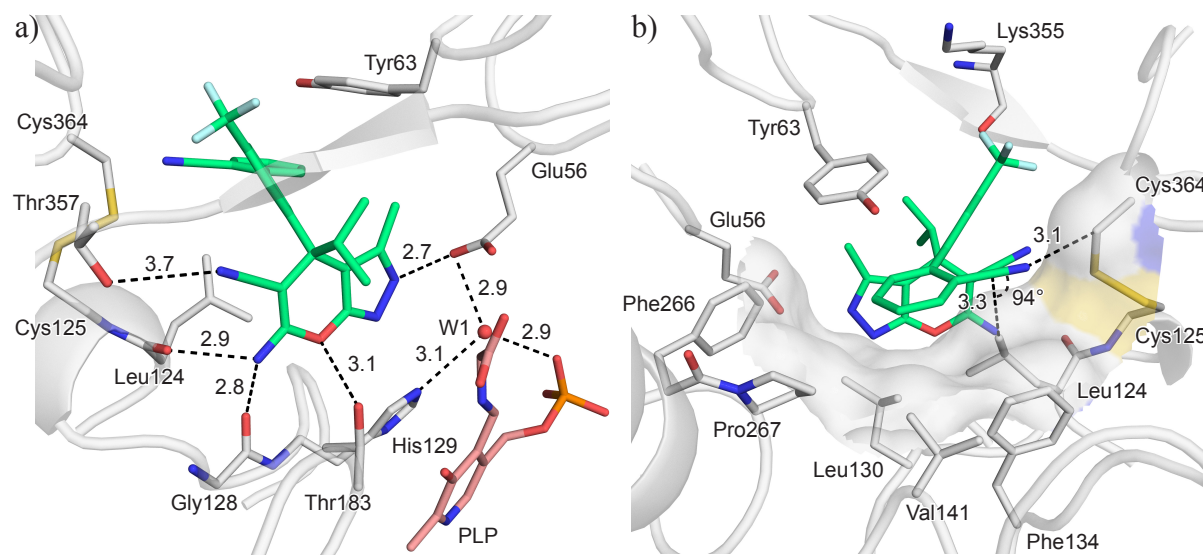


Figure 52. Co-crystal structure (PDB code 5XMT, 2.6 Å) showing the protein–ligand interactions of pyrazolopyran (+)-**222** (lime) and PvSHMT (grey) in the second active site with the disulfide bridge in its oxidized form. a) Polar interactions between (+)-**222** and the protein. b) Apolar interactions involving the biphenyl moiety in the *p*ABA channel. The surface spans the volume of the *p*ABA channel. The water molecule (W1) is represented as a red sphere. PLP is omitted for clarity in b). Distances are given in Å. Color code: C_{protein} grey, C₍₊₎₋₂₂₂ lime, C_{PLP} salmon, F light cyan, N blue, O red, P orange, S yellow.

3.2. Aryl Sulfonamide/Aryl Sulfone Series

Sulfonamide and sulfone motifs are commonly incorporated into small molecule drugs, as illustrated with the antimalarial sulfadoxine (**21**), and in the recently approved active substances Belinostat (**224**, antitumor agent), Apremilast (**225**, treatment of active psoriatic arthritis), Vonoprazan fumarate (**226**, treatment of gastric ulcer), Polmacoxib (**227**, treatment of colorectal cancer), and Selexipag (**228**, treatment of pulmonary arterial hypertension) (Figure 53).^[184,185] It is therefore of paramount importance to have a comprehensive understanding of their preferred conformations.

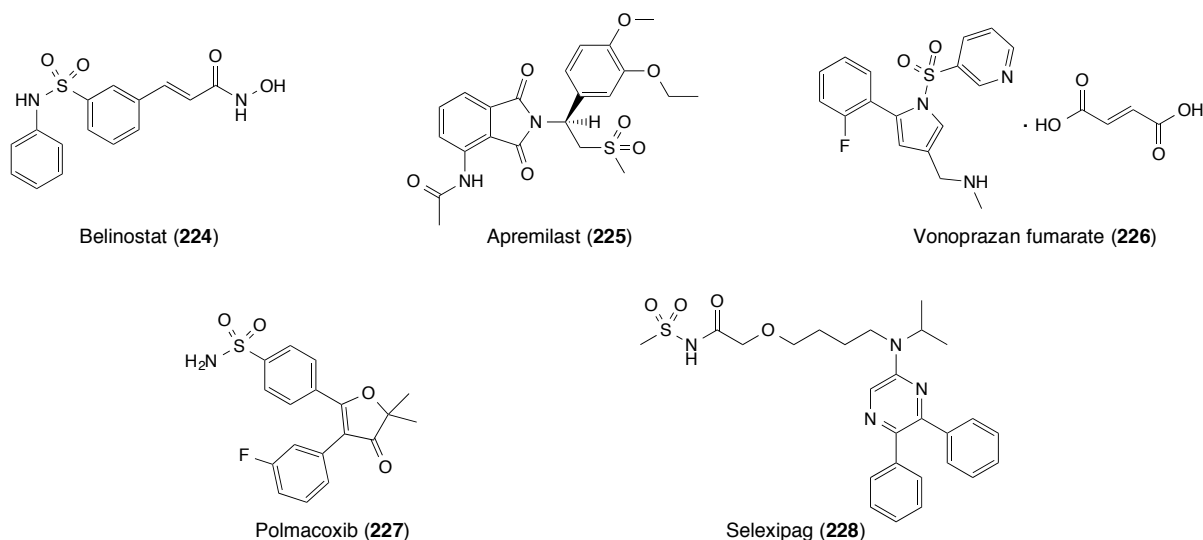


Figure 53. Non-exhaustive list of recently approved drugs containing either a sulfonamide or sulfone moiety.^[184,185]

3.2.1. Conformational Analysis

Aryl sulfonamide and aryl sulfone motifs were incorporated into pyrazolopyran-based inhibitors and a special attention was put during modeling onto the preferred conformation of these moieties. Prior reports have shown that the sulfonamide conformation can considerably affect target affinity as in the development of factor Xa inhibitors.^[186,187] There are two distinct dihedrals in aryl sulfonamides and one in aryl sulfones that determine the conformational preferences of these fragments.

The first is the torsion angle about the C_{sp^2} -S bond in both moieties. In 1986, Beddoes *et al.* described for the first time a conformation for aryl sulfonamide in which the π orbital of the *ipso*-carbon atom bisects the O-S-O angle.^[188] This observation was later confirmed by Brameld *et al.* in an extensive CSD search.^[137] New searches were performed to update the previous results, as the number of structures deposited in the CSD has more than doubled since

3. Conformational Aspects in the Design of Inhibitors for SHMT: Biphenyl, Aryl Sulfonamide, and Aryl Sulfone Motifs

the work by Brameld *et al.*^[137] In both motifs, the $C_{sp^2}-C_{sp^2}-S-N$ torsion angles (τ) converge towards 90° , which is characteristic of the conformation discussed above (Figure 54a). That way, the sulfonyl moiety orients orthogonally its two opposite substituents. Similar results were retrieved from the PDB (Figure 54b), although, a broader distribution was observed resulting from the lower accuracy in the determination of small molecule conformations in macromolecular X-ray structures. This can be accounted for the several ligand poses that can be fitted to electron densities.^[189] These results were underpinned by dihedral scans computed by density functional theory (DFT) (Figures 54c and 54d).

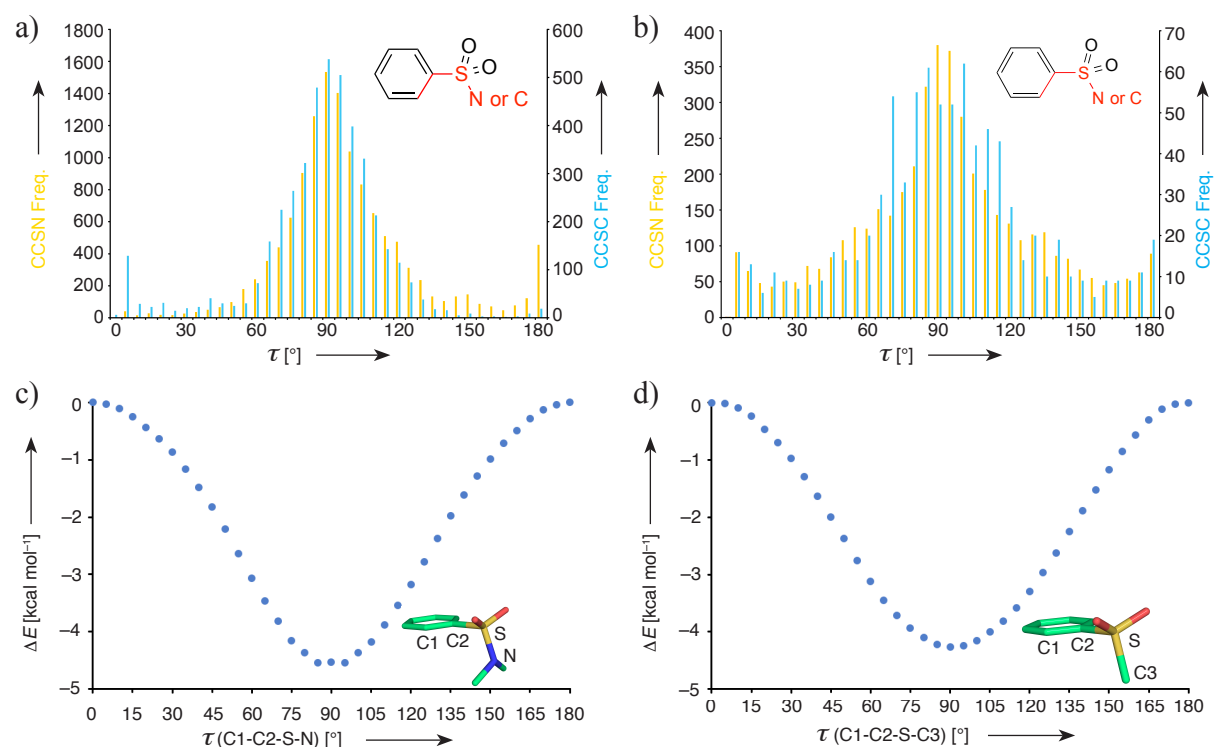


Figure 54. Torsion histograms for aryl sulfonamides (yellow) and aryl sulfones (blue) derived from a) CSD ligands and b) bound ligands in the PDB. c) Relative energy while driving the dihedral angle τ (C1-C2-S-N) of an aryl sulfonamide from 0–180°. d) Relative energy while driving the dihedral angle τ (C1-C2-S-C3) of an aryl sulfone from 0–180°. DFT-B3LYP/cc-pVDZ calculations carried out in water (with polarizable continuum solvent model) using Gaussian 09.^[169]

The second dihedral of interest is the $C_{sp^2}-S-N-C_{sp^3}$ angle. This latter can adopt two different conformations: eclipsed or staggered (Figure 55). Initially, the eclipsed conformation was believed to be the more favorable,^[190,191] as suggested by *ab initio* calculations on *N*-methylmethanesulfonamide ($\Delta G_{\text{eclipsed} \rightarrow \text{staggered}} \approx 1.46\text{--}2.63 \text{ kcal mol}^{-1}$). However, these were questioned by the crystal structure of *N*-methylmethanesulfonamide that adopted the staggered conformation only.^[192]

3. Conformational Aspects in the Design of Inhibitors for SHMT: Biphenyl, Aryl Sulfonamide, and Aryl Sulfone Motifs

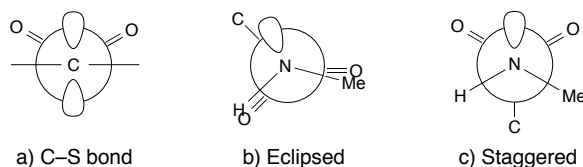


Figure 55. a) Stable conformation for aryl sulfonamides/aryl sulfones relative to the C_{sp^2} -S bond. b) and c) Two energetically stable conformations of sulfonamides relative to the N-S bond.

In the majority of the CSD and PDB ligands, the C_{sp^2} -S-N- C_{sp^3} torsion angles are in a range of 60° to 90° (Figure 56) that depict the conformation in which the N-lone pair bisects the SO_2 angle (staggered conformation). An increase of the N-pyramidalization can be observed at lower C_{sp^2} -S-N- C_{sp^3} torsion angles. Interestingly, the nitrogen atom is generally less pyramidal in sulfonamides than in acyclic tertiary amines. This observation can be derived from the $N\cdots$ plane distances that are shorter in sulfonamides ($< 0.40 \text{ \AA}$) than in acyclic tertiary amines ($d(N\cdots\text{plane}) \approx 0.45 \text{ \AA}$) (Figure 56).

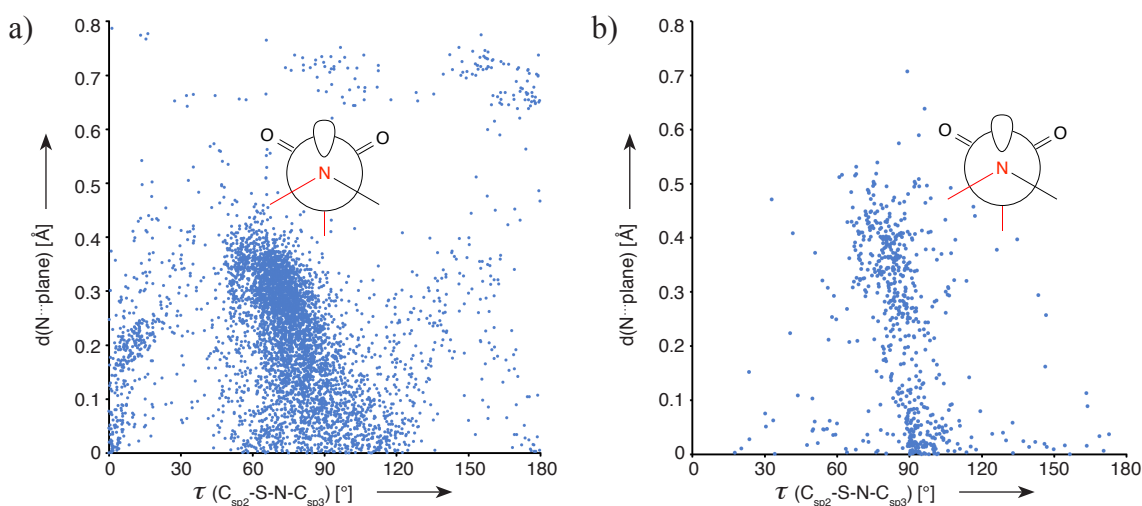


Figure 56. Scatterplot for N,N -disubstituted sulfonamides derived from a) CSD ligands and b) bound ligands in the PDB. The distance between N and the plane of its three substituents is plotted against the C_{sp^2} -S-N- C_{sp^3} torsion angle. The absolute value of the larger of the two alternative C_{sp^2} -S-N- C_{sp^3} torsion angles was chosen.

Additionally, PES at the B3LYP/cc-pVDZ and B3LYP/cc-pVTZ levels of theory (in water with polarizable continuum solvent model) for the fragments PhSO_2NH_2 , PhSO_2NHMe , and $\text{PhSO}_2\text{NMe}_2$ also support the preference for the staggered conformation (Figure 57). The preference for this conformation can be explained on stereoelectronic and steric grounds. Indeed, the N-lone pair interacts in an antiperiplanar orientation with the σ^* orbital of the weakest bond that is the C_{sp^2} -S bond. Furthermore, steric repulsion might also favor the

3. Conformational Aspects in the Design of Inhibitors for SHMT: Biphenyl, Aryl Sulfonamide, and Aryl Sulfone Motifs

staggered over the eclipsed conformation, in particular if larger substituents are attached to the N-atom.

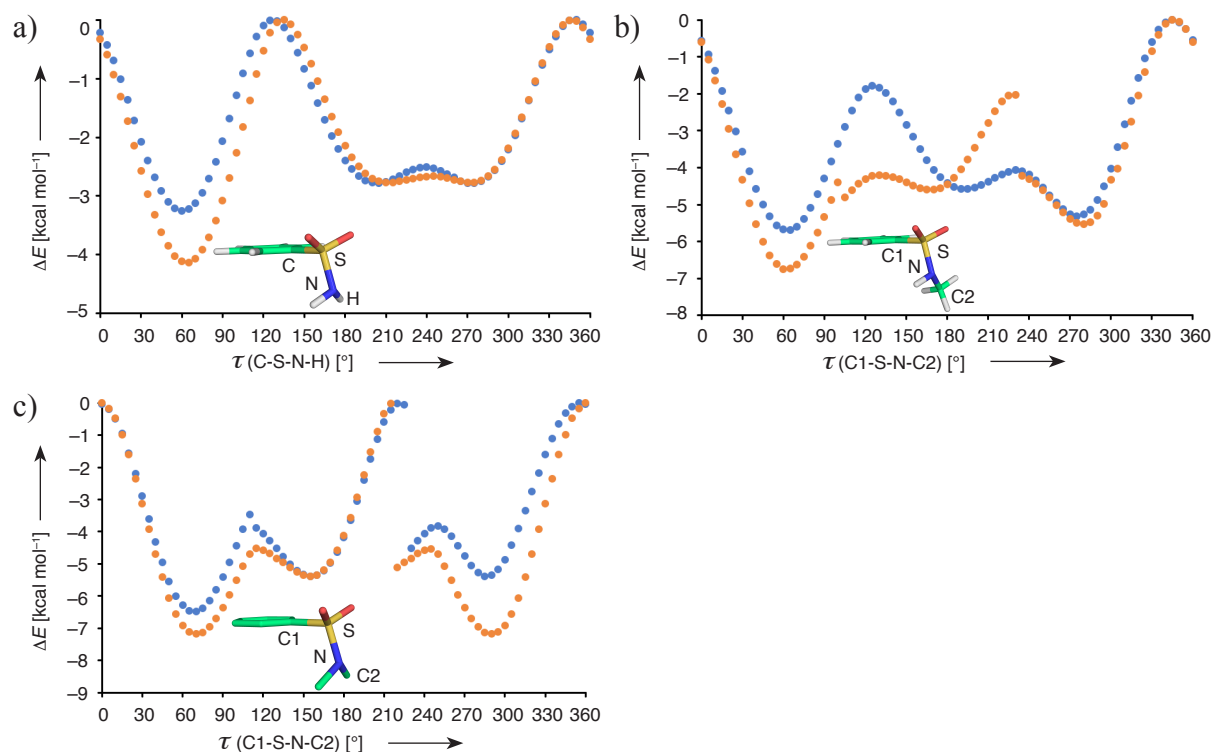


Figure 57. Relative energy while driving the dihedral angle from 0–360°: a) τ (C-S-N-H) of a PhSO₂NH₂ fragment; b) τ (C1-S-N-C2) of a PhSO₂NHMe fragment; c) τ (C1-S-N-C2) of a PhSO₂NMe₂ fragment. DFT-B3LYP/cc-pVDZ (blue) and DFT-B3LYP/cc-pVTZ (orange) calculations carried out in water (with polarizable continuum solvent model) using Gaussian 09.^[169]

3.2.2. Design and Synthesis of Ligands (±)-229–237, (±)-263–265, and (±)-269,270

A series of nine ligands bearing an aryl sulfonamide moiety ((±)-229–237, for the full structures see Section 3.2.4, Table 9) was designed with the intention to establish hydrophobic interactions at the entry of the *p*ABA channel. The sulfonamide motif was key to direct properly different apolar fragments of various size attached to the N-atom. In the modeling, the SO₂ group was oriented towards the solvent, whereas the small lipophilic fragments were all pointing to the apolar side chains of Phe134, Lys139, Val141, Ser263, and Pro267 (Figure 58). Also, it was envisioned to displace the water molecule (W1) that is in a small hydrophobic cavity (Figure 58b).

3. Conformational Aspects in the Design of Inhibitors for SHMT: Biphenyl, Aryl Sulfonamide, and Aryl Sulfone Motifs

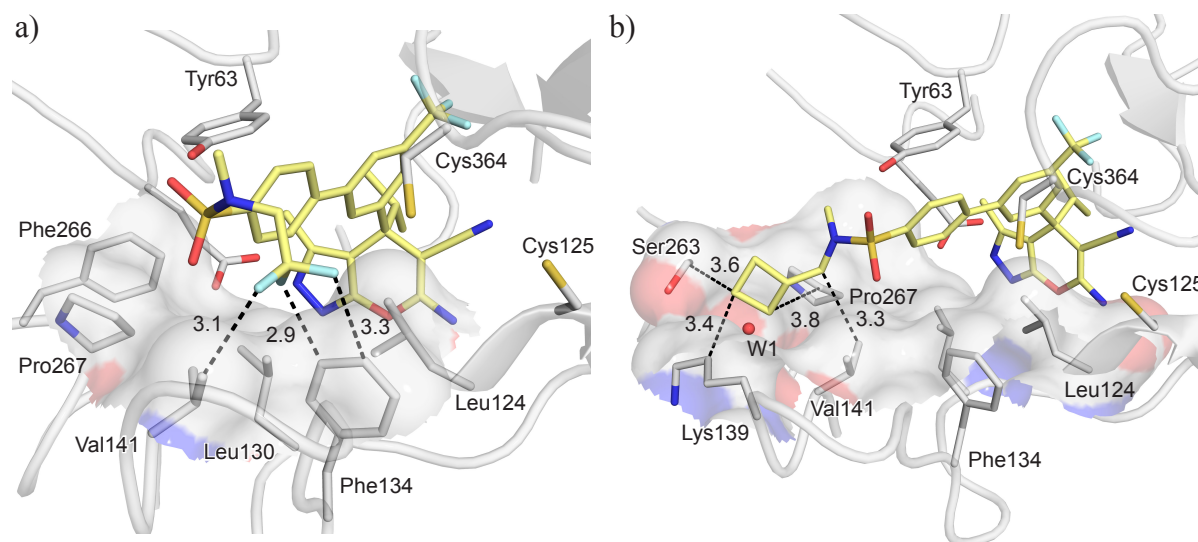
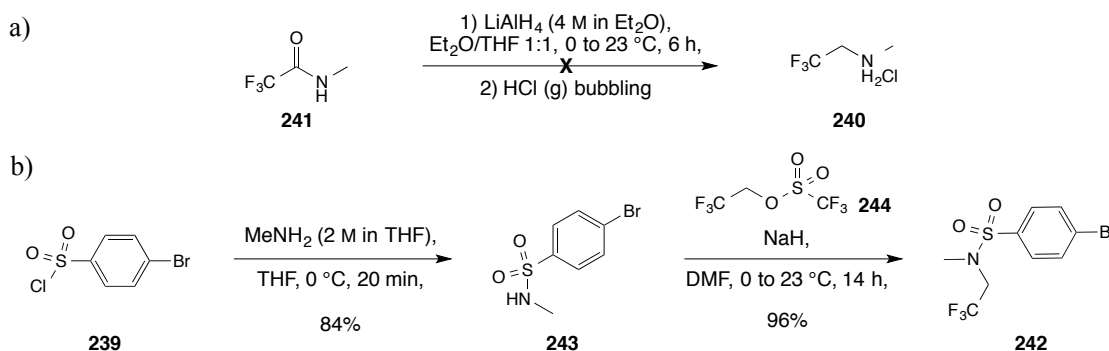


Figure 58. Proposed binding mode of ligands a) (+)-**231** and b) (+)-**234** within the active site of *PvSHMT* (PDB code 4TMR, 2.6 Å) as modeled with MOLOC. PLP is omitted for clarity. Distances are given in Å. Color code: C_{PvSHMT} grey, $C_{Ligands}$ gold, F cyan, N blue, O red, S yellow.

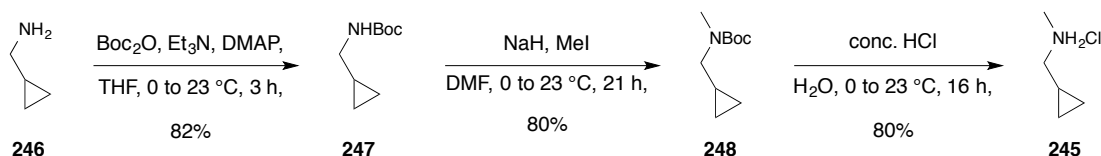
Brominated aryl sulfonamides building blocks **238a–h** were synthesized by reacting 4-bromo-benzenesulfonylchloride (**239**) with the corresponding secondary amines (see Scheme 26 below). Few of these amines were not commercially available, such as trifluoromethyl amine **240**. The synthesis of the latter from **241** is reported in the literature (Scheme 21a).^[193] The reduction with lithium aluminium hydride (LiAlH_4) proceeded well, however, most of the free amine **240** that was formed was lost during the work-up due to its high volatility. To overcome this difficulty, crystalline sulfonamide **242** was prepared directly (Scheme 21b). First, 4-bromo-benzenesulfonylchloride (**239**) was converted to *N*-methylsulfonamide **243**, then, the CH_2CF_3 moiety was attached to the sulfonamide by reacting **243** with NaH followed by the addition of sulfonate **244**. It is noteworthy that other reagents were tried first, such as 2,2,2-trifluoroethylmethanesulfonate or 2,2,2-trifluoroethylmethylbenzenesulfonate, without any success.



Scheme 21. a) Attempt to synthesize trifluoromethyl amine **240**. b) Preparation of sulfonamide **242**.

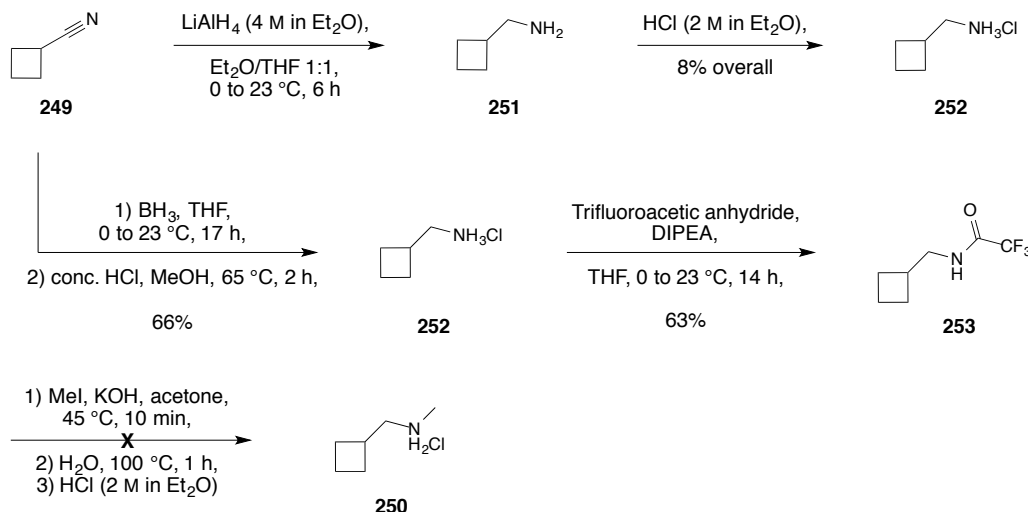
3. Conformational Aspects in the Design of Inhibitors for SHMT: Biphenyl, Aryl Sulfonamide, and Aryl Sulfone Motifs

N-Methylcyclopropylmethamine (**245**) was synthesized in three steps from cyclopropylmethamine (**246**) (Scheme 22).^[194] The latter was first mono-protected to **247**, a subsequent *N*-methylation gave **248** that was deprotected to give the hydrochloride salt of **245**.



Scheme 22. Preparation of *N*-methylcyclopropylmethamine (**245**).

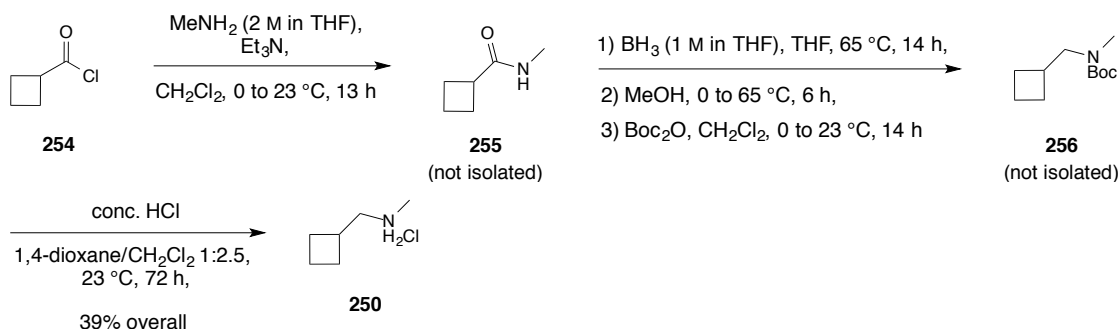
Cyclobutyl nitrile **249** was chosen as starting material for the synthesis of the *N*-methylated amine **250**. Initially, **249** was reduced to **251** with LiAlH_4 by adapting a literature procedure (Scheme 23).^[195] The primary amine **251** was isolated as its hydrochloride salt **252** but in a poor yield of 8%. A significant amount of **251** was presumably lost during the work-up of the first step due to its high volatility. Alternatively, reduction of **249** using a borane-THF complex^[196] and subsequent formation of the HCl salt allowed to isolate **252** in good yield (Scheme 23). This intermediate was successfully protected as a trifluoroacetamide (**253**) by following a known protocol.^[197] However, *N*-methylation followed by deprotection yielded only traces of **250** (Scheme 23).



Scheme 23. Attempts to synthesize *N*-methyl amine **250**. DIPEA = *N,N*-diisopropylethylamine.

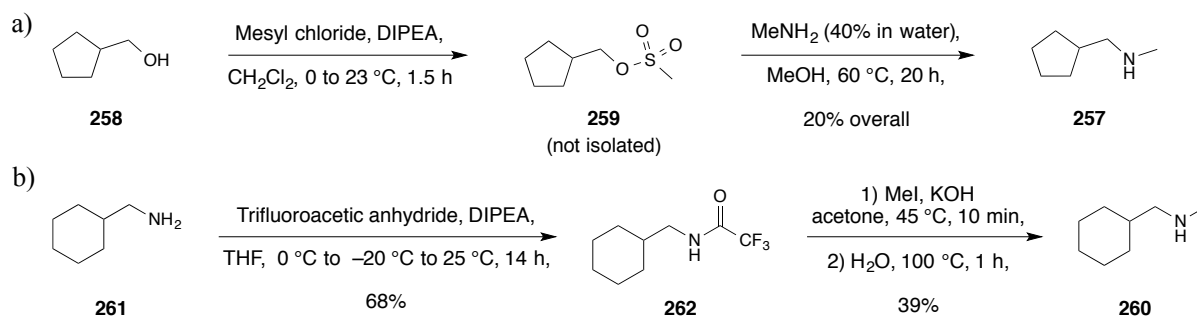
Gratifyingly, the cyclobutyl building block **250** was obtained by adapting a known procedure.^[198] Acyl chloride **254** was converted to the *N*-methylethylamide **255** by treatment with *N*-methylamine, reduced, and Boc-protected to **256** (Scheme 24). Cleavage of the protecting group gave the hydrochloride salt of **250** in an overall yield of 39%.

3. Conformational Aspects in the Design of Inhibitors for SHMT: Biphenyl, Aryl Sulfonamide, and Aryl Sulfone Motifs



Scheme 24. Successful preparation of *N*-methyl-cyclobutylmethamine **250**.

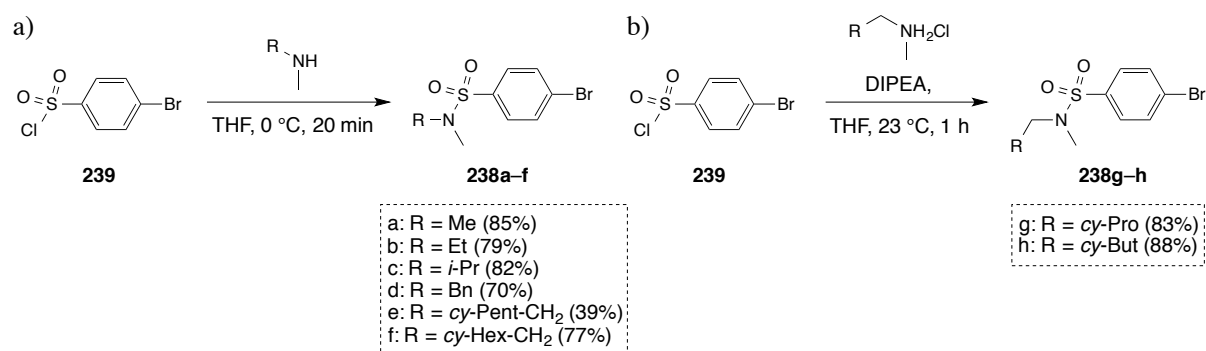
Cyclopentyl **257** was prepared from cyclopentylmethanol (**258**) *via* mesylate **259** following a reported protocol (Scheme 25a).^[199] The synthesis of 1-cyclohexyl-*N*-methylmethanamine (**260**) started by the mono-protection of cyclohexylmethanamine (**261**), followed by *N*-methylation of **262** and deprotection (Scheme 25b).



Scheme 25. a) Synthesis of cyclopentyl **257**. b) Synthesis of cyclohexyl **260**. DIPEA = *N,N*-diisopropylethylamine.

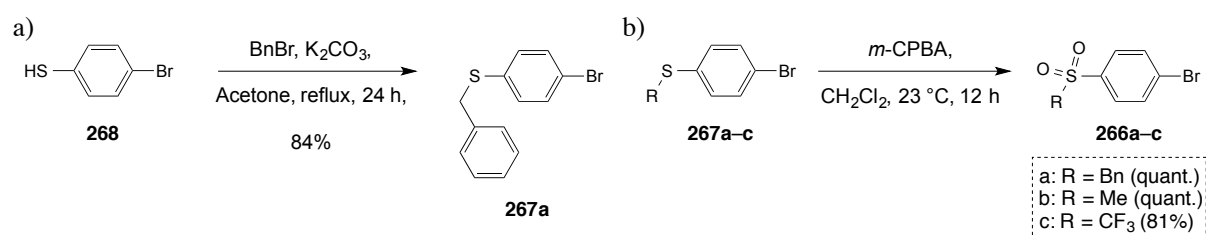
Aryl sulfonamide building blocks **238a–h** were consequently synthesized by reacting **239** with the corresponding secondary amines purchased (for **238a–d**) or prepared in house (for **238e–h**) (Scheme 26). In case of amines used as their hydrochloride salt, *N,N*-diisopropylamine (DIPEA) was added to the mixture to obtain the free amines *in situ*. Brominated **238a–h** and **242** were then utilized for the preparation of ligands (\pm)-**229–237** following the synthetic route depicted in Scheme 13.

3. Conformational Aspects in the Design of Inhibitors for SHMT: Biphenyl, Aryl Sulfonamide, and Aryl Sulfone Motifs



Scheme 26. Synthesis of sulfonamides building blocks **238a–h** from a) free amines or b) hydrochloride salts.

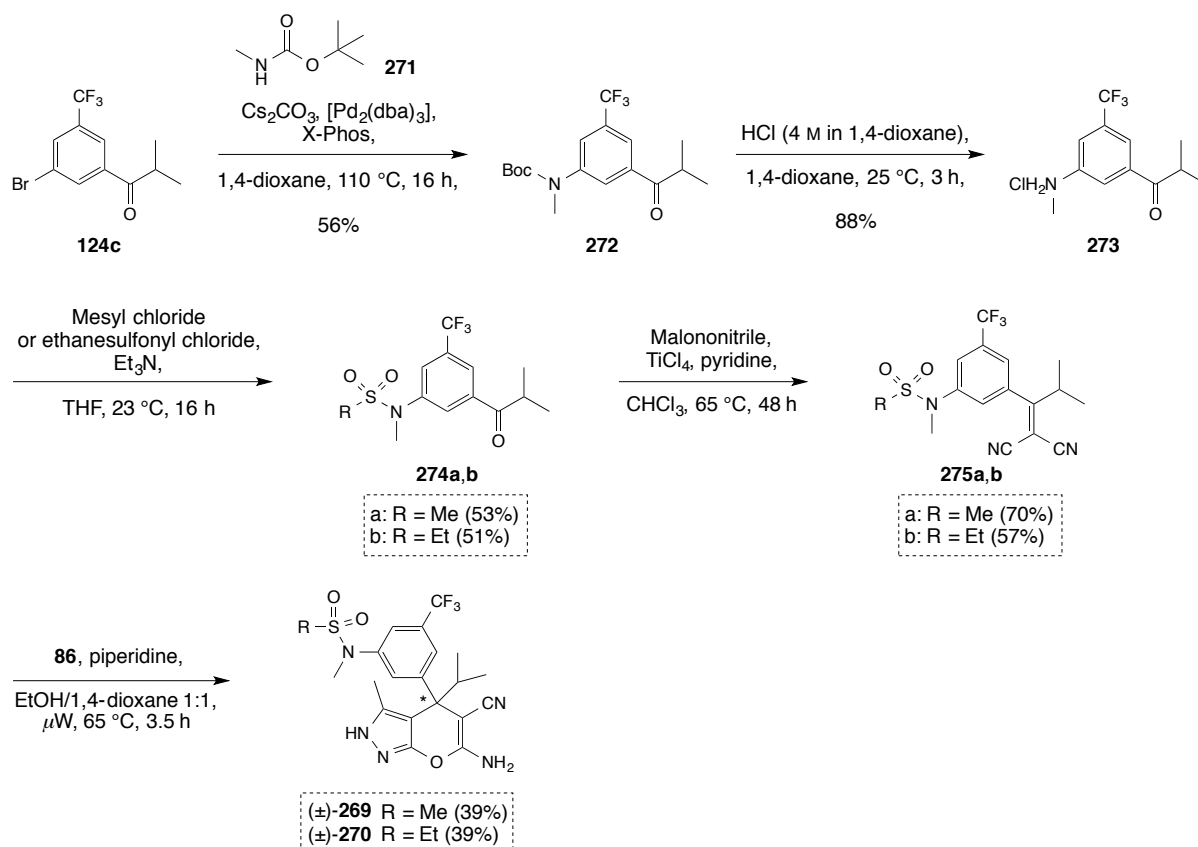
Three sulfone-containing ligands ((±)-**263–265**) were prepared as well. The bromoaryls **266a–c** were readily prepared by oxidation of **267a–c** using *meta*-chloroperbenzoic acid (*m*-CPBA) (Scheme 27b). Note that **267a** was obtained by alkylation of benzenethiol **268** (Scheme 27a). Precursors **266a–c** were subsequently used to synthesize target molecules (±)-**263–265**.



Scheme 27. a) Alkylation **268** of to **267a**. b) Synthesis of **266a–c** by oxidation of **267a–c**.

Finally, two reverse sulfonamides ((±)-**269** and (±)-**270**) were synthesized (Scheme 28). Their preparation started with a Buchwald-Hartwig amination involving brominated **124c** and carbamate **271**, which afforded protected aniline **272**. Boc-cleavage led to the hydrochloride salt of **273**, and a subsequent reaction with mesyl chloride or ethanesulfonyl chloride gave sulfonamides **274a,b**. Then, ligands (±)-**269** and (±)-**270** were obtained *via* **275a,b**.

3. Conformational Aspects in the Design of Inhibitors for SHMT: Biphenyl, Aryl Sulfonamide, and Aryl Sulfone Motifs



Scheme 28. Preparation of reverse sulfonamides (±)-**269** and (±)-**270**.

3.2.3. Small Molecule X-ray Crystal Structures

Three small molecule X-ray crystal structures were recorded for (±)-**229**, (±)-**231**, and (±)-**236**. In all of them, the aryl sulfonamide motif was found in its preferred conformation (Figure 59 and Appendix, Section 9.5) as discussed above.

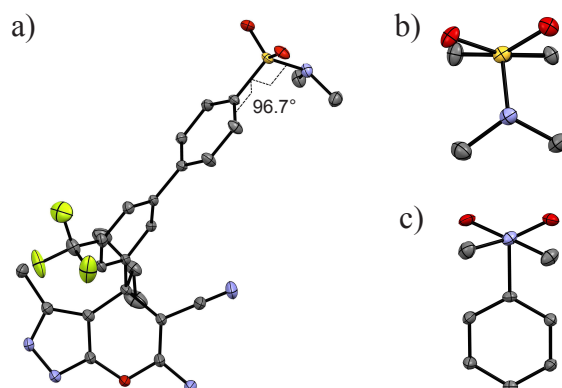


Figure 59. a) ORTEP plot at the 50% probability level of the small molecule X-ray crystal structure of (±)-**229** (for clarity hydrogen atoms are omitted and only (+)-**229** is shown). b) Front view of the sulfonamide from (+)-**229** showing the π orbital of the *ipso*-carbon atom bisecting the O-S-O angle. c) Front view of the sulfonamide from (+)-**229** showing the N-lone pair bisecting the O-S-O angle.

3. Conformational Aspects in the Design of Inhibitors for SHMT: Biphenyl, Aryl Sulfonamide, and Aryl Sulfone Motifs

The π orbital of the *ipso*-carbon atom bisects finely the O-S-O angle, with C_{sp^2} - C_{sp^2} -S-N torsion angles equal to 96.7° , 90.9° and 79.9° , respectively. The sulfonamides are in the staggered conformation with C_{sp^2} -S-N- C_{sp^3} dihedrals equal to 74.4° , 70.7° , and 74.1° , respectively, which are characteristic of the N-lone pair bisecting the O-S-O angle (Figure 59c).

Additionally, the N-aryl sulfonamide of (\pm)-**269** was also found in a staggered conformation with a C_{sp^3} -N-S- C_{sp^3} torsion angle of -71.8° (Figure 60). This moiety is twisted almost orthogonally with respect to the phenyl ring with a C_{sp^2} - C_{sp^2} -N-S torsion angle of 77.6° , as the two substituents on the nitrogen atom prevent a planar conformation where the N-lone pair is conjugated with the π -system of the aromatic ring. One of the S=O moieties of the sulfonamide is at a short distance ($d(S=O \cdots N) = 2.9 \text{ \AA}$) to the exocyclic amino moiety of a second molecule (Appendix, Section 9.5, Figure 118).

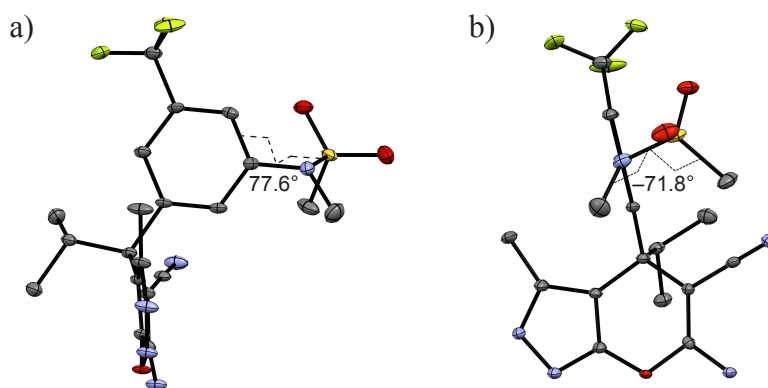


Figure 60. ORTEP plot at the 50% probability level of the small molecule X-ray crystal structure of (\pm)-**269** (for clarity hydrogen atoms are omitted and only (+)-**269** is shown). a) Side view showing the N-lone pair bisecting the O-S-O angle. b) Front view showing the C_{sp^3} -N-S- C_{sp^3} torsion angle.

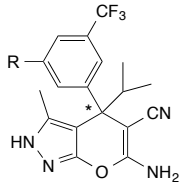
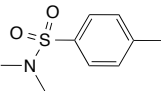
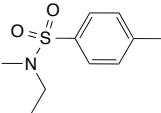
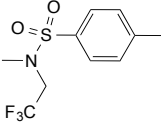
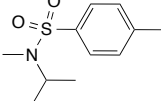
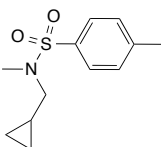
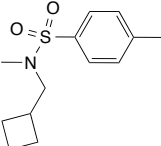
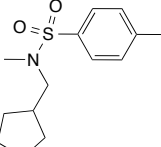
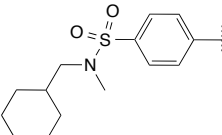
3.2.4. Biological Activities

The biological activities of the aryl sulfonamide ligands (\pm)-**229–237** were rather unsatisfactory (Table 9). Although, acceptable affinities were measured for *At*SHMT ($IC_{50} = 22.8\text{--}87.7 \text{ nM}$), no meaningful SAR was recognizable in both enzymatic assays. And no significant activity gain was measured, regardless of the size of the apolar moiety grafted onto the sulfonamide. Mixed results were also obtained in the cell-based assay (Table 9), ligands (\pm)-**229** and (\pm)-**237** displayed good efficacy ($EC_{50} = 144$ and 104 nM , respectively), whereas all others were significantly less potent. The two enantiomers of (\pm)-**237** were separated by chiral-phase HPLC and effective chiral recognition was observed. Indeed, (+)-**237** was considerably more potent ($IC_{50} = 150 \text{ nM}$, $EC_{50} = 56 \text{ nM}$) than (–)-**237** (38% inhibition of *Pf*SHMT at $250 \mu\text{M}$, $EC_{50} = 1584 \text{ nM}$) in target- and cell-based assays. The biological activities

3. Conformational Aspects in the Design of Inhibitors for SHMT: Biphenyl, Aryl Sulfonamide, and Aryl Sulfone Motifs

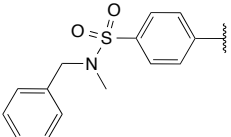
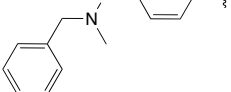

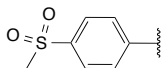
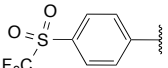
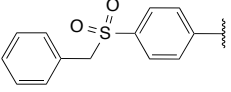
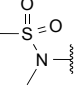
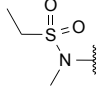
of aryl sulfones ((±)-**263–265**) and reverse sulfonamides ((±)-**269** and (±)-**270**) were in a similar range to the aryl sulfonamide ligands (Table 9). The lack of affinity gain in these ligands bearing diverse apolar moieties at their extremity could be rationalized by virtue of three co-crystal structures with C364A-PvSHMT mutant (*vide supra*).

Table 9. Biological activities and microsomal half-lives of aryl sulfonamides ((±)-**229–237**, (±)-**269** and (±)-**270**) and aryl sulfones ((±)-**263–265**) analogues.

Cpd.		EC ₅₀ <i>Pf</i> NF54 [nM]	IC ₅₀ <i>Pf</i> SHMT ± SD [nM] ^[a]	IC ₅₀ <i>At</i> SHMT [nM]	<i>t</i> _{1/2} [min] ^[b]
R					
(±)- 229		114	328 ± 8	22.8	2
(±)- 230		210	232 ± 4	74.4	n.d. ^[c]
(±)- 231		657	220 ± 6	43.0	n.d.
(±)- 232		400	322 ± 9	39.1	n.d.
(±)- 233		391	200 ± 6	29.0	n.d.
(±)- 234		374	699 ± 90	87.7	n.d.
(±)- 235		872	3378 ± 196	79.1	n.d.
(±)- 236		838	62% inhibition at 250 μM	85.6	n.d.

3. Conformational Aspects in the Design of Inhibitors for SHMT: Biphenyl, Aryl Sulfonamide, and Aryl Sulfone Motifs

Table 9 continued.

(±)- 237		104	2031 ± 252	73.9	n.d.
(+)- 237		56	150 ± 5	n.d.	n.d.
(-)- 237		1584	38% inhibition at 250 μM	n.d.	n.d.
(±)- 263		91	310 ± 8	16.8	3
(±)- 264		1399	393 ± 9	n.d.	6
(±)- 265		557	358 ± 11	24.5	< 2
(±)- 269		200	221 ± 6	22.4	n.d.
(±)- 270		186	158 ± 2	19.2	n.d.

[a] Standard deviations are given. [b] *In vitro* metabolic stability measured in human liver microsomes. [c] n.d. = not determined.

Although, some compounds displayed good cellular efficacy, such as enantiopure (+)-**237** ($EC_{50} = 56$ nM), the work on this series was not pursued further due to the poor microsomal stability measured in liver microsomes (Table 9). The terminal fragments on the phenyl ring departing from the pyrazolopyran core are presumably responsible for this intrinsic instability and not the pyrazolopyran core. Indeed, pyrazolopyran-based ligands with half-lives up to 4 h were identified later in this optimization program (see Chapter 4).

3.2.5. Co-crystal Structures with C364A-PvSHMT Mutant Highlighting the Lipophilic Character of the SO_2 Moiety

Several attempts were made to co-crystallize either (±)-**231**, (±)-**237**, or (±)-**265** with wild-type PvSHMT, however, no electron density of the bound ligands could be seen and partial or full formation of the disulfide bridge between Cys125 and Cys364 was observed. It is conceivable that the oxidation resulted from an extended crystallization period and molecular O_2 presumably acted as oxidant. To circumvent the cysteine oxidation and prevent the disulfide bridge formation, Cys364 was mutated to Ala364. This way, three new co-crystals of (±)-**231**,

3. Conformational Aspects in the Design of Inhibitors for SHMT: Biphenyl, Aryl Sulfonamide, and Aryl Sulfone Motifs

(±)-**237**, or (±)-**265** with the C364A-*Pv*SHMT mutant could be obtained and solved (Figure 61). The co-crystals diffracted at 2.4, 2.2, and 2.6 Å resolution, respectively, and belong to the C2 space group. Despite using a racemic mixture of ligands for co-crystallization, only the (+)-(*S*) enantiomer was present in all structures. In the 3 protein–ligand complexes, both active sites were found populated by a ligand.

The binding mode of the three ligands is identical as the one observed with wild-type *Pv*SHMT. The key interactions of the core with the side chain of Glu56, Thr183, and Thr357 and the backbone carbonyl of Leu124 and Gly128 are conserved (Figure 61). And the bicyclic scaffolds departing from the stereogenic center address the *p*ABA channel. In all complexes, the SO₂ moiety points to the hydrophobic side chain of the residues lining the *p*ABA channel (Figure 61), which contrasts with the expected orientation of the sulfonamide/sulfone moiety (Figure 58). Indeed, the SO₂ groups of (+)-**231**, (+)-**237**, and (+)-**265** establish several van der Waals interactions with apolar atoms of Val141 and Pro267, and form weak hydrogen bonds with non-polarized C α –H donors.^[200] Consequently, the apolar fragments attached at the termini of the ligands point to the solvent, thereby, not providing additional interactions as proposed by modeling. These observations enabled to explain why, regardless of the size of the apolar moiety, no activity gain could be measured.

These three co-crystal structures highlight the low hydrophilicity of the SO₂ group, which resembles the one of the nitro group that also prefers pointing into hydrophobic pockets rather than into solvent.^[201] Searches in both CSD and PDB for H-bonding from strong H-bond donors (excluding C–H) to the SO₂ moiety in aryl sulfonamides and aryl sulfones were performed to underscore these outcomes (Table 10). Only 1239 sulfonamides of the 7856 hits in the CSD formed one H-bond, while in the PDB cases of single H-bond were more frequent (847 hits out of 1410). A limited number of hits were retrieved in both the CSD and PDB when searching for 2 H-bonds. Concerning aryl sulfones, 344 hits out of the 2352 in the CSD established one H-bond, and approximately half of the hits in the PDB. The distance of the H-bonds to the SO₂ group range from 2.8 to 3.5 Å (Figure 62), and no specific directionality was observed as the H-bonds cover the hemisphere surrounding a S=O bond (Figure 63).

3. Conformational Aspects in the Design of Inhibitors for SHMT: Biphenyl, Aryl Sulfonamide, and Aryl Sulfone Motifs

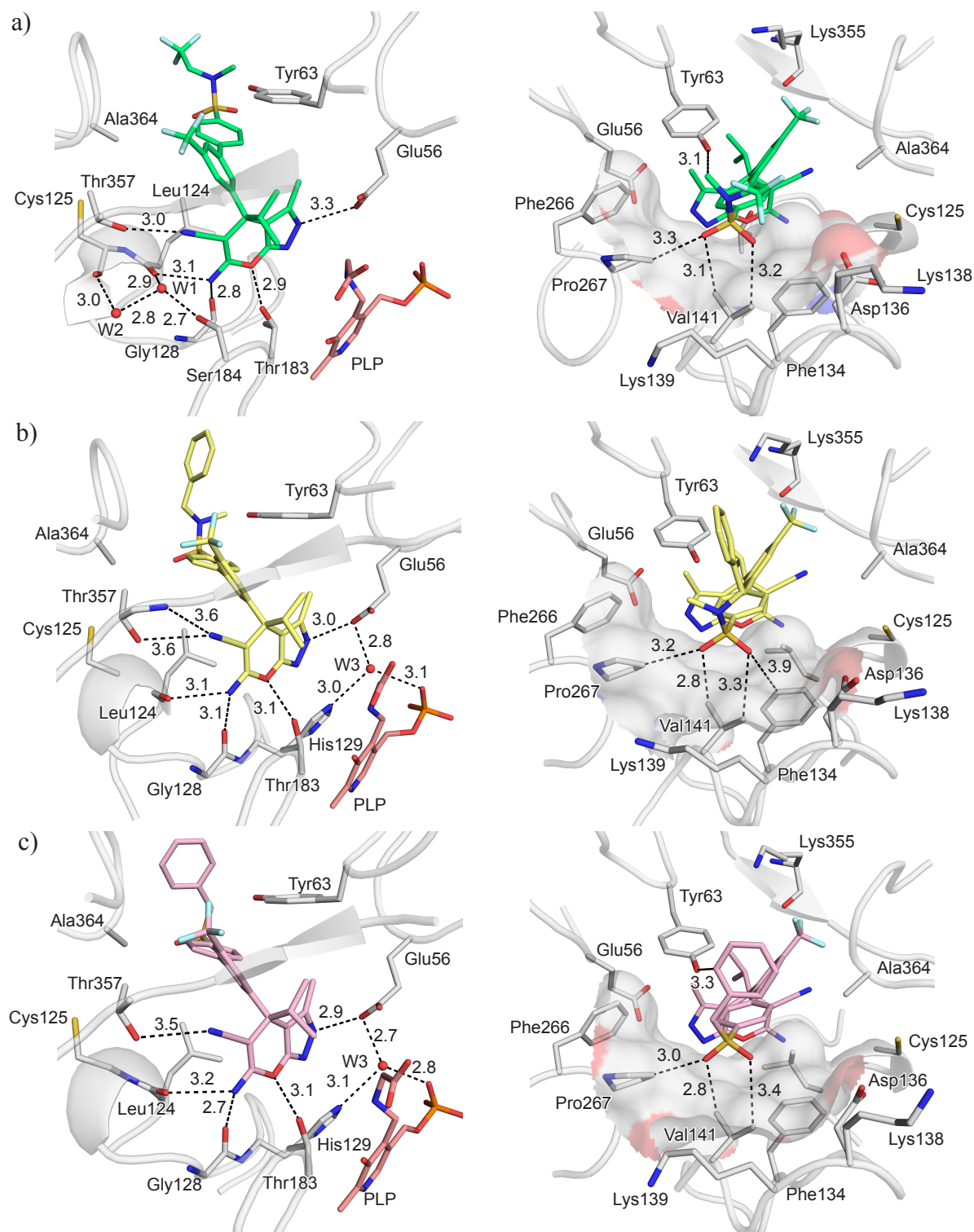


Figure 61. Co-crystal structures of C364A-PvSHMT mutant with a) (+)-**231** (PDB code 5XMP, 2.4 Å); b) (+)-**237** (PDB code 5XMQ, 2.2 Å); and c) (+)-**265** (PDB code 5XMR, 2.6 Å). The surface spans the volume of the *p*ABA channel. Water molecules are represented as red spheres. Distances are given in Å. Color code: C_{protein} grey, C₍₊₎₋₂₃₁ lime, C₍₊₎₋₂₃₇ gold, C₍₊₎₋₂₆₅ pink, C_{PLP} salmon, F light cyan, N blue, O red, P orange, S yellow.

3. Conformational Aspects in the Design of Inhibitors for SHMT: Biphenyl, Aryl Sulfonamide, and Aryl Sulfone Motifs

Table 10. Total number of hits from the CSD and PDB forming one or two H-bonds with strong H-bond donors. Search range: 2.0–3.5 Å (sum of the van der Waals radii^[202] –1.0 Å and +0.5 Å). All hits from the PDB were manually sorted so that only one active site per enzyme was considered to avoid replicates.

H-bond Acceptor	Total number of hits	H-bond Donor			
		O–H		N–H	
		1 H-bond	2 H-bonds	1 H-bond	2 H-bonds
Aryl Sulfonamide	CSD: 7856	CSD: 456	CSD: 0	CSD: 783	CSD: 37
	PDB: 1410	PDB: 170	PDB: 0	PDB: 677	PDB: 496
Aryl Sulfone	CSD: 2352	CSD: 174	CSD: 0	CSD: 170	CSD: 7
	PDB: 208	PDB: 5	PDB: 1	PDB: 107	PDB: 72

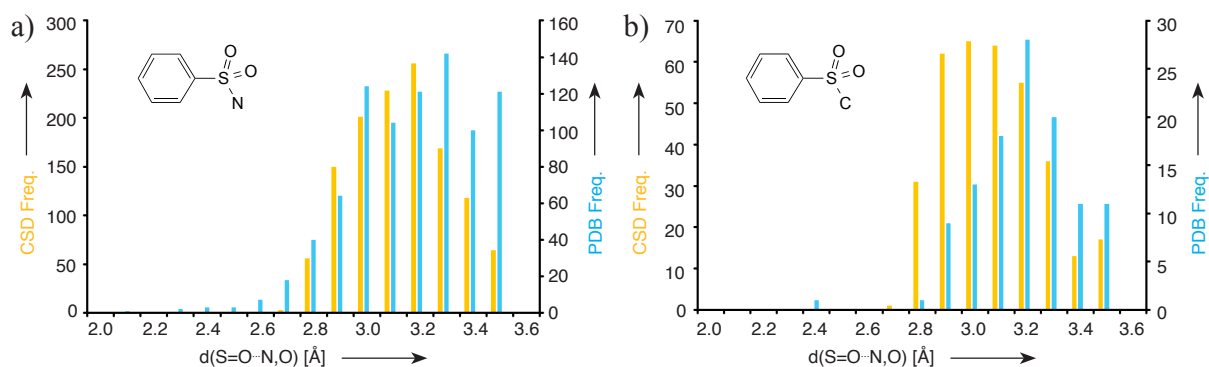


Figure 62. Distance ($d(\text{S}=\text{O}\cdots\text{N},\text{O})$) histogram derived from CSD and PDB ligands forming one H-bond with strong H-bond donors. a) Aryl sulfonamide fragments. b) Aryl sulfone fragments. The searches were conducted with ConQuest 1.19 in CSD 5.38 and with Relibase+ (v3.2.0) in PDB (June 2017).

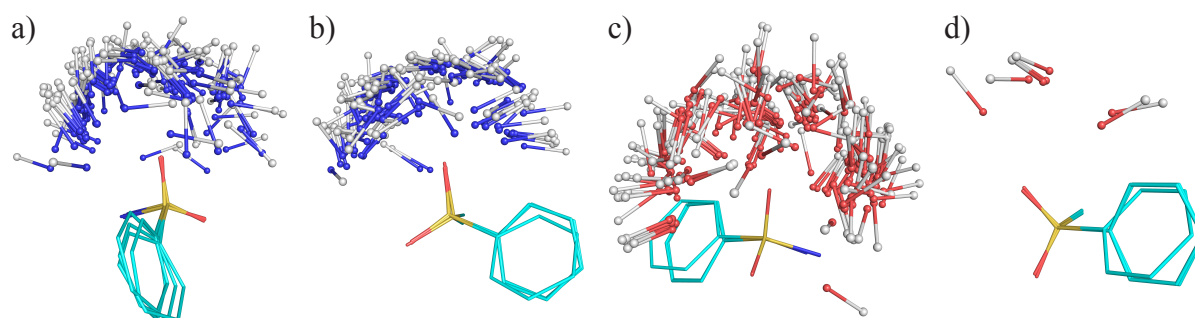


Figure 63. Superposition of the intermolecular contacts $\text{S}=\text{O}\cdots\text{N}-\text{H}$ retrieved in the PDB for a) aryl sulfonamide and b) aryl sulfone unit. Superposition of the intermolecular contacts $\text{S}=\text{O}\cdots\text{O}-\text{H}$ retrieved in the PDB for c) aryl sulfonamide and d) aryl sulfone unit. Only 3 fragments shown for clarity.

3.3. Tautomerism of the Pyrazolopyran Core

Two tautomers can be drawn for the pyrazolopyran core, or more precisely, for its pyrazole ring. Either the N(1) atom can be protonated or the N(2) atom (Figure 64). The positioning of the proton is crucial to interact with the side chain of Glu56, when the ligand is bound to PvSHMT.

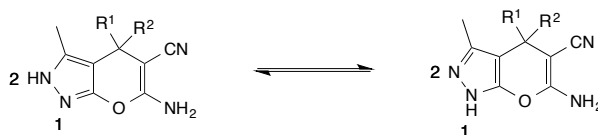


Figure 64. Two possible tautomers of the pyrazolopyran core.

In all protein–ligand complexes discussed in the previous sections, the N(2) atom is in close proximity to Glu56 ($d(\text{N}\cdots\text{O}_{\text{Glu56}}) = 2.5\text{--}3.5 \text{ \AA}$), suggesting that the N(2) atom is protonated, otherwise strong electrostatic repulsion would occur. The protonation at N(2) is also seen in the unbound state, as evidence by several small molecule X-ray crystal structures (Figure 65 and Appendix, Section 9.5). The preference for this tautomer is supported by the bond length in the pyrazole ring, as well as by intermolecular interactions within the crystal lattice.

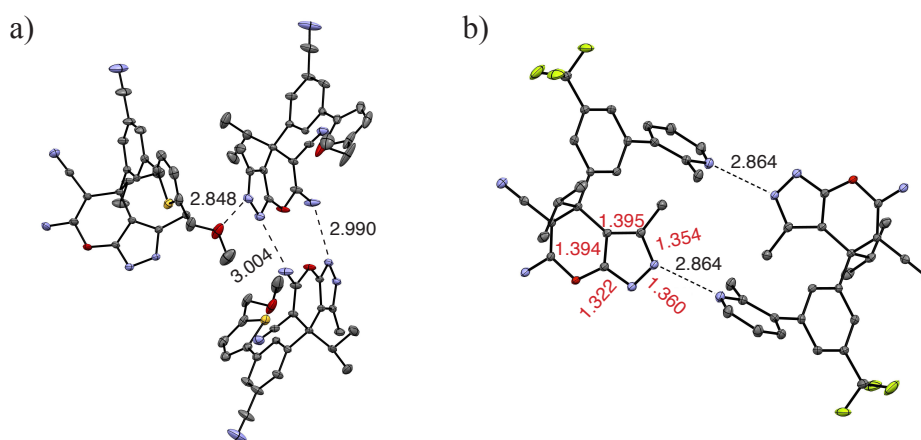


Figure 65. Small molecule X-ray crystal structures of a) thiophene ether (\pm)-**112** and b) pyridyl (\pm)-**209**. The intermolecular interactions are represented as dashed lines. Distances are given in Å.

In addition, $^1\text{H}\text{--}^{15}\text{N}\text{--HSQC}$ and $^1\text{H}\text{--}^{15}\text{N}\text{--HMBC}$ were recorded for ligand (\pm)-**269** in order to pinpoint the preferred tautomer in solution. First, the signals of interest in the ^1H NMR should be identified (Figure 66). The proton on the pyrazole ring has a chemical shift (δ) of 11.37 ppm, while the ones of the exocyclic amino group and the methyl moiety on C(3) have chemical shifts of 6.26 and 1.85 ppm, respectively.

3. Conformational Aspects in the Design of Inhibitors for SHMT: Biphenyl, Aryl Sulfonamide, and Aryl Sulfone Motifs

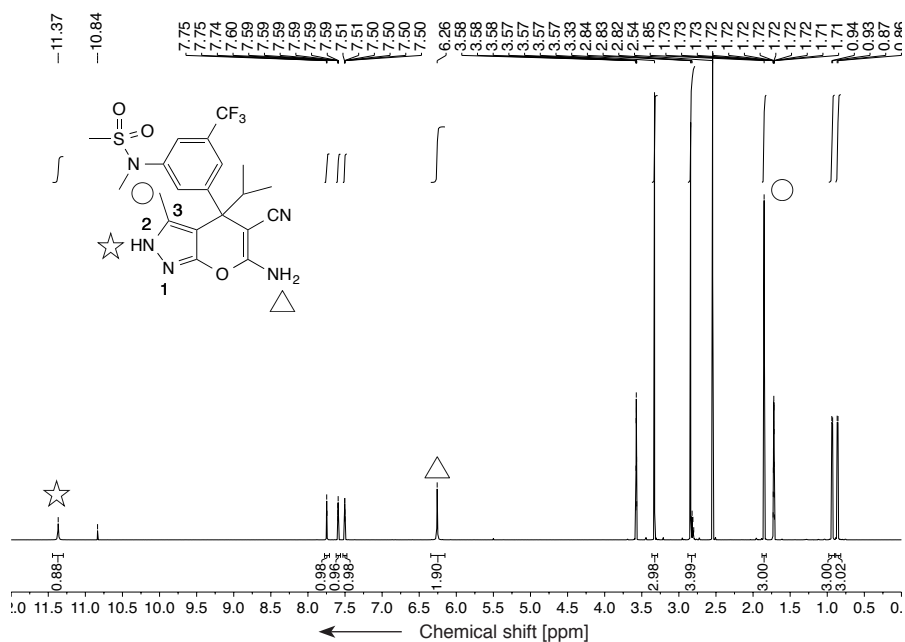


Figure 66. ^1H NMR (600 MHz) spectra of compound (\pm)-**269** in $\text{THF-}d_8$ at 298 K.

^1H - ^{15}N -HSQC allowed to determine the chemical shift of the protonated nitrogen in the ring ($\delta = -193.93$ ppm) (Figure 67), however, it is impossible to discriminate between N(1) and N(2) with this sole experiment.

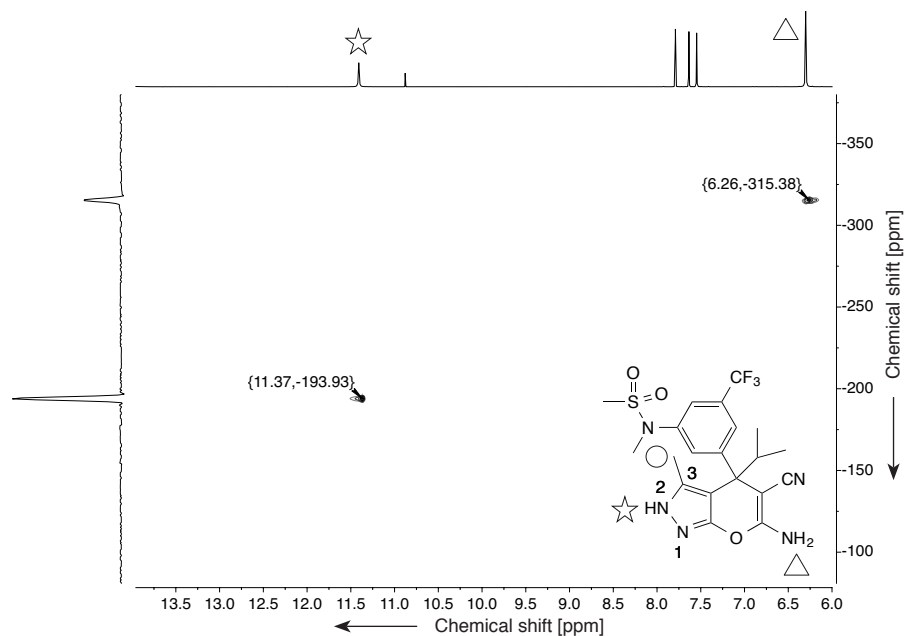


Figure 67. ^1H - ^{15}N -HSQC NMR spectra of compound (\pm)-**269** in $\text{THF-}d_8$ at 298 K.

On the other hand, ^1H - ^{15}N -HMBC enabled to assign the chemical shift corresponding to N(2). Indeed, only the long range heteronuclear correlation between N(2) and the protons

3. Conformational Aspects in the Design of Inhibitors for SHMT: Biphenyl, Aryl Sulfonamide, and Aryl Sulfone Motifs

of the methyl group on C(3) should give a signal. According to the ^1H - ^{15}N -HMBC spectra, N(2) has a chemical shift of -193.93 ppm (Figure 68). Combining this information with the one of the ^1H - ^{15}N -HSQC experiment allowed to conclude unambiguously that the proton is located onto N(2), thus, the major tautomer present in solution is identical to the one seen in solid state.

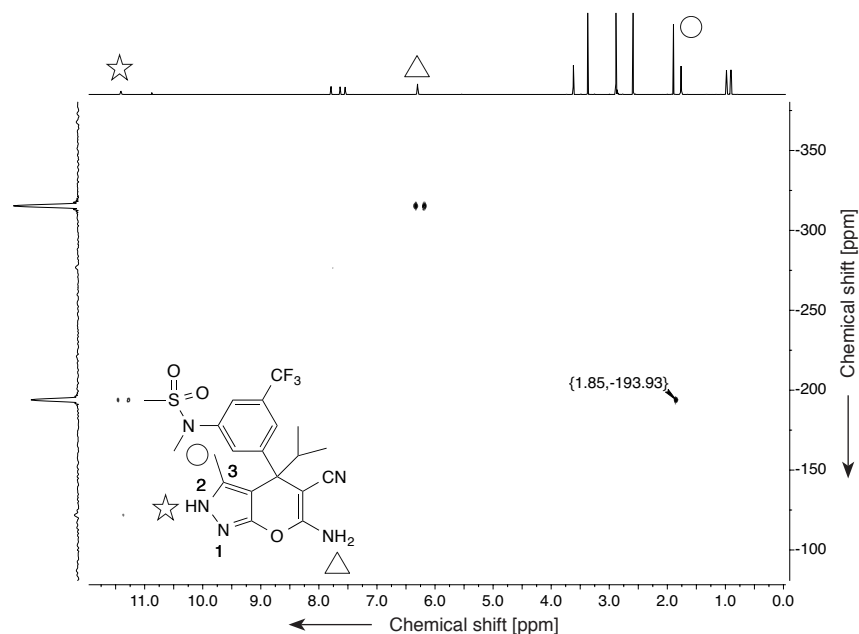


Figure 68. ^1H - ^{15}N -HMBC NMR spectra of compound (\pm)-**269** in $\text{THF-}d_8$ at 298 K.

Finally, DFT calculations (B3LYP/6-31G(d)) also support the tautomer in which the pyrazole NH is vicinal to the methyl group (Figure 69).

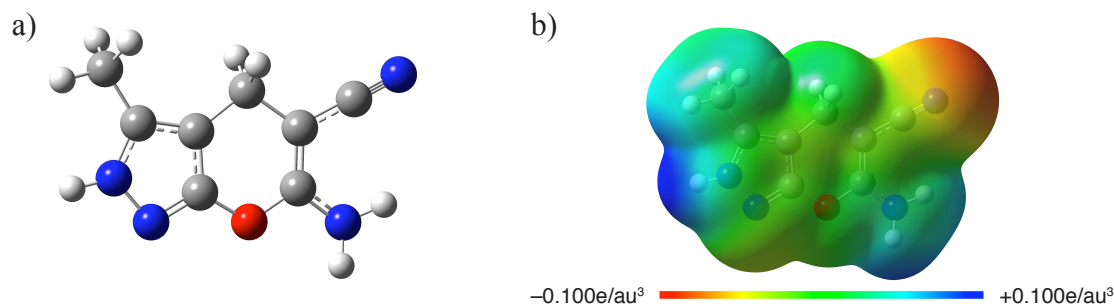


Figure 69. a) Optimized structure of the pyrazolopyran core. b) Electrostatic density from Total SCF Density of the pyrazolopyran core (isovalue = 0.0004; mapped with electrostatic potential). The calculations were performed at the B3LYP/6-31G(d) level of theory using the software package Gaussian 09.^[169]

3.4. Summary on Biphenyl and Aryl Sulfonamide/Aryl Sulfone Analogues and their Conformational Preferences

The significance of small molecule conformation in drug design was highlighted with two series of ligands bearing either a biphenyl or an aryl sulfonamide/aryl sulfone motif.

While the torsion angle of the biphenyl fragment (in (\pm)-**217–223**) did not affect much target affinity, a steep SAR was observed in the cell-based assay. The torsion angles of the considered *ortho*-substituted biphenyl motifs were investigated by CSD and PDB searches, as well as by theoretical calculations, in order to understand this result. It was shown that the variation of the torsion angle, which is governed by the size of the *ortho*-substituent on the terminal ring, correlates with the cellular efficacy. And that, in pyrazolopyran-based inhibitors, large *ortho*-substituents are detrimental to efficacy. It is postulated that the conformation at the biphenyl affects cell-penetration and/or transporter mediated uptake and efflux. Four ligands of this series were co-crystallized with wild-type *Pv*SHMT. Interestingly, in the complexes with (+)-**218** and (+)-**220**, the *ortho*-halo substituents undergo antiparallel dipolar C–F/C–Cl \cdots C–O interactions with the nearby C–O bond of Tyr63. The co-crystal structures with (+)-**219** and (+)-**222** contrast with these latter, as their respective methyl and nitrile *ortho*-substituent point to Cys364 to avoid steric repulsion with Tyr63. Nonetheless, those structural differences had only minor effect on the affinities for *Pf*SHMT.

The preferred conformations of aryl sulfonamides and aryl sulfones was described by CSD and PDB searches, as well as by theoretical calculations and small molecule X-ray crystallography. These motifs preferentially adopt a conformation in which the π orbital of the *ipso*-carbon atom bisects the O–S–O angle. Additionally, in aryl sulfonamides, the N-lone pair bisect the O–S–O angle resulting in a characteristic staggered conformation. The small lipophilic fragments attached at the termini of these aryl sulfonamide/aryl sulfone analogues did not provide an appreciable improvement of affinity for SHMT and no distinguishable SAR was observed. These results were explained with the help of three co-crystal structures with C364A-*Pv*SHMT mutant. The respective aryl sulfonamide/aryl sulfone moieties of (+)-**231**, (+)-**237**, and (+)-**265** were found in their favored conformation, however, their SO₂ groups are all pointing towards the lipophilic residues of the *p*ABA channel. Therefore, the apolar moieties grafted onto the sulfonamides (or sulfones) are pointing to the solvent and does not participate to the binding. These complexes underscored the low hydrophilicity of the SO₂ moiety, which prefers to point to hydrophobic environments rather than to polar ones. This was further underpinned by searches in the CSD and PDB revealing that only half or less of

3. Conformational Aspects in the Design of Inhibitors for SHMT: Biphenyl, Aryl Sulfonamide, and Aryl Sulfone Motifs

the reported structures bearing a SO₂ moiety establish strong H-bonds with surrounding residues. Finally, it was shown that the preferred tautomer of the pyrazolopyran core, in solution and in solid state, is the one with the pyrazole NH vicinal to the methyl group on C(3), enabling critical H-bonding interactions with Glu56 of PvSHMT.

4. In Vivo Validation of SHMT as a Druggable Antimalarial Target

The following results were published in the *Journal of Medicinal Chemistry*.^[117] The target-based assays on *Pf*SHMT and *At*SHMT were performed in the group of Dr. Pimchai Chaiyen by Dr. Ubolsree Leartsakulpanich and Aritsara Jaruwat (National Center for Genetic Engineering and Biotechnology, Thailand), and by Dr. Raphael Aponte (BASF-SE, Germany), respectively. The cell-based assays were performed in the group of Dr. Matthias Rottmann (Swiss Tropical and Public Health Institute, Basel) by Anja Schäfer. The co-crystal structures with *Pv*SHMT were solved by Dr. Penchit Chitnumsub and Wanwipa Ittarat (National Center for Genetic Engineering and Biotechnology, Thailand). The metabolic stability and plasma protein binding measurements were performed by Dr. Karen L. White (Monash University, Australia). Dr. Mel Lloyd supervised the mutagenicity evaluation (Covance Laboratories, United Kingdom). The *in vivo* mouse model study was carried out by Dr. Sergio Wittlin, Ursula Lehmann, and Christin Gump (Swiss Tropical and Public Health Institute, Basel). Marc Siggel contributed with a semester project to the molecular dynamic simulations.

4. In Vivo Validation of SHMT as a Druggable Antimalarial Target

Plotting the measured half-lives of most compounds from the optimization program obtained at this point against their calculated $\log D_{7.4}$ (Figure 70a) revealed that lipophilic ligands ($c\log D_{7.4} > 3$) were poorly stable. In contrast, more polar ligands ($c\log D_{7.4} < 2$) displayed interesting $t_{1/2}$ values. Among which is the carboxylic acid (\pm)-**66**, others are molecules bearing an 2-indolinone scaffold (discussed in Chapter 5). Inhibitor (\pm)-**66** displayed a promising microsomal half-life ($t_{1/2} = 137$ min), good target affinities, but only a moderate cell-based efficacy ($EC_{50} = 340$ nM) (Figure 70b). The challenge was therefore to improve its potency while keeping a $t_{1/2}$ above 2 h. In this respect, a series of carboxylic acid analogues was prepared using the knowledge learned from the previous rounds of optimization.

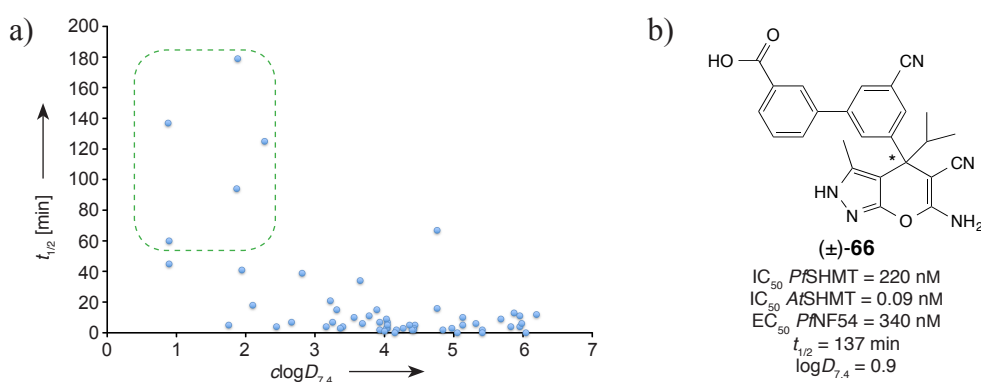


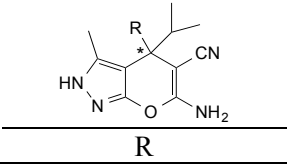
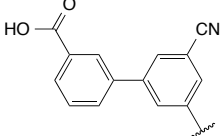
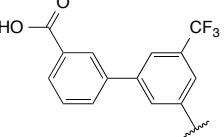
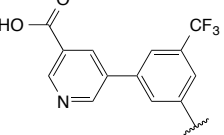
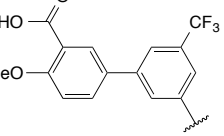
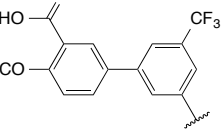
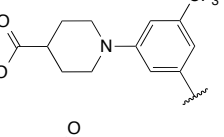
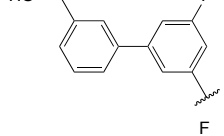
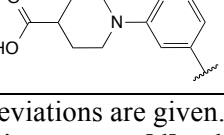
Figure 70. a) Half-lives in human liver microsomes ($t_{1/2}$) plotted against the $c\log D_{7.4}$ of selected compounds. All $c\log D_{7.4}$ were calculated with the software package ACD/Labs.^[203] b) Ligand (\pm)-**66** and selected biological data.

4.1. Identification of an in Vivo Candidate and Animal Model

In Chapter 2, it was shown that replacing the *meta*-nitrile moiety on the phenyl ring for a CF_3 greatly enhanced potency. Also, *N*-heterocyclic ligands, such as *N*-pyridyl analogues (\pm)-**199** and (\pm)-**200**, were highly potent. These structural motifs were therefore used to improve the cellular efficacy of carboxylate (\pm)-**66** and the consequences on metabolic stability were monitored. A series of *meta*- CF_3 analogues ((\pm)-**276–280**) was prepared (Table 11), and as expected the substitution $CN \rightarrow CF_3$ resulted in a significant potency boost (EC_{50} (\pm)-**276** = 54 nM). Only moderate efficacy was measured for the nicotinic acid (\pm)-**277** and for the *ortho*-substituted carboxylates (\pm)-**278** and (\pm)-**279** (Table 11).

4. *In Vivo* Validation of SHMT as a Druggable Antimalarial Target

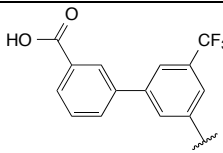
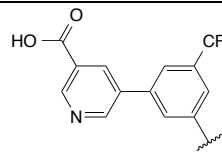
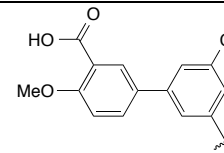
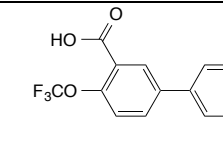
Table 11. Biological activities, $\log D_{7.4}$ values, and microsomal half-lives of carboxylate-based ligands (\pm)-276–282.

Cpd.		EC_{50} <i>Pf</i> NF54 [nM]	IC_{50} <i>Pf</i> SHMT \pm SD [nM] ^[a]	IC_{50} <i>At</i> SHMT [nM]	$\log D_{7.4}$ ^[b]	$t_{1/2}$ ^[c] [min]
R						
(\pm)-66		340	220 \pm 70	0.088	1.4	137
(\pm)-276		54	189 \pm 7	19.1	1.8	41
(\pm)-277		632	119 \pm 6	n.d. ^[d]	n.d.	64
(\pm)-278		822	77 \pm 1	n.d.	1.7	59
(\pm)-279		172	268 \pm 15	n.d.	n.d.	70
(\pm)-280		116	312 \pm 10	41.9	1.6	55
(\pm)-281		194	56 \pm 1	27.8	1.5	157
(\pm)-282		154	75 \pm 1	26.2	1.2	226

[a] Standard deviations are given. [b] Measured by HPLC. [c] *In vitro* metabolic stability measured in human liver microsomes. [d] n.d. = not determined.

The discrepancies might be linked to the variation of pK_a of the carboxylate in (\pm)-276–279. Calculated pK_a values are summarized in Table 12; while (\pm)-276 has a pK_a value of 3.4, the other analogues are either more acidic ((\pm)-277 and (\pm)-279) or more basic ((\pm)-278). In addition, an intramolecular H-bond interaction might occur in (\pm)-278 between the carboxylate and the neighboring OMe moiety, which might alter the potency of this latter.

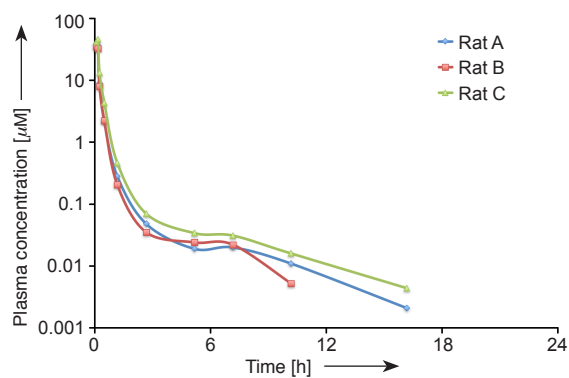
Table 12. Calculated pK_a values for carboxylates (\pm)-**276**–**279**.

Cpd.				
	(\pm)- 276	(\pm)- 277	(\pm)- 278	(\pm)- 279
pK_a ^[a]	3.4	2.8	4.2–4.3	3.1

[a] Calculated with Jaguar from the software package Maestro (V.9.9.013).

The terminal carboxylate was also attached onto a piperidine moiety ((\pm)-**280**), and good efficacy was measured but (\pm)-**280** was still 2-fold less potent than (\pm)-**276**. Although an improved EC_{50} could be measured for (\pm)-**276**, its half-life was reduced compared to (\pm)-**66** ($t_{1/2}$ = 41 vs. 137 min, respectively) (Table 11). Reasoning that a good potency/stability balance might be obtained with a ligand having a lipophilicity within the range of (\pm)-**66** and (\pm)-**276** ($\log D_{7.4}$ = 1.4 and 1.8, respectively), the *meta*-fluoro derivative (\pm)-**281** was prepared. As anticipated, an intermediate potency was obtained (EC_{50} = 194 nM), however, the metabolic stability measured for (\pm)-**281** ($t_{1/2}$ = 157 min) surpassed all other ligands tested so far (Table 11). Ligand (\pm)-**281** was also incubated in rat liver microsomes resulting in a comparable half-life of 95 min.

a)



b)

Parameter	IV administration			
	Rat A	Rat B	Rat C	Mean \pm SD
Measured dose [mg/kg]	4.8	4.8	5.1	4.8 \pm 0.2
Apparent $t_{1/2}$ [h]	2.7	c.n.d. ^[a]	3.2	3.0
Plasma CL [mL/min/kg]	22.7	23.8 ^[b]	17.1	21.2 \pm 3.6
Plasma V_{ss} [L/kg]	0.5	0.6 ^[b]	0.4	0.5 \pm 0.06
$AUC_{0-\infty}$ [h \cdot μ M]	8.2	7.7 ^[b]	11.4	9.1 \pm 2.0
%Dose in urine over 24 h	< LLQ	< LLQ	< LLQ	< LLQ

Figure 71. a) Plasma concentration of (\pm)-**281** in male Sprague Dawley rats following i.v. administration at 5 mg/kg. b) Pharmacokinetic parameters for (\pm)-**281**. [a] c.n.d. = Could not determined. [b] Parameters estimated by extrapolating the area under the curve (AUC) using the average terminal rate constant from rats A and C. LLQ = lower limit of quantification.

These results were further confirmed in an *in vivo* rat model, in which an apparent *in vivo* half-life of 3 h was measured (Figure 71). The disparities between *in vitro* and *in vivo* experiments can possibly be attributed to plasma protein or microsome binding. A minor potency loss was observed when applying the $\text{CF}_3 \rightarrow \text{F}$ replacement strategy to piperidine derivative (\pm)-**280**. Remarkably, a considerable stability gain was measured for (\pm)-**282** ($t_{1/2} = 226$ min) (Table 11). Finally, ligands (\pm)-**281** and (\pm)-**282** inhibited *Pf*- and *At*SHMT in the two-digit nanomolar range.

Subsequent to these encouraging results, it was envisioned that the potency of these analogues could be further improved by extending their carboxylate side chain (ligands (\pm)-**283–290**, Table 13). As seen in the co-crystal structure of 5-CHO-H₄F (**54**) bound to *Pv*SHMT (PDB code 4OYT, 2.4 Å),^[113] the two carboxylates of its terminal glutamate are located at the periphery of the *p*ABA channel (Figure 72a). MOLOC modeling suggested that addition of one or two carbon unit into the carboxylate side chain would allow to position the COOH moiety in analogy to **54** (Figure 72b).

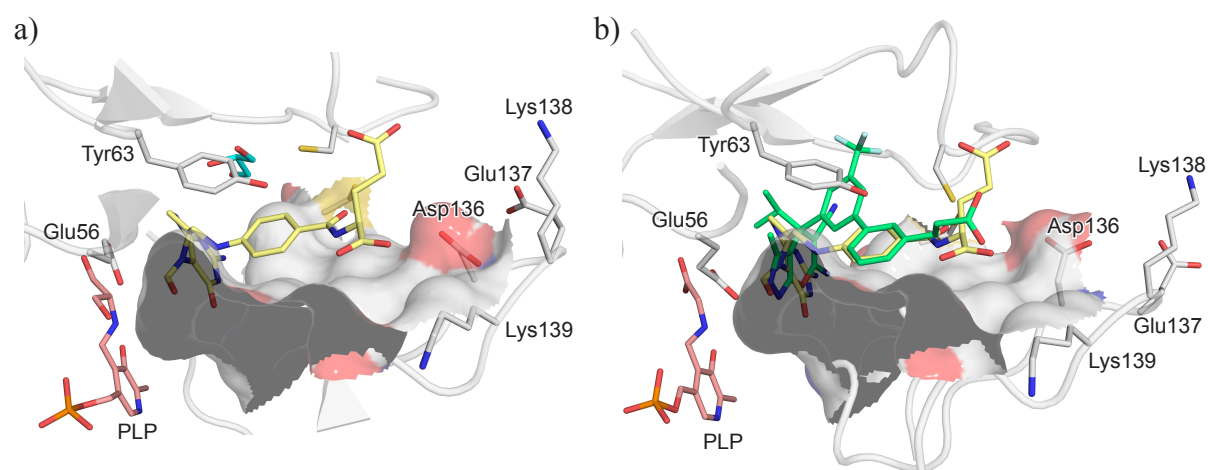
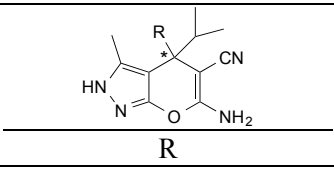
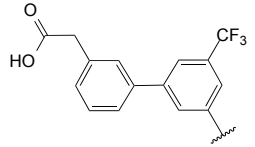
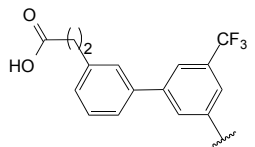
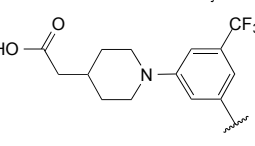
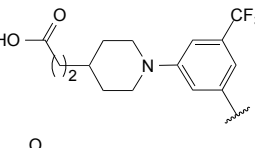
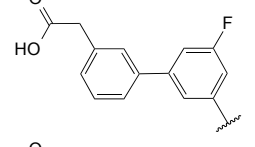
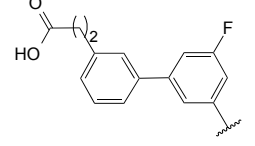
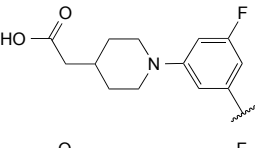
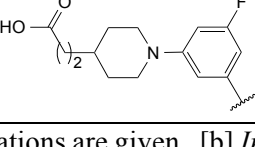


Figure 72. a) Co-crystal structure of **54** with *Pv*SHMT (PDB code 4OYT, 2.4 Å).^[113] b) Modeled carboxylate (+)-**284** within the active site of *Pv*SHMT (PDB code 4TMR, 2.6 Å) superposed with **54**. The surface spans the volume of the *p*ABA channel. Color code: C_{protein} grey, C_{54} gold, $C_{(+)-284}$ lime, C_{glycerol} cyan, C_{PLP} salmon, F light cyan, N blue, O red, P orange, S yellow.

Remarkably, increasing the length of the carboxylate side-chain led to compelling cell-based efficacy improvement for all analogues (\pm)-**283–290** (Table 13). Head-to-head comparisons revealed that the potency was enhanced up to 3-fold by adding a carbon unit in both CF_3 - and F-series (e.g.: EC_{50} values (\pm)-**276** 54 nM > (\pm)-**283** 22 nM > (\pm)-**284** 10 nM or (\pm)-**282** 154 nM > (\pm)-**289** 55 nM > (\pm)-**290** 17 nM). Efficacy gain came along with a loss in metabolic stability, which became unacceptable in the CF_3 -series (Table 13). Overall, this

SAR yielded ligands with attractive profiles, such as (±)-**284** that is highly potent but moderately stable ($EC_{50} = 10$ nM; $t_{1/2} = 31$ min), while the high stability of (±)-**287** and (±)-**289** compensate for their modest efficacy ($EC_{50} = 52$ nM; $t_{1/2} = 159$ min and $EC_{50} = 55$ nM; $t_{1/2} = 194$ min, respectively).

Table 13. Biological activities and microsomal half-lives of ligands (±)-**283–290** with extended carboxylate side chains.

Cpd.		EC_{50} <i>Pf</i> /NF54 [nM]	IC_{50} <i>Pf</i> /SHMT ± SD [nM] ^[a]	IC_{50} <i>At</i> /SHMT [nM]	$t_{1/2}$ [min] ^[b]
(±)- 283		22	186 ± 9	59.0	54
(±)- 284		10	165 ± 7	27.0	31
(±)- 285		84	186 ± 7	13.5	36
(±)- 286		17	168 ± 11	18.2	12
(±)- 287		52	172 ± 10	22.4	159
(±)- 288		19	90 ± 4	33.6	95
(±)- 289		55	97 ± 1	37.1	194
(±)- 290		17	130 ± 4	13.8	50

[a] Standard deviations are given. [b] *In vitro* metabolic stability measured in human liver microsomes.

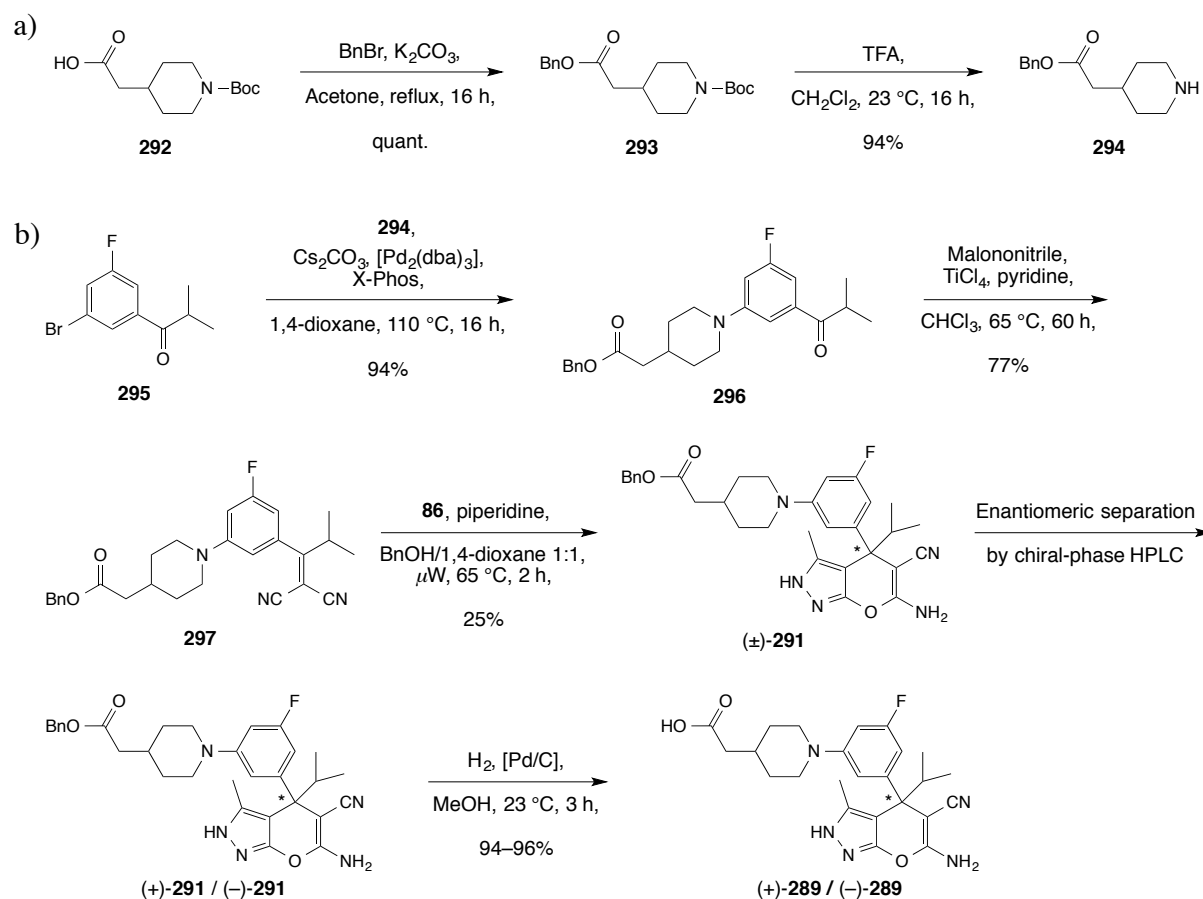
Plasma protein binding was assessed *via* ultracentrifugation in mouse plasma for (±)-**284** and (±)-**289**, as acidic ligands tend to have a high affinity for proteins present in the liquid portion of blood, such as albumin.^[204,205] Ligand (±)-**284** was found to be almost completely bound to plasma proteins (99.2 % bound) (Table 14), whereas the free fraction of piperidine (±)-**289** was much greater (82.9% bound), implying that an acceptable amount of (±)-**289** would be available to target SHMT *in vivo*. Taking all parameters into account, (±)-**289** was seemingly the compound with the most attractive profile, and the optimal balance between potency and microsomal stability.

Table 14. Protein binding data for (±)-**284** and (±)-**289** in mouse plasma.

Cpd.	Fraction unbound in mouse plasma (% Bound)
(±)- 284	0.008 ± 0.0015 (99.2% bound)
(±)- 289	0.171 ± 0.0065 (82.9% bound)

Accordingly, the pure enantiomers of (±)-**289** were investigated. For this purpose, the (+)- and (-)-enantiomers of the direct precursor ((±)-**291**) of (±)-**289** were separated by chiral phase HPLC prior to hydrogenation to yield (+)-**289** and (-)-**289** (Scheme 29). Synthesis of (±)-**291** started by the esterification of acetic acid **292** to give **293** that was subsequently deprotected to yield piperidine **294** (Scheme 29a). The latter was then coupled with fluoroaryl **295** to obtain the bicyclic scaffold **296**. The pyrazolopyran (±)-**291** was easily prepared *via* **297** as detailed in the previous sections (Scheme 29b). As expected, the affinity of (+)-**289** for *Pf*- and *At*SHMT is much greater than the one of (-)-**289** (Table 15). This trend was also observed in the cell-based assay, (+)-**289** inhibited cell proliferation efficiently ($EC_{50} = 35$ nM), conversely, (-)-**289** exhibited an EC_{50} value only in the micromolar range ($EC_{50} = 6143$ nM). In addition, a gain in microsomal stability was measured for the enantiopure (+)-**289** ($t_{1/2} > 255$ min) in comparison to (-)-**289** and the racemic mixture (±)-**289** (Table 15). Following these impressive results, (+)-**289** was selected for *in vivo* efficacy evaluation in a *Pf*SCID mouse model.

4. In Vivo Validation of SHMT as a Druggable Antimalarial Target



Scheme 29. a) Preparation of the piperidine building block **294**. b) Preparation of enantiopure (+)-**289** and (–)-**289**.

Table 15. Biological activities and microsomal half-lives of enantiopure ligands (+)-**289** and (–)-**289**.

Cpd.	EC ₅₀ <i>Pf</i> NF54 [nM]	IC ₅₀ <i>Pf</i> SHMT ± SD [nM] ^[a]	IC ₅₀ <i>At</i> SHMT [nM]	<i>t</i> _{1/2} [min] ^[b]
(±)- 289	55	97 ± 1	37.1	194
(+)- 289	35	110 ± 2	12.6	>255 ^[c]
(–)- 289	6143	1581 ± 49	977	206

[a] Standard deviations are given. [b] *In vitro* metabolic stability measured in human liver microsomes.

[c] This compound showed minimal degradation (<15%) over the course of the incubation.

The *in vivo* efficacy of (+)-**289** was studied at 4 × 50 mg/kg (p.o.) in a *Pf*SCID mouse model. Subsequent to the administration of (+)-**289** on days 3, 4, 5, and 6 after infection, a significant reduction of parasitemia of 73% (vs. untreated mice) was measured on day 7 after infection (Figure 73 and Table 16). Although, complete clearance was not achieved, this outcome constitutes a true proof of concept and shows for the first time that an inhibitor targeting SHMT can induce a compelling decrease of the proliferation of malaria parasites *in vivo*.

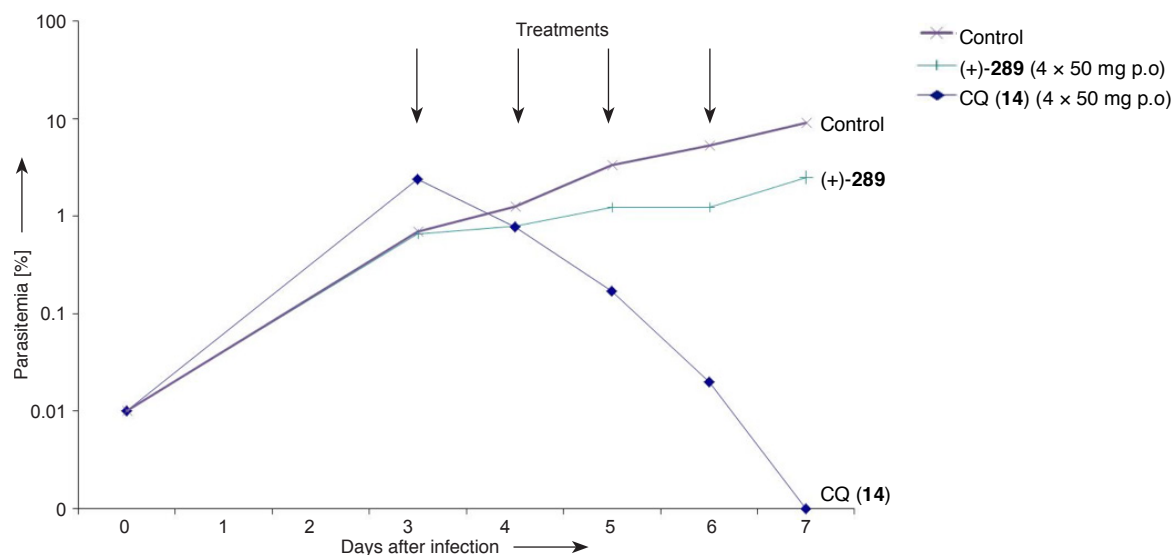


Figure 73. Therapeutic efficacy of (+)-289 against *Pf3D7*^{0087/N9}. The arrows indicate the days of treatment in the 4-day test by Peters. Values are the level of parasitemia in peripheral blood of $n = 2$ mice/group. CQ = chloroquine (14).

Table 16. *In vivo* efficacy of (+)-289 against *Pf3D7*^{0087/N9}. Shown are all values of parasitemia on day 7 post-infection. RBC = red blood cells.

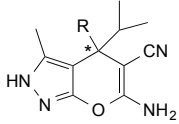
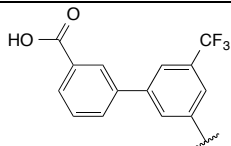
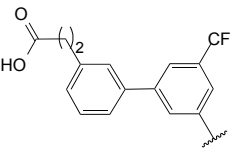
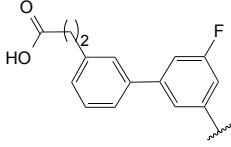
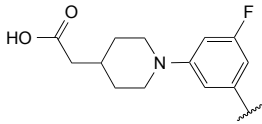
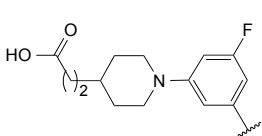
Substances	Dosage [mg/kg]: 4 ×	Route	Parasitized RBC over 100				Avg.	% of control	% Activity
			M1	M2	M3	M4			
(+)-289	50	p.o.	3.00	2.00	-	-	2.50	27.36	73
Control Day 7	-	-	8.95	9.10	9.80	8.70	9.14	-	-

4.2. Cytotoxicity and Mutagenicity Evaluation

Cytotoxicity of selected compounds was determined against rat myoblast L6 cells in a 72 h cytotoxicity assay (Table 17). None of the ligands was found to be cytotoxic with IC_{50} values in the high micromolar range and excellent safety indexes. In addition, the mutagenicity of the pyrazolopyran class of molecules was evaluated *via* an AMES assay employing (\pm)-281 as reference compound (Appendix, Section 9.4).^[206] This assay is a short-term bacterial reverse mutation assay, which was designed to detect chemical substances that can produce genetic damage leading to gene mutation. Out of the five strains examined (TA98, TA100, TA102, TA1535, and TA1537), reproducible evidence of mutagenicity (characterized by a 2-fold increase in revertant colony numbers over concurrent vehicle controls) was observed only in strain TA98 without metabolic activation at 5000 $\mu\text{g}/\text{plate}$ in a first experiment, and at

1250 $\mu\text{g}/\text{plate}$ and above in a second experiment. Hence, it is reasonable to state that this class of compounds does not induce significant mutagenicity that would preclude any further investigations.

Table 17. *In vitro* activities of selected pyrazolopyran ligands on *PfNF54* and rat myoblast L6-cell.

Cpd.		$\text{EC}_{50} \pm \text{SD}$ [nM] ^[a]	IC_{50} Rat myoblast L6-cell [μM]	Safety Index
(±)-276		54 ± 20	> 200	> 3800
(±)-284		10 ± 1	93.1	9702
(±)-288		19 ± 2	143.8	7688
(±)-289		55 ± 2	> 200	> 4000
(±)-290		14 ± 2	> 200	> 15000

[a] Standard deviation are given.

4.3. Co-crystal Structures of Carboxylate Analogues with *PvSHMT*

4.3.1. Binding Mode of the Biaryl Series

Co-crystal structures of either (+)-283, (+)-284, or (+)-288 with *PvSHMT* were resolved each at 2.3 Å resolution, and belong to the *C2* space group (Figure 74). They were all obtained using a racemic mixture of the respective ligands. In comparison to previously discussed *PvSHMT*–ligand complexes, subtle differences in the binding mode of these analogues can be observed. In the three co-crystal structures, the terminal carboxylate side chains protrude from the *pABA* channel. Two water molecules (W1 and W2) participate to the binding of the core of (+)-283 (Figure 74b). W1 takes part to a tripod-shaped interaction that bridges the N(2) of

the pyrazole ring with the side chain of Glu56 and His129. The second water molecule (W2) bridges the backbone C=O of Leu124 and the side chain of Thr357 *via* two hydrogen bonds, and is at van der Waals distance to the nonbasic NH₂ moiety of (+)-**283** (3.1 Å). However, analysis of the bond angles suggests more favorable interactions of the core NH₂ group with the backbone C=O of Leu124 and Gly128 than with W2.

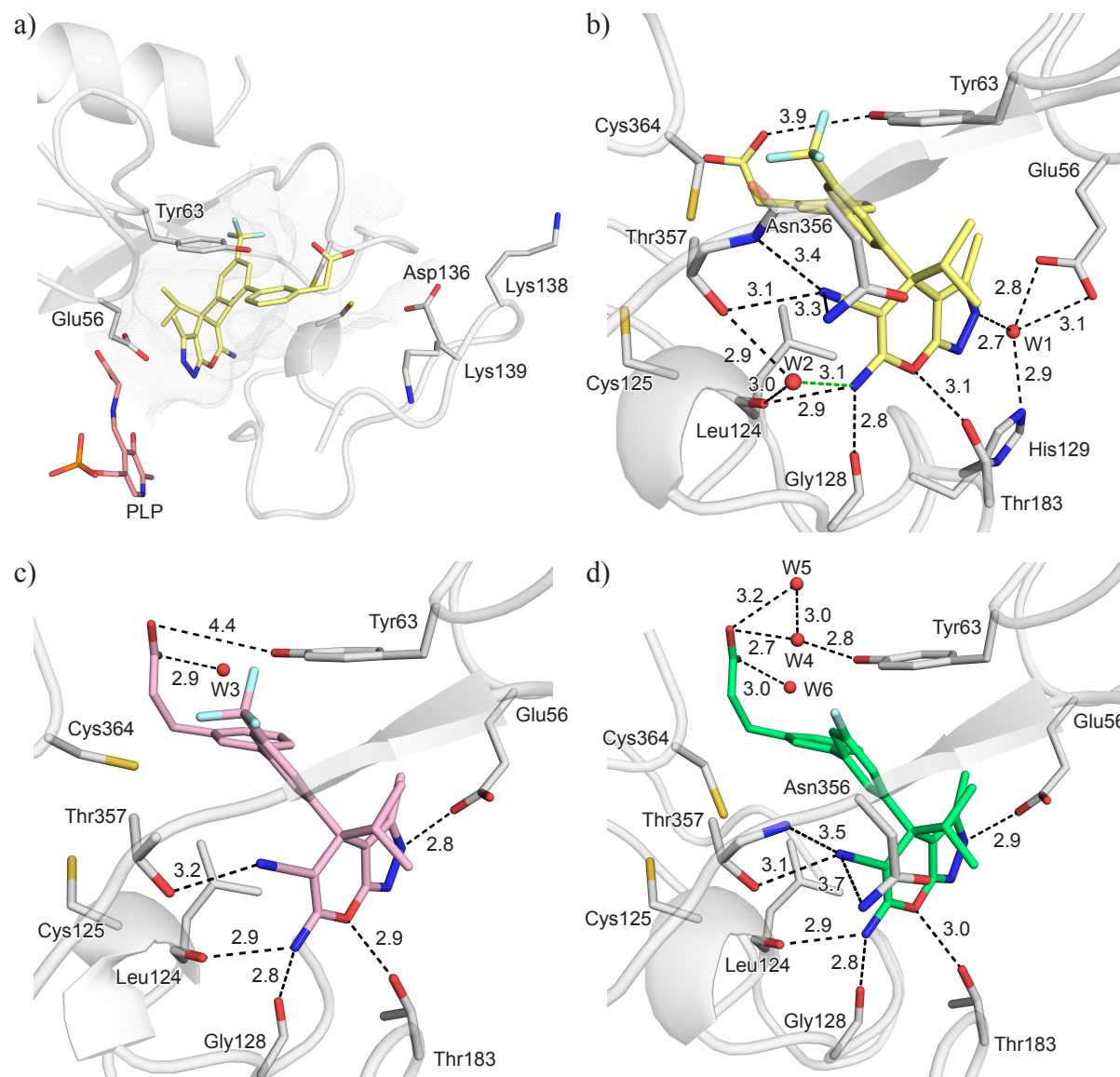


Figure 74. Co-crystal structures of (+)-**283**, (+)-**284**, and (+)-**288** with *Pv*SHMT. a) Occupancy of the active site by (+)-**283** (PDB code 5GVM, 2.3 Å). The mesh spans the volume of the binding pocket. b) Polar interactions between (+)-**283** and the protein. c) Binding mode of (+)-**284** (PDB code 5GVP, 2.3 Å). d) Binding mode of (+)-**288** (PDB code 5GVN, 2.3 Å). PLP is omitted for clarity. The water molecules are represented as red spheres. Distances are given in Å. Color code: C_{protein} grey, C₍₊₎₋₂₈₃ gold, C₍₊₎₋₂₈₄ pink, C₍₊₎₋₂₈₈ lime, C_{PLP} salmon, F light cyan, N blue, O red, P orange, S yellow.

In the complex with (+)-**284**, a water molecule (W3) solvates the carboxylate moiety of the ligand, however, no polar interaction is established with Tyr63 (Figure 74c). On the other hand, a small water cluster composed of W4, W5, and W6 was resolved in the vicinity of Tyr63 and the carboxylate of (+)-**288** (Figure 74d). Indeed, the latter is engaged in a water-mediated interaction with Tyr63 *via* W4 ($d(O^- \cdots O_{W4}) = 2.7 \text{ \AA}$ and $d(O_{W4} \cdots O_{Tyr}) = 2.8 \text{ \AA}$), while W5 and W6 solvate the carboxylate moiety.

Solvation of Tyr63 was also observed in the complexes with the biphenyl analogues (+)-**219** and (+)-**220** (Section 3.1.2, Figure 51). Superposition of the four co-crystal structures revealed a quasi-identical positioning of W1, W2, W4, and W5 nearby Tyr63 (Figure 75a). Whereas, W3 and W6, which solvate the respective carboxylate of (+)-**284** and (+)-**288**, are almost overlapping.

During the optimization program, it was hypothesized that extension of the carboxylate chain in (+)-**288** might allow to form a salt-bridge with Lys138 or Lys139. This interaction was suggested by molecular dynamics simulation where Lys139 was found to be able to swing towards the ligand (Figure 75b). However, this was not observed in any of the *Pv*SHMT–ligand complexes depicted in Figure 74.

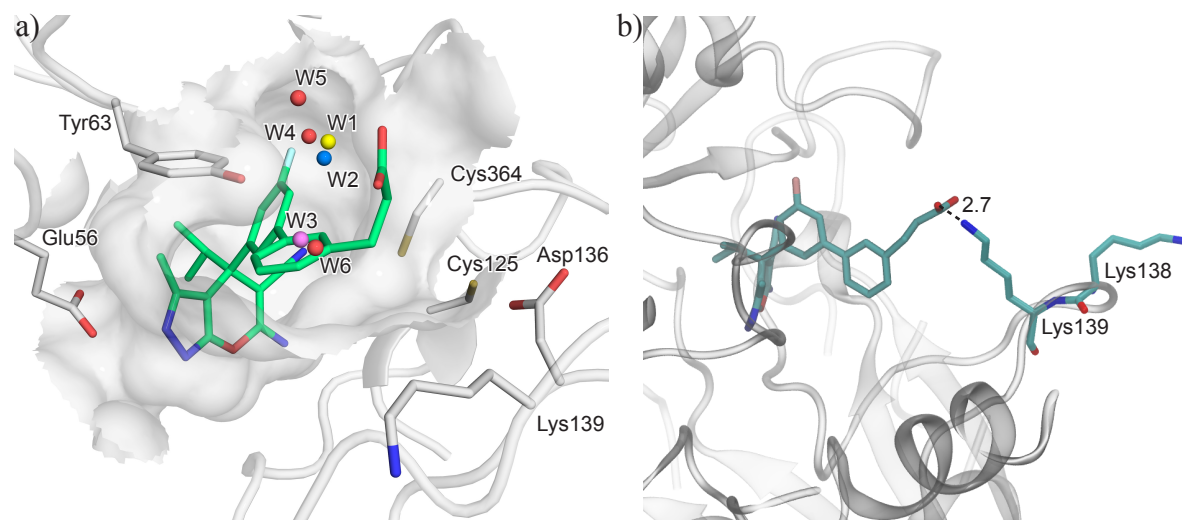


Figure 75. a) Superposition of the four co-crystal structures (PDB codes 5GVN, 5GVP, 5XMU, and 5XMV) revealing the positioning of the water molecules around Tyr63 in the context of 5GVN. Water molecules are represented as spheres. W1 (yellow) is extracted from PDB code 5XMU. W2 (marine) is extracted from PDB code 5XMV. W3 (purple) is extracted from PDB code 5GVP. W4, W5, and W6 (red) are from PDB code 5GVN. PLP is omitted for clarity. Color code: C_{protein} grey, $C_{(+)-288}$ lime, F light cyan, N blue, O red, S yellow. b) Snapshot of the MD simulation with (+)-**288** in *Pv*SHMT (PDB code 4PFF, 2.3 Å), showing the interaction between the carboxylate and Lys139. The distance is given in Å.

Ligands (+)-**283**, (+)-**284**, and (+)-**288** establish an array of dipolar and hydrophobic interactions with amino acids of *Pv*SHMT (Figure 76). The CF₃ moiety in (+)-**283** and (+)-**284** fills nicely the small lateral pocket lined by Lys355 and Pro367, and participates in short dipolar C–F···H–C and C–F···C=O interactions.^[207–209] One C–F bond is nearly orthogonal to the backbone carbonyl of Lys355 ($d(\text{F}\cdots\text{C}_{\text{Lys355}}) = 3.4\text{--}3.7 \text{ \AA}$, angle $\text{F}\cdots\text{C}=\text{O} = 67\text{--}71^\circ$) (Figures 76a and 76b). Another C–F bond is in close proximity to the side chain of Lys355 and forms $\text{F}\cdots\text{NH}^+$ interactions ($d(\text{F}\cdots\text{NH}^+) = 3.4 \text{ \AA}$).

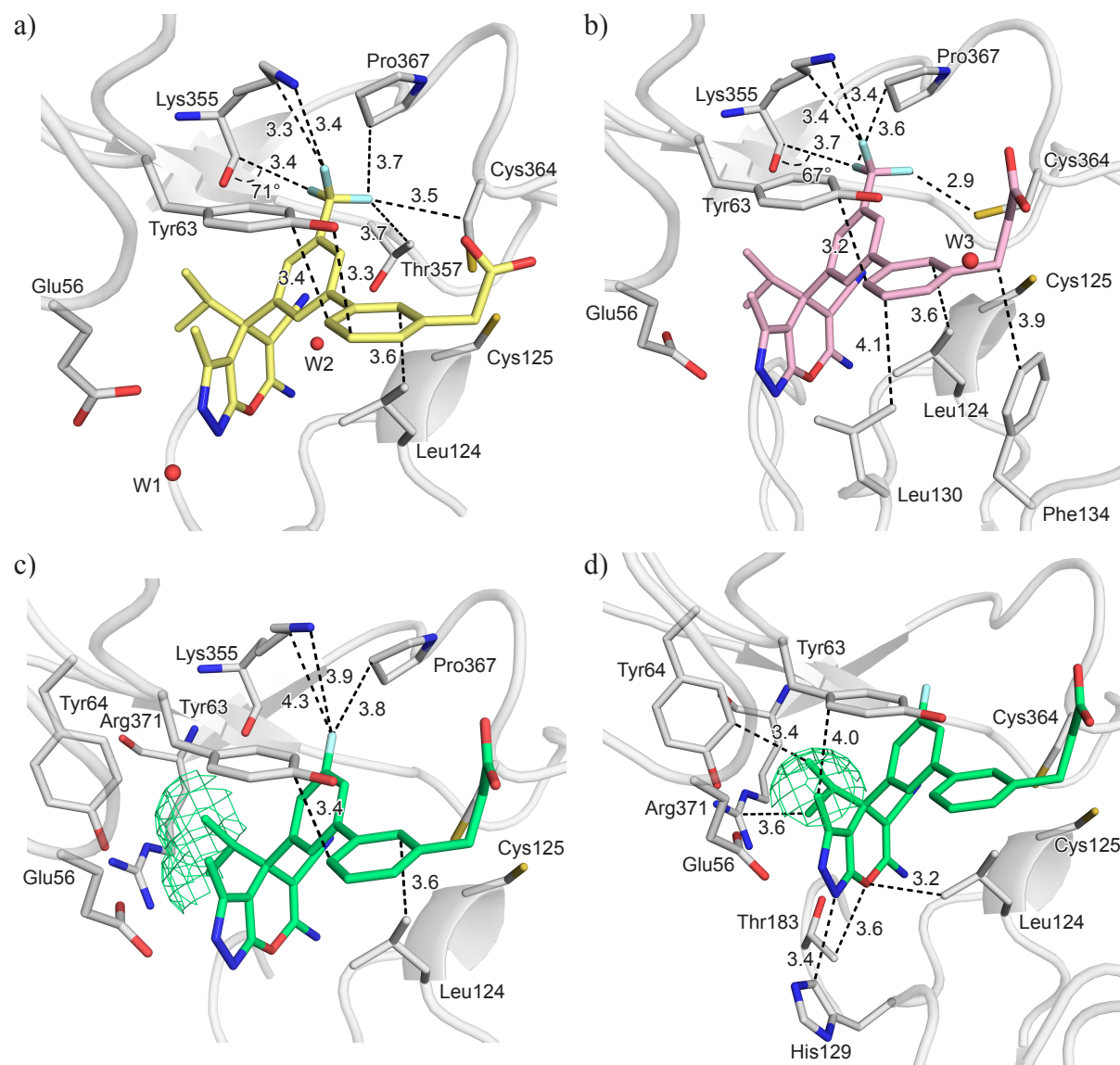


Figure 76. Dipolar and hydrophobic interactions of *Pv*SHMT with ligands: a) (+)-**283** (PDB code 5GVM, 2.3 Å); b) (+)-**284** (PDB code 5GVP, 2.3 Å); c) and d) (+)-**288** (PDB code 5GVN, 2.3 Å). The mesh spans the volumes of the methyl and isopropyl moieties. PLP is omitted for clarity. The water molecules are represented as red spheres. Distances are given in Å. Color code: C_{protein} grey, C₍₊₎₋₂₈₃ gold, C₍₊₎₋₂₈₄ pink, C₍₊₎₋₂₈₈ lime, F light cyan, N blue, O red, S yellow.

Similarly, the *meta*-fluorine of (+)-**288** is involved in hydrophobic contacts with Lys355 and Pro367 (Figure 76c). In addition, the methyl and isopropyl moieties attached onto the core provide an optimal filling of small lipophilic pockets as shown in Figures 76c and 76d. The isopropyl group addresses Tyr64 and Arg371, while the methyl group is at close distance to Tyr63 ($d(\text{C}-\text{H}\cdots\text{C}_{\text{Tyr63}}) = 4.0 \text{ \AA}$). It is also interesting to note that in the co-crystal structure with (+)-**284**, Cys364 points towards the ligand at a $\text{S}\cdots\text{F}$ distance of 2.9 \AA (Figure 76b) possibly forming a weak H-bond type interaction.^[210]

4.3.2. Binding Mode of the *N*-Piperidine-Aryl Series

Co-crystal structures with the piperidine analogues (+)-**282**, (+)-**285**, (+)-**286**, (+)-**289**, and (+)-**290** were also recorded (Figures 77 and 78). They diffracted at 2.3, 2.3, 2.4, 2.2, and 2.2 \AA resolution, respectively, and belong to the $C2$ space group. All complexes were obtained from a racemic mixture of ligands, excepted for the co-crystal structure with (+)-**289**, which was grown using enantiopure (+)-**289**.

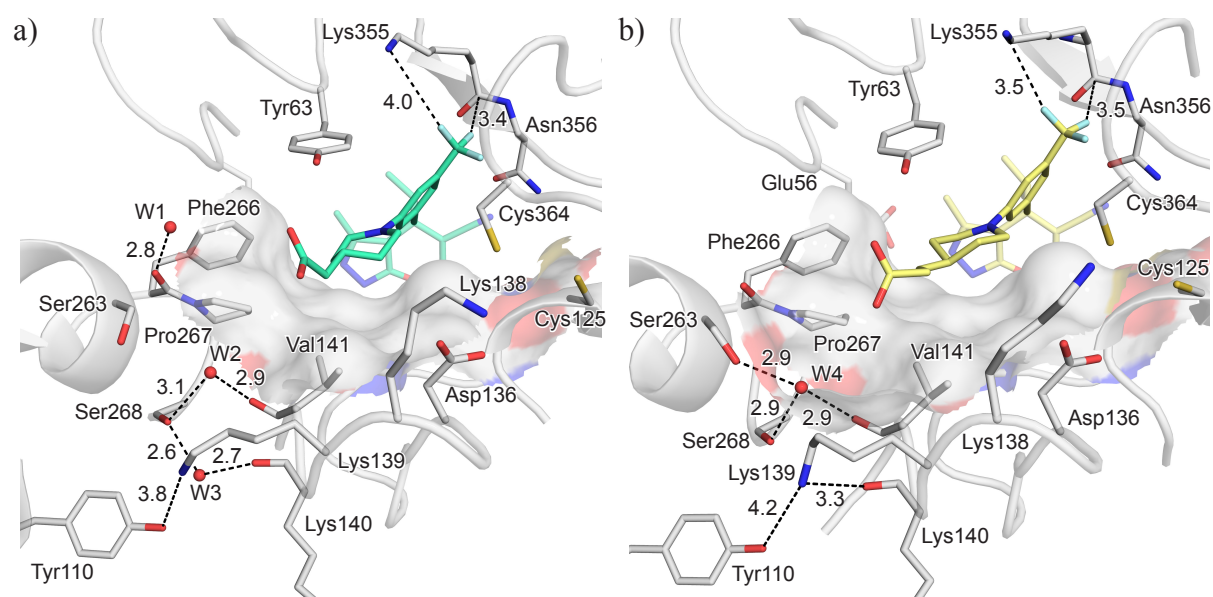


Figure 77. Co-crystal structures of *Pv*SHMT with: a) (+)-**285** (PDB code 5YG0, 2.3 \AA); and b) (+)-**286** (PDB code 5YG1, 2.4 \AA). PLP is omitted for clarity. The water molecules are represented as red spheres. Distances are given in \AA . Color code: $\text{C}_{\text{protein}}$ grey, $\text{C}_{(+)-285}$ cyan, $\text{C}_{(+)-286}$ gold, F light cyan, N blue, O red, S yellow.

Conversely than in the complex with ligand (+)-**288** described above, the respective carboxylate moieties of these analogues do not bind to Tyr63 *via* a water mediated interaction, and only the carboxylate of (+)-**290** is solvated by two water molecules in the recorded

co-crystal structures (Figure 78c). The carboxylate of (+)-**289** is at short distance to the phenolic ring ($d(\text{O}^- \cdots \text{O}_{\text{Tyr}}) = 3.4 \text{ \AA}$), however, its orientation, below the plane formed by Tyr63, does not favor a H-bond (Figure 78b).

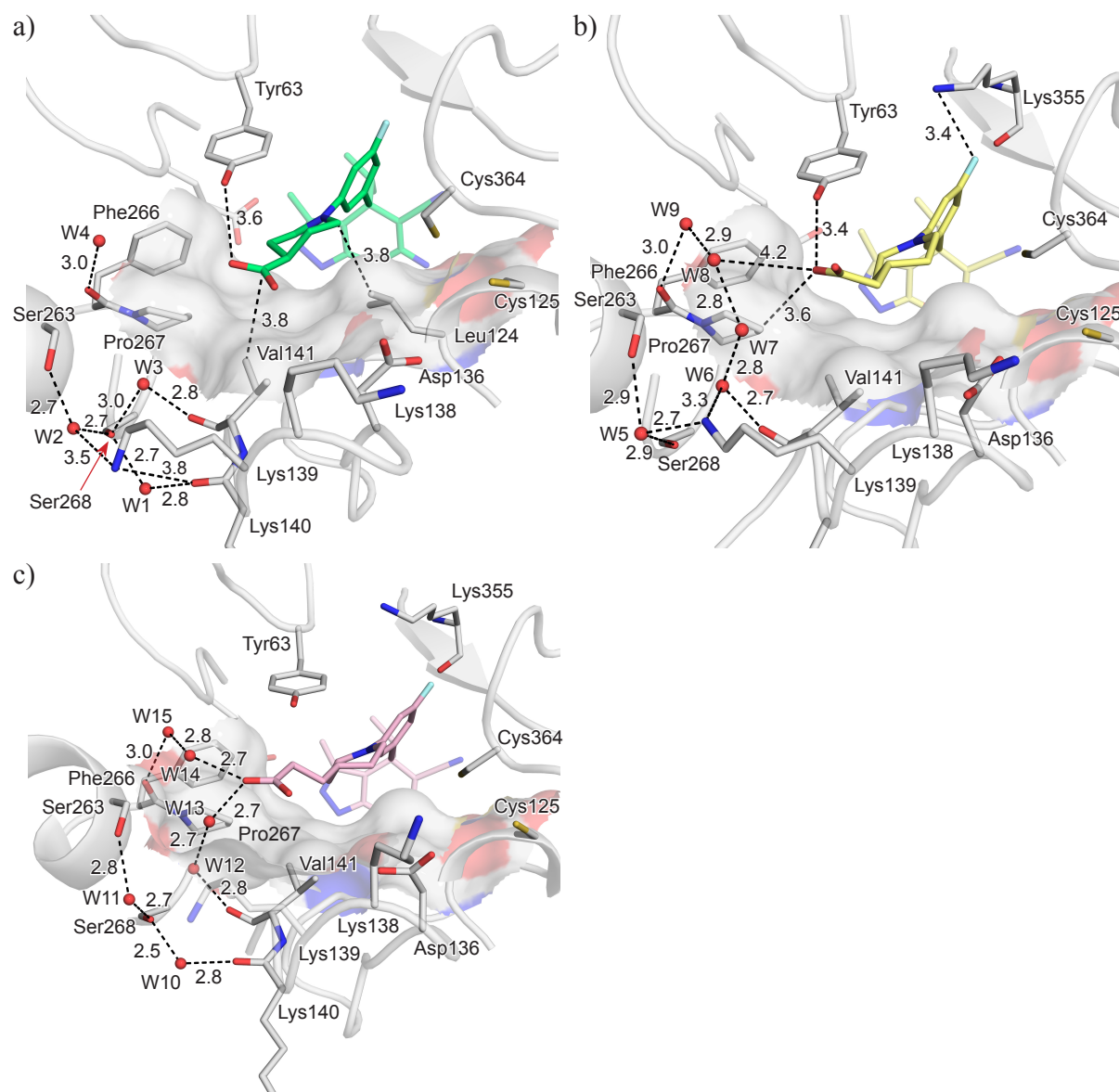


Figure 78. Co-crystal structures of *Pv*SHMT with: a) (+)-**282** (PDB code 5YFY, 2.3 Å); b) (+)-**289** (PDB code 5YFZ, 2.2 Å); c) (+)-**290** (PDB code 5YG2, 2.2 Å). PLP is omitted for clarity. The water molecules are represented as red spheres. Distances are given in Å. Color code: C_{protein} grey, $C_{(+)-282}$ lime, $C_{(+)-289}$ gold, $C_{(+)-290}$ pink, F light cyan, N blue, O red, S yellow.

All carboxylate side chains extend linearly from the ligands in the *p*ABA channel towards a small, rather lipophilic, pocket lined by the side chains of Lys139, Val141, Ser263, and Pro267 (Figures 77 and 78). Interestingly, this pocket hosts few water molecules that enjoy several polar contacts with the side chain of Tyr110, Lys139, Ser263, and Ser268 together with the backbone C=O of Lys140 and Val141. A lace composed of five water molecules (W5, W6,

W7, W8, and W9) was resolved in the co-crystal structure with (+)-**289** (Figure 78b). A similar arrangement of four water molecules is observed in the complex with (+)-**290** (Figure 78c).

Two water molecules (W2 and W3) resolved in the co-crystal structures with (+)-**289** and (+)-**290** act as a third binding partner and solvate the protein–ligand complexes (Figure 79a).^[211–213] The carboxylate at the termini of ligands (+)-**289** and (+)-**290** possibly stabilizes the water cluster. To verify this hypothesis, these two structures were superimposed with ligand structures without carboxylate and of equal resolution (2.2 Å) (Figure 79). Interestingly, five water molecules (W1–W5) are seen at identical positions in the co-crystal structure with *ortho*-chlorinated (+)-**220**, although the ligand does not interact with the latter (Figure 79a). Conversely, only the two water molecules (W4 and W5) in the vicinity of Lys139 are conserved when aryl sulfonamide (+)-**237** is bound to *Pv*SHMT (Figure 79b).

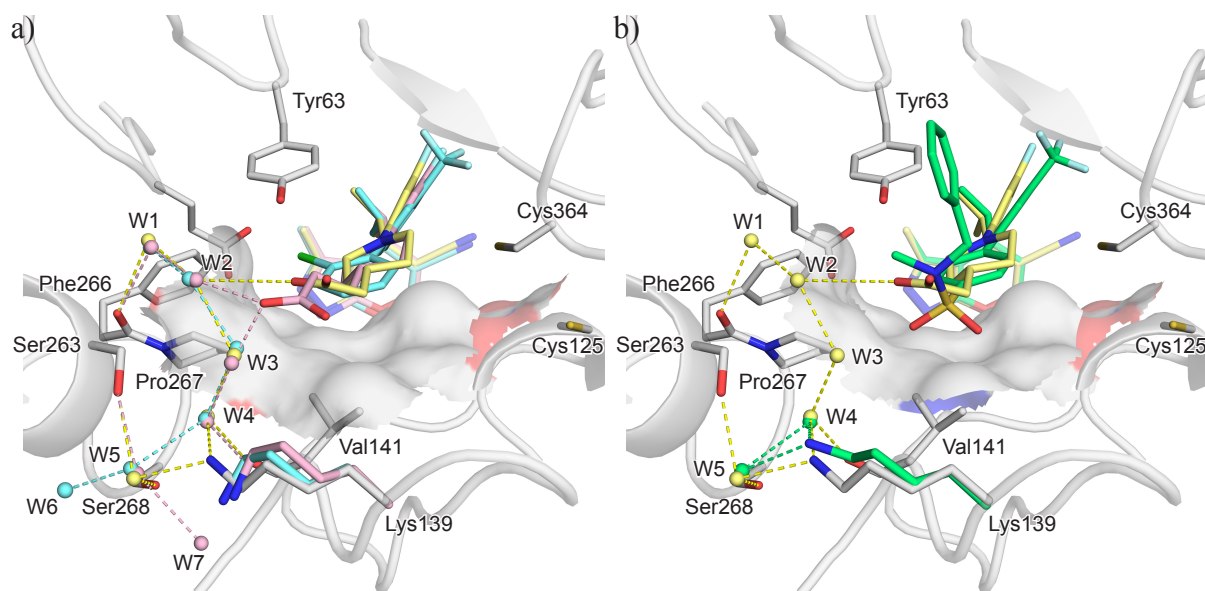


Figure 79. a) Superposition of the *Pv*SHMT–ligand complexes with (+)-**220** (cyan; PDB code 5XMV, 2.2 Å), (+)-**289** (gold; PDB code 5YFZ, 2.2 Å), and (+)-**290** (pink; PDB code 5YG2, 2.2 Å). b) Superposition of the *Pv*SHMT–ligand complexes (+)-**237** (lime; PDB code 5XMQ, 2.2 Å) and (+)-**289** (gold; PDB code 5YFZ, 2.2 Å). Water molecules are represented as spheres and are colored as their corresponding ligand. PLP is omitted for clarity. The dashes represent H-bonding interactions. Color code: C_{protein} grey, F light cyan, N blue, O red, S yellow.

In the five complexes with the *N*-piperidine-aryl analogues presented above, Lys139 points into the small pocket at the periphery of the *p*ABA channel, establishes several H-bonds with water molecules and/or amino acid residues, and adopts two slightly different orientations independently of the nature of the water cluster (Figures 77, 78, and 79). Thus, possibly explaining why it does not rotate towards any ligands to interact with their carboxylate side

chain as suggested by molecular dynamics (*vide supra*). Finally, a dipolar contact between the acetic acid moiety of (+)-**289** and Pro267 can be pinpointed ($d(\text{O}^- \cdots \text{H}-\text{C}_{\text{Pro267}}) = 3.6 \text{ \AA}$) (Figure 78b).

4.3.3. Spatial Location of the Carboxylate Moiety in the PvSHMT–Ligand Complexes

Superposition of ligands (+)-**283**, (+)-**284**, and (+)-**288** with 5-CHO-H₄F (**54**) shows a good match between the pyrazolopyran-based ligands and **54** (Figure 80a). The position of the terminal phenyl ring of the three inhibitors matches well with the *para*-aminobenzoyl side chain of the H₄F derivative **54**. The carboxylate moiety of each inhibitor points upwards in the similar direction to the glutamate side chain of the natural substrate. The binding modes of ligands (+)-**286**, (+)-**289**, and (+)-**290** also match nicely with the one of **54** (Figure 80b). Albeit, the position of the piperidine ring is slightly off compared to the *para*-aminobenzoyl side chain of **54**. Interestingly, the orientation of their respective carboxylate differs from the one seen in the biaryl series. They point linearly, in the same direction as the second COOH moiety of **54**.

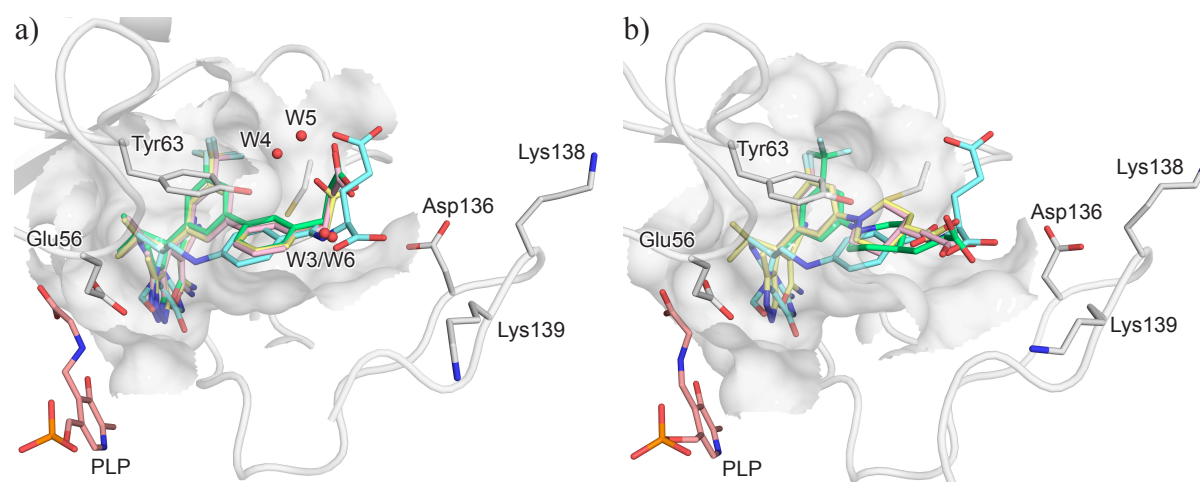


Figure 80. a) Overlay of (+)-**283** (from PDB code 5GVM, 2.3 Å), (+)-**284** (from PDB code 5GVP, 2.3 Å), (+)-**288** (from PDB code 5GVN, 2.3 Å), and **54** (from PDB code 4OYT, 2.4 Å) in PvSHMT (protein coordinates taken from PDB code 5GVN, 2.3 Å). The water molecules are represented as red spheres. Color code: C₅₄ cyan, C₍₊₎₋₂₈₃ gold, C₍₊₎₋₂₈₄ pink, C₍₊₎₋₂₈₈ lime. b) Overlay of (+)-**286** (PDB code 5YG1, 2.4 Å), (+)-**289** (PDB code 5YFZ, 2.2 Å), (+)-**290** (PDB code 5YG2, 2.2 Å) and **54** (from PDB code 4OYT, 2.4 Å) in PvSHMT (protein coordinates taken from PDB code 5YG1, 2.2 Å). The surface spans the volume of the binding pocket. Color code: C_{protein} grey, C₍₊₎₋₂₈₆ lime, C₍₊₎₋₂₈₉ gold, C₍₊₎₋₂₉₀ pink, C_{PLP} salmon, F light cyan, N blue, O red, P orange, S yellow.

It is noteworthy that grafting the monoglutamate tail of **54** onto the terminal phenyl/piperidine ring was not attempted, as modeling suggested only a poor overlay with the

corresponding fragment of **54**. Furthermore, this strategy was previously attempted on the thienyl ligand (4*R/S*,2''*S*)-**68**, giving inhibition only in the micromolar IC₅₀ range (Section 2.1).

4.3.4. Cys364–Loop Movement

The loop containing Cys364, named herein as Cys364–loop, is highly flexible as a consequence of its unique feature to exist either in a reduced or oxidized state, in which a covalent disulfide bond between Cys125 and Cys364 is formed. This flexibility is not limited to the plasmodial SHMT, but is also found in human SHMT despite its inability to form the disulfide bridge.^[214] The numerous co-crystal structures obtained throughout this program offered the possibility of studying the conformation of the Cys364–loop based on crystallographic information. As shown in Figure 81, the position of this loop varies substantially and its movements are undoubtedly linked to the presence of a ligand within the binding pocket, more precisely, to the nature of the *meta*-substituent on the phenyl ring.

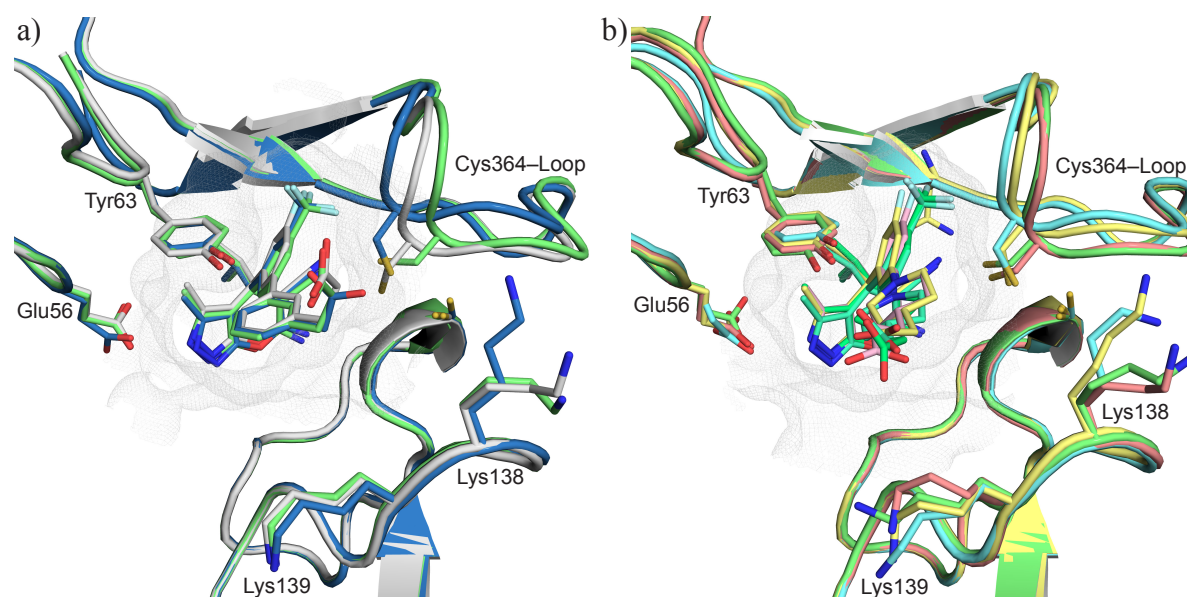


Figure 81. a) Superposition of the complexes of *Pv*SHMT with (+)-**283**, (+)-**284**, and (+)-**288**. b) Superposition of the complexes with (+)-**285**, (+)-**286**, (+)-**289**, and (+)-**290**. The protein loops and β -strands are represented as cartoon; the active site surface is represented as grey mesh. PLP and water molecules are omitted for clarity. Color code: *C_{PvSHMT-(+)-283}* marine, *C_{PvSHMT-(+)-284}* green, *C_{PvSHMT-(+)-285}* cyan, *C_{PvSHMT-(+)-286}* gold, *C_{PvSHMT-(+)-288}* grey, *C_{PvSHMT-(+)-289}* lime, *C_{PvSHMT-(+)-290}* salmon, F light cyan, N blue, O red, S yellow.

This flexibility is well exemplified by the $C\alpha \cdots C\alpha$ distance between Cys125 and Cys364, which ranges from 5.7 to 7.7 Å in the seven complexes depicted in Figure 81. The

shorter distances are measured for the structures with a *meta*-F substituent, while it increases for the CF₃ analogues. This reflects the ability of the Cys364-loop to adapt its conformation depending on the overall volume occupied by the ligand bound to *Pv*SHMT.

The high degree of flexibility of the Cys364-loop is further exhibited by overlaying co-crystal structures with *meta*-CN analogues (Figure 82). Again, the position of the loop fluctuates largely with C α ···C α distances up to 7.7 Å. From an activity point of view, these changes had limited impact on target affinity. Head-to-head comparison revealed that *meta*-F ligands have lower IC₅₀ values on *Pf*SHMT than the *meta*-CF₃ (e.g. IC₅₀ (±)-**284** 165 nM > (±)-**288** 90 nM or (±)-**286** 168 nM > (±)-**290** 130 nM). Hence, it is tempting to reason that small *meta*-substituents induce a Cys364-loop conformation that resemble the inactive oxidized state of the enzyme. However, the minor differences in affinity values prevent to draw any clear conclusion on this matter.

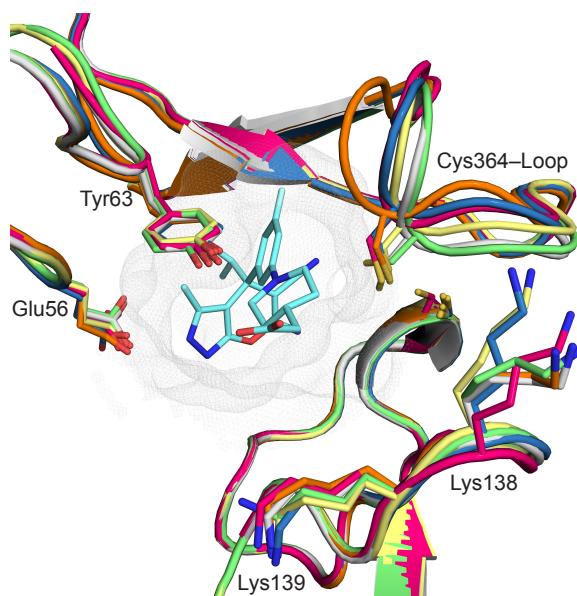


Figure 82. Superposition of the complexes with (+)-**67**, (+)-**112**, (+)-**283**, (+)-**286**, (+)-**288**, (+)-**289**. Only ligand (+)-**289** is shown for clarity. The protein loops and β -strands are represented as cartoon; the active site surface is represented as grey mesh. PLP and water molecules are omitted for clarity. Color code: C_{*Pv*SHMT-(+)-67} pink, C_{*Pv*SHMT-(+)-112} orange, C_{*Pv*SHMT-(+)-283} marine, C_{*Pv*SHMT-(+)-286} gold, C_{*Pv*SHMT-(+)-288} grey, C_{*Pv*SHMT-(+)-289} lime, C₍₊₎₋₂₈₉ cyan, F light cyan, N blue, O red, S yellow.

4.4. Summary on the Discovery of a Potent *In Vivo* Inhibitor and Co-crystal Structures Analysis

Based on rational design, highly metabolically stable pyrazolopyran-based ligands bearing a carboxylate moiety could be identified. The key adjustment was to substitute the *meta*-CF₃ substituent on the phenyl ring departing from the stereogenic center for a fluoride. This led to an acceptable loss of potency, however, it allowed to identify molecules with half-lives exceeding 3 h. The potency of these halo-ligands could be further improved by increasing the length of their carboxylate side chain, as suggested by structure-based design. Ultimately, the two enantiomers of ligand (±)-**289**, which exhibited a promising biological profile (EC₅₀ = 55 nM and *t*_{1/2} = 3.2 h), were separated by chiral-phase HPLC. Gratifyingly, pure (+)-**289** was more potent and more stable than the racemic mixture. It is noteworthy that given the early stage of the project, metabolism *via* non-microsomal enzymes was not explored and the potential for other routes of metabolism (*e.g.* phase II conjugation) cannot be ruled out at this stage. Candidate (+)-**289** displayed a significant *in vivo* efficacy, at 4 × 50 mg/kg (p.o.) in a *Pf*SCID mouse model, with a reduction of 73% of parasitemia compared to untreated mice. Hence, validating SHMT as a druggable antimalarial target. Besides, no cytotoxicity, neither mutagenicity was observed for this class of ligands.

Seven new co-crystal structure with *Pv*SHMT showed the good fit of the ligands with the bound substrate 5-CHO-H₄F (**54**); the pyrazolopyran core occupies the pterin binding pocket, the substituted bicyclic scaffold at the stereogenic center fills the *p*ABA channel, and the carboxylate side chains at the termini of the ligands imitate the terminal glutamate side chain of 5-CHO-H₄F (**54**). An interesting water-mediated interaction between the carboxylate of (+)-**288** and Tyr63 was observed for the first time. In addition, a small pocket hosting relatively conserved water molecules was identified in four complexes. In contrary to molecular dynamics predictions, Lys139 points towards this pocket, rather than to the ligands. Finally, the relative flexibility of the Cys364-loop was highlighted in the overlay of several co-crystal structures.

5. Investigation of Novel Scaffolds Inhibiting SHMT

The target-based assays on *Pf*SHMT and *At*SHMT were performed in the group of Dr. Pimchai Chaiyen by Dr. Ubolsree Leartsakulpanich and Aritsara Jaruwat (National Center for Genetic Engineering and Biotechnology, Thailand), and by Dr. Raphael Aponte (BASF-SE, Germany), respectively. The cell-based assays were performed in the group of Dr. Matthias Rottmann (Swiss Tropical and Public Health Institute, Basel) by Anja Schäfer. The co-crystal structures with *Pv*SHMT were solved by Dr. Penchit Chitnumsub and Wanwipa Ittarat (National Center for Genetic Engineering and Biotechnology, Thailand). The metabolic stability measurements were performed by Dr. Karen L. White (Monash University, Australia). Single molecule X-ray crystal structures were resolved by Dr. Nils Trapp. Marc Siggel contributed with his Master thesis to the synthesis of most of the pyrimidine-based ligands.

5. Investigation of Novel Scaffolds Inhibiting SHMT

Alternative scaffolds were investigated to identify novel active substances towards SHMT. Computer-assisted modeling, together with the knowledges acquired during the aforementioned optimization rounds, guided their design. The synthesis of two distinct series of molecules was pursued, the first focused on spirocyclic analogues featuring a pyrazolopyran core, the second targeted ligands with a *N*-heterocyclic core (pyrimidine or triazine).

5.1. Spirocyclic Analogues Featuring a Pyrazolopyran Core

5.1.1. Spiro-2-indolinone Series

To diversify the portfolio of SHMT inhibitors, it was envisaged to install a 2-indolinone scaffold onto the pyrazolopyran core. A significant number of active substances feature a 2-indolinone scaffold,^[215] a prominent example is the antimalarial NITD609 (**31**)^[72] discussed in the introduction. It has also been successfully incorporated in drugs for cancer treatment,^[216] such as in tyrosine kinase inhibitors,^[217–219] and is found in natural products,^[220] such as in the welwitindolinone alkaloids.^[221] In addition, this motif has been used to conformationally lock biologically active molecules in form of spirocycles.^[222]

Four 2-indolinone derivatives were designed, bearing terminal *ortho*-tolyl ((±)-**298**), 3-pyridyl ((±)-**299**), 4-pyridyl ((±)-**300**), and aryl sulfonamide ((±)-**301**) rings (Figure 83a). MOLOC modeling of the 3-pyridyl analogue (+)-**299** suggested that two favorable H-bond interactions could be formed *via* the 2-indolinone motif of (+)-**299** with the side chain of Asn354 and the backbone C=O of Lys355 (Figure 83b). All other key interactions of the core with the surrounding amino acids were retained.

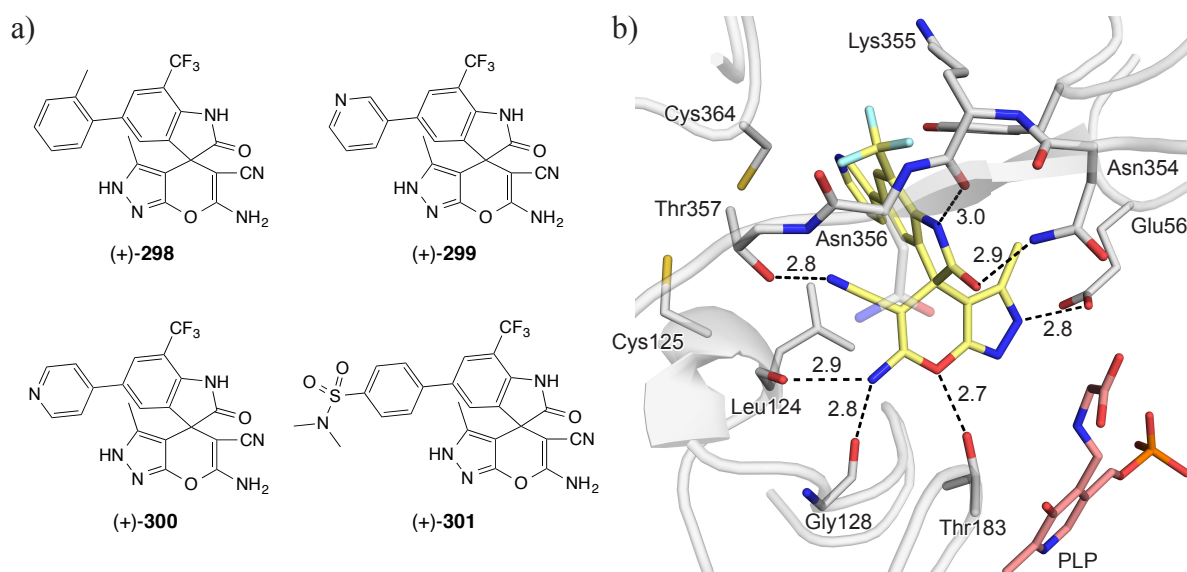
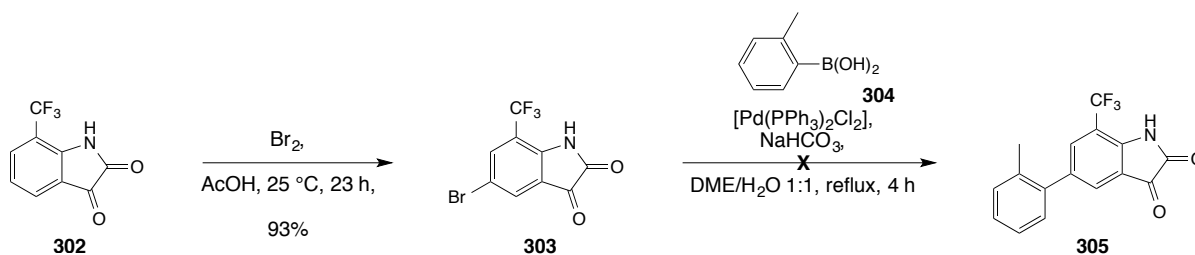


Figure 83. a) Designed ligands (\pm)-298–301 incorporating a 2-indolinone scaffold. b) Proposed binding mode of (+)-299 within the active site of P ν SHMT (PDB code 4TMR, 2.6 Å) as modeled with MOLOC. Distances are given in Å. Color code: C_{P ν SHMT} grey, C_{Ligand} gold, C_{PLP} salmon, F light cyan, N blue, O red, P orange, S yellow.

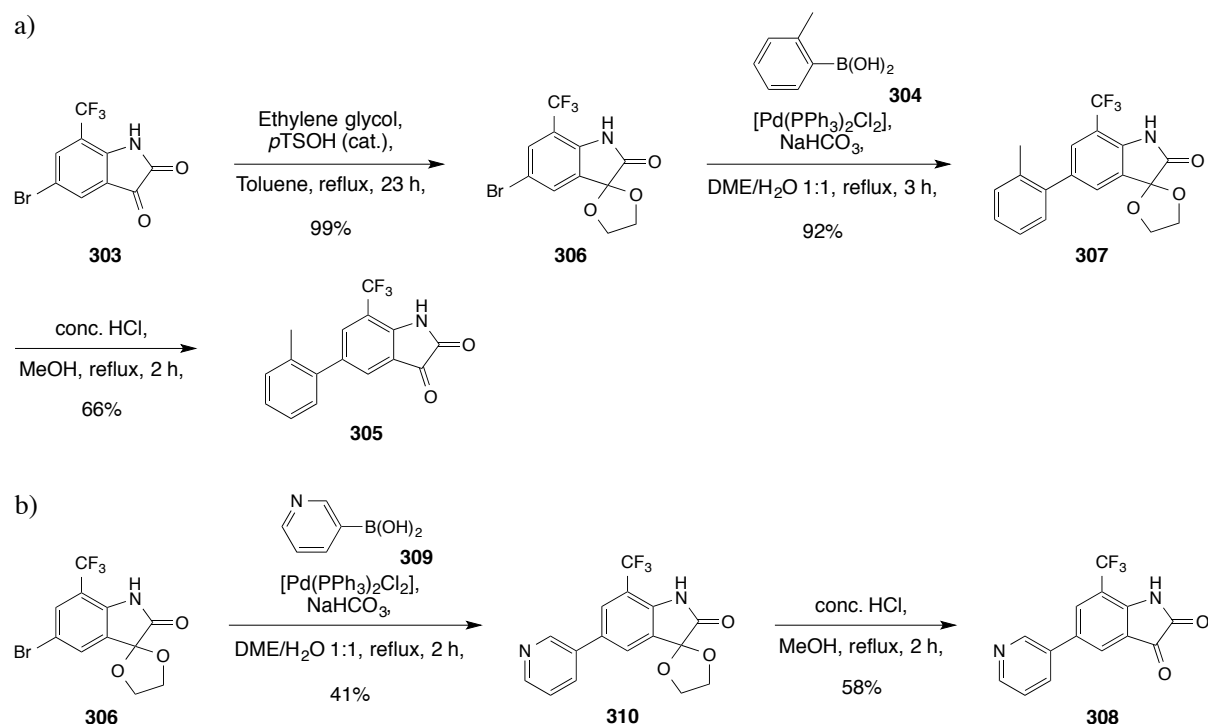
The synthesis started with a selective bromination^[223] of 7-trifluoromethyl-isatin **302** (Scheme 30), after which a direct cross-coupling between brominated **303** and *ortho*-tolyl boronic acid (**304**) was attempted. However, the bicyclic scaffold **305** did not form under the conditions reported in Scheme 30.



Scheme 30. Synthesis of brominated **303** and attempt to prepare *ortho*-tolyl isatin **305**.

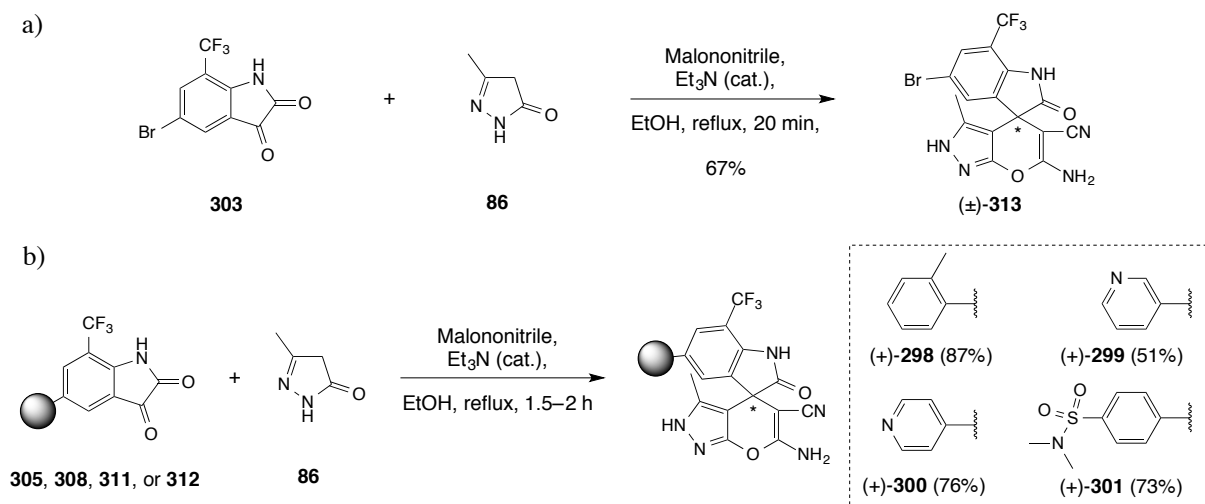
Wang *et al.* reported that cross-coupling involving 5-bromo-isatin derivatives can be impeded by the free carbonyl (ketone) group, therefore, they converted the ketone moiety to a ketal and subsequently performed a cross-coupling with success.^[224] Inspired by this report, **303** was transformed quantitatively to ketal **306**, then subjected to a Suzuki-Miyaura cross-coupling with **304** leading to the desired product **307** in excellent yield (Scheme 31a). A simple deprotection using conc. HCl gave access to **305**. Similarly, 3-pyridyl intermediate **308** was obtained by reacting ketal **306** with 3-pyridylboronic acid (**309**) to give **310**, which was

subsequently deprotected to afford ketone **308** (Scheme 31b). The isatin precursors **311** and **312**, for the synthesis of 4-pyridyl (\pm)-**300** and aryl sulfonamide (\pm)-**301**, were obtained free-of-charge from TCG LifeSciences.



Scheme 31. a) Successful synthesis of **305** via ketal **306**. b) Preparation of 3-pyridyl intermediate **308**.
pTSOH = *para*-toluenesulfonic acid

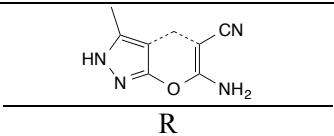
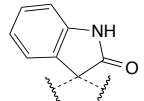
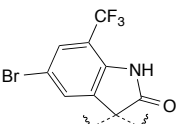
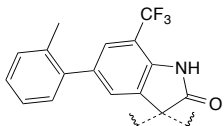
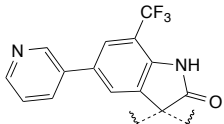
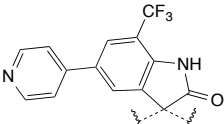
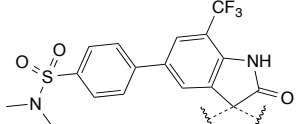
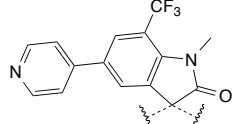
Pyrazolopyran derivatives are known to be accessible *via* a multi-component reaction.^[130,131,225,226] In the ligands reported in the previous sections, the steric hindrance induced by the isopropyl group precluded this approach and preparation of dinitrile intermediates was required prior to the formation of the pyrazolopyran core. Regarding the isatin building blocks **305**, **308**, **311**, and **312**, the keto group is more accessible, hence, a test reaction involving 5-bromo-isatin **303**, malononitrile, and 3-methyl-1*H*-pyrazol-5(4*H*)-one (**86**) was carried out (Scheme 32a). Complete conversion of **303** to (\pm)-**313** was achieved in only 20 min, and the target molecule (\pm)-**313** was isolated in 67% yield. This approach was applied to isatins **305**, **308**, **311**, and **312** leading to the synthesis of ligands (\pm)-**298–301** in moderate to high yields (Scheme 32b).



Scheme 32. a) Multi-component reaction involving **303**, malononitrile, and pyrazolone **86**. b) Synthesis of ligands (±)-**298–301**.

The core alone ((±)-**314**) did not exhibit any efficacy in all assays, while, its functionalization at both *meta*-positions led to minor improvements (Table 18). With the exception of *ortho*-tolyl (±)-**298**, which displayed low enzymatic activities (IC_{50} *Pf*SHMT = 5.2 μ M; IC_{50} *At*SHMT = 1.2 μ M), all other ligands ((±)-**299–301** and (±)-**313**) were inactive in the target assays. Cell-based efficacies were also unsatisfactory with measured EC_{50} values in the two-digit micromolar range. Ligand (±)-**300** was *N*-methylated and resulted in an enhanced potency (EC_{50} (±)-**315** = 1.5 μ M), which might be the result of a better cell-permeation. However, enzymatic activity still remained in the micromolar range (Table 18). Although few ligands possessed interesting microsomal stability ($t_{1/2}$ = 34–125 min), the work on this series was stopped and modifications of the 2-indolinone scaffold were undertaken. It is conceivable that introduction of polar groups at this position of the molecule is detrimental to activity, in fact, only ligands bearing an isopropyl moiety on the stereogenic center proved to be highly efficacious at this point.

Table 18. Biological activities and microsomal half-lives of ligands (\pm)-**298–301** and (\pm)-**313–315** bearing a 2-indolinone scaffold.

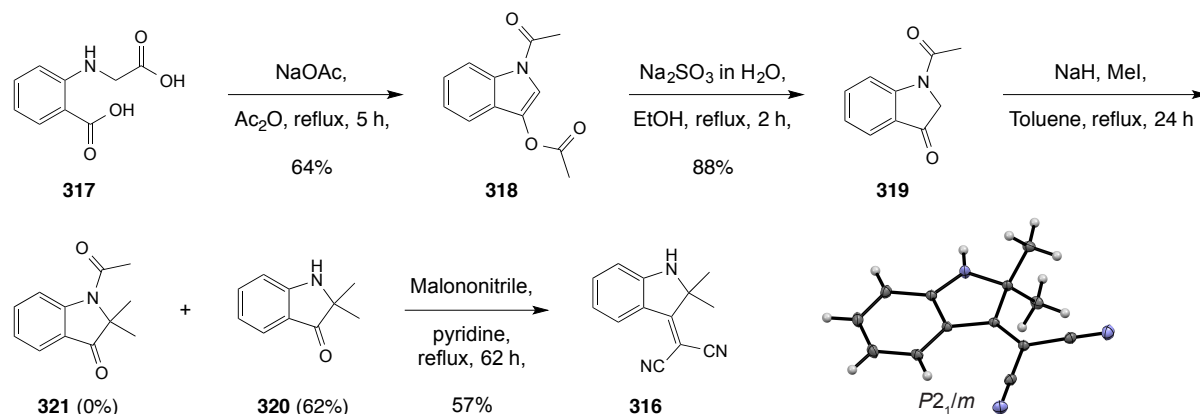
Cpd.		EC ₅₀ <i>Pf</i> NF54 [μ M]	IC ₅₀ <i>Pf</i> SHMT \pm SD [μ M] ^[a]	IC ₅₀ <i>At</i> SHMT [μ M]	<i>t</i> _{1/2} [min] ^[b]
(\pm)- 314		> 34	> 250	12% inhibition at 100 μ M	n.d. ^[c]
(\pm)- 313		22.7	> 250	14.3	125
(\pm)- 298		22.1	5.2 \pm 0.4	1.2	34
(\pm)- 299		22.8	> 250	48% inhibition at 100 μ M	94
(\pm)- 300		11.6	> 250	34.2	54
(\pm)- 301		16.7	n.d.	n.d.	n.d.
(\pm)- 315		1.5	> 250	9.6	7

[a] Standard deviations are given. [b] *In vitro* metabolic stability measured in human liver microsomes. [c] n.d. = not determined.

5.1.2. Spiro-dihydroindene Series

To test this hypothesis, we set out to prepare a molecule with a *gem*-dimethyl moiety instead of the carbonyl group. It is worth noting that the *gem*-dimethyl group is widely found in natural products and is used by medicinal chemists to modulate a broad range of properties, such as target affinity, metabolic stability, and the conformation of small molecules.^[227] The synthesis of the dinitrile precursor **316** was recently reported in the literature.^[228] It started with an intramolecular aldol-type condensation of diacid **317** to give indole **318** (Scheme 33). Selective deprotection of the enol employing sodium sulfite led to the dihydroindol-3-one **319**.

The latter was treated with sodium hydride and iodomethane, however, the deprotected *gem*-dimethyl-indol-3-one **320** was obtained in 62% yield instead of the intended product **321**. It is likely that the sodium hydride used was not fresh and possibly contained impurities of sodium hydroxide, which consequently led to the cleavage of the acetyl moiety. Subsequently, a Knoevenagel condensation with malononitrile was performed on **320** in pyridine at reflux to obtain dinitrile **316**. This molecule has a characteristic bright-red color and its structure was confirmed by X-ray crystallography (Scheme 33).

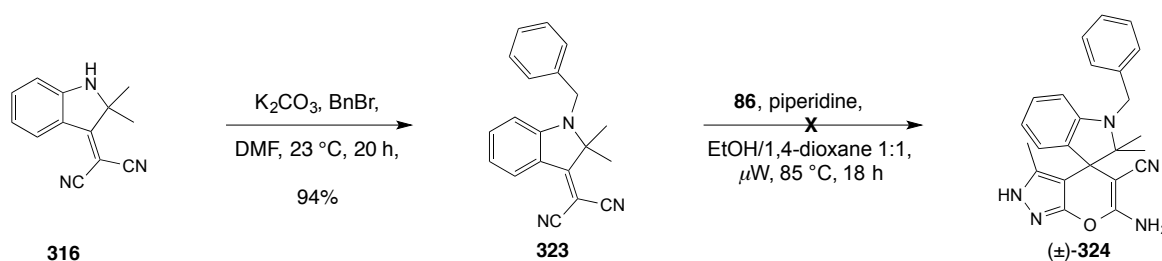


Scheme 33. Preparation of the *gem*-dimethyl building block **316**.

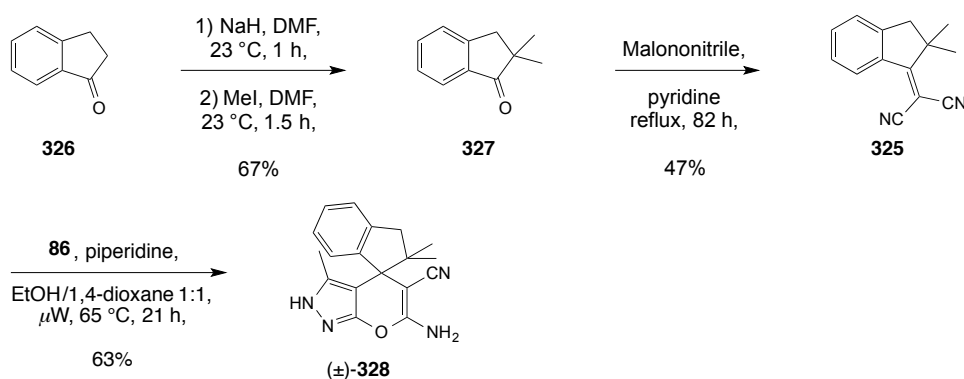
Unfortunately, all attempts to convert **316** to the target molecule (\pm)-**322** remained unsuccessful (Table 19). Numerous reaction conditions were investigated, however, neither changing the base, the solvent, nor the temperature had an effect on the outcome of the reaction. In fact, the starting material **316** remained unreacted, regardless of the reaction conditions. Considering previous efforts on the successful synthesis of ligands bearing an isopropyl group on the pyrazolopyran core, it can be excluded that this lack of reactivity is due to the steric hindrance of the *gem*-dimethyl group. Alternatively, the electron-donating ability of the dihydroindole scaffold might decrease the nucleophilicity of the exocyclic C=C double bond in **316**, hence, making this moiety less reactive towards the addition of pyrazolone **86**. Molecule **316** was therefore N-benzylated to **323**, but the pyrazolopyran (\pm)-**324** could not be synthesized either due to lack of reactivity (Scheme 34). The use of a stronger electron-withdrawing group, such as *para*-nitrobenzyl on the nitrogen atom could be an alternative, with the downside being its difficulties in removal afterwards. This approach was therefore not further pursued.

Table 19. Screening of the reaction conditions for the conversion **316** of to (\pm)-**322**.

Entry	Base	Solvent	Temp. / Time	Result
1	Et ₃ N (0.2 eq.)	EtOH	Reflux / 24 h	Unreacted 316
2	Piperidine (10.0 eq.)	EtOH/1,4-dioxane 1:1	65 °C (μ w) / 6 h	Unreacted 316
3	Piperidine (10.0 eq.)	EtOH/1,4-dioxane 1:1	85 °C (μ w) / 2 h	Unreacted 316
4	Hünig's base (1.0 eq)	MeOH/THF 4:1	50 °C / 62 h	Unreacted 316
5	Hünig's base (1.0 eq)	MeOH/THF 4:1	100 °C (μ w) / 3.5 h	Unreacted 316

**Scheme 34.** Synthesis of *N*-benzyl analogue **323** and attempt to convert it to (\pm)-**324**.

To test whether the stereoelectronic properties of **316** prevented any reaction with **86**, dihydroindene **325** was prepared in two steps from dihydroindenone **326** *via* **327** (Scheme 35). By applying the conditions generally used to synthesize pyrazolopyran-based ligands (*vide supra*), the spirocyclic molecule (\pm)-**328** was obtained in good yield, albeit, a longer reaction time (21 h vs. 3.5 h) was necessary to achieve a full conversion of **325**.

**Scheme 35.** Synthesis of spiroindene analogue (\pm)-**328**.

The structure of (\pm)-**328** was confirmed by X-ray crystallography (Figure 84). Intermolecular interactions within the crystal lattice revealed that the core was protonated at the N(2) as described in Section 3.3 (Figure 84c).

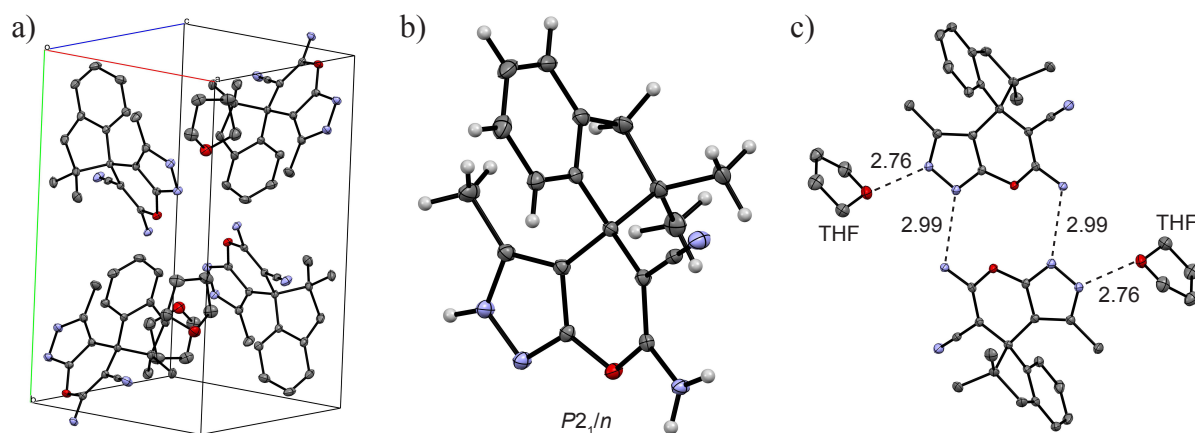
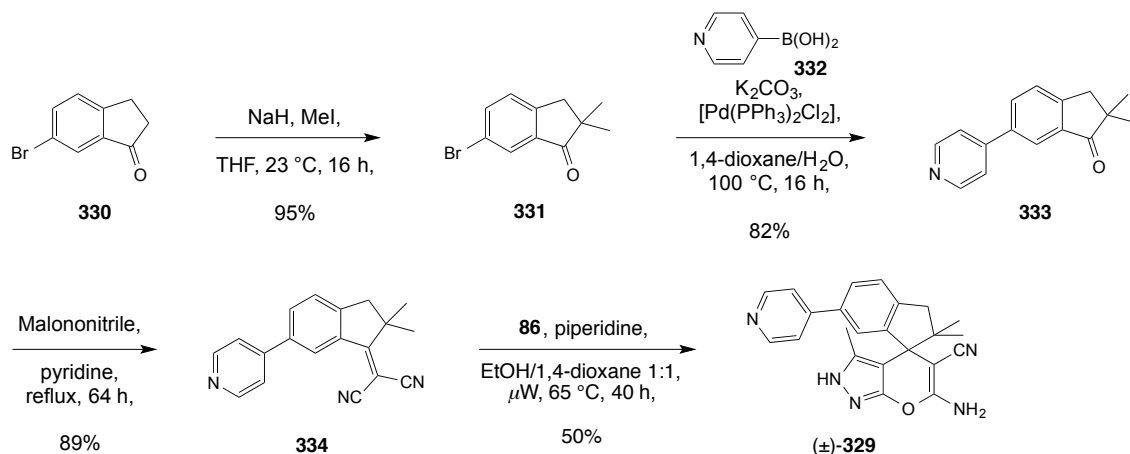


Figure 84. X-ray crystal structure of (\pm)-**328**. a) Crystal packing. b) Single enantiomer (+)-**328**. c) Intermolecular H-bond interactions involving THF molecules. Hydrogen atoms are omitted for clarity in a) and c). Distances are given in Å.

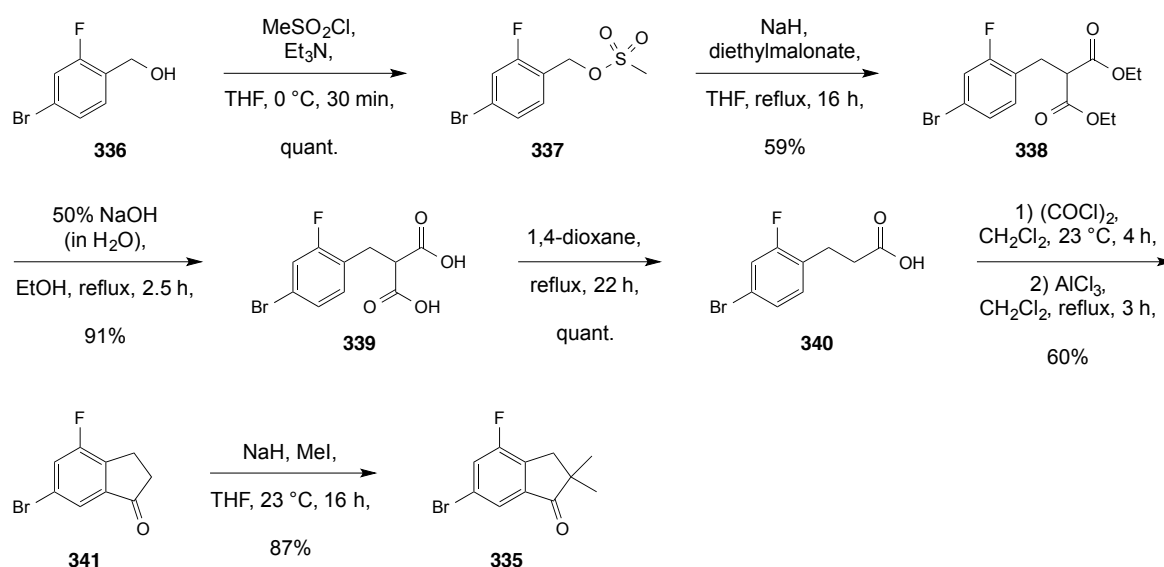
Encouraged by this outcome, several derivatives of (\pm)-**328** were designed and synthesized, starting from the 4-pyridyl analogue (\pm)-**329**. Following the synthetic approach depicted in Scheme 35, brominated **330** was efficiently bis-methylated *alpha* to the keto group to give **331**, followed by cross-coupling with 4-pyridylboronic acid (**332**) yielding **333** (Scheme 36). The conformationally locked analogue (\pm)-**329** was then synthesized *via* **334**.



Scheme 36. Preparation of the 4-pyridyl analogue (\pm)-**329**.

As described in the previous sections, introduction of a *meta*-substituent on the phenyl ring departing from the stereogenic center is crucial to achieve high potency and stability. Therefore, a fluoride was introduced on the 4-position and the 4-fluoro-dihydro-indenone

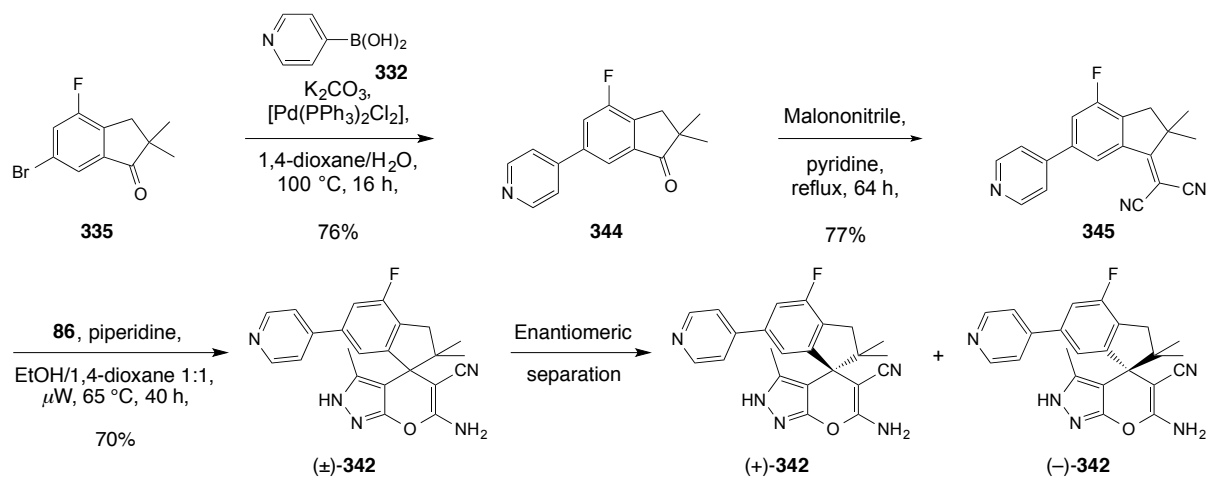
scaffold **335** was synthesized in six steps from benzylic alcohol **336** (Scheme 37). The latter was first converted quantitatively to sulfonate **337**^[229] and further reacted with diethyl malonate in the presence of sodium hydride to yield **338**.^[230] Saponification gave diacid **339** in high yield,^[230] after which mono-decarboxylation occurred upon heating **339** in 1,4-dioxane to reflux to form quantitatively the propionic acid **340**.^[231] Intermediate **340** was first treated with oxalyl chloride, followed by aluminium chloride to prepare the 2,3-dihydro-indenone scaffold **341** via a Friedel-Craft-type acylation.^[232] Finally, **335** was synthesized by bis-methylation of **341**.



Scheme 37. Multi-step synthesis of the 4-fluoro-dihydro-indenone scaffold **335**.

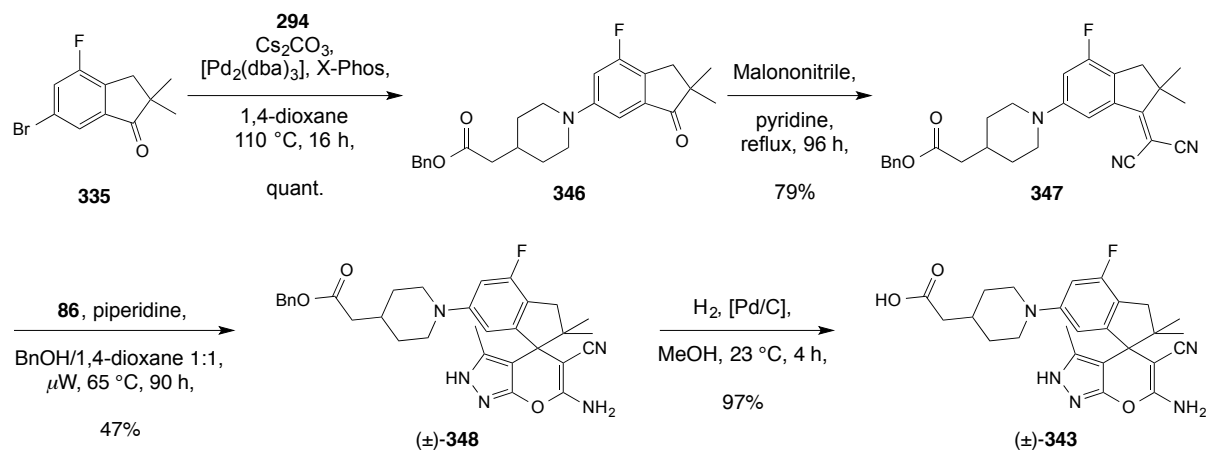
Scaffold **335** was subsequently subjected to Suzuki-Miyaura cross-coupling conditions with 4-pyridylboronic acid (**332**) towards the preparation of 4-pyridyl derivative (\pm)-**342** (Scheme 38). Alternatively, a Buchwald-Hartwig amination with benzyl (piperidin-4-yl)acetate (**294**) afforded the carboxylate (\pm)-**343** (Scheme 39). Those two terminal fragments were selected as they are known from previous optimization rounds to provide ligands with high potency and microsomal stability.

Hence, mixing dihydroindenone **335** with **332** in the presence of a Pd-based catalyst led to the formation of the bicyclic building block **344** in high yield (Scheme 38). Next, dinitrile **345** was synthesized prior to the core formation that gave the target molecule (\pm)-**342** in good yield. Enantiomeric separation by HPLC using a chiral-phase with a solvent mixture of hexane/EtOAc/*i*-PrOH 60:30:10 allowed to obtain enantiomerically pure (+)-**342** and (–)-**342** (see Experimental Part, Section 8.1.5 for the HPLC traces).



Scheme 38. Preparation of ligand (\pm)-**342** and isolation of enantiomerically pure (+)-**342** and (–)-**342**.

The piperidine fragment **294** was efficiently coupled with **335** to obtain **346** quantitatively, which was further reacted with malononitrile in pyridine at reflux to yield dinitrile **347** (Scheme 39). Then, the spirocyclic ligand (\pm)-**348** was prepared in a moderate yield and subsequent palladium-catalysed hydrogenation gave carboxylate (\pm)-**343**. Chiral separation using the same conditions described above allowed to isolate enantiopure (+)-**348** and (–)-**348** (see Experimental Part, Section 8.1.5 for the HPLC traces), which were deprotected to obtain (+)-**343** and (–)-**343**, respectively.

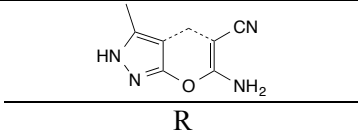
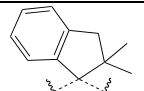
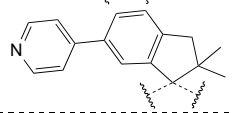
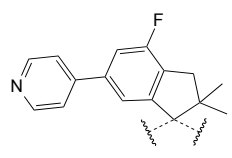
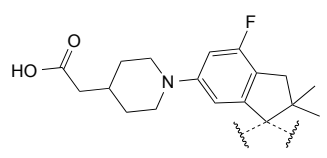
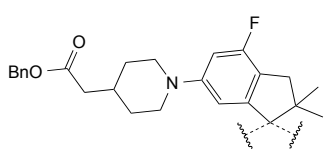
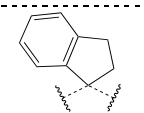


Scheme 39. Preparation of carboxylate (\pm)-**343**.

The spiro-dihydroindene ligands presented above were tested against *At*- and *Pf*SHMT, and in the cell-based assay against the *Pf*NF54 strain (Table 20). The sole core shows good sub-micromolar affinity for *Pf*SHMT (IC_{50} (\pm)-**328** = 0.201 μM), which is in contrast to the inactive 2-indolinone analogues (Table 18). Interestingly, a considerable affinity gain was measured for (\pm)-**329** featuring a terminal 4-pyridyl moiety (IC_{50} (\pm)-**329** = 0.030 μM), highlighting the importance of filling the *p*ABA channel to inhibit efficiently *Pf*SHMT.

Introducing a fluoride in ligand (\pm)-**342** did not affect substantially target affinity, and enzymatic activities were also in the two-digit nanomolar range for (\pm)-**343** and (\pm)-**348** (Table 20). These results were nicely underpinned by the inhibitory constants against *At*SHMT, even though, the affinity values were generally one order of magnitude lower (Table 20).

Table 20. Biological activities of spiro-dihydroindene ligands.

Cpd.		EC ₅₀ <i>Pf</i> NF54 [μ M]	IC ₅₀ <i>Pf</i> SHMT \pm SD [μ M] ^[a]	IC ₅₀ <i>At</i> SHMT \pm SD [μ M] ^[a]
(\pm)- 328		25.5	0.201 \pm 0.004	2.86 \pm 0.280
(\pm)- 329		2.358	0.030 \pm 0.001	0.173 \pm 0.009
(\pm)- 342		0.619	0.039 \pm 0.001	0.195 \pm 0.004
(+)- 342		0.334	0.014 \pm 0.002	0.281 \pm 0.016
(-)- 342		10.213	0.339 \pm 0.006	2.27 \pm 0.156
(\pm)- 343		2.131	0.061 \pm 0.001	0.112 \pm 0.006
(+)- 343		0.861	0.043 \pm 0.002	0.163 \pm 0.007
(-)- 343		> 21.5	2.51 \pm 0.03	4.69 \pm 0.200
(\pm)- 348		0.252	0.076 \pm 0.002	0.648 \pm 0.038
(+)- 348		0.165	0.060 \pm 0.002	0.494 \pm 0.043
(-)- 348		2.487	> 25.0	4.79 \pm 0.861
(\pm)- 349		> 36.0	4.36 \pm 0.72	47% inhibition at 100 μ M

[a] Standard deviations are given.

The cell-based SAR is in good agreement with target affinities (Table 20). More than 10-fold potency improvement was measured upon occupying the *p*ABA channel with a 4-pyridyl fragment (EC₅₀ (\pm)-**328** = 25.5 μ M > EC₅₀ (\pm)-**329** = 2.358 μ M). Addition of a fluoride to the *meta*-position had a significant impact, exemplified by the sub-micromolar potency measured for (\pm)-**342** (EC₅₀ = 0.619 μ M). A better EC₅₀ value was measured for benzyl ester

(±)-**348** ($EC_{50} = 0.252 \mu\text{M}$) that is presumably the result of an improved cellular permeation due to hydrophobic effects, as the corresponding carboxylate (±)-**343** is 10-fold less potent ($EC_{50} = 2.131 \mu\text{M}$).

Chiral recognition is also effective for this class of molecules (Table 20). As measured for pyrazolopyran-based ligands (*vide supra*), the (+)-enantiomer is much more active on target than the (–)-enantiomer in all head-to-head comparison pairs (*e.g.* (–)-**342**: 339 nM > (+)-**342**: 14 nM and (–)-**343**: 2510 nM > (+)-**343**: 43 nM). The strong preference for the (+)-enantiomer was also observed in the cellular assay, where ligand (+)-**348** displayed the best potency of the series ($EC_{50} = 165 \text{ nM}$). It is noteworthy that the *gem*-dimethyls on the indene scaffold are essential for activity, as their removal led to a considerable loss of affinity (ligand (±)-**349**: $IC_{50} P_f\text{SHMT} = 4.36 \mu\text{M}$; $EC_{50} > 36 \mu\text{M}$) (Table 20).

5.1.3. Binding Mode of Spiro-dihydroindene Analogues

Co-crystal structures of (+)-**342** and (+)-**343** with *Pv*SHMT were resolved at 2.4 and 2.3 Å resolution, respectively, and belong to the *C2* space group (Figure 85). They were both obtained using the (+)-enantiomer of the respective ligands. From the two complexes, it can be derived that (+)-**342** and (+)-**343** are (*S*)-configured. The overall conformation of the spiroindene core in each co-crystal structure is in good agreement with the small molecule X-ray crystal structure of (±)-**328** depicted in Figure 84. The binding mode of these ligands resembles the one of previous pyrazolopyran-based molecules, however, subtle differences are distinguishable. The core undergoes three strong H-bond interactions *via* the vinylogous cyanamide with the side chain of Thr357 and the backbone C=O of Leu124 and Gly128 (Figures 85a and 85c). The sp^3 oxygen atom of the pyran ring is at a short distance from Thr183 establishing a favorable H-bond, but it is also in proximity to the backbone C=O of Gly128 ($d(\text{O}\cdots\text{O}=\text{C}) = 3.4 \text{ \AA}$), which presumably results in a slightly repulsive interaction (Figure 85c). The core is slightly turned in such a way that the pyrazole NH cannot interact directly with Glu56. Indeed, the X-ray co-crystal structures show that the pyrazolopyran core is not aligned with Glu56, which precludes the formation of a strong direct ionic H-bond with the carboxylate. In the structure with (+)-**342**, only a weak H-bonding contact with $d(\text{N}\cdots\text{O}^-) = 3.6 \text{ \AA}$ is observed (Figure 85a). Nonetheless, a contact between the N(2)–H of (+)-**343** and Glu56 is mediated *via* H-bridging to a water molecule W2 (Figure 85c).

Due to the constrained core in (+)-**342** and (+)-**343** the small lateral pocket lined by the Cys364–loop is not properly filled by the fused phenyl ring and its *meta*-fluoro substituent,

leading to a small void. In the complex with (+)-**343**, a water molecule (W4) occupies this small cavity, solvates the CN moiety, and establishes a short orthogonal dipolar interaction with the C–F bond ($d(\text{O}\cdots\text{C}_{\text{sp}^2}\text{-F}) = 3.1 \text{ \AA}$, angle $(\text{F-C}_{\text{sp}^2}\text{-O}) = 78^\circ$) (Figure 85c). The lower resolution of the co-crystal structure with (+)-**342** did not allow refinement of water molecules with high accuracy in this small pocket.

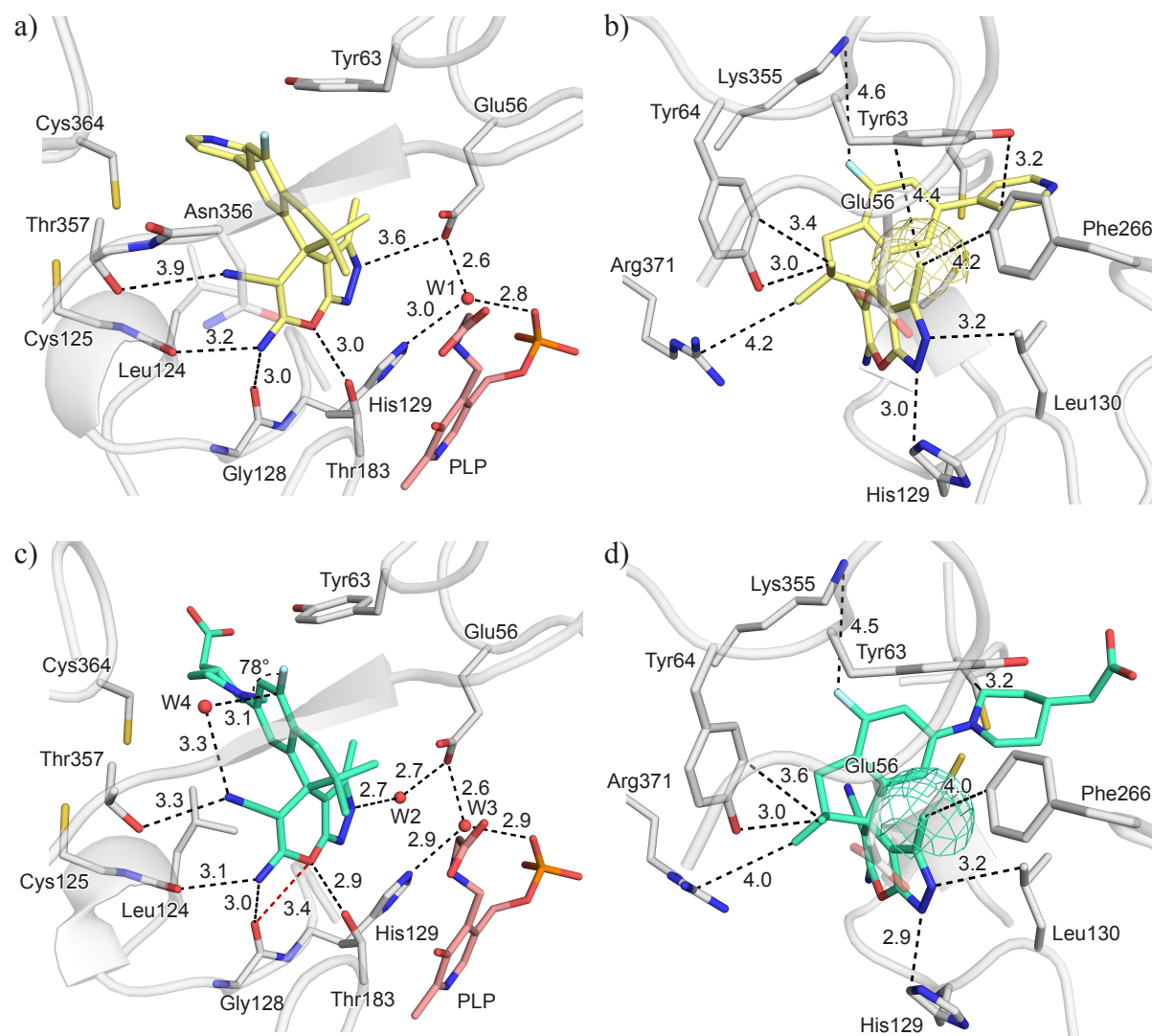


Figure 85. Co-crystal structures of *Pv*SHMT with: a) and b) (+)-**342** (PDB code 5YG3, 2.4 Å); c) and d) (+)-**343** (PDB code 5YG4, 2.3 Å). The water molecules are represented as red spheres. The mesh represents the volume of the methyl moiety. Distances are given in Å. Color code: C_{protein} grey, $C_{(+)\text{-342}}$ gold, $C_{(+)\text{-343}}$ cyan, C_{PLP} salmon, F light cyan, N blue, O red, P orange, S yellow.

In both structures, the methyl group on the pyrazole ring is surrounded by the lipophilic side chains of Tyr63 and Phe266, while the *gem*-dimethyl moiety on the core interacts with both Tyr64 and Arg371 (Figures 85b and 85d). Additional dipolar interactions can be pinpointed between the pyrazole ring and *Pv*SHMT residues, namely His129 and Leu130.

The terminal substituents on the spiroindene core nicely occupy the *p*ABA channel (Figure 85). The carboxylate of (+)-**343** is solvated by a water molecule (W5), which is at short distance of a second water molecule (W6) ($d(\text{O}\cdots\text{O}) = 2.9 \text{ \AA}$) (Figure 86a). As detailed previously, a network of water molecules was refined at the entrance of the *p*ABA channel (Figure 86a).

Superposition of the *Pv*SHMT–(+)-**343** complex with the one of its closely related analogue (+)-**289** revealed a good structural match (Figure 86b). On the one hand, the terminal carboxylate moiety and the vinylogous cyanamide overlay perfectly. The latter clearly anchors the ligands within the *Pv*SHMT binding pocket, and the molecules are oriented according to this moiety and their respective preferred conformations. On the other hand, the phenyl rings departing from the stereogenic center adopt two distinct orientations. As discussed above, in (+)-**289**, the phenyl ring is oriented towards the lateral cavity lined by the Cys364–loop, whereas in (+)-**343**, the fused phenyl ring is rotated by 19.6° with respect to the plane of the aforementioned moiety, and W4 occupies the cavity instead (Figure 86b). Additionally, the spiro-cyclic motif in (+)-**343** forces the pyrazolopyran core to adopt a significantly less planar conformation than in (+)-**289**. Consequently, the pyrazole fragment of (+)-**343** is not aligned with Glu56 and deviates by 12.5° compared to the original binding mode (Figure 86b).

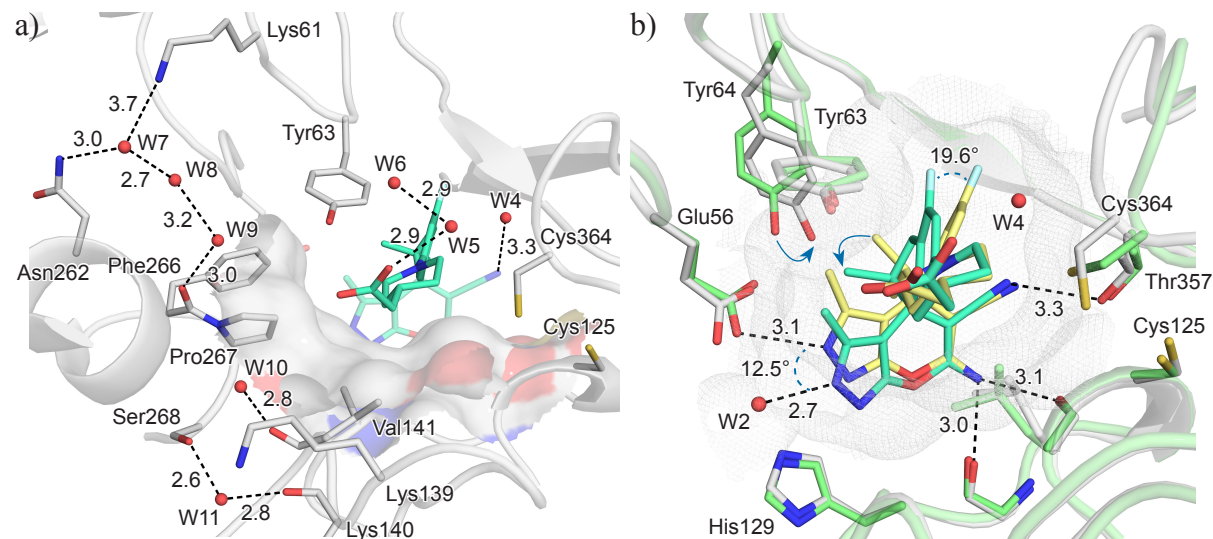


Figure 86. a) Occupancy of the *p*ABA channel by (+)-**343** within the *Pv*SHMT binding site (PDB code 5YG4, 2.3 Å). b) Overlay of the *Pv*SHMT–ligand complexes obtained with (+)-**289** (PDB code 5YFZ, 2.2 Å) and (+)-**343** (PDB code 5YG4, 2.3 Å). The water molecules are represented as red spheres. The surface and the mesh represent the volume of the binding pocket. Distances are given in Å. Color code: $C_{PvSHMT-(+)-289}$ green, $C_{PvSHMT-(+)-343}$ grey, $C_{(+)-289}$ gold, $C_{(+)-343}$ cyan, F light cyan, N blue, O red, S yellow.

Finally, the positioning of one CH₃ group (from the isopropyl moiety in (+)-**289** and the *gem*-dimethyl moiety in (+)-**343**) in the back of the pocket varies markedly. Accordingly, Tyr64 swings away (shift of the phenolic O-atom by 1.6 Å) in order to compensate for the small void created by the different positioning of this methyl moiety in the PvSHMT-(+)-**343** complex (Figure 86b). These two co-crystal structures underline the paramount importance of the vinylogous cyanamide in the binding mode of both ligands classes to PvSHMT, in contrast, they suggest that the pyrazole fragment can possibly be replaced by alternative moieties without affecting much target affinity (IC₅₀ (+)-**289** = 110 nM; IC₅₀ (+)-**343** = 43 nM).

5.2. De novo Design of Inhibitors for SHMT

5.2.1. Design and Synthesis of Pyrimidine-based Ligands

A class of ligands based on a pyrimidine core was investigated. The vinylogous cyanamide was kept as key structural element in the *de novo* design approach. An exocyclic amide was installed on the core of pyrimidine **350** in order to interact with Glu56 (Figure 87). As exemplified above, filling the *p*ABA channel is crucial for high affinity, hence, it is necessary to properly orient the vector departing from the core of the molecule. A cyclopropyl moiety was therefore introduced, as it is known to orient its two geminal substituents in an almost perpendicular fashion.^[233] Alternatively, the cyclopropyl moiety was replaced by an SO₂ group (in ligand **351**) that also leads to the desired orientation.

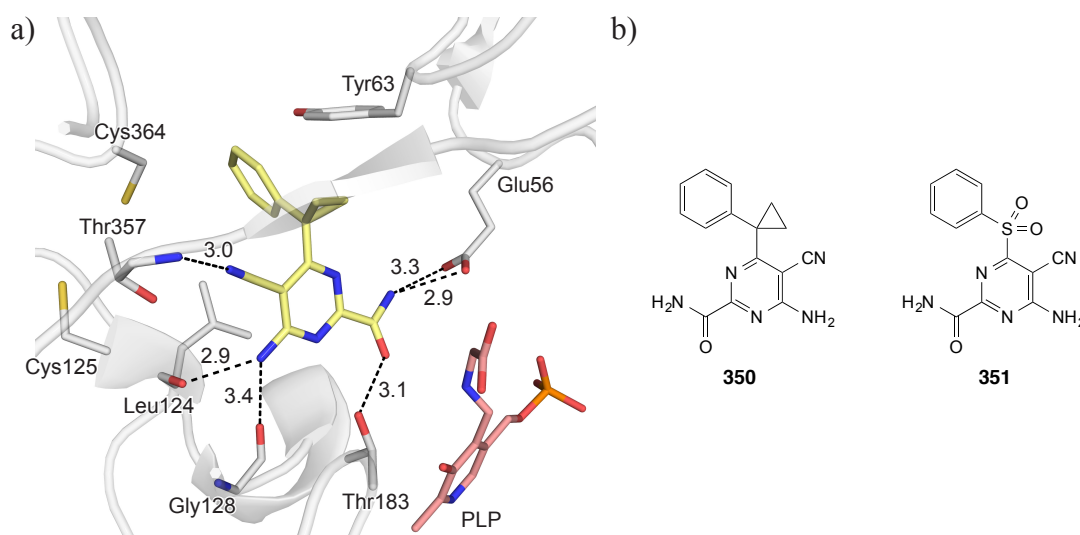


Figure 87. a) Proposed binding mode of **350** within the active site of PvSHMT (PDB code 4TMR, 2.6 Å) as modeled with MOLOC. Distances are given in Å. Color code: C_{PvSHMT} grey, C_{Ligand} gold, C_{PLP} salmon, N blue, O red, P orange, S yellow. b) Molecular structure of ligands **350** and **351**.

In the CSD, the retrieved mean $C_{sp^2}-C_{sp^3}-C_{sp^2}$ (or $C_{sp^2}-S-C_{sp^2}$) angle is equal to 112° and 104° for cyclopropyl- and sulfone-containing molecules, respectively (Figure 88). The main advantage of these molecules is that they do not contain a stereogenic center, and thus does not require enantiomeric separation. Additionally, they feature functional groups commonly used in drug design that are known to have good metabolic stability.

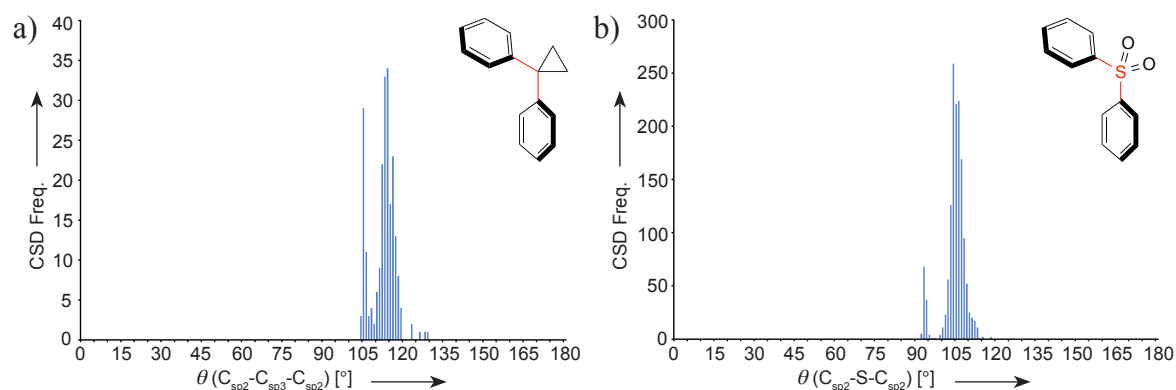
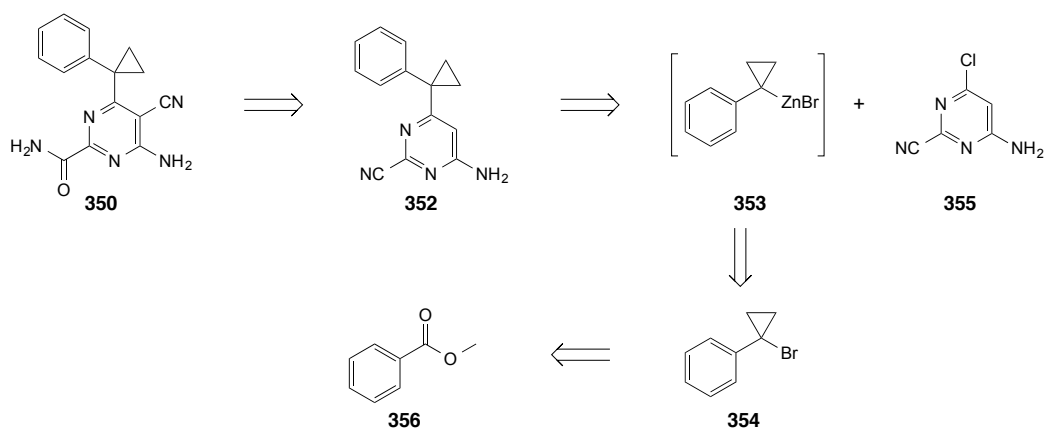


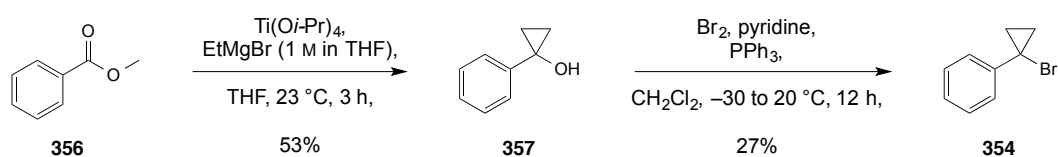
Figure 88. a) Angle histogram for *gem*-disubstituted-cyclopropyls derived from CSD ligands. b) Angle histogram for aryl sulfones derived from CSD ligands.

Compound **350** was targeted to test the feasibility of the synthetic approach. However, additional installation of a terminal moiety filling the *p*ABA channel would be required for high affinity. It was envisioned that ligand **350** could be obtained in few steps from aminopyrimidine **352** (Scheme 40). The key step involves a Negishi cross-coupling^[146] between the organozinc species **353** generated *in situ* from the brominated cyclopropyl **354** and chloropyrimidine **355**. The respective brominated cyclopropyl moiety of **354** was to be synthesized through a Kulinkovich reaction^[234] involving methyl benzoate (**356**) followed by a bromination. This convergent approach is particularly attractive, as it offers the possibility of using various organozinc derivatives in the cross-coupling step, hence, enabling the synthesis of multiple target molecules.



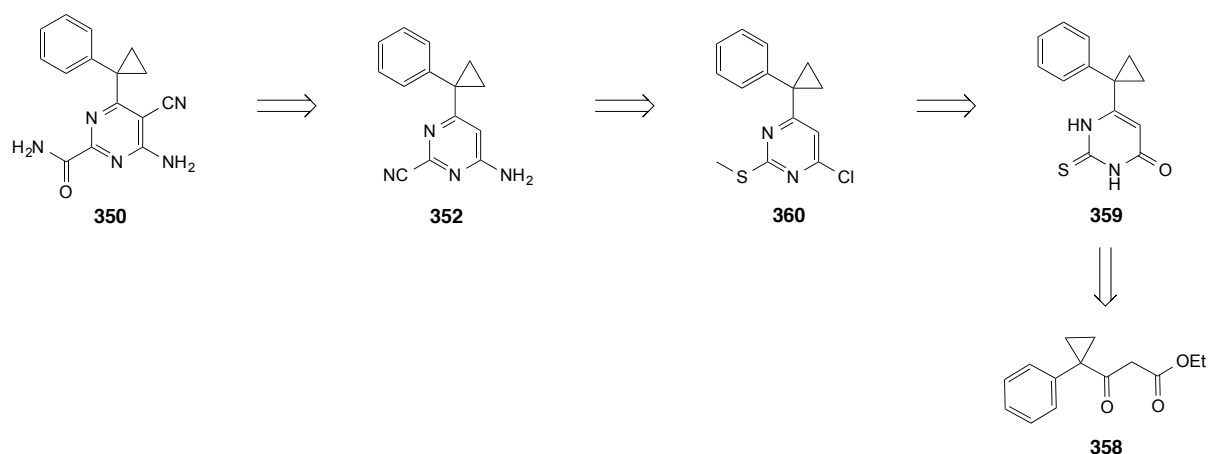
Scheme 40. Retrosynthesis of ligand **350** via a convergent approach.

As expected, cyclopropyl alcohol **357** was formed in moderate yield using Kulinkovich's method by reacting methyl benzoate (**356**) with ethyl magnesium bromide in presence of titanium isopropoxide ($\text{Ti}(\text{O}i\text{-Pr})_4$) (Scheme 41). Bromination of alcohol **357** turned out to be more difficult than anticipated. Use of PBr_3 , which reacts *via* a carbocation, resulted in complete decomposition of the cyclopropyl moiety *via* ring opening to an alkene derivative. While, the milder Appel reaction employing CBr_4 and PPh_3 , proceeding *via* a $\text{S}_{\text{N}}2$ mechanism,^[235] led to full decomposition of the starting material **357**. Alternatively, brominated **354** was prepared in low yield by adapting a methodology reported by de Meijere *et al.*, which involves pre-mixing triphenylphosphine with bromine and then adding of a solution of **357** in pyridine (Scheme 41).^[236] Intermediates **354** and **357** proved to be relatively unstable and could not be stored over several days. Given the low reaction yields and this intrinsic instability, it was decided to follow an alternative and more reliable route for the preparation of ligand **350**.



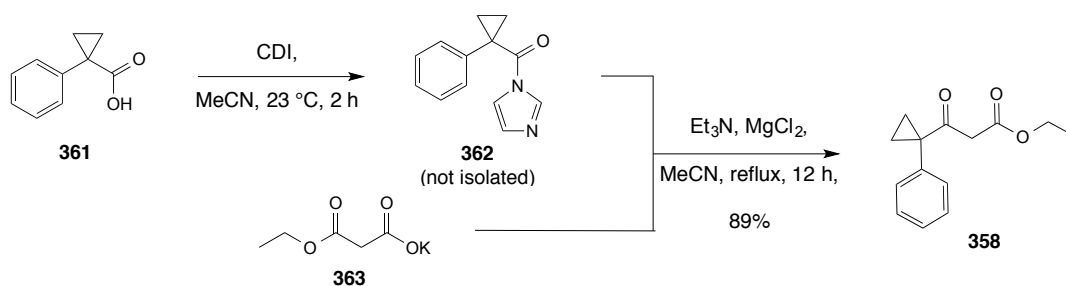
Scheme 41. Synthesis of brominated cyclopropyl intermediate **354**.

The alternative synthetic route differed in the preparation of the intermediate **352** and relied on the synthesis of the pyrimidine core from β -ketoester **358** in order to avoid the use of a cross-coupling reaction to install the cyclopropylphenyl fragment onto the pyrimidine (Scheme 42). The key intermediates towards **352** are the 2-thioxo-dihydropyrimidinone **359** and the methylthiopyrimidine **360**.



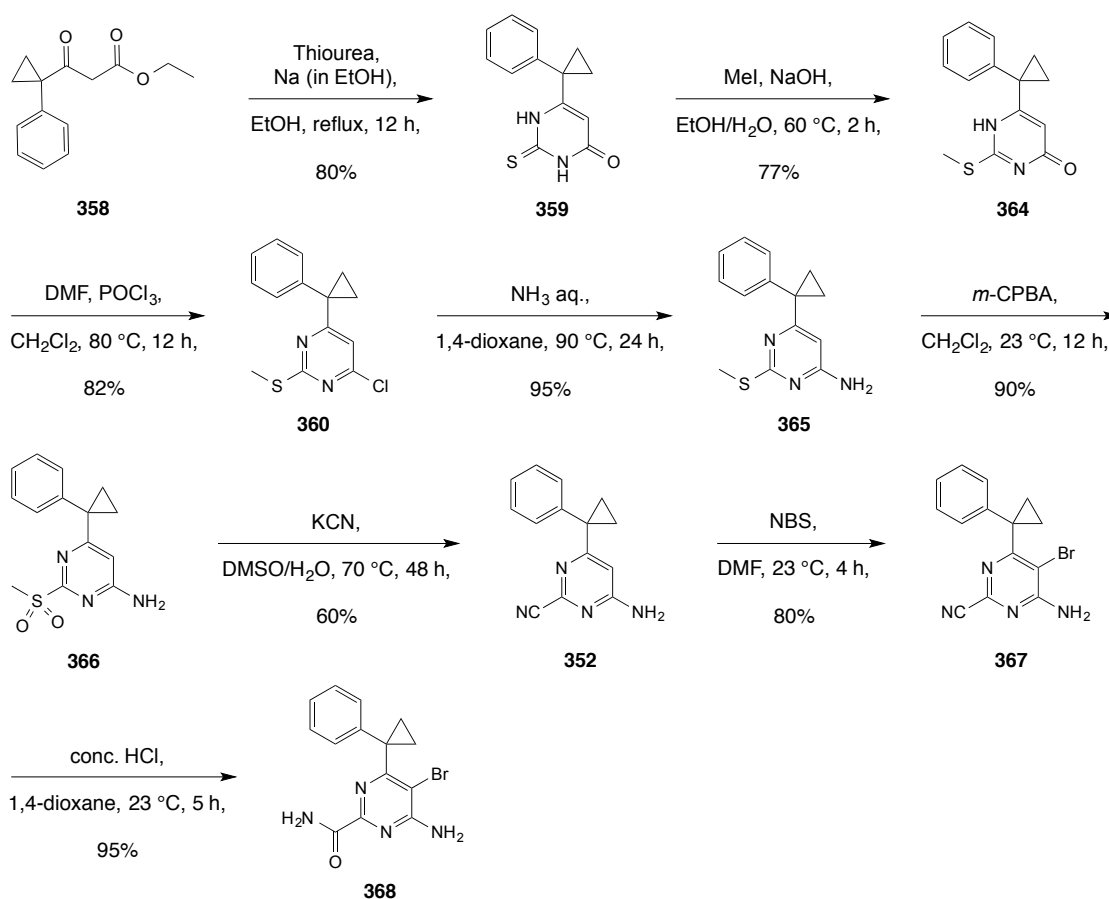
Scheme 42. Retrosynthesis of ligand **350** via a linear synthetic approach.

The synthesis started by reacting the commercially available carboxylate **361** with CDI to form the activated amide **362**, which was further reacted with malonate **363** to give the β -ketoester **358** in 89% yield (Scheme 43).^[237]



Scheme 43. Preparation of β -ketoester **358**.

β -Ketoester **358** was then reacted with thiourea to form 2-thioxo-dihydropyrimidinone **359**,^[237] which was subsequently S-methylated to give **364** (Scheme 44). Aromatization occurred upon chlorination of **364** and led to the formation of chloropyrimidine **360** in high yield. It should be noted that the reaction proceeded only when using the Vilsmeier reagent generated *in situ*,^[238] while the sole use of POCl_3 did not yield the desired product **360**. Next, amination of **360** gave aminopyrimidine **365** in an excellent yield. The latter was treated with *m*-CPBA to selectively oxidize the methyl thioether group to sulfone **366**, which was then substituted by a nitrile when reacted with potassium cyanide leading to cyanopyrimidine **352** in good yield. Brominated **367** was prepared using *N*-bromosuccinimide (NBS) as brominating reagent, and its treatment with conc. HCl allowed to convert the nitrile moiety of **367** to the corresponding amide **368** (Scheme 44).



Scheme 44. Multi-step preparation of amide **368**.

Multiple reaction conditions were screened for the cyanation of **368** to the target molecule **350** (Table 21).^[239–242] Unfortunately, none of the reported procedures led to the successful preparation of **350**, regardless of the catalyst, the cyanide source, or the temperature. In most of the cases, the starting material **368** remained unreacted, while minor conversion was observed when using a combination of $[\text{Pd}(\text{PPh}_3)_4]$ and CuCN with eventual decomposition of **368** (Entry 5). A mild cyanation method reported by Cohen and Buchwald employing a third generation of Pd-based catalyst ($[t\text{-BuXPhosPd}]$ (G3)),^[243] which proved to be successful for other electron-poor pyrimidines, did not yield any product either (Entry 1).

Table 21. Screening of the reaction conditions for the cyanation of **368** to **350**.

Entry	Catalyst	Reagent	Temperature	Result
1	[<i>t</i> -BuXPhosPd] (G3)	Zn(CN) ₂	40–145 °C	Unreacted 368
2	[Pd ₂ (dba) ₃], dppf	Zn(CN) ₂	100–140 °C	Unreacted 368
3	[Pd(PPh ₃) ₄]	Zn(CN) ₂	100–140 °C	Unreacted 368
4	-	CuCN	100–145 °C	Unreacted 368
5	[Pd(PPh ₃) ₄]	CuCN	100–145 °C	Decomposition of 368
6	[Pd(OAc) ₂]	Na ₂ CO ₃ , K ₃ (FeCN) ₆	140 °C	Unreacted 368

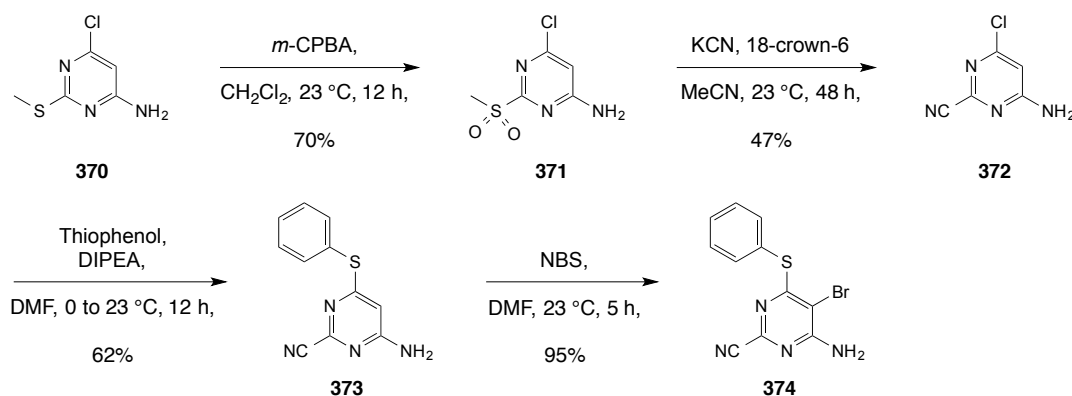
The lack of reactivity of **368** might be due to its amide moiety, which possibly coordinates to the catalyst and consequently inactivates its catalytic activity. To test this hypothesis, cyanation was attempted on pyrimidine **367**, which features a nitrile at the 2-position instead of an amide group. However, this approach remained unsuccessful too, as no trace of product **369** could be recorded by LC/MS analyses (Table 22).

Table 22. Tested conditions for the cyanation of **367** to **369**.

Entry	Catalyst	Reagent	Temperature	Result
1	[<i>t</i> -BuXPhosPd] (G3)	Zn(CN) ₂	100 °C	Unreacted 367
2	[Pd(PPh ₃) ₄]	CuCN	100–145 °C	Unreacted 367

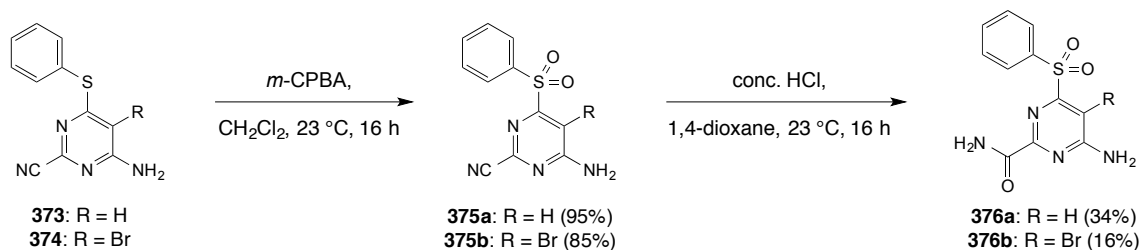
The synthetic strategy towards sulfone **351** was devised similarly as for the cyclopropyl series. Commercially available 6-chloro-2-(methylthio)-pyrimidine **370** was selected as starting point to efficiently discriminate between positions 2 and 6, and avoid regioselectivity issues. Hence, oxidation of **370** followed by a nucleophilic cyanation of **371** led to the 2-cyanopyrimidine **372** (Scheme 45). Nucleophilic addition of thiophenol assisted by a base

(DIPEA) gave the 6-(phenylthio)-pyrimidine **373** prior to bromination with NBS that yielded intermediate **374**.



Scheme 45. Synthesis of 6-(phenylthio)-pyrimidine **374**.

Oxidation of the sulfur to the corresponding sulfone had to be performed prior to the hydrolysis of the nitrile, as such amides generally show poor solubility in organic solvents limiting the scope of usable solvents. Test reactions were performed on **373** to explore the feasibility of the approach. *m*-CPBA oxidation gave sulfone **375a** in almost quantitative yield, and hydrolysis using a large excess of conc. HCl led to amide **376a** in moderate yield (Scheme 46). In a similar manner, brominated **374** was oxidized to **375b** (Scheme 46), however, its hydrolysis proved to be more delicate. With a large excess of conc. HCl, several by-products were observed by LC/MS analysis, among which, one corresponded to cleavage of the aryl sulfone fragment. The best compromise between conversion of **375b** and limited formation of by-products was obtained by using 10–12 equivalent of conc. HCl. Compound **376b** was obtained in 16% yield after purification by reverse-phase HPLC. Brominated **376b** appeared to be unstable in solution over a short period of time as a mixture of products was observed when measuring its ^1H and ^{13}C NMR spectra in $(\text{CD}_3)_2\text{SO}$. An LC/MS analysis of the NMR sample confirmed this observation, as an unknown by-product was seen in non-negligible amount. Given the instability of **376b** and the difficulties previously encountered for the final cyanation step, the work towards ligand **351** was put to a halt.



Scheme 46. *m*-CPBA oxidation to **375a,b** and hydrolysis to **376a,b**.

Ligand **377** featuring a 2-aminopyrimidine scaffold was investigated as well (Figure 89). Replacing the amide moiety of ligand **350** by an exocyclic amino group induced a slight shift of the ligand towards Glu56 as modeled with MOLOC (Figure 89a). Hence, the second amino group of **377**, which is on position 6 of the pyrimidine ring, is in close proximity to the side chain of Thr183 and the backbone C=O of Gly128, but it is too far away from the backbone C=O of Leu124 to establish a H-bond interaction.

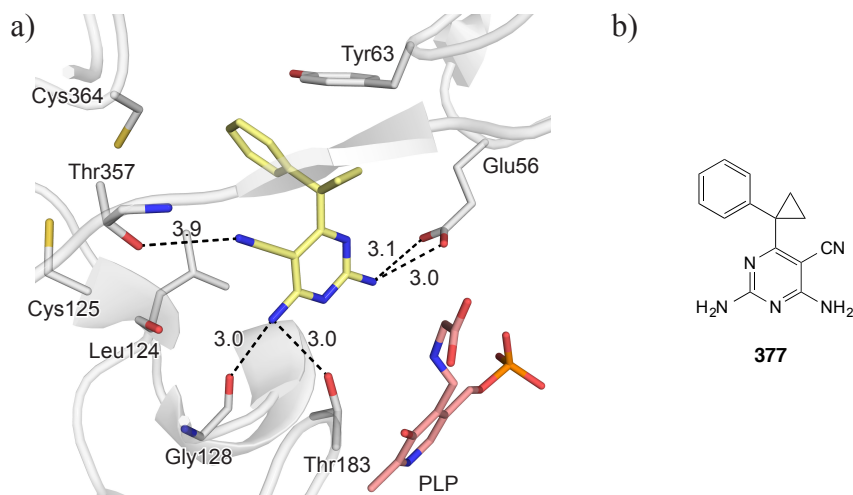
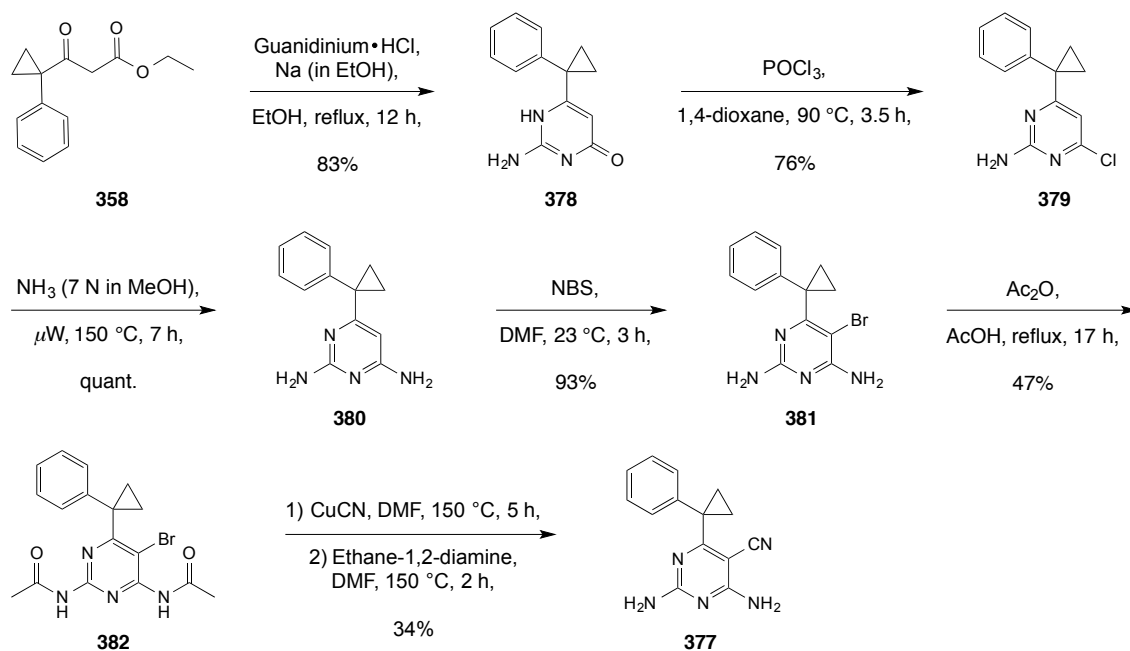


Figure 89. a) Proposed binding mode of **377** within the active site of *PvSHMT* (PDB code 4TMR, 2.6 Å) as modeled with MOLOC. Distances are given in Å. Color code: C_{PvSHMT} grey, C_{Ligand} gold, C_{PLP} salmon, N blue, O red, P orange, S yellow. b) Molecular structure of ligand **377**.

Preparation of ligand **377** is based on the synthetic route detailed above for amido-pyrimidine **350**. Reacting the versatile β -ketoester **358** with guanidinium hydrochloride gave 2-amino-dihydropyrimidinone **378** (Scheme 47). Chlorinated pyrimidine **379** was synthesized by chlorination of **378** using $POCl_3$, and subsequent microwave-assisted amination led to 2,6-diamino-pyrimidine **380** that was further brominated to **381**. In a publication by Marchetti *et al.* dealing with the synthesis of comparable molecules, it was reported that conversion of a 2,6-diaminopyrimidine scaffold to a *N,N*-diacetyl derivative was crucial prior to the cyanation step for ease of purification.^[241] Accordingly, *N,N*-diacetyl **382** was prepared by heating **381** in acetic anhydride, then, treated with copper cyanide and ethane-1,2-diamine to give ligand **377** with a concomitant loss of the acetyl groups (Scheme 47).



Scheme 47. Preparation ligand 377.

5.2.2. Design and Synthesis of Triazine-based Ligands

As the installation of a cyano group on the 5-position of the pyrimidine ring of **368** was abortive, an alternative molecule was designed. The nitrile moiety was initially introduced to act as an H-bond acceptor. Accordingly, the triazine-based molecule **383** was designed to maintain the possibility of acting as a H-bond acceptor and to interact with the receptor *via* a bridging water molecule. Indeed, the N(5) atom of **383** is in reasonable proximity to Thr357 ($d(\text{N}\cdots\text{O}(\text{H})) = 4.8 \text{ \AA}$) for a H_2O -mediated H-bridge (Figure 90).

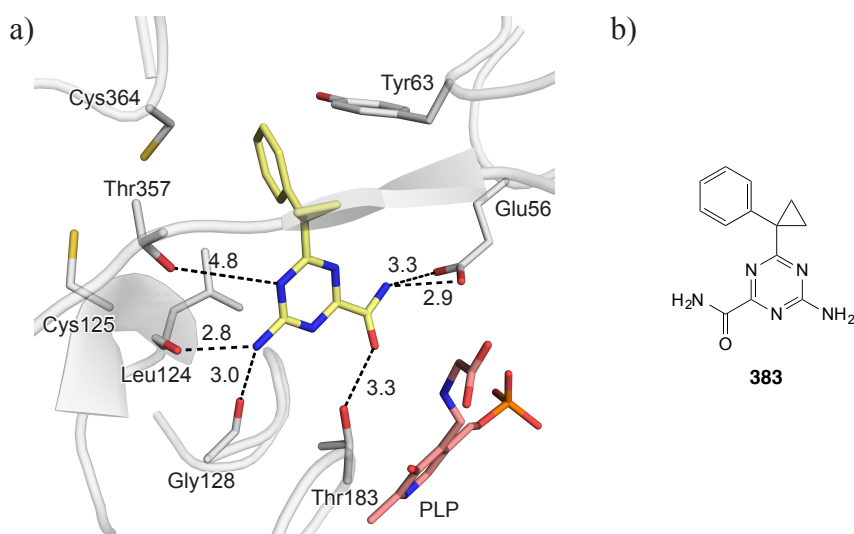
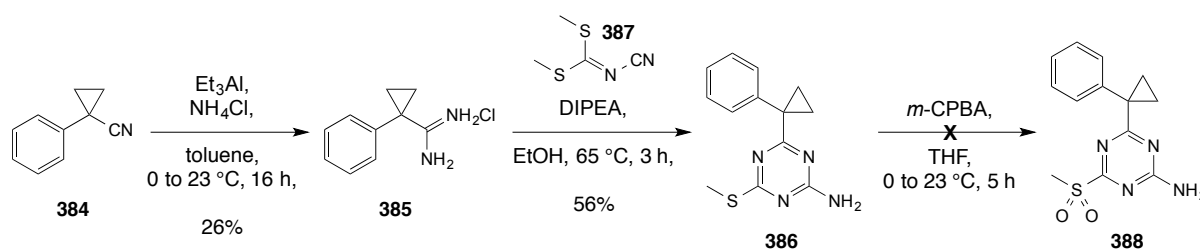


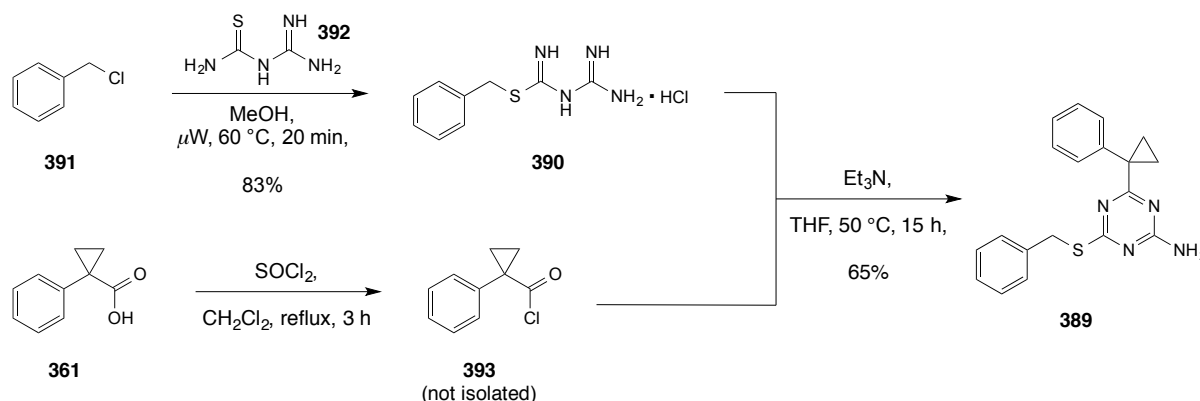
Figure 90. a) Proposed binding mode of **383** within the active site of *Pv*SHMT (PDB code 4TMR, 2.6 Å) as modeled with MOLOC. Distances are given in Å. Color code: C_{PvSHMT} grey, C_{Ligand} gold, C_{PLP} salmon, N blue, O red, P orange, S yellow. b) Molecular structure of ligand **383**.

Analogous to the synthetic route depicted above, the preparation of **383** started from cyclopropane carbonitrile **384**, which was converted to amidinium salt **385** according to a reported procedure^[244] (Scheme 48). The triazine core in **386** was formed by reacting **385** with *S,S*-dimethyl-*N*-cyanodithioiminocarbonate (**387**),^[245] and oxidation with *m*-CPBA led to methyl sulfone **388**, however, the latter decomposed during the work-up to form a product that is presumably an hydroxyl-substituted triazine according to NMR and LC/MS analyses.



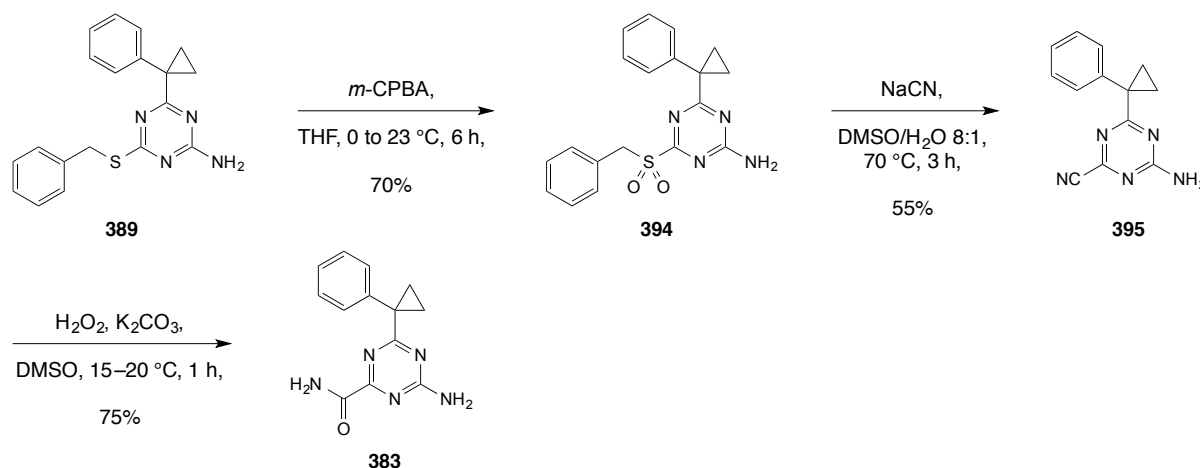
Scheme 48. Attempt to prepare triazine amide **383** via methyl sulfone **388**.

To tackle this issue, the synthetic strategy was modified to introduce a benzylthio moiety at the 2-position. Triazine **389** was readily synthesized by reacting thiourea **390**, which was prepared by mixing benzyl chloride (**391**) with 2-imino-4-thiobiuret (**392**),^[246] with acyl chloride **393** generated *in situ* from carboxylic acid **361** (Scheme 49).



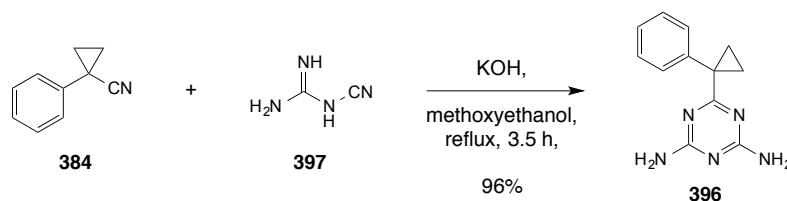
Scheme 49. Preparation of 2-benzylthio-triazine **389**.

In analogy to the work by Courme *et al.*,^[247] benzyl sulfone **394** was synthesized in 70% yield, without stability issues, and was reacted with sodium cyanide to give 2-cyanotriazine **395** (Scheme 50). Finally, the target molecule **383** was prepared by hydrolysis of nitrile **395** using a mixture of hydrogen peroxide and potassium carbonate in DMSO.



Scheme 50. Preparation of triazine amide **383**.

Additionally, the triazine analogue **396** of 2,6-diaminopyrimidine **377** was prepared for comparison. The synthesis of 6-substituted-2,4-diaminotriazine typically involves the condensation of a carbonitrile with dicyandiamide.^[248,249] Therefore, cyclopropane carbonitrile **384** was reacted with cyanoguanidine (**397**) in presence of potassium hydroxide to give **396** almost quantitatively (Scheme 51).

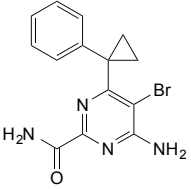
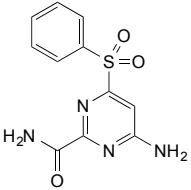
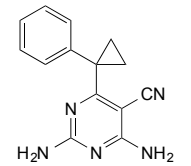
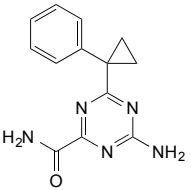
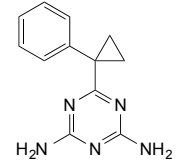


Scheme 51. One-step preparation of 2,6-diamino-triazine **396**.

5.2.3. Biological Activities

The biological activities of selected pyrimidine- (**368**, **376a**, and **377**) and triazine-based ligands (**383** and **396**) were evaluated against *At*- and *Pf*SHMT, as well as on the *Pf*NF54 strain (Table 23). Unfortunately, all compounds were completely inactive in all assays. Although, high affinity was not anticipated with these small molecules, it was postulated that they could exhibit inhibitory activity in the low micromolar range. The lack of activity might be due to the missing nitrile moiety in **368** and **376a**, which presumably prevented the ligands to bind properly to the receptor as in the predicted binding mode (Figure 87). Ligand **377** features a vinylogous cyanamide, but lacks the amide group at the 2-position to potentially interact with Glu56. It is also possible that no appreciable activity could be measured due to the absence of a terminal substituent on the phenyl ring to occupy the *p*ABA channel.

Table 23. Biological activities of pyrimidine- and triazine-based ligands **368**, **376a**, **377**, **383**, and **396**.

Cpd.	Molecular Structure	EC ₅₀ <i>Pf</i> NF54 [μ M]	IC ₅₀ <i>Pf</i> SHMT \pm SD [μ M] ^[a]	<i>At</i> SHMT Inhibition
368		> 30	72% remaining activity at 500 μ M	< 5% at 100 μ M
376a		n.d. ^[b]	n.d.	< 5% at 100 μ M
377		> 30	81% remaining activity at 500 μ M	< 5% at 100 μ M
383		n.d.	c.n.d. ^[c]	< 5% at 100 μ M
396		> 30	78% remaining activity at 500 μ M	< 5% at 100 μ M

[a] Standard deviations are given. [b] n.d. = not determined. [c] c.n.d. = could not determine due to solubility limitations.

5.3. Summary on the Discovery of a Novel Potent Class of SHMT Inhibitors

Alternative active substances to the original pyrazolopyran analogues were investigated. Nineteen spirocyclic ligands featuring a pyrazolopyran core were rationally designed and synthesized. Within this series, seven analogues based on a 2-indolinone scaffold were essentially inactive despite the fact that modeling suggested the establishment of two favorable polar interaction with residues of *Pv*SHMT, in addition to those arising from the core of the molecules. Sub-micromolar affinity were obtained by replacement of the 2-indolinone scaffold by a *gem*-dimethyl-dihydroindene motif. The molecular structure of these strained pyrazolopyran analogues was confirmed by small molecule X-ray crystallography. An important affinity gain was achieved by properly occupying the *p*ABA channel with terminal

fragments attached to the core of the molecules. While, adding a fluoride on the *meta*-position of the fused phenyl ring did not affect target affinity, it considerably improved cell-based efficacy. Additionally, the *gem*-dimethyl moiety on the indene scaffold proved to be indispensable, as its removal led to a complete loss of efficacy. Chiral recognition was also effective with this class of ligands, where in the three head-to-head comparison pairs, the (+)-(*S*)-enantiomer was always significantly more potent than the (-)-(*R*). Benzyl ester (+)-**348** displayed the best cellular potency of the series with an EC₅₀ value of 165 nM.

Two co-crystal structures of (+)-**342** and (+)-**343** with PvSHMT could be resolved. The binding mode of these conformationally constrained analogues resembles the one of previous pyrazolopyran-based ligands, with the vinylogous cyanamide serving as an anchor to bind to the receptor. Nonetheless, subtle changes were observed. In the spiro-cyclic analogues (+)-**342** and (+)-**343**, the orientation of the fused phenyl ring is substantially different to the one observed with other non-spirocyclic pyrazolopyran-based ligands, such as carboxylate (+)-**289**. Consequently, the small lateral pocket lined by the Cys364-loop is not properly filled by the ligands, which allows for the insertion of a water molecule. The short ionic H-bond between the pyrazole ring and Glu56 was lost due to the specific conformation of (+)-**342** and (+)-**343**, in favor of a water mediated interaction. In addition, a repositioning of Tyr64 was observed to compensate for the vacant space in the vicinity of the *gem*-dimethyl moiety attached to the ligands. Overall, these new analogues bind strongly to PvSHMT through a myriad of H-bond and dipolar interactions, which is nicely reflected by high target affinities.

A *de novo* design approach led to the investigation of novel *N*-heterocyclic analogues for the inhibition of SHMT. A large part of the work was dedicated to the establishment of synthetic routes towards these pyrimidine- and triazine-based ligands. Not all target molecules could be prepared, mainly due to the fact that the final cyanation step onto the pyrimidine core remained unsuccessful for amide **368**. Nonetheless, five compounds were tested for their biological properties, however, no significant activity was measured, even at high micromolar concentration. This lack of affinity may be rationalized by the absence of a terminal substituent on the phenyl ring departing from the core to occupy the *p*ABA channel.

6. Affinity Assessment Towards Human SHMT and Metabolomics Study

The metabolomics study was initiated by Dr. Matthias Witschel (BASF-SE, Germany), designed and performed by Dr. Ulrike Rennefahrt, Sandra González Maldonado, and Dr. Oliver Schmitz (Metanomics GmbH, Germany). The cells were cultivated by Dr. Tzutzy Ramirez Hernandez (BASF-SE, Germany). The target-based assays on *Pf*SHMT and *hc*SHMT were performed in the group of Dr. Ubolsree Leartsakulpanich (National Center for Genetic Engineering and Biotechnology, Thailand) by Aritsara Jaruwat. The cell-based assays, including the cytotoxicity assays, were performed in the group of Dr. Matthias Rottmann (Swiss Tropical and Public Health Institute, Basel) by Anja Schäfer.

6. Affinity Assessment Towards Human SHMT and Metabolomics Study

As discussed in the introduction, cancer and malaria cells have in common to be both rapidly dividing cells and to require high levels of metabolites to support the *de novo* biosynthesis of purine and pyrimidines.^[93] Hence, metabolomic pathways or enzymes targeted by antimalarials can potentially be used for the treatment of cancer and vice versa. In this regard, the folate synthesis pathway is targeted by anticancer drugs, such as 5-fluorouracil (5-FU, **398**; for the structure see Figure 92 in Section 6.2) that inhibits TS, resulting in impairment of the methylation of dUMP (**50**) to dTMP (**49**) and folate cycle disruption.^[250] Methotrexate (MTX, **41**) and pemetrexed bind to human SHMT *in vitro*, and are currently used as frontline chemotherapy for a diverse range of cancers.^[89,251,252] Similarly, pyrazolopyran-based inhibitors of *Pf*SHMT were tested against human SHMT, and their effect on viable human cells were monitored *via* a metabolomics analysis.

6.1. Affinity Assessment for Human SHMT

In humans, the *SHMT1* gene codes for the cytoplasmic isozyme (SHMT1) and the *SHMT2* gene codes for the mitochondrial isozyme (SHMT2).^[253] SHMT1 polymorphisms have been associated with increased lung cancer risks, while it has been shown that SHMT2 is upregulated in colon and breast cancer.^[214,254] In addition, experimental studies suggest that SHMT2 activity limits that of pyruvate kinase (PKM2) and reduces oxygen consumption, leading to a profound survival advantage to cells in poorly vascularized tumour environments.^[255] *Pf*SHMT shares approximately 47% sequence identity with mammalian SHMTs.^[110] In fact, the active sites of *Pv*SHMT and SHMT2 share many similarities in the pterin binding pocket, as well as in the *p*ABA channel (Figure 91). Importantly, the cysteine switch is absent in human SHMTs, as Cys125 and Cys364 are replaced by Pro146 and Ser396, respectively. In the pterin binding site, all residues are conserved, except of Thr183 and Ser184, which are replaced by Ser205 and Ala206 in SHMT2, respectively (Figure 91), whereas in the *p*ABA channel, Phe134 is replaced by Tyr155. Hence, these high structural similarities render the discovery of selective inhibitors for a given species highly challenging.

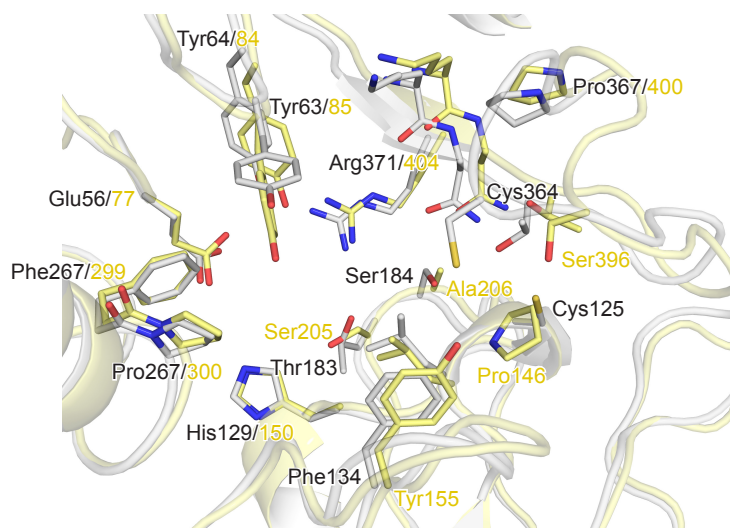
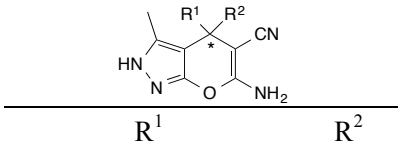
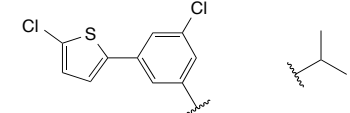
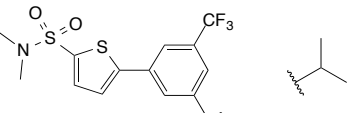
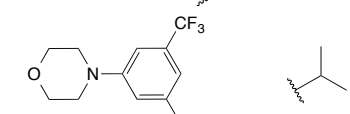
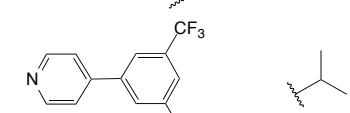
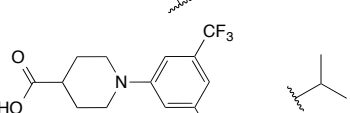
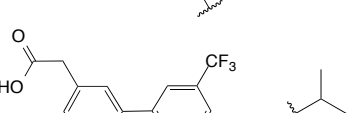
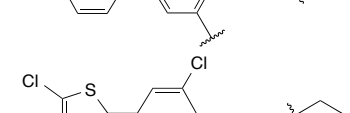
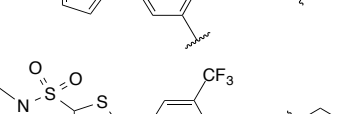
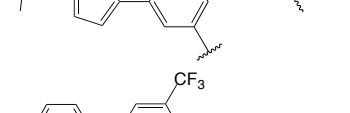


Figure 91. Overlay of *Pv*SHMT (grey, PDB code 4TMR, 2.6 Å) and SHMT2 (gold, PDB code 4PVF, 2.6 Å)^[256] with key amino acids shown in stick representation. PLP is omitted for clarity. Color code: C_{*Pv*SHMT} grey, C_{SHMT2} gold, N blue, O red, S yellow.

A notable difference between *Plasmodium* and human SHMTs lies in their kinetics. Indeed, Pinthong *et al.* reported that SHMT1 has a turnover ($k_{\text{cat}} = 28.0 \text{ s}^{-1}$), which is more than 30 times faster than the ones of *Pf*SHMT ($k_{\text{cat}} = 0.74 \text{ s}^{-1}$) and *Pv*SHMT ($k_{\text{cat}} = 0.98 \text{ s}^{-1}$).^[257]

Selected pyrazolopyran-based ligands were tested against SHMT1 (Table 24). All compounds bearing an isopropyl moiety on the stereogenic center displayed affinities values for SHMT1 in the low nanomolar range and lower IC₅₀ values compared to *Pf*SHMT. The selectivity was reversed by exchanging the isopropyl for an ethyl group (in (±)-**399**), however, this result could not be confirmed with the other two ethyl derivatives (±)-**137** and (±)-**400**, which were more potent on SHMT1 than *Pf*SHMT (Table 24). It is likely that the IC₅₀ value of chlorinated (±)-**399** for SHMT1 is an outlier value. Additionally, from a structural point of view, there is no apparent explanation to rationalize this change in selectivity, as both enzymes are structurally identical in the region where the isopropyl/ethyl moiety binds, namely in the vicinity of Tyr64/84 and Arg371/404 (Figure 91). It has to be noted that the higher affinities for SHMT1 over *Pf*SHMT might be due to the much faster catalytic turnover of the human enzyme.

Table 24. Biological activities of selected ligands including *in vitro* affinities for *h*SHMT1.

Cpd.		EC_{50} <i>Pf</i> NF54 [nM]	IC_{50} <i>Pf</i> SHMT \pm SD [nM] ^[a]	IC_{50} <i>h</i> SHMT1 \pm SD [nM] ^[a]	IC_{50} Rat myoblast L6-cell [μ M]
(\pm)-117		485	255 \pm 16	80 \pm 20	n.d. ^[b]
(\pm)-129		18	375 \pm 20	90 \pm 20	9.9
(\pm)-158		26	179 \pm 9	34 \pm 1	37.4
(\pm)-200		3.2	243 \pm 14	70 \pm 10	16.7
(\pm)-280		116	312 \pm 10	56 \pm 2	n.d.
(\pm)-283		22	186 \pm 9	110 \pm 3	n.d.
(\pm)-399		7094	80 \pm 10	150 \pm 10	n.d.
(\pm)-137		340	153 \pm 4	100 \pm 30	n.d.
(\pm)-400		60	110 \pm 30	110 \pm 20	n.d.

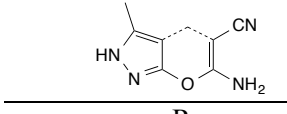
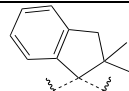
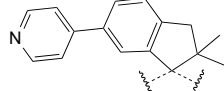
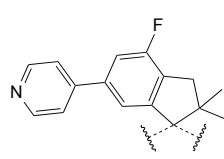
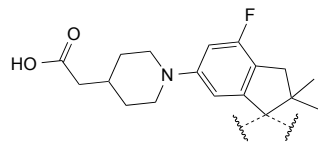
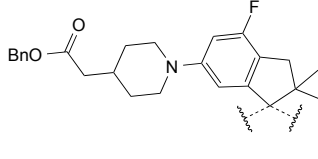
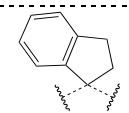
[a] Standard deviations (SD) are given. [b] n.d. = not determined.

Despite the significant target affinities measured for human SHMT1, none of the ligands proved to be cytotoxic as discussed in the previous sections and shown in Table 24 for (\pm)-129, (\pm)-158, and (\pm)-200. Indeed, all IC_{50} values measured against rat myoblast L6 cells remained in the high micromolar range. The absence of cytotoxicity reflects the fact that human cells do not primarily rely on the folate synthesis pathway for the *de novo* biosynthesis of purine, and can use the salvage pathway to fulfil their need in metabolites. This observation

was nicely underpinned in a recent study by Kim *et al.*, who showed that “knockdown of SHMT2 did not affect the proliferation or survival of multiple cell-lines under normal culture conditions”.^[255]

Interestingly, spiro-dihydroindene analogues (\pm)-**328** and (\pm)-**349** are highly selective for *Pf*SHMT (Table 25), while other ligands of this series are either slightly selective (*e.g.* (+)-**342**) or have comparable affinities for both species (*e.g.* (\pm)-**343**) (Table 25). The SAR is identical for both species: occupying the *p*AHA channel with a terminal fragment significantly enhanced activity ((\pm)-**328** vs. (\pm)-**329**), and adding a fluoride on the fused phenyl ring did not affect target affinity. It is also noteworthy that the chiral recognition is less pronounced with SHMT1. For instance, there is a 23-fold difference in affinity for SHMT1 between (+)-**343** and (–)-**343** (IC_{50} SHMT1 = 0.019 and 0.440 μ M, respectively), while the affinity discrepancy is considerably larger for *Pf*SHMT (IC_{50} *Pf*SHMT = 0.043 and 2.51 μ M, respectively).

Table 25. Biological affinities of spiro-dihydroindene ligands for *Pf*SHMT and *h*SHMT1.

Cpd.		IC_{50} <i>Pf</i> SHMT \pm SD [μ M] ^[a]	IC_{50} <i>h</i> SHMT1 \pm SD [μ M] ^[a]
(\pm)- 328		0.201 \pm 0.004	8.86 \pm 0.68
(\pm)- 329		0.030 \pm 0.001	0.047 \pm 0.002
(\pm)- 342		0.039 \pm 0.001	0.047 \pm 0.001
(+)- 342		0.014 \pm 0.002	0.027 \pm 0.001
(–)- 342		0.339 \pm 0.006	0.125 \pm 0.003
(\pm)- 343		0.061 \pm 0.001	0.057 \pm 0.001
(+)- 343		0.043 \pm 0.002	0.019 \pm 0.001
(–)- 343		2.51 \pm 0.030	0.440 \pm 0.010
(\pm)- 348		0.069 \pm 0.002	0.029 \pm 0.001
(+)- 348		0.060 \pm 0.002	0.029 \pm 0.001
(–)- 348		> 250	0.248 \pm 0.005
(\pm)- 349		4.36 \pm 0.72	> 250

[a] Standard deviations are given.

Serine and glycine are the primary metabolites of interest, as they are directly involved in the catalytic transformation performed by SHMT. Dose-dependent responses were measured after treatment with (\pm)-**158** (Figure 93). As expected, the level of serine increased significantly upon addition of the pyrazolopyran-based ligand, while glycine levels decreased proportionally. These observations confirmed the mode of action of (\pm)-**158**, which binds to SHMT and inhibits its catalytic activity. 5-FU (**398**) did not alter the levels of serine and glycine, as it acts only on the downstream TS enzyme (Figure 93).

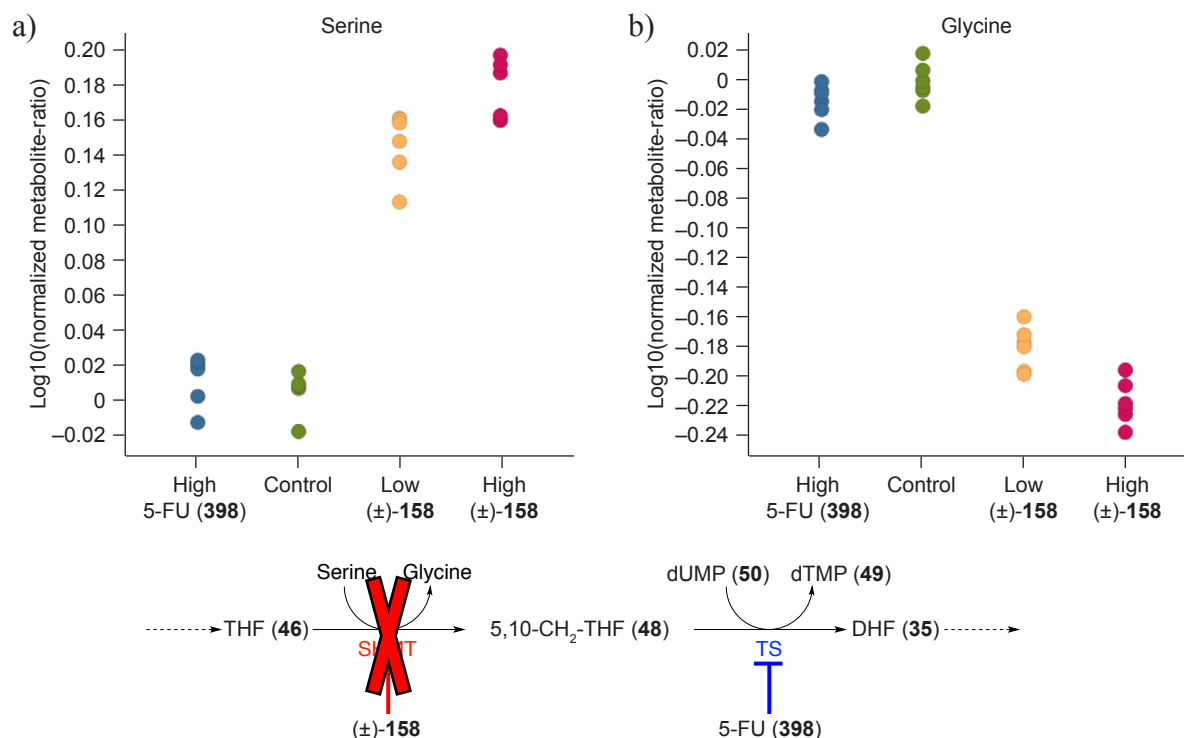


Figure 93. Variation of key metabolites following treatment with (\pm)-**158** or **398**: a) serine and b) glycine.

Next, the levels of dUMP (**50**) and dTMP (**49**) were monitored. Treatment with 5-FU (**398**) led to a compelling increase in dUMP (**50**) and a decrease in dTMP (**49**), as a result of the disruption of the catalytic activity of TS (Figure 94). Conversely, the SHMT inhibitor (\pm)-**158** did not alter the amount of these metabolites compared to the control experiment (Figure 94). This is rather surprising, as (\pm)-**158** effectively inhibits SHMT (*vide supra*), which diminishes the production of 5,10-CH₂-H₄F (**48**). This latter provides the one-carbon unit required for the methylation of dUMP by TS. Subsequently, it can be expected that a diminution of the production of 5,10-CH₂-H₄F (**48**) disturbs the downstream conversion of dUMP to dTMP. It is possible that intracellular 5,10-CH₂-H₄F (**48**) resources are used to compensate its depletion subsequent to the inhibition of SHMT.

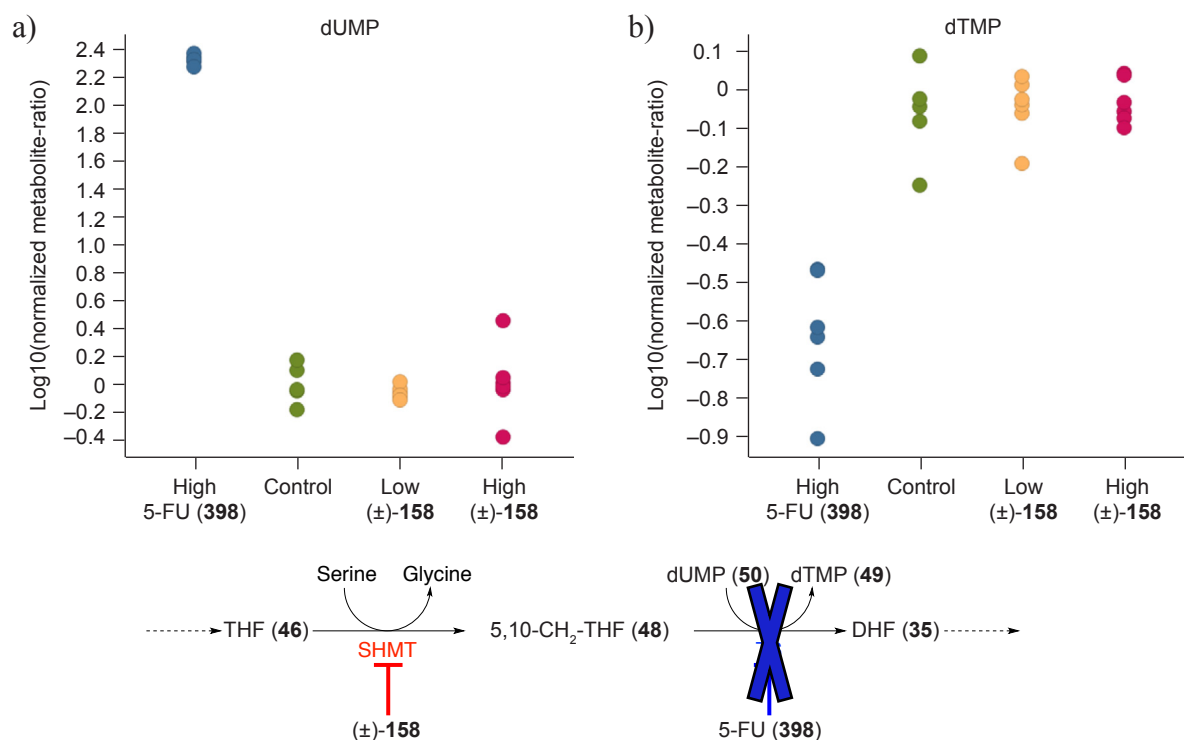


Figure 94. Variation of key metabolites following treatment with (±)-158 or 398: a) dUMP (50) and b) dTMP (49).

An overview of the changes induced by (±)-158 on all metabolites was obtained by performing an analysis of variance (ANOVA), which is a statistical model used to investigate the influence of cofounding or experimental factors on variables. Glycine and serine were the most affected metabolites together with the purine intermediate 5-aminoimidazole-4-carboxamide-1 β -ribofuranosyl-5'-monophosphate (AICAR, 401) as shown by the volcano plot on Figure 95.

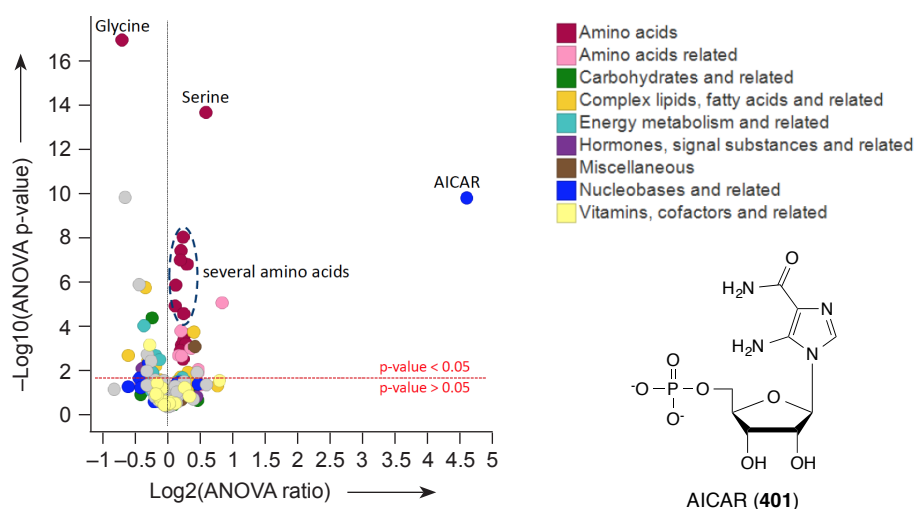
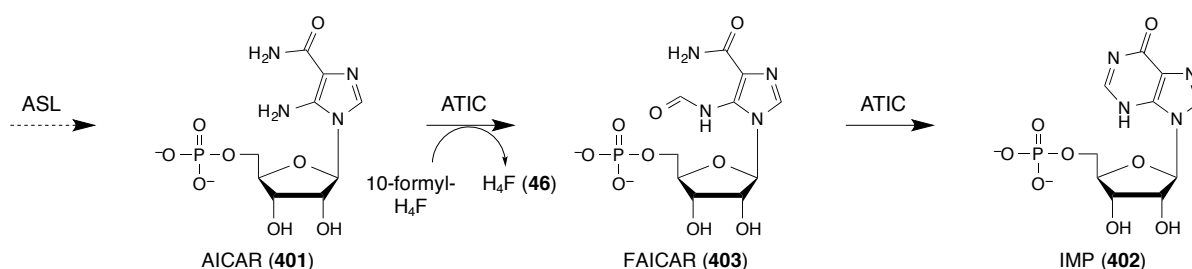


Figure 95. Volcano plot for (±)-158 showing the variations of the metabolites upon treatment with (±)-158 and molecular structure of AICAR (401).

AICAR (**401**) is one of the last intermediates in the *de novo* biosynthesis of inosine monophosphate (IMP, **402**) (Scheme 52).^[258] It is first formylated to 5-formamidoimidazole-4-carboxamide ribotide (FAICAR, **403**) by the bifunctional enzyme AICAR transformylase (ATIC),^[259,260] which uses 10-formyl-H₄F as a source of the formyl moiety. ATIC further promotes an intramolecular condensation in FAICAR (**403**) to form IMP (**402**), referred to as cyclohydrolase activity.



Scheme 52. Last two steps of the *de novo* purine biosynthesis. ASL = Adenylosuccinate lyase.

A closer look at the AICAR (**401**) levels revealed a dramatic increase of **401** following treatments with (\pm)-**158** and a dose-dependent effect (Figure 96a). IMP (**402**) was only slightly decreased at a high dose of (\pm)-**158** (Figure 96b). It is hypothesized that IMP-levels were replenished by salvage of adenosine monophosphate (AMP) through deamination of IMP. Accumulation of AICAR (**401**) might be a consequence of the inhibition of ATIC by (\pm)-**158**. If 10-formyl-H₄F would be the limiting factor, accumulations further upstream would have been observed, which was not the case here.

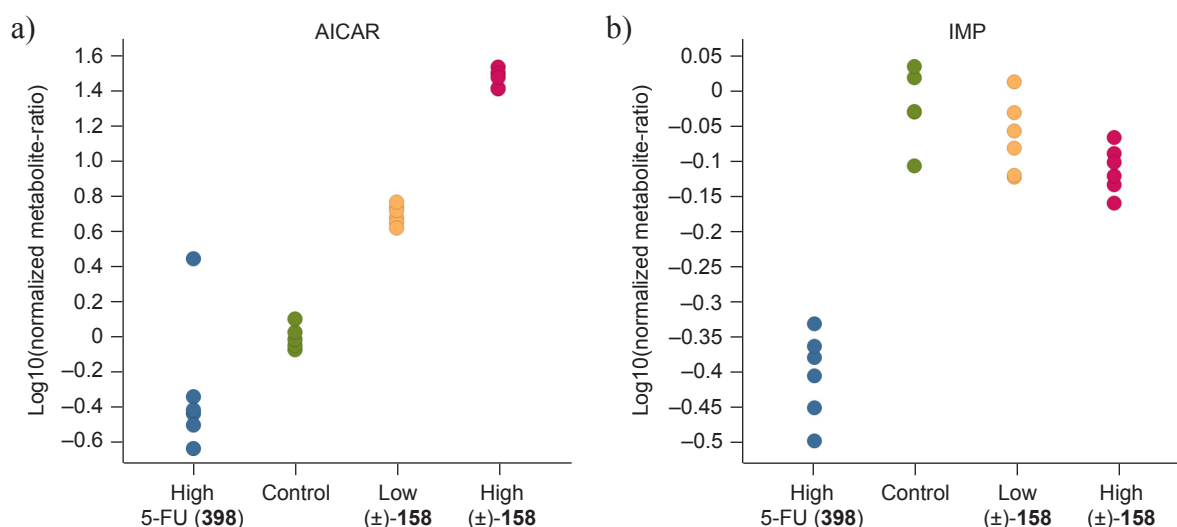


Figure 96. Variation of a) AICAR metabolites and b) IMP metabolites following treatment with (\pm)-**158** or **398**.

Several antifolates, such as MTX (**41**) and pemetrexed, are known to non-specifically inhibitATIC.^[261–265] Nonetheless, it cannot be excluded that the increase of AICAR is due to the depletion of 10-formyl-H₄F. This hypothesis is supported by the work of Kim *et al.*, who reported that the increase of AICAR “can be explained because 10-formyl-H₄F is required for the conversion of AICAR to FAICAR”.^[255] Importantly, most purine metabolism-associated diseases result in AICAR accumulation.

Interestingly, cells with low steady-state adenosine triphosphate (ATP) content and high proliferation rate seem to be more sensitive to AICAR.^[266] This metabolite activates AMP-activated kinase (AMPK),^[264,267,268] which is a central metabolic sensor protecting against environmental and nutritional stress, and replenishing ATP levels through down-regulation of anabolic and up-regulation of catabolic pathways. Few reports showed that an elongated AMPK activation inhibits the proliferation of cancer cells and induces apoptosis, including hepatocellular carcinoma.^[265,269] Therefore, an increase of AICAR-levels, subsequent to a treatment with (±)-**158**, might enable to indirectly disrupt the proliferation of cancer cells.

The significant depletion of glycine content following treatment with the SHMT inhibitor (±)-**158** might be valuable to selectively target glycine vulnerability in tumor cells. Indeed, it has been shown that glycine consumption and expression is strongly correlated with rates of proliferation across cancer cells.^[270] The consumed glycine supports in part the *de novo* purine biosynthesis, and contributes to the biosynthetic requirements of ATP and NADPH in cancer cells.^[271] In mitochondria, it fuels heme biosynthesis, which sustains oxidative phosphorylation.^[271] Additionally, Jain and co-workers reported that the mitochondrial SHMT2 is a key source of glycine in proliferating cells.^[270] However, glycine depletion can also lead to unwanted side effects, as it is a major source of methyl groups for the one carbon pool, which is essential for the synthesis of proteins and purines, for instance. It can engender a reduced synthesis of glutathione, which is the main antioxidant of the cell and a key amino acid required to maintain the cellular redox balance.

Serine is also a key precursor in cancer metabolism but its accumulation can induce unwanted side effects. It might affect the synthesis of sphingolipids, phospholipids, lipid messenger molecules, and cysteine.^[272] It also might influence cell proliferation, as it is an indirect precursor of purines and pyrimidines. Besides, it has to be noted that increased serine levels have been observed in the plasma and urine of patients with schizophrenia and psychosis, thus, it is possibly linked to these diseases.^[273]

Finally, it is noteworthy that over the course of this project other research groups investigated pyrazolopyran-based inhibitors against cancer cells.^[214,274] The work by Marani *et al.* revealed that this class of ligands preferentially inhibits SHMT1 with IC₅₀ values in the double-digit micromolar range.^[214] This observation was rationalized by molecular dynamics simulations, which suggested that the loop lining the *p*ABA channel (referred to as Cys364–loop in *Pv*SHMT) encloses the ligand in human SHMT1 more effectively than in SHMT2. The total SHMT activity in lung and colon cancer cells was significantly reduced upon treatment with the compounds of interests, albeit, only at high concentrations ranging from 11.5 to 200 μ M.

6.3. Summary on the Inhibition of Human SHMT and the Metabolomics Study

The structure of SHMT is highly conserved across all species, which offers the possibility of studying molecules primarily optimized for the inhibition of *Pf*SHMT towards human SHMT. A set of selected pyrazolopyran-based ligands was tested against the cytosolic isozyme of SHMT (reported as SHMT1). With the exception of one analogue, all compounds displayed higher affinities for SHMT1 than for *Pf*SHMT. This might be a concern regarding the toxicity of these active substances in human, nonetheless, the cytotoxicity measurements for this class of ligands counter this hypothesis, as no adverse effects were observed on rat myoblast L6 cell lines. These results were underpinned by recent reports, which showed that the knockdown of human SHMT does not affect the proliferation or survival of cell lines under normal culture conditions. Conversely to this series of molecules, a couple of spiro-dihydroindene analogues are highly selective for *Pf*SHMT, while others have comparable affinities for both species.

A metabolome study was performed in order to precisely determine which metabolites are affected upon treatment of HepG2 cell lines with the morpholino analogue (\pm)-**158**. The primary mode of action of the latter was confirmed by the accumulation of serine and the decrease of glycine levels. Interestingly, a significant increase of AICAR metabolites was measured, which might indicate an incomplete inhibition of purine biosynthesis. The explanation for this observation is still unclear. It might be due to the inhibition of ATIC by (\pm)-**158** or to a depletion of 10-formyl-H₄F. Importantly, AICAR might act as a potential master regulator in cells by activating AMPK, which is particularly detrimental to the proliferation of cancer cells. Therefore, it would be particularly interesting to perform an in-depth evaluation of the effects of SHMT inhibitors on cancer cells in order to determine their therapeutic potential. Finally, additional metabolomics studies would be required to unravel

the full repertoire of SHMT-inhibitor-induced consequences and determine its *in vivo* toxicity. Indeed, over time and by elongated treatment, the inhibition of purine biosynthesis could become a concern in malaria patients due to a blockage of liver cell proliferation and regeneration that could cause liver damages.

7. Conclusions and Outlook

7. Conclusions and Outlook

7.1. General Conclusions

A comprehensive and detailed study dealing with the development of novel antimalarials targeting SHMT is presented. While potent inhibitors, such as the methyl ester (\pm)-**67**, which were formerly developed for crop protection, were readily identified, most of the work was dedicated to the improvement of the metabolic stability of the pyrazolopyran class of ligands in order to reach significant *in vivo* efficacy.

Based on structural information, the substituents on the pyrazolopyran core were systematically altered (Figure 97). The consequences of these structural alterations on the affinity for *At*- and *Pf*SHMT, and *in vitro* on the sensitive strain *Pf*NF54 were carefully studied.

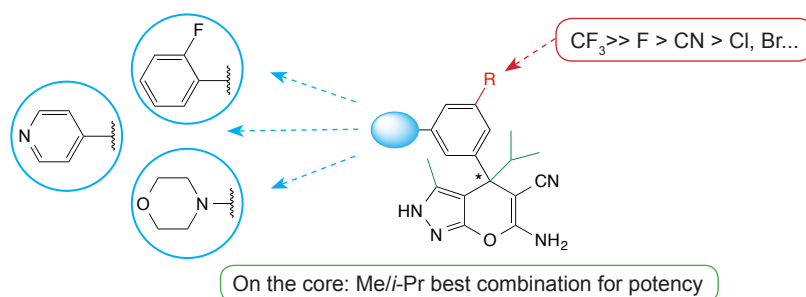


Figure 97. Summary of the SAR for pyrazolopyran-based inhibitors.

Initially, the focus was set on replacing the terminal thienyl fragment due to its particular sensitivity to metabolic degradation. We found that numerous alternative moieties can efficiently replace this fragment and retain activity in the medium to low nanomolar range. Nonetheless, modifications at other positions of the molecule were required to reach the desired single-digit nanomolar activity. In this regard, an extensive SAR study showed that the lipophilic substituents on the stereogenic center and on the pyrazole ring were not amenable to broad changes, and the methyl/*iso*-propyl combination remained optimal for high potency. Conversely, cellular efficacy was profoundly influenced by the nature of the *meta*-substituent on the phenyl ring departing from the stereogenic center. Indeed, up to 10-fold potency improvement was measured by replacing the nitrile for a CF_3 moiety. The coveted efficacy was eventually obtained for several ligands featuring diverse aromatic *N*-heterocycle, however, still lacking sufficient stability in human liver microsomes.

The predominant significance of small molecule conformation in drug design was underscored with two series of inhibitors bearing widely used chemical motifs, namely biphenyl and aryl sulfonamide/aryl sulfone. Across a series of *ortho*-substituted biphenyl

analogues, we observed that the nature of the *ortho*-substituent does not affect target affinity much, but rather influences cell-based efficacy with a steep SAR and discrepancies up to 37-fold. By databases mining and theoretical calculations, we showed that the loss of cellular efficacy correlates with the torsion angle of the biphenyl fragment. Thereby, it is postulated that cell permeation is impacted by the conformational changes of the biphenyls.

Additionally, we examined the preferred conformations of aryl sulfonamides and aryl sulfones by CSD and PDB searches, as well as by DFT calculations. Both structural elements preferably adopt a conformation in which the π orbital of the *ipso*-carbon atom bisects the O-S-O angle. In addition, aryl sulfonamides are usually present in a so-called staggered conformation with the N-lone pair of sulfonamides bisecting the O-S-O angle. The peculiar lipophilic character of the sulfonyl moiety was underlined thanks to three co-crystal structures with C364A-*Pv*SHMT mutant, where the respective SO₂ groups point towards non-polarized C-H bonds of hydrophobic residues. Consequently, the terminal apolar fragments that were intended to interact with the protein are directed to the bulk, which explains the lack of affinity gain within this series. The observations made in these three complexes were underpinned by CSD and PDB searches and highlight the low hydrophilicity of the SO₂ group, which prefers to point to hydrophobic environments rather than into polar ones.

In parallel, a set of carboxylates with considerably improved half-lives were discovered. The log*D* of these analogues was finely tuned by applying a CF₃ → F substitution, which led to ligands with an optimal compromise between potency and stability. Importantly, chiral recognition at the active site of SHMT is effective, and large discrepancies in activity between enantiomers of optically resolved ligands were observed. Among the carboxylate analogues, piperidine (+)-**289** presented the best compound profile (EC₅₀ = 35 nM; *t*_{1/2} > 4.3 h), and was therefore studied in a *Pf*SCID mouse model. Remarkably, (+)-**289** induced a significant reduction of parasitemia of 73% on day 7 after treatment, which constitutes the very first example of the treatment of a malaria infection by an SHMT inhibitor. Hence, we showed that SHMT is a druggable target for antimalarials, which was the primary goal of this Thesis.

Overall, eighteen co-crystal structures with *Pv*SHMT were solved at 2.2–2.6 Å resolution, which enabled us to perform an in-depth elucidation of the binding mode of the pyrazolopyran class of molecules. The good structural match between these active substances and the natural substrate H₄F is undoubtedly a cornerstone for the high affinity of the ligands. The pterin binding pocket is perfectly occupied by the pyrazolopyran core, while the bicyclic scaffold extends into the *p*ABA channel, which is crucial for strong activity.

The knowledge gained from this extensive SAR served for the design of alternative scaffolds. Pyrimidines- and triazines-based ligands were investigated in a *de novo* design approach, but did not display any appreciable activity. In contrast, nanomolar affinity was measured for a series of novel spirocyclic compounds featuring a pyrazolopyran core. Their binding mode does not differ much from the one of the original lead series. However, two major changes resulting from their conformationally locked core were pinpointed. First, the small lateral pocket lined by the Cys364-loop is not properly filled by the ligand, hence, allowing the insertion of a water molecule in this cavity. Second, the small void resulting from the different position of one methyl moiety in the back of the pocket is compensated by the movement of Tyr64.

Finally, a metabolomics study employing viable human cells did not only confirm the mode of action of pyrazolopyran-based inhibitors, but also suggested that this class of ligands can potentially find applications against the proliferation of cancer cells.

7.2. Outlook and Perspectives

Targeting SHMT is a promising alternative to existing antimalarial treatments as demonstrated in this Thesis. The next step will be to develop an inhibitor able to reach full efficacy in animal models, and possibly at a single dose.

This might be feasible by designing a hybrid drug featuring an endoperoxide motif with a dual mode of action. Indeed, a ligand such as (*S*)-**404** would have the potential to effectively inhibit *Pf*SHMT thanks to the well established pyrazolopyran core (Figure 98a). In analogy to artemisinin and other active substances containing a pharmacophoric endoperoxide bridge,^[50,69,71,275] cleavage of this latter in red blood cells would generate highly reactive carbon-centered radicals that are toxic to parasites. The dispiro ozonide fragment **405** is known to be active *in vitro*,^[49] its preparation *via* a Griesbaum cross-ozonolysis reaction is straightforward,^[276] and it can presumably be coupled to building block **295** (Figure 98a). Large and apolar fragments occupying the *p*ABA channel are well suited for the inhibition of SHMT as aforementioned, and modeling of (*S*)-**404** suggested a good fit of the ligand within the *Pv*SHMT binding site (Figure 98b). Reaction of the endoperoxide warhead with ferrous iron would generate carbon-centered radicals (*e.g.* **406**), along with the pyrazolopyran-based ligand (*S*)-**407** as a side product (Figure 98c).

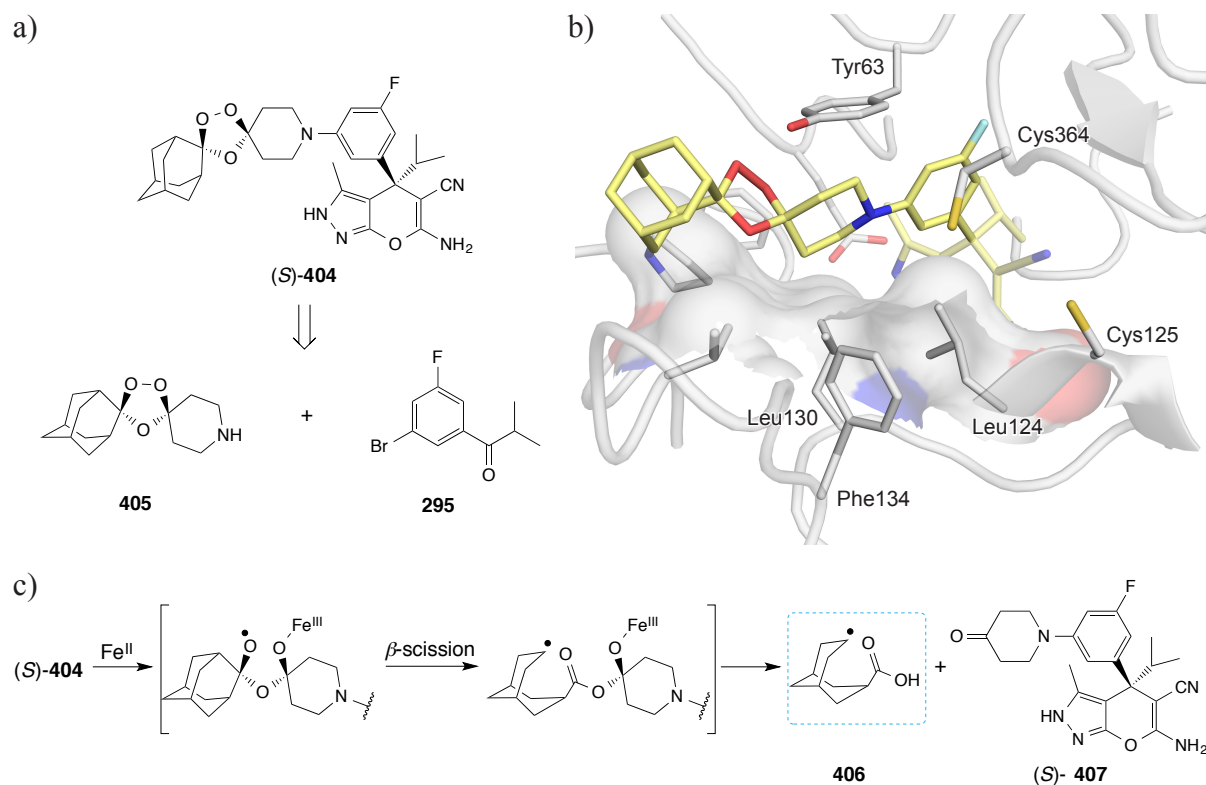


Figure 98. a) Proposed hybrid drug (S)-404 and its simplified synthesis. b) Proposed binding mode of (S)-404 within the active site of PvSHMT (PDB code 4TMR, 2.6 Å) as modeled with MOLOC. Color code: C_{PvSHMT} grey, C_{Ligand} gold, F light cyan, N blue, O red, S yellow. c) Proposed reaction of ozonide (S)-404 with ferrous iron leading to the generation of a carbon-centered radical.

Alternative lead structures are also highly desirable. Therefore, a new screening campaign would certainly yield novel active fragments that could be further tuned by structure-based design using the knowledge learned from the SAR described herein. In addition, the numerous structural informations available for PvSHMT give the opportunity of conceiving potentially active substances by *de novo* design approaches. Future generations of SHMT inhibitors could be based on a purine scaffold, such as **408** (Figure 99). The exocyclic amide on one side and the amino group on the other side are incorporated to ensure a good binding of the core, while the cyclopropyl linker directs the phenyl fragment towards the *p*ABA channel. Molecules featuring a tetrahydronaphthyridine core, as in ligand **409**, are another possibility (Figure 99). The vinylogous cyanamide is preserved to ensure a good anchoring of the molecule within the binding site, and the isoindole could be further derivatized by N-methylation. The core could be synthesized by reacting a dinitrile, such as **410**, with benzylpiperidin-3-one (**411**) in presence of ammonium acetate. In this respect, preliminary experiments confirmed the feasibility of this synthetic approach. A proposed SAR study is depicted in Figure 99. On the core, ring contraction could be envisioned, which would require

the use of readily accessible pyrrolidone building blocks. Introducing one or two methyl moieties at the 5-position of this ring might be crucial for an optimal filling of the pterin binding site. The upper isoindole fragment could be reduced to the corresponding isoindoline, which might be more synthetically accessible and more chemically stable than the isoindole. In addition, the fused phenyl ring could be decorated with various functional groups, including halo-substituents.

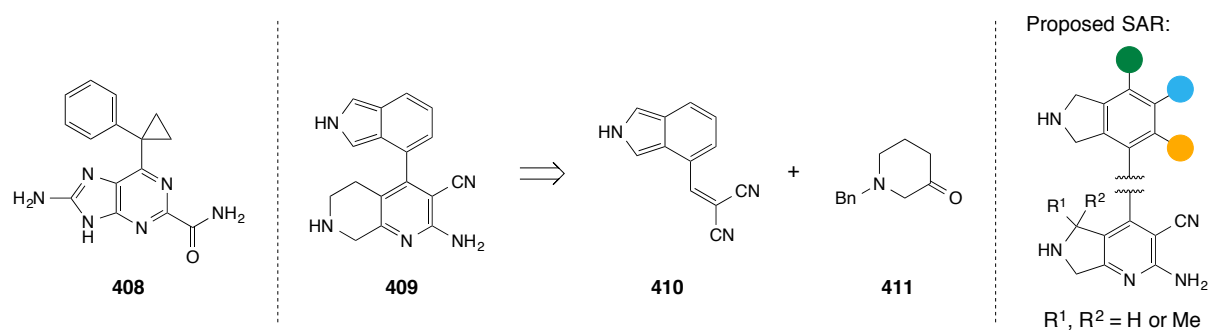


Figure 99. Proposed ligands based either on a purine core (**408**) or on a tetrahydronaphthyridine core (**409**).

Finally, the metabolomics study opened exciting opportunities for the use of pyrazolopyran-based inhibitors against the proliferation of cancer cells. Therefore, it would be highly interesting to study the effects of this class of ligands on different cancer cell lines.

8. Experimental Part

8. Experimental Part

8.1. Synthetic Protocols and Characterization of Selected Ligands

Synthesis and characterization of all intermediates and final compounds that are already published can be found online in the respective Supporting Information.^[116,117,150] Nonetheless, protocols for the synthesis of representative building blocks and ligands, together with their characterization are reported in the following. Additionally, preparation and characterization of all molecules discussed in Chapter 5 are available in this section.

8.1.1. Materials and Experimental Methods

Reagents (ABCR, Acros, Aldrich, Fluorochem, Fluka, and TCI) were purchased as reagent grade and used without further purification.

Solvents for extraction or column chromatography were distilled from technical grade.

Dry solvents (THF, CH₂Cl₂, diethyl ether, MeCN, and toluene) for reactions were purified by a solvent drying system from LC Technology Solutions Inc. SP-105 under nitrogen atmosphere (H₂O content < 10 ppm as determined by Karl-Fischer titration). All other solvents were purchased in p.a. quality.

Reactions in the absence of air and moisture were performed in oven-dried glassware under Ar or N₂ atmosphere.

Flash column chromatography were performed using SiO₂ (60 Å, 230–400 mesh, particle size 0.040–0.063 mm, Fluka) at 23 °C with a head pressure of 0.0–0.5 bar or with SiO₂ columns (230–400 mesh, particle size 0.035–0.070 mm, RediSep R_f Normal-phase Flash Columns) packed on RediSep R_f Cartridges on a CombiFlash R_f 200 psi flash chromatography system. The solvent compositions are reported individually in parentheses.

Analytical thin layer chromatography (TLC) was performed on aluminium sheets coated with silica gel 60 F254 (Merck, Macherey-Nagel). Visualization was achieved using UV light (254 or 366 nm).

Evaporation *in vacuo* was performed at 25–60 °C and 900–10 mbar.

Reported yields refer to spectroscopically and chromatographically pure compounds that were dried under high vacuum (0.1–0.05 mbar) before analytical characterization.

^1H , ^{13}C , and ^{19}F nuclear magnetic resonance (NMR) spectra were recorded on Varian Gemini 300, Varian Mercury 300, Bruker ARX 300, Bruker DRX 400, and Bruker AV 400 spectrometers at 300 MHz or 400 MHz (^1H), 75 MHz or 101 MHz (^{13}C), and 377 MHz (^{19}F), respectively. Chemical shifts δ are reported in ppm downfield from tetramethylsilane using the residual deuterated solvent signals as an internal reference (CDCl_3 : $\delta_{\text{H}} = 7.26$ ppm, $\delta_{\text{C}} = 77.16$ ppm; $\text{THF-}d_8$: $\delta_{\text{H}} = 1.72$ ppm, $\delta_{\text{C}} = 25.31$ ppm; CD_3OD : $\delta_{\text{H}} = 3.31$ ppm, $\delta_{\text{C}} = 49.00$ ppm; $(\text{CD}_3)_2\text{SO}$: $\delta_{\text{H}} = 2.50$ ppm, $\delta_{\text{C}} = 39.52$ ppm). For ^1H NMR, coupling constants J are given in Hz and the resonance multiplicity is described as s (singlet), d (doublet), t (triplet), q (quartet), quint (quintet), sext (sextet), sept (septet), m (multiplet), and br. (broad). All spectra were recorded at 298 K. The assignments are based on HSQC and HMBC experiments.

Infrared (IR) spectra were recorded on a Perkin-Elmer Spectrum 1600 FT-IR spectrometer (ATR, Golden Gate) and are reported as wavenumbers $\tilde{\nu}$ (cm^{-1}) with band intensities indicated as s (strong), m (medium), w (weak), br. (broad).

High-resolution mass spectrometry (HR-MS) was performed by the MS-service of the Laboratory of Organic Chemistry at the ETH Zurich on a Waters Micromass AutoSpec-Ultima spectrometer (EI) or on a Bruker maXis spectrometer (ESI).

Elemental analyses were performed by the Microanalytical Laboratory of the Laboratory of Organic Chemistry at the ETH Zurich with a LECO CHNS-932 instrument. In case of fluorine-containing molecules, the oxygen content could not be measured.

High-performance liquid chromatography (HPLC) analysis was performed on a Merck Hitachi LaChrom HPLC System (D-7000 Interface, L-7100 Pump, L-7200 Autosampler and L-7400 UV Detector). Separations under acidic conditions were performed using 0.1% vol. formic acid in eluent H_2O and MeCN on a Merck Superspher 100 RP-18e (100 Å, 4 μm), 250 \times 4 mm column. A flow rate of 1 mL/min was used, and the UV detector was set to 254 nm (optical path length = 10 mm). A sample concentration of 0.5 mg/mL was used, and 20 μL of this solution were injected. The following gradient was used: $\text{H}_2\text{O}/\text{MeCN}$ 60:40 for 8 min, gradient to $\text{H}_2\text{O}/\text{MeCN}$ 0:100 over 12 min, $\text{H}_2\text{O}/\text{MeCN}$ 0:100 for 5 min.

Nomenclature follows the suggestions proposed by the software ACD Name from ACD/Labs.^[203] Numbering of atoms in the structures follows the numbering of the IUPAC name.

8.1.2. General Procedures

General Procedure GP1 for the Preparation of Alkylated Bromoarenes

Oven dried glassware and distilled solvents were used. The reaction was carried out under Ar atmosphere.

A solution of a 1,3-dibromoarene (4.94 mmol, 1.0 eq) in Et₂O (25 mL) was cooled to -78 °C, treated dropwise with 1.6 M *n*-BuLi in hexane (3.08 mL, 4.94 mmol, 1.0 eq), stirred at -78 °C for 15 min, and treated dropwise with the corresponding isobutyramide derivative (4.94 mmol, 1.0 eq). The mixture was stirred at -78 °C for 30 min, allowed to warm up to 23 °C, stirred for 3 h, diluted with water (15 mL) and EtOAc (15 mL). The two layers were separated, and the aqueous layer was extracted three times with EtOAc (3 × 20 mL). The combined organic layers were washed with brine, dried over Na₂SO₄, filtered, and evaporated to afford the crude alkylated bromoarene.

General Procedure GP2 for the Borylation

The reaction was performed under Ar atmosphere and distilled solvents were used.

A mixture of a bromoarene ketone (7.93 mmol, 1.0 eq), 4,4,4',4',5,5,5',5'-octamethyl-2,2'-bi(1,3,2-dioxaborolane) (**96**) (8.73 mmol, 1.1 eq), and KOAc (23.80 mmol, 3.0 eq) in toluene (38 mL) was degassed under Ar for 10 min, treated with [PdCl₂(dppf)·CH₂Cl₂] (0.159 mmol, 0.02 eq), degassed under Ar for 5 min, stirred at 150 °C for 6 min in a microwave oven, then passed through a pad of celite eluting with EtOAc. The mother liquor was evaporated to afford the crude borylated product.

General Procedure GP3 for the Suzuki Cross-coupling Using a Bromoarene Ketone

The reaction was performed under Ar atmosphere.

A solution of the bromoarene ketone (1.59 mmol, 1.0 eq), the corresponding boronic acid (or pinacol boronate) (1.59 mmol, 1.0 eq), and Na₂CO₃ (1.90 mmol, 1.2 eq) in a mixture of THF/H₂O 4:1 (20 mL) was degassed with Ar under sonication for 15 min. The solution was treated with [Pd(PPh₃)₂Cl₂] (0.079 mmol, 0.05 eq), degassed with Ar under sonication for 5 min, stirred at 63 °C for 5.5 h, cooled to 23 °C, and diluted with EtOAc (15 mL) and water (15 mL). The two layers were separated, and the aqueous layer was extracted twice with EtOAc (2 × 15 mL). The combined organic layers were washed with brine, dried over Na₂SO₄, filtered, and evaporated to afford the crude coupling product.

General Procedure GP4 for the Suzuki Cross-coupling Using a Pinacol Boronate Ketone

The reaction was performed under Ar atmosphere.

A solution of the pinacol boronate ketone (10.64 mmol, 1.15 eq), the corresponding brominated coupling partner (9.25 mmol, 1.0 eq), and Na₂CO₃ (1.177 g, 11.10 mmol, 11.10 eq) in a mixture of THF/H₂O 4:1 (118.75 mL) was degassed with Ar under sonication for 15 min. The solution was treated with [Pd(PPh₃)₂Cl₂] (0.463 mmol, 0.05 eq), degassed with Ar under sonication for 5 min, stirred at 63 °C for 6 h, cooled to 23 °C, and diluted with H₂O (25 mL) and EtOAc (25 mL). The two layers were separated, and the aqueous layer was extracted three times with EtOAc (3 × 40 mL). The combined organic layers were washed with brine, dried over Na₂SO₄, filtered, and evaporated to afford the crude coupling product.

General Procedure GP5 for the Buchwald-Hartwig Coupling

Dried solvent was used and the reaction was performed under Ar atmosphere in a Biotage[®] Microwave sealed flask.

A solution of bromoarene ketone (20.33 mmol, 1.0 eq) in 1,4-dioxane (30 mL) was treated with Cs₂CO₃ (30.50 mmol, 1.5 eq) and the corresponding secondary amine (24.34 mmol, 1.2 eq), the mixture was degassed with Ar for 10 min, treated with [Pd₂(dba)₃] (0.41 mmol, 0.02 eq) and X-Phos (**163**) (1.63 mmol, 0.08 eq), heated at 110 °C for 16 h, and diluted with water and EtOAc. The two layers were separated, and the aqueous layer was extracted three times with EtOAc (3 × 20 mL). The combined organic layers were dried over Na₂SO₄, filtered, and evaporated to afford the crude coupling product.

General Procedure GP6 for the Knoevenagel Condensation

HPLC grade chloroform distilled on CaCl₂ and dried on molecular sieves was used. The reaction was performed under Ar atmosphere in a Biotage[®] Microwave sealed flask.

The ketone (0.701 mmol, 1.0 eq) and malononitrile (3.51 mmol, 5.0 eq) were treated with CHCl₃ (2.0 mL). An emulsion was obtained. A dropwise addition of a freshly prepared solution of TiCl₄ (0.842 mmol, 1.2 eq) in dry toluene (0.9 mL) led to a yellow precipitate. Pyridine (3.51 mmol, 4.0 eq) was added, and a black mixture was obtained. The mixture was stirred at 65 °C for 48 h, and cooled to 23 °C. Addition of 1 M HCl (3.0 mL) led to a brown precipitate. The mixture was diluted with CH₂Cl₂ (20 mL) and water (20 mL). The two layers were separated, and the aqueous layer was filtered to get rid of the precipitate. The aqueous layer was extracted three times with CH₂Cl₂ (3 × 20 mL). The combined organic layers were washed with brine, dried over Na₂SO₄, filtered, and evaporated to afford the crude dinitrile.

General Procedure GP7 for the Synthesis of the Pyrazolopyran Core

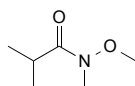
Distilled solvents were used and the reaction was carried out under Ar atmosphere.

A mixture of the dinitrile (0.331 mmol, 1.0 eq) and the corresponding pyrazolone (0.364 mmol, 1.1 eq) was suspended in a mixture of ethanol/1,4-dioxane 1:1 (0.80 mL). Addition of distilled piperidine (3.31 mmol, 10.0 eq) led to an orange solution. The mixture was stirred at 65 °C for 3.5 h in a microwave oven, and diluted with water (10 mL) and EtOAc (10 mL). The two layers were separated, and the aqueous layer was extracted three times with EtOAc (3 × 10 mL). The combined organic layers were washed with brine, dried over Na₂SO₄, filtered, and evaporated to afford the crude pyrazolopyran.

N.B.: in case of benzyl protected analogues, benzyl alcohol was used instead of ethanol to prevent transesterification.

General Procedure GP8 for the Benzyl Deprotection

A solution of the benzyl ester (0.175 mmol, 1.0 eq) in MeOH (2.0 mL) was treated with 10% [Pd/C] (0.047 mmol, 0.27 eq), and H₂ was bubbled through the solution for 10 min. The mixture was stirred at 23 °C for 3 h, and filtered through a PTFE microfilter (45/25). The mother liquor was evaporated to afford the carboxylic acid.

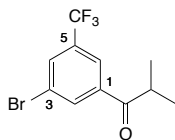
*8.1.3. Synthetic Procedures and Characterizations of Selected Compounds for Chapters 2–4****N*-Methoxy-*N*,2-dimethylpropanamide (76)^[277]**

A suspension of *N*,*O*-dimethylhydroxylammonium chloride (10.32 g, 106 mmol) in CH₂Cl₂ (265 mL) was cooled to 0 °C, and treated dropwise over 15 min with Et₃N (29.5 mL, 212 mmol) leading to a white precipitate. Isobutyryl chloride (**77**) (11.08 mL, 106 mmol) was added dropwise while maintaining the internal temperature below 4 °C. Then the mixture was stirred at 23 °C for 1 h and diluted with sat. NaHCO₃ solution (160 mL). The two layers were separated, and the aqueous layer was extracted twice with CH₂Cl₂ (2 × 60 mL). The combined organic layers were washed with 1 M HCl (50 mL) and brine (50 mL), dried over Na₂SO₄, filtered, and evaporated to afford **76** (12.56 g, 91%) as a colorless oil.

¹H NMR (400 MHz, CDCl₃): δ = 1.12 (d, *J* = 6.8 Hz, 6 H: CHMe₂), 2.96 (sept., *J* = 6.8 Hz, 1 H; CHMe₂), 3.18 (s, 3 H; NMe), 3.69 ppm (s, 3 H; OMe); ¹³C NMR (101 MHz, CDCl₃): δ =

19.27 (CHMe₂), 29.97 (CHMe₂), 32.32 (weak, NMe), 61.56 (OMe) 178.41 ppm (weak, C=O); IR (ATR): $\tilde{\nu}$ = 2971 (m), 2938 (w), 1661 (s), 1471 (m), 1414 (m), 1384 (m), 1361 (w), 1301 (w), 1176 (m), 1093 (m), 996 (s), 927 (w), 866 (w), 738 cm⁻¹ (m).

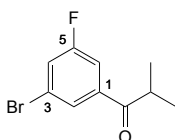
1-[3-Bromo-5-(trifluoromethyl)phenyl]-2-methylpropan-1-one (124c)



Following **GP1**, column chromatography (SiO₂; cyclohexane) gave **124c** (3.24 g, 83%) as a colorless oil.

R_f = 0.47 (SiO₂; cyclohexane); ¹H NMR (400 MHz, CDCl₃): δ = 1.24 (d, J = 6.8 Hz, 6 H; CHMe₂), 3.49 (sept., J = 6.8 Hz, 1 H; CHMe₂), 7.94 (br. t, J = 1.8 Hz, 1 H; H-C(4)), 8.11 (br. t, J = 1.7 Hz, 1 H; H-C(6)), 8.24 ppm (br. s, 1 H; H-C(2)); ¹³C NMR (100 MHz, CDCl₃): δ = 19.03 (CHMe₂), 35.92 (CHMe₂), 123.58 (C(3)), 123.86 (q, ³ J (C, F) = 3.8 Hz; C(4)), 132.37 (q, ³ J (C, F) = 3.7 Hz; C(6)), 133.25 (q, ¹ J (C, F) = 273.2 Hz; CF₃), 133.08 (q, ² J (C, F) = 33.4 Hz; C(5)), 134.76 (q, ⁵ J (C, F) = 1.1 Hz; C(2)), 138.59 (C(1)), 201.75 ppm (C=O); ¹⁹F NMR (377 MHz, CDCl₃): δ = -62.88 ppm (s; CF₃); IR (ATR): $\tilde{\nu}$ = 3078 (w), 2976 (w), 2937 (w), 2873 (w), 1694 (s), 1606 (w), 1579 (w), 1469 (m), 1435 (m), 1386 (m), 1370 (m), 1352 (m), 1314 (s), 1259 (m), 1207 (s), 1172 (s), 1161 (s), 1129 (s), 1100 (s), 1083 (m), 1013 (m), 964 (w), 923 (w), 888 (m), 824 (w), 811 (m), 777 (m), 767 (m), 746 (m), 690 (s), 659 (m), 616 cm⁻¹ (w); HR-EI-MS: m/z (%): 295.9836 (12, [M]⁺, calcd for C₁₁H₁₀⁸¹BrF₃O⁺: 295.9841), 293.9865 (11, [M]⁺, calcd for C₁₁H₁₀⁷⁹BrF₃O⁺: 293.9862), 252.9294 (100, [M - C₃H₇]⁺, calcd for C₈H₃⁸¹BrF₃O⁺: 252.9293), 250.9316 (98, [M - C₃H₇]⁺, calcd for C₈H₃⁷⁹BrF₃O⁺: 250.9314).

1-(3-Bromo-5-fluorophenyl)-2-methylpropan-1-one (295)

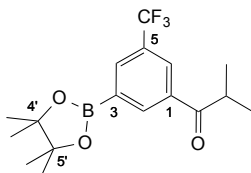


Following **GP1**, column chromatography (SiO₂; cyclohexane/EtOAc 100:0 → 97:03) gave **295** (3.20 g, 82%) as a greenish oil.

R_f = 0.60 (SiO₂; cyclohexane/EtOAc 95:05); ¹H NMR (400 MHz, CDCl₃): δ = 1.22 (d, J = 6.8 Hz, 6 H; CHMe₂), 3.43 (sept., J = 6.8 Hz, 1 H; CHMe₂), 7.43 (ddd, ³ J (H, F) = 7.7 Hz, J = 2.4, 1.7 Hz, 1 H; H-C(6)), 7.57 (ddd, ³ J (H, F) = 8.9 Hz, J = 2.4, 1.4 Hz, 1 H; H-C(4)), 7.83–7.89 ppm (m, 1 H; H-C(2)); ¹³C NMR (101 MHz, CDCl₃): δ = 19.08 (CHMe₂), 35.93 (CHMe₂),

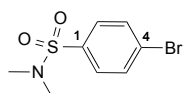
114.30 (d, $^2J(\text{C}, \text{F}) = 22.3$ Hz; C(4)), 123.21 (C(3)), 123.32 (d, $^2J(\text{C}, \text{F}) = 24.7$ Hz; C(6)), 127.50 (d, $^4J(\text{C}, \text{F}) = 3.2$ Hz; C(2)), 139.48 (d, $^3J(\text{C}, \text{F}) = 6.3$ Hz; C(1)), 162.86 (d, $^1J(\text{C}, \text{F}) = 252.7$ Hz; C(5)), 201.88 ppm (d, $^4J(\text{C}, \text{F}) = 2.0$ Hz; C=O); ^{19}F NMR (377 MHz, CDCl_3): $\delta = -109.51$ to -109.17 ppm (m; F); IR (ATR): $\tilde{\nu} = 2971$ (m), 1689 (s), 1601 (m), 1557 (w), 1448 (m), 1385 (w), 1361 (w), 1339 (m), 1279 (s), 1213 (s), 1157 (m), 1128 (s), 1085 (m), 1018 (m), 899 (w), 878 (w), 834 (m), 808 (w), 777 (w), 750 (m), 697 (m), 663 (m), 637 cm^{-1} (m); HR-EI-MS: m/z (%): 245.9874 (15, $[\text{M}]^+$, calcd for $\text{C}_{10}\text{H}_{10}^{81}\text{BrFO}^+$: 245.9879), 243.9900 (15, $[\text{M}]^+$, calcd for $\text{C}_{10}\text{H}_{10}^{79}\text{BrFO}^+$: 243.9894), 202.9325 (100, $[\text{M} - \text{C}_3\text{H}_7]^+$, calcd for $\text{C}_8\text{H}_3^{81}\text{BrFO}^+$: 202.9325), 200.9343 (100, $[\text{M} - \text{C}_3\text{H}_7]^+$, calcd for $\text{C}_8\text{H}_3^{79}\text{BrFO}^+$: 200.9346).

2-Methyl-1-[3-(4,4,5,5-tetramethyl-1,3,2-dioxaborolan-2-yl)-5-(trifluoromethyl)phenyl]-propan-1-one (144)



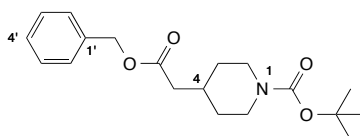
Following **GP2**, column chromatography (SiO_2 ; cyclohexane/EtOAc 100:0 \rightarrow 90:10) and trituration in cyclohexane gave **144** (4.35 g, 98%) as a white solid.

$R_f = 0.58$ (SiO_2 ; cyclohexane/EtOAc 80:20); m.p. 62–64 °C; ^1H NMR (400 MHz, CDCl_3): $\delta = 1.23$ (d, $J = 6.8$ Hz, 6 H; CHMe_2), 1.37 (s, 12 H; $(\text{CMe}_2)_2$), 3.62 (sept., $J = 6.8$ Hz, 1 H; CHMe_2), 8.22 (br. s, 1 H; H–C(4)), 8.27 (br. s, 1 H; H–C(6)), 8.49 ppm (br. s, 1 H; H–C(2)); ^{13}C NMR (101 MHz, CDCl_3): $\delta = 19.15$ (CHMe_2), 25.03 ($(\text{CMe}_2)_2$), 35.72 (CHMe_2), 84.78 ($(\text{CMe}_2)_2$), 124.01 (q, $^1J(\text{C}, \text{F}) = 272.7$ Hz; CF_3), 127.79 (q, $^3J(\text{C}, \text{F}) = 3.7$ Hz; C(6)), 130.96 (q, $^2J(\text{C}, \text{F}) = 32.8$ Hz; C(5)), 135.41 (q, $^3J(\text{C}, \text{F}) = 3.5$ Hz; C(4)), 136.39 (C(1)), 137.53 (C(2)), 203.57 ppm (C=O), C(3) hidden by the noise; ^{19}F NMR (377 MHz, CDCl_3): $\delta = -62.70$ ppm (s; CF_3); IR (ATR): $\tilde{\nu} = 3066$ (w), 2978 (m), 2938 (w), 2876 (w), 1690 (m), 1654 (w), 1606 (w, sh), 1596 (m), 1474 (m), 1456 (m), 1428 (m), 1415 (m), 1392 (m), 1380 (m), 1373 (m), 1344 (s), 1311 (m), 1294 (s), 1263 (m), 1205 (s), 1175 (s), 1162 (s), 1134 (s), 1111 (s), 1100 (s), 1018 (m), 964 (m), 910 (m), 886 (m), 872 (m), 843 (s), 801 (m), 762 (m), 744 (w), 733 (w), 705 (s), 681 (s), 666 (s), 613 cm^{-1} (m); HR-ESI-MS: m/z (%): 343.1692 (5, $[\text{M} + \text{H}]^+$, calcd for $\text{C}_{17}\text{H}_{23}^{11}\text{BF}_3\text{O}_3^+$: 343.1692), 289.1220 (100, $[\text{M} + \text{H}_2\text{O} - \text{C}_4\text{H}_7\text{O}]^+$, calcd for $\text{C}_{13}\text{H}_{17}^{11}\text{BF}_3\text{O}_3^+$: 289.1223), 288.1258 (24, $[\text{M} + \text{H}_2\text{O} - \text{C}_4\text{H}_7\text{O}]^+$, calcd for $\text{C}_{13}\text{H}_{17}^{10}\text{BF}_3\text{O}_3^+$: 288.1259).

4-Bromo-*N,N*-dimethylbenzene-1-sulfonamide (238a)^[278]

A solution of 4-bromobenzene-1-sulfonyl chloride (**239**) (1.70 g, 6.65 mmol) in THF (35 mL) was cooled to 0 °C, treated slowly with diethylamine (2 M in THF) (13.97 mL, 27.9 mmol), stirred at 0 °C for 20 min, allowed to warm up to 23 °C, and diluted with H₂O (34 mL) and EtOAc (70 mL). The two layers were separated, and the aqueous layer was extracted twice with EtOAc (2 × 15 mL). The combined organic layers were washed with brine, dried over Na₂SO₄, filtered, and evaporated. Column chromatography (SiO₂, cyclohexane/EtOAc 90:10 → 85:15) gave **238a** (1.50 g, 85%) as a white solid.

R_f = 0.25 (SiO₂; cyclohexane/EtOAc 80:20); m.p. 92–94 °C ([273]: 94 °C); ¹H NMR (400 MHz, CDCl₃): δ = 2.71 (s, 6 H; NMe₂), 7.61–7.66 (m, 2 H; H–C(3, 5)), 7.67–7.73 ppm (m, 1 H; H–C(2, 6)); ¹³C NMR (101 MHz, CDCl₃): δ = 38.02 (NMe₂), 127.90 (C(4)), 129.35 (C(2, 6)), 132.48 (C(3, 5)), 134.83 ppm (C(1)); IR (ATR): $\tilde{\nu}$ = 3092 (w), 2963 (w), 1928 (w), 1576 (m), 1467 (m), 1457 (m), 1390 (m), 1336 (s), 1292 (w), 1276 (m), 1263 (m), 1163 (s), 1148 (s), 1104 (w), 1085 (m), 1064 (m), 1052 (w), 1007 (s), 973 (w), 944 (s), 820 (s), 746 (s), 707 (s), 687 cm⁻¹ (s); HR-EI-MS: m/z (%): 264.9595 (46, [M]⁺, calcd for C₈H₁₀⁸¹BrNO₂S⁺: 264.9590), 262.9610 (46, [M]⁺, calcd for C₈H₁₀⁷⁹BrNO₂S⁺: 262.9611), 44.0482 (100).

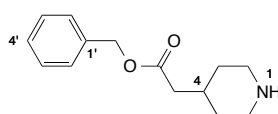
***tert*-Butyl 4-[2-(Benzyloxy)-2-oxoethyl]piperidine-1-carboxylate (293)**

A solution of 2-(1-(*tert*-butoxycarbonyl)piperidin-4-yl)acetic acid (**292**) (1.35 g, 5.55 mmol) in acetone (20 mL) was treated with K₂CO₃ (0.767 g, 5.55 mmol), followed by benzyl bromide (0.726 mL, 6.10 mmol), stirred at reflux for 16 h, allowed to cool to 23 °C, and evaporated. The residue was taken up in Et₂O and water. The two layers were separated, and the aqueous layer was extracted three times with Et₂O (3 × 20 mL). The combined organic layers were washed with brine, dried over Na₂SO₄, filtered, and evaporated to give **293** (1.85 g, 100%) as a colorless oil.

R_f = 0.14 (SiO₂; cyclohexane/EtOAc 95:05); ¹H NMR (400 MHz, CDCl₃): δ = 1.15 (qd, J = 12.4, 4.4 Hz, 2 H; H_{ax}-C(3, 5)), 1.44 (s; C(CH₃)) 1.62–1.75 (m, 2 H; H_{eq}-C(3, 5)), 1.95 (m, 1 H; H–C(4)), 2.29 (d, J = 7.1 Hz, 2 H; CH₂C=O), 2.58–2.86 (m, 2 H; H_{ax}-C(2, 6)), 3.96–4.20

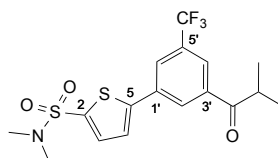
(m, 2 H; H_{eq} -C(2, 6)), 5.12 (s, 2 H; CH₂O), 7.28–7.42 ppm (m, 5 H; H-C(2', 3', 4', 5', 6')); ¹³C NMR (101 MHz, CDCl₃): δ = 28.60 (C(CH₃)), 31.94 (C(3, 5)), 33.26 (C(4)), 41.20 (CH₂C=O), 43.87 (C(2, 6)), 66.36 (CH₂O), 79.49 (C(CH₃)), 128.35 (C(2', 6')), 128.41 (C(4')), 128.72 (C(3', 5')), 136.06 (C(1')), 154.93 (COOtBu), 172.37 ppm (COOBn); IR (ATR): $\tilde{\nu}$ = 2975 (w), 2929 (w), 2119 (w), 1733 (m), 1686 (s), 1448 (w), 1419 (m), 1391 (w), 1365 (m), 1313 (w), 1285 (m), 1232 (m), 1151 (s), 1117 (m), 1003 (m), 979 (m), 948 (w), 864 (m), 737 (m), 696 cm⁻¹ (s); HR-EI-MS: m/z (%): 276.1229 (100, [M - C₄H₉]⁺, calcd for C₁₅H₁₈NO₄⁺: 276.1231).

Benzyl (Piperidin-4-yl)acetate (**294**)^[279]



A solution of *tert*-butyl 4-(2-(benzyloxy)-2-oxoethyl)piperidine-1-carboxylate (**293**) (1.75 g, 5.25 mmol) in CH₂Cl₂ (2.40 mL) was cooled in an ice bath, treated dropwise with TFA (1.20 mL, 15.58 mmol), stirred at 23 °C for 16 h, and evaporated. The residue was taken up in EtOAc (30 mL) and a sat. aq. K₂CO₃ solution (30 mL). The two layers were separated, and the aqueous layer was extracted three times with EtOAc (3 × 20 mL). The combined organic layers were washed with brine, dried over Na₂SO₄, filtered, and evaporated to give **294** (1.15 g, 94%) as a colorless oil which was directly used for the next step.

5-[3-(Isobutyryl)-5-(trifluoromethyl)phenyl]-*N,N*-dimethylthiophene-2-sulfonamide (**145**)

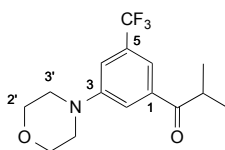


Following **GP4**, column chromatography (SiO₂; cyclohexane/EtOAc 95:05 → 85:15) gave **145** (2.86 g, 76%) as an off-white solid.

R_f = 0.36 (SiO₂; cyclohexane/EtOAc 80:20); m.p. 107–110 °C; ¹H NMR (400 MHz, CDCl₃): δ = 1.27 (d, J = 6.8 Hz, 6 H; CHMe₂), 2.83 (s, 6 H; NMe₂), 3.58 (sept., J = 6.9 Hz, 1 H; CHMe₂), 7.45 (d, J = 3.9 Hz, 1 H; H-C(3)), 7.56 (d, J = 3.9 Hz, 1 H; H-C(4)), 8.00 (br. s, 1 H; H-C(4')), 8.15 (br. s, 1 H; H-C(6')), 8.32 ppm (t, J = 1.6 Hz, 1 H; H-C(2')); ¹³C NMR (101 MHz, CDCl₃): δ = 19.09 (CHMe₂), 35.96 (CHMe₂), 38.20 (NMe₂), 123.46 (d, ¹ J (C, F) = 273.1 Hz; CF₃), 125.14 (C(3)), 125.19 (q, ³ J (C, F) = 3.7 Hz; C(6')), 126.71 (q, ³ J (C, F) = 3.6 Hz; C(4')),

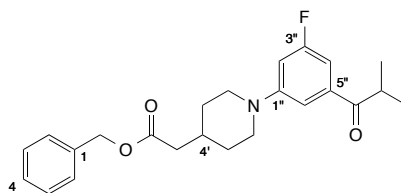
129.15 (d, $^3J(\text{C}, \text{F}) = 1.4$ Hz; C(2')), 132.57 (q, $^2J(\text{C}, \text{F}) = 33.2$ Hz; C(5')), 133.29 (C(4)), 134.57 (C(3')), 136.40 (C(5)), 138.01 (C(1')), 147.94 (C(2)), 202.45 ppm (C=O); ^{19}F NMR (377 MHz, CDCl_3): $\delta = -62.85$ ppm (s; CF_3); IR (ATR): $\tilde{\nu} = 3090$ (w), 2980 (w), 2909 (w), 1682 (s), 1603 (w), 1530 (w), 1460 (m), 1430 (w), 1391 (m), 1373 (w), 1350 (s), 1326 (w), 1303 (s), 1272 (w), 1246 (m), 1217 (m), 1197 (w), 1172 (w), 1157 (s), 1125 (s), 1112 (w), 1056 (w), 1016 (m), 985 (m), 953 (s), 908 (w), 893 (m), 880 (w), 828 (m), 820 (w), 769 (w), 746 (w), 716 (s), 698 (s), 689 (s), 666 (w), 655 cm^{-1} (m); HR-ESI-MS: m/z (%): 406.0758 (100, $[\text{M} + \text{H}]^+$, calcd for $\text{C}_{17}\text{H}_{19}\text{F}_3\text{NO}_3\text{S}_2^+$: 406.0753).

2-Methyl-1-[3-(morpholin-4-yl)-5-(trifluoromethyl)phenyl]propan-1-one (162g)



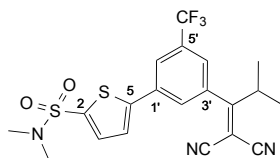
Following **GP5**, column chromatography (SiO_2 ; cyclohexane/EtOAc 100:0 \rightarrow 90:10) gave **162g** (270 mg, 88%) as an orange oil.

$R_f = 0.26$ (SiO_2 ; cyclohexane/EtOAc 90:10); ^1H NMR (400 MHz, CDCl_3): $\delta = 1.22$ (d, $J = 6.8$ Hz, 6 H; CHMe_2), 3.17–3.36 (m, 4 H; H–C(3', 5')), 3.52 (sept., $J = 6.8$ Hz, 1 H; CHMe_2), 3.80 – 3.97 (m, 4 H; H–C(2', 6')), 7.58–7.65 ppm (m, 2 H; H–C(2, 4)), H–C(6) hidden under the residual solvent peak; ^{13}C NMR (101 MHz, CDCl_3): $\delta = 19.22$ (CHMe_2), 35.77 (CHMe_2), 48.70 (C(3', 5')), 66.74 (C(2', 6')), 115.66 (q, $^3J(\text{C}, \text{F}) = 3.8$ Hz; C(6)), 115.82 (q, $^3J(\text{C}, \text{F}) = 3.9$ Hz; C(4)), 117.69 (d, $^5J(\text{C}, \text{F}) = 1.1$ Hz; C(2)), 124.04 (q, $^1J(\text{C}, \text{F}) = 272.8$ Hz; CF_3), 132.10 (q, $^2J(\text{C}, \text{F}) = 32.2$ Hz; C(5)), 137.92 (C(1)), 151.94 (C(3)), 203.65 ppm (C=O); ^{19}F NMR (377 MHz, CDCl_3): $\delta = -62.76$ ppm (s; CF_3); IR (ATR): $\tilde{\nu} = 2971$ (w), 2857 (w), 1687 (m), 1604 (m), 1466 (w), 1451 (m), 1308 (w), 1296 (m), 1268 (w), 1238 (m), 1205 (w), 1156 (m), 1117 (s), 1070 (w), 1027 (w), 990 (m), 966 (w), 953 (s), 865 (m), 821 (w), 811 (w), 782 (w), 751 (m), 706 (m), 691 (m), 664 cm^{-1} (m); HR-EI-MS: m/z (%): 301.1294 (89, $[\text{M}]^+$, calcd for $\text{C}_{15}\text{H}_{18}\text{F}_3\text{NO}_2^+$: 301.1285), 258.0739 (58, $[\text{M} - \text{C}_3\text{H}_7]^+$, calcd for $\text{C}_{12}\text{H}_{11}\text{F}_3\text{NO}_2^+$: 258.0737), 200.0321 (100).

Benzyl {1-[3-Fluoro-5-(2-methylpropanoyl)phenyl]piperidin-4-yl}acetate (296)

Following **GP5**, the crude was absorbed on SiO₂ and column chromatography (SiO₂; cyclohexane/EtOAc grad. 100:0 → 90:10) gave **296** (6.1 g, 94%) as a yellow oil.

R_f = 0.16 (SiO₂; cyclohexane/EtOAc 90:10); ¹H NMR (400 MHz, CDCl₃): δ = 1.20 (d, J = 6.8 Hz, 6 H; CHMe₂), 1.39 (dtd, J = 13.2, 11.8, 3.9 Hz, 2 H; H_{ax}-C(3', 5')), 1.76–1.89 (m, 2 H; H_{eq}-C(3', 5')), 2.00 (ttt, J = 10.9, 7.1, 3.7 Hz, 1 H; H-C(4')), 2.34 (d, J = 7.0 Hz, 2 H; CH₂C=O), 2.80 (td, J = 12.4, 2.6 Hz, 2 H; H_{ax}-C(2', 6')), 3.44 (sept., J = 6.8 Hz, 1 H; CHMe₂), 3.63–3.79 (m, 2 H; H_{eq}-C(2', 6')), 5.14 (s, 2 H; CH₂O), 6.74 (dt, J = 11.8, 2.3 Hz, 1 H; H-C(4'')), 7.01 (ddd, J = 8.9, 2.2, 1.3 Hz, 1 H; H-C(2'')), 7.26–7.28 (m, 1 H; H-C(6'')), 7.29–7.45 ppm (m, 5 H; H-C(2, 3, 4, 5, 6)); ¹³C NMR (101 MHz, CDCl₃): δ = 19.29 (CHMe₂), 31.61 (C(3', 5')), 32.93 (C(4')), 35.74 (CHMe₂), 41.10 (CH₂C=O), 49.05 (C(2', 6')), 66.41 (CH₂O), 105.21 (d, ² J (C, F) = 23.0 Hz; C(2'')), 106.84 (d, ² J (C, F) = 25.3 Hz; C(4'')), 111.24 (d, ⁴ J (C, F) = 2.1 Hz; C(6'')), 128.38 (C(2, 6)), 128.44 (C(4)), 128.74 (C(3, 5)), 136.06 (C(1)), 138.58 (d, ³ J (C, F) = 8.0 Hz; C(5'')), 153.17 (d, ³ J (C, F) = 9.7 Hz; C(1'')), 163.94 (d, ¹ J (C, F) = 244.0 Hz; C(3'')), 172.35 (OC=O), 203.93 ppm (d, ⁴ J (C, F) = 2.7 Hz; C=O); ¹⁹F NMR (377 MHz, CDCl₃): δ = -111.80 ppm (dd, ³ J (H, F) = 11.8, 8.9 Hz; F); IR (ATR): $\tilde{\nu}$ = 2971 (w), 2932 (w), 1731 (s), 1684 (s), 1606 (s), 1583 (s), 1443 (m), 1383 (m), 1288 (m), 1248 (w), 1149 (s), 1089 (w), 994 (m), 976 (m), 904 (w), 852 (m), 779 (w), 748 (s), 696 (s), 675 cm⁻¹ (w); HR-ESI-MS: m/z (%): 398.2124 (100, [M + H]⁺, calcd for C₂₄H₂₉FNO₃⁺: 398.2126).

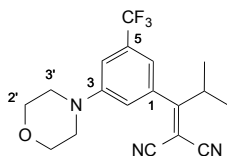
5-[3-(1,1-Dicyano-3-methylbut-1-en-2-yl)-5-(trifluoromethyl)phenyl]-N,N-dimethylthiophene-2-sulfonamide (146)

Following **GP6**, column chromatography (SiO₂; cyclohexane/EtOAc 90:10 → 83:17) gave **146** (2.70 g, 88%) as an off-white solid.

R_f = 0.15 (SiO₂; cyclohexane/EtOAc 80:20); m.p. 130–133 °C; ¹H NMR (400 MHz, CDCl₃): δ = 1.24 (d, J = 6.9 Hz, 6 H; CHMe₂), 2.83 (s, 6 H; NMe₂), 3.52 (sept., J = 6.9 Hz, 1 H; CHMe₂),

7.39–7.47 (m, 2 H; H–C(3, 6')), 7.53–7.59 (m, 2 H; H–C(4, 4')), 7.96 ppm (br. s, 1 H; H–C(2')); ^{13}C NMR (101 MHz, CDCl_3): δ = 20.72 (CHMe_2), 36.31 (CHMe_2), 38.19 (NMe_2), 88.78 ($\text{C}(\text{CN})_2$), 111.00 (CN), 111.45 (CN), 123.11 (q, $^1J(\text{C}, \text{F}) = 273.3$ Hz; CF_3), 123.76 (q, $^3J(\text{C}, \text{F}) = 3.7$ Hz; C(6')), 124.90 (q, $^3J(\text{C}, \text{F}) = 3.7$ Hz; C(4')), 125.53 (C(3)), 127.86 (C(2')), 132.90 (q, $^2J(\text{C}, \text{F}) = 33.5$ Hz; C(5')), 133.26 (C(4)), 134.96 (C(3')), 135.94 (C(1')), 137.04 (C(5)), 147.01 (C(2)), 183.50 ppm ($\text{C}=\text{C}(\text{CN})_2$); ^{19}F NMR (377 MHz, CDCl_3): δ = –62.93 ppm (s; CF_3); IR (ATR): $\tilde{\nu}$ = 3100 (w), 2974 (w), 2239 (w), 1607 (w), 1583 (w), 1531 (w), 1456 (w), 1439 (w), 1428 (w), 1362 (m), 1342 (s), 1315 (m), 1277 (s), 1243 (w), 1211 (w), 1177 (w), 1154 (s), 1122 (s), 1103 (m), 1043 (m), 1015 (m), 991 (w), 949 (m), 914 (w), 889 (s), 849 (w), 819 (m), 802 (m), 715 (s), 703 (w), 688 (s), 662 cm^{-1} (s); HR-ESI-MS: m/z (%): 471.1126 (100, $[\text{M} + \text{NH}_4]^+$, calcd for $\text{C}_{20}\text{H}_{22}\text{F}_3\text{N}_4\text{O}_2\text{S}_2^+$: 471.1131).

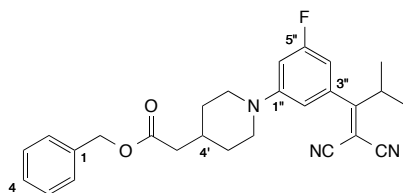
{2-Methyl-1-[3-(morpholin-4-yl)-5-(trifluoromethyl)phenyl]propylidene}propane-dinitrile (164g)



Following **GP6**, column chromatography (SiO_2 ; cyclohexane/EtOAc 95:05 \rightarrow 85:15) gave **164g** (534 mg, 77%) as a yellow solid.

R_f = 0.20 (SiO_2 ; cyclohexane/EtOAc 80:20); m.p. 92–95 °C; ^1H NMR (400 MHz, CDCl_3): δ = 1.21 (d, $J = 6.9$ Hz, 6 H; CHMe_2), 3.13–3.36 (m, 4 H; H–C(3', 5')), 3.46 (sept., $J = 6.9$ Hz, 1 H; CHMe_2), 3.75–4.02 (m, 4 H; H–C(2', 6')), 6.77 (t, $J = 2.0$ Hz, 1 H; H–C(2)), 6.85 (td, $J = 1.5, 0.7$ Hz, 1 H; H–C(6)), 7.18 ppm (ddd, $J = 2.2, 1.5, 0.7$ Hz, 1 H; H–C(4)); ^{13}C NMR (101 MHz, CDCl_3): δ = 20.75 (CHMe_2), 36.32 (CHMe_2), 48.39 (C(3', 5')), 66.60 (C(2', 6')), 87.73 ($\text{C}(\text{CN})_2$), 111.46 (CN), 111.80 (CN), 113.34 (q, $^3J(\text{C}, \text{F}) = 3.8$ Hz; C(4)), 113.75 (q, $^3J(\text{C}, \text{F}) = 3.9$ Hz; C(6)), 116.54 (d, $^5J(\text{C}, \text{F}) = 1.5$ Hz; C(2)), 123.70 (q, $^1J(\text{C}, \text{F}) = 273.0$ Hz; CF_3), 132.54 (q, $^2J(\text{C}, \text{F}) = 32.6$ Hz; C(5)), 135.66 (C(1)), 151.72 (C(3)), 185.41 ppm ($\text{C}=\text{C}(\text{CN})_2$); ^{19}F NMR (377 MHz, CDCl_3): δ = –62.95 ppm (s; CF_3); IR (ATR): $\tilde{\nu}$ = 3079 (w), 2972 (w), 2862 (w), 2234 (w), 1608 (w), 1578 (m), 1467 (m), 1449 (m), 1389 (w), 1377 (m), 1309 (w), 1298 (w), 1258 (m), 1228 (m), 1175 (m), 1161 (m), 1110 (s), 1069 (m), 1029 (w), 989 (w), 974 (s), 934 (w), 916 (s), 894 (m), 873 (m), 848 (m), 806 (w), 740 (w), 729 (w), 699 (m), 684 (m), 659 (w), 643 cm^{-1} (w); HR-ESI-MS: m/z (%): 350.1475 (22, $[\text{M} + \text{H}]^+$, calcd for $\text{C}_{18}\text{H}_{19}\text{F}_3\text{N}_3\text{O}_+$: 350.1475), 301.1524 (100).

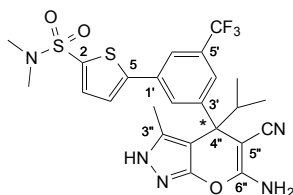
Benzyl {1-[3-(1,1-Dicyano-3-methylbut-1-en-2-yl)-5-fluorophenyl]piperidin-4-yl}acetate (297)



Following **GP6**, the crude was absorbed on SiO₂ and column chromatography (SiO₂; cyclohexane/EtOAc grad. 100:0 → 90:10) gave **297** (5.0 g, 77%) as an orange oil.

R_f = 0.29 (SiO₂; cyclohexane/EtOAc 80:20); ¹H NMR (400 MHz, CDCl₃): δ = 1.20 (d, J = 6.9 Hz, 6 H; CHMe₂), 1.31–1.47 (m, 2 H; H_{ax}-C(3', 5')), 1.78–1.89 (m, 2 H; H_{eq}-C(3', 5')), 2.01 (ddt, J = 18.7, 11.2, 4.1 Hz, 1 H; H-C(4')), 2.34 (d, J = 7.0 Hz, 2 H; CH₂C=O), 2.82 (td, J = 12.5, 2.7 Hz, 2 H; H_{ax}-C(2', 6')), 3.41 (sept., J = 6.9 Hz, 1 H; CHMe₂), 3.65 (dq, J = 12.7, 2.2, 1.6 Hz, 2 H; H_{eq}-C(2', 6')), 5.14 (s, 2 H; CH₂O), 6.28 (ddd, ³ J (H, F) = 8.3 Hz, J = 2.2, 1.4 Hz, 1 H; H-C(4'')), 6.38 (dd, J = 2.4, 1.4 Hz, 1 H; H-C(2'')), 6.64 (dt, ³ J (H, F) = 12.2 Hz, J = 2.3 Hz, 1 H; H-C(6'')), 7.28–7.46 ppm (m, 5 H; H-C(2, 3, 4, 5, 6)); ¹³C NMR (101 MHz, CDCl₃): δ = 20.78 (CHMe₂), 31.48 (C(3', 5')), 32.84 (C(4')), 36.30 (CHMe₂), 41.02 (CH₂C=O), 48.77 (C(2', 6')), 66.43 (CH₂O), 87.08 (C(CN)₂), 103.50 (d, ² J (C, F) = 24.4 Hz; C(4'')), 104.14 (d, ² J (C, F) = 25.1 Hz; C(6'')), 110.01 (d, ⁴ J (C, F) = 2.4 Hz; C(2'')), 111.72 (CN), 111.99 (CN), 128.38 (C(2, 6)), 128.45 (C(4)), 128.74 (C(3, 5)), 135.91 (d, ³ J (C, F) = 10.4 Hz; C(3'')), 136.03 (C(1)), 153.19 (d, ³ J (C, F) = 10.7 Hz; C(1'')), 163.72 (d, ¹ J (C, F) = 245.6 Hz; C(5'')), 172.29 (C=O), 186.23 ppm (d, ⁴ J (C, F) = 2.6 Hz; C=C(CN)₂); ¹⁹F NMR (377 MHz, CDCl₃): δ = -110.29 ppm (dd, J = 12.4, 8.4 Hz; F); IR (ATR): $\tilde{\nu}$ = 2933 (w), 2231 (w), 1730 (s), 1608 (m), 1574 (s), 1462 (m), 1385 (m), 1280 (w), 1240 (w), 1145 (s), 1110 (w), 1093 (w), 1058 (w), 977 (m), 832 (m), 747 (m), 696 (s), 631 cm⁻¹ (w); HR-ESI-MS: m/z (%): 446.2236 (100, [M + H]⁺, calcd for C₂₇H₂₉FN₃O₂⁺: 446.2238).

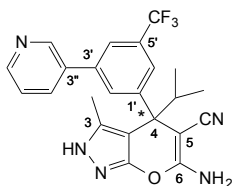
(±)-5-{3-[6-Amino-5-cyano-3-methyl-4-isopropyl-2,4-dihydropyrano[2,3-*c*]pyrazol-4-yl]-5-(trifluoromethyl)phenyl}-*N,N*-dimethylthiophene-2-sulfonamide ((±)-**129**)



Following **GP7**, column chromatography (SiO₂; cyclohexane/EtOAc 70:30 → 50:50) and recrystallization from CH₂Cl₂/hexane gave (±)-**129** (65 mg, 27%) as a white solid.

R_f = 0.14 (SiO₂; cyclohexane/EtOAc 50:50); m.p. 155–158 °C; ¹H NMR (400 MHz, THF-*d*₈): δ = 0.88 and 0.97 (d, J = 6.6 Hz, 6 H; CHMe₂), 1.86 (s, 3 H; Me), 2.73 (s, 6 H; NMe₂), 2.89 (sept., J = 6.6 Hz, 1 H; CHMe₂), 6.30 (br. s, 2 H; NH₂), 7.53 (d, J = 3.9 Hz, 1 H; H-C(3)), 7.58 (d, J = 3.9 Hz, 1 H; H-C(4)), 7.67 (br. s, 1 H; H-C(6')), 7.86 (br. s, 1 H; H-C(4')), 7.93 (br. s, 1 H; H-C(2')), 11.36 ppm (br. s, 1 H; NH); ¹³C NMR (101 MHz, THF-*d*₈): δ = 12.17 (Me), 18.68 and 19.20 (CHMe₂), 36.36 (CHMe₂), 38.11 (NMe₂), 48.83 (C(4'')), 62.76 (C(5'')), 99.35 (C(3a'')), 119.94 (CN), 121.72 (q, ³ J (C, F) = 3.8 Hz; C(4')), 125.12 (q, ¹ J (C, F) = 272.4 Hz; CF₃), 125.86 (C(4)), 126.27 (q, ³ J (C, F) = 3.8 Hz; C(6')), 130.55 (C(2')), 131.90 (q, ² J (C, F) = 31.8 Hz; C(5')), 134.01 (C(3)), 134.66 (C(1')), 135.76 (C(3'')), 136.82 (C(5)), 148.12 (C(3')), 149.60 (C(2)), 157.43 (C(7a'')), 162.75 ppm (C(6'')); ¹⁹F NMR (377 MHz, THF-*d*₈): δ = -63.42 ppm (s; CF₃); IR (ATR): $\tilde{\nu}$ = 3427 (w), 3336 (w), 3217 (w), 2963 (w), 2192 (m), 1644 (s), 1604 (s), 1588 (m), 1487 (m), 1460 (w), 1427 (w), 1398 (s), 1384 (w), 1308 (m), 1272 (w), 1239 (w), 1159 (s), 1128 (s), 1099 (w), 1048 (m), 1009 (w), 958 (m), 919 (w), 897 (w), 812 (w), 724 (w), 709 (s), 692 (w), 659 cm⁻¹ (m); HR-ESI-MS: m/z (%): 569.1611 (100, [M + NH₄]⁺, calcd for C₂₄H₂₈F₃N₆O₃S₂⁺: 569.1611), 552.1343 (15, [M + H]⁺, calcd for C₂₄H₂₅F₃N₅O₃S₂⁺: 552.1345); elemental analysis calcd (%) for C₂₄H₂₄F₃N₅O₃S₂ (551.6): C 52.26, H 4.39, N 12.70, F 10.33, S 11.63; found: C 52.25, H 4.32, N 12.66, F 10.23, S 11.49.

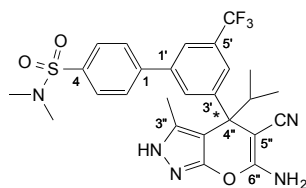
(±)-6-Amino-3-methyl-4-isopropyl-4-[3-(pyridin-3-yl)-5-(trifluoromethyl)phenyl]-2,4-dihydropyrano[2,3-c]pyrazole-5-carbonitrile ((±)-199)



Following **GP7**, column chromatography (SiO₂; cyclohexane/EtOAc 60:40 → 20:80) and recrystallization from CH₂Cl₂/hexane gave (±)-**199** (135 mg, 42%) as a white solid.

$R_f = 0.14$ (SiO₂; cyclohexane/EtOAc 20:80); m.p. 153–156 °C; ¹H NMR (400 MHz, THF-*d*₈): $\delta = 0.88$ and 0.98 (d, $J = 6.6$ Hz, 6 H; CHMe₂), 1.87 (s, 3 H; Me), 2.93 (sept., $J = 6.6$ Hz, 1 H; CHMe₂), 6.27 (br. s, 2 H; NH₂), 7.38 (ddd, $J = 7.9, 4.8, 0.9$ Hz, 1 H; H-C(5'')), 7.68 (br. s, 1 H; H-C(6')), 7.82 (br. s, 1 H; H-C(4')), 7.94 (br. s, 1 H; H-C(2')), 7.98 (ddd, $J = 7.9, 2.4, 1.6$ Hz, 1 H; H-C(4'')), 8.56 (dd, $J = 4.8, 1.6$ Hz, 1 H; H-C(6'')), 8.85 (dd, $J = 2.4, 0.9$ Hz, 1 H; H-C(2'')), 11.35 ppm (br. s, 1 H; NH); ¹³C NMR (101 MHz, THF-*d*₈): $\delta = 12.23$ (Me), 18.72 and 19.25 (CHMe₂), 36.40 (CHMe₂), 48.91 (C(4)), 63.02 (C(5)), 99.50 (C(3a)), 120.15 (CN), 122.82 (q, ³ J (C, F) = 3.8 Hz; C(4')), 124.24 (C(5'')), 125.40 (q, ¹ J (C, F) = 272.4 Hz; CF₃), 125.47 (q, ³ J (C, F) = 3.8 Hz; C(6')), 131.49–131.80 (m, 2 C; C(2', 5')), 135.09 (C(4'')), 135.73 (C(3)), 136.24 (C(3')), 139.88 (C(3'')), 147.58 (C(1')), 149.33 (C(2'')), 150.07 (C(6'')), 157.45 (C(7a)), 162.67 ppm (C(6)); ¹⁹F NMR (377 MHz, THF-*d*₈): $\delta = -63.18$ ppm (s; CF₃); IR (ATR): $\tilde{\nu} = 3477$ (w), 3125 (m), 2971 (w), 2182 (s), 1636 (s), 1595 (s), 1513 (w), 1489 (m), 1465 (w), 1441 (w), 1401 (s), 1380 (m), 1345 (m), 1265 (s), 1190 (w), 1158 (m), 1124 (s), 1076 (w), 1056 (w), 1024 (w), 981 (w), 934 (w), 897 (w), 880 (w), 866 (w), 834 (w), 810 (m), 796 (m), 751 (m), 709 (s), 692 (m), 651 (m), 623 cm⁻¹ (w); HR-ESI-MS: m/z (%): 440.1692 (100, [M + H]⁺, calcd for C₂₃H₂₁F₃N₅O⁺: 440.1693); elemental analysis calcd (%) for C₂₃H₂₀F₃N₅O (439.4): C 62.86, H 4.59, N 15.94, F 12.97; found: C 62.93, H 4.49, N 16.03, F 12.72.

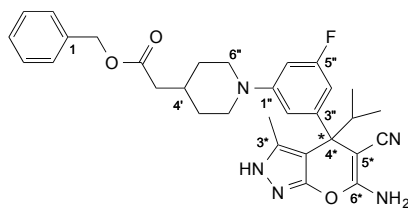
(±)-3'-[6-Amino-5-cyano-3-methyl-4-isopropyl-2,4-dihydropyrano[2,3-*c*]pyrazol-4-yl]-*N,N*-dimethyl-5'-(trifluoromethyl)[1,1'-biphenyl]-4-sulfonamide ((±)-**229**)



Following **GP7**, column chromatography (SiO₂; cyclohexane/EtOAc 80:20 → 60:40) and recrystallization from CH₂Cl₂/hexane gave (±)-**229** (95 mg, 31%) as a white solid.

R_f = 0.05 (SiO₂; cyclohexane/EtOAc 60:40); m.p. 200–203 °C; ¹H NMR (400 MHz, THF-*d*₈): δ = 0.88 and 0.98 (d, J = 6.5 Hz, 6 H; CHMe₂), 1.88 (s, 3 H; Me), 2.67 (s, 6 H; NMe₂), 2.92 (sept., J = 6.6 Hz, 1 H; CHMe₂), 6.28 (br. s, 2 H; NH₂), 7.69 (br. s, 1 H; H-C(4')), 7.84–7.86 (m, 5 H; H-C(2, 3, 5, 6, 6')), 7.97 (br. s, 1 H; H-C(2')), 11.35 ppm (br. s, 1 H; NH); ¹³C NMR (101 MHz, THF-*d*₈): δ = 12.24 (Me), 18.70 and 19.24 (CHMe₂), 36.46 (CHMe₂), 38.01 (NMe₂), 48.94 (C(4'')), 63.06 (C(5'')), 99.40 (C(3a'')), 120.18 (CN), 123.03 (q, ³ J (C, F) = 3.9 Hz; C(6')), 125.37 (q, ¹ J (C, F) = 272.4 Hz; CF₃), 125.47–125.98 (m; C(4')), 128.73 (C(2, 6)), 129.35 (C(3, 5)), 131.54 (q, ² J (C, F) = 32.1 Hz; C(5')), 132.01 (C(2')), 135.73 (C(3)), 136.54 (C(1')), 141.28 (C(1)), 144.89 (C(4)), 147.57 (C(3')), 157.48 (C(7a'')), 162.65 ppm (C(6'')); ¹⁹F NMR (377 MHz, THF-*d*₈): δ = -63.19 ppm (s; CF₃); IR (ATR): $\tilde{\nu}$ = 3501 (w), 3399 (w), 3254 (w), 2971 (w), 2191 (s), 1642 (s), 1585 (s), 1484 (m), 1454 (m), 1392 (s), 1350 (w), 1335 (s), 1261 (s), 1155 (s), 1118 (s), 1098 (m), 1071 (w), 1051 (w), 1016 (w), 949 (m), 905 (m), 852 (w), 828 (w), 796 (w), 758 (m), 737 (m), 724 (w), 709 (s), 688 (m), 677 (m), 651 cm⁻¹ (w); HR-ESI-MS: m/z (%): 546.1780 (100, [M + H]⁺, calcd for C₂₆H₂₇F₃N₅O₃S⁺: 546.1781); elemental analysis calcd (%) for C₂₆H₂₆F₃N₅O₃S (545.6): C 57.24, H 4.80, N 12.84, F 10.45, S 5.88; found: C 56.97, H 4.93, N 12.64, F 10.49, S 5.78.

(±)-Benzyl (1-{3-[6-Amino-5-cyano-3-methyl-4-isopropyl-2,4-dihydropyrano[2,3-*c*]pyrazole-4-yl]-5-fluorophenyl}piperidin-4-yl)acetate ((±)-**291**)



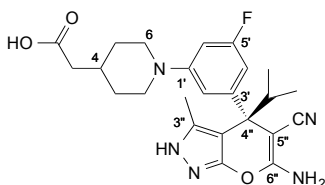
Following **GP7**, column chromatography (SiO₂; cyclohexane/EtOAc 80:20 → 55:45) and recrystallization from CH₂Cl₂/hexane gave (±)-**291** (145 mg, 25%) as a white solid.

R_f = 0.23 (SiO₂; cyclohexane/EtOAc 50:50); m.p. 198–201 °C; ¹H NMR (400 MHz, THF-*d*₈): δ = 0.85 and 0.94 (d, J = 6.6 Hz, 6 H; CHMe₂), 1.35 (qd, J = 12.1, 4.0 Hz, 2 H; H_{ax}-C(3', 5')), 1.74–1.82 (m, 2 H; H_{eq}-C(3', 5')), 1.87 (s, 4 H; H-C(4') and Me), 2.29 (d, J = 7.0 Hz, 2 H; CH₂C=O), 2.61–2.84 (m, 3 H; H_{ax}-C(2', 6') and CHMe₂), 3.59–3.70 (m, 2 H; H_{eq}-C(2', 6')), 5.08 (s, 2 H; CH₂O), 6.04 (br. s, 2 H; NH₂), 6.47 (m, 2 H; H-C(4'', 6'')), 6.78 (t, J = 1.9 Hz, 1 H; H-C(2'')), 7.18–7.50 (m, 5 H; H-C(2, 3, 4, 5, 6)), 11.18 ppm (br. s, 1 H; NH); ¹³C NMR (101 MHz, THF-*d*₈): δ = 12.31 (Me), 18.95 and 19.42 (CHMe₂), 32.58 (C(3', 5')), 33.91 (C(4')), 36.31 (CHMe₂), 41.41 (CH₂C=O), 48.69 (d, J = 2.1 Hz; C(4*)), 50.10 and 50.29 (C(2', 6')), 63.77 (C(5*)), 66.36 (CH₂O), 100.35 (C(3a*)), 101.66 (d, ² J (C, F) = 25.3 Hz; C(4'')), 106.51 (d, ² J (C, F) = 23.3 Hz; C(6'')), 113.23 (d, ⁴ J (C, F) = 2.1 Hz; C(2'')), 120.16 (CN), 128.66 (C(4)), 128.87 (C(1, 6)), 129.12 (C(3, 5)), 135.71 (C(3*)), 137.72 (C(1)), 147.95 (d, ³ J (C, F) = 8.2 Hz; C(3'')), 153.93 (d, ³ J (C, F) = 10.4 Hz; C(1'')), 157.35 (C(7a*)), 162.33 (C(6*)), 164.62 (d, ¹ J (C, F) = 239.9 Hz; C(5'')), 172.20 ppm (C=O); ¹⁹F NMR (377 MHz, THF-*d*₈): δ = -114.59 ppm (m; F); IR (ATR): $\tilde{\nu}$ = 3416 (w), 3228 (w), 3153 (w), 2965 (w), 2195 (s), 1714 (s), 1636 (m), 1612 (w), 1584 (s), 1484 (m), 1462 (w), 1398 (s), 1376 (m), 1347 (w), 1302 (w), 1257 (s), 1174 (m), 1144 (w), 1104 (w), 1075 (w), 1058 (w), 1003 (m), 958 (w), 944 (w), 904 (w), 838 (w), 823 (w), 742 (s), 698 (s), 618 cm⁻¹ (w); HR-ESI-MS: m/z (%): 544.2719 (100, [M + H]⁺, calcd for C₃₁H₃₅FN₅O₃⁺: 544.2718).

Separation of (±)-**291** enantiomers by chiral-phase HPLC (column, Daicel, Chiralpak-IA 250 mm × 20 mm; flow, 15 mL/min; detection, 254 nm; eluent, hexane/EtOAc/*i*PrOH 60:30:10). The sample was dissolved in eluent (7 mg/mL) and injected. (–)-**291**: t_R = 8.41 min (ee > 99%), $[\alpha]_D^{22} = -100.6^\circ$ (*c* 0.51, CHCl₃). (+)-**291**: t_R = 9.42 min (ee > 99%), $[\alpha]_D^{22} = 103.9^\circ$ (*c* 0.51, CHCl₃); for the HPLC traces see Section 8.1.5, Figures 100, 101, and 102.

6.9 Hz, 2 H; CH_2COOH), 2.59–2.87 (m, 3 H; $\text{H}_{\text{ax}}\text{-C}(2, 6)$ and CHMe_2), 3.63 (dt, $J = 12.8$, 3.3 Hz, 2 H; $\text{H}_{\text{eq}}\text{-C}(2, 6)$), 6.50–6.60 (m, 2 H; $\text{H-C}(4', 6')$), 6.78 ppm (t, $J = 1.9$ Hz, 1 H; $\text{H-C}(2')$); (+)-**289**: $[\alpha]_{\text{D}}^{23} = 86.4^\circ$ (c 0.50, MeOH).

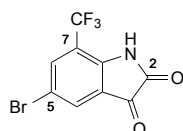
(-)-(1-{3-[6-Amino-5-cyano-3-methyl-4-isopropyl-2,4-dihydropyrano[2,3-*c*]pyrazol-4-yl]-5-fluorophenyl}piperidin-4-yl)acetic Acid ((-)-289)



Following **GP8** starting from (-)-**291**, (-)-**289** (133 mg, 94%) was obtained as a white solid. ^1H NMR (400 MHz, CD_3OD): $\delta = 0.87$ and 0.99 (d, $J = 6.6$ Hz, 6 H; CHMe_2), 1.38 (qt, $J = 12.7$, 6.0 Hz, 2 H; $\text{H}_{\text{ax}}\text{-C}(3, 5)$), 1.70–1.98 (m, 6 H; $\text{H}_{\text{eq}}\text{-C}(3, 5)$, $\text{H-C}(4)$ and Me), 2.25 (d, $J = 6.9$ Hz, 2 H; CH_2COOH), 2.69–2.77 (m, 3 H; $\text{H}_{\text{ax}}\text{-C}(2, 6)$ and CHMe_2), 3.63 (dt, $J = 12.7$, 3.4 Hz, 2 H; $\text{H}_{\text{eq}}\text{-C}(2, 6)$), 6.50–6.60 (m, 2 H; $\text{H-C}(4', 6')$), 6.77 ppm (d, $J = 2.0$ Hz, 1 H; $\text{H-C}(2')$); (-)-**289**: $[\alpha]_{\text{D}}^{23} = -88.0^\circ$ (c 0.50, MeOH).

8.1.4. Synthetic Procedures and Characterizations for Chapter 5

5-Bromo-7-(trifluoromethyl)-1*H*-indole-2,3-dione (303)^[223]

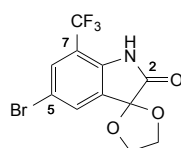


A solution of 7-(trifluoromethyl)-1*H*-indole-2,3-dione (**302**) (5.28 g, 24.54 mmol) in acetic acid (52 mL) was treated dropwise with Br_2 (6.57 mL, 128 mmol), and stirred at 23°C for 18 h after which an orange precipitate appeared. Br_2 (1.30 mL) was added. The mixture was stirred at 23°C for 5 h, poured onto an excess of ice, and stirred until the ice had melted. The mixture was filtered, and the resulting solid was washed several times with water and dried under vacuum to afford **303** (6.69 g, 93%) as an orange solid.

$R_f = 0.23$ (SiO_2 ; cyclohexane/EtOAc 80:20); m.p. $230\text{--}232^\circ\text{C}$; ^1H NMR (400 MHz, $(\text{CD}_3)_2\text{SO}$): $\delta = 7.95$ (d, $J = 2.0$ Hz, 1 H; $\text{H-C}(4)$), 8.03 (d, $J = 2.0$ Hz, 1 H; $\text{H-C}(6)$), 11.58 ppm (br. s, 1 H; NH); ^{13}C NMR (101 MHz, $(\text{CD}_3)_2\text{SO}$): $\delta = 113.89$ (C(5)), 114.04 (q, $^2J(\text{C}, \text{F}) = 33.6$ Hz; C(7)), 121.59 (C(3a)), 122.10 (q, $^1J(\text{C}, \text{F}) = 273.0$ Hz; CF_3), 130.59 (C(4)), 134.88 (q, $^3J(\text{C}, \text{F}) = 4.5$ Hz; C(6)), 146.13 (q, $^3J(\text{C}, \text{F}) = 2.1$ Hz; C(7a)), 159.40 (C(2)), 181.12 ppm

(C(3)); ^{19}F NMR (377 MHz, $(\text{CD}_3)_2\text{SO}$): $\delta = -60.48$ ppm (s; CF_3); IR (ATR): $\tilde{\nu} = 3224$ (m), 3123 (w), 1752 (s), 1746 (s), 1611 (m), 1458 (m), 1428 (w), 1400 (m), 1332 (m), 1305 (w), 1294 (w), 1266 (m), 1211 (w), 1170 (w), 1144 (w), 1130 (s), 1084 (m), 987 (m), 923 (w), 894 (s), 852 (m), 812 (w), 740 (m), 700 (s), 671 (m), 618 cm^{-1} (w); HR-EI-MS: m/z (%): 294.9274 (50, $[\text{M}]^+$, calcd for $\text{C}_9\text{H}_3^{81}\text{BrF}_3\text{NO}_2^+$: 294.9273), 292.9296 (52, $[\text{M}]^+$, calcd for $\text{C}_9\text{H}_3^{79}\text{BrF}_3\text{NO}_2^+$: 292.9294), 266.9325 (99, $[\text{M} - \text{CO}]^+$, calcd for $\text{C}_8\text{H}_3^{81}\text{BrF}_3\text{NO}^+$: 266.9330), 264.9341 (100, $[\text{M} - \text{CO}]^+$, calcd for $\text{C}_8\text{H}_3^{79}\text{BrF}_3\text{NO}^+$: 264.9350).

5'-Bromo-7'-(trifluoromethyl)spiro[1,3-dioxolane-2,3'-indol]-2'(1'H)-one (306) (adapted from Wang *et al.*^[224])

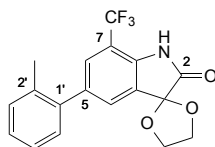


A mixture of 5-bromo-7-(trifluoromethyl)-1*H*-indole-2,3-dione (**303**) (2.80 g, 9.52 mmol), ethylene glycol (10.1 mL, 181 mmol), and *p*TsOH·H₂O (91 mg, 0.48 mmol) in toluene (86 mL) was placed in a 250 mL round-bottomed flask equipped with a Dean-Stark apparatus and stirred at reflux for 15 h. After addition of ethylene glycol (12 mL), the mixture was stirred at reflux for 3 h, and allowed to cool to 23 °C and evaporated. The residue was taken up in CH_2Cl_2 (30 mL) and washed with a sat. NaHCO_3 solution (35 mL). The aqueous layer was extracted three times with CH_2Cl_2 (3×30 mL). The combined organic layers were dried over Na_2SO_4 , filtered, and evaporated. Column chromatography (SiO_2 ; cyclohexane/EtOAc 100:0 → 90:10) gave **306** (3.18 g, 99%) as a yellowish solid.

$R_f = 0.10$ (SiO_2 ; cyclohexane/EtOAc 90:10); m.p. 193–196 °C; ^1H NMR (400 MHz, CDCl_3): $\delta = 4.27$ – 4.40 and 4.50 – 4.63 (2 m, 4 H; $\text{OCH}_2\text{CH}_2\text{O}$), 7.63 (m, 1 H; H–C(4)), 7.66 (m, 1 H; H–C(6)), 7.72 ppm (br. s, 1 H; NH); ^{13}C NMR (101 MHz, CDCl_3): $\delta = 66.26$ ($\text{OCH}_2\text{CH}_2\text{O}$), 100.42 (C(3)), 114.34 (q, $^2J(\text{C}, \text{F}) = 34.2$ Hz; C(7)), 115.73 (C(5)), 122.80 (q, $^1J(\text{C}, \text{F}) = 272.6$ Hz; CF_3), 128.09 (C(3a)), 131.13 (q, $^3J(\text{C}, \text{F}) = 4.2$ Hz; C(6)), 132.27 (C(4)), 138.50 (C(7a)), 173.49 ppm (C(2)); ^{19}F NMR (377 MHz, CDCl_3): $\delta = -60.94$ ppm (s; CF_3); IR (ATR): $\tilde{\nu} = 3202$ (m), 3129 (w), 2961 (w), 2896 (w), 1746 (s), 1625 (m), 1460 (m), 1438 (w), 1417 (w), 1337 (m), 1278 (w), 1259 (m), 1230 (m), 1188 (s), 1162 (w), 1131 (s), 1030 (s), 999 (s), 944 (s), 840 (m), 774 (m), 743 (m), 697 (s), 670 (w), 646 (m), 621 cm^{-1} (w); HR-EI-MS: m/z (%): 338.9538 (24, $[\text{M}]^+$, calcd for $\text{C}_{11}\text{H}_7^{81}\text{BrF}_3\text{NO}_3^+$: 338.9535), 336.9554 (24, $[\text{M}]^+$, calcd for

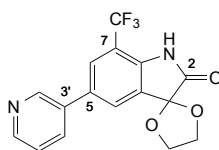
$C_{11}H_7^{79}BrF_3NO_3^+$: 336.9556), 310.9584 (97, $[M - CO]^+$, calcd for $C_{10}H_7^{81}BrF_3NO_2^+$: 310.9592), 308.9604 (100, $[M - CO]^+$, calcd for $C_{10}H_7^{79}BrF_3NO_2^+$: 308.9612).

5'-(2-Methylphenyl)-7'-(trifluoromethyl)spiro[1,3-dioxolane-2,3'-indol]-2'(1'H)-one (307)



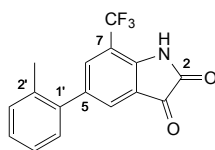
A solution of 5'-bromo-7'-(trifluoromethyl)spiro[1,3-dioxolane-2,3'-indol]-2'(1'H)-one (**306**) (650 mg, 1.92 mmol) in DME (5.2 mL) was degassed under Ar for 5 min, treated with $[Pd(PPh_3)_2Cl_2]$ (40.5 mg, 0.06 mmol), stirred at 23 °C for 15 min, treated with *o*-tolylboronic acid (**304**) (392 mg, 2.88 mmol), $NaHCO_3$ (485 mg, 5.77 mmol), and H_2O (5.20 mL) upon which a solid crushed out of the mixture. The suspension was stirred at reflux for 3 h, allowed to cool to 23 °C, and evaporated. The residue was taken up in CH_2Cl_2 (15 mL) and washed with a sat. solution of $NaHCO_3$. The aqueous layer was extracted three times with CH_2Cl_2 (3 × 15 mL). The combined organic layers were dried over Na_2SO_4 , filtered, and evaporated. Column chromatography (SiO_2 ; cyclohexane/EtOAc 100:0 → 90:10) gave **307** (615 mg, 92%) as an off-white solid.

R_f = 0.10 (SiO_2 ; cyclohexane/EtOAc 90:10); m.p. 164–166 °C; 1H NMR (400 MHz, $CDCl_3$): δ = 2.26 (s, 3 H; Me), 4.26–4.40 and 4.50–4.66 (2 m, 4 H; OCH_2CH_2O), 7.18–7.31 (m, 4 H; H–C(3', 4', 5', 6')), 7.48 (dq, J = 1.8 Hz, $^3J(H, F)$ = 0.8 Hz, 1 H; H–C(4)), 7.50 (dq, J = 1.5 Hz, $^3J(H, F)$ = 0.7 Hz, 1 H; H–C(6)), 7.65 ppm (br. s, 1 H; NH); ^{13}C NMR (101 MHz, $CDCl_3$): δ = 20.51 (Me), 66.14 (OCH_2CH_2O), 100.94 (C(3)), 112.61 (q, $^2J(C, F)$ = 33.4 Hz; C(7)), 123.72 (q, $^1J(C, F)$ = 272.1 Hz; CF_3), 126.23 (C(5)), 128.22 (C(4)), 128.94 (q, $^3J(C, F)$ = 4.0 Hz; C(6)), 129.81 (C(5', 6')), 129.83 (C(3a)), 130.72 (C(3')), 135.42 (C(2')), 137.62 (C(1')), 138.15 (d, $^4J(C, F)$ = 2.1 Hz; C(5)), 139.53 (C(7a)), 174.13 ppm (C(2)); ^{19}F NMR (377 MHz, $CDCl_3$): δ = –60.94 ppm (s; CF_3); IR (ATR): $\tilde{\nu}$ = 3192 (m), 3121 (w), 2898 (w), 1752 (s), 1633 (m), 1621 (m), 1498 (w), 1471 (m), 1448 (m), 1417 (w), 1373 (m), 1326 (w), 1293 (m), 1281 (m), 1264 (m), 1242 (m), 1182 (s), 1162 (s), 1115 (s), 1058 (m), 1030 (s), 999 (s), 948 (m), 898 (m), 864 (w), 849 (m), 803 (w), 792 (w), 759 (s), 742 (m), 727 (s), 702 (s), 670 (m), 649 (w), 626 (w), 605 cm^{-1} (w); HR-EI-MS: m/z (%): 372.0817 (38, $[M + Na]^+$, calcd for $C_{18}H_{14}F_3NNaO_3^+$: 372.0818), 350.0999 (12, $[M + H]^+$, calcd for $C_{18}H_{15}F_3NO_3^+$: 350.0999), 306.0734 (100, $[M - C_2H_4O]^+$, calcd for $C_{16}H_{11}F_3NO_2^+$: 306.0736).

5'-(Pyridin-3-yl)-7'-(trifluoromethyl)spiro[1,3-dioxolane-2,3'-indol]-2'(1'H)-one (310)

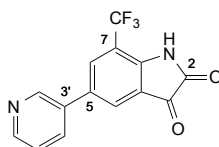
A solution of 5'-bromo-7'-(trifluoromethyl)spiro[1,3-dioxolane-2,3'-indol]-2'(1'H)-one (**306**) (650 mg, 1.92 mmol) in DME (5.2 mL) was degassed under Ar for 5 min, treated with [Pd(PPh₃)₂Cl₂] (41 mg, 0.06 mmol), stirred at 23 °C for 15 min, treated with pyridin-3-ylboronic acid (**309**) (354 mg, 2.88 mmol), NaHCO₃ (485 mg, 5.77 mmol), and H₂O (5.20 mL) upon which a solid crushed out of the mixture. The suspension was stirred at reflux for 3 h, allowed to cool to 23 °C, and evaporated. The residue was taken up in CH₂Cl₂ and washed with a sat. NaHCO₃ solution. The aqueous layer was extracted three times with CH₂Cl₂ (3 × 15 mL). The combined organic layers were dried over Na₂SO₄, filtered, and evaporated. The crude was absorbed on SiO₂ and column chromatography (SiO₂; cyclohexane/EtOAc 80:20 → 60:40) gave **310** (265 mg, 41%) as a white solid.

$R_f = 0.09$ (SiO₂; cyclohexane/EtOAc 60:40); m.p. 214–216 °C; ¹H NMR (400 MHz, CDCl₃): $\delta = 4.30$ – 4.47 and 4.51 – 4.71 (2 m, 4 H; OCH₂CH₂O), 7.39 (ddd, $J = 7.9, 4.9, 0.9$ Hz, 1 H; H–C(5')), 7.72 (dq, $J = 1.8$ Hz, $^4J(\text{H}, \text{F}) = 0.8$ Hz, 1 H; H–C(6)), 7.75 (d, $J = 1.8$ Hz, 1 H; H–C(4)), 7.85 (ddd, $J = 8.0, 2.5, 1.6$ Hz, 1 H; H–C(4')), 7.91 (br. s, 1 H; NH), 8.64 (dd, $J = 4.9, 1.6$ Hz, 1 H; H–C(6')), 8.82 ppm (dd, $J = 2.5, 0.9$ Hz, 1 H; H–C(2')); ¹³C NMR (101 MHz, CDCl₃): $\delta = 66.20$ (OCH₂CH₂O), 100.74 (C(3)), 113.55 (q, $^2J(\text{C}, \text{F}) = 33.7$ Hz; C(7)), 123.53 (q, $^1J(\text{C}, \text{F}) = 272.1$ Hz; CF₃), 123.85 (C(5')), 127.12 (q, $^3J(\text{C}, \text{F}) = 4.1$ Hz; C(6)), 127.23 (C(3a)), 127.76 (C(4)), 133.71 (C(5)), 134.26 (C(4')), 134.73 (C(3')), 139.41 (C(7a)), 148.01 (C(2')), 149.32 (C(6')), 173.99 ppm (C(2)); ¹⁹F NMR (377 MHz, CDCl₃): $\delta = -60.75$ ppm (s; CF₃); IR (ATR): $\tilde{\nu} = 2971$ (br. w), 1746 (s), 1633 (w), 1622 (w), 1464 (w), 1453 (w), 1372 (w), 1297 (w), 1272 (w), 1173 (s), 1103 (s), 1025 (m), 999 (s), 945 (w), 892 (w), 804 (w), 755 (w), 705 cm⁻¹ (m); HR-ESI-MS: m/z (%): 337.0793 (100, [M + H]⁺, calcd for C₁₆H₁₂F₃N₂O₃⁺: 337.0795).

5-(2-Methylphenyl)-7-(trifluoromethyl)-1*H*-indole-2,3-dione (305)

A solution of 5'-(2-methylphenyl)-7'-(trifluoromethyl)spiro[1,3-dioxolane-2,3'-indol]-2'(1'*H*)-one (**307**) (500 mg, 1.43 mmol) in MeOH (7.3 mL) was treated with conc. HCl (3.0 mL, 99 mmol). A yellowish solid crushed out of the solution. The suspension was stirred at reflux for 2 h. An orange solution was obtained. The mixture was allowed to cool to 23 °C and evaporated. The residue was taken up in CH₂Cl₂ and washed with a sat. NaHCO₃ solution. The aqueous layer was extracted three times with CH₂Cl₂ (3 × 15 mL). The combined organic layers were dried over Na₂SO₄, filtered, and evaporated. The crude was absorbed on SiO₂ and column chromatography (SiO₂; cyclohexane/EtOAc 100:0 → 90:10) gave **305** (290 mg, 66%) as an orange solid.

R_f = 0.11 (SiO₂; cyclohexane/EtOAc 90:10); m.p. 165–167 °C; ¹H NMR (400 MHz, CDCl₃): δ = 2.27 (s, 3 H; Me), 7.10–7.22 (m, 1 H; H–C(3')), 7.27–7.38 (m, 3 H; H–C(4', 5', 6')), 7.73 (dq, J = 1.7 Hz, ⁴ J (H, F) = 0.8 Hz, 1 H; H–C(6)), 7.78 (dq, J = 1.8, 0.7 Hz, 1 H; H–C(4)), 8.33 ppm (br. s, 1 H; NH); ¹³C NMR (101 MHz, CDCl₃): δ = 20.43 (Me), 114.34 (q, ² J (C, F) = 33.7 Hz; C(7)), 119.08 (C(3a)), 125.37 (q, ¹ J (C, F) = 171.1 Hz; CF₃), 126.56 (C(4')), 128.84 (C(5')), 129.59 (2 C; C(4, 6')), 131.03 (C(3')), 135.11 (q, ³ J (C, F) = 3.9 Hz; C(6)), 135.26 (C(1')), 138.19 (C(2')), 138.40 (C(5)), 144.66 (q, ³ J (C, F) = 1.7 Hz; C(7a)), 158.11 (C(2)), 181.36 ppm (C(3)); ¹⁹F NMR (377 MHz, CDCl₃): δ = –60.73 ppm (s; CF₃); IR (ATR): $\tilde{\nu}$ = 3212 (br. w), 3129 (br. w), 2987 (br. w), 1750 (s), 1616 (m), 1475 (w), 1355 (w), 1291 (w), 1247 (w), 1183 (w), 1170 (w), 1122 (s), 1003 (w), 980 (w), 903 (w), 761 (w), 743 (w), 713 cm^{–1} (m); HR-ESI-MS: m/z (%): 328.0556 (100, [M + Na]⁺, calcd for C₁₆H₁₀F₃NNaO₂⁺: 328.0556), 306.0737 (99, [M + H]⁺, calcd for C₁₆H₁₁F₃NO₂⁺: 306.0736).

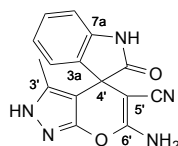
5-(Pyridin-3-yl)-7-(trifluoromethyl)-1*H*-indole-2,3-dione (308)

A solution of 5'-(pyridin-3-yl)-7'-(trifluoromethyl)spiro[1,3-dioxolane-2,3'-indol]-2'(1'*H*)-one (**310**) (230 mg, 0.68 mmol) in MeOH (7.0 mL) was treated with conc. HCl (2.2 mL, 26.8 mmol), stirred at reflux for 20 h, allowed to cool to 23 °C, and evaporated. The residue

was taken up in CH₂Cl₂ and washed with a sat. NaHCO₃ solution. The aqueous layer was extracted three times with CH₂Cl₂ (3 × 15 mL). The combined organic layers were dried over Na₂SO₄, filtered, and evaporated. The crude was absorbed on SiO₂ and column chromatography (SiO₂; cyclohexane/EtOAc 60:40 → 40:60) gave **308** (115 mg, 58%) as an orange solid.

R_f = 0.49 (SiO₂; CH₂Cl₂/MeOH 90:10); m.p. 250 °C (decomp.); ¹H NMR (400 MHz, THF-*d*₈): δ = 7.39 (dd, J = 7.9, 4.8 Hz, 1 H; H-C(5')), 8.03 (dt, J = 7.9, 2.0 Hz, 1 H; H-C(4')), 8.08 (d, J = 1.9 Hz, 1 H; H-C(6)), 8.11 (d, J = 1.9 Hz, 1 H; H-C(4)), 8.56 (dd, J = 4.8, 1.6 Hz, 1 H; H-C(6')), 8.91 (d, J = 2.5 Hz, 1 H; H-C(2')), 10.62 ppm (br. s, 1 H; NH); ¹³C NMR (101 MHz, THF-*d*₈): δ = 114.62 (q, ² J (C, F) = 33.8 Hz; C(7)), 121.83 (C(3a)), 124.34 (q, ¹ J (C, F) = 271.1 Hz; CF₃), 124.23 (C(5')), 126.98 (C(4)), 132.06 (q, ³ J (C, F) = 4.4 Hz; C(6)), 133.65 (C(5)), 134.39 (C(4')), 134.58 (C(3')), 147.83 (C(7a)), 148.81 (C(2')), 150.10 (C(6')), 159.89 (C(2)), 182.25 ppm (C(3)); ¹⁹F NMR (377 MHz, THF-*d*₈): δ = -62.63 ppm (s; CF₃); IR (ATR): $\tilde{\nu}$ = 2970 (br. w), 1741 (m), 1627 (w), 1575 (w), 1477 (w), 1432 (w), 1363 (w), 1296 (w), 1267 (m), 1179 (m), 1109 (s), 1067 (w), 1042 (w), 987 (w), 802 (w), 723 cm⁻¹ (w); HR-EI-MS: m/z (%): 293.0533 (100, [M + H]⁺, calcd for C₁₄H₈F₃N₂O₂⁺: 293.0532).

(±)-6'-Amino-3'-methyl-2-oxo-1,2-dihydro-2'H-spiro[indole-3,4'-pyrano[2,3-*c*]pyrazole]-5'-carbonitrile ((±)-314)

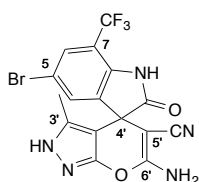


A solution of indoline-2,3-dione (150 mg, 1.02 mmol) in EtOH (5.5 mL) was treated with malononitrile (67 mg, 1.02 mmol), 3-methyl-1*H*-pyrazol-5(4*H*)-one (**86**) (100 mg, 1.02 mmol), and Et₃N (28 μ L, 0.20 mmol) and stirred at reflux for 1.5 h after which a white precipitate appeared. The mixture was allowed to cool to 23 °C and filtered. The resulting solid was washed with EtOH to give (±)-**314** (187 mg, 63%) as a white solid.

R_f = 0.23 (SiO₂; CH₂Cl₂/MeOH 90:10); m.p. 280 °C (decomp.); ¹H NMR (400 MHz, (CD₃)₂SO): δ = 1.53 (s, 3 H; Me), 6.90 (dt, J = 7.7, 0.8 Hz, 1 H; H-C(5)), 7.01 (dtd, J = 14.6, 7.4, 1.3 Hz, 2 H; H-C(6, 7)), 7.10–7.33 (m, 3 H; H-C(4) and NH₂), 10.58 (br. s, 1 H; NH), 12.27 ppm (br. s, 1 H; NH); ¹³C NMR (101 MHz, (CD₃)₂SO): δ = 8.95 (Me), 47.28 (C(3)), 55.16 (C(5')), 95.40 (C(3a')), 109.65 (C(5)), 118.72 (CN), 122.49 (C(6)), 124.51 (C(7)), 128.88 (C(4)), 132.68 (C(7a)), 134.68 (C(3')), 141.51 (C(3a)), 155.25 (C(7a')), 162.46 (C(6')),

178.00 ppm (C=O); IR (ATR): $\tilde{\nu}$ = 3334 (m), 3129 (m), 2182 (s), 1706 (s), 1640 (m), 1604 (m), 1581 (s), 1518 (w), 1497 (m), 1481 (w), 1470 (s), 1408 (s), 1379 (m), 1319 (w), 1287 (w), 1207 (m), 1152 (m), 1098 (w), 1079 (w), 1053 (m), 982 (w), 929 (m), 916 (w), 863 (m), 810 (w), 754 (s), 726 (w), 692 (s), 675 (s), 645 (w), 619 cm^{-1} (m); HR-ESI-MS: m/z (%): 294.0983 (100, $[M + H]^+$, calcd for $\text{C}_{15}\text{H}_{12}\text{N}_5\text{O}_2^+$: 294.0986); elemental analysis calcd (%) for $\text{C}_{15}\text{H}_{11}\text{N}_5\text{O}_2$ (293.3): C 61.43, H 3.78, N 23.88, O 10.91; found: C 61.63, H 3.73, N 23.98, O 11.10.

(±)-6'-Amino-5-bromo-3'-methyl-2-oxo-7-(trifluoromethyl)-1,2-dihydro-2'H-spiro[indole-3,4'-pyrano[2,3-c]pyrazole]-5'-carbonitrile ((±)-313)

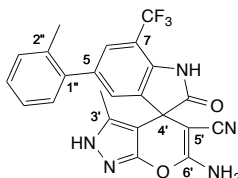


A solution of 5-bromo-7-(trifluoromethyl)-1*H*-indole-2,3-dione (**303**) (150 mg, 0.51 mmol) in EtOH (2.0 mL) was treated with malononitrile (34 mg, 0.51 mmol), 3-methyl-1*H*-pyrazol-5(4*H*)-one (**86**) (50 mg, 0.51 mmol), and Et_3N (14 μL , 0.10 mmol) and stirred at reflux for 20 min after which a white precipitate appeared. The mixture was allowed to cool to 23 °C and filtered. The resulting solid was washed with EtOH to afford (±)-**313** (150 mg, 67%) as a white solid.

R_f = 0.28 (SiO_2 ; $\text{CH}_2\text{Cl}_2/\text{MeOH}$ 90:10); m.p. 290 °C (decomp.); ^1H NMR (400 MHz, $\text{THF-}d_8$): δ = 1.67 (s, 3 H; Me), 6.64 (br. s, 2 H; NH_2), 7.46 (d, J = 2.1 Hz, 1 H; H-C(4)), 7.66 (dq, J = 1.9 Hz, $^4J(\text{H}, \text{F})$ = 0.7 Hz, 1 H; H-C(6)), 10.21 (br. s, 1 H; NH), 11.45 ppm (s, 1 H; NH); ^{13}C NMR (101 MHz, $\text{THF-}d_8$): δ = 9.44 (Me), 47.98 (C(3)), 56.77 (C(5')), 95.84 (C(3a')), 113.79 (q, $^2J(\text{C}, \text{F})$ = 33.8 Hz; C(7)), 115.19 (C(5)), 117.86 (CN), 124.07 (q, $^1J(\text{C}, \text{F})$ = 271.1 Hz; CF_3), 128.95 (q, $^3J(\text{C}, \text{F})$ = 4.7 Hz; C(6)), 132.53 (C(4)), 135.58 (C(3')), 138.60 (C(3a)), 139.69 (C(7a)), 156.78 (C(7a')), 163.72 (C(6')), 177.75 ppm (C(2)); ^{19}F NMR (377 MHz, $\text{THF-}d_8$): δ = -62.54 ppm (s; CF_3); IR (ATR): $\tilde{\nu}$ = 3447 (m), 3318 (m), 3087 (w), 3012 (w), 2803 (w), 2198 (s), 1723 (s), 1639 (s), 1608 (s), 1587 (s), 1529 (m), 1494 (m), 1461 (m), 1429 (w), 1397 (s), 1332 (s), 1296 (m), 1264 (w), 1210 (m), 1185 (s), 1118 (s), 1076 (w), 1046 (w), 996 (w), 973 (w), 951 (w), 929 (w), 911 (m), 885 (m), 878 (m), 830 (w), 747 (w), 697 (s), 660 (m), 611 cm^{-1} (m); HR-ESI-MS: m/z (%): 441.9944 (100, $[M + H]^+$, calcd for $\text{C}_{16}\text{H}_{10}^{81}\text{BrF}_3\text{N}_5\text{O}_2^+$: 441.9946), 439.9962 (97, $[M + H]^+$, calcd for $\text{C}_{16}\text{H}_{10}^{79}\text{BrF}_3\text{N}_5\text{O}_2^+$: 439.9964); elemental

analysis calcd (%) for C₁₆H₉BrF₃N₅O₂ (440.2): C 43.66, H 2.06, N 15.91, O 7.27, Br 18.15, F 12.95; found: C 43.79, H 1.94, N 15.79, Br 17.89, F 13.19.

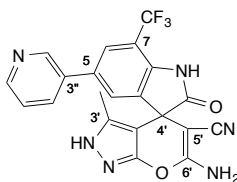
(±)-6'-Amino-3'-methyl-5-(2-methylphenyl)-2-oxo-7-(trifluoromethyl)-1,2-dihydro-2'H-spiro[indole-3,4'-pyrano[2,3-c]pyrazole]-5'-carbonitrile ((±)-298)



A solution of 5-(2-methylphenyl)-7-(trifluoromethyl)-1*H*-indole-2,3-dione (**305**) (150 mg, 0.49 mmol) in EtOH (2.0 mL) was treated with malononitrile (33 mg, 0.49 mmol), 3-methyl-1*H*-pyrazol-5(4*H*)-one (**86**) (48 mg, 0.49 mmol), and Et₃N (14 μL, 0.01 mmol) and stirred at reflux for 1.5 h after which a white precipitate appeared. The mixture was allowed to cool to 23 °C and filtered. The resulting solid was washed with EtOH to give (±)-**298** (196 mg, 87%) as a white solid.

R_f = 0.29 (SiO₂; CH₂Cl₂/MeOH 90:10); m.p. 260 °C (decomp.); analyt. HPLC: t_R = 14.50 min (purity = 95%); ¹H NMR (400 MHz, THF-*d*₈): δ = 1.68 (s, 3 H; Me-C(3')), 2.19 (s, 3 H; Me-C(1')), 6.55 (br. s, 2 H; NH₂), 7.08–7.23 (m, 4 H; H-C(3'', 4'', 5'', 6'')), 7.26 (d, J = 1.7 Hz, 1 H; H-C(4)), 7.44 (d, J = 1.7 Hz, 1 H; H-C(6)), 10.08 (br. s, 1 H; NH), 11.35 ppm (br. s, 1 H; NH); ¹³C NMR (101 MHz, THF-*d*₈): δ = 9.46 (Me-C(3')), 20.49 (Me-C(1')), 47.88 (C(3)), 57.30 (C(5')), 96.53 (C(3a')), 112.07 (q, ² J (C, F) = 33.0 Hz; C(7)), 118.02 (CN), 125.02 (q, ¹ J (C, F) = 271.7 Hz; CF₃), 126.52–126.63 (m, 2 C; C(6, 6'')), 128.40 (C(4'')), 130.43 (2 C; C(4, 5'')), 131.08 (C(3'')), 135.40 (C(3')), 136.12 (C(3a)), 136.15 (C(2'')), 137.26 (C(5)), 139.37 (q, ³ J (C, F) = 2.2 Hz; (C(7a))), 141.13 (C(1'')), 156.91 (C(7a')), 163.79 (C(6')), 178.36 ppm (C=O); ¹⁹F NMR (377 MHz, THF-*d*₈): δ = -62.04 ppm (s; CF₃); IR (ATR): $\tilde{\nu}$ = 3413 (w), 3334 (w), 3164 (w), 2987 (m), 2901 (w), 2196 (w), 1698 (m), 1643 (w), 1606 (w), 1591 (w), 1496 (w), 1473 (w), 1406 (s), 1358 (w), 1258 (w), 1212 (w), 1153 (w), 1133 (s), 1065 (s), 901 (w), 890 (w), 841 (w), 761 (w), 701 cm⁻¹ (m); HR-ESI-MS: m/z (%): 452.1330 (100, [M + H]⁺, calcd for C₂₃H₁₇F₃N₅O₂⁺: 452.1329).

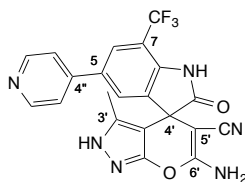
(±)-6'-Amino-3'-methyl-2-oxo-5-(pyridin-3-yl)-7-(trifluoromethyl)-1,2-dihydro-2'H-spiro[indole-3,4'-pyrano[2,3-c]pyrazole]-5'-carbonitrile ((±)-299)



A solution of 5-(pyridin-3-yl)-7-(trifluoromethyl)-1*H*-indole-2,3-dione (**308**) (85 mg, 0.29 mmol) in EtOH (17 mL) was treated with malononitrile (19 mg, 0.29 mmol), 3-methyl-1*H*-pyrazol-5(4*H*)-one (**86**) (29 mg, 0.29 mmol), and Et₃N (8.11 μL, 0.06 mmol) and stirred at reflux for 1.5 h upon which a white precipitate appeared. The mixture was allowed to cool to 23 °C and filtered. The resulting solid was washed with EtOH to give (±)-**299** (65 mg, 51%) as a white solid.

R_f = 0.18 (SiO₂; CH₂Cl₂/MeOH 90:10); m.p. 260 °C (decomp.); ¹H NMR (400 MHz, THF-*d*₈): δ = 1.67 (s, 3 H; Me), 6.61 (br. s, 2 H; NH₂), 7.31 (ddd, J = 7.9, 4.8, 0.9 Hz, 1 H; H-C(5'')), 7.64 (d, J = 1.8 Hz, 1 H; H-C(4)), 7.81 (d, J = 1.8 Hz, 1 H; H-C(6)), 7.95 (ddd, J = 8.0, 2.5, 1.6 Hz, 1 H; H-C(4'')), 8.49 (dd, J = 4.8, 1.6 Hz, 1 H; H-C(6'')), 8.82 (dd, J = 2.5, 0.9 Hz, 1 H; H-C(2'')), 10.19 (br. s, 1 H; NH), 11.41 ppm (br. s, 1 H; NH); ¹³C NMR (101 MHz, THF-*d*₈): δ = 9.47 (Me), 48.01 (C(3)), 57.22 (C(5')), 96.35 (C(3a')), 112.90 (q, ² J (C, F) = 33.8 Hz; C(7)), 118.03 (CN), 124.05 (C(5'')), 124.76 (q, ³ J (C, F) = 4.3 Hz; C(6)), 124.91 (q, ¹ J (C, F) = 271.1 Hz; CF₃), 127.97 (C(4)), 133.54 (C(5)), 134.42 (C(4'')), 135.49 (C(3'')), 135.56 (C(3')), 137.36 (C(3a)), 140.32 (d, ³ J (C, F) = 2.3 Hz; C(7a)), 148.89 (C(2'')), 149.55 (C(6'')), 156.92 (C(7a')), 163.77 (C(6')), 178.28 ppm (C(2)); ¹⁹F NMR (377 MHz, THF-*d*₈): δ = -62.20 ppm (s; CF₃); IR (ATR): $\tilde{\nu}$ = 3330 (br. w), 2987 (m), 2901 (w), 2186 (w), 1728 (m), 1653 (w), 1605 (w), 1587 (m), 1497 (w), 1472 (w), 1404 (m), 1364 (w), 1271 (w), 1211 (w), 1156 (w), 1119 (s), 1065 (s), 897 (w), 814 (w), 758 (w), 711 cm⁻¹ (m); HR-ESI-MS: m/z (%): 439.1121 (100, [M + H]⁺, calcd for C₂₁H₁₄F₃N₆O₂⁺: 439.1125).

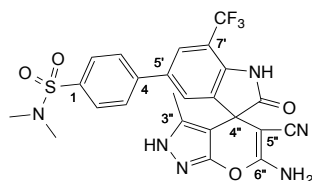
(±)-6'-Amino-3'-methyl-2-oxo-5-(pyridin-4-yl)-7-(trifluoromethyl)-1,2-dihydro-2'H-spiro[indole-3,4'-pyrano[2,3-c]pyrazole]-5'-carbonitrile ((±)-300)



A solution of 5-(pyridin-4-yl)-7-(trifluoromethyl)-1*H*-indole-2,3-dione (150 mg, 0.51 mmol) in EtOH (64 mL) was treated with malononitrile (34 mg, 0.51 mmol), 3-methyl-1*H*-pyrazol-5(4*H*)-one (**86**) (50 mg, 0.51 mmol), and Et₃N (14 μL, 0.10 mmol) and stirred at reflux for 2 h, allowed to cool to 23 °C, and evaporated. The residue was triturated in EtOH and filtered to give (±)-**300** (171 mg, 76%) as a pinkish solid.

$R_f = 0.15$ (SiO₂; CH₂Cl₂/MeOH 90:10); m.p. 220 °C (decomp.); analyt. HPLC: $t_R = 4.78$ min (purity = 95%); ¹H NMR (400 MHz, THF-*d*₈): $\delta = 1.66$ (s, 3 H; Me), 6.63 (br. s, 2 H; NH₂), 7.51–7.62 (m, 2 H; H–C(3''), 5''), 7.72 (d, $J = 1.8$ Hz, 1 H; H–C(4)), 7.90 (d, $J = 1.8$ Hz, 1 H; H–C(6)), 8.46–8.63 (m, 2 H; H–C(2''), 6''), 10.26 (br. s, 1 H; NH), 11.42 ppm (br. s, 1 H; NH); ¹³C NMR (101 MHz, THF-*d*₈): $\delta = 9.47$ (Me), 48.01 (C(3)), 57.12 (C(5')), 96.25 (C(3a')), 112.91 (q, ² J (C, F) = 33.3 Hz; C(7)), 117.99 (CN), 121.62 (C(3''), 5''), 124.85 (q, ¹ J (C, F) = 271.8 Hz; CF₃), 124.87 (q, ³ J (C, F) = 4.3 Hz; C(6)), 127.77 (C(4)), 133.52 (C(4'')), 135.58 (C(3')), 137.40 (C(3a)), 141.21 (C(7a)), 146.70 (C(5)), 151.15 (C(2''), 6''), 156.90 (C(7a')), 163.79 (C(6')), 178.31 ppm (C=O); ¹⁹F NMR (377 MHz, THF-*d*₈): $\delta = -62.29$ ppm (s; CF₃); IR (ATR): $\tilde{\nu} = 3334$ (br. w), 2987 (m), 2900 (w), 2179 (w), 1739 (m), 1715 (m), 1636 (w), 1599 (m), 1470 (w), 1442 (w), 1403 (m), 1393 (m), 1265 (w), 1202 (w), 1114 (s), 1065 (s), 821 (w), 702 cm⁻¹ (m); HR-ESI-MS: m/z (%): 439.1118 (100, [M + H]⁺, calcd for C₂₁H₁₄F₃N₆O₂⁺: 439.1125).

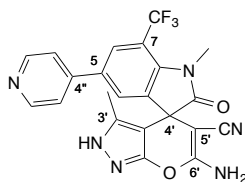
(±)-4-[6'-Amino-5'-cyano-3'-methyl-2-oxo-7-(trifluoromethyl)-1,2-dihydro-2'H-spiro[indole-3,4'-pyrano[2,3-c]pyrazol]-5-yl]-N,N-dimethylbenzene-1-sulfonamide ((±)-301)



A solution of 4-(2,3-dioxo-7-(trifluoromethyl)indolin-5-yl)-*N,N*-dimethylbenzenesulfonamide (150 mg, 0.38 mmol) in EtOH (9.0 mL) was treated with malononitrile (25 mg, 0.38 mmol), 3-methyl-1*H*-pyrazol-5(4*H*)-one (**86**) (37 mg, 0.38 mmol), and Et₃N (10.5 μL, 0.08 mmol) and stirred at reflux for 2 h upon which a white precipitate appeared. The suspension allowed to cool to 23 °C, and filtered. The resulting solid was washed with EtOH to give (±)-**301** (150 mg, 73%) as a white solid.

$R_f = 0.28$ (SiO₂; CH₂Cl₂/MeOH 90:10); m.p. 240 °C (decomp.); analyt. HPLC: $t_R = 8.94$ min (purity = 95%); ¹H NMR (400 MHz, THF-*d*₈): $\delta = 1.67$ (s, 3 H; Me), 2.63 (s, 6 H; NMe₂), 6.63 (br. s, 2 H; NH₂), 7.68 (d, $J = 1.8$ Hz, 1 H; H-C(4')), 7.72–7.81 (m, 2 H; H-C(3, 5)), 7.82–7.89 (m, 3 H; H-C(2, 6, 6')), 10.23 (br. s, 1 H; NH), 11.42 ppm (br. s, 1 H; NH); ¹³C NMR (101 MHz, THF-*d*₈): $\delta = 9.48$ (Me), 38.01 (NMe₂), 48.02 (C(3')), 57.14 (C(5'')), 96.31 (C(3a'')), 112.87 (q, ² J (C, F) = 33.3 Hz; C(7')), 118.03 (CN), 124.88 (q, ¹ J (C, F) = 271.1 Hz; CF₃), 125.12 (q, ³ J (C, F) = 4.3 Hz; C(6')), 128.03 (C(2, 6)), 128.13 (C(4')), 129.18 (C(3, 5)), 134.79 (C(5')), 135.57 (C(3'')), 135.71 (C(1)), 137.34 (C(3a')), 140.69 (d, ³ J (C, F) = 2.2 Hz; C(7a')), 144.17 (C(4)), 156.91 (C(7a'')), 163.79 (C(6'')), 178.29 ppm (C(2'')); ¹⁹F NMR (377 MHz, THF-*d*₈): $\delta = -62.23$ ppm (s; CF₃); IR (ATR): $\tilde{\nu} = 3416$ (w), 3297 (w), 3097 (br. w), 2987 (w), 2179 (m), 1725 (s), 1645 (w), 1631 (w), 1604 (w), 1581 (m), 1502 (w), 1471 (w), 1413 (m), 1340 (m), 1301 (w), 1158 (s), 1121 (s), 1088 (w), 1065 (w), 965 (w), 896 (w), 830 (w), 713 cm⁻¹ (m); HR-ESI-MS: m/z (%): 545.1210 (100, [M + H]⁺, calcd for C₂₄H₂₀F₃N₆O₄S⁺: 545.1213).

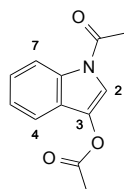
(±)-6'-Amino-1,3'-dimethyl-2-oxo-5-(pyridin-4-yl)-7-(trifluoromethyl)-1,2-dihydro-2'H-spiro[indole-3,4'-pyrano[2,3-c]pyrazole]-5'-carbonitrile ((±)-**315**)



A solution of 1-methyl-5-(pyridin-4-yl)-7-(trifluoromethyl)-1*H*-indole-2,3-dione (150 mg, 0.49 mmol) in EtOH (2.0 mL) was treated with malononitrile (32 mg, 0.49 mmol), 3-methyl-1*H*-pyrazol-5(4*H*)-one (**86**) (48 mg, 0.49 mmol), and Et₃N (14 μL, 0.10 mmol) and stirred at reflux for 1.5 h, allowed to cool to 23 °C, and evaporated. The residue was triturated in EtOH and filtered to give (±)-**315** (110 mg, 50%) as a light pink solid.

$R_f = 0.23$ (SiO₂; CH₂Cl₂/MeOH 90:10); m.p. 250 °C (decomp.); analyt. HPLC: $t_R = 6.88$ min (purity = 95%); ¹H NMR (400 MHz, THF-*d*₈): $\delta = 1.59$ (s, 3 H; Me), 3.46 (q, ¹ J (H, F) = 2.5 Hz, 3 H; NMe), 6.68 (br. s, 2 H; NH₂), 7.59 (d with virtual coupling, $J = 6.2$ Hz, 2 H; H-C(3'', 5'')), 7.77 (d, $J = 2.0$ Hz, 1 H; H-C(4)), 8.03 (d, $J = 2.0$ Hz, 1 H; H-C(6)), 8.53 (d with virtual coupling, $J = 6.2$ Hz, 2 H; H-C(2'', 6'')), 11.43 ppm (br. s, 1 H; NH); ¹³C NMR (101 MHz, THF-*d*₈): $\delta = 9.44$ (Me), 29.35 (q, ² J (C, F) = 6.3 Hz; NMe), 47.22 (C(3)), 57.08 (C(5')), 96.16 (C(3a')), 113.10 (q, ² J (C, F) = 32.9 Hz; C(7)), 117.89 (CN), 121.58 (C(3'', 5'')), 124.74 (q, ¹ J (C, F) = 271.6 Hz; CF₃), 126.10 (q, ³ J (C, F) = 5.9 Hz; C(6)), 127.63 (C(4)), 133.67 (C(5)), 135.51 (C(3')), 137.76 (C(3a)), 142.99 (C(7a)), 146.27 (C(4'')), 151.29 (C(2'', 6'')), 156.90 (C(7a')), 163.83 (C(6')), 177.83 ppm (C=O); ¹⁹F NMR (377 MHz, THF-*d*₈): $\delta = -53.93$ ppm (q, ² J (H, F) = 2.3 Hz; CF₃); IR (ATR): $\tilde{\nu} = 3280$ (w), 2987 (m), 2901 (w), 2191 (m), 1711 (m), 1642 (w), 1594 (m), 1493 (w), 1470 (w), 1394 (m), 1342 (m), 1223 (w), 1158 (w), 1102 (m), 1073 (s), 1057 (w), 1041 (m), 941 (w), 823 (m), 766 (w), 704 cm⁻¹ (m); HR-ESI-MS: m/z (%): 453.1277 (100, [M + H]⁺, calcd for C₂₂H₁₆F₃N₆O₂⁺: 453.1281).

1-Acetyl-1*H*-indol-3-yl Acetate (**318**)^[228]

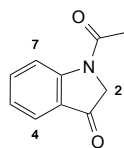


A mixture of 2-((carboxymethyl)amino)benzoic acid (**317**) (3 g, 15.4 mmol) and anhydride acetic acid (64 mL, 678 mmol) was treated with sodium acetate (1.261 g, 15.4 mmol), stirred at reflux for 5 h, cooled to 23 °C, and evaporated (55 mbar, temp. of bath: 65 °C). Water

(20 mL) was added. The two layers were separated, and the aqueous layer was extracted four times with EtOAc (4 × 20 mL). The combined organic layers were washed with brine, dried over Na₂SO₄, filtered, and evaporated. Column chromatography (SiO₂; cyclohexane/EtOAc 100:0 → 90:10) gave **318** (2.12 g, 64%) as a brownish solid.

$R_f = 0.09$ (SiO₂; cyclohexane/EtOAc 90:10); m.p. 76–79 °C; ¹H NMR (400 MHz, CDCl₃): $\delta = 2.39$ (s, 3 H; NC(=O)Me), 2.61 (s, 3 H; OC(=O)Me), 7.31 (td, $J = 6.8, 1.0$ Hz, 1 H; H–C(6)), 7.35–7.45 (m, 1 H; H–C(5)), 7.54 (dt, $J = 7.8, 1.3$, 1 H; H–C(4)), 7.72 (s, 1 H; H–C(2)), 8.46 ppm (br. d, $J = 8.8$ Hz, 1 H; H–C(7)); ¹³C NMR (101 MHz, CDCl₃): $\delta = 21.20$ (NC=OMe), 24.08 (OC=OMe), 113.44 (C(2)), 116.85 (C(7)), 117.61 (C(4)), 123.74 (C(3)), 123.89 (C(6)), 126.36 (C(5)), 133.03 (C(3a)), 134.78 (C(7a)), 168.00 (NC(=O)Me), 168.85 ppm (OC(=O)Me); IR (ATR): $\tilde{\nu} = 1739$ (m), 1692 (m), 1571 (w), 1448 (m), 1386 (m), 1366 (m), 1345 (m), 1328 (m), 1237 (w), 1206 (s), 1008 (w), 932 (m), 892 (w), 732 (s), 689 (m), 632 cm⁻¹ (w); HR-EI-MS: m/z (%): 217.0734 (19, [M]⁺, calcd for C₁₂H₁₁NO₃⁺: 217.0734), 133.0517 (100, [M – C₄H₄O₂]⁺, calcd for C₈H₇NO⁺: 133.0528).

1-Acetyl-1,2-dihydro-3H-indol-3-one (**319**)^[228]

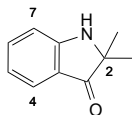


A solution of 1-acetyl-1H-indol-3-yl acetate (**318**) (2.00 g, 9.2 mmol) in ethanol (23 mL) was treated with a solution of Na₂SO₃ (1.16 g, 9.2 mmol) in H₂O (7.70 mL) leading to a white precipitate. The mixture was stirred at reflux for 2 h, cooled to 23 °C, and evaporated. The residue was diluted with water (12 mL) and EtOAc (30 mL). The layers were separated, and the aqueous layer was extracted three times with EtOAc (3 × 20 mL). The combined organic layers were washed with brine, dried over Na₂SO₄, filtered, and evaporated. The crude was absorbed on SiO₂ and column chromatography (SiO₂; cyclohexane/EtOAc 70:30 → 60:40) gave **319** (1.42 g, 88%) as a yellowish solid.

$R_f = 0.15$ (SiO₂; cyclohexane/EtOAc 60:40); m.p. 139–142 °C; ¹H NMR (400 MHz, CDCl₃): $\delta = 2.32$ (s, 3 H; Me), 4.29 (s, 2 H; H₂–C(2)), 7.21 (td, $J = 8.0, 0.9$ Hz, 1 H; H–C(6)), 7.66 (td, $J = 7.3, 1.5$ Hz, 1 H; H–C(5)), 7.74 (br. d, $J = 7.5$ Hz, 1 H; H–C(4)), 8.55 ppm (br. d, $J = 8.4$ Hz, 1 H; H–C(7)); ¹³C NMR (101 MHz, CDCl₃): $\delta = 24.40$ (Me), 56.26 (C(2)), 118.76 (C(7)), 123.83 (C(4)), 124.36 (C(6)), 125.01 (C(7a)), 137.51 (C(5)), 153.88 (C(3a)), 168.27 (NC=O), 194.85 ppm (C=O); IR (ATR): $\tilde{\nu} = 1715$ (s), 1673 (s), 1604 (w), 1585 (w), 1459 (s), 1417 (w),

1380 (m), 1353 (m), 1281 (s), 1234 (w), 1192 (w), 1138 (m), 1103 (w), 1061 (w), 1009 (w), 924 (w), 760 (s), 735 (m), 647 cm^{-1} (m); HR-ESI-MS: m/z (%): 175.0640 (77, $[M]^+$, calcd for $\text{C}_{10}\text{H}_9\text{NO}_2^+$: 175.0628), 133.0521 (100, $[M - \text{Ac} + \text{H}]^+$, calcd for $\text{C}_8\text{H}_7\text{NO}^+$: 133.0523).

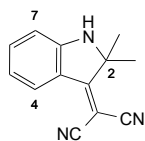
2,2-Dimethyl-1,2-dihydro-3H-indol-3-one (320)^[228]



The reaction was performed under Ar atmosphere and dry solvent was used.

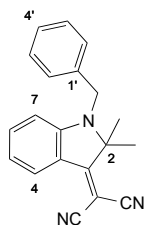
A solution of 1-acetyl-1,2-dihydro-3H-indol-3-one (**319**) (1.3 g, 7.42 mmol) in dry toluene (39 mL) was cooled in an ice bath, treated carefully with 60% NaH in mineral oil (950 mg, 23.75 mmol) and MeI (1.62 mL, 26.0 mmol), and stirred at reflux for 2.5 h. MeI (1.60 mL) was added and the mixture stirred at reflux for 3 h. Another portion of MeI (1.60 mL) was added and the mixture stirred at reflux for 4 h. One more portion of MeI (0.80 mL) was added and the mixture stirred at reflux for 13 h. The yellow mixture was cooled to 23 °C and poured into brine (39 mL). The aqueous layer was extracted three times with EtOAc (3 × 30 mL). The combined organic layers were washed with brine, dried over Na_2SO_4 , filtered, and evaporated. Column chromatography (SiO_2 ; cyclohexane/EtOAc 95:05 → 90:10) gave **320** (740 mg, 62%) as brown needles.

R_f = 0.07 (SiO_2 ; cyclohexane/EtOAc 90:10); m.p. 83–86 °C; ^1H NMR (400 MHz, CDCl_3): δ = 1.33 (s, 6 H; CMe_2), 4.59 (br. s, 1 H; NH), 6.76–6.89 (m, 2 H; H–C(5, 7)), 7.45 (td, J = 7.1, 1.4 Hz, 1 H; H–C(6)), 7.62 ppm (dt, J = 7.1, 0.8 Hz, 1 H; H–C(4)); ^{13}C NMR (101 MHz, CDCl_3): δ = 24.64 (CMe_2), 64.10 (C(2)), 112.64 (C(7)), 118.99 (C(5)), 119.83 (C(3a)), 125.23 (C(4)), 137.30 (C(6)), 159.69 (C(7a)), 205.21 ppm (C=O); IR (ATR): $\tilde{\nu}$ = 3363 (m), 2968 (w), 1674 (s), 1614 (s), 1486 (m), 1471 (m), 1406 (w), 1374 (w), 1326 (m), 1308 (w), 1290 (m), 1179 (w), 1143 (w), 1100 (w), 993 (w), 958 (w), 760 (s), 717 (m), 703 (w), 647 cm^{-1} (m); HR-EI-MS: m/z (%): 161.0837 (75, $[M]^+$, calcd for $\text{C}_{10}\text{H}_{11}\text{NO}^+$: 161.0836), 132.0807 (100, $[M - \text{CHO}]^+$, calcd for $\text{C}_9\text{H}_{10}\text{N}^+$: 132.0808).

(2,2-Dimethyl-1,2-dihydro-3*H*-indol-3-ylidene)propanedinitrile (316)^[228]

A solution of 2,2-dimethyl-1,2-dihydro-3*H*-indol-3-one (**320**) (500 mg, 3.10 mmol) in dry pyridine (6.2 mL) was treated with a solution of malononitrile (287 mg, 4.34 mmol) in dry pyridine (2.7 mL), stirred at reflux for 38 h, treated with a solution of malonitrile (287 mg) in dry pyridine (2.7 mL), stirred at reflux for 24 h, cooled to 23 °C, and diluted with water (3 mL) and 1 M HCl (6 mL). The layers were separated, and the aqueous layer was extracted three times with EtOAc (3 × 20 mL). The combined organic layers were washed with 1 M HCl (15 mL) and brine (15 mL), dried over Na₂SO₄, filtered, and evaporated. The crude was absorbed on SiO₂ and column chromatography (SiO₂; cyclohexane/EtOAc 90:10 → 70:30) gave **316** (370 mg, 57%) as a bright red solid.

$R_f = 0.33$ (SiO₂; cyclohexane/EtOAc 60:40); m.p. 225 °C (decomp.); ¹H NMR (400 MHz, CDCl₃): $\delta = 1.70$ (s, 6 H; CMe₂), 4.92 (br. s, 1 H; NH), 6.76 (dt, $J = 8.4, 0.8$ Hz, 1 H; H-C(7)), 6.83 (td, $J = 7.1, 1.0$ Hz, 1 H; H-C(5)), 7.45 (td, $J = 7.1, 1.2$ Hz, 1 H; H-C(6)), 8.24 ppm (ddd, $J = 8.4, 1.3, 0.7$ Hz, 1 H; H-C(4)); ¹³C NMR (101 MHz, CDCl₃): $\delta = 25.43$ (CMe₂), 66.58 (C(CN)₂), 67.22 (C(2)), 111.39 (C(7)), 114.62 (CN), 114.82 (CN), 119.87 (C(5)), 119.99 (C(3a)), 126.87 (C(4)), 138.50 (C(6)), 155.45 (C(7a)), 178.41 ppm (C=C(CN)₂); IR (ATR): $\tilde{\nu} = 3386$ (br. w), 2207 (m), 1615 (m), 1531 (m), 1498 (m), 1453 (m), 1407 (m), 1377 (w), 1334 (m), 1291 (m), 1227 (w), 1147 (m), 884 (w), 772 (w), 744 (s), 681 cm⁻¹ (w); HR-EI-MS: m/z (%): 209.0946 (31, [M]⁺, calcd for C₁₃H₁₁N₃⁺: 209.0948), 194.0719 (100, [M - CH₃]⁺, calcd for C₁₂H₈N₃⁺: 194.0713).

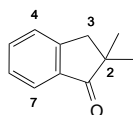
(1-Benzyl-2,2-dimethyl-1,2-dihydro-3*H*-indol-3-ylidene)propanedinitrile (323)

A solution of (2,2-dimethyl-1,2-dihydro-3*H*-indol-3-ylidene)propanedinitrile (**316**) (200 mg, 0.96 mmol) in DMF (5 mL) was treated with K₂CO₃ (330 mg, 2.39 mmol) and benzyl bromide (0.34 mL, 2.87 mmol), stirred at 23 °C for 20 h, and diluted with H₂O and CH₂Cl₂. The two layers were separated, and the organic layer was extracted three times with H₂O (3 × 10 mL).

The combined aqueous layers were extracted three times with CH_2Cl_2 (3×10 mL). The combined organic layers were dried over Na_2SO_4 , filtered, and evaporated. Column chromatography (SiO_2 ; cyclohexane/EtOAc 90:10 \rightarrow 80:20) gave **323** (270 mg, 94%) as a bright red solid.

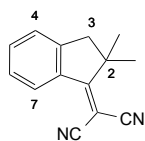
^1H NMR (400 MHz, CDCl_3): δ = 1.67 (s, 6 H; CMe_2), 4.60 (s, 2 H; CH_2), 6.43 (dt, J = 8.5, 0.9 Hz, 1 H; H-C(7)), 6.77 (td, J = 8.2, 0.9 Hz, 1 H; H-C(6)), 7.20 (ddt, J = 7.1, 1.4, 0.7 Hz, 2 H; H-C(2', 6')), 7.27–7.41 (m, 4 H; H-C(5, 3', 4', 5')), 8.31 ppm (dt, J = 8.3, 0.7 Hz, 1 H; H-C(4)); ^{13}C NMR (101 MHz, CDCl_3): δ = 22.96 (CMe_2), 45.35 (CH_2), 65.15 ($\text{C}(\text{CN})_2$), 70.90 (CMe_2), 109.52 (C(7)), 114.97 (CN), 115.29 (CN), 118.86 (C(6)), 119.30 (C(7a)), 126.32 (C(2', 6')), 126.99 (C(4)), 127.81 (C(4')), 129.12 (C(3', 5')), 136.78 (C(1')), 138.86 (C(5)), 155.75 (C(3a)), 177.25 ppm ($\text{C}=\text{C}(\text{CN})_2$); HR-ESI-MS: m/z (%): 322.1310 (100, $[\text{M} + \text{Na}]^+$, calcd for $\text{C}_{20}\text{H}_{17}\text{N}_3\text{Na}^+$: 322.1315), 300.1490 (33, $[\text{M} + \text{H}]^+$, calcd for $\text{C}_{20}\text{H}_{18}\text{N}_3^+$: 300.1495).

2,2-Dimethyl-2,3-dihydro-1*H*-inden-1-one (**327**)^[280]



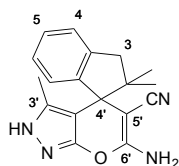
A suspension of 60% NaH in mineral oil (999 mg, 24.97 mmol) in DMF (15 mL) was treated with 2,3-dihydro-1*H*-inden-1-one (**326**) (1.5 g, 11.35 mmol). The mixture was stirred at 23 °C for 1 h leading to a dark green mixture. MeI (4.97 mL, 79.0 mmol) was added dropwise leading to an orange mixture, which was stirred at 23 °C for 1.5 h, and diluted with water and Et_2O . The layers were separated, and the aqueous layer was extracted three times with Et_2O (3×15 mL). The combined organic layers were washed with water four times, dried over Na_2SO_4 , filtered, and evaporated. The crude was absorbed on SiO_2 and column chromatography (SiO_2 ; cyclohexane/EtOAc 100:0 \rightarrow 95:05) gave **327** (1.21 g, 67%) as a brown oil.

R_f = 0.39 (SiO_2 ; cyclohexane/EtOAc 90:10); ^1H NMR (400 MHz, CDCl_3): δ = 1.24 (s, 6 H; CMe_2), 3.01 (s, 2 H; $\text{H}_2\text{-C}(3)$), 7.37 (td, J = 7.8, 0.9 Hz, 1 H; H-C(6)), 7.43 (dt, J = 7.7, 0.9 Hz, 1 H; H-C(4)), 7.59 (td, J = 7.5, 1.2 Hz, 1 H; H-C(5)), 7.77 ppm (dt, J = 7.7, 0.6 Hz, 1 H; H-C(7)); ^{13}C NMR (101 MHz, CDCl_3): δ = 25.43 (CMe_2), 43.04 (C(3)), 45.64 (C(2)), 124.61 (C(7)), 126.77 (C(4)), 127.56 (C(6)), 134.94 (C(5)), 135.53 (C(7a)), 152.36 (C(3a)), 211.52 ppm (C=O); IR (ATR): $\tilde{\nu}$ = 2960 (w), 2925 (w), 1711 (s), 1608 (m), 1466 (m), 1436 (w), 1379 (w), 1324 (w), 1288 (m), 1205 (w), 1178 (w), 1090 (w), 990 (m), 938 (m), 797 (m), 734 (s), 714 cm^{-1} (w); HR-EI-MS: m/z (%): 160.0885 (59, $[\text{M}]^+$, calcd for $\text{C}_{11}\text{H}_{12}\text{O}^+$: 160.0883), 145.0647 (100, $[\text{M} - \text{CH}_3]^+$, calcd for $\text{C}_{10}\text{H}_9\text{O}^+$: 145.0648).

(2,2-Dimethyl-2,3-dihydro-1*H*-inden-1-ylidene)propanedinitrile (325)

A solution of 2,2-dimethyl-2,3-dihydro-1*H*-inden-1-one (**327**) (740 mg, 4.62 mmol) in dry pyridine (9.3 mL) was treated with a solution of malononitrile (427 mg, 6.47 mmol) in dry pyridine (4.0 mL), stirred at reflux for 82 h, cooled to 23 °C, and diluted with water (4 mL) and 1 M HCl (7 mL). The layers were separated, and the aqueous layer was extracted three times with EtOAc (3 × 20 mL). The combined organic layers were washed with 1 M HCl (17 mL) and brine (17 mL), dried over Na₂SO₄, filtered, and evaporated. The crude was absorbed on SiO₂ and column chromatography (SiO₂; cyclohexane/EtOAc 100:0 → 90:10) followed by trituration in cyclohexane gave **325** (448 mg, 47%) as a white solid.

R_f = 0.22 (SiO₂; cyclohexane/EtOAc 90:10); m.p. 182–184 °C; ¹H NMR (400 MHz, CDCl₃): δ = 1.58 (s, 6 H; CMe₂), 3.07 (s, 2 H; H₂–C(3)), 7.35–7.49 (m, 2 H; H–C(4, 6)), 7.60 (td, J = 7.5, 1.1 Hz, 1 H; H–C(5)), 8.50 ppm (dt, J = 8.2, 0.8 Hz, 1 H; H–C(7)); ¹³C NMR (101 MHz, CDCl₃): δ = 26.89 (CMe₂), 46.94 (C(2)), 48.65 (C(3)), 74.82 (C(CN)₂), 113.58 (CN), 114.08 (CN), 126.01 (C(4)), 126.85 (C(7)), 128.29 (C(6)), 135.17 (C(3a)), 135.45 (C(5)), 150.14 (C(7a)), 185.19 ppm (C=C(CN)₂); IR (ATR): $\tilde{\nu}$ = 2972 (w), 2223 (m), 1601 (w), 1558 (s), 1464 (m), 1432 (m), 1385 (w), 1363 (w), 1311 (m), 1228 (w), 1160 (m), 982 (w), 785 (s), 723 (s), 664 cm⁻¹ (w); HR-EI-MS: m/z (%): 208.0994 (59, [M]⁺, calcd for C₁₄H₁₂N₂⁺: 208.0995), 193.0761 (100, [M – CH₃]⁺, calcd for C₁₃H₉N₂⁺: 193.0760).

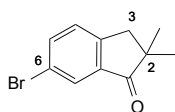
(±)-6'-Amino-2,2,3'-trimethyl-2,3-dihydro-2'*H*-spiro[indene-1,4'-pyrano[2,3-*c*]pyrazole]-5'-carbonitrile ((±)-328)

Following **GP7** (the mixture was stirred at 65 °C for 21 h in a microwave oven), the crude was absorbed on SiO₂, column chromatography (SiO₂; cyclohexane/EtOAc 70:30 → 55:45) and recrystallization from a THF/CH₂Cl₂/hexane mixture gave (±)-**328** (140 mg, 63%) as a white solid.

R_f = 0.08 (SiO₂; cyclohexane/EtOAc 60:40); m.p. 220 °C (decomp.); analyt. HPLC: t_R = 10.53 min (purity > 99%); ¹H NMR (400 MHz, THF-*d*₃): δ = 0.79 and 1.09 (2 s, 6 H; CMe₂),

1.54 (s, 3 H; Me-C(3')), 2.70 and 2.92 (2 d, $J = 15.4$ Hz, 2 H; H₂-C(3)), 6.17 (br. s, 2 H; NH₂), 7.02–7.09 (m, 1 H; H-C(6)), 7.11–7.22 (m, 3 H; H-C(4, 5, 7)), 11.10 ppm (s, 1 H; NH); ¹³C NMR (101 MHz, THF-*d*₈): $\delta = 10.92$ (Me-C(3')), 46.49 (C(3)), 52.44 (C(2)), 54.86 (C(1)), 61.95 (C(5')), 101.29 (C(3a')), 120.44 (CN), 125.45 (C(4)), 126.56 (C(6)), 127.41 (C(7)), 128.14 (C(5)), 135.37 (C(3')), 143.55 (C(7a)), 146.39 (C(3a)), 157.80 (C(7a')), 163.77 ppm (C(6')); IR (ATR): $\tilde{\nu} = 3145$ (br. w), 2186 (m), 1635 (m), 1583 (s), 1486 (m), 1396 (s), 1362 (w), 1295 (w), 1164 (w), 1050 (m), 905 (m), 755 (s), 726 (w), 656 cm⁻¹ (w); HR-ESI-MS: m/z (%): 307.1556 (100, [M + H]⁺, calcd for C₁₈H₁₉N₄O⁺: 307.1553).

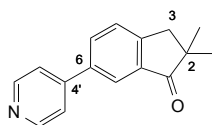
6-Bromo-2,2-dimethyl-2,3-dihydro-1H-inden-1-one (331)^[281]



The reaction was performed under Ar atmosphere and dry solvent was used.

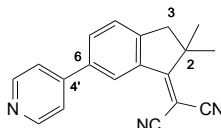
A solution of 6-bromo-2,3-dihydro-1H-inden-1-one (**330**) (1.5 g, 7.11 mmol) in dry THF (45 mL) was treated with MeI (1.11 mL, 17.77 mmol), stirred at 23 °C for 15 min, treated in small portions with 60% NaH in mineral oil (0.711 g, 17.77 mmol), stirred at 23 °C for 16 h, and carefully diluted with water (30 mL) and EtOAc. The layers were separated, and the aqueous layer was extracted three times with EtOAc (3 × 20 mL). The combined organic layers were washed with brine, dried over Na₂SO₄, filtered, and evaporated. Column chromatography (SiO₂; cyclohexane/EtOAc 100:0 → 95:05) gave **331** (1.62 g, 95%) as an orange oil.

$R_f = 0.44$ (SiO₂; cyclohexane/EtOAc 90:10); ¹H NMR (400 MHz, CDCl₃): $\delta = 1.23$ (s, 6 H; CMe₂), 2.94 (s, 2 H; H₂-C(3)), 7.31 (dd, $J = 8.1, 0.9$ Hz, 1 H; H-C(4)), 7.69 (dd, $J = 8.1, 2.0$ Hz, 1 H; H-C(5)), 7.88 ppm (dd, $J = 1.8, 0.6$ Hz, 1 H; H-C(7)); ¹³C NMR (101 MHz, CDCl₃): $\delta = 25.35$ (CMe₂), 42.61 (C(3)), 46.29 (C(2)), 121.70 (C(7a)), 127.54 (C(7)), 128.36 (C(4)), 137.40 (C(3a)), 137.68 (C(5)), 150.82 (C(6)), 209.99 ppm (C=O); IR (ATR): $\tilde{\nu} = 2960$ (w), 1711 (s), 1597 (w), 1466 (m), 1436 (m), 1413 (w), 1315 (w), 1286 (w), 1257 (m), 1188 (m), 1172 (w), 815 (w), 771 (w), 729 (w), 642 (w), 608 cm⁻¹ (w); HR-EI-MS: m/z (%): 239.9991 (70, [M]⁺, calcd for C₁₁H₁₁⁸¹BrO⁺: 239.9967), 238.0009 (70, [M]⁺, calcd for C₁₁H₁₁⁷⁹BrO⁺: 237.9988), 224.9743 (98, [M - CH₃]⁺, calcd for C₁₀H₈⁸¹BrO⁺: 224.9733), 222.9758 (100, [M - CH₃]⁺, calcd for C₁₀H₈⁷⁹BrO⁺: 222.9753).

2,2-Dimethyl-6-(pyridin-4-yl)-2,3-dihydro-1H-inden-1-one (333)

A solution of 6-bromo-2,2-dimethyl-2,3-dihydro-1H-inden-1-one (**331**) (1.0 g, 4.18 mmol) in 1,4-dioxane/water 5:1 (7.56 mL) was treated with pyridin-4-ylboronic acid (**332**) (771 mg, 6.27 mmol) followed by K_2CO_3 (1.734 g, 12.55 mmol). The mixture was degassed with Ar for 15 min, treated with $[Pd(PPh_3)_2Cl_2]$ (147 mg, 0.21 mmol), degassed with Ar for 5 min, stirred at 100 °C for 16 h, cooled to 23 °C, and diluted with EtOAc and water. The layers were separated, and the aqueous layer was extracted three times with EtOAc (3×15 mL). The combined organic layers were washed with brine, dried over Na_2SO_4 , filtered, and evaporated. Column chromatography (SiO_2 ; cyclohexane/EtOAc 85:15 \rightarrow 75:25) gave **333** (817 mg, 82%) as a white solid.

R_f = 0.11 (SiO_2 ; cyclohexane/EtOAc 60:40); m.p. 120–122 °C; 1H NMR (400 MHz, $CDCl_3$): δ = 1.28 (s, 6 H; CMe_2), 3.06 (s, 2 H; $H_2-C(3)$), 7.52 (d with virtual coupling, J = 6.2 Hz, 2 H; $H-C(3', 5')$), 7.56 (dq, J = 8.0, 0.9 Hz, 1 H; $H-C(4)$), 7.87 (dd, J = 7.9, 1.9 Hz, 1 H; $H-C(5)$), 8.03 (dd, J = 1.9, 0.7 Hz, 1 H; $H-C(7)$), 8.68 ppm (d with virtual coupling, J = 6.2 Hz, 2 H; $H-C(2', 6')$); ^{13}C NMR (101 MHz, $CDCl_3$): δ = 25.42 (CMe_2), 42.85 (C(3)), 46.22 (C(2)), 121.68 (C(3', 5')), 122.89 (C(7)), 127.60 (C(4)), 133.58 (C(5)), 136.43 (C(3a)), 137.93 (C(4')), 147.38 (C(6)), 150.61 (C(2', 6')), 153.01 (C(7a)), 211.06 ppm (C=O); IR (ATR): $\tilde{\nu}$ = 3027 (w), 2954 (w), 2923 (w), 1698 (s), 1614 (m), 1596 (m), 1544 (w), 1480 (w), 1436 (w), 1427 (w), 1407 (w), 1358 (w), 1307 (w), 1180 (m), 1170 (m), 1002 (m), 931 (w), 811 (s), 774 (m), 705 (m), 624 cm^{-1} (w); HR-ESI-MS: m/z (%): 238.1228 (100, $[M + H]^+$, calcd for $C_{16}H_{16}NO^+$: 238.1226).

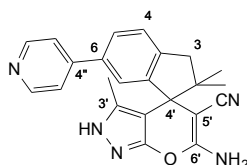
[2,2-Dimethyl-6-(pyridin-4-yl)-2,3-dihydro-1H-inden-1-ylidene]propanedinitrile (334)

A solution of 2,2-dimethyl-6-(pyridin-4-yl)-2,3-dihydro-1H-inden-1-one (**333**) (670 mg, 2.82 mmol) in dry pyridine (5.6 mL) was treated with a solution of malononitrile (261 mg, 3.95 mmol) in dry pyridine (2.4 mL), stirred at reflux for 40 h, treated with a solution of malononitrile (261 mg) in dry pyridine (2.4 mL), stirred at reflux for additional 24 h, cooled to 23 °C, diluted with water (6 mL) and 1 M HCl (10 mL). The aqueous layer was extracted three

times with EtOAc (3 × 20 mL). The combined organic layers were washed with 1 M HCl (13 mL) and brine (20 mL), dried over Na₂SO₄, filtered, and evaporated. Column chromatography (SiO₂; cyclohexane/EtOAc 70:30 → 50:50) gave **334** (720 mg, 89%) as a beige solid.

R_f = 0.07 (SiO₂; cyclohexane/EtOAc 60:40); m.p. 189–192 °C; ¹H NMR (400 MHz, CDCl₃): δ = 1.62 (s, 6 H; CMe₂), 3.13 (s, 2 H; H₂-C(3)), 7.46–7.59 (m, 3 H; H-C(4, 3', 5')), 7.88 (dd, J = 8.0, 1.6 Hz, 1 H; H-C(5)), 8.71 (d with virtual coupling, J = 6.2 Hz, 2 H; H-C(2', 6')), 8.79 ppm (dd, J = 1.5, 0.7 Hz, 1 H; H-C(7)); ¹³C NMR (101 MHz, CDCl₃): δ = 26.95 (CMe₂), 47.45 (C(2)), 48.39 (C(3)), 75.79 (C(CN)₂), 113.22 (CN), 114.01 (CN), 121.57 (C(3', 5')), 125.00 (C(7)), 126.79 (C(4)), 133.99 (C(5)), 136.12 (C(7a)), 138.62 (C(3a)), 146.77 (C(4')), 150.66 (C(6)), 150.80 (C(2', 6')), 184.51 ppm (C=C(CN)₂); IR (ATR): $\tilde{\nu}$ = 2222 (m), 1608 (w), 1592 (m), 1557 (s), 1546 (m), 1481 (m), 1429 (w), 1385 (w), 1312 (w), 1288 (w), 1219 (w), 1196 (w), 992 (w), 817 (s), 735 (w), 678 (w), 610 cm⁻¹ (m); HR-ESI-MS: m/z (%): 286.1344 (100, [M + H]⁺, calcd for C₁₉H₁₆N₃⁺: 286.1339).

(±)-6'-Amino-2,2,3'-trimethyl-6-(pyridin-4-yl)-2,3-dihydro-2'H-spiro[indene-1,4'-pyrano[2,3-c]pyrazole]-5'-carbonitrile ((±)-329)

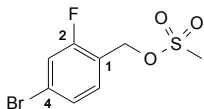


Following **GP7** (the mixture was stirred at 65 °C for 40 h in a microwave oven), column chromatography (SiO₂; cyclohexane/EtOAc 30:70 → 0:100) and recrystallization from a THF/CH₂Cl₂/hexane mixture gave (±)-**329** (233 mg, 50%) as a white solid.

R_f = 0.09 (SiO₂; EtOAc); m.p. 235 °C (decomp.); analyt. HPLC: t_R = 8.53 min (purity > 99%); ¹H NMR (400 MHz, THF-*d*₈): δ = 0.83 and 1.12 (s, 6 H; CMe₂), 1.61 (s, 3 H; Me-C(3')), 2.77 and 2.99 (2 d, J = 15.8 Hz, 2 H; H₂-C(3)), 6.29 (br. s, 2 H; NH₂), 7.33 (dd, J = 7.8, 0.8 Hz, 1 H; H-C(4)), 7.45 (d, J = 1.8 Hz, 1 H; H-C(7)), 7.51 (d with virtual coupling, J = 6.2 Hz, 2 H; H-C(3'', 5'')), 7.61 (dd, J = 7.8, 1.8 Hz, 1 H; H-C(5)), 8.52 (d with virtual coupling, J = 6.2 Hz, 2 H; H-C(2'', 6'')), 11.20 ppm (br. s, 1 H; NH); ¹³C NMR (101 MHz, THF-*d*₈): δ = 11.07 (Me-C(3')), 46.21 (C(3)), 52.80 (C(2)), 55.02 (C(1)), 61.63 (C(5')), 100.98 (C(3a')), 120.52 (CN), 121.96 (C(3'', 5'')), 125.08 (C(7)), 126.26 (C(4)), 127.15 (C(5)), 135.40 (C(3'')), 137.97 (C(6)), 144.91 (C(7a)), 147.60 (C(3a)), 148.76 (C(4'')), 151.06 (C(2'', 6'')), 157.83 (C(7a')), 163.89 ppm (C(6')), CMe₂ hidden under the residual solvent peak; IR (ATR): $\tilde{\nu}$ = 3144 (br. w),

2172 (m), 1644 (w), 1601 (s), 1583 (s), 1485 (m), 1399 (s), 1381 (w), 1362 (w), 1220 (w), 1156 (w); 1050 (m), 1009 (w), 909 (w), 804 (w), 792 (w), 612 cm^{-1} (m); HR-ESI-MS: m/z (%): 384.1821 (100, $[M + H]^+$, calcd for $\text{C}_{23}\text{H}_{22}\text{N}_5\text{O}^+$: 384.1819).

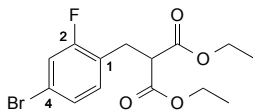
(4-Bromo-2-fluorophenyl)methyl Methanesulfonate (337)^[229]



A solution of (4-bromo-2-fluorophenyl)methanol (**336**) (10 g, 48.8 mmol) in THF (103 mL) was treated with Et_3N (8.84 mL, 63.4 mmol), cooled in an ice bath, and treated dropwise with methanesulfonyl chloride (4.54 mL, 58.5 mmol) upon which a white precipitate appeared. The mixture was stirred at 0 °C for 30 min and diluted with water and EtOAc. The layers were separated, and the aqueous layer was extracted three times with EtOAc (3 × 20 mL). The combined organic layers were washed with brine, dried over Na_2SO_4 , filtered, and evaporated to give **337** (13.81 g, 100%) as a yellow oil.

R_f = 0.06 (SiO_2 ; cyclohexane/EtOAc 90:10); ^1H NMR (400 MHz, CDCl_3): δ = 3.01 (s, 3 H; Me), 5.25 (d, $^4J(\text{H}, \text{F})$ = 1.2 Hz, 2 H; CH_2O), 7.28–7.42 ppm (m, 3 H; H–C(3, 5, 6)); ^{13}C NMR (101 MHz, CDCl_3): δ = 38.20 (Me), 64.59 (d, $^3J(\text{C}, \text{F})$ = 3.9 Hz; CH_2O), 119.71 (d, $^2J(\text{C}, \text{F})$ = 24.2 Hz; C(3)), 120.24 (d, $^2J(\text{C}, \text{F})$ = 14.5 Hz; C(1)), 124.41 (d, $^3J(\text{C}, \text{F})$ = 9.5 Hz; C(4)), 128.14 (d, $^4J(\text{C}, \text{F})$ = 3.8 Hz; C(5)), 132.31 (d, $^3J(\text{C}, \text{F})$ = 3.9 Hz; C(6)), 160.89 ppm (d, $^1J(\text{C}, \text{F})$ = 254.4 Hz; C(2)); ^{19}F NMR (377 MHz, CDCl_3): δ = –114.59 ppm (dd, $^3J(\text{H}, \text{F})$ = 9.1 Hz, $^4J(\text{H}, \text{F})$ = 5.9 Hz; F); IR (ATR): $\tilde{\nu}$ = 1608 (m), 1580 (w), 1487 (m), 1408 (w), 1350 (m), 1221 (w), 1169 (s), 1125 (w), 1068 (w), 929 (s), 883 (m), 807 (m), 749 (w), 704 cm^{-1} (w); HR-ESI-MS: m/z (%): 306.9240 (100, $[M + \text{Na}]^+$, calcd for $\text{C}_8\text{H}_8^{81}\text{BrFNaO}_3\text{S}^+$: 306.9233), 304.9261 (100, $[M + \text{Na}]^+$, calcd for $\text{C}_8\text{H}_8^{79}\text{BrFNaO}_3\text{S}^+$: 304.9254).

Diethyl [(4-bromo-2-fluorophenyl)methyl]propanedioate (338)^[230]



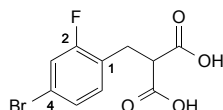
Oven-dried glassware and dry solvent were used.

A suspension of 60% NaH in mineral oil (3.67 g, 92.0 mmol) in THF (62 mL) was cooled to –10 °C. Diethyl malonate (9.11 mL, 59.7 mmol) was slowly added. The mixture was stirred for 30 min at 23 °C, slowly treated at –10 °C with a solution of 4-bromo-2-fluorobenzyl methanesulfonate (**337**) (13.0 g, 45.9 mmol) in THF (42 mL), stirred at reflux for 14 h, cooled

to 23 °C, and diluted with water and EtOAc. The layers were separated, and the aqueous layer was extracted three times with EtOAc (3 × 20 mL). The combined organic layers were washed with brine, dried over Na₂SO₄, filtered, and evaporated. Column chromatography (SiO₂; cyclohexane/EtOAc 100:0 → 95:05) gave **338** (9.77 g, 61%) as a colorless oil.

$R_f = 0.26$ (SiO₂; cyclohexane/EtOAc 90:10); ¹H NMR (400 MHz, CDCl₃): $\delta = 1.21$ (t, $J = 7.1$ Hz, 6 H; 2 OCH₂CH₃), 3.19 (d, $J = 7.9$ Hz, 2 H; CH₂CH(COOEt)₂), 3.67 (t, $J = 7.9$ Hz, 1 H; CH₂CH(COOEt)₂), 4.16 (qt, $J = 7.1, 3.7$ Hz, 4 H; 2 OCH₂CH₃), 7.09 (t, $J = 8.2$ Hz, 1 H; H-C(6)), 7.15–7.24 ppm (m, 2 H; H-C(3, 5)); ¹³C NMR (101 MHz, CDCl₃): $\delta = 14.14$ (2 OCH₂CH₃), 28.23 (d, ³ J (C, F) = 2.1 Hz; CH₂CH(COOEt)₂), 51.91 (d, ⁴ J (C, F) = 1.5 Hz; CH₂CH(COOEt)₂), 61.77 (2 OCH₂CH₃), 119.17 (d, ² J (C, F) = 25.2 Hz; C(3)), 121.07 (d, ³ J (C, F) = 9.6 Hz; C(4)), 124.14 (d, ² J (C, F) = 15.5 Hz; C(1)), 127.49 (d, ⁴ J (C, F) = 3.7 Hz; C(5)), 132.61 (d, ³ J (C, F) = 5.2 Hz; C(6)), 161.18 (d, ¹ J (C, F) = 250.7 Hz; C(2)), 168.58 ppm (2 C=O); ¹⁹F NMR (377 MHz, CDCl₃): $\delta = -114.62$ ppm (t, ³ J (H, F) = 8.7 Hz; F); IR (ATR): $\tilde{\nu} = 2982$ (w), 1730 (s), 1605 (w), 1577 (w), 1485 (m), 1404 (w), 1369 (w), 1331 (w), 1265 (w), 1227 (m), 1149 (m), 1114 (m), 1095 (w), 1063 (w), 1032 (m), 886 (m), 855 (w), 811 cm⁻¹ (w); HR-ESI-MS: m/z (%): 349.0275 (99, [M + H]⁺, calcd for C₁₄H₁₇⁸¹BrFO₄⁺: 349.0270), 347.0294 (100, [M + H]⁺, calcd for C₁₄H₁₇⁷⁹BrFO₄⁺: 347.0289).

[(4-Bromo-2-fluorophenyl)methyl]propanedioic Acid (**339**)^[230]

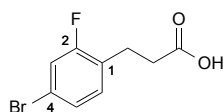


A solution of diethyl [(4-bromo-2-fluorophenyl)methyl]propanedioate (**338**) (9.77 g, 28.1 mmol) in ethanol (320 mL) was treated with a 50% aq. NaOH solution (32 mL), and stirred at reflux for 2.5 h upon which a white precipitate was obtained. The suspension was cooled to 23 °C and evaporated. The residue was acidified to pH 4 with a 1 M HCl solution and extracted three times with Et₂O (3 × 40 mL). The combined organic layers were washed with water and brine, dried over Na₂SO₄, filtered, and evaporated to give **339** (7.73 g, 94%) as a white solid.

$R_f = 0.15$ (SiO₂; cyclohexane/EtOAc/formic acid 70:30:01); m.p. 165–167 °C; ¹H NMR (400 MHz, THF-*d*₈): $\delta = 3.12$ (dd, $J = 7.7, 1.2$ Hz, 2 H; CH₂CH(COOH)₂), 7.14–7.25 (m, 2 H; H-C(5, 6)), 7.25–7.39 ppm (m, 1 H; H-C(3)), CH₂CH(COOH)₂ hidden under the residual solvent peak; ¹³C NMR (101 MHz, THF-*d*₈): $\delta = 28.69$ (d, ³ J (C, F) = 2.3 Hz; CH₂CH(COOH)₂), 52.10 (d, ⁴ J (C, F) = 1.3 Hz; CH₂CH(COOH)₂), 119.47 (d, ² J (C, F) = 25.7 Hz; C(3)), 121.15 (d,

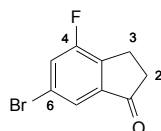
$^3J(\text{C}, \text{F}) = 9.7 \text{ Hz}$; C(4)), 126.20 (d, $^3J(\text{C}, \text{F}) = 15.5 \text{ Hz}$; C(1)), 128.08 (d, $^4J(\text{C}, \text{F}) = 3.7 \text{ Hz}$; C(5)), 133.65 (d, $^3J(\text{C}, \text{F}) = 5.2 \text{ Hz}$; C(6)), 162.12 (d, $^1J(\text{C}, \text{F}) = 249.8 \text{ Hz}$; C(2)), 170.04 ppm (2 C=O); ^{19}F NMR (377 MHz, CDCl_3): $\delta = -113.41$ to -119.49 ppm (m; F); IR (ATR): $\tilde{\nu} = 2873$ (br. w), 1702 (s), 1608 (w), 1577 (w), 1485 (m), 1445 (w), 1402 (m), 1324 (w), 1264 (m), 1219 (s), 1166 (w), 941 (m), 870 (s), 812 (m), 792 (w), 771 (w), 678 cm^{-1} (m); HR-ESI-MS (negative mode): m/z (%): 290.9506 (45, $[\text{M} - \text{H}]^-$, calcd for $\text{C}_{10}\text{H}_7^{81}\text{BrFO}_4^-$: 290.9498), 288.9524 (37, $[\text{M} - \text{H}]^-$, calcd for $\text{C}_{10}\text{H}_7^{79}\text{BrFO}_4^-$: 288.9517).

3-(4-Bromo-2-fluorophenyl)propanoic Acid (**340**)^[231]



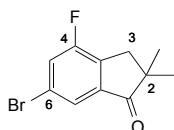
A solution of [(4-bromo-2-fluorophenyl)methyl]propanedioic acid (**339**) (7.6 g, 26.1 mmol) in 1,4-dioxane (170 mL) was stirred at reflux for 22 h, cooled to 23 °C, and evaporated. The residue was diluted with water and Et_2O . The layers were separated, and the aqueous layer was extracted three times with Et_2O ($3 \times 30 \text{ mL}$). The combined organic layers were washed with water and brine, dried over Na_2SO_4 , filtered, and evaporated to give **340** (6.44 g, quant.) as a white solid.

$R_f = 0.47$ (SiO_2 ; cyclohexane/ EtOAc /formic acid 70:30:1); m.p. 97–99 °C; ^1H NMR (400 MHz, $\text{THF}-d_8$): $\delta = 2.52$ (t, $J = 7.7 \text{ Hz}$, 2 H; $\text{CH}_2\text{CH}_2\text{COOH}$), 2.87 (td, $J = 7.6 \text{ Hz}$, $^4J(\text{H}, \text{F}) = 1.2 \text{ Hz}$, 2 H; $\text{CH}_2\text{CH}_2\text{COOH}$), 7.14–7.25 (m, 2 H; H–C(5, 6)), 7.25–7.35 (m, 1 H; H–C(3)), 10.82 ppm (br. s, 1 H; COOH); ^{13}C NMR (101 MHz, $\text{THF}-d_8$): $\delta = 24.68$ (d, $^3J(\text{C}, \text{F}) = 2.6 \text{ Hz}$; $\text{CH}_2\text{CH}_2\text{COOH}$), 34.01 (d, $^4J(\text{C}, \text{F}) = 1.4 \text{ Hz}$; $\text{CH}_2\text{CH}_2\text{COOH}$), 119.44 (d, $^2J(\text{C}, \text{F}) = 25.7 \text{ Hz}$; C(3)), 120.63 (d, $^3J(\text{C}, \text{F}) = 9.7 \text{ Hz}$; C(4)), 128.17 (d, $^4J(\text{C}, \text{F}) = 3.7 \text{ Hz}$; C(5)), 128.32 (d, $^2J(\text{C}, \text{F}) = 15.7 \text{ Hz}$; C(1)), 132.95 (d, $^3J(\text{C}, \text{F}) = 5.5 \text{ Hz}$; C(6)), 161.96 (d, $^1J(\text{C}, \text{F}) = 249.1 \text{ Hz}$; C(2)), 173.37 ppm (C=O); ^{19}F NMR (377 MHz, CDCl_3): $\delta = -116.85$ to -116.75 ppm (m; F); IR (ATR): $\tilde{\nu} = 3400$ –2400 (br. w), 1697 (s), 1602 (w), 1578 (w), 1484 (s), 1434 (m), 1404 (m), 1301 (m), 1273 (w), 1218 (s), 1116 (m), 1068 (w), 1047 (w), 1007 (w), 923 (w), 877 (s), 858 (s), 815 (m), 778 (w), 672 cm^{-1} (w); HR-ESI-MS (negative mode): m/z (%): 246.9606 (43, $[\text{M} - \text{H}]^-$, calcd for $\text{C}_9\text{H}_7^{81}\text{BrFO}_2^-$: 246.9598), 244.9626 (44, $[\text{M} - \text{H}]^-$, calcd for $\text{C}_9\text{H}_7^{79}\text{BrFO}_2^-$: 244.9619).

6-Bromo-4-fluoro-2,3-dihydro-1H-inden-1-one (341)^[232]

A solution of 3-(4-bromo-2-fluorophenyl)propanoic acid (**340**) (6.44 g, 26.1 mmol) in CH₂Cl₂ (38 mL) was treated with few drops of DMF and dropwise with oxalyl chloride (4.56 mL, 52.1 mmol), stirred at 23 °C for 4 h, evaporated, and diluted with CH₂Cl₂ (20 mL). This solution was added to a suspension of AlCl₃ (4.34 g, 32.6 mmol) in CH₂Cl₂ (20 mL). The mixture was stirred at reflux for 3.5 h, cooled to 23 °C, poured onto ice/water, and diluted with CH₂Cl₂ and a sat. NH₄Cl solution. The layers were separated, and the aqueous layer was extracted three times with CH₂Cl₂ (3 × 20 mL). The combined organic layers were washed with a sat. NH₄Cl solution and brine, dried over Na₂SO₄, filtered, and evaporated. The crude was absorbed on SiO₂ and column chromatography (SiO₂; cyclohexane/EtOAc 100:0 → 90:10) gave **341** (3.88 g, 65%) as a white solid.

R_f = 0.28 (SiO₂; cyclohexane/EtOAc 90:10); m.p. 123–125 °C; ¹H NMR (400 MHz, CDCl₃): δ = 2.65–2.83 (m, 2 H; H₂–C(3)), 3.01–3.20 (m, 2 H; H₂–C(2)), 7.42 (dd, ³ J (H, F) = 7.9 Hz, J = 1.6 Hz, 1 H; H–C(5)), 7.69 ppm (d, J = 1.5 Hz, 1 H; H–C(7)); ¹³C NMR (101 MHz, CDCl₃): δ = 21.60 (C(2)), 36.09 (C(3)), 122.01 (d, ³ J (C, F) = 7.1 Hz; C(6)), 122.90 (d, ⁴ J (C, F) = 4.1 Hz; C(7)), 124.01 (d, ² J (C, F) = 23.2 Hz; C(5)), 139.92 (d, ² J (C, F) = 19.8 Hz; C(3a)), 141.15 (d, ³ J (C, F) = 5.3 Hz; C(7a)), 160.00 (d, ¹ J (C, F) = 255.6 Hz; C(4)), 203.97 ppm (d, ⁴ J (C, F) = 2.4 Hz; C=O); ¹⁹F NMR (377 MHz, CDCl₃): δ = –116.06 ppm (d, ³ J (H, F) = 7.9 Hz; F); IR (ATR): $\tilde{\nu}$ = 3068 (w), 1704 (s), 1609 (w), 1588 (w), 1466 (m), 1452 (m), 1395 (w), 1262 (s), 1221 (w), 1065 (m), 980 (w), 957 (m), 907 (w), 879 (m), 841 (w), 820 (w), 729 (m), 641 cm^{–1} (w); HR-EI-MS: m/z (%): 229.9566 (99, [M]⁺, calcd for C₉H₆⁸¹BrFO⁺: 229.9560), 227.9582 (100, [M]⁺, calcd for C₉H₆⁷⁹BrFO⁺: 227.9581).

6-Bromo-4-fluoro-2,2-dimethyl-2,3-dihydro-1H-inden-1-one (335)

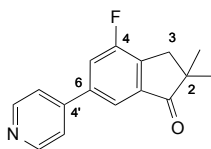
The reaction was performed under Ar atmosphere and dry solvent was used.

A solution of 6-bromo-4-fluoro-2,3-dihydro-1H-inden-1-one (**341**) (2.1 g, 9.17 mmol) in THF (59 mL) was treated with MeI (1.43 mL, 22.92 mmol), stirred at 23 °C for 15 min, treated portion wise with 60% NaH in mineral oil (0.917 g, 22.92 mmol), stirred at 23 °C for 16 h, and

carefully diluted with water (15 mL) and EtOAc (15 mL). The layers were separated, and the aqueous layer was extracted three times with EtOAc (3 × 15 mL). The combined organic layers were washed with brine, dried over Na₂SO₄, filtered, and evaporated. The crude was absorbed on SiO₂ and column chromatography (SiO₂; cyclohexane/EtOAc 100:0 → 95:05) gave **335** (2.04 g, 87%) as a beige solid.

R_f = 0.61 (SiO₂; cyclohexane/EtOAc 90:10); m.p. 100–103 °C; ¹H NMR (400 MHz, CDCl₃): δ = 1.25 (s, 6 H; CMe₂), 2.94 (s, 2 H; H₂-C(3)), 7.43 (dd, ³ J (H, F) = 7.9 Hz, J = 1.6 Hz, 1 H; H-C(5)), 7.70 ppm (d, J = 1.6 Hz, 1 H; H-C(7)); ¹³C NMR (101 MHz, CDCl₃): δ = 25.30 (CMe₂), 38.27 (C(3)), 46.07 (C(2)), 121.98 (d, ³ J (C, F) = 7.0 Hz; C(6)), 123.54 (d, ⁴ J (C, F) = 4.1 Hz; C(7)), 124.23 (d, ² J (C, F) = 23.4 Hz; C(5)), 137.11 (d, ² J (C, F) = 19.8 Hz; C(3a)), 139.50 (d, ³ J (C, F) = 5.4 Hz; C(7a)), 160.07 (d, ¹ J (C, F) = 255.3 Hz; C(4)), 208.62 ppm (d, ⁴ J (C, F) = 2.6 Hz; C=O); ¹⁹F NMR (377 MHz, CDCl₃): δ = -115.98 ppm (d, ³ J (H, F) = 7.9 Hz; F); IR (ATR): $\tilde{\nu}$ = 3070 (w), 2981 (w), 2964 (w), 2933 (w), 1709 (s), 1606 (w), 1584 (m), 1471 (w), 1459 (m), 1428 (m), 1384 (w), 1290 (w), 1256 (s), 1219 (w), 1168 (m), 1039 (m), 973 (w), 930 (w), 900 (w), 877 (m), 853 (m), 811 (w), 717 (m), 622 cm⁻¹ (w); HR-EI-MS: m/z (%): 257.9875 (71, [M]⁺, calcd for C₁₁H₁₀⁸¹BrFO⁺: 257.9879), 255.9894 (72, [M]⁺, calcd for C₁₁H₁₀⁷⁹BrFO⁺: 255.9894), 242.9640 (99, [M - CH₃]⁺, calcd for C₁₀H₇⁸¹BrFO⁺: 242.9638), 240.9661 (100, [M - CH₃]⁺, calcd for C₁₀H₇⁷⁹BrFO⁺: 240.9659).

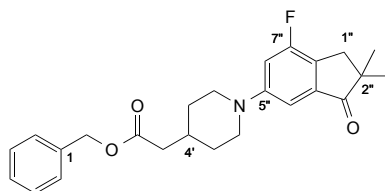
4-Fluoro-2,2-dimethyl-6-(pyridin-4-yl)-2,3-dihydro-1H-inden-1-one (344)



A solution of 6-bromo-4-fluoro-2,2-dimethyl-2,3-dihydro-1H-inden-1-one (**335**) (800 mg, 3.11 mmol) in a mixture of 1,4-dioxane/H₂O 5:1 (5.64 mL) was treated with pyridin-4-ylboronic acid (**332**) (574 mg, 4.67 mmol) and K₂CO₃ (1290 mg, 9.33 mmol), degassed with Ar for 15 min, treated with [Pd(PPh₃)₂Cl₂] (109 mg, 0.16 mmol), degassed with Ar for 5 min, stirred at 100 °C for 16 h, cooled to 23 °C, and diluted with EtOAc and water. The layers were separated, and the aqueous layer was extracted three times with EtOAc (3 × 15 mL). The combined organic layers were washed with brine, dried over Na₂SO₄, filtered, and evaporated. Column chromatography (SiO₂; cyclohexane/EtOAc 80:20 → 70:30) gave **344** (605 mg, 76%) as a white solid.

$R_f = 0.14$ (SiO₂; cyclohexane/EtOAc 60:40); m.p. 131–133 °C; ¹H NMR (400 MHz, CDCl₃): $\delta = 1.29$ (s, 6 H; CMe₂), 3.06 (s, 2 H; H₂-C(3)), 7.50 (d with virtual coupling, $J = 6.2$ Hz, 2 H; H-C(3', 5')), 7.56 (dd, $^3J(\text{H}, \text{F}) = 9.3$ Hz, $J = 1.5$ Hz, 1 H; H-C(5)), 7.85 (d, $J = 1.4$ Hz, 1 H; H-C(7)), 8.70 ppm (d with virtual coupling, $J = 6.2$ Hz, 2 H; H-C(2', 6')); ¹³C NMR (101 MHz, CDCl₃): $\delta = 25.37$ (CMe₂), 38.48 (C(3)), 46.24 (C(2)), 118.62 (d, $^4J(\text{C}, \text{F}) = 3.7$ Hz; C(7)), 119.57 (d, $^2J(\text{C}, \text{F}) = 21.6$ Hz; C(5)), 121.59 (C(3', 5')), 138.67 (d, $^2J(\text{C}, \text{F}) = 20.0$ Hz; C(3a)), 139.27 (d, $^3J(\text{C}, \text{F}) = 5.5$ Hz; C(7a)), 140.47 (d, $^3J(\text{C}, \text{F}) = 6.0$ Hz; C(6)), 146.26 (d, $^4J(\text{C}, \text{F}) = 1.8$ Hz; C(4')), 150.76 (C(2', 6')), 160.71 (d, $^1J(\text{C}, \text{F}) = 251.6$ Hz; C(4)), 209.74 ppm (d, $^4J(\text{C}, \text{F}) = 2.7$ Hz; C=O); ¹⁹F NMR (377 MHz, CDCl₃): $\delta = -117.74$ ppm (d, $^3J(\text{H}, \text{F}) = 9.3$ Hz; F); IR (ATR): $\tilde{\nu} = 2961$ (w), 2929 (w), 2868 (w), 1712 (s), 1627 (w), 1597 (m), 1550 (w), 1475 (w), 1404 (w), 1380 (w), 1324 (m), 1283 (w), 1240 (w), 1208 (w), 1165 (w), 1040 (m), 932 (w), 879 (w), 822 (s), 770 (w), 649 cm⁻¹ (m); HR-ESI-MS: m/z (%): 256.1137 (57, [M + H]⁺, calcd for C₁₆H₁₅FNO⁺: 256.1132), 227.1184 (100, [M - C₂H₆ + H]⁺, calcd for C₁₄H₁₀FNO⁺: 227.0741).

Benzyl [1-(7-Fluoro-2,2-dimethyl-3-oxo-2,3-dihydro-1H-inden-5-yl)piperidin-4-yl]acetate (346)

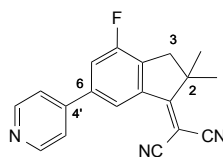


Following **GP5**, the crude was absorbed on SiO₂ and column chromatography (SiO₂; cyclohexane/EtOAc 100:0 → 90:10) gave **346** (1.67 g, 100%) as an orange oil.

$R_f = 0.13$ (SiO₂; cyclohexane/EtOAc 90:10); ¹H NMR (400 MHz, CDCl₃): $\delta = 1.23$ (s, 6 H; CMe₂), 1.31–1.45 (m, 2 H; H_{ax}-C(3', 5')), 1.76–1.88 (m, 2 H; H_{eq}-C(3', 5')), 1.93–2.03 (m, 1 H; H-C(4')), 2.33 (d, $J = 7.1$ Hz, 2 H; CH₂C=O), 2.78 (td, $J = 12.4, 2.6$ Hz, 2 H; H_{ax}-C(2', 6')), 2.88 (s, 2 H; H₂-C(1'')), 3.60–3.74 (m, 2 H; H_{eq}-C(2', 6')), 5.14 (s, 2 H; CH₂O), 6.87 (dd, $^3J(\text{H}, \text{F}) = 11.8$ Hz, $J = 2.2$ Hz, 1 H; H-C(6'')), 7.01 (d, $J = 2.2$ Hz, 1 H; H-C(4'')), 7.29–7.41 ppm (m, 5 H; C₆H₅); ¹³C NMR (101 MHz, CDCl₃): $\delta = 25.47$ (CMe₂), 31.59 (C(3', 5')), 32.92 (C(4')), 37.96 (C(1'')), 41.11 (CH₂C=O), 46.10 (C(2'')), 49.55 (C(2', 6')), 66.41 (CH₂O), 105.72 (d, $^4J(\text{C}, \text{F}) = 2.9$ Hz; C(4'')), 110.00 (d, $^2J(\text{C}, \text{F}) = 23.7$ Hz; C(6'')), 128.26 (d, $^2J(\text{C}, \text{F}) = 20.7$ Hz; C(7a'')), 128.39 (C(2, 6)), 128.44 (C(4)), 128.73 (3, 5), 136.06 (C(1)), 138.56 (d, $^3J(\text{C}, \text{F}) = 6.8$ Hz; C(3a'')), 153.26 (d, $^3J(\text{C}, \text{F}) = 7.9$ Hz; C(5'')), 160.67 (d, $^1J(\text{C}, \text{F}) = 247.8$ Hz;

C(7'')), 172.36 (COOBn), 210.70 ppm (d, $^4J(\text{C}, \text{F}) = 3.2$ Hz; C=O); ^{19}F NMR (377 MHz, CDCl_3): $\delta = -118.37$ ppm (d, $^3J(\text{H}, \text{F}) = 11.9$ Hz; F); IR (ATR): $\tilde{\nu} = 2925$ (br, w), 1731 (w), 1712 (s), 1628 (m), 1577 (w), 1496 (m), 1446 (w), 1381 (w), 1360 (w), 1289 (m), 1248 (w), 1142 (s), 1046 (w), 979 (w), 902 (w), 852 (w), 744 (m), 696 cm^{-1} (m); HR-ESI-MS: m/z (%): 410.2130 (100, $[M + \text{H}]^+$, calcd for $\text{C}_{25}\text{H}_{29}\text{FNO}_3^+$: 410.2126).

[4-Fluoro-2,2-dimethyl-6-(pyridin-4-yl)-2,3-dihydro-1*H*-inden-1-ylidene]propane-dinitrile (345)

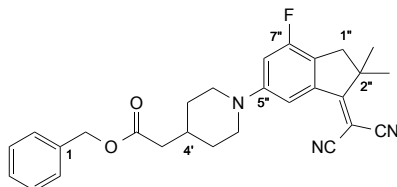


A solution of 4-fluoro-2,2-dimethyl-6-(pyridin-4-yl)-2,3-dihydro-1*H*-inden-1-one (**344**) (550 mg, 2.15 mmol) in dry pyridine (4.3 mL) was treated with a solution of malononitrile (199 mg, 3.02 mmol) in dry pyridine (1.8 mL), stirred at reflux for 43 h, treated with a solution of malononitrile (200 mg) in dry pyridine (1.8 mL), stirred at reflux for 20 h, cooled to 23 °C, and diluted with water (6 mL) and 1 M HCl (8 mL). The layers were separated, and the aqueous layer was extracted three times with EtOAc (3 × 20 mL). The combined organic layers were washed with 1 M HCl (15 mL) and brine (20 mL), dried over Na_2SO_4 , filtered, and evaporated. Column chromatography (SiO_2 ; cyclohexane/EtOAc 75:25 → 60:40) gave **345** (505 mg, 77%) as a yellow solid.

$R_f = 0.13$ (SiO_2 ; cyclohexane/EtOAc 60:40); m.p. 190–192 °C; ^1H NMR (400 MHz, CDCl_3): $\delta = 1.64$ (s, 6 H; CMe_2), 3.13 (s, 2 H; $\text{H}_2\text{-C}(3)$), 7.50 (d with virtual coupling, $J = 6.2$ Hz, 2 H; $\text{H-C}(3', 5')$), 7.58 (dd, $^3J(\text{H}, \text{F}) = 9.1$ Hz, $J = 1.4$ Hz, 1 H; $\text{H-C}(5)$), 8.60 (d, $J = 1.3$ Hz, 1 H; $\text{H-C}(7)$), 8.74 ppm (d with virtual coupling, $J = 6.2$ Hz, 2 H; $\text{H-C}(2', 6')$); ^{13}C NMR (101 MHz, CDCl_3): $\delta = 26.95$ (CMe_2), 44.20 (d, $^3J(\text{C}, \text{F}) = 1.2$ Hz; C(3)), 47.94 (C(2)), 112.71 (CN), 113.59 (CN), 119.68 (d, $^2J(\text{C}, \text{F}) = 20.9$ Hz; C(5)), 120.83 (d, $^4J(\text{C}, \text{F}) = 3.8$ Hz; C(7)), 121.46 (C(3', 5')), 136.44 (d, $^2J(\text{C}, \text{F}) = 20.1$ Hz; C(3a)), 138.69 (d, $^3J(\text{C}, \text{F}) = 6.4$ Hz; C(7a)), 141.19 (d, $^3J(\text{C}, \text{F}) = 6.4$ Hz; C(6)), 145.72 (d, $^4J(\text{C}, \text{F}) = 2.1$ Hz; C(4')), 150.96 (C(2', 6')), 159.62 (d, $^1J(\text{C}, \text{F}) = 250.5$ Hz; C(4)), 183.33 ppm (d, $^4J(\text{C}, \text{F}) = 2.8$ Hz; $\text{C}=\text{C}(\text{CN})_2$), $\text{C}(\text{CN})_2$ hidden under the residual solvent peak; ^{19}F NMR (377 MHz, CDCl_3): $\delta = -114.66$ ppm (d, $^3J(\text{H}, \text{F}) = 9.2$ Hz; F); IR (ATR): $\tilde{\nu} = 2966$ (w), 2220 (m), 1712 (m), 1584 (w), 1560 (s), 1468 (m), 1406 (w), 1331 (m), 1287 (w), 1260 (m), 1212 (w), 1173 (w), 1049 (w), 904 (w), 817 (s), 731 (m),

610 cm^{-1} (m); HR-ESI-MS: m/z (%): 304.1249 (100, $[M + H]^+$, calcd for $\text{C}_{19}\text{H}_{15}\text{FN}_3^+$: 304.1245).

Benzyl {1-[3-(Dicyanomethylidene)-7-fluoro-2,2-dimethyl-2,3-dihydro-1*H*-inden-5-yl]piperidine-4-yl}acetate (347)

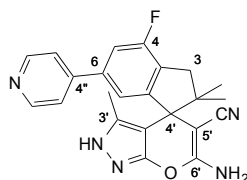


A solution of benzyl [1-(7-fluoro-2,2-dimethyl-3-oxo-2,3-dihydro-1*H*-inden-5-yl)piperidin-4-yl]acetate (**346**) (1.5 g, 3.66 mmol) in dry pyridine (7.2 mL) was treated with a solution of malononitrile (339 mg, 5.13 mmol) in dry pyridine (3.1 mL), stirred at reflux for 43 h, treated with a solution of malononitrile (339 mg) in dry pyridine (3.1 mL), stirred at reflux for 60 h, cooled to 23 °C, and diluted with water (10 mL) and 1 M HCl (14 mL). The layers were separated, and the aqueous layer was extracted three times with EtOAc (3 × 20 mL). The combined organic layers were washed with 1 M HCl (20 mL) and brine (25 mL), dried over Na_2SO_4 , filtered, and evaporated. The crude was absorbed in SiO_2 and column chromatography (SiO_2 ; cyclohexane/EtOAc 100:0 → 90:10) gave **347** (1.32 g, 79%) as a yellow/orange solid.

R_f = 0.48 (SiO_2 ; cyclohexane/EtOAc 80:20); m.p. 89–90 °C; ^1H NMR (400 MHz, CDCl_3): δ = 1.30–1.44 (m, 2 H; $\text{H}_{\text{eq}}\text{-C}(3', 5')$), 1.57 (s, 6 H; CMe_2), 1.77–1.89 (m, 2 H; $\text{H}_{\text{ax}}\text{-C}(3', 5')$), 1.92–2.08 (m, 1 H; $\text{H-C}(4')$), 2.34 (d, J = 7.0 Hz, 2 H; $\text{CH}_2\text{C=O}$), 2.74–2.91 (m, 2 H; $\text{H}_{\text{eq}}\text{-C}(2', 6')$), 2.95 (s, 2 H; $\text{H}_2\text{-C}(1'')$), 3.66 (dt, J = 12.4, 2.8 Hz, 2 H; $\text{H}_{\text{ax}}\text{-C}(2', 6')$), 5.13 (s, 2 H; CH_2O), 6.88 (dd, $^3J(\text{H}, \text{F})$ = 11.7 Hz, J = 2.0 Hz, 1 H; $\text{H-C}(6'')$), 7.30–7.42 (m, 5 H; C_6H_5), 7.76 ppm (d, J = 2.0 Hz, 1 H; $\text{H-C}(4'')$); ^{13}C NMR (101 MHz, CDCl_3): δ = 26.96 (CMe_2), 31.51 ($\text{C}(3', 5')$), 32.83 ($\text{C}(4')$), 41.04 ($\text{CH}_2\text{C=O}$), 43.90 ($\text{C}(1'')$), 47.88 ($\text{C}(2'')$), 49.41 ($\text{C}(2', 6')$), 66.44 (CH_2O), 75.31 ($\text{C}(\text{CN})_2$), 107.71 (d, $^4J(\text{C}, \text{F})$ = 3.1 Hz; $\text{C}(4'')$), 110.32 (d, $^2J(\text{C}, \text{F})$ = 23.1 Hz; $\text{C}(6'')$), 113.36 (CN), 114.12 (CN), 126.22 (d, $^2J(\text{C}, \text{F})$ = 20.7 Hz; $\text{C}(7\text{a}'')$), 128.39 ($\text{C}(3, 5)$), 128.45 ($\text{C}(4)$), 128.74 ($\text{C}(2, 6)$), 136.03 ($\text{C}(1)$), 137.96 (d, $^3J(\text{C}, \text{F})$ = 8.0 Hz; $\text{C}(3\text{a}'')$), 153.52 (d, $^3J(\text{C}, \text{F})$ = 8.7 Hz; $\text{C}(5'')$), 159.65 (d, $^1J(\text{C}, \text{F})$ = 246.0 Hz; $\text{C}(7'')$), 172.28 (C=O), 184.84 ppm (d, $^4J(\text{C}, \text{F})$ = 3.1 Hz; $\text{C=C}(\text{CN})_2$); ^{19}F NMR (377 MHz, CDCl_3): δ = -115.71 ppm (d, $^3J(\text{H}, \text{F})$ = 11.8 Hz; F); IR (ATR): $\tilde{\nu}$ = 2963 (w), 2929 (w), 2845 (w), 2220 (w), 1731 (s), 1620 (m), 1558 (m), 1495 (m), 1458 (m), 1368 (m), 1320 (w), 1274 (m), 1250 (m), 1211 (w),

1152 (s), 1049 (w), 987 (m), 969 (w), 907 (w), 838 (m), 795 (w), 738 (m), 694 (m) 618 cm^{-1} (w); HR-ESI-MS: m/z (%): 458.2246 (100, $[M + H]^+$, calcd for $\text{C}_{28}\text{H}_{29}\text{FN}_3\text{O}_2^+$: 458.2238).

(±)-6'-Amino-4-fluoro-2,2,3'-trimethyl-6-(pyridin-4-yl)-2,3-dihydro-2'H-spiro[indene-1,4'-pyrano[2,3-c]pyrazole]-5'-carbonitrile ((±)-342)



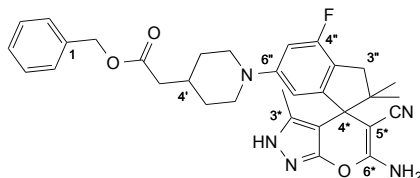
Following **GP7** (the mixture was stirred at 65 °C for 23 h in a microwave oven), the crude was absorbed on SiO_2 . Column chromatography (SiO_2 ; $\text{CH}_2\text{Cl}_2/\text{MeOH}$ 97.5:2.5 \rightarrow 93:07) and recrystallization from a THF/ CH_2Cl_2 /hexane mixture gave (±)-**342** (370 mg, 70%) as a white solid.

R_f = 0.46 (SiO_2 ; $\text{CH}_2\text{Cl}_2/\text{MeOH}$ 90:10); m.p. 238 °C (decomp.); ^1H NMR (400 MHz, THF- d_8): δ = 0.86 and 1.14 (s, 6 H; CMe_2), 1.68 (s, 3 H; Me-C(3')), 2.78 and 3.02 (2 d, J = 16.1 Hz, 2 H; H_2 -C(3)), 6.35 (br. s, 2 H; NH_2), 7.29 (d, J = 1.5 Hz, 1 H; H-C(7)), 7.41 (dd, $^3J(\text{H}, \text{F})$ = 10.0 Hz, J = 1.5 Hz, 1 H; H-C(5)), 7.54 (d with virtual coupling, J = 6.2 Hz, 2 H; H-C(3'', 5'')), 8.54 (d with virtual coupling, J = 6.2 Hz, 2 H; H-C(2'', 6'')), 11.26 ppm (br. s, 1 H; NH); ^{13}C NMR (101 MHz, THF- d_8): δ = 11.21 (Me-C(3')), 26.08 (CMe_2), 41.73 (C(3)), 53.03 (C(2)), 55.55 (d, $^4J(\text{C}, \text{F})$ = 2.3 Hz; C(1)), 61.32 (C(5')), 100.28 (C(3a')), 113.49 (d, $^2J(\text{C}, \text{F})$ = 22.4 Hz; C(5)), 120.36 (CN), 120.83 (d, $^4J(\text{C}, \text{F})$ = 2.9 Hz; C(7)), 121.97 (C(3'', 5'')), 130.56 (d, $^2J(\text{C}, \text{F})$ = 19.2 Hz; C(3a)), 135.51 (C(3')), 140.47 (d, $^3J(\text{C}, \text{F})$ = 6.9 Hz; C(6)), 147.50 (d, $^4J(\text{C}, \text{F})$ = 2.1 Hz; C(4'')), 151.15 (d, $^3J(\text{C}, \text{F})$ = 6.1 Hz; C(7a)), 151.21 (C(2'', 6'')), 157.77 (C(7a')), 160.78 (d, $^1J(\text{C}, \text{F})$ = 246.3 Hz; C(4)), 163.76 ppm (C(6')); ^{19}F NMR (377 MHz, THF- d_8): δ = -119.81 ppm (d, $^3J(\text{H}, \text{F})$ = 9.9 Hz; F); IR (ATR): $\tilde{\nu}$ = 3361 (w), 3116 (br. w), 2181 (s), 1634 (w), 1601 (w), 1585 (s), 1549 (w), 1486 (m), 1449 (w), 1392 (s), 1381 (w), 1365 (w), 1328 (w), 1157 (m), 1064 (s), 1011 (m), 901 (m), 865 (w), 830 (m), 816 (m), 805 (w), 685 (m), 607 cm^{-1} (m); HR-ESI-MS: m/z (%): 402.1728 (100, $[M + H]^+$, calcd for $\text{C}_{23}\text{H}_{21}\text{FN}_5\text{O}^+$: 402.1725); elemental analysis calcd (%) for $\text{C}_{23}\text{H}_{20}\text{FN}_5\text{O}$ (401.4): C 68.82, H 5.02, N 17.45, O 3.99, F 4.73; found: C 69.01, H 5.12, N 17.27, F 4.75.

Separation of (±)-**342** enantiomers by chiral-phase HPLC (column, Daicel, Chiralpak-IA 250 mm \times 20 mm; flow, 15 mL/min; detection, 280 nm; eluent, hexane/EtOAc/*i*PrOH 60:30:10). The sample was dissolved in eluent (7 mg/mL) and injected. (–)-**342**: t_R = 9.18 min

(ee > 99%), $[\alpha]_D^{26} = -93.0^\circ$ (c 0.48, CH₃OH). (+)-**342**: $t_R = 12.48$ min (ee > 99%), $[\alpha]_D^{26} = 98.7^\circ$ (c 0.50, CH₃OH); for the HPLC traces see Section 8.1.5, Figures 103, 104, and 105.

(±)-Benzyl [1-(6'-Amino-5'-cyano-4-fluoro-2,2,3'-trimethyl-2,3-dihydro-2'H-spiro[indene-1,4'-pyrano[2,3-c]pyrazol]-6-yl)piperidin-4-yl]acetate ((±)-**348**)



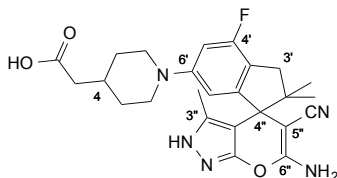
Following **GP7** (the mixture was stirred at 65 °C for 90 h in a microwave oven), column chromatography (SiO₂; cyclohexane/EtOAc 80:20 → 50:50) and recrystallization from CH₂Cl₂/hexane gave (±)-**348** (450 mg, 35%) as a white solid.

$R_f = 0.10$ (SiO₂; cyclohexane/EtOAc 50:50); m.p. 198–201 °C; ¹H NMR (400 MHz, THF-*d*₈): $\delta = 0.78$ and 1.08 (2 s, 6 H; CMe₂), 1.26 – 1.42 (m, 2 H; H_{ax}-C(3', 5')), 1.64 (s, 3 H; Me-C(3*)), 1.74 – 1.81 (m, 2 H; H_{eq}-C(3', 5')), 1.80 – 1.94 (m, 1 H; H-C(4')), 2.28 (d, $J = 7.0$ Hz, 2 H; CH₂C=O), 2.59 (d, $J = 15.1$ Hz, 1 H; H_a-C(3'')), 2.65 (ddt, $J = 9.7, 6.8, 3.4$ Hz, 2 H; H_{ax}-C(2', 6'')), 2.82 (d, $J = 15.2$ Hz, 1 H; H_b-C(3'')), 3.59 – 3.68 (m, 2 H; H_{eq}-C(2', 6'')), 5.08 (s, 2 H; CH₂O), 6.21 (br. s, 2 H; NH₂), 6.48 (d, $J = 2.1$ Hz, 1 H; H-C(7'')), 6.53 (dd, $^3J(\text{H}, \text{F}) = 12.2$ Hz, $J = 2.1$ Hz, 1 H; H-C(5'')), 7.20 – 7.39 (m, 5 H; C₆H₅), 11.12 ppm (br. s, 1 H; NH); ¹³C NMR (101 MHz, THF-*d*₈): $\delta = 11.01$ (Me-C(3*)), 25.83 and 26.01 (CMe₂), 32.68 and 32.70 (C(3', 5')), 33.88 (C(4')), 41.38 (C(3'')), 41.42 (CH₂C=O), 50.40 and 50.66 (C(2', 6'')), 52.92 (C(2'')), 55.37 (d, $^4J(\text{C}, \text{F}) = 2.8$ Hz; C(1'')), 61.65 (C(5*)), 66.34 (CH₂O), 101.04 (C(3a*)), 102.95 (d, $^2J(\text{C}, \text{F}) = 24.4$ Hz; C(5'')), 110.35 (d, $^4J(\text{C}, \text{F}) = 2.6$ Hz; C(7'')), 119.16 (d, $^2J(\text{C}, \text{F}) = 19.8$ Hz; C(3a'')), 120.41 (CN), 128.64 (C(4)), 128.87 (C(2, 6)), 129.11 (C(3, 5)), 135.37 (C(3*)), 137.72 (C(1)), 149.85 (d, $^3J(\text{C}, \text{F}) = 7.6$ Hz; C(7a'')), 154.34 (d, $^3J(\text{C}, \text{F}) = 8.7$ Hz; C(6'')), 157.71 (C(7a*)), 160.74 (d, $^1J(\text{C}, \text{F}) = 242.9$ Hz; C(4'')), 163.77 (C(6*)), 172.19 ppm (C=O); ¹⁹F NMR (377 MHz, THF-*d*₈): $\delta = -120.12$ ppm (d, $^3J(\text{H}, \text{F}) = 12.1$ Hz; F); IR (ATR): $\tilde{\nu} = 3315$ (br. w), 2931 (w), 2194 (m), 1728 (m), 1646 (s), 1587 (s), 1496 (w), 1479 (w), 1442 (w), 1389 (m), 1289 (w), 1252 (w), 1158 (m), 1138 (s), 1069 (w), 991 (w), 898 (w), 865 (w), 786 (w), 737 (w), 697 cm⁻¹ (m); HR-ESI-MS: m/z (%): 556.2722 (100, [M + H]⁺, calcd for C₃₁H₃₅FN₅O₃⁺: 556.2718).

Separation of (±)-**348** enantiomers by chiral-phase HPLC (column, Daicel, Chiralpak-IA 250 mm × 20 mm; flow, 15 mL/min; detection, 280 nm; eluent, hexane/EtOAc/*i*PrOH 60:30:10). The sample was dissolved in eluent (7 mg/mL) and injected. (–)-**348**: $t_R = 7.39$ min

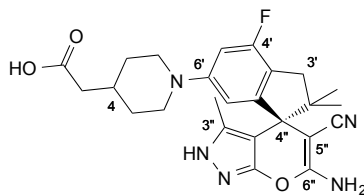
(ee > 99%), $[\alpha]_{\text{D}}^{22} = -44.3^\circ$ (*c* 0.53, CHCl₃). (+)-**348**: $t_{\text{R}} = 10.04$ min (ee > 99%), $[\alpha]_{\text{D}}^{22} = 44.5^\circ$ (*c* 0.49, CHCl₃); for the HPLC traces see Section 8.1.5, Figures 106, 107, and 108.

(±)-[1-(6'-Amino-5'-cyano-4-fluoro-2,2,3'-trimethyl-2,3-dihydro-2'H-spiro[indene-1,4'-pyrano[2,3-c]pyrazol]-6-yl)piperidin-4-yl]acetic acid ((±)-343)



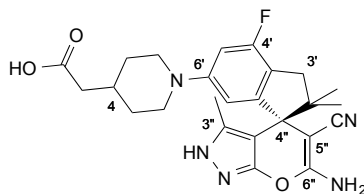
Following **GP8** starting from (±)-**348**, (±)-**343** (245 mg, 97%) was obtained as a white solid. $R_{\text{f}} = 0.08$ (SiO₂; cyclohexane/EtOAc/formic acid 40:60:01); m.p. 185 °C (decomp.); analyt. HPLC: $t_{\text{R}} = 8.91$ min (purity = 97%); ¹H NMR (400 MHz, CD₃OD): $\delta = 0.82$ and 1.11 (2 s, 6 H; CMe₂), 1.28–1.47 (m, 2 H; H_{ax}-C(3, 5)), 1.69 (s, 3 H, Me-C(3'')), 1.77–1.96 (m, 3 H; H_{ax}-C(3, 5) and H-C(4)), 2.24 (d, $J = 6.9$ Hz, 2 H; CH₂C=O), 2.59–2.75 (m, 3 H; H_{ax}-C(2, 6) and H_a-C(3')), 2.83 (d, $J = 15.5$ Hz, 1 H; H_b-C(3')), 3.53–3.68 (m, 2 H; H_{eq}-C(2, 6)), 6.52 (d, $J = 2.1$ Hz, 1 H; H-C(7')), 6.63 ppm (dd, ³ $J(\text{H}, \text{F}) = 12.1$ Hz, $J = 2.1$ Hz, 1 H; H-C(5')); ¹³C NMR (101 MHz, CD₃OD): $\delta = 10.98$ (Me-C(3'')), 25.85 and 25.97 (CMe₂), 32.76 and 32.78 (C(3, 5)), 34.06 (C(4)), 41.58 (C(3')), 41.86 (CH₂C=O), 51.22 and 51.45 (C(2, 6)), 53.32 (C(2'')), 55.65 (d, ⁴ $J(\text{C}, \text{F}) = 2.8$ Hz; C(1')), 60.77 (C(5'')), 101.41 (C(3a'')), 104.09 (d, ² $J(\text{C}, \text{F}) = 24.6$ Hz; C(5')), 110.83 (d, ⁴ $J(\text{C}, \text{F}) = 2.7$ Hz; C(7')), 120.33 (d, ² $J(\text{C}, \text{F}) = 19.8$ Hz; C(3a'')), 122.15 (CN), 137.30 (C(3'')), 149.85 (d, ³ $J(\text{C}, \text{F}) = 7.6$ Hz; C(7a'')), 154.80 (d, ³ $J(\text{C}, \text{F}) = 8.8$ Hz; C(6')), 157.86 (C(7a'')), 161.22 (d, ¹ $J(\text{C}, \text{F}) = 243.4$ Hz; C(4')), 165.01 (C(6'')), 176.38 ppm (C=O); ¹⁹F NMR (377 MHz, CD₃OD): $\delta = -120.20$ ppm (d, ³ $J(\text{H}, \text{F}) = 12.0$ Hz; F); IR (ATR): $\tilde{\nu} = 3400$ –2400 (br. w), 2957 (w), 2804 (w), 2189 (m), 1712 (w), 1627 (s), 1579 (s), 1482 (m), 1442 (w), 1390 (m), 1381 (m), 1249 (w), 1162 (m), 1151 (m), 1070 (w), 965 (w), 906 (w), 831 (w), 786 (w), 734 (w), 709 cm⁻¹ (w); HR-ESI-MS: m/z (%): 466.2256 (100, [M + H]⁺, calcd for C₂₅H₂₉FN₅O₃⁺: 466.2249).

(+)-[1-(6'-Amino-5'-cyano-4-fluoro-2,2,3'-trimethyl-2,3-dihydro-2'H-spiro[indene-1,4'-pyrano[2,3-c]pyrazol]-6-yl)piperidin-4-yl]acetic acid ((+)-343)



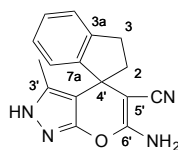
Following **GP8** starting from (+)-**348**, (+)-**343** (85 mg, 92%) was obtained as a light pink solid. ^1H NMR (400 MHz, CD_3OD): δ = 0.82 and 1.11 (2 s, 6 H; CMe_2), 1.41 (q, J = 12.2 Hz, 2 H; $\text{H}_{\text{ax}}\text{-C}(3, 5)$), 1.69 (s, 3 H; $\text{Me-C}(3'')$), 1.76–1.98 (m, 3 H; $\text{H}_{\text{ax}}\text{-C}(3, 5)$ and $\text{H-C}(4)$), 2.25 (d, J = 6.9 Hz, 2 H; $\text{CH}_2\text{C=O}$), 2.67 (d, J = 15.5 Hz, 1 H; $\text{H}_a\text{-C}(3')$), 2.77 (t, J = 12.3 Hz, 2 H; $\text{H}_{\text{ax}}\text{-C}(2, 6)$), 2.85 (d, J = 15.5 Hz, 1 H; $\text{H}_b\text{-C}(3')$), 3.62 (dp, J = 12.7, 2.8 Hz, 2 H; $\text{H}_{\text{eq}}\text{-C}(2, 6)$), 6.52 (d, J = 2.1 Hz, 1 H; $\text{H-C}(7')$), 6.63 ppm (dd, $^3J(\text{H}, \text{F})$ = 12.1 Hz, J = 2.1 Hz, 1 H; $\text{H-C}(5')$); $[\alpha]_{\text{D}}^{21} = 56.6^\circ$ (c 0.48, CH_3OH).

(-)-[1-(6'-Amino-5'-cyano-4-fluoro-2,2,3'-trimethyl-2,3-dihydro-2'H-spiro[indene-1,4'-pyrano[2,3-c]pyrazol]-6-yl)piperidin-4-yl]acetic acid ((-)-343)



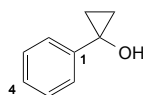
Following **GP8** starting from (-)-**348**, (-)-**343** (85 mg, 92%) was obtained as a light yellow solid.

^1H NMR (400 MHz, CD_3OD): δ = 0.82 and 1.11 (2 s, 6 H; CMe_2), 1.40 (tq, J = 11.6, 4.3 Hz, 2 H; $\text{H}_{\text{ax}}\text{-C}(3, 5)$), 1.69 (s, 3 H; $\text{Me-C}(3'')$), 1.76–1.99 (m, 3 H; $\text{H}_{\text{ax}}\text{-C}(3, 5)$ and $\text{H-C}(4)$), 2.25 (d, J = 6.9 Hz, 2 H; $\text{CH}_2\text{C=O}$), 2.67 (d, J = 15.5 Hz, 1 H; $\text{H}_a\text{-C}(3')$), 2.77 (t, J = 12.3 Hz, 2 H; $\text{H}_{\text{ax}}\text{-C}(2, 6)$), 2.85 (d, J = 15.5 Hz, 1 H; $\text{H}_b\text{-C}(3')$), 3.52–3.72 (m, 2 H; $\text{H}_{\text{eq}}\text{-C}(2, 6)$), 6.52 (d, J = 2.1 Hz, 1 H; $\text{H-C}(7')$), 6.63 ppm (dd, $^3J(\text{H}, \text{F})$ = 12.1 Hz, J = 2.1 Hz, 1 H; $\text{H-C}(5')$); $[\alpha]_{\text{D}}^{21} = -53.9^\circ$ (c 0.49, CH_3OH).

(±)-6'-Amino-3'-methyl-2,3-dihydro-2'H-spiro[indene-1,4'-pyrano[2,3-c]pyrazole]-5'-carbonitrile ((±)-349)

A solution of 2,3-dihydro-1*H*-inden-1-one (100 mg, 0.76 mmol) in EtOH (3.0 mL) was treated with malononitrile (50 mg, 0.76 mmol), 3-methyl-1*H*-pyrazol-5(4*H*)-one (**86**) (74 mg, 0.76 mmol), and Et₃N (21 μL, 0.15 mmol) and stirred at reflux for 4 h after which a precipitate appeared. The suspension was allowed to cool to 23 °C and filtered. The resulting solid was washed with EtOH to give (±)-**349** (80 mg, 38%) as a yellowish solid.

$R_f = 0.09$ (SiO₂; cyclohexane/EtOAc 60:40); m.p. 215 °C (decomp.); ¹H NMR (400 MHz, (CD₃)₂SO): $\delta = 1.61$ (s, 3 H; Me), 2.33 (dd, $J = 8.1, 6.6$ Hz, 2 H; H₂-C(2)), 2.90–3.20 (m, 2 H; H₂-C(3)), 6.77 (br. s, 2 H; NH₂), 6.83–6.93 (m, 1 H; H-C(7)), 7.11–7.34 (m, 3 H; H-C(4, 5, 6)), 12.08 ppm (br. s, 1 H; NH); ¹³C NMR (101 MHz, (CD₃)₂SO): $\delta = 9.79$ (Me), 30.29 (C(3)), 42.68 (C(2)), 46.32 (C(1)), 62.98 (C(5')), 102.27 (C(3a')), 120.24 (CN), 124.22 (C(7)), 124.34 (C(4)), 127.09 (C(5)), 127.23 (C(6)), 134.78 (C(3')), 141.90 (C(3a)), 147.45 (C(7a)), 154.20 (C(7a')), 159.92 ppm (C(6')); IR (ATR): $\tilde{\nu} = 3365$ (s), 3311 (w), 3259 (w), 3172 (m), 2936 (w), 2856 (w), 2189 (s), 1647 (s), 1603 (s), 1587 (s), 1510 (w), 1487 (s), 1472 (w), 1453 (w), 1422 (w), 1399 (s), 1378 (w), 1320 (w), 1307 (w), 1286 (w), 1245 (w), 1214 (w), 1171 (w), 1149 (w), 1095 (w), 1064 (m), 1010 (m), 986 (w), 948 (w), 909 (m), 835 (w), 802 (w), 777 (s), 746 (m), 726 (s), 714 (w), 687 (w), 659 (s), 607 cm⁻¹ (m); HR-ESI-MS: m/z (%): 279.1236 (100, [M + H]⁺, calcd for C₁₆H₁₅N₄O⁺: 279.1240).

1-Phenylcyclopropan-1-ol (357)^[234]

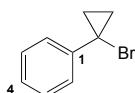
Oven dried glassware was used and the reaction was performed under N₂ atmosphere.

A solution of methyl benzoate (**356**) (6.16 mL, 50 mmol) in Et₂O (160 mL) was treated with titanium isopropoxide (1.5 mL, 5 mmol), then dropwise with a 1 M EtMgBr solution in Et₂O (35.3 mL, 106 mmol) over 1.5 h, stirred at 23 °C for 16 h, quenched with a sat. NH₄Cl solution until liberation of gas ceased, and extracted three times with EtOAc (3 × 20 mL). The combined organic layers were washed with sat. NaHCO₃ solution, water and brine, dried over

anhydrous Na₂SO₄, filtered, and evaporated. Column chromatography (SiO₂; hexane/EtOAc 90:10) gave **357** (3.5 g, 53%) as a colorless oil.

¹H NMR (400 MHz, CDCl₃): δ = 1.02–1.08 and 1.24–1.30 (2 m, 4 H; C(CH₂)₂), 7.19–7.38 ppm (m, 5 H; C₆H₅), OH hidden in the noise. The data corresponded to the literature values.^[234]

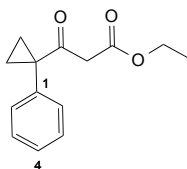
(1-Bromocyclopropyl)benzene (354) (Adapted from de Meijere *et al.*^[236])



A solution of triphenyl phosphine (3.16 g, 12.2 mmol) in CH₂Cl₂ (14 mL) was cooled to –30 °C, treated dropwise with Br₂ (0.64 mL, 12.2 mmol), stirred at –30 °C for 15 min, treated with a solution of 1-phenylcyclopropan-1-ol (**357**) (1.6 g, 11.6 mmol) in pyridine (0.963 mL, 11.6 mmol) at –15 °C, and stirred at 23 °C for 16 h. The mixture was evaporated, treated with SiO₂, and evaporated. Column chromatography (SiO₂; hexane) gave **354** (680 mg, 27%) as colorless oil.

¹H NMR (400 MHz, CDCl₃): δ = 1.27–1.32 and 1.48–1.52 (2 m, 4 H, C(CH₂)₂), 7.22–7.55 ppm (m, 5 H; C₆H₅); ¹³C NMR (101 MHz, CDCl₃): δ = 17.49 (C(CH₂)₂), 32.67 (C(CH₂)₂), 128.11 (C(4)), 128.63 (C(2, 6)), 128.75 (C(3, 5)), 143.54 ppm (C(1)).

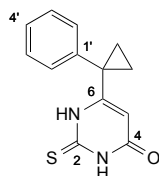
Ethyl-3-oxo-3-(1-phenylcyclopropyl)propanoate (358)^[237]



A mixture of potassium ethyl malonate (**363**) (19.8 g, 117.0 mmol) and magnesium chloride (13.4 g, 138.6 mmol) in acetonitrile (180 mL) was treated with distilled Et₃N (177.5 mmol, 24.7 mL) and stirred at 23 °C for 2 h. At the same time, in a separate flask, a solution of 1-phenyl-1-cyclopropyl carboxylic acid (**361**) (9.0 g, 55.8 mmol) in acetonitrile (54 mL) was treated portion wise with *N,N*-carbonyldiimidazole (10.8 g, 66.6 mmol), stirred at 23 °C for 2 h, and added dropwise to the previous solution. The mixture was stirred at 23 °C for 16 h and treated with a 13% HCl solution (324 mL) while keeping the internal temperature at 10 °C. The two layers were separated, the organic solvent evaporated, and the residue taken up in EtOAc. The aqueous layer was extracted three times with EtOAc (3 × 40 mL). The combined organic layers were washed with a sat. NaHCO₃ solution (3 × 30 mL), brine (3 × 30 mL), dried over anhydrous Na₂SO₄, filtered, and evaporated to give **358** (11.5 g, 89%) as a colorless oil.

$R_f = 0.25$ (SiO₂; cyclohexane/EtOAc 95:05); ¹H NMR (400 MHz, CDCl₃): $\delta = 1.21$ (t, $J = 7.2$ Hz, 3 H; OCH₂CH₃), 1.25 and 1.69 (2 q, $J = 3.6$ Hz, 4 H; C(CH₂)₂), 3.33 (s, 2 H; CH₂), 4.09 (q, $J = 7.1$ Hz, 2 H; OCH₂CH₃), 7.26–7.41 ppm (m, 5 H; C₆H₅); ¹³C NMR (101 MHz, CDCl₃): $\delta = 14.16$ (OCH₂CH₃), 19.84 (C(CH₂)₂), 37.61 (C(CH₂)₂), 48.54 (CH₂), 61.20 (OCH₂CH₃), 128.00 (C(4)), 128.91 (C(2, 6)), 131.13 (C(3, 5)), 139.84 (C(1)), 167.57 (C(=O)OEt), 203.49 ppm (C=O); IR (ATR): $\tilde{\nu} = 2982$ (w, br.), 1737 (s), 1695 (s), 1601 (w), 1316 (s), 1274 (m), 1237 (m), 1209 (m), 1146 (m), 1108 (w), 1062 (m), 1020 (s), 945 (m), 760 (m), 702 cm⁻¹ (s); HR-MALDI-MS: m/z (%): 233.1174 (100, [M + H]⁺, calcd for C₁₂H₁₇O₃⁺: 233.1172).

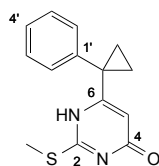
6-(1-Phenylcyclopropyl)-2-sulfanylidene-2,3-dihydropyrimidin-4(1H)-one (359)^[237]



Oven dried glassware was used and the reaction was performed under N₂ atmosphere.

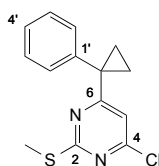
Sodium (1.51 g, 65.0 mmol) was dissolved in anhydrous ethanol (58 mL), cooled to 23 °C, treated with thiourea (3.54 g, 46.2 mmol) and ethyl 3-oxo-3-(1-phenylcyclopropyl)propanoate (**358**) (8 g, 33.3 mmol), stirred at reflux for 16 h, cooled to 23 °C, and evaporated. The residue was dissolved in water and acidified to pH 3 using a 3 N HCl solution upon which a white precipitate appeared. The suspension was filtered, washed with Et₂O, and dried under high vacuum to give **359** (5.56 g, 80%) as greyish solid, which was used without further purification.

$R_f = 0.15$ (SiO₂; cyclohexane/EtOAc 75:25); m.p. 178–180 °C^[237]: 180 °C); ¹H NMR (400 MHz, (CD₃)₂SO): $\delta = 1.19$ and 1.33 (2 dd, $J = 5.0, 2.0$ Hz, 2 H; C(CH₂)₂), 5.93 (s, 1 H; H–C(5)), 7.13–7.50 (m; 5 H, C₆H₅), 12.35 (br. s, 1 H; NH), 12.40 ppm (br. s, 1 H; NH); ¹³C NMR (101 MHz, (CD₃)₂SO): $\delta = 14.91$ (C(CH₂)₂), 27.31 (C(CH₂)₂), 104.99 (C(5)), 126.70 (C(4')), 127.38 (C(2', 6')), 128.39 (C(3', 5')), 141.13 (C(1')), 157.90 (C(6)), 161.27 (C(4)), 176.34 ppm (C(2)); IR (ATR): $\tilde{\nu} = 3092$ (w, br.), 2872 (w, br.), 1674 (s), 1622 (s), 1573 (s), 1493 (w), 1421 (s), 1363 (w), 1307 (w), 1232 (w), 1167 (s), 1154 (s), 1126 (m), 945 (w), 883 (w), 826 (w), 762 (w), 702 (s), 694 cm⁻¹ (s); HR-ESI-MS: m/z (%): 245.0744 (100, [M + H]⁺, calcd for C₁₃H₁₃N₂OS⁺: 245.0743).

2-(Methylsulfanyl)-6-(1-phenylcyclopropyl)pyrimidin-4(1H)-one (364)

A solution of 6-(1-phenylcyclopropyl)-2-sulfanylidene-2,3-dihydropyrimidin-4(1H)-one (**359**) (5.5 g, 1.4 mmol) in EtOH/H₂O 2:1 (68 mL) was treated with sodium hydroxide (869 mg, 22.6 mmol) and dropwise with MeI (1.41 mL, 22.6 mmol) and stirred at 60 °C for 1 h. The formed precipitate was filtered, washed with water, and dried under high vacuum to give **364** (4.5 g, 77%) as white solid, which was used without further purification.

$R_f = 0.15$ (SiO₂; cyclohexane/EtOAc 75:25); m.p. 268–270 °C; ¹H NMR (400 MHz, (CD₃)₂SO): $\delta = 1.21$ and 1.65 (2 q, $J = 3.6$ Hz, 4 H; C(CH₂)₂), 2.45 (s, 3 H; SMe), 5.20 (s, 1 H; H-C(5)), 7.25 – 7.47 (m; 5 H; C₆H₅), 12.47 ppm (br. s, 1 H; NH); ¹³C NMR (101 MHz, (CD₃)₂SO): $\delta = 12.77$ (SMe), 16.27 (C(CH₂)₂), 30.82 (C(CH₂)₂), 105.69 (C(5), weak signal), 127.29 (C(4')), 128.58 (C(2', 6')), 130.77 (C(3', 5')), 141.17 (C(1')), 162.40 (C(2), weak signal), 169.71 ppm (C(6), weak signal); IR (ATR): $\tilde{\nu} = 2921$ (w, br.), 2824 (w, br.), 1639 (s), 1567 (m), 1541 (m), 1458 (m), 1397 (m), 1313 (s), 1271 (s), 1245 (m), 1207 (s), 1131 (m), 1085 (m), 1061 (s), 1027 (s), 1000 (s), 930 (m), 877 (s), 833 (m), 794 (s), 762 (s), 700 (s), 622 cm⁻¹ (m); HR-MALDI-MS: m/z (%): 259.0901 (100, [M + H]⁺, calcd for C₁₄H₁₅N₂SO⁺: 259.0900).

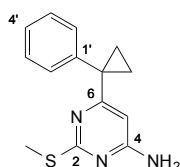
4-Chloro-2-(methylsulfanyl)-6-(1-phenylcyclopropyl)pyrimidine (360)

A mixture of POCl₃ (5.32 mL, 15.2 mmol) and DMF (4.72 mL, 15.2 mmol) was stirred at 23 °C for 30 min. A solution of 2-(methylsulfanyl)-6-(1-phenylcyclopropyl)pyrimidin-4(1H)-one (**364**) (4 g, 15.2 mmol) in CH₂Cl₂ (30 mL) was treated dropwise with the prepared Vilsmeier reagent, stirred at reflux for 16 h, cooled to 23 °C, carefully washed with water twice, dried over anhydrous Na₂SO₄, filtered, and evaporated to give **360** (3.5 g, 82%) as an off-white solid, which was used without further purification.

$R_f = 0.24$ (SiO₂; cyclohexane); m.p. 71–73 °C; ¹H NMR (400 MHz, CDCl₃): $\delta = 1.40$ and 1.81 (2 q, $J = 3.7$ Hz, 4 H; C(CH₂)₂), 2.53 (s, 3 H; SMe), 6.37 (s, 1 H; H-C(5)), 7.30 – 7.48 ppm (m, 5 H; C₆H₅); ¹³C NMR (101 MHz, CDCl₃): $\delta = 14.36$ (SMe), 19.85 (C(CH₂)), 31.68 (C(CH₂)),

114.18 (C(5)), 127.89 (C(4')), 129.09 (C(2', 6')), 131.21 (C(3', 5')), 140.62 (C(1')), 160.67 (C(4)), 172.61 (C(2)), 175.65 ppm (C(6)); HR-MALDI-MS: m/z (%): 279.0532 (33, $[M + H]^+$, calcd for $C_{14}H_{14}^{39}ClN_2S^+$: 279.0531), 277.0560 (100, $[M + H]^+$, calcd for $C_{14}H_{14}^{37}ClN_2S^+$: 277.0561).

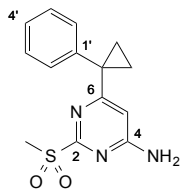
2-(Methylsulfanyl)-6-(1-phenylcyclopropyl)pyrimidin-4-amine (365)



A solution of 4-chloro-2-(methylsulfanyl)-6-(1-phenylcyclopropyl)pyrimidine (**360**) (1.1 g, 4.0 mmol) in 1,4-dioxane (24 mL) was treated with conc. ammonia (30.3 mL, 400 mmol), stirred at 90 °C for 24 h, and cooled to 23 °C. The formed white precipitate was filtered, washed with water, and dried under high vacuum to give **365** (950 mg, 93%) as white solid.

R_f = 0.16 (SiO₂; cyclohexane/EtOAc 85:15); m.p. 166–168 °C; ¹H NMR (400 MHz, CDCl₃): δ = 1.26 and 1.78 (2 q, J = 3.5 Hz, 4 H; C(CH₂)₂), 2.51 (s, 3 H; SMe), 4.56 (br. s, 2 H; NH₂), 5.51 (s, 1 H; H–C(5)), 7.29–7.45 ppm (m, 5 H; C₆H₅); ¹³C NMR (101 MHz, CDCl₃): δ = 14.02 (SMe), 17.59 (C(CH₂)), 31.18 (C(CH₂)), 98.77 (C(5)), 127.28 (C(4')), 128.68 (C(2', 6')), 131.40 (C(3', 5')), 142.25 (C(1')), 162.38 (C(4)), 170.91 (C(2)), 172.27 ppm (C(6)); IR (ATR): $\tilde{\nu}$ = 3380 (w, br.), 3308 (w, br.), 3144 (m, br.), 1643 (s), 1579 (s), 1533 (s), 1466 (w), 1446 (w), 1407 (m), 1276 (s), 1138 (w), 1109 (m), 1078 (m), 1002 (m), 931 (m), 868 (m), 832 (m), 767 (m), 737 (w), 701 (s), 651 (m), 616 cm⁻¹ (m); HR-ESI-MS: m/z (%): 258.1061 (100, $[M + H]^+$, calcd for $C_{14}H_{16}N_3S^+$: 258.1059).

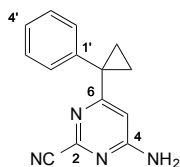
2-(Methanesulfonyl)-6-(1-phenylcyclopropyl)pyrimidin-4-amine (366)



A solution of 2-(methylsulfanyl)-6-(1-phenylcyclopropyl)pyrimidin-4-amine (**365**) (1.7 g, 6.8 mmol) in CH₂Cl₂ (68 mL) was treated with *m*-CPBA (3.44 g, 13.9 mmol), stirred at 23 °C for 4 h, and evaporated. The resulting solid was triturated in a sat. NaHCO₃ solution, filtered, and dried under high vacuum to give **366** (1.74 g, 90%) as a brownish solid.

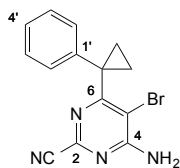
$R_f = 0.25$ (SiO₂; cyclohexane/EtOAc 75:25); m.p. 224–225 °C; ¹H NMR (400 MHz, (CD₃)₂SO): $\delta = 1.28$ and 1.63 (2 q, $J = 3.7$ Hz, 4 H; C(CH₂)₂), 3.24 (s, 3 H; SO₂Me), 5.90 (s, 1 H; H–C(5)), 7.26 – 7.41 ppm (m, 7 H; C₆H₅ and NH₂); ¹³C NMR (400 MHz, (CD₃)₂SO): $\delta = 17.34$ (C(CH₂)₂), 30.58 (C(CH₂)₂), 38.56 (SO₂Me), 103.53 (C(5)), 127.39 (C(4')), 128.78 (C(2', 6')), 130.84 (C(3', 5')), 141.01 (C(1')), 164.25 (C(4)), 165.44 (C(2)), 170.88 ppm (C(6)); IR (ATR): $\tilde{\nu} = 3424$ (m, br.), 3314 (m, br.), 3207 (m, br.), 3010 (w), 2928 (w), 1640 (s), 1590 (s), 1519 (m), 1425 (w), 1320 (s), 1305 (s), 1142 (s), 1126 (s), 1057 (w), 964 (s), 930 (w), 878 (w), 853 (w), 760 (s), 700 (s), 659 cm⁻¹ (m); HR-ESI-MS: m/z (%): 290.0958 (100, [M + H]⁺, calcd for C₁₄H₁₆N₃O₂S⁺: 290.0958).

4-Amino-6-(1-phenylcyclopropyl)pyrimidine-2-carbonitrile (**352**)



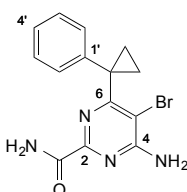
A solution of 2-(methanesulfonyl)-6-(1-phenylcyclopropyl)pyrimidin-4-amine (**366**) (910 mg, 3.14 mmol) in DMSO/H₂O 6:1 (11.7 mL) was treated with sodium cyanide (155 mg, 3.14 mmol), stirred at 70 °C for 3 days, and diluted with water (15 mL) and EtOAc (25 mL). The two layers were separated, the organic layer was washed with water (3 × 10 mL) and the aqueous layer extracted once with ethyl acetate (25 mL). Each aqueous layer was extracted with EtOAc (5 × 15 mL). The combined organic layers were washed with water (15 mL), brine (3 × 30 mL), dried over anhydrous Na₂SO₄, filtered, and evaporated. Column chromatography (SiO₂, cyclohexane/EtOAc 80:20 → 60:40) gave **352** (430 mg, 60%) as a yellowish solid.

$R_f = 0.23$ (SiO₂; cyclohexane/EtOAc 75:25); m.p. 148–150 °C; ¹H NMR (400 MHz, (CD₃)₂SO): $\delta = 1.26$ and 1.56 (2 q, $J = 3.8$ Hz, 4 H; C(CH₂)₂), 5.94 (s, 1 H; H–C(5)), 7.31 (br. s, 2 H, NH₂), 7.33 – 7.45 ppm (m, 5 H; C₆H₅); ¹³C NMR (400 MHz, (CD₃)₂SO): $\delta = 17.74$ (C(CH₂)₂), 30.88 (C(CH₂)₂), 104.85 (C(5)), 116.96 (CN), 127.89 (C(4')), 129.27 (C(2', 6')), 131.28 (C(3', 5')), 141.39 (C(1')), 144.23 (C(2)), 163.97 (C(4)), 171.33 ppm (C(6)); IR (ATR): $\tilde{\nu} = 3414$ (m, br.), 3324 (m, br.), 3192 (m, br.), 1648 (s), 1588 (s), 1523 (s), 1476 (m), 1418 (m), 1346 (s), 1247 (w), 1063 (w), 1020 (m), 969 (m), 942 (s), 853 (w), 778 (m), 764 (m), 702 (s), 677 (m), 632 cm⁻¹ (w); HR-ESI-MS: m/z (%): 237.1133 (100, [M + H]⁺, calcd for C₁₄H₁₃N₄⁺: 237.1135).

4-Amino-5-bromo-6-(1-phenylcyclopropyl)pyrimidine-2-carbonitrile (367)

A solution of 4-amino-6-(1-phenylcyclopropyl)pyrimidine-2-carbonitrile (**352**) (660 mg, 2.8 mmol) in DMF (2.4 mL) was treated with *N*-bromosuccinimide (597 mg, 3.4 mmol), stirred at 23 °C for 5 h, and diluted with water and EtOAc. The layers were separated, and the organic layer was washed with water (3 × 5 mL). The aqueous layer was extracted with EtOAc (3 × 10 mL). The combined organic layers were washed with brine, dried over Na₂SO₄, filtered, and evaporated to give **367** (710 mg, 80%) as a yellowish solid.

$R_f = 0.17$ (SiO₂, cyclohexane/EtOAc 85:15); m.p. 202–204 °C; ¹H NMR (400 MHz, (CD₃)₂SO): $\delta = 1.34$ – 1.42 (m, 4 H; C(CH₂)₂), 7.04–7.31 (m, 5 H; C₆H₅), 7.44 and 8.25 ppm (br. s, 2 H; NH₂); ¹³C NMR (101 MHz, (CD₃)₂SO): $\delta = 17.11$ (C(CH₂)₂), 31.11 (C(CH₂)₂), 108.74 (C(5)), 116.02 (CN), 125.85 (C(2'), 6'), 125.93 (C(4')), 128.30 (C(3'), 5')), 141.39 (C(1')), 141.54 (C(2)), 161.78 (C(4)), 166.63 ppm (C(6)); IR (ATR): $\tilde{\nu} = 3479$ (m, br.), 3344 (m, br.), 2922 (w, br.), 1614 (s), 1555 (s), 1493 (s), 1469 (m), 1410 (w), 1346 (s), 1265 (w), 1030 (m), 1014 (s), 958 (w), 894 (m), 785 (m), 753 (s), 694 (s), 680 cm⁻¹ (m); HR-ESI-MS: m/z (%): 317.0218 (100, [M + H]⁺, calcd for C₁₄H₁₂⁸¹BrN₄⁺: 317.0220), 315.0236 (99, [M + H]⁺, calcd for C₁₄H₁₂⁷⁹BrN₄⁺: 315.0240).

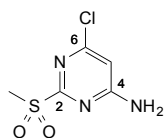
4-Amino-5-bromo-6-(1-phenylcyclopropyl)pyrimidine-2-carboxamide (368)

A solution of 4-amino-5-bromo-6-(1-phenylcyclopropyl)pyrimidine-2-carbonitrile (**367**) (690 mg, 2.18 mmol) in 1,4-dioxane (4.8 mL) was treated dropwise with conc. HCl (4.8 mL), stirred at 23 °C for 5 h, carefully made basic with a sat. NaHCO₃ solution, and extracted three times with EtOAc (3 × 15 mL). The combined organic layers were washed with brine, dried over Na₂SO₄, filtered, and dried to give **368** (660 mg, 91%) as an off-white solid.

$R_f = 0.15$ (SiO₂, CH₂Cl₂/MeOH/Acetic Acid 95:05:01); m.p. 260 °C (decomp.); ¹H NMR (400 MHz, (CD₃)₂SO): $\delta = 1.37$ and 1.44 (2 m, 4 H; C(CH₂)₂), 7.03–7.29 (m, 5 H; C₆H₅), 7.63 and 7.85 ppm (br. s, 2 H; CONH₂); ¹³C NMR (101 MHz, (CD₃)₂SO): $\delta = 17.15$ (C(CH₂)₂),

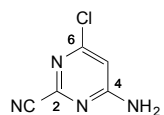
31.18 (C(CH₂)₂), 106.26 (C(5)), 125.71 (C(4')), 125.83 (C(2', 6')), 128.19 (C(3', 5')), 142.08 (C(1')), 156.54 (C=O), 161.79 (C(2)), 164.77 (C(4)), 165.75 ppm (C(6)); IR (ATR): $\tilde{\nu}$ = 3458 (m), 3219 (m, br.), 1701 (m), 1669 (s), 1615 (s), 1554 (s), 1492 (m), 1443 (w), 1298 (s), 1255 (w), 1063 (m), 1025 (m), 1010 (s), 789 (s), 735 (w), 699 cm⁻¹ (s); HR-ESI-MS: *m/z* (%): 335.0329 (94, [M + H]⁺, calcd for C₁₄H₁₅⁸¹BrN₄O⁺: 355.0326), 333.0349 (97, [M + H]⁺, calcd for C₁₄H₁₅⁷⁹BrN₄O⁺: 333.0345).

6-Chloro-2-(methanesulfonyl)pyrimidin-4-amine (371)



A solution of 6-chloro-2-(methanesulfonyl)pyrimidin-4-amine (**370**) (5 g, 28.0 mmol) in CH₂Cl₂ (28 mL) was treated portion wise with *m*-CPBA (16 g, 67.4 mmol) and stirred at 23 °C for 5 h. The solvent was evaporated, the residue was triturated in a sat. NaHCO₃ solution, filtered, and dried under high vacuum. Recrystallization from ethanol gave **371** (3 g, 70%, purity ca. 75%). *R_f* = 0.14 (SiO₂; CH₂Cl₂/MeOH 98:02); m.p. 229–231 °C; ¹H NMR (400 MHz, (CD₃)₂SO): δ = 3.27 (s, 3 H; SO₂Me), 6.64 (s, 1 H; H–C(5)), 7.91 and 8.10 ppm (br. s, 2 H; NH₂); ¹³C NMR (101 MHz, (CD₃)₂SO): δ = 38.74 (SO₂Me), 105.17 (C(5)), 157.91 (C(6)), 165.33 (C(2)), 164.41 ppm (C(4)); IR (ATR): $\tilde{\nu}$ = 3413 (m), 3306 (m), 3194 (m), 3082 (w), 1636 (s), 1569 (s), 1513 (s), 1393 (m), 1309 (s), 1343 (s), 1111 (s), 1048 (m), 991 (m), 957 (s), 876 (m), 830 (m), 821 (m), 770 (w), 750 (s), 699 (w), 662 (w), 629 cm⁻¹ (w); HR-ESI-MS: *m/z* (%): 209.9912 (38, [M + H]⁺, calcd for C₅H₇³⁹ClN₃O₂S⁺: 209.9913) 207.9941 (100, [M + H]⁺, calcd for C₅H₇³⁷ClN₃O₂S⁺: 207.9942).

4-Amino-6-chloropyrimidine-2-carbonitrile (372)

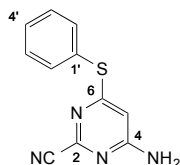


A solution of 6-chloro-2-(methanesulfonyl)pyrimidin-4-amine (**371**) (3 g, 14.4 mmol) in acetonitrile (78 mL) was treated with KCN (930 mg, 14.4 mmol) and 18-crown-6 (38 mg, 0.14 mmol), stirred at 23 °C for 16 h, treated with KCN (1.58 g, 24.32 mmol), and stirred at 23 °C for 16 h. The solvent was evaporated and the residue taken up in EtOAc and water. The two layers were separated and the organic layer was dried over Na₂SO₄, filtered, and

evaporated. Crude **372** (1.8 g, 80%, purity ca. 90%) was directly used in the next step without further purification.

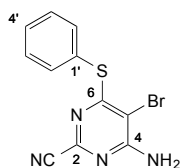
$R_f = 0.16$ (SiO₂; cyclohexane/EtOAc 60:40); m.p. 170–173 °C; ¹H NMR (400 MHz, CDCl₃): $\delta = 6.68$ (s, 1 H; H–C(5)), 7.84 and 7.98 ppm (br. s, 2 H, NH₂); ¹³C NMR (101 MHz, CDCl₃): $\delta = 106.13$ (C(5)), 115.38 (CN), 143.46 (C(4)), 157.46 (C(6)), 164.70 ppm (C(2)); IR (ATR): $\tilde{\nu} = 3401$ (m), 3328 (m), 3194 (m, br.), 2987 (m), 1650 (s), 1569 (s), 1521 (s), 1476 (w), 1385 (m), 1335 (m), 1276 (m), 1134 (w), 1011 (w), 968 (m), 879 (s), 851 (s), 764 (s), 663 (w), 610 cm⁻¹ (w); HR-ESI-MS: m/z (%): 155.0120 (18, [M + H]⁺, calcd for C₅H₄³⁷CIN₄⁺: 155.0119).

4-Amino-6-(phenylsulfanyl)pyrimidine-2-carbonitrile (**373**)



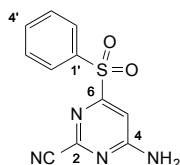
A solution of 4-amino-6-chloropyrimidine-2-carbonitrile (**372**) (1.6 g, 10.3 mmol) in DMF (16 mL) was cooled to 0 °C, treated with DIPEA (1.0 mL, 11 mmol) and thiophenol (1.12 mL, 10.7 mmol), stirred at 23 °C for 16 h, and diluted with water and EtOAc. The two layers were separated, and the aqueous layer was extracted three times with EtOAc (3 × 20 mL). The combined organic layers were washed with water, a sat. NaHCO₃ solution and brine, dried over Na₂SO₄, filtered, and evaporated. Column chromatography (SiO₂; cyclohexane/EtOAc 80:20 → 60:40) gave **373** (1.44 g, 62%) as a yellowish solid.

$R_f = 0.18$ (SiO₂; cyclohexane/EtOAc 60:40); m.p. 247–249 °C; ¹H NMR (400 MHz, CDCl₃): $\delta = 5.93$ (s, 1 H; H–C(5)), 7.47 (br. s, 2 H, NH₂), 7.53–7.58 (m, 3 H, H–C(1', 2', 6')) 7.58–7.65 ppm (m, 2 H; H–C(3', 5')); ¹³C NMR (101 MHz, CDCl₃): $\delta = 101.04$ (C(5)), 115.89 (CN), 126.94 (C(1')), 130.32 (C(2', 6')), 130.52 (C(4')), 135.54 (C(3', 5')), 143.12 (C(2)), 163.25 (C(4)), 169.40 ppm (C(6)); IR (ATR): $\tilde{\nu} = 3401$ (m), 3322 (m), 3184 (m), 1653 (m), 1565 (s), 1515 (s), 1473 (m), 1439 (m), 1387 (s), 1334 (m), 1276 (w), 1124 (m), 965 (m), 871 (s), 844 (m), 764 (w), 747 (s), 705 (m) 688 (m), 670 cm⁻¹ (w) ; HR-ESI-MS: m/z (%): 229.0548 (100, [M + H]⁺, calcd for C₁₁H₉N₄S: 229.0542).

4-Amino-5-bromo-6-(phenylsulfanyl)pyrimidine-2-carbonitrile (374)

A solution of 4-amino-6-chloropyrimidine-2-carbonitrile (**373**) (200 mg, 0.88 mmol) in DMF (0.8 mL) was treated with *N*-bromosuccinimide (184 mg, 1.04 mmol), stirred at 23 °C for 4 h, diluted with EtOAc and water, and the two layers were separated. The aqueous layer was extracted three times with EtOAc (3 × 10 mL). The combined organic layers were washed twice with brine, dried over Na₂SO₄, filtered, and evaporated to give **374** (277 mg, 95%) as yellow solid.

R_f = 0.28 (SiO₂; cyclohexane/EtOAc 75:25); m.p. 200–202 °C; ¹H NMR (400 MHz, (CD₃)₂SO): δ = 7.45–7.60 (m, 5 H, C₆H₅), 8.22 ppm (br. s, 1 H, NH₂ second proton not observed); ¹³C NMR (101 MHz, (CD₃)₂SO): δ = 100.25 (C(5)), 115.66 (CN), 127.51 (C(4')), 129.36 (C(1')), 129.88 (C(2', 5')), 135.47 (C(3', 5')), 140.88 (C(2)), 159.69 (C(4)), 166.23 ppm (C(6)); IR (ATR): $\tilde{\nu}$ = 3382 (m), 3317 (m), 3183 (m), 1649 (s), 1554 (s), 1473 (m), 1439 (w), 1357 (s), 1315 (m), 1250 (m), 1042 (w), 1025 (w), 1005 (s), 872 (m), 766 (s), 740 (s), 704 (m), 658 cm⁻¹ (s); HR-ESI-MS: m/z (%): 308.9629 (100, [M + H]⁺, calcd for C₁₁H₈⁸¹BrN₄S⁺: 308.9627), 306.9650 (97, [M + H]⁺, calcd for C₁₁H₈⁷⁹BrN₄S⁺: 306.9648).

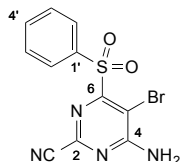
4-Amino-6-(benzenesulfonyl)pyrimidine-2-carbonitrile (375a)

A suspension of 4-amino-6-(phenylsulfanyl)pyrimidine-2-carbonitrile (**373**) (100 mg, 0.45 mmol) in CH₂Cl₂ (1.5 mL) was treated portionwise with *m*-CPBA (200 mg, 0.81 mmol), stirred at 23 °C for 16 h, and evaporated. The residue triturated in a sat. NaHCO₃ solution, filtered, and dried under high vacuum to give **375a** (110 mg, 95%) as an off-white solid.

R_f = 0.23 (SiO₂; cyclohexane/EtOAc 60:40); m.p. 257 °C (decomp.); ¹H NMR (400 MHz, (CD₃)₂SO): δ = 7.33 (s, 1 H; H–C(5)), 7.66–7.99 (m, 5 H; C₆H₅), 8.32 and 8.46 ppm (br. s, 2 H; NH₂); ¹³C NMR (101 MHz, (CD₃)₂SO): δ = 105.65 (C(5)), 115.45 (CN), 128.81 (C(2', 6')), 129.97 (C(3', 5')), 134.96 (C(4')), 136.66 (C(1')), 144.25 (C(2)), 163.24 (C(4)), 164.90 ppm (C(6)); IR (ATR): $\tilde{\nu}$ = 3450 (m), 3352 (m), 1636 (s), 1586 (s), 1523 (m), 1482 (w), 1447 (w), 1399 (m), 1335 (w), 1313 (m), 1302 (s), 1153 (s), 1120 (w), 1074 (m), 999 (w), 964 (m), 848

(m), 755 (m), 723 (s), 680 (m), 642 cm^{-1} (m); HR-ESI-MS: m/z (%): 261.0445 (100, $[M + H]^+$, calcd for $\text{C}_{11}\text{H}_9\text{N}_4\text{O}_2\text{S}^+$: 261.0441).

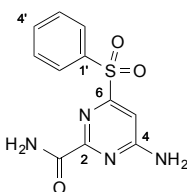
4-Amino-5-bromo-6-(benzenesulfonyl)pyrimidine-2-carbonitrile (**375b**)



A suspension of 4-amino-5-bromo-6-(phenylsulfanyl)pyrimidine-2-carbonitrile (**374**) (100 mg, 0.33 mmol) in CH_2Cl_2 (1.5 mL) was treated portionwise with *m*-CPBA (150 mg, 0.67 mmol), stirred at 23 °C for 16 h, and evaporated. The residue was triturated in a sat. NaHCO_3 solution, filtered, and dried under high vacuum to give **375b** (95 mg, 85%) as an off-white solid.

R_f = 0.14 (SiO_2 ; cyclohexane/EtOAc 60:40); m.p. 240 °C (decomp.); ^1H NMR (400 MHz, $(\text{CD}_3)_2\text{SO}$): δ = 7.67–7.99 (m, 5 H; C_6H_5), 8.95 and 8.14 ppm (br. s, 2 H; NH_2); ^{13}C NMR (101 MHz, $(\text{CD}_3)_2\text{SO}$): δ = 102.38 (C(5)), 115.18 (CN), 129.18 (C(2'), 6'), 129.37 (C(3'), 5'), 135.88 (C(4')), 136.48 (C(1')), 140.79 (C(2)), 160.68 (C(4)), 163.15 ppm (C(6)); IR (ATR): $\tilde{\nu}$ = 3448 (w), 3351 (w, br), 1774 (w), 1638 (m), 1582 (w), 1544 (w), 1544 (m), 1447 (m), 1400 (w), 1376 (m), 1310 (s), 1220 (m), 1153 (s), 1084 (w), 1074 (w), 1037 (w), 1009 (w), 964 (w), 857 (w), 758 (w), 722 (s), 60 (m), 640 cm^{-1} (m); HR-ESI-MS: m/z (%): 340.9523 (100, $[M + H]^+$ calcd for $\text{C}_{11}\text{H}_8^{81}\text{BrN}_4\text{O}_2\text{S}^+$: 340.9525), 338.9544 (97, $[M + H]^+$ calcd for $\text{C}_{11}\text{H}_8^{79}\text{BrN}_4\text{O}_2\text{S}^+$: 338.9546).

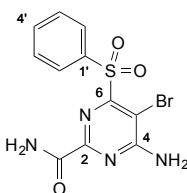
4-Amino-6-(benzenesulfonyl)pyrimidine-2-carboxamide (**376a**)



A solution of 4-amino-6-(benzenesulfonyl)pyrimidine-2-carbonitrile (**375a**) (55 mg, 0.21 mmol) in 1,4-dioxane (0.5 mL) was treated dropwise with conc. HCl (200 μL , 2.4 mmol), stirred at 23 °C for 5 h, carefully made basic with a sat. NaHCO_3 solution, and extracted three times with EtOAc (3×10 mL). The combined organic layers were evaporated, and the residue was purified by preparative HPLC ($\text{H}_2\text{O}/\text{MeCN}$ 70:30 for 8 min, gradient to $\text{H}_2\text{O}/\text{MeCN}$ 0:100 over 12 min, $\text{H}_2\text{O}/\text{MeCN}$ 0:100 for 5 min) to give **376a** (20 mg, 34%) as an off-white solid.

$R_f = 0.37$ (SiO₂; CH₂Cl₂/MeOH/Acetic Acid 95:05:0.1); m.p. 204 °C (decomp.); ¹H NMR (400 MHz, (CD₃)₂SO): $\delta = 7.20$ (s, 1 H; H-C(5)), 7.64–7.69 (m, 2 H; H-C(3', 5')), 7.87–7.72 (br. s, 2 H; NH₂), 7.75–7.80 (m, 1 H; H-C(4')), 7.90 and 7.70 (br. s, 2 H; NH₂), 8.01–8.04 ppm (m, 2 H; H-C(2', 6')); ¹³C NMR (101 MHz, (CD₃)₂SO): $\delta = 102.88$ (C(5)), 128.82 (C(2', 6')), 129.59 (C(3', 5')), 134.59 (C(4')), 137.36 (C(1')), 159.85 (C(2)), 163.81 (C=O), 163.95 (C(4)), 165.33 ppm (C(6)); HR-ESI-MS: m/z (%): 279.0554 (100, [M + H]⁺, calcd for C₁₁H₁₁N₄O₃S⁺: 279.0546).

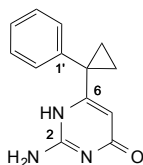
4-Amino-6-(benzenesulfonyl)-5-bromopyrimidine-2-carboxamide (376b)



A solution of 4-amino-5-bromo-6-(benzenesulfonyl)pyrimidine-2-carbonitrile (**375b**) (70 mg, 0.21 mmol) in 1,4-dioxane (0.5 mL) was treated dropwise with conc. HCl (200 μ L, 2.4 mmol), stirred at 23 °C for 5 h, carefully made basic with a sat. NaHCO₃ solution, and extracted three times with EtOAc (3 \times 10 mL). The combined organic layers were evaporated, and the residue was purified by preparative HPLC (H₂O/MeCN 70:30 for 8 min, gradient to H₂O/MeCN 0:100 over 12 min, H₂O/MeCN 0:100 for 5 min) to give **376b** (12 mg, 16%) as an off-white solid.

$R_f = 0.50$ (SiO₂; CH₂Cl₂/MeOH/Acetic Acid 95:05:0.1); m.p. 180 °C (decomp.); HR-ESI-MS: m/z (%): 358.9637 (100, [M + H]⁺, calcd for C₁₁H₈⁸¹BrN₄O₂S⁺: 358.9631), 356.9651 (100, [M + H]⁺, calcd for C₁₁H₈⁷⁹BrN₄O₂S⁺: 356.9658).

2-Amino-6-(1-phenylcyclopropyl)pyrimidin-4(1H)-one (378) (Adapted from Mai *et al.*^[282])

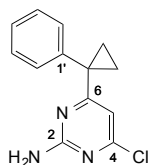


Sodium (2.47 g, 108 mmol) was added in small portion to absolute EtOH (214 mL). When a clear solution was obtained, guanidinium hydrochloride (6.17 g, 64.6 mmol) was added, followed by ethyl 3-oxo-3-(1-phenylcyclopropyl)propanoate (**358**) (10 g, 43.1 mmol). The mixture was stirred at reflux for 12 h, cooled to 23 °C, and evaporated. The residue was diluted with water (66 mL) and neutralized with a 2 M HCl solution upon which a white precipitate

appeared. The suspension was filtered, the resulting solid was washed with water, and dried under high vacuum to give **378** (8.15 g, 83%) as a white solid.

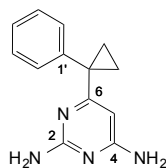
$R_f = 0.13$ (SiO₂; CH₂Cl₂/MeOH 95:05); m.p. 280 °C (decomp.); ¹H NMR (400 MHz, (CD₃)₂SO): $\delta = 1.07$ and 1.50 (2 q, $J = 3.5$ Hz, 4 H; C(CH₂)₂), 4.76 (s, 1 H; H-C(5)), 6.47 (br. s, 2 H; NH₂), 7.22 – 7.47 (m, 5 H; C₆H₅), 10.59 ppm (br. s, 1 H; NH); ¹³C NMR (101 MHz, (CD₃)₂SO): $\delta = 15.40$ (C(CH₂)₂), 30.75 (C(CH₂)₂), 99.77 (C(5)), 126.88 (C(4')), 128.31 (C(2', 6')), 130.64 (C(3', 5')), 142.28 (C(1')), 155.50 (C(2)), 162.33 (C=O), 171.80 ppm (C(6)); IR (ATR): $\tilde{\nu} = 3311$ (br. w), 3067 (br. w), 1661 (s), 1651 (s), 1608 (w), 1493 (m), 1471 (s), 1371 (m), 1323 (w), 1266 (w), 1135 (w), 983 (w), 953 (w), 833 (m), 765 (s), 723 (w), 700 (s), 634 cm⁻¹ (w); HR-ESI-MS: m/z (%): 228.1135 (100, [M + H]⁺, calcd for C₁₃H₁₄N₃O⁺: 228.1131).

4-Chloro-6-(1-phenylcyclopropyl)pyrimidin-2-amine (379)



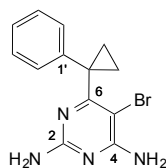
A suspension of 2-amino-6-(1-phenylcyclopropyl)pyrimidin-4(1*H*)-one (**378**) (2.0 g, 8.8 mmol) in 1,4-dioxane (32 mL) was treated with POCl₃ (6.32 mL, 67.8 mmol). The mixture was placed in a pre-heated oil bath at 90 °C, stirred for 3.5 h, cooled to 23 °C, added to ice and neutralized with a sat. NaHCO₃ solution upon which a white precipitate appeared. The suspension was diluted with EtOAc. The two layers were separated, and the aqueous layer was extracted three times with EtOAc (3 × 20 mL). The combined organic layers were washed with brine, dried over Na₂SO₄, filtered, and evaporated to give **379** (1.64 g, 76%) as an off-white solid.

$R_f = 0.78$ (SiO₂; CH₂Cl₂/MeOH 95:05); m.p. 141–142 °C; ¹H NMR (400 MHz, CDCl₃): $\delta = 1.32$ and 1.71 (2 q, $J = 3.7$ Hz, 4 H; C(CH₂)₂), 5.10 (s, 2 H; NH₂), 6.08 (s, 1 H; H-C(5)), 7.27 – 7.49 ppm (m, 5 H; C₆H₅); ¹³C NMR (101 MHz, CDCl₃): $\delta = 18.99$ (C(CH₂)₂), 31.34 (C(CH₂)₂), 109.50 (C(5)), 127.64 (C(4')), 128.90 (C(2', 6')), 131.18 (C(3', 5')), 141.21 (C(1')), 161.23 (C(4)), 162.49 (C(2)), 176.75 ppm (C(6)); IR (ATR): $\tilde{\nu} = 3482$ (w), 3307 (w), 3184 (w), 1685 (w), 1626 (m), 1567 (s), 1525 (s), 1466 (m), 1318 (m), 1229 (w), 1201 (w), 1002 (w), 938 (s), 854 (m), 808 (m), 787 (w), 734 (w), 695 (s), 619 cm⁻¹ (m); HR-ESI-MS: m/z (%): 248.0769 (32, [M + H]⁺, calcd for C₁₃H₁₃³⁹ClN₃⁺: 248.0766), 246.0795 (100, [M + H]⁺, calcd for C₁₃H₁₃³⁷ClN₃⁺: 246.0793).

6-(1-Phenylcyclopropyl)pyrimidine-2,4-diamine (380)

A suspension of 4-chloro-6-(1-phenylcyclopropyl)pyrimidin-2-amine (**379**) (1.65 g, 6.72 mmol) in dry ammonia (7 N in MeOH) (5.76 mL, 40.3 mmol) was stirred in a microwave oven at 150 °C for 7 h, cooled to 23 °C, and evaporated. The residue was diluted with water and EtOAc. The two layers were separated, and the aqueous layer was extracted three times with EtOAc (3 × 15 mL). The combined organic layers were washed with brine, dried over Na₂SO₄, filtered, and evaporated to give **380** (1.52 g, 100%) as a white solid.

R_f = 0.11 (SiO₂; CH₂Cl₂/MeOH 95:05); m.p. 198–201 °C; ¹H NMR (400 MHz, THF-*d*₈): δ = 0.99 and 1.59 (2 q, J = 3.2 Hz, 4 H; C(CH₂)₂), 5.08 (s, 1 H; H-C(5)), 5.11 (br. s, 2 H; NH₂), 5.29 (br. s, 2 H; NH₂), 7.13–7.24 (m, 1 H; H-C(4')), 7.24–7.30 (m, 2 H; H-C(2', 6')), 7.31–7.45 ppm (m, 2 H; H-C(3', 5')); ¹³C NMR (101 MHz, THF-*d*₈): δ = 16.46 (C(CH₂)₂), 31.30 (C(CH₂)₂), 94.20 (C(5)), 127.23 (C(4')), 128.89 (C(2', 6')), 132.11 (C(3', 5')), 144.65 (C(1')), 164.67 (C(4)), 165.53 (C(2)), 172.22 ppm (C(6)); IR (ATR): $\tilde{\nu}$ = 3464 (w), 3329 (w), 3192 (w), 1611 (s), 1550 (s), 1457 (w), 1408 (s), 1256 (w), 1103 (w), 1060 (w), 983 (w), 950 (w), 808 (m), 769 (w), 704 (m), 633 cm⁻¹ (w); HR-ESI-MS: m/z (%): 227.1295 (100, [M + H]⁺, calcd for C₁₃H₁₅N₄⁺: 227.1291).

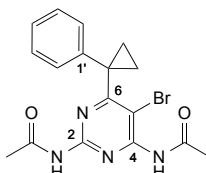
5-Bromo-6-(1-phenylcyclopropyl)pyrimidine-2,4-diamine (381)

A solution of 6-(1-phenylcyclopropyl)pyrimidine-2,4-diamine (**380**) (700 mg, 3.09 mmol) in DMF (2.8 mL) was treated with *N*-bromosuccinimide (661 mg, 3.71 mmol). The solution turned yellow, and a white precipitate appeared rapidly. The suspension was stirred at 23 °C for 3 h, treated with water (56 mL), and filtered. The resulting solid was dried under high vacuum to give **381** (875 mg, 93%) as a light yellow solid.

R_f = 0.27 (SiO₂; CH₂Cl₂/MeOH 95:05); m.p. 120 °C (decomp.); ¹H NMR (400 MHz, THF-*d*₈): δ = 1.18–1.29 and 1.25–1.37 (2 m, 4 H; C(CH₂)₂), 5.60 (br. s, 2 H; NH₂), 5.97 (br. s, 2 H; NH₂), 7.00–7.10 (m, 1 H; H-C(4')), 7.10–7.19 (m, 2 H; H-C(2', 6')), 7.19–7.26 ppm (m, 2 H; H-C(3', 5')); ¹³C NMR (101 MHz, THF-*d*₈): δ = 16.95 (C(CH₂)₂), 31.96 (C(CH₂)₂), 93.87 (C(5)),

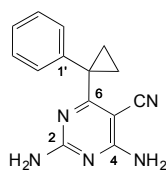
126.20 (C(4')), 127.46 (C(3', 5')), 128.59 (C(2', 6')), 143.96 (C(1')), 162.71 ppm (C(2, 4)), C(6) hidden in the noise; IR (ATR): $\tilde{\nu}$ = 3397 (w), 3146 (br. w), 1670 (w), 1627 (m), 1554 (w), 1533 (s), 1494 (w), 1430 (m), 1387 (w), 1265 (w), 1093 (w), 1029 (w), 967 (w), 789 (m), 760 (m), 695 (m), 659 cm^{-1} (m); HR-ESI-MS: m/z (%): 307.0382 (96, $[M + H]^+$, calcd for $\text{C}_{13}\text{H}_{14}^{81}\text{BrN}_4^+$: 307.0377), 305.0401 (100, $[M + H]^+$, calcd for $\text{C}_{13}\text{H}_{14}^{79}\text{BrN}_4^+$: 305.0396).

***N,N'*-[5-Bromo-6-(1-phenylcyclopropyl)pyrimidine-2,4-diyl]diacetamide (382)**



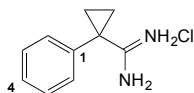
A solution of 5-bromo-6-(1-phenylcyclopropyl)pyrimidine-2,4-diamine (**381**) (2.0 g, 6.55 mmol) in anhydride acetic (15.46 mL) and acetic acid (16 mL) was stirred at reflux for 17 h, cooled to 23 °C, poured onto ice, neutralized with conc. ammonia, and diluted with EtOAc. The two layers were separated, and the aqueous layer was extracted three times with EtOAc (3 × 25 mL). The combined organic layers were washed with a sat. NaHCO_3 solution (100 mL) and water (50 mL), dried over Na_2SO_4 , filtered, and evaporated. Column chromatography (SiO_2 ; cyclohexane/EtOAc 80:20 → 30:70) gave **382** (1.2 g, 47%) as a brown solid.

R_f = 0.21 (SiO_2 ; cyclohexane/EtOAc 50:50); m.p. 67–70 °C; ^1H NMR (400 MHz, CDCl_3): δ = 1.42–1.48 (m, 4 H; $\text{C}(\text{CH}_2)_2$), 2.53 (s, 3 H; Me), 2.59 (s, 3 H; Me), 7.06–7.25 (m, 5 H; C_6H_5), 8.07 (br. s, 1 H; NH), 8.17 ppm (s, 1 H; NH); ^{13}C NMR (101 MHz, CDCl_3): δ = 16.55 ($\text{C}(\text{CH}_2)_2$), 25.52 (Me), 25.87 (Me), 32.31 ($\text{C}(\text{CH}_2)_2$), 126.71 (C(4')), 127.01 (C(3', 5)), 128.59 (C(2', 6')), 140.97 (C(1')), 154.82 (C(4)), 156.05 (C(2)), 170.44 (C=O), 170.89 ppm (C(6)); IR (ATR): $\tilde{\nu}$ = 3165 (br. w), 1663 (s), 1574 (s), 1495 (w), 1420 (w), 1369 (m), 1305 (w), 1230 (w), 1191 (w), 1016 (s), 790 (w), 755 (m), 696 cm^{-1} (s); HR-ESI-MS: m/z (%): 391.0595 (77, $[M + H]^+$, calcd for $\text{C}_{17}\text{H}_{18}^{81}\text{BrN}_4\text{O}_2^+$: 391.0589), 389.0612 (82, $[M + H]^+$, calcd for $\text{C}_{17}\text{H}_{18}^{79}\text{BrN}_4\text{O}_2^+$: 389.0608), 349.0486 (100, $[M - \text{C}_2\text{H}_2\text{O}]^+$, calcd for $\text{C}_{15}\text{H}_{16}^{81}\text{BrN}_4\text{O}^+$: 349.0482), 347.0507 (99, $[M - \text{C}_2\text{H}_2\text{O}]^+$, calcd for $\text{C}_{15}\text{H}_{16}^{79}\text{BrN}_4\text{O}^+$: 347.0502).

2,4-Diamino-6-(1-phenylcyclopropyl)pyrimidine-5-carbonitrile (377)

A solution of *N,N'*-[5-bromo-6-(1-phenylcyclopropyl)pyrimidine-2,4-diyl]diacetamide (**382**) (270 mg, 0.69 mmol) in DMF (5.4 mL) was treated with copper cyanide (75 mg, 0.83 mmol), stirred at reflux for 8 h, treated with ethylenediamine (13.3 mL, 197 mmol), stirred at 80 °C for 1 h and at 23 °C for 13 h, filtered through a pad of celite eluting with DMF, and diluted with water and EtOAc. The two layers were separated, and the aqueous layer was extracted three times with EtOAc (3 × 15 mL). The combined organic layers were washed with brine, dried over Na₂SO₄, filtered, and evaporated. Column chromatography (SiO₂; CH₂Cl₂/MeOH 97.5/2.5) and recrystallization from a MeOH/hexane mixture gave **377** (60 mg, 34%) as white needles.

$R_f = 0.35$ (SiO₂; CH₂Cl₂/MeOH 95:05); m.p. 222–224 °C; ¹H NMR (400 MHz, THF-*d*₈): $\delta = 1.10$ – 1.26 and 1.28 – 1.43 (2 m, 4 H; C(CH₂)₂), 6.16 (br. s, 2 H; NH₂), 6.32 (br. s, 2 H; NH₂), 7.08–7.15 (m, 1 H; H–C(4')), 7.15–7.26 (m, 2 H; H–C(2', 6')), 7.35–7.47 ppm (m, 2 H; H–C(3', 5')); ¹³C NMR (101 MHz, THF-*d*₈): $\delta = 14.82$ (C(CH₂)₂), 32.22 (C(CH₂)₂), 80.95 (C(5)), 116.90 (CN), 127.13 (C(4')), 128.78 (C(2', 6')), 129.28 (C(3', 5')), 143.50 (C(1')), 164.70 (C(4)), 166.42 (C(2)), 175.64 ppm (C(6)); IR (ATR): $\tilde{\nu} = 3468$ (w), 3452 (w), 3319 (br. w), 3110 (br. w), 2217 (m), 1645 (m), 1623 (s), 1557 (s), 1533 (s), 1498 (m), 1449 (s), 1290 (w), 968 (w), 929 (w), 803 (w), 773 (w), 737 (w), 708 cm⁻¹ (m); HR-ESI-MS: m/z (%): 252.1249 (100, [M + H]⁺, calcd for C₁₄H₁₄N₅⁺: 252.1244).

1-Phenylcyclopropane-1-carboximidamide – hydrogen chloride 1:1 (385)^[244]

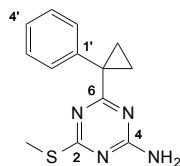
Oven dried glassware was used and the reaction was performed under Ar atmosphere.

A suspension of NH₄Cl (4.7 g, 87.5 mmol) in anhydrous toluene (32 mL) was cooled to 0 °C, treated dropwise with trimethylaluminium (2 M in toluene) (40.3 mL, 80.6 mmol), stirred at 23 °C for 1 h until methane evolution ceased, treated dropwise with a solution of 1-phenyl-1-cyclopropanecarbonitrile (**384**) (7 mL, 48.8 mmol) in toluene (16.1 mL), stirred at 80 °C for 16 h, cooled to 23 °C, poured into a slurry of SiO₂ (24.5 g) and CHCl₃ (84 mL), filtered, and washed with MeOH. The filtrate was concentrated to 30 mL, filtered, and washed with

MeOH/toluene. The filtrate was treated with HCl (1.23 M in MeOH) (126 mL) and Et₂O (650 mL), and stirred at 23 °C for 16 h. The resulting suspension was filtered, dissolved in *i*PrOH/acetone 4:1 (245 mL), and stirred at 23 °C for 16 h. The mixture was filtered, the filtrate concentrated (30 mL), treated with Et₂O (500 mL), stirred at 23 °C for 1 h, filtered, and the solid was dried under high vacuum to give **385** (2.5 g, 26 %) as an off-white solid.

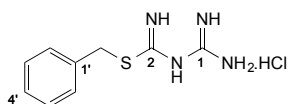
$R_f = 0.30$ (SiO₂; CH₂Cl₂/MeOH/Acetic Acid 95:05:0.1); m.p. 231–233 °C; ¹H NMR (400 MHz, (CD₃)₂SO): $\delta = 1.24$ – 1.27 and 1.46 – 1.50 (2 m, 4 H; C(CH₂)₂), 7.23–7.49 (m, 5 H; C₆H₅) 9.05 and 9.08 ppm (br. s, 4 H; C(=NH)NH₂); ¹³C NMR (101 MHz, (CD₃)₂SO): $\delta = 14.52$ (C(CH₂)₂), 28.30 (C(CH₂)₂), 127.79 (C(4')), 128.52 (C(2', 6')), 128.70 (C(3', 5')), 138.58 (C(1')), 171.40 ppm (C(=NH)NH₂); IR (ATR): $\tilde{\nu} = 3227$ (m), 3077 (m), 1676 (s), 1514 (m), 1501 (w), 1448 (w), 1427 (w), 1243 (w), 1097 (m), 1035 (w), 951 (m), 767 (m), 706 cm⁻¹ (s); HR-ESI-MS: m/z (%): 161.1074 (100, [M + H]⁺, calcd for C₁₀H₁₃N₂⁺: 161.1073).

4-(Methylsulfanyl)-6-(1-phenylcyclopropyl)-1,3,5-triazin-2-amine (386) (Adapted from Brough *et al.*^[245])



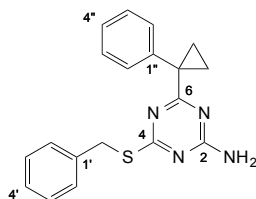
A solution of 1-phenylcyclopropane-1-carboximidamide – hydrogen chloride 1:1 (**385**) (1.5 g, 7.6 mmol) in EtOH (37.5 mL) was treated with *S,S*-dimethyl-*N*-cyanodithioiminocarbonate (**387**) (1.13 g, 7.6 mmol) and DIPEA (2.7 mL, 18 mmol), stirred at 65 °C for 16 h, cooled to 23 °C, treated with SiO₂, and evaporated. Column chromatography (SiO₂; cyclohexane/EtOAc 80:20) gave **386** (1.1 g, 57%) as a white solid.

$R_f = 0.37$ (SiO₂; cyclohexane/EtOAc 80:20); m.p. 165–167 °C; ¹H NMR (400 MHz, (CD₃)₂SO): $\delta = 1.23$ and 1.61 (2 q, $J = 3.6$ Hz, 4 H; C(CH₂)₂), 2.29 (s, 3 H, SMe), 7.19–7.33 ppm (m, 7 H; C₆H₅ and NH₂); ¹³C NMR (101 MHz, (CD₃)₂SO): $\delta = 12.25$ (SMe), 17.53 (C(CH₂)₂), 31.47 (C(CH₂)₂), 126.37 (C(4')), 127.77 (C(2', 6')), 130.72 (C(3', 5')), 141.52 (C(1')), 164.98 (C(4)), 178.54 (C(6)), 179.52 ppm (C(2)); IR (ATR): $\tilde{\nu} = 3322$ (m, br.), 3119 (m, br.), 1651 (m), 1513 (s), 1444 (m), 1396 (m), 1327 (m), 1277 (s), 1225 (m), 1209 (w), 1096 (w), 1032 (w), 1022 (w), 932 (m), 879 (s), 817 (s), 749 (m), 693 (s), 627 (m), 606 cm⁻¹ (m); HR-ESI-MS: m/z (%): 259.1012 (100, [M + H]⁺, calcd for C₁₃H₁₄N₄S⁺: 259.1012).

Benzyl *N*-Carbamimidoylcarbamimidothioate – hydrogen chloride 1:1 (390)^[246]

A solution of benzyl chloride (**391**) (2.73 mL, 23.70 mmol) in MeOH (48 mL) was treated with 2-imino-4-thiobiuret (**392**) (2.80 g, 23.70 mmol), stirred at 60 °C in a microwave oven for 20 min, cooled to 23 °C, and evaporated. The residue was triturated in acetonitrile (25 mL), filtered, and dried under high vacuum to give **390** (4.80 g, 83%) as a white solid.

m.p. 188–190 °C; ¹H NMR (400 MHz, (CD₃)₂SO): δ = 4.24 (s, 2 H; CH₂S), 7.13–7.52 (m, 5 H; C₆H₅), 8.04 (br. s, 4 H; NH), 8.10 ppm (br. s, 2 H; NH); ¹³C NMR (101 MHz, (CD₃)₂SO): δ = 34.62 (CH₂S), 127.34 (C(4')), 128.56 (C(2', 6') or C(3', 5')), 128.97 (C(2', 6') or C(3', 5')), 136.88 (C(1')), 162.21 (C(1)), 163.61 ppm (C(2)); IR (ATR): $\tilde{\nu}$ = 3294 (br. m), 3153 (br. m), 1650 (m), 1630 (m), 1611 (m), 1523 (s), 1329 (w), 1236 (w), 1178 (w), 1069 (w), 923 (m), 750 (w), 708 (w), 695 (w), 631 cm⁻¹ (m); HR-ESI-MS: *m/z* (%): 209.0859 (100, [M + H]⁺, calcd for C₉H₁₃N₄S⁺: 209.0855).

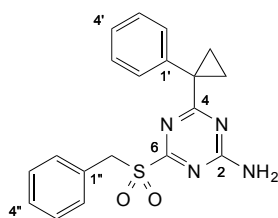
4-(Benzylsulfanyl)-6-(1-phenylcyclopropyl)-1,3,5-triazin-2-amine (389)

A solution of 1-phenylcyclopropanecarboxylic acid (**361**) (1.5 g, 9.3 mmol) in CH₂Cl₂ (75 mL) was treated with thionyl chloride (6.75 mL, 92.0 mmol), stirred at reflux for 3 h, cooled to 23 °C, and evaporated. The residue was diluted with dry THF (24 mL), treated with benzyl *N*-carbamimidoylcarbamimidothioate – hydrogen chloride 1:1 (**390**) (2.26 g, 9.3 mmol) and Et₃N (3.87 mL, 27.7 mmol). The mixture was stirred at 50 °C for 15 h, cooled to 23 °C, and diluted with water and EtOAc. The two layers were separated, and the aqueous layer was extracted three times with EtOAc (3 × 15 mL). The combined organic layers were washed with brine, dried over Na₂SO₄, filtered, and evaporated. The crude was absorbed on SiO₂ and column chromatography (SiO₂; cyclohexane/EtOAc 95:05 → 85:15) gave **389** (2.0 g, 65%) as a white solid.

*R*_f = 0.29 (SiO₂; cyclohexane/EtOAc 80:20); m.p. 133–135 °C; ¹H NMR (400 MHz, CDCl₃): δ = 1.33 and 1.73 (2 q, *J* = 3.7 Hz, 4 H; C(CH₂)₂), 4.18 (s, 2 H; CH₂S), 5.18 (br. s, 2 H; NH₂), 7.11–7.26 (m, 5 H; C₆H₅), 7.27–7.54 ppm (m, 5 H; C₆H₅); ¹³C NMR (101 MHz, CDCl₃): δ =

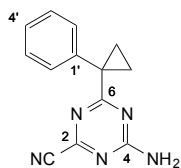
18.80 (C(CH₂)₂), 32.08 (C(CH₂)₂), 34.16 (CH₂S), 126.93 (C(4'')), 127.16 (C(4')), 128.15 (C(2'', 6'')), 128.52 (C(3'', 5'')), 129.01 (C(2', 6')), 131.38 (C(3', 5')), 138.08 (C(1')), 141.66 (C(1'')), 165.18 (C(2)), 180.27 (C(6)), 180.39 ppm (C(4)); IR (ATR): $\tilde{\nu}$ = 3440 (w), 3317 (br. w), 3209 (br. w), 1637 (m), 1516 (s), 1442 (w), 1395 (w), 1318 (w), 1284 (w), 1233 (w), 1215 (w), 1019 (w), 930 (w), 885 (m), 814 (m), 766 (w), 712 (w), 701 (m), 692 cm⁻¹ (m); HR-ESI-MS: m/z (%): 335.1323 (100, [M + H]⁺, calcd for C₁₉H₁₉N₄S⁺: 335.1325).

4-(1-Phenylcyclopropyl)-6-(phenylmethanesulfonyl)-1,3,5-triazin-2-amine (394)



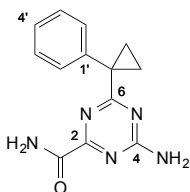
A solution of 4-(benzylthio)-6-(1-phenylcyclopropyl)-1,3,5-triazin-2-amine (**389**) (1.70 g, 5.1 mmol) in THF (240 mL) at 0 °C was treated portionwise with *m*-CPBA (2.73 g, 12.2 mmol), stirred at 0 °C for 2 h and at 23 °C for 3 h, diluted with a sat. NaHCO₃ solution and EtOAc. The two layers were separated, and the aqueous layer was extracted three times with EtOAc (3 × 25 mL). The combined organic layers were washed with water and brine, dried over Na₂SO₄, filtered, and evaporated. The crude was absorbed on SiO₂ and column chromatography (SiO₂; cyclohexane/EtOAc 85:15 → 70:30) gave **394** (1.31 g, 70%) as a white solid.

R_f = 0.30 (SiO₂; cyclohexane/EtOAc 60:40); m.p. 126–129 °C; ¹H NMR (400 MHz, CDCl₃): δ = 1.50 and 1.82 (2 q, J = 3.8 Hz, 4 H; C(CH₂)₂), 4.49 (s, 2 H; CH₂SO₂), 5.69 and 6.75 (br. s, 2 H; NH₂), 7.05–7.23 and 7.27–7.52 ppm (2 m, 10 H; 2 C₆H₅); ¹³C NMR (101 MHz, CDCl₃): δ = 20.21 (C(CH₂)₂), 32.68 (C(CH₂)₂), 56.23 (CH₂SO₂), 126.65 (C(1'')), 127.46 (C(4')), 128.33 (C(2', 6')), 128.80 (C(3', 5')), 128.98 (C(4'')), 131.40 (C(3'', 5'')), 131.49 (C(2'', 6'')), 140.38 (C(1')), 166.69 (C(2)), 172.70 (C(6)), 183.60 ppm (C(4)); IR (ATR): $\tilde{\nu}$ = 3317 (w), 3250 (w), 1643 (m), 1567 (s), 1512 (w), 1489 (w), 1412 (m), 1319 (m), 1185 (w), 1137 (s), 963 (w), 932 (w), 912 (w), 817 (w), 772 (w), 696 (m), 638 (w), 616 cm⁻¹ (m); HR-ESI-MS: m/z (%): 367.1231 (100, [M + H]⁺, calcd for C₁₉H₁₉N₄O₂S⁺: 367.1223).

4-Amino-6-(1-phenylcyclopropyl)-1,3,5-triazine-2-carbonitrile (395)

A solution of 4-(1-phenylcyclopropyl)-6-(phenylmethanesulfonyl)-1,3,5-triazin-2-amine (**394**) (1.30 g, 3.55 mmol) in DMSO/water 8:1 (16.8 mL) was treated with NaCN (0.261 g, 5.32 mmol) and stirred at 70 °C for 3 h, which led to a red solution. The mixture was cooled to 23 °C and diluted with EtOAc and water. The two layers were separated, and the organic layer was extracted three times with water (3 × 15 mL). Each aqueous layer was extracted three times with EtOAc (3 × 10 mL). The combined organic layers were washed with brine, dried over Na₂SO₄, filtered, and evaporated. The crude was absorbed on SiO₂ and column chromatography (SiO₂; cyclohexane/EtOAc 95:05 → 80:20) gave **395** (461 mg, 55%) as a white solid.

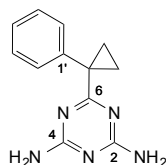
R_f = 0.24 (SiO₂; cyclohexane/EtOAc 80:20); m.p. 145–147 °C; ¹H NMR (400 MHz, CDCl₃): δ = 1.45 and 1.81 (2 q, J = 3.8 Hz, 4 H; C(CH₂)₂), 5.26 and 5.75 (br. s, 2 H; NH₂), 7.27–7.44 ppm (m, 5 H; C₆H₅); ¹³C NMR (101 MHz, CDCl₃): δ = 20.43 (C(CH₂)₂), 32.42 (C(CH₂)₂), 114.89 (CN), 127.41 (C(4')), 128.47 (C(3', 5')), 131.34 (C(2', 6')), 140.34 (C(1')), 152.65 (C(2)), 165.74 (C(4)), 183.46 ppm (C(6)); IR (ATR): $\tilde{\nu}$ = 3418 (m), 3336 (w), 3208 (br. w), 1654 (s), 1562 (m), 1548 (m), 1514 (s), 1493 (w), 1444 (w), 1404 (m), 1355 (m), 1300 (w), 1192 (w), 1099 (w), 1022 (w), 1031 (w), 964 (m), 937 (s), 906 (w), 817 (s), 743 (w), 697 (s), 638 cm⁻¹ (m); HR-ESI-MS: m/z (%): 238.1091 (100, [M + H]⁺, calcd for C₁₃H₁₂N₅⁺: 238.1087).

4-Amino-6-(1-phenylcyclopropyl)-1,3,5-triazine-2-carboxamide (383)

A solution of 4-amino-6-(1-phenylcyclopropyl)-1,3,5-triazine-2-carbonitrile (**395**) (350 mg, 1.5 mmol) in DMSO (9.1 mL) was treated with K₂CO₃ (561 mg, 4.1 mmol), cooled in an ice bath, and treated dropwise with 30% H₂O₂ (18.1 mL, 177 mmol) upon which a white precipitate appeared. The mixture was stirred at 15–20 °C for 1 h, diluted with water, filtered, and the resulting solid was dried under high vacuum to give **383** (282 mg, 75%) as a white solid.

$R_f = 0.24$ (SiO₂; CH₂Cl₂/MeOH/Acetic Acid 95:05:0.1); m.p. 300 °C (decomp.); ¹H NMR (400 MHz, (CD₃)₂SO): $\delta = 1.28$ and 1.72 (2 q, $J = 3.6$ Hz, 4 H; C(CH₂)₂), 7.18–7.26 (m, 1 H; H–C(4')), 7.27–7.40 (m, 4 H; H–C(2', 3', 5', 6')), 7.50 (br. s, 1 H; NH), 7.62 (br. s, 1 H; NH), 7.68 (br. s, 1 H; NH), 7.71 ppm (br. s, 1 H; NH); ¹³C NMR (101 MHz, (CD₃)₂SO): $\delta = 18.09$ (C(CH₂)₂), 31.73 (C(CH₂)₂), 126.48 (C(4')), 127.94 (C(3', 5')), 130.73 (C(2', 6')), 141.44 (C(1')), 164.57 (C(4)), 165.72 (C=O), 166.88 (C(2)), 180.84 ppm (C(6)); IR (ATR): $\tilde{\nu} = 3407$ (m), 3323 (br. w), 3188 (br. m), 1702 (s), 1652 (s), 1572 (w), 1559 (m), 1517 (s), 403 (m), 1317 (m), 1210 (m), 1102 (w), 1060 (w), 1025 (w), 954 (m), 838 (w), 800 (m), 755 (w), 717 (w), 699 (s), 670 (w), 601 cm⁻¹ (s); HR-ESI-MS: m/z (%): 256.1197 (100, [M + H]⁺, calcd for C₁₃H₁₄N₅O⁺: 256.1193).

6-(1-Phenylcyclopropyl)-1,3,5-triazine-2,4-diamine (396)



A solution of 1-phenylcyclopropanecarbonitrile (**384**) (0.10 mL, 0.70 mmol) in methoxyethanol (0.6 mL) was treated with cyanoguanidine (**397**) (71 mg, 0.84 mmol) and KOH (24 mg, 0.42 mmol), stirred at reflux for 3.5 h, and cooled to 23 °C upon which a white precipitate appeared. Water (2.4 mL) was added and the suspension filtered. The resulting solid was washed with water, dried under high vacuum, and recrystallized from a EtOH/water 1:1 mixture to give **396** (153 mg, 96%) as white needles.

$R_f = 0.25$ (SiO₂; CH₂Cl₂/MeOH 95:05); m.p. 236–239 °C; ¹H NMR (400 MHz, THF-*d*₈): $\delta = 1.06$ and 1.59 (2 q, $J = 3.3$ Hz, 4 H; C(CH₂)₂), 5.73 (br. s, 2 H; NH₂), 5.87 (br. s, 2 H; NH₂), 7.02–7.14 (m, 1 H; H–C(4')), 7.14–7.23 (m, 2 H; H–C(2', 6')), 7.23–7.37 ppm (m, 2 H; H–C(3', 5')); ¹³C NMR (101 MHz, THF-*d*₈): $\delta = 17.18$ (C(CH₂)₂), 32.18 (C(CH₂)₂), 126.53 (C(4')), 128.19 (C(2', 5')), 132.01 (C(3', 5')), 144.24 (C(1')), 168.55 (C(2, 4)), 181.01 ppm (C(6)); IR (ATR): $\tilde{\nu} = 3442$ (w), 3308 (w), 3190 (w), 1649 (m), 1625 (m), 1530 (s), 1453 (m), 1403 (m), 1312 (w), 1252 (w), 1232 (w), 1023 (w), 986 (m), 958 (m), 820 (s), 769 (w), 702 (s), 611 cm⁻¹ (w); HR-ESI-MS: m/z (%): 228.1247 (100, [M + H]⁺, calcd for C₁₂H₁₃N₅⁺: 228.1244).

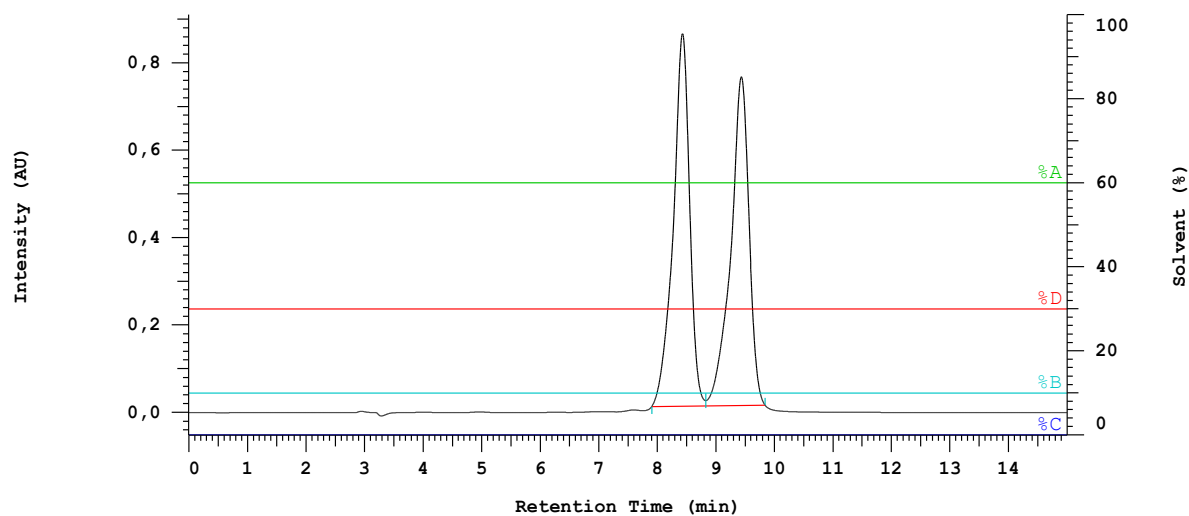
8.1.5. HPLC Chromatograms of (\pm)-**291**, (+)-**291**, (-)-**291**, (\pm)-**342**, (+)-**342**, (-)-**342**, (\pm)-**348**, (+)-**348**, and (-)-**348**

Figure 100. HPLC chromatogram of (\pm)-**291** (column, Daicel, Chiralpak-IA 250 mm \times 20 mm; flow, 1 mL/min; detection, 254 nm; eluent, hexane/EtOAc/*i*PrOH 60:30:10). (-)-**291**: t_R = 8.43 min and (+)-**291**: t_R = 9.43 min. T = 23 °C.

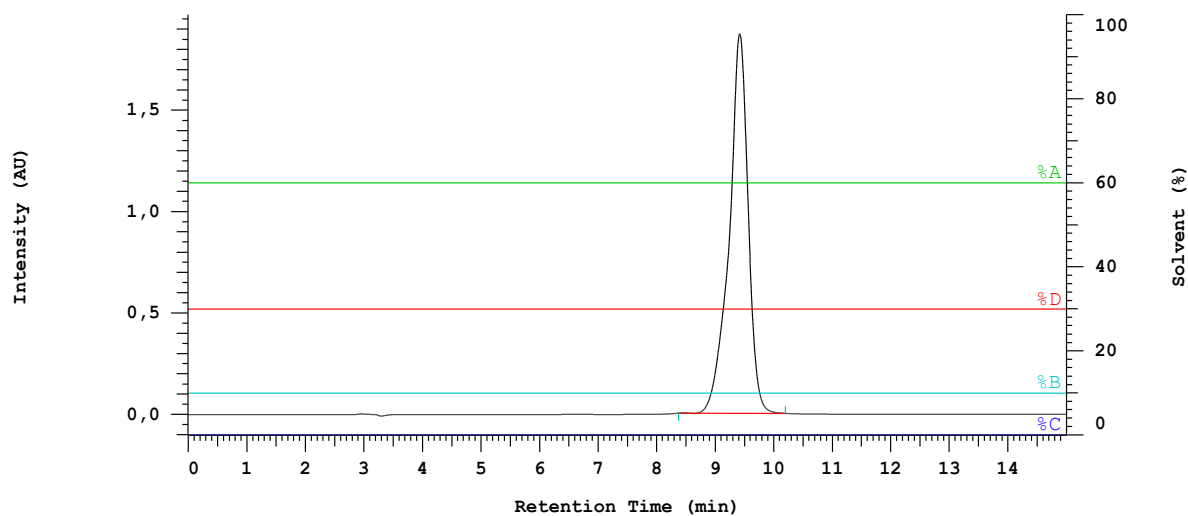


Figure 101. HPLC chromatogram of (+)-**291** (column, Daicel, Chiralpak-IA 250 mm \times 20 mm; flow, 1 mL/min; detection, 254 nm; eluent, hexane/EtOAc/*i*PrOH 60:30:10). (+)-**291**: t_R = 9.42 min (ee > 99%). T = 23 °C.

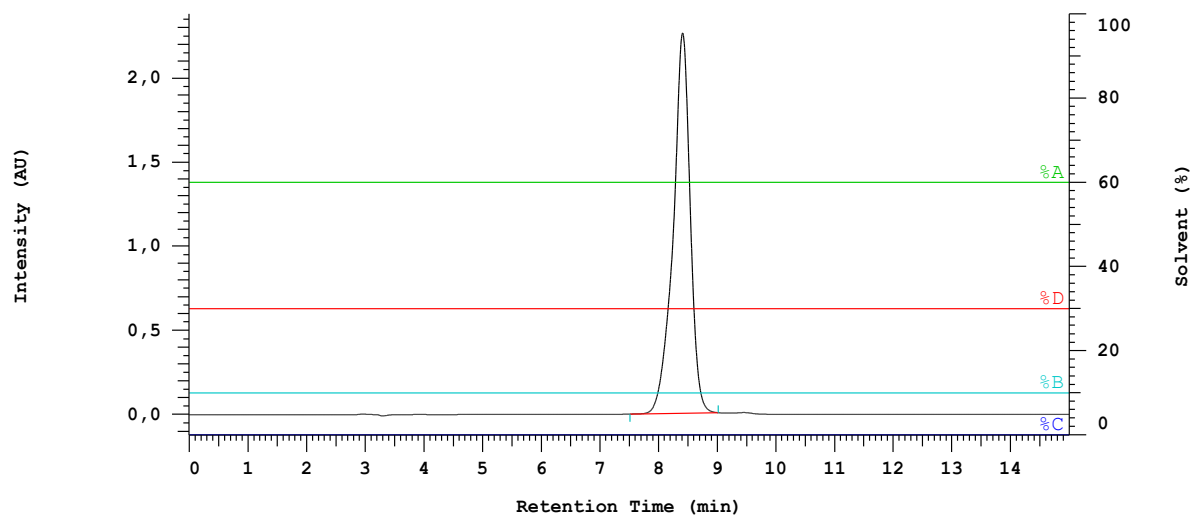


Figure 102. HPLC chromatogram of (-)-**291** (column, Daicel, Chiralpak-IA 250 mm × 20 mm; flow, 1 mL/min; detection, 254 nm; eluent, hexane/EtOAc/*i*PrOH 60:30:10). (-)-**291**: $t_R = 8.41$ min (ee > 99%). $T = 23$ °C.

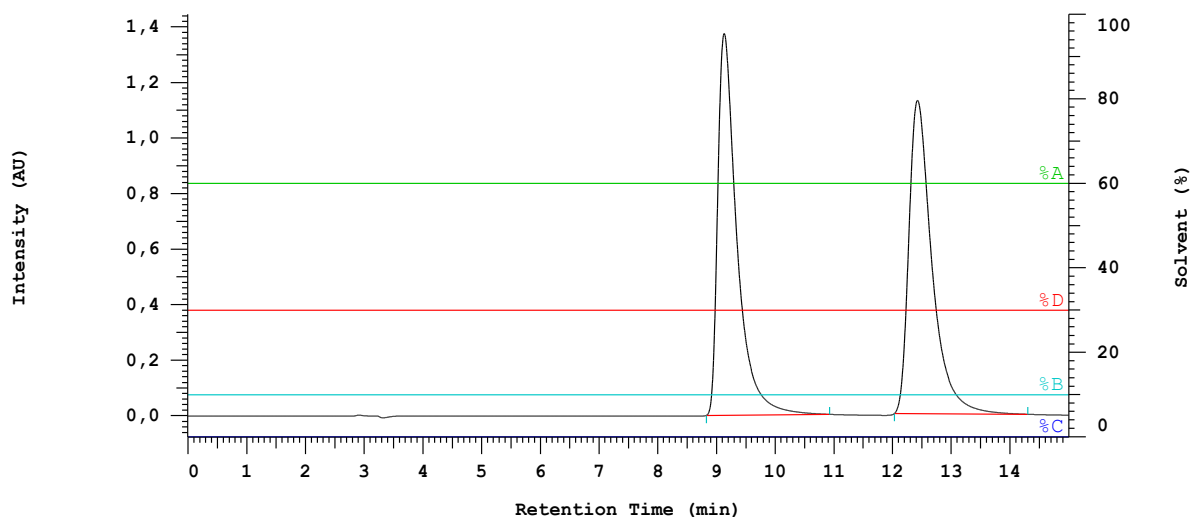


Figure 103. HPLC chromatogram of (±)-**342** (column, Daicel, Chiralpak-IA 250 mm × 20 mm; flow, 1 mL/min; detection, 254 nm; eluent, hexane/EtOAc/*i*PrOH 60:30:10). (-)-**342**: $t_R = 9.13$ min and (+)-**342**: $t_R = 12.42$ min. $T = 23$ °C.

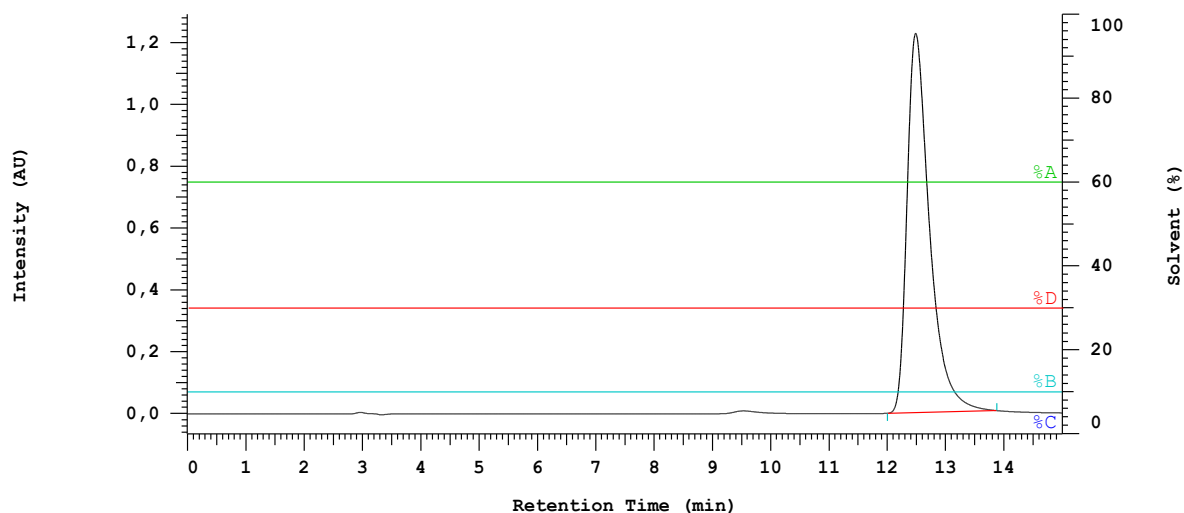


Figure 104. HPLC chromatogram of (+)-**342** (column, Daicel, Chiralpak-IA 250 mm \times 20 mm; flow, 1 mL/min; detection, 254 nm; eluent, hexane/EtOAc/*i*PrOH 60:30:10). (+)-**342**: $t_R = 12.48$ min (ee > 99%). $T = 23$ °C.

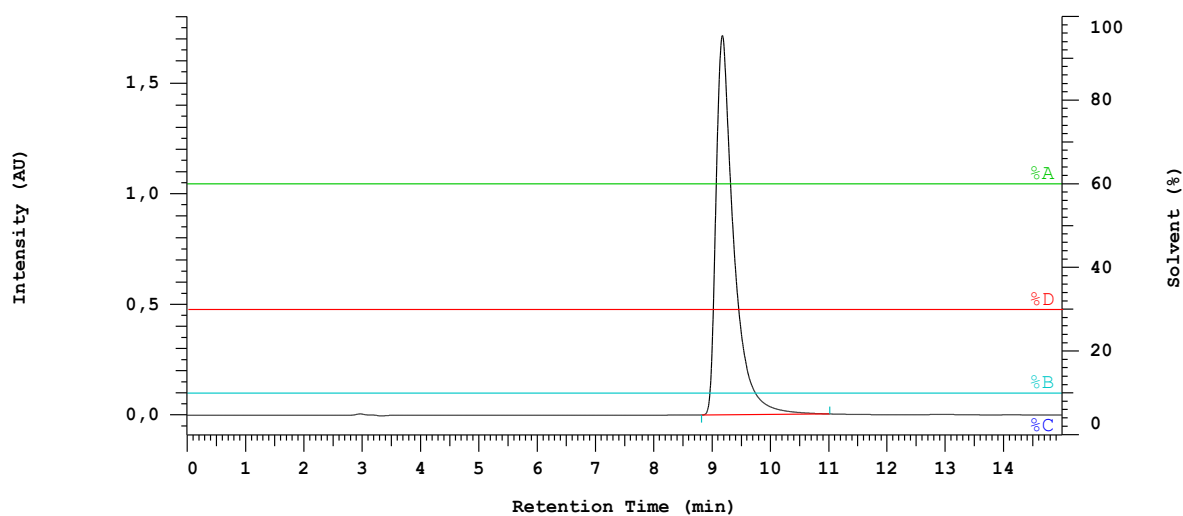


Figure 105. HPLC chromatogram of (-)-**342** (column, Daicel, Chiralpak-IA 250 mm \times 20 mm; flow, 1 mL/min; detection, 254 nm; eluent, hexane/EtOAc/*i*PrOH 60:30:10). (-)-**342**: $t_R = 9.18$ min (ee > 99%). $T = 23$ °C.

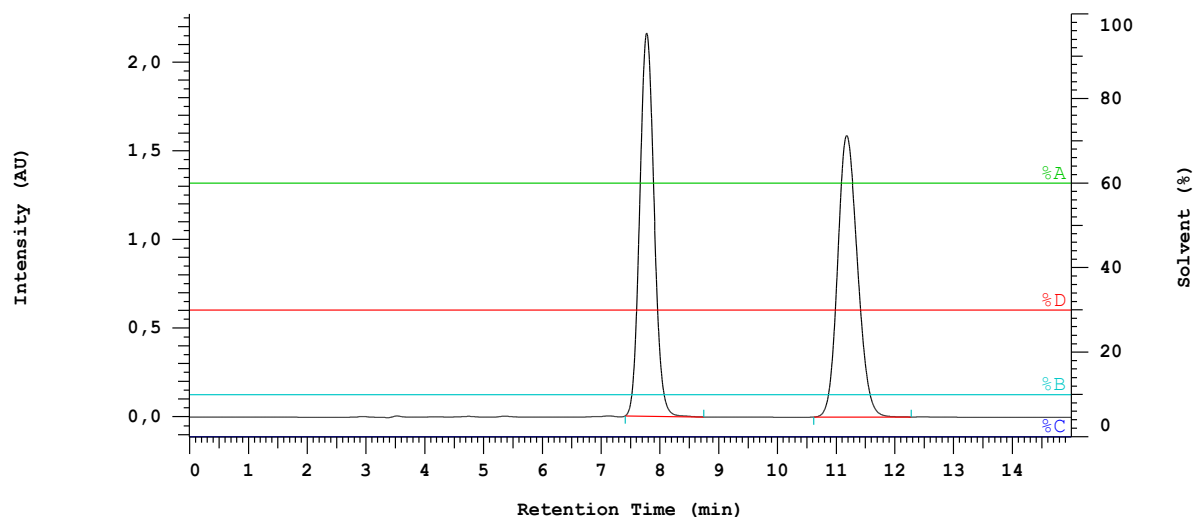


Figure 106. HPLC chromatogram of (±)-**348** (column, Daicel, Chiralpak-IA 250 mm × 20 mm; flow, 1 mL/min; detection, 254 nm; eluent, hexane/EtOAc/*i*PrOH 60:30:10). (–)-**348**: $t_R = 7.78$ min and (+)-**348**: $t_R = 11.18$ min. $T = 23$ °C.

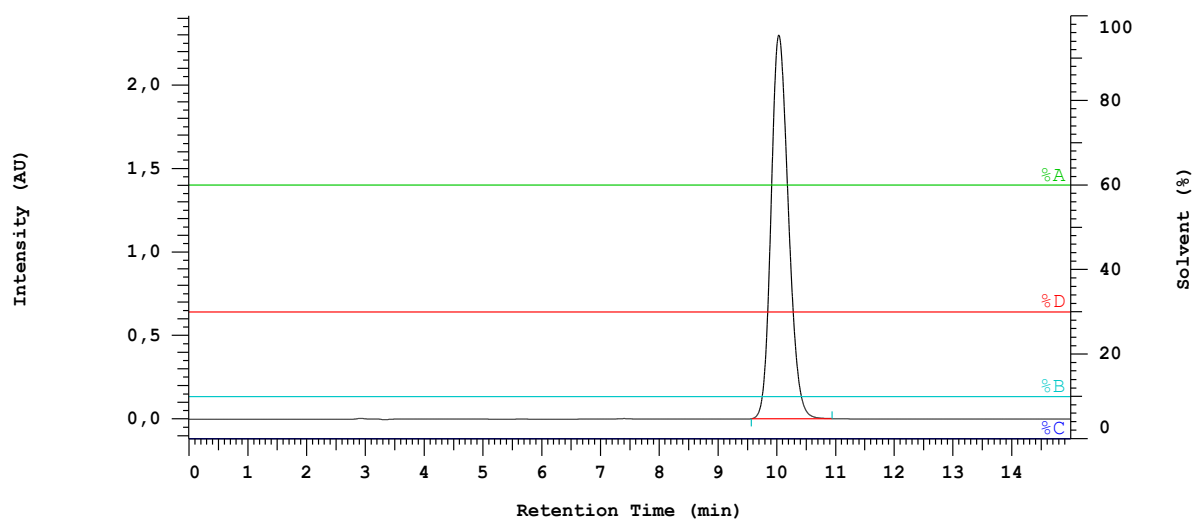


Figure 107. HPLC chromatogram of (+)-**348** (column, Daicel, Chiralpak-IA 250 mm × 20 mm; flow, 1 mL/min; detection, 254 nm; eluent, hexane/EtOAc/*i*PrOH 60:30:10). (+)-**348**: $t_R = 10.04$ min (ee > 99%). $T = 23$ °C.

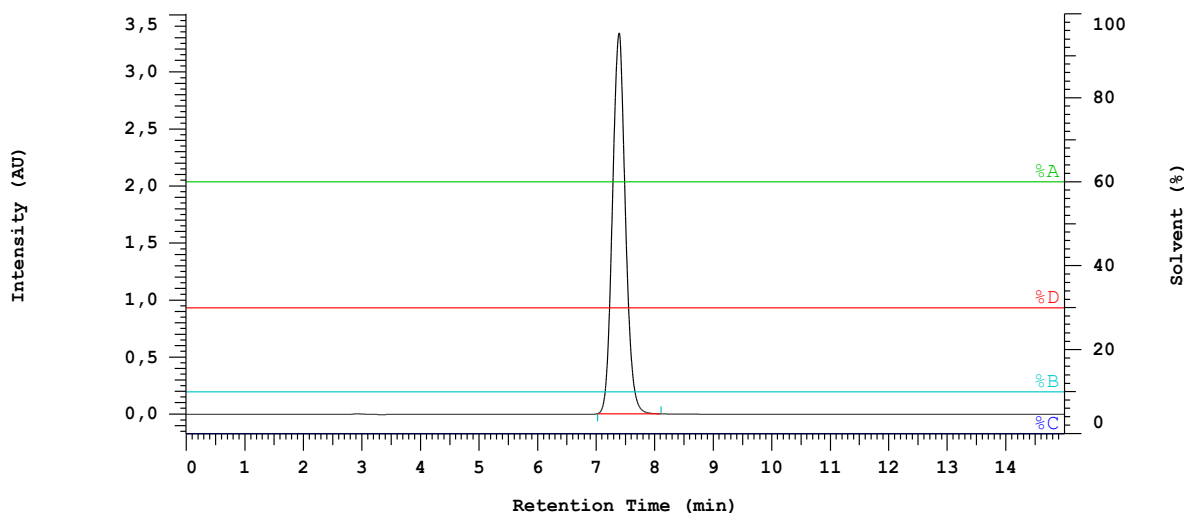


Figure 108. HPLC chromatogram of (-)-**348** (column, Daicel, Chiralpak-IA 250 mm × 20 mm; flow, 1 mL/min; detection, 254 nm; eluent, hexane/EtOAc/*i*PrOH 60:30:10). (-)-**348**: $t_R = 7.39$ min (ee > 99%). $T = 23$ °C.

8.2. Biological Assays and Co-crystallization with *Pv*SHMT

8.2.1. In Vitro Experiments

In Vitro Antimalarial Activity. *Plasmodium falciparum* drug-sensitive NF54 strain was cultivated in a variation of the medium previously described, consisting of RPMI 1640 supplemented with 0.5% ALBUMAX® II, 25 mM Hepes, 25 mM NaHCO₃ buffer (pH = 7.3), 0.36 mM hypoxanthine, and 100 µg/mL neomycin.^[283,284] Human erythrocytes served as host cells. Cultures were maintained in an atmosphere of 3% O₂, 4% CO₂, and 93% N₂ in modular chambers at 37 °C. Compounds were dissolved in DMSO (10 mg/mL), diluted in hypoxanthine-free culture medium, and titrated in duplicates over a 64-fold range in 96 well plates. Infected erythrocytes (1.25% final hematocrit and 0.3% final parasitemia) were added into the wells. After 48 h incubation, 0.25 µCi of [³H]hypoxanthine was added and plates were incubated for an additional 24 h. Parasites were harvested onto glass-fiber filters, and radioactivity was counted using a MicroBeta2 plate liquid scintillation counter (Perkin Elmer). The results were recorded and expressed as a percentage of the untreated controls. Fifty percent effective concentrations (EC₅₀) were estimated by linear interpolation.^[285]

Enzymatic *Pf*SHMT-Assay. Assay reactions (200 µL total volume) contained SHMT (~0.5 µM), L-serine (2 mM), (6*S*)-H₄F (0.4 mM), β-NADP⁺ (0.25 mM), and the coupling enzyme methylene tetrahydrofolate dehydrogenase (Fold, 5 µM) in 50 mM HEPES pH 7.0

containing 1 mM DTT and 0.5 mM EDTA. To this mixture, 1 μ L of inhibitors with various concentrations were added and initial rates of the reaction monitored to measure the activity of the enzyme. The inhibitors were dissolved in DMSO, and the control assays without inhibitor but in the presence of 0.5% DMSO (final concentration) were also carried out.

Enzymatic *At*SHMT-Assay. Assay reactions (200 μ L total volume) contained SHMT (1 μ g), L-serine (20 mM), (6*S*)-H₄F (0.3 mM), β -NAD⁺ (2 mM) and the coupling enzyme methylene tetrahydrofolate dehydrogenase (FOLD, 20 μ g) in 50 mM potassium phosphate buffer pH 7.4, containing 7.5 mM DTT. To this mixture, 10 μ L of inhibitors with various concentrations (final concentrations from 1–1000 nM) were added and initial rates of the reaction monitored to measure the amount of non-inhibited enzyme. The inhibitors were dissolved in 80% DMSO, and the control assays without inhibitor in the presence of 1% DMSO (final concentration) were also carried out. The accumulation of NADH was followed for 20 minutes at 340 nm using a BioTek Synergy HTX plate reader.

The metabolic stability assay was performed by incubating each test compound in human liver microsomes (XenoTech LLC, Lenexa, KS) along with appropriate co-factors at a substrate concentration of either 0.5 or 1 μ M and a microsomal protein concentration of 0.4 mg/mL using methods previously described.^[79] Loss of parent compound was monitored by LC/MS (Micromass Quattro Ultima Pt triple quadrupole or Micromass QTOF mass spectrometer coupled to an Alliance HPLC all from Waters) and intrinsic clearance values (*in vitro* CL_{int}) were calculated using the depletion rate constant. Hepatic blood clearance and the corresponding hepatic extraction ratio (E_H) were calculated using the well stirred model of hepatic extraction in each species, according to the "*in vitro* t_{1/2}" approach described by Obach.^[286]

In Vitro Cytotoxicity. Rat skeletal myoblasts cells (L6 cells) in RPMI 1640 medium with 10% FCS and 2 mM L-glutamine were added to each well of a 96-well microtiter plate and incubated at 37 °C under a 5% CO₂ atmosphere for 24 h. Compounds were added directly into the wells, and subsequently serial drug dilutions were prepared covering a range from 100–0.002 μ M. The plates were incubated for another 72 h. 10 μ L of Alamar Blue (12.5 mg resazurin dissolved in 100 mL water) were then added to each well and incubation continued for a further 1–4 h. The plates were read with a *Spectramax Gemini XS* microplate fluorometer (Molecular Devices Cooperation, Sunnyvale, CA, USA) using an excitation wavelength of

536 nm and an emission wavelength of 588 nm. Data were analyzed using the software *Softmax Pro* (Molecular Devices Cooperation, Sunnyvale, CA, USA). Decrease of fluorescence (= inhibition) was expressed as percentage of the fluorescence of control cultures and plotted against the drug concentrations. From the sigmoidal inhibition curves, the IC₅₀ values were calculated. Podophyllotoxin was used as positive control in the assay (IC₅₀ = 0.0082 μM).

hERG Inhibition. The method used was a modification of the method described previously.^[287] Briefly, hERG functional activity was measured in an inducible hERG T-RExTM-CHO Cell line (ThermoFisher #K1237) using thallium influx as a surrogate indicator of potassium ion channel activity. Thallium enhances the fluorescent signal of BTC-AM dye (ThermoFisher #B6791). A total of 384 well plates were seeded at 15,000 cells/well with doxycycline hyclate included to induce expression of the hERG channel and grown for 48 h. Media was removed, and cells were loaded with 4 μM dye for 90 mins in a low potassium buffer, dye removed, and compound added to the cells in a high potassium buffer in a 6 pt. 1:3 dilution dose response (top concentration of 30 μM final). Stock solutions of compounds in DMSO were prepared fresh. After 30 mins of compound incubation, channel activity was recorded upon addition of thallium buffer using a Tetra plate reader. The slope of the kinetic read was used to calculate channel activity.

Plasma Protein Binding Assessment via Ultracentrifugation. Mouse plasma from female Swiss outbred mice was collected inhouse under tissue harvesting protocols approved by the Monash Institute of Pharmaceutical Sciences Animal Ethics Committee. Plasma was stored frozen at -20 °C and thawed in a water bath maintained at 37 °C on the day of experiment. DMSO/acetonitrile/water solutions of each compound were spiked into aliquots of mouse plasma to a nominal compound concentration of 1000 ng/mL. The final DMSO and acetonitrile concentrations were 0.2% (v/v) and 0.4% (v/v), respectively. Spiked plasma samples were centrifuged (Beckman Ultracentrifuge Rotor type 42.2 Ti; 223,000 × g, 37 °C) for 4.2 h to separate proteins. This is a modification of a method reported previously by Nakai *et al.*,^[288] and was confirmed to result in >99.8% protein removal during in-house validation studies. An aliquot of protein-free supernate was analyzed by UPLC-MS (employing either a Xevo TQ or micromass Quattro Premier coupled to an Acquity UPLC all from Waters) to obtain the unbound concentration (C_{unbound}). Total compound concentrations in plasma (C_{total})

were determined in non-centrifuged samples incubated similarly in parallel for either 0.5 h and 4.2 h.

The unbound fraction (f_u) of (\pm)-**284** and (\pm)-**289** in mouse plasma was calculated using the average values for C_{total} and C_{unbound} as per the following equation:

$$f_u = \frac{C_{\text{unbound}}}{C_{\text{total}}}$$

A standard deviation (SD) for the f_u value determined within this experiment was calculated using the propagation of errors approach (which takes into account the standard deviations for replicate measurements of C_{total} and C_{unbound}) using the following equation:

$$SD_{f_u} = \sqrt{\left(\frac{SD_{\text{unbound}}}{C_{\text{unbound}}}\right)^2 + \left(\frac{SD_{\text{total}}}{C_{\text{total}}}\right)^2} \times \left(\frac{C_{\text{unbound}}}{C_{\text{total}}}\right)$$

The value for f_u was alternatively expressed as % bound using the following equation:

$$\% \text{ Bound} = (1 - f_u) \times 100\%$$

Partition coefficient values ($\log D_{7.4}$) of the test compounds were estimated by correlation of their chromatographic retention properties against the characteristics of a series of standard compounds with known partition coefficient values. The method employed is a gradient HPLC based derivation of the method developed by Lombardo *et al.*^[289]

8.2.2. *In Vivo* Experiments

Pharmacokinetics of (\pm)-281** in Male Sprague Dawley Rats Following IV Administration.**

The intravenous (IV) pharmacokinetics of (\pm)-**281** were studied in male Sprague Dawley rats (weight range 275–291 g) using study protocols reviewed and approved by the Monash Institute of Pharmaceutical Sciences Animal Ethics Committee. Animals were fasted overnight but free had access to water throughout the pre- and post-dose sampling period. Access to food was re-instated 4 h after dosing. Compound (\pm)-**281** was administered at 5 mg/kg as a 10 min constant rate infusion *via* an indwelling jugular vein cannula in 10% (v/v) DMSO/isotonic phosphate buffered saline (pH 6.5). Samples of arterial blood were collected up to 24 h post-dose into heparinized vials (at 4 °C) containing Complete® (a protease inhibitor cocktail), potassium fluoride, and EDTA to minimize potential for *ex vivo* degradation of (\pm)-**281** in blood/plasma samples. Once collected, blood samples were centrifuged, supernatant plasma was removed and stored frozen (–80 °C) until analysis by LC/MS. Total pooled urine was also

collected over the 24 h post-dose period and analyzed to obtain an estimate of urinary excretion. Plasma concentration versus time data (Figure 71) were analyzed using non-compartmental methods (PKSolver Version 2.0) and pharmacokinetic parameters are summarized in Figure 71b.

Plasmodium Falciparum Acute in Vivo Model. Mice (*NODscidIL2R γ ^{null}* mice, females, 20–22 g) are engrafted daily with 0.6 mL human blood i.v. in the tail for 14 days before use and are kept in individually ventilated cages (IVC), but otherwise under standard conditions with 22 °C and 60–70% relative humidity, pellets (PAB45 – NAFAG 9009, Provimi Kliba AG, CH-4303, Kaiseraugst, Switzerland) and water *ad libitum*. From a donor mouse with approximately 5–10% parasitemia (*Plasmodium falciparum* strain *Pf3D7^{0087/N9}*),^[139] heparinized blood (containing 100 microliter of 200 u/mL Heparin) is taken and diluted in physiological saline to 10⁸ parasitized erythrocytes per mL. Of this suspension, 0.2 mL is injected intravenously (i.v.) into experimental groups and a control group of n = 3–5 mice. Compounds are solubilised (suspended) in a solution consisting of 70% Tween-80 (d = 1.08 g/mL) and 30% ethanol (d = 0.81 g/mL), followed by a 10-fold dilution in H₂O. 3, 4, 5 and 6 days post-infection, the experimental groups are treated with a single daily dose by the oral (p.o.) route. The drug concentration is adjusted in a way that 10 mL/kg has to be injected. 3, 5, 6 and 7 days post-infection, 2 microliter tail blood is taken and parasitemia, as well as hematocrit, determined by FACS. On days 3–7, parasitemia is also determined by microscopy. The difference of the mean infection rate of the control group (= 100%) to the test group is calculated and expressed as percent reduction on day 7.

8.2.3. Co-crystallization with PvSHMT

Crystallization of Recombinant PvSHMT and Selected Ligands. PvSHMT (or C364A-PvSHMT) was crystallized using a microbatch method in a 60-well plate (\varnothing 1 mm at bottom of each well) covered with 6 mL of baby oil (Johnson; a mixture of mineral oil, olive oil, and vitamin E, PZ Johnson, Thailand). Protein–ligand complexes were prepared by mixing 60 μ L of purified PvSHMT protein (20–25 mg/mL) with 1 mM PLP, 60 mM β -mercaptoethanol, 90 mM of glycine, and 5.7 mM of the respective ligands. The mixture was equilibrated on ice for 30 min to allow complete complex formation. The crystallization drop was composed of 1 μ L each of a crystallization solution and the protein complex. Protein crystals of PvSHMT

were grown at 293 K in 20–24% w/v PEG4000, 0.06–0.12 M NaCl, 0.1 M Tris-HCl buffer pH 8.5.

***PvSHMT* Crystal Structure Data Collection, Structure Determination, and Refinement.**

A single crystal was flash-vitrified in liquid nitrogen using 20% glycerol in crystallizing agent as a cryoprotectant. X-ray diffraction data were collected at 100 K at wavelength of 1 Å using ADSC Quantum-315 CCD detector at beamline 13B1, NSRRC, Taiwan. Data were processed using the HKL2000 package. X-ray diffraction data and refinement statistics are available online.^[116,117,150] The structure of *PvSHMT* (or C364A-*PvSHMT*) was determined by molecular replacement using *Phaser* in CCP4 suite^[290] with a chain A protomer of *PvSHMT* coordinate (PDB code 4OYT)^[113] as the template. Model building and structure refinement were carried out using *Coot*^[291] and *Refmac5*.^[292] The ligand structure was prepared using *HYPERCHEM*.^[293]

9. Appendix

9. Appendix

9.1. Alignment of *At*SHMT with *Pf*- and *Pv*SHMT

The sequence of *At*SHMT (unpublished structure), *Pv*SHMT (PDB code 4O6Z) and *Pf*SHMT (PDB code 4TMR) were aligned using the online program PRALINE from the Centre for Integrative Bioinformatics VU of the university of Amsterdam.^[294]

Table 26. Results of the sequences alignment using PRALINE.

	Alignment <i>At</i> SHMT/ <i>Pf</i> SHMT	Alignment <i>At</i> SHMT/ <i>Pv</i> SHMT
Alignment score	5778.00	5614.00
Alignment score per aligned residue pair	12.53	12.70
Sequence identities	206	198
Percent sequence identity	45%	45%
Number of sequences	2	2
Alignment length	507	488
Number of residues	968	930
Number of gaps	46	46

9. Appendix

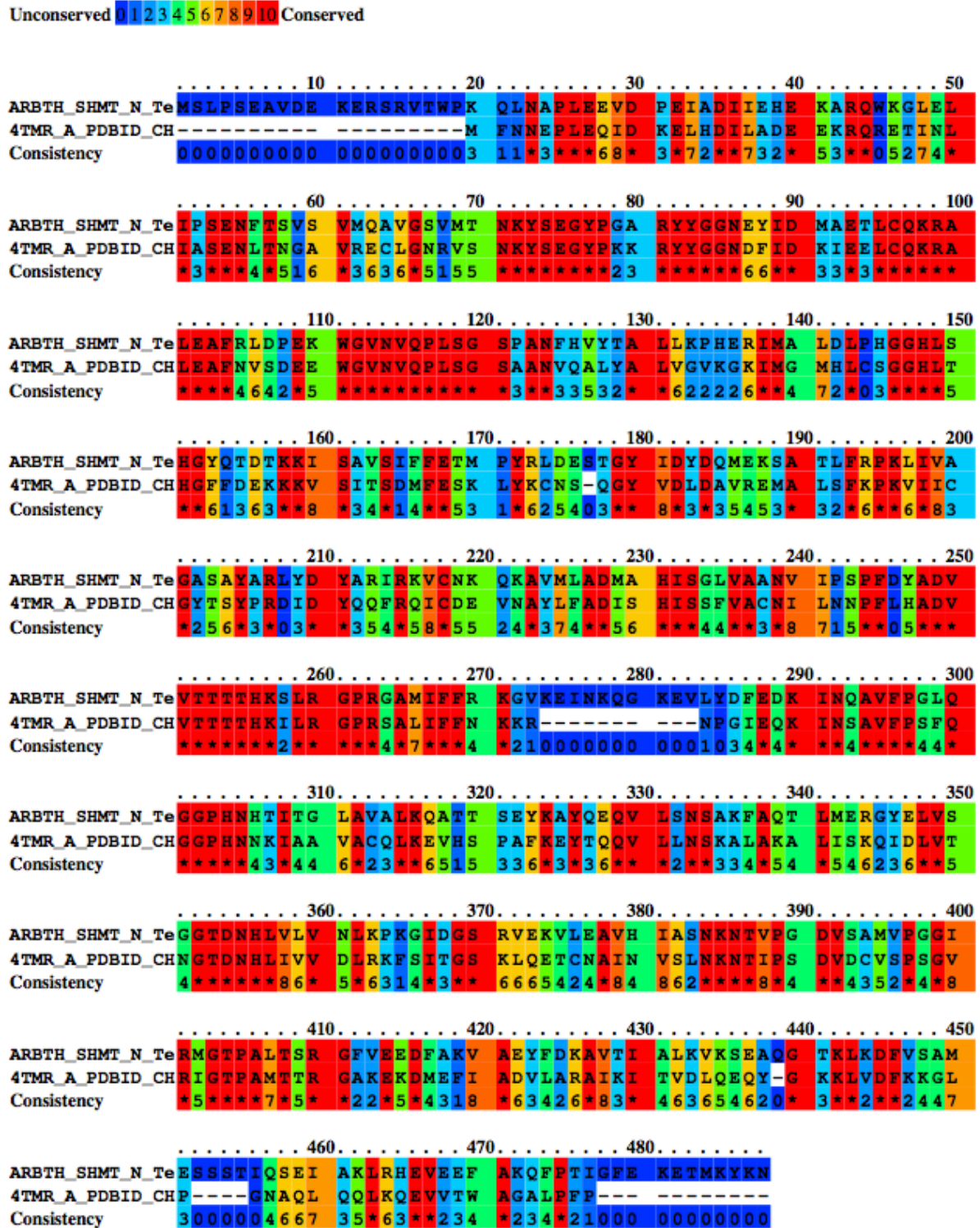


Figure 110. Amino acid conservation *AtSHMT/PvSHMT*.

9.2. Metabolites Identification from Ligands (±)-69, (±)-129, (±)-130, and (±)-151

In order to enhance metabolite formation and identification ligands (±)-69, (±)-129, (±)-130, and (±)-151 were incubated in human liver microsomes (XenoTech LLC, Lenexa, KS) at a higher substrate (50 μ M) and higher microsomal protein concentrations (1 mg/mL) than used for the metabolic stability assay described above. Following a 60 min incubation, supernatant samples were quenched using an equal volume of acetonitrile before analysis by LC/MS using conditions described in Table 27 below. Potential metabolites for each compound were searched for and identified using accurate mass monitoring and were confirmed by MS/MS fragmentation where possible. A summary of the structure-based metabolic transformations assessed for (±)-69, (±)-129, (±)-130, and (±)-151 is presented in Tables 28, 29, 31, and 33, respectively. To estimate the most abundant metabolite(s) and hence the site(s) most susceptible to metabolism, the metabolite profiles for each compound based on relative metabolite peak areas are presented in Tables 30, 32, and 34, however, it must be noted that metabolite profiles for (±)-69, (±)-129, (±)-130, and (±)-151 were calculated assuming comparable response factors for each component and authentic standards would be required for quantitative confirmation.

Table 27. LC/MS Analytical conditions for the sample analysis.

Instrument	Waters Micromass Xevo G2 QTOF coupled to a Waters Acquity UPLC
Detection	Positive mode electrospray ionisation under MS ^E acquisition mode
Cone/CID voltage	45 / 20-70 ((±)-69, (±)-129, (±)-130) 40 / 15-20 ((±)-151)
Column	Ascentis Express Amide column (50 × 2.1 mm, 2.7 μ m)
LC conditions	Gradient cycle time: 6 min; Injection volume: 5 μ L; Flow rate: 0.4 mL/min
Mobile phase	Acetonitrile-water gradient with 0.05% formic acid
Metabolite identification	Metabolites were confirmed by accurate mass and MS/MS fragmentation where possible

Table 28. Potential metabolites of (\pm)-**69** monitored in human liver microsomes under ESI positive ionization mode. D = detected, ND = not detected, t_R = retention time.

Metabolite Description	Δ Mass [Daltons]	$[M + H]^+$	D/ND	t_R [min]	Metabolite code
Parent ((\pm)- 69)	-	536	D	2.70	-
Mono-oxygenation	+16	552	D	2.36	M + 16 (I)
				2.64	M + 16 (II)
Ester Hydrolysis	-90	446	D	2.13	M - 90
Ester Hydrolysis	-427	109	ND	-	-
Nitrile Hydrolysis	+18	554	ND	-	-
Nitrile Hydrolysis	+19	555	ND	-	-
Dehydrogenation	-2	534	ND	-	-
Reduction	+2	538	ND	-	-
Mono-oxygenation + dehydrogenation	+14	550	ND	-	-
Bis-oxygenation	+32	568	ND	-	-
Bis-oxygenation + dehydrogenation	+30	566	ND	-	-

Table 29. Potential metabolites of (\pm)-**129** monitored in human liver microsomes under ESI positive ionization mode. D = detected, ND = not detected, t_R = retention time.

Metabolite Description	Δ Mass [Daltons]	$[M + H]^+$	D/ND	t_R [min]	Metabolite Code
(\pm)- 129	-	552	D	4.53	-
Reduction	+2	554	D	4.17	M + 2 (I)
				4.37	M + 2 (II)
				4.29	M + 16 (I)
Oxygenation	+16	568	D	4.35	M + 16 (II)
				4.48	M + 16 (III)
				4.33	M + 32 (I)
Bis-oxygenation	+32	584	D	4.44	M + 32 (II)
				4.41	M - 14
N-demethylation	-14	538	D	4.41	M - 14
Bis-N-demethylation	-28	524	D	4.31	M - 28
Dehydrogenation	-2	550	ND	-	-
Oxygenation & dehydrogenation	+14	566	ND	-	-
Methyl to acid	+30	582	ND	-	-
Primary amine deamination	+1	553	ND	-	-
Nitrile hydrolysis to amide	+18	570	ND	-	-
Nitrile hydrolysis to acid	+19	571	ND	-	-
Sulfonamide hydrolysis	-27	525	ND	-	-

Table 30. Metabolite profiles for (\pm)-**129** in NADPH-supplemented human liver microsomes after 60 minutes.

% Substrate Consumed	Relative Peak Area (as % of total metabolite peak area formed after 60 minutes)								
	<i>M</i> +2 (I)	<i>M</i> +2 (II)	<i>M</i> +16 (I)	<i>M</i> +16 (II)	<i>M</i> +16 (III)	<i>M</i> +32 (I)	<i>M</i> +32 (II)	<i>M</i> -14	<i>M</i> -28
50	< 1	12	1	< 1	50	< 1	< 1	33	3

Table 31. Potential metabolites of (\pm)-**130** monitored in human liver microsomes under ESI positive ionization mode. D = detected, ND = not detected, t_R = retention time.

Metabolite Description	Δ Mass [Daltons]	[<i>M</i> + H] ⁺	D/ND	t_R [min]	Metabolite Code
(\pm)- 130	–	555	D	4.53	–
Reduction	+2	557	D	4.17	<i>M</i> +2 (I)
				4.37	<i>M</i> +2 (II)
				4.29	<i>M</i> +16 (I)
Oxygenation	+16	571	D	4.35	<i>M</i> +16 (II)
				4.48	<i>M</i> +16 (III)
				4.33	<i>M</i> +32 (I)
Bis-oxygenation	+32	587	D	4.44	<i>M</i> +32 (II)
<i>N</i> -demethylation	-14	541	D	4.41	<i>M</i> -14
Bis- <i>N</i> -demethylation	-28	527	D	4.31	<i>M</i> -28
Dehydrogenation	-2	553	ND	–	–
Oxygenation & dehydrogenation	+14	569	ND	–	–
Methyl to acid	+30	585	ND	–	–
Primary amine deamination	+1	556	ND	–	–
Nitrile hydrolysis to amide	+18	573	ND	–	–
Nitrile hydrolysis to acid	+19	574	ND	–	–
Sulfonamide hydrolysis	-27	528	ND	–	–

Table 32. Metabolite profiles for (\pm)-**130** in NADPH-supplemented human liver microsomes after 60 minutes.

% Substrate Consumed	Relative Peak Area (as % of total metabolite peak area formed after 60 minutes)								
	<i>M</i> +2 (I)	<i>M</i> +2 (II)	<i>M</i> +16 (I)	<i>M</i> +16 (II)	<i>M</i> +16 (III)	<i>M</i> +32 (I)	<i>M</i> +32 (II)	<i>M</i> -14	<i>M</i> -28
50	< 1	12	1	< 1	51	< 1	< 1	33	3

Table 33. Potential metabolites of (\pm)-**151** monitored in human liver microsomes under ESI positive ionization mode. D = detected, ND = not detected, t_R = retention time.

Metabolite Description	Δ Mass [Daltons]	$[M + H]^+$	D/ND	t_R [min]	Metabolite Code
(\pm)- 151	–	366	D	4.30	–
				3.87	$M + 16$ (I)
Oxygenation	+16	382	D	3.97	$M + 16$ (II)
				4.25	$M + 16$ (III)
Bis-oxygenation	+32	398	D	3.90	$M + 32$ (I)
				4.22	$M + 32$ (II)
Dehydrogenation	–2	364	ND	–	–
Primary amine deamination	+1	367	ND	–	–
Reduction	+2	368	ND	–	–
Oxygenation & dehydrogenation	+14	380	ND	–	–
Nitrile hydrolysis to amide	+18	384	ND	–	–
Nitrile hydrolysis to acid	+19	385	ND	–	–
Chlorine displacement (Cl to OH)	–18	348	ND	–	–

Table 34. Metabolite profiles for (\pm)-**151** in NADPH-supplemented human liver microsomes after 60 minutes.

% Substrate Consumed	Relative Peak Area (as % of total metabolite peak area formed after 60 minutes) [#]				
	$M + 16$ (I)	$M + 16$ (II)	$M + 16$ (III)	$M + 32$ (I)	$M + 32$ (II)
57	4	11	83	2	< 1

9.3. In Vivo Efficacy Evaluation in SCID Mouse Models

Table 35. Average parasitemia values used for Figure 43.

Post-Inf. (Days)	Average %Para.			
	(\pm)- 200 4 \times 50 mg/kg p.o.	Chloroquine 4 \times 10 mg/kg p.o.	Chloroquine 4 \times 50 mg/kg p.o.	Control
0	0.01	0.01	0.01	0.01
1	-	-	-	-
2	-	-	-	-
3	1.77	1.16	2.40	2.35
4	2.18	1.47	0.78	3.59
5	5.79	0.12	0.17	7.08
6	9.90	0.02	0.02	17.25
7	13.43	0.00	0.00	18.00

Table 36. *In vivo* efficacy of (±)-**200** against *P. falciparum* Pf3D7^{0087/N9}. Shown are all values of parasitemia on day 7 post-infection.

Substances	Dosage [mg/kg]: 4 ×	Route	Parasitized		Avg.	% of control	% Activity
			RBC over 100 M1	RBC over 100 M2			
(±)- 200	50	p.o.	12.94	13.92	13.43	74.61	25.39
Control Day 7	-	-	17.80	18.20	18.00	-	-

9.4. AMES Study

All the results of the study and experimental details have been published in the *Journal of Medicinal Chemistry*.^[117] Herein are reported only the data for (±)-**281** on strain TA98 without metabolic activation.

Table 37. Raw plate counts and calculated mutagenicity data for (±)-**281**, mutation experiment 1 and 2 –S–9 on strain TA98.

Strain	Compound	Without metabolic activation					
		Conc. Level [μg/plate]	Mean	Standard Deviation	Fold Increase	Revertant Number per Plate	
TA98	DMSO	-	34.7	6.0	-	34, 29, 41	
	(±)- 281	5	31.0	7.1	0.9	36, 26	
		16	35.0	1.4	1.0	34, 36	
		50	33.0	17.0	1.0	21, 45	
		160	38.0	2.8	1.1	36, 40	
		500	48.5	0.7	1.4	49, 48	
		1600	49.0	1.4	1.4	48, 50	
		5000	103.0	31.1	3.0	125 S, 81 S	
		2NF	5	734.0	258.8	21.2	551, 917
TA98	DMSO	-	16.7	-	-	12, 9, 29	
	(±)- 281	156.3	26.5	-	1.6	29, 24	
		312.5	20.0	-	1.2	20, 20	
		625	28.0	-	1.7	37, 19	
		1250	47.5	-	2.9	50, 45	
		2500	64.5	-	3.9	62, 67	
		5000	92.0	-	5.5	88, 96	
		2NF	5	512.0	-	30.7	572, 452
		Positive control			Postfixes		
2NF	2-nitrofluorene		S	Slight thinning of background bacterial lawn			

Test article formulation. (±)-**281** was formulated in anhydrous analytical grade DMSO at a maximum concentration of 50.00 mg/mL, with appropriate dilutions performed in DMSO to provide final treatment concentrations over the range 5 to 5000 µg/plate. (±)-**281** was tested for mutation (and toxicity) using a plate incorporation treatment methodology, in the absence and presence of S-9. Appropriate vehicle and positive controls were included. As a positive result was observed following treatment with strain TA98 in the absence of S-9 in Experiment 1, (±)-**281** was further tested for mutation and toxicity using plate incorporation methodology, in the absence of S-9 in Experiment 2. Appropriate vehicle and positive controls were included.

Toxicity and precipitation. Following treatments of all the test strains in Experiment 1, evidence of toxicity in the form of a slight thinning of the background bacterial lawn was observed at 5000 µg/plate in strains TA98, TA100, TA1535 and TA102 in the absence and presence of S-9 and in strain TA1537 in the absence of S-9 only. The test article was completely soluble in the aqueous assay system at all concentrations tested.

Mutation. Following treatments of all the test strains in the absence and presence of S-9 in Experiment 1, treatment of strain TA98 in the absence of S-9 at 5000 µg/plate resulted in an increase in revertant colony numbers that was 3.0-fold greater than the concurrent vehicle controls. As this increase in revertant numbers was observed at a toxic concentration, Experiment 2 was performed in strain TA98 in the absence of S-9 only to verify this. Following Experiment 2 treatments, increases in revertant numbers of > 2-fold the concurrent vehicle controls were observed at 1250 µg/plate and above. As evidence of reproducibility was observed between experiments, the increases in revertants in strain TA98 in the absence of S-9 were considered as evidence of mutagenic activity in this assay. No other increases in revertant numbers were observed that were ≥ 1.5-fold (TA102), ≥ 2-fold (TA98 and TA100) or ≥ 3-fold (TA1535 and TA1537) the concurrent control. Data from the control treatments provided confirmation of the correct strain and assay functioning, and the study data were therefore accepted as valid.

9.5. Small Molecule X-ray Crystal Structures

Single crystalline samples were measured on a Bruker Kappa APEX-II Duo diffractometer with sealed tube Mo-K α radiation ($\lambda = 0.71073 \text{ \AA}$), a microfocus sealed tube Cu-K α radiation with mirror optics ($\lambda = 1.54178 \text{ \AA}$), or a Bruker/Nonius Kappa APEX II diffractometer with microfocus sealed tube Mo-K α radiation using mirror optics ($\lambda = 0.71073 \text{ \AA}$). All measurements were carried out at 100 K (unless specifically noted) using an Oxford Cryosystems program suite and corrected absorption effects using the multi-scan method (SADABS).^[295] The structures were solved using SHELXS,^[296] SHELXT,^[297] or Superflip^[298,299] and refined by full-matrix least-squares analysis (SHELXL)^[296,300] using the program package OLEX2.^[301] Data were corrected for absorption effects using the multi-scan method (SADABS).^[300] Unless otherwise indicated below, all non-hydrogen atoms were refined anisotropically and hydrogen atoms were constrained to ideal geometries and refined with fixed isotropic displacement parameters (in terms of a riding model). The structures were deposited in the CSD with the following CCDC access codes: 1032749 ((\pm)-**71**), 1515139 ((\pm)-**112**), 1515140 ((\pm)-**209**), 1515141 ((\pm)-**215**), 1546904 ((\pm)-**221**), 1546905 ((\pm)-**229**), 1546906 ((\pm)-**231**), 1546907 ((\pm)-**236**), 1546908 ((\pm)-**269**), 1577720 (**316**), and 1577716 ((\pm)-**328**).

Crystal Data for (±)-71

Crystal data at 100 K for $C_{25}H_{24}N_6O_2S$, $M = 472.56 \text{ g mol}^{-1}$, triclinic, space group $P\bar{1}$, $a = 9.096(3) \text{ \AA}$, $b = 10.603(3) \text{ \AA}$, $c = 12.824(4) \text{ \AA}$, $\alpha = 76.544(8)^\circ$, $\beta = 86.026(8)^\circ$, $\gamma = 72.249(8)^\circ$, $V = 1145.6(6) \text{ \AA}^3$, $Z = 2$, $D_c = 1.370 \text{ g/cm}^3$, $\mu(\text{MoK}\alpha) = 0.178 \text{ mm}^{-1}$. Colorless crystal (linear dimensions approx. $0.16 \text{ mm} \times 0.14 \text{ mm} \times 0.03 \text{ mm}$) were grown from slow evaporation of THF/hexane solution at $23 \text{ }^\circ\text{C}$. Number of measured and unique reflections 14658 and 3692, respectively ($R_{\text{int}} = 0.0446$). Final $R_1 = 0.0617$, $wR_2 = 0.1629$ for 2618 independent reflections with $I > 2\sigma(I)$, 279 parameters and $3.266 < 2\theta < 48.744^\circ$ (corresponding R values based on all 3692 reflections are 0.0617 and 0.1823, respectively).

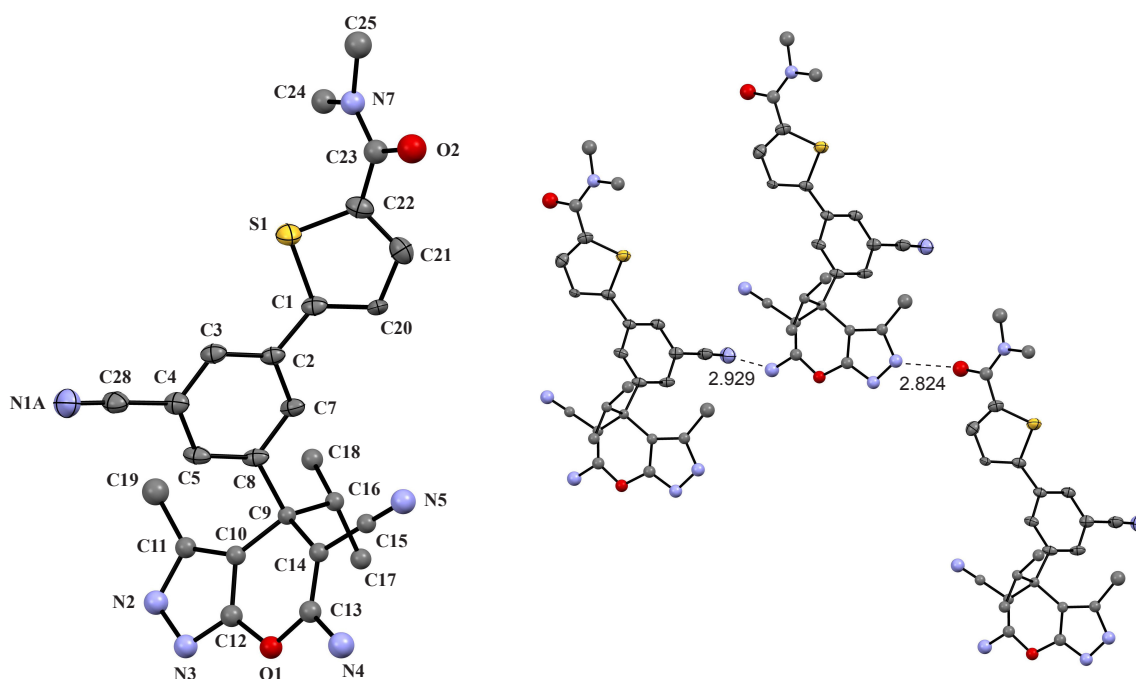


Figure 111. ORTEP plot of (±)-71, arbitrary numbering, H-atoms are omitted for clarity. Atomic displacement parameters at 100 K are drawn at 50% probability level. Selected bond lengths (\AA), angles ($^\circ$), and torsional angles ($^\circ$): S1–C1 1.711(4), S1–C22 1.387(4), N1A–C28 1.148(5), O1–C12 1.387(13), O1–C13 1.353(14), O2–C23 1.288(19), N2–N3 **1.366(13)**, N2–C11 **1.391(15)**, N3–C12 **1.332(15)**, N4–C13 1.371(15), N5–C15 1.121(2), N7–C23 1.319(19), N7–C24 1.467(17), N7–C25 1.458(17), C10–C11 1.385(14), C16–C9–C8 113.7(8), S1–C1–C2–C3 $-22.6(4)$, S1–C22–C23–O2 126.1(11), C8–C9–C16–C18 50.5(11).

Crystal Data for (±)-112

Crystal data at 100 K for $C_{54}H_{59}N_{10}O_4S_2$, $M = 976.23 \text{ g mol}^{-1}$, monoclinic, space group $P2_1$, $a = 11.664(3) \text{ \AA}$, $b = 16.775(4) \text{ \AA}$, $c = 13.975(3) \text{ \AA}$, $\alpha = 90^\circ$, $\beta = 105.749(5)^\circ$, $\gamma = 90^\circ$, $V = 2631.9(10) \text{ \AA}^3$, $Z = 2$, $D_c = 1.232 \text{ g/cm}^3$, $\mu(\text{MoK}\alpha) = 0.156 \text{ mm}^{-1}$. Colorless crystal (linear dimensions approx. $0.30 \text{ mm} \times 0.24 \text{ mm} \times 0.16 \text{ mm}$) were grown from slow evaporation of $\text{CH}_2\text{Cl}_2/\text{hexane}$ solution at 23°C . Number of measured and unique reflections 23320 and 11615, respectively ($R_{\text{int}} = 0.0236$). Final $R_1 = 0.0511$, $wR_2 = 0.1340$ for 10624 independent reflections with $I > 2\sigma(I)$, 687 parameters and $3.028 < 2\theta < 55.1^\circ$ (corresponding R values based on all 11615 reflections are 0.0511 and 0.1340, respectively).

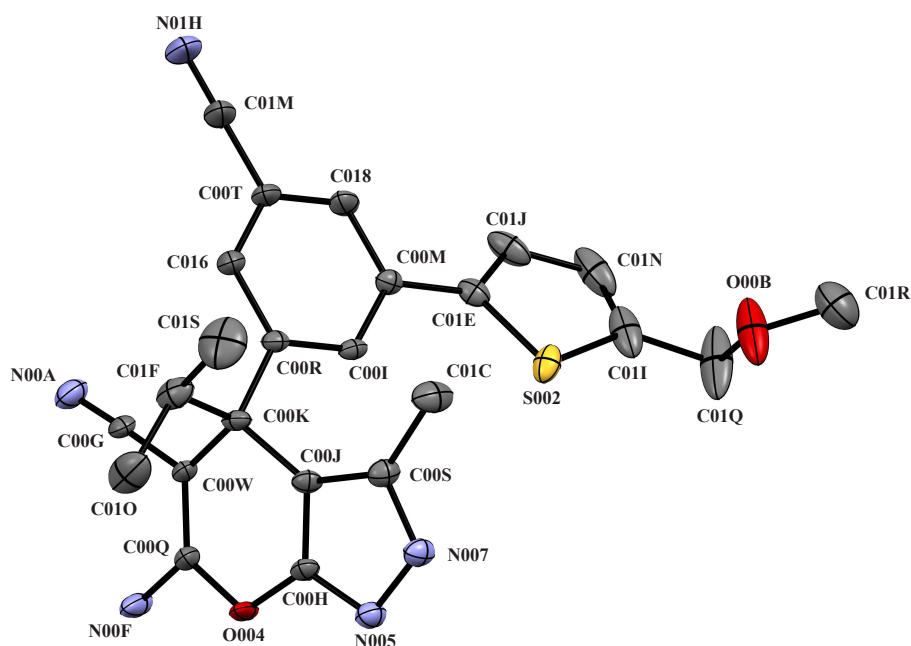


Figure 112. ORTEP plot of (±)-112, arbitrary numbering, H-atoms are omitted for clarity. Atomic displacement parameters at 100 K are drawn at 50% probability level. Selected bond lengths (\AA), angles ($^\circ$), and torsional angles ($^\circ$): $\text{S002-C01E } 1.721(4)$, $\text{S002-C01I } 1.739(5)$, $\text{O004-C00H } 1.372(4)$, $\text{O004-C00Q } 1.371(4)$, $\text{N005-N007 } 1.371(4)$, $\text{N005-C00H } 1.320(4)$, $\text{N007-C00S } 1.353(5)$, $\text{N00A-C00G } 1.154(5)$, $\text{N00F-CC00Q } 1.349(5)$, $\text{N01H-C01M } 1.147(5)$, $\text{C00H-C00J } 1.396(4)$, $\text{C00J-C00K } 1.520(5)$, $\text{C00K-C00W } 1.535(5)$, $\text{C00J-C00S } 1.389(5)$, $\text{C00Q-C00W } 1.367(5)$, $\text{C00R-C00K-C01F } 112.1(3)$, $\text{S002-C01I-C01Q-O00B } -63.3$, $\text{S002-C01E-C00M-C00I } -26.2$.

Crystal Data for (±)-209

Crystal data at 100 K for $C_{24}H_{22}F_3N_5O$, $M = 453.47 \text{ g mol}^{-1}$, triclinic, space group $P-1$, $a = 11.389(4) \text{ \AA}$, $b = 11.456(3) \text{ \AA}$, $c = 12.388(4) \text{ \AA}$, $\alpha = 72.397(8)^\circ$, $\beta = 70.668(8)^\circ$, $\gamma = 68.692(9)^\circ$, $V = 1390.0(7) \text{ \AA}^3$, $Z = 1$, $D_c = 1.342 \text{ g/cm}^3$, $\mu(\text{MoK}\alpha) = 0.101 \text{ mm}^{-1}$. Colorless crystal (linear dimensions approx. $0.10 \text{ mm} \times 0.08 \text{ mm} \times 0.07 \text{ mm}$) were grown from slow evaporation of THF solution at 23°C . Number of measured and unique reflections 23465 and 6397, respectively ($R_{\text{int}} = 0.0313$). Final $R_1 = 0.0476$, $wR_2 = 0.1267$ for 5120 independent reflections with $I > 2\sigma(I)$, 450 parameters and $4.666 < 2\theta < 55.192^\circ$ (corresponding R values based on all 6397 reflections are 0.0476 and 0.1267, respectively).

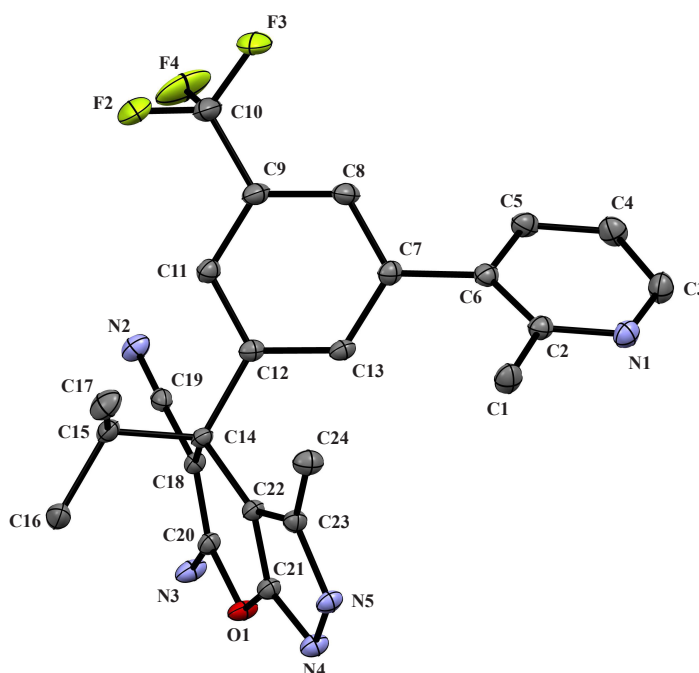


Figure 113. ORTEP plot of (±)-209, arbitrary numbering, H-atoms are omitted for clarity. Atomic displacement parameters at 100 K are drawn at 50% probability level. Selected bond lengths (\AA), angles ($^\circ$), and torsional angles ($^\circ$): F2–C10 1.341(2), O1–C20 1.700(17), O1–C21 1.3718(18), N1–C2 1.347(2), N1–C3 1.343(2), N2–C19 1.152(2), N3–C20 1.349(2), N4–N5 1.3604(18), N4–C21 1.3220(19), N5–C23 1.3534(19), C1–C2 1.507(2), C14–C18 1.541(2), C14–C22 1.5133(19), C18–C20 1.364(2), C21–C22 1.394(2), C22–C23 1.395(2), C12–C14–C15 112.74(12), C13–C7–C6–C2 49.4(2).

Crystal Data for (±)-215

Crystal data at 100 K for $C_{27}H_{22}F_3N_5O$, $M = 489.50 \text{ g mol}^{-1}$, monoclinic, space group $P2_1/c$, $a = 20.4652(10) \text{ \AA}$, $b = 9.7295(6) \text{ \AA}$, $c = 21.3194(13) \text{ \AA}$, $\alpha = 90^\circ$, $\beta = 137.384(2)^\circ$, $\gamma = 90^\circ$, $V = 2874.3(3) \text{ \AA}^3$, $Z = 4$, $D_c = 1.327 \text{ g/cm}^3$, $\mu(\text{MoK}\alpha) = 0.275 \text{ mm}^{-1}$. Colorless crystal (linear dimensions approx. $0.38 \text{ mm} \times 0.32 \text{ mm} \times 0.08 \text{ mm}$) were grown from slow evaporation of $\text{CH}_2\text{Cl}_2/\text{hexane}$ solution at 23°C . Number of measured and unique reflections 49705 and 6598, respectively ($R_{\text{int}} = 0.0527$). Final $R_1 = 0.0802$, $wR_2 = 0.2270$ for 5019 independent reflections with $I > 2\sigma(I)$, 406 parameters and $4.01 < 2\theta < 54.968^\circ$ (corresponding R values based on all 6598 reflections are 0.0802 and 0.2270, respectively).

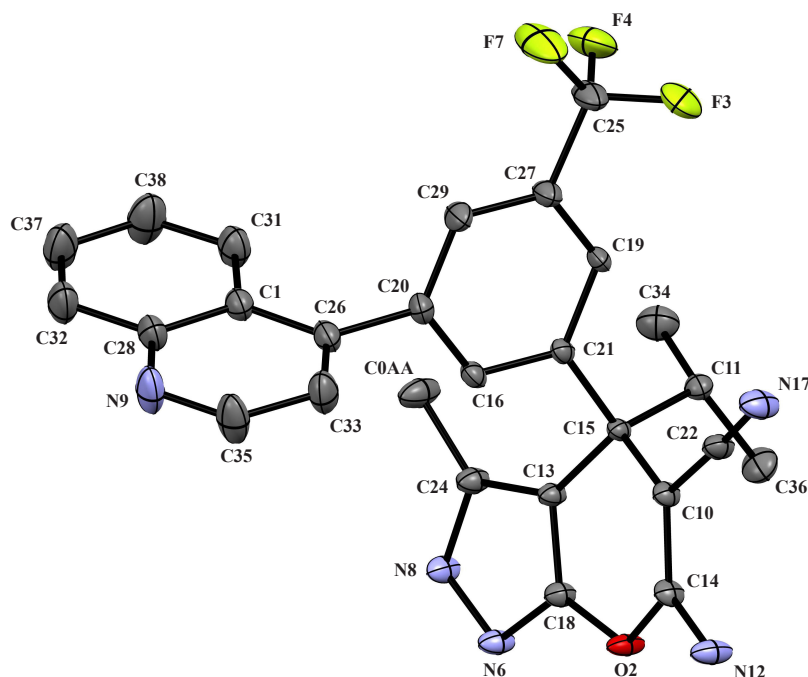


Figure 114. ORTEP plot of (±)-215, arbitrary numbering, H-atoms are omitted for clarity. Atomic displacement parameters at 100 K are drawn at 50% probability level. Selected bond lengths (\AA), angles ($^\circ$), and torsional angles ($^\circ$): F3–C25 1.327(4), O2–C14 1.362(3), O2–C18 1.366(3), N6–N8 1.361(3), N6–C18 1.314(3), N8–C24 1.348(4), N9–C28 1.362(4), N9–C35 1.306(4), N12–C14 1.326(4), N17–C22 1.146(4), C10–C14 1.368(4), C10–C15 1.534(3), C13–C15 1.498(3), C13–C18 1.386(4), C13–C24 1.393(4), C21–C15–C11 112.6(2), C16–C20–C26–C33 $-76.7(4)$.

Crystal Data for (±)-221

Crystal data at 100 K for $C_{24}H_{20}BrF_3N_4O$, $M = 517.40 \text{ g mol}^{-1}$, monoclinic, space group $C2/c$, $a = 38.787(4) \text{ \AA}$, $b = 9.8919(11) \text{ \AA}$, $c = 14.1063(15) \text{ \AA}$, $\alpha = 90^\circ$, $\beta = 99.703(3)^\circ$, $\gamma = 90^\circ$, $V = 5334.8(10) \text{ \AA}^3$, $Z = 8$, $D_c = 1.288 \text{ g/cm}^3$, $\mu(\text{MoK}\alpha) = 1.583 \text{ mm}^{-1}$. Colorless crystal (linear dimensions approx. $0.28 \text{ mm} \times 0.19 \text{ mm} \times 0.07 \text{ mm}$) were grown from slow evaporation of $\text{CH}_2\text{Cl}_2/\text{hexane}$ solution at 23°C . Number of measured and unique reflections 23037 and 6144, respectively ($R_{\text{int}} = 0.0380$). Final $R_1 = 0.0569$, $wR_2 = 0.1745$ for 4742 independent reflections with $I > 2\sigma(I)$, 366 parameters and $4.254 < 2\theta < 55.192^\circ$ (corresponding R values based on all 6144 reflections are 0.0569 and 0.1745, respectively). The structure contains unidentified disordered solvent molecules, thus a masked refinement was performed (OLEX2). The CF_3 -group is strongly disordered and the F-atom positions were described by three partially occupied orientations. The heterocyclic part of the molecule is disordered too, resulting in ellipsoids with large differences of the main axes. Overall crystal quality was poor, the data described herein represents the best of several tested samples.

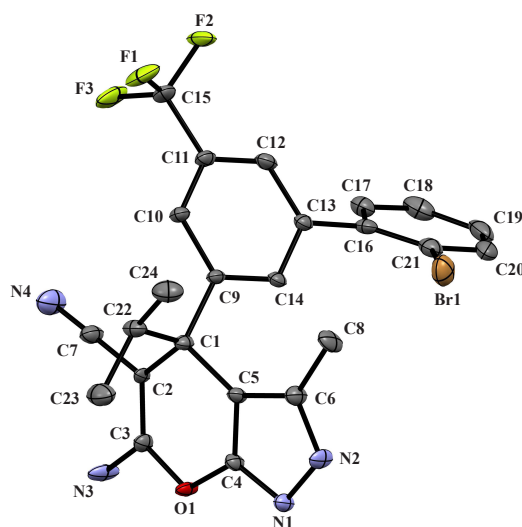


Figure 115. ORTEP plot of (±)-221, arbitrary numbering, H-atoms are omitted for clarity. Atomic displacement parameters at 100 K are drawn at 50% probability level. Selected bond lengths (\AA), angles ($^\circ$), and torsion angles ($^\circ$): $\text{Br1-C21 } 1.893(4)$, $\text{N1-N2 } 1.362(4)$, $\text{N1-C4 } 1.324(4)$, $\text{N2-C6 } 1.333(4)$, $\text{N3-C3 } 1.334(4)$, $\text{N4-C7 } 1.140(5)$, $\text{O1-C3 } 1.354(3)$, $\text{O1-C4 } 1.368(4)$, $\text{C1-C2 } 1.539(4)$, $\text{C1-C5 } 1.510(4)$, $\text{C2-C3 } 1.367(4)$, $\text{C2-C7 } 1.420(4)$, $\text{C4-C5 } 1.387(4)$, $\text{C5-C6 } 1.404(4)$, $\text{C22-C1-C9 } 113.5(3)$, $\text{C14-C13-C16-C21 } 57.5(5)$.

Crystal Data for (±)-229

Crystal data at 100 K for $C_{26}H_{26}F_3N_5O_3S$, $M = 545.58 \text{ g mol}^{-1}$, monoclinic, space group $P2_1/c$, $a = 22.7123(7) \text{ \AA}$, $b = 9.6826(3) \text{ \AA}$, $c = 14.1227(4) \text{ \AA}$, $\alpha = 90^\circ$, $\beta = 98.1350(10)^\circ$, $\gamma = 90^\circ$, $V = 3074.53(16) \text{ \AA}^3$, $Z = 4$, $D_c = 1.179 \text{ g/cm}^3$, $\mu(\text{MoK}\alpha) = 0.156 \text{ mm}^{-1}$. Colorless crystal (linear dimensions approx. $0.24 \text{ mm} \times 0.13 \text{ mm} \times 0.10 \text{ mm}$) were grown from slow evaporation of THF/ CH_2Cl_2 solution at 23°C . Number of measured and unique reflections 28903 and 7072, respectively ($R_{\text{int}} = 0.0357$). Final $R_1 = 0.0515$, $wR_2 = 0.1511$ for 5041 independent reflections with $I > 2\sigma(I)$, 357 parameters and $4.58 < 2\theta < 55.1^\circ$ (corresponding R values based on all 7072 reflections are 0.0515 and 0.1511, respectively). The structure contains unidentified disordered solvent molecules, thus a masked refinement was performed (OLEX2).

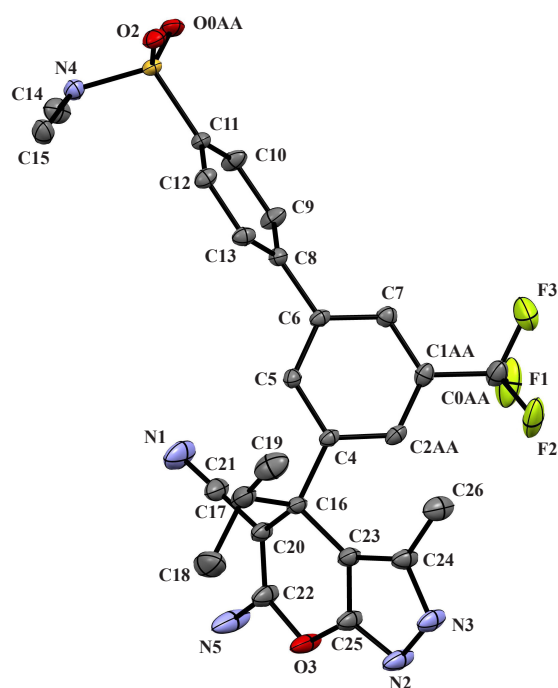


Figure 116. ORTEP plot of (±)-229, arbitrary numbering, H-atoms are omitted for clarity. Atomic displacement parameters at 100 K are drawn at 50% probability level. Selected bond lengths (\AA), angles ($^\circ$), and torsion angles ($^\circ$): S1–O2 1.4308(14), S1–O0AA 1.4327(13), S1–N4 1.6362(17), S1–C11 1.7664(18), F1–C0AA 1.313(3), N1–C21 1.152(3), N2–N3 1.362(3), N2–C25 1.313(3), N3–C24 1.343(3), N4–C14 1.472(3), O3–C22 1.360(3), O3–C25 1.370 (3), C16–C20 1.543(3), C16–C23 1.506(3), C20–C22 1.361(3), C23–C24 1.383(3), C23–C25 1.397(3), O2–S1–O0AA $119.80(8)$, C4–C16–C17 $112.02(15)$, N4–S1–C11–C10 $96.66(16)$, N4–S1–C11–C12 $-83.09(16)$, C9–C8–C6–C7 $51.9(3)$.

Crystal Data for (±)-231

Crystal data at 100 K for $C_{28.5}H_{29}Cl_3F_6N_5O_3S$, $M = 741.98 \text{ g mol}^{-1}$, triclinic, space group $P-1$, $a = 9.7486(6) \text{ \AA}$, $b = 11.7562(7) \text{ \AA}$, $c = 14.6615(9) \text{ \AA}$, $\alpha = 92.403(3)^\circ$, $\beta = 95.931(3)^\circ$, $\gamma = 104.298(3)^\circ$, $V = 1615.57(17) \text{ \AA}^3$, $Z = 2$, $D_c = 1.525 \text{ g/cm}^3$, $\mu(\text{MoK}\alpha) = 0.423 \text{ mm}^{-1}$. Colorless crystal (linear dimensions approx. $0.24 \text{ mm} \times 0.20 \text{ mm} \times 0.10 \text{ mm}$) were grown from slow evaporation of CH_2Cl_2 solution at 23°C . Number of measured and unique reflections 27810 and 7453, respectively ($R_{\text{int}} = 0.0325$). Final $R_1 = 0.0521$, $wR_2 = 0.1321$ for 5749 independent reflections with $I > 2\sigma(I)$, 469 parameters and $4.392 < 2\theta < 55.144^\circ$ (corresponding R values based on all 7453 reflections are 0.0521 and 0.1321, respectively). The asymmetric unit contains two disordered CH_2Cl_2 , one of which is split over two positions and additionally disordered about the inversion center. Both disordered sites could be modelled, but strong restraints were necessary.

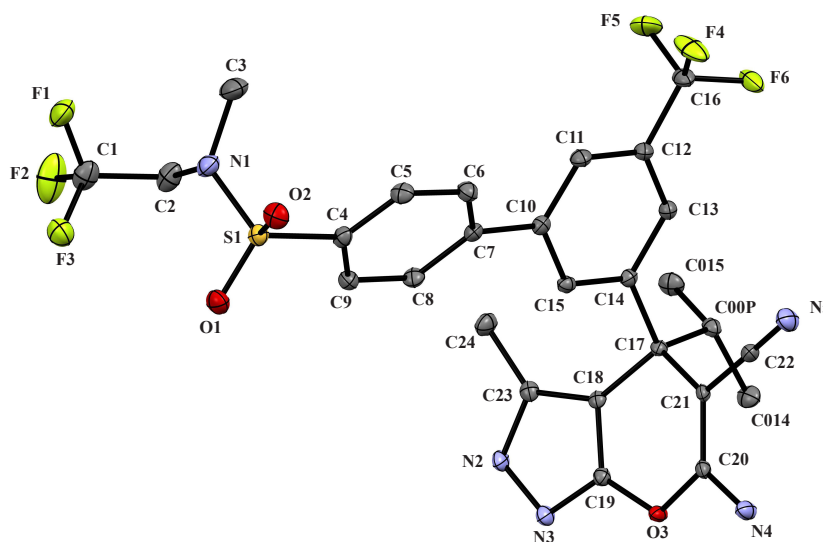


Figure 117. ORTEP plot of (±)-231, arbitrary numbering, H-atoms and the disordered CH_2Cl_2 molecule are omitted for clarity. Atomic displacement parameters at 100 K are drawn at 50% probability level. Selected bond lengths (\AA), angles ($^\circ$), and torsion angles ($^\circ$): S1–O1 1.4284(17), S1–O2 1.4256(17), S1–N1 1.638(2), S1–C4 1.760(2), F1–C1 1.341(3), F4–C16 1.339(3), N2–N3 1.362(3), N2–C23 1.351(3), N3–C19 1.317(3), N4–C20 1.329(3), N5–C22 1.149(3), O3–C19 1.366(3), O3–C20 1.363(3), C17–C18 1.505(3), C17–C21 1.536(3), C18–C19 1.394(3), C18–C23 1.384(3), C20–C21 1.368(3), O2–S1–O1 121.20(10), C14–C17–C00P 112.09(17), N1–S1–C4–C5 $-87.5(2)$, N1–S1–C4–C9 $90.9(2)$, C11–C10–C7–C6 $30.3(3)$.

Crystal Data for (±)-236

Crystal data at 100 K for $C_{33}H_{38}Cl_2F_3N_5O_3S$, $M = 712.64 \text{ g mol}^{-1}$, triclinic, space group $P-1$, $a = 9.7725(3) \text{ \AA}$, $b = 11.1037(4) \text{ \AA}$, $c = 16.9521(8) \text{ \AA}$, $\alpha = 93.995(4)^\circ$, $\beta = 106.743(3)^\circ$, $\gamma = 94.322(3)^\circ$, $V = 1748.43(12) \text{ \AA}^3$, $Z = 2$, $D_c = 1.354 \text{ g/cm}^3$, $\mu(\text{MoK}\alpha) = 2.712 \text{ mm}^{-1}$. Colorless crystal (linear dimensions approx. $0.12 \text{ mm} \times 0.015 \text{ mm} \times 0.005 \text{ mm}$) were grown from slow evaporation of CH_2Cl_2 /hexane solution at 23°C . Number of measured and unique reflections 22357 and 6048, respectively ($R_{\text{int}} = 0.1104$). Final $R_1 = 0.0679$, $wR_2 = 0.1896$ for 3082 independent reflections with $I > 2\sigma(I)$, 487 parameters and $5.468 < 2\theta < 133.53^\circ$ (corresponding R values based on all 6048 reflections are 0.0679 and 0.1896, respectively).

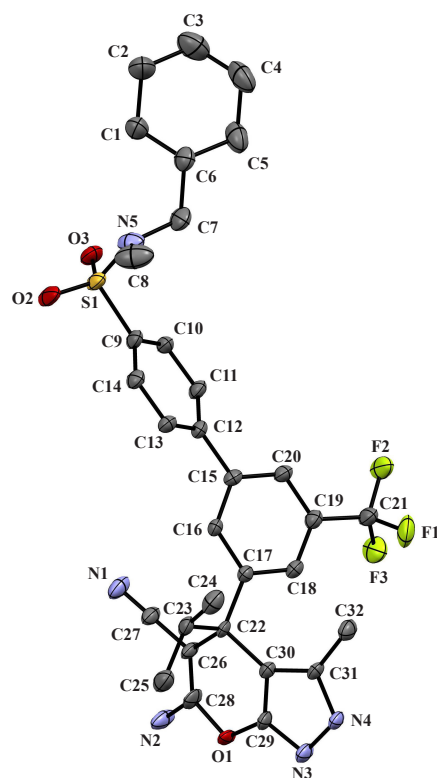


Figure 118. ORTEP plot of (±)-236, arbitrary numbering, H-atoms and the disordered CH_2Cl_2 molecule are omitted for clarity. Atomic displacement parameters at 100 K are drawn at 50% probability level. Selected bond lengths (\AA), angles ($^\circ$), and torsion angles ($^\circ$): S1–O2 1.427(3), S1–O3 1.424(3), S1–N5 1.631(4), S1–C9 1.758(4), F1–C21 1.348(5), N1–C27 1.150(5), N2–C28 1.358(10), N3–N4 1.372(4), N3–C29 1.317(4), N4–C31 1.355(4), N5–C7 1.477(5), O1–C28 1.363(9), O1–C29 1.401(9), C1–C2 1.532(7), C2–C3 1.514(7), C26–C27 1.418(5), C22–C26 1.548(5), C22–C30 1.511(4), C26–C28 1.351(11), C29–C30 1.377(5), C30–C31 1.383(5), O3–S1–O2 119.9(2), C17–C22–C23 112.5(3), N5–S1–C9–C10 $-98.1(4)$, N5–S1–C9–C14 79.9(4), C11–C12–C15–C20 38.2(5).

Crystal Data for (±)-269

Crystal data at 100 K for $C_{42}H_{48}Cl_4F_6N_{10}O_6S_2$, $M = 1108.82 \text{ g mol}^{-1}$, triclinic, space group $P-1$, $a = 10.4435(14) \text{ \AA}$, $b = 14.920(2) \text{ \AA}$, $c = 16.658(2) \text{ \AA}$, $\alpha = 98.908(5)^\circ$, $\beta = 103.069(5)^\circ$, $\gamma = 100.227(5)^\circ$, $V = 2436.2(6) \text{ \AA}^3$, $Z = 2$, $D_c = 1.512 \text{ g/cm}^3$, $\mu(\text{MoK}\alpha) = 0.410 \text{ mm}^{-1}$. Colorless crystal (linear dimensions approx. $0.32 \text{ mm} \times 0.28 \text{ mm} \times 0.08 \text{ mm}$) were grown from slow evaporation of $\text{CH}_2\text{Cl}_2/\text{hexane}$ solution at $23 \text{ }^\circ\text{C}$. Number of measured and unique reflections 39606 and 11296, respectively ($R_{\text{int}} = 0.0458$). Final $R_1 = 0.0728$, $wR_2 = 0.2065$ for 8382 independent reflections with $I > 2\sigma(I)$, 732 parameters and $4.106 < 2\theta < 55.354^\circ$ (corresponding R values based on all 11296 reflections are 0.0728 and 0.2065, respectively).

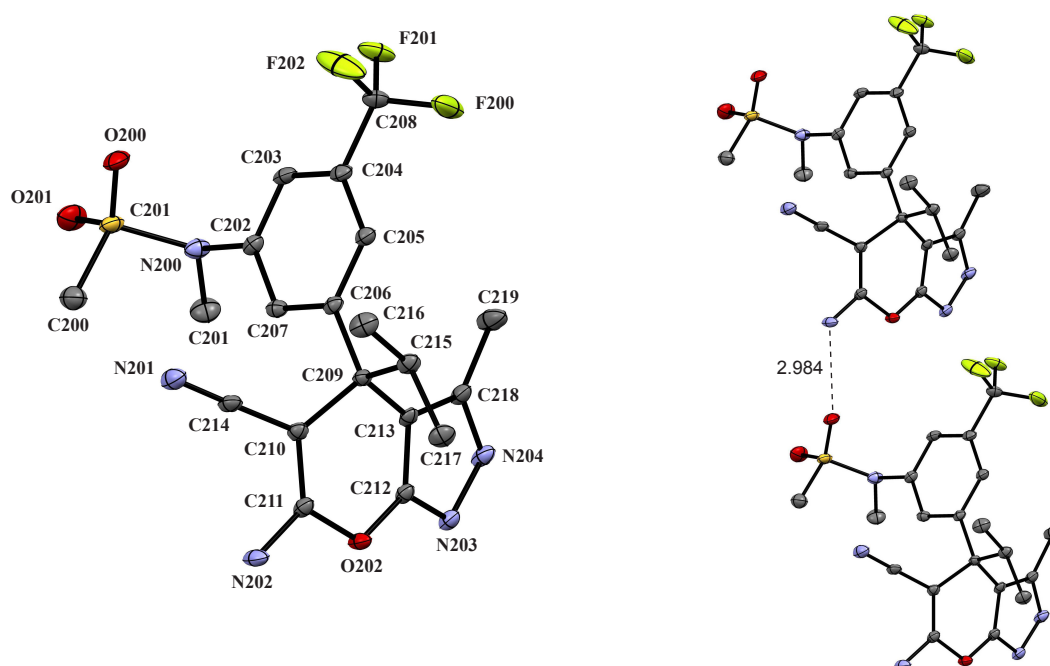


Figure 119. ORTEP plot of (±)-269 with arbitrary numbering (left), and intermolecular H-bond involving the SO_2 moiety (right). H-atoms are omitted for clarity. Atomic displacement parameters at 100 K are drawn at 50% probability level. Selected bond lengths (\AA), angles ($^\circ$), and torsion angles ($^\circ$): S200-O200 1.434(3), S200-O201 1.428(3), S200-N200 1.650(3), S200-C200 1.754(4), F200-C208 1.332(4), N200-C201 1.482(5), N200-C202 1.437(4), N201-C214 1.150(4), N202-C211 1.337(4), N203-N204 1.368(4), N204-C218 1.354(4), N203-C212 1.316(4), O202-C211 1.374(4), O202-C212 1.363(4), C209-C210 1.533(4), C209-C213 1.504(4), C210-C211 1.367(4), C212-C213 1.399(4), C213-C218 1.380(4), C202-N200-S200 116.1(2), O200-S200-O201 118.07(16), C206-C209-C215 112.2(3), $\text{S200-N200-C202-C203}$ 77.6 (3), $\text{C200-S200-N200-C201}$ $-71.8(3)$.

Crystal Data for 316

Crystal data at 100 K for $C_{13}H_{11}N_3$, $M = 209.25 \text{ g mol}^{-1}$, monoclinic, space group $P2_1/m$, $a = 8.6587(5) \text{ \AA}$, $b = 7.0815(4) \text{ \AA}$, $c = 9.2920(5) \text{ \AA}$, $\alpha = 90^\circ$, $\beta = 111.0600(10)^\circ$, $\gamma = 90^\circ$, $V = 531.70(5) \text{ \AA}^3$, $Z = 2$, $D_c = 1.307 \text{ g/cm}^3$, $\mu(\text{MoK}\alpha) = 0.081 \text{ mm}^{-1}$. Orange crystal (linear dimensions approx. $0.2 \text{ mm} \times 0.17 \text{ mm} \times 0.09 \text{ mm}$) were grown from slow evaporation of CDCl_3 solution at 23°C . Number of measured and unique reflections 8157 and 1708, respectively ($R_{\text{int}} = 0.0190$). Final $R_1 = 0.0382$, $wR_2 = 0.1040$ for 1520 independent reflections with $I > 2\sigma(I)$, 98 parameters and $5.042 < 2\theta < 61.02^\circ$ (corresponding R values based on all 1708 reflections are 0.0382 and 0.1093, respectively).

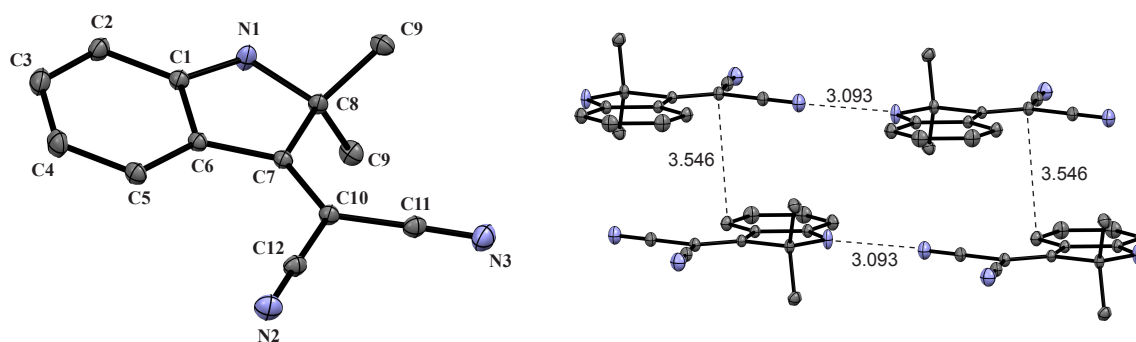


Figure 120. ORTEP plot of **316**, arbitrary numbering, H-atoms are omitted for clarity (left) and crystal packing (right). Distances are given in \AA . Atomic displacement parameters at 100 K are drawn at 50% probability level. Selected bond lengths (\AA), angles ($^\circ$), and torsion angles ($^\circ$): **N1–C1 1.3490(14)**, **N1–C8 1.4650(14)**, **N2–C12 1.1528(16)**, **N3–C11 1.1530(16)**, **C1–C6 1.4161(15)**, **C6–C7 1.4313(14)**, **C7–C8 1.5303(15)**, **C7–C10 1.3767(15)**, **C10–C11 1.4299(15)**, **C6–C7–C10–C12 0.000(1)**.

Crystal Data for (±)-328

Crystal data at 100 K for $C_{22}H_{26}N_4O_2$, $M = 378.47 \text{ g mol}^{-1}$, monoclinic, space group $P2_1/n$, $a = 11.4679(11) \text{ \AA}$, $b = 15.1421(16) \text{ \AA}$, $c = 12.6305(13) \text{ \AA}$, $\alpha = 90^\circ$, $\beta = 112.981(2)^\circ$, $\gamma = 90^\circ$, $V = 2019.2(4) \text{ \AA}^3$, $Z = 4$, $D_c = 1.245 \text{ g/cm}^3$, $\mu(\text{MoK}\alpha) = 0.082 \text{ mm}^{-1}$. Colorless crystal (linear dimensions approx. $0.2 \text{ mm} \times 0.1 \text{ mm} \times 0.08 \text{ mm}$) were grown from slow evaporation of CH_2Cl_2 /hexane solution at 23°C . Number of measured and unique reflections 34231 and 4638, respectively ($R_{\text{int}} = 0.0320$). Final $R_1 = 0.0377$, $wR_2 = 0.0922$ for 3879 independent reflections with $I > 2\sigma(I)$, 265 parameters and $4.074 < 2\theta < 55.05^\circ$ (corresponding R values based on all 4638 reflections are 0.0377 and 0.0922, respectively).

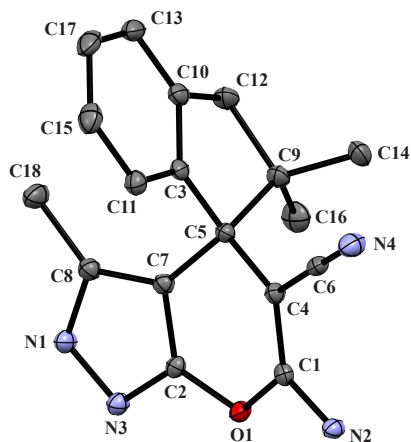


Figure 121. ORTEP plot of (±)-328, arbitrary numbering, H-atoms are omitted for clarity. Atomic displacement parameters at 100 K are drawn at 50% probability level. Selected bond lengths (\AA), angles ($^\circ$), and torsion angles ($^\circ$): O1–C1 1.3705(13), O1–C2 1.3705(13), N1–N3 1.3625(13), N1–C8 1.3515(15), N2–C1 1.3366(14), N3–C2 1.3181(14), N4–C6 1.1514(15), C1–C4 1.3711(15), C2–C7 1.3895(13), C4–C5 1.5279(15), C5–C7 1.5133(14), C7–C8 1.3897(15), C14–C9–C16 108.83(9), C7–C5–C3–C11 75.37(16).

10. References

10. References

- [1] World Health Organization. *Global Health Observatory (GHO) Data: Life Expectancy*. Available via the following link: http://www.who.int/gho/mortality_burden_disease/life_tables/situation_trends_text/en/, accessed on May 16, **2017**.
- [2] D. Pitt, J.-M. Aubin, *Can. J. Surg.* **2012**, *55*, E8–E9. Joseph Lister: Father of Modern Surgery.
- [3] Z. Lv, Y. Chu, Y. Wang, *HIV/AIDS-Res. Pall. Care* **2015**, *7*, 95–104. HIV Protease Inhibitors: A Review of Molecular Selectivity and Toxicity.
- [4] A. Krohn, S. Redshaw, J. C. Ritchie, *J. Med. Chem.* **1991**, *34*, 3340–3342. Novel Binding Mode of Highly Potent HIV-Proteinase Inhibitors Incorporating the (*R*)-Hydroxyethylamine Isostere.
- [5] U.S. Food and Drug Administration. Roche, Fortovase® (Saquinavir). Available via the following link: https://www.accessdata.fda.gov/drugsatfda_docs/nda/97/020828_fortovase_toc.cfm, accessed on May 22, **2017**.
- [6] B. Turk, *Nat. Rev. Drug Discov.* **2006**, *5*, 785–799. Targeting Proteases: Successes, Failures and Future Prospects.
- [7] R. Capdeville, E. Buchdunger, J. Zimmermann, A. Matter, *Nat. Rev. Drug Discov.* **2002**, *1*, 493–502. Gleevec (STI571, Imatinib), a Rationally Developed, Targeted Anticancer Drug.
- [8] P. W. Manley, S. W. Cowan-Jacob, J. Mestan, *Biochim. Biophys. Acta* **2005**, *1754*, 3–13. Advances in the Structural Biology, Design and Clinical Development of Bcr-Abl Kinase Inhibitors for the Treatment of Chronic Myeloid Leukaemia.
- [9] E. Weisberg, P. W. Manley, W. Breitenstein, J. Brügger, S. W. Cowan-Jacob, A. Ray, B. Huntly, D. Fabbro, G. Fendrich, E. Hall-Meyers, A. L. Kung, J. Mestan, G. Q. Daley, L. Callahan, L. Catley, C. Cavazza, A. Mohammed, D. Neuberg, R. D. Wright, D. G. Gilliland, J. D. Griffin, *Cancer Cell* **2005**, *7*, 129–141. Characterization of AMN107, a Selective Inhibitor of Native and Mutant Bcr-Abl.
- [10] M. Breccia, G. Alimena, *Leuk. Res.* **2010**, *34*, 129–134. Nilotinib: A Second-Generation Tyrosine Kinase Inhibitor for Chronic Myeloid Leukemia.
- [11] I. Kola, J. Landis, *Nat. Rev. Drug Discov.* **2004**, *3*, 711–715. Can the Pharmaceutical Industry Reduce Attrition Rates?
- [12] M. Hay, D. W. Thomas, J. L. Craighead, C. Economides, J. Rosenthal, *Nat. Biotech.* **2014**, *32*, 40–51. Clinical Development Success Rates for Investigational Drugs.

- [13] J. A. DiMasi, H. G. Grabowski, R. W. Hansen, *J. Health. Econ.* **2016**, *47*, 20–33. Innovation in the Pharmaceutical Industry: New Estimates of R&D Costs.
- [14] C. A. Lipinski, F. Lombardo, B. W. Dominy, P. J. Feeney, *Adv. Drug Delivery Rev.* **1997**, *23*, 3–25. Experimental and Computational Approaches to Estimate Solubility and Permeability in Drug Discovery and Development Settings.
- [15] M. J. Waring, J. Arrowsmith, A. R. Leach, P. D. Leeson, S. Mandrell, R. M. Owen, G. Pairaudeau, W. D. Pennie, S. D. Pickett, J. Wang, O. Wallace, A. Weir, *Nat. Rev. Drug Discov.* **2015**, *14*, 475–486. An Analysis of the Attrition of Drug Candidates from Four Major Pharmaceutical Companies.
- [16] M. Njoroge, N. M. Njuguna, P. Mutai, D. S. B. Ongarora, P. W. Smith, K. Chibale, *Chem. Rev.* **2014**, *114*, 11138–11163. Recent Approaches to Chemical Discovery and Development Against Malaria and the Neglected Tropical Diseases Human African Trypanosomiasis and Schistosomiasis.
- [17] Y. Cha, T. Erez, I. J. Reynolds, D. Kumar, J. Ross, G. Koytiger, R. Kusko, B. Zeskind, S. Risso, E. Kagan, S. Papapetropoulos, I. Grossmann, D. Laifenfeld, *Br. J. Pharmacol.* **2017**. DOI: 10.1111/bph.13798. Pharma Perspective on Drug Repurposing.
- [18] A. Martorana, U. Perricone, A. Lauria, *Curr. Top. Med. Chem.* **2016**, *16*, 2088–2106. The Repurposing of Old Drugs or Unsuccessful Lead Compounds by *in Silico* Approaches: New Advances and Perspectives.
- [19] Q. Vanhaelen, P. Mamoshina, A. M. Aliper, A. Artemov, K. Lezhnina, I. Ozerov, I. Labat, A. Zhavoronkov, *Drug Discov. Today* **2017**, *22*, 210–222. Design of Efficient Computational Workflows for *in Silico* Drug Repurposing.
- [20] T. T. Ashburn, K. B. Thor, *Nat. Rev. Drug Discov.* **2004**, *3*, 673–683. Drug Repositioning: Identifying and Developing New Uses for Existing Drugs.
- [21] D. M. Klug, M. H. Gelb, M. P. Pollastri, *Bioorg. Med. Chem. Lett.* **2016**, *26*, 2569–2576. Repurposing Strategies for Tropical Disease Drug Discovery.
- [22] A. M. Thayer, *Chem. Eng. News* **2012**, *90*, 15–25. Drug Repurposing.
- [23] S. C. Gupta, B. Sung, S. Prasad, L. J. Webb, B. B. Aggarwal, *Trends Pharmacol. Sci.* **2013**, *34*, 508–517. Cancer Drug Discovery by Repurposing: Teaching New Tricks to Old Dogs.
- [24] D. C. Gilbert, C. Vale, R. Haire, C. Coyle, R. E. Langley, *Clin. Oncol.* **2016**, *28*, 36–41. Repurposing Vitamin D as an Anticancer Drug.
- [25] M. Yarchoan, S. E. Arnold, *Diabetes* **2014**, *63*, 2253–2261. Repurposing Diabetes Drugs for Brain Insulin Resistance in Alzheimer Disease.

- [26] K. B. Thor, M. A. Katofiasc, *J. Pharmacol. Exp. Ther.* **1995**, *274*, 1014–1024. Effects of Duloxetine, a Combined Serotonin and Norepinephrine Reuptake Inhibitor, on Central Neural Control of Lower Urinary Tract Function in the Chloralose-Anesthetized Female Cat.
- [27] P. A. Norton, N. R. Zinner, I. Yalcin, R. C. Bump, *Am. J. Obstet. Gynecol.* **2002**, *187*, 40–48. Duloxetine Versus Placebo in the Treatment of Stress Urinary Incontinence.
- [28] I. H. Osterloh in *Sildenafil* (Ed. U. Dünzendorfer), Birkhäuser Basel, Basel, **2004**, pp. 1–13. The Discovery and Development of Viagra® (Sildenafil Citrate).
- [29] Pfizer. *Appendix A 2016 Financial Report*. Available via the following link: https://s21.q4cdn.com/317678438/files/doc_financials/Annual/2016/2016-financial-report.pdf, accessed on June 05, **2017**.
- [30] World Health Organization. *2016 World Malaria Report*; World Health Organization: Geneva December **2016**.
- [31] B. M. Greenwood, K. Bojang, C. J. M. Whitty, G. A. T. Targett, *Lancet* **2005**, *365*, 1487–1498. Malaria.
- [32] M. A. Phillips, J. N. Burrows, C. Manyando, R. H. van Huijsduijnen, W. C. Van Voorhis, T. N. C. Wells, *Nat. Rev. Dis. Primers* **2017**, *3*, Article Number 17050. Malaria.
- [33] T. N. C. Wells, W. E. Gutteridge in *Neglected Diseases and Drug Discovery* (Eds.: M. J. Palmer, T. N. C. Wells), RCS Publishing, Cambridge, **2012**, pp. 1–32. Malaria: New Medicines for Its Control and Eradication.
- [34] A. S. Paul, E. S. Egan, M. T. Duraisingh, *Curr. Opin. Hematol.* **2015**, *22*, 220–226. Host–Parasite Interactions That Guide Red Blood Cell Invasion by Malaria Parasites.
- [35] L. Bannister, G. Mitchell, *Trends Parasitol.* **2003**, *19*, 209–213. The Ins, Outs and Roundabouts of Malaria.
- [36] A. Trampuz, M. Jereb, I. Muzlovic, R. M. Prabhu, *Crit. Care* **2003**, *7*, 315–323. Clinical Review: Severe Malaria.
- [37] S. C. Wassmer, T. E. Taylor, P. K. Rathod, S. K. Mishra, S. Mohanty, M. Arevalo-Herrera, M. T. Duraisingh, J. D. Smith, *Am. J. Trop. Med. Hyg.* **2015**, *93*, 42–56. Investigating the Pathogenesis of Severe Malaria: A Multidisciplinary and Cross-Geographical Approach.
- [38] World Health Organization. *Malaria Prevention Works: Let’s Close the Gap*; World Health Organization: Geneva April **2017**.

- [39] World Health Organization. *Malaria Vector Control Policy Recommendations and Their Applicability to Product Evaluation*; World Health Organization: Geneva May **2017**.
- [40] J. A. Turner, C. N. E. Ruscoe, T. R. Perrior, *Chimia* **2016**, *70*, 684–693. Discovery to Development: Insecticides for Malaria Vector Control.
- [41] H. Ranson, R. N’Guessan, J. Lines, N. Moiroux, Z. Nkuni, V. Corbel, *Trends Parasitol.* **2011**, *27*, 91–98. Pyrethroid Resistance in African Anopheline Mosquitoes: What Are the Implications for Malaria Control?
- [42] T. E. Nkya, I. Akhouayri, W. Kisinza, J.-P. David, *Insect Biochem. Mol. Biol.* **2013**, *43*, 407–416. Impact of Environment on Mosquito Response to Pyrethroid Insecticides: Facts, Evidences and Prospects.
- [43] M. Schlitzer, *ChemMedChem* **2007**, *2*, 944–986. Malaria Chemotherapeutics Part I: History of Antimalarial Drug Development, Currently Used Therapeutics, and Drugs in Clinical Development.
- [44] R. G. Ridley, *Nature* **2002**, *415*, 686–693. Medical Need, Scientific Opportunity and the Drive for Antimalarial Drugs.
- [45] I. B. Müller, J. E. Hyde, *Mol. Biochem. Parasitol.* **2013**, *188*, 63–77. Folate Metabolism in Human Malaria Parasites—75 Years On.
- [46] W. Chin, P. G. Contacos, G. R. Coatney, H. K. King, *Am. J. Trop. Med. Hyg.* **1966**, *15*, 823–829. The Evaluation of Sulfonamides, Alone or in Combination with Pyrimethamine, in the Treatment of Multi-Resistant *Falciparum* Malaria.
- [47] J. D. Chulay, W. M. Watkins, D. G. Sixsmith, *Am. J. Trop. Med. Hyg.* **1984**, *33*, 325–330. Synergistic Antimalarial Activity of Pyrimethamine and Sulfadoxine Against *Plasmodium Falciparum* in Vitro.
- [48] J. G. Kublin, F. K. Dzinjalama, D. D. Kamwendo, E. M. Malkin, J. F. Cortese, L. M. Martino, R. A. G. Mukadam, S. J. Rogerson, A. G. Lescano, M. E. Molyneux, P. A. Winstanley, P. Chimpeni, T. E. Taylor, C. V. Plowe, *J. Infect. Dis.* **2002**, *185*, 380–388. Molecular Markers for Failure of Sulfadoxine-Pyrimethamine and Chlorproguanil-Dapsone Treatment of *Plasmodium falciparum* Malaria.
- [49] L. Tilley, S. A. Charman, J. L. Vennerstrom in *Neglected Diseases and Drug Discovery* (Eds.: M. J. Palmer, T. N. C. Wells), RCS Publishing, Cambridge, **2012**, pp. 33–64. Semisynthetic Artemisinin and Synthetic Peroxide Antimalarials.
- [50] Y. Tu, *Nat. Med.* **2011**, *17*, 1217–1220. The Discovery of Artemisinin (Qinghaosu) and Gifts from Chinese Medicine.

- [51] Y. Tu, *Angew. Chem. Int. Ed.* **2016**, *55*, 2–19; *Angew. Chem.* **2016**, *128*, 10366–10382. Artemisinin—a Gift from Traditional Chinese Medicine to the World (Nobel Lecture).
- [52] P. M. O'Neill, V. E. Barton, S. A. Ward, *Molecules* **2010**, *15*, 1705–1721. The Molecular Mechanism of Action of Artemisinin—The Debate Continues.
- [53] P. A. Stocks, P. G. Bray, V. E. Barton, M. Al-Helal, M. Jones, N. C. Araujo, P. Gibbons, S. A. Ward, R. H. Hughes, G. A. Biagini, J. Davies, R. Amewu, A. E. Mercer, G. Ellis, P. M. O'Neill, *Angew. Chem. Int. Ed.* **2007**, *46*, 6278–6283. Evidence for a Common Non-Heme Chelatable-Iron-Dependent Activation Mechanism for Semisynthetic and Synthetic Endoperoxide Antimalarial Drugs.
- [54] N. Klonis, M. P. Crespo-Ortiz, I. Bottova, N. Abu-Bakar, S. Kenny, P. J. Rosenthal, L. Tilley, *Proc. Natl. Acad. Sci. U. S. A.* **2011**, *108*, 11405–11410. Artemisinin Activity against *Plasmodium falciparum* Requires Hemoglobin Uptake and Digestion.
- [55] J. Wang, C.-J. Zhang, W. N. Chia, C. C. Y. Loh, Z. Li, Y. M. Lee, Y. He, L.-X. Yuan, T. K. Lim, M. Liu, C. X. Liew, Y. Q. Lee, J. Zhang, N. Lu, C. T. Lim, Z.-C. Hua, B. Liu, H.-M. Shen, K. S. W. Tan, Q. Lin, *Nat. Commun.* **2015**, *6*, 1–11. Haem-Activated Promiscuous Targeting of Artemisinin in *Plasmodium falciparum*.
- [56] R. N. Price, *Exp. Opin. Invest. Drugs* **2000**, *9*, 1815–1827. Artemisinin Drugs: Novel Antimalarial Agents.
- [57] M. P. Anthony, J. N. Burrows, S. Duparc, J. Moehrle, T. N. C. Wells, *Malar. J.* **2012**, *11*, 316. The Global Pipeline of New Medicines for the Control and Elimination of Malaria.
- [58] A. Mbengue, S. Bhattacharjee, T. Pandharkar, H. Liu, G. Estiu, R. V. Stahelin, S. S. Rizk, D. L. Njimoh, Y. Ryan, K. Chotivanich, C. Nguon, M. Ghorbal, J.-J. Lopez-Rubio, M. Pfrender, S. Emrich, N. Mohandas, A. M. Dondorp, O. Wiest, K. Haldar, *Nature* **2015**, *520*, 683–687. A Molecular Mechanism of Artemisinin Resistance in *Plasmodium falciparum* Malaria.
- [59] J. Burrows, *Nature* **2015**, *520*, 628–629. Malaria Runs Rings Round Artemisinin.
- [60] A. M. Dondorp, R. M. Fairhurst, L. Slutsker, J. R. MacArthur, J. G. Breman, P. J. Guerrin, T. E. Wellems, P. Ringwald, R. D. Newman, C. V. Plowe, *N. Engl. J. Med.* **2011**, *365*, 1073–1075. The Threat of Artemisinin-Resistant Malaria.
- [61] E. A. Ashley, M. Dhorda, R. M. Fairhurst, C. Amaratunga, P. Lim, S. Suon, S. Sreng, J. M. Anderson, S. Mao, B. Sam, C. Sopha, C. M. Chuor, C. Nguon, S. Sovannaroth, S. Pukrittayakamee, P. Jittamala, K. Chotivanich, K. Chutasmit, C. Suchatsoonthorn, R. Runchaen, T. T. Hien, N. T. Thuy-Nhien, N. V. Thanh, N. H. Phu, Y. Htut, K.-T.

- Han, K. H. Aye, O. A. Mokuolu, R. R. Olaosebikan, O. O. Folaranmi, M. Mayxay, M. Khanthavong, B. Hongvanthong, P. N. Newton, M. A. Onyamboko, C. I. Fanello, A. K. Tshefu, N. Mishra, N. Valecha, A. P. Phyo, F. Nosten, P. Yi, R. Tripura, S. Borrmann, M. Bashraheil, J. Peshu, M. A. Faiz, A. Ghose, M. A. Hossain, R. Samad, M. R. Rahman, M. M. Hasan, A. Islam, O. Miotto, R. Amato, B. MacInnis, J. Stalker, D. P. Kwiatkowski, Z. Bozdech, A. Jeeyapant, P. Y. Cheah, T. Sakulthaew, J. Chalk, B. Intharabut, K. Silamut, S. J. Lee, B. Vihokhern, C. Kunasol, M. Imwong, J. Tarning, W. J. Taylor, S. Yeung, C. J. Woodrow, J. A. Flegg, D. Das, J. Smith, M. Venkatesan, C. V. Plowe, K. Stepniewska, P. J. Guerin, A. M. Dondorp, N. P. Day, N. J. White, N. *Engl. J. Med.* **2014**, *371*, 411–423. Spread of Artemisinin Resistance in *Plasmodium falciparum* Malaria.
- [62] World Health Organization. *Artemisinin and Artemisinin-based Combination Therapy Resistance*. World Health Organization: Geneva October **2016**.
- [63] L. Paloque, A. P. Ramadani, O. Mercereau-Puijalon, J.-M. Augereau, F. Benoit-Vical, *Malar. J.* **2016**, *15*, 149. *Plasmodium falciparum*: Multifaceted Resistance to Artemisinins.
- [64] J. Straimer, N. F. Gnädig, B. Witkowski, C. Amaratunga, V. Duru, A. P. Ramadani, M. Dacheux, N. Khim, L. Zhang, S. Lam, P. D. Gregory, F. D. Urnov, O. Mercereau-Puijalon, F. Benoit-Vical, R. M. Fairhurst, D. Ménard, D. A. Fidock, *Science* **2015**, *347*, 428–431. K13-Propeller Mutations Confer Artemisinin Resistance in *Plasmodium falciparum* Clinical Isolates.
- [65] L. Tilley, J. Straimer, N. F. Gnädig, S. A. Ralph, D. A. Fidock, *Trends Parasitol.* **2016**, *32*, 682–696. Artemisinin Action and Resistance in *Plasmodium falciparum*.
- [66] N. J. White, *J. Clin. Invest.* **2004**, *113*, 1084–1092. Antimalarial Drug Resistance.
- [67] T. N. C. Wells, R. H. van Huijsduijnen, W. C. Van Voorhis, *Nat. Rev. Drug Discov.* **2015**, *14*, 424–442. Malaria Medicines: A Glass Half Full?
- [68] R. K. Haynes, B. Fugmann, J. Stetter, K. Rieckmann, H.-D. Heilmann, H.-W. Chan, M.-K. Cheung, W.-L. Lam, H.-N. Wong, S. L. Croft, L. Vivas, L. Rattray, L. Stewart, W. Peters, B. L. Robinson, M. D. Edstein, B. Kotecka, D. E. Kyle, B. Beckermann, M. Gerisch, M. Radtke, G. Schmuck, W. Steinke, U. Wollborn, K. Schmeer, A. Römer, *Angew. Chem. Int. Ed.* **2006**, *45*, 2082–2088; *Angew. Chem.* **2006**, *118*, 2136–2142. Artemisone—A Highly Active Antimalarial Drug of the Artemisinin Class.
- [69] S. A. Charman, S. Arbe-Barnes, I. C. Bathurst, R. Brun, M. Campbell, W. N. Charman, Francis C. K. Chiu, J. Chollet, J. C. Craft, D. J. Creek, Y. Dong, H. Matile, M. Maurer,

- J. Morizzi, T. Nguyen, P. Papastogiannidis, C. Scheurer, D. M. Shackleford, K. Sriraghavan, L. Stingelin, Y. Tang, H. Urwyler, X. Wang, K. L. White, S. Wittlin, L. Zhou, J. L. Vennerstrom, *Proc. Natl. Acad. Sci. U. S. A.* **2011**, *108*, 4400-4405. Synthetic Ozonide Drug Candidate OZ439 Offers New Hope for a Single-dose Cure of Uncomplicated Malaria.
- [70] H. M. Ismail, V. E. Barton, M. Panchana, S. Charoensutthivarakul, G. A. Biagini, S. A. Ward, P. M. O'Neill, *Angew. Chem. Int. Ed.* **2016**, *55*, 6401–6405; *Angew. Chem.* **2016**, *128*, 6511–6515. A Click Chemistry-Based Proteomic Approach Reveals that 1,2,4-Trioxolane and Artemisinin Antimalarials Share a Common Protein Alkylation Profile.
- [71] P. M. O'Neill, R. K. Amewu, S. A. Charman, S. Sabbani, N. F. Gnädig, J. Straimer, D. A. Fidock, E. R. Shore, N. L. Roberts, M. H.-L. Wong, W. D. Hong, C. Pidathala, C. Riley, B. Murphy, G. Aljayyousi, F. J. Gamo, L. Sanz, J. Rodrigues, C. G. Cortes, E. Herreros, I. Angulo-Barturén, M. B. Jiménez-Díaz, S. F. Bazaga, M. S. Martínez-Martínez, B. Campo, R. Sharma, E. Ryan, D. M. Shackleford, S. Campbell, D. A. Smith, G. Wirjanata, R. Noviyanti, R. N. Price, J. Marfurt, M. J. Palmer, I. M. Copple, A. E. Mercer, A. Ruecker, M. J. Delves, R. E. Sinden, P. Siegl, J. Davies, R. Rochford, C. H. M. Kocken, A.-M. Zeeman, G. L. Nixon, G. A. Biagini, S. A. Ward, *Nat. Commun.* **2017**, *8*, 15159. A Tetraoxane-Based Antimalarial Drug Candidate that Overcomes *PfK13-C580Y* Dependent Artemisinin Resistance.
- [72] M. Rottmann, C. McNamara, B. K. S. Yeung, M. C. S. Lee, B. Zou, B. Russell, P. Seitz, D. M. Plouffe, N. V. Dharia, J. Tan, S. B. Cohen, K. R. Spencer, G. E. González-Páez, S. B. Lakshminarayana, A. Goh, R. Suwanarusk, T. Jegla, E. K. Schmitt, H.-P. Beck, R. Brun, F. Nosten, L. Renia, V. Dartois, T. H. Keller, D. A. Fidock, E. A. Winzeler, T. T. Diagana, *Science* **2010**, *329*, 1175–1180. Spiroindolones, a Potent Compound Class for the Treatment of Malaria.
- [73] N. J. White, S. Pukrittayakamee, A. P. Phyto, R. Rueangweerayut, F. Nosten, P. Jittamala, A. Jeeyapant, J. P. Jain, G. Lefèvre, R. Li, B. Magnusson, T. T. Diagana, F. J. Leong, *N. Engl. J. Med.* **2014**, *371*, 403–410. Spiroindolone KAE609 for Falciparum and Vivax Malaria.
- [74] T. Wu, A. Nagle, K. Kuhen, K. Gagaring, R. Borboa, C. Franceck, Z. Chen, D. Plouffe, A. Goh, S. B. Lakshminarayana, J. Wu, H. Q. Ang, P. Zeng, M. L. Kang, W. Tan, M. Tan, N. Ye, X. Lin, C. Caldwell, J. Ek, S. Skolnik, F. Liu, J. Wang, J. Chang, C. Li, T. Hollenbeck, T. Tuntland, J. Isbell, C. Fischli, R. Brun, M. Rottmann, V. Dartois, T. Keller, T. Diagana, E. Winzeler, R. Glynn, D. C. Tully, A. K. Chatterjee, *J. Med.*

- Chem.* **2011**, *54*, 5116–5130. Imidazolopiperazines: Hit to Lead Optimization of New Antimalarial Agents.
- [75] A. Nagle, T. Wu, K. Kuhen, K. Gagaring, R. Borboa, C. Francek, Z. Chen, D. Plouffe, X. Lin, C. Caldwell, J. Ek, S. Skolnik, F. Liu, J. Wang, J. Chang, C. Li, B. Liu, T. Hollenbeck, T. Tuntland, J. Isbell, T. Chuan, P. B. Alper, C. Fischli, R. Brun, S. B. Lakshminarayana, M. Rottmann, T. T. Diagana, E. A. Winzeler, R. Glynn, D. C. Tully, A. K. Chatterjee, *J. Med. Chem.* **2012**, *55*, 4244–4273. Imidazolopiperazines: Lead Optimization of the Second-Generation Antimalarial Agents.
- [76] K. L. Kuhen, A. K. Chatterjee, M. Rottmann, K. Gagaring, R. Borboa, J. Buenviaje, Z. Chen, C. Francek, T. Wu, A. Nagle, S. W. Barnes, D. Plouffe, M. C. S. Lee, D. A. Fidock, W. Graumans, M. van de Vegte-Bolmer, G. J. van Gemert, G. Wirjanata, B. Sebayang, J. Marfurt, B. Russell, R. Suwanarusk, R. N. Price, F. Nosten, A. Tungtaeng, M. Gettayacamin, J. Sattabongkot, J. Taylor, J. R. Walker, D. Tully, K. P. Patra, E. L. Flannery, J. M. Vinetz, L. Renia, R. W. Sauerwein, E. A. Winzeler, R. J. Glynn, T. T. Diagana, *Antimicrob. Agents Chemother.* **2014**, *58*, 5060–5067. KAF156 Is an Antimalarial Clinical Candidate with Potential for Use in Prophylaxis, Treatment, and Prevention of Disease Transmission.
- [77] F. J. Leong, R. Zhao, S. Zeng, B. Magnusson, T. T. Diagana, P. Pertel, *Antimicrob. Agents Chemother.* **2014**, *58*, 6437–6443. A First-in-Human Randomized, Double-Blind, Placebo-Controlled, Single- and Multiple-Ascending Oral Dose Study of Novel Imidazolopiperazine KAF156 to Assess Its Safety, Tolerability, and Pharmacokinetics in Healthy Adult Volunteers.
- [78] N. J. White, T. T. Duong, C. Uthaisin, F. Nosten, A. P. Phy, B. Hanboonkunupakarn, S. Pukrittayakamee, P. Jittamala, K. Chuthasmit, M. S. Cheung, Y. Feng, R. Li, B. Magnusson, M. Sultan, D. Wieser, X. Xun, R. Zhao, T. T. Diagana, P. Pertel, F. J. Leong, *N. Engl. J. Med.* **2016**, *375*, 1152–1160. Antimalarial Activity of KAF156 in *Falciparum* and *Vivax* Malaria.
- [79] J. M. Coteron, M. Marco, J. Esquivias, X. Deng, K. L. White, J. White, M. Koltun, F. El Mazouni, S. Kokkonda, K. Katneni, R. Bhamidipati, D. M. Shackleford, I. Angulo-Barturen, S. B. Ferrer, M. B. Jiménez-Díaz, F.-J. Gamo, E. J. Goldsmith, W. N. Charman, I. Bathurst, D. Floyd, D. Matthews, J. N. Burrows, P. K. Rathod, S. A. Charman, M. A. Phillips, *J. Med. Chem.* **2011**, *54*, 5540–5561. Structure-Guided Lead Optimization of Triazolopyrimidine-Ring Substituents Identifies Potent *Plasmodium*

- falciparum* Dihydroorotate Dehydrogenase Inhibitors with Clinical Candidate Potential.
- [80] M. A. Phillips, J. Lotharius, K. Marsh, J. White, A. Dayan, K. L. White, J. W. Njoroge, F. El Mazouni, Y. Lao, S. Kokkonda, D. R. Tomchick, X. Deng, T. Laird, S. N. Bhatia, S. March, C. L. Ng, D. A. Fidock, S. Wittlin, M. Lafuente-Monasterio, F. J. G. Benito, L. M. Sanz Alonso, M. S. Martinez, M. B. Jimenez-Diaz, S. F. Bazaga, I. Angulo-Barturen, J. N. Haselden, J. Louttit, Y. Cui, A. Sridhar, A.-M. Zeeman, C. Kocken, R. Sauerwein, K. Dechering, V. M. Avery, S. Duffy, M. Delves, R. Sinden, A. Ruecker, K. S. Wickham, R. Rochford, J. Gahagen, L. Iyer, E. Riccio, J. Mirsalis, I. Bathhurst, T. Rueckle, X. Ding, B. Campo, D. Leroy, M. J. Rogers, P. K. Rathod, J. N. Burrows, S. A. Charman, *Sci. Transl. Med.* **2015**, *7*, 296ra111. A Long-Duration Dihydroorotate Dehydrogenase Inhibitor (DSM265) for Prevention and Treatment of Malaria.
- [81] Y. Yuthavong, B. Tarnchompoo, T. Vilaivan, P. Chitnumsub, S. Kamchonwongpaisan, S. A. Charman, D. N. McLennan, K. L. White, L. Vivas, E. Bongard, C. Thongpanchang, S. Taweechai, J. Vanichtanankul, R. Rattanajak, U. Arwon, P. Fantauzzi, J. Yuvaniyama, W. N. Charman, D. Matthews, *Proc. Natl. Acad. Sci. U. S. A.* **2012**, *109*, 16823–16828. Malarial Dihydrofolate Reductase as a Paradigm for Drug Development against a Resistance-Compromised Target.
- [82] *The PyMOL Molecular Graphic System*, Version 1.8.0.5., Schrödinger LLC, **2017**.
- [83] D. L. Doolan, C. Dobaño, J. K. Baird, *Clin. Microbiol. Rev.* **2009**, *22*, 13–36. Acquired Immunity to Malaria.
- [84] L. A. Kirkman, K. W. Deitsch, *Curr. Opin. Microbiol.* **2012**, *15*, 456–462. Antigenic Variation and the Generation of Diversity in Malaria Parasites.
- [85] R. Rappuoli, A. Aderem, *Nature* **2011**, *473*, 463–469. A 2020 Vision for Vaccines against HIV, Tuberculosis and Malaria.
- [86] World Health Organization. *Rainbow Tables*. Available via the following link: http://www.who.int/immunization/research/development/Rainbow_tables/en/, accessed on June 02, **2017**.
- [87] The RTS,S Clinical Trials Partnership, *PLoS Medicine* **2014**, *11*, e1001685. Efficacy and Safety of the RTS,S/AS01 Malaria Vaccine During 18 Months after Vaccination: A Phase 3 Randomized, Controlled Trial in Children and Young Infants at 11 African Sites.

- [88] A. K. Chatterjee, E. A. Winkler in *Neglected Diseases and Drug Discovery* (Eds.: M. J. Palmer, T. N. C. Wells), RCS Publishing, Cambridge, **2012**, pp. 88–111. Human Targets Repositioning and Cell-Based Approaches for Antimalarial Discovery.
- [89] A. Nzila, Z. Ma, K. Chibale, *Future Med. Chem.* **2011**, *3*, 1413–1426. Drug Repositioning in the Treatment of Malaria and TB.
- [90] Z. Yu, J. A. Brannigan, D. K. Moss, A. M. Brzozowski, A. J. Wilkinson, A. A. Holder, E. W. Tate, R. J. Leatherbarrow, *J. Med. Chem.* **2012**, *55*, 8879–8890. Design and Synthesis of Inhibitors of *Plasmodium falciparum* N-Myristoyltransferase, a Promising Target for Antimalarial Drug Discovery.
- [91] M. D. Rackham, J. A. Brannigan, D. K. Moss, Z. Yu, A. J. Wilkinson, A. A. Holder, E. W. Tate, R. J. Leatherbarrow, *J. Med. Chem.* **2013**, *56*, 371–375. Discovery of Novel and Ligand-Efficient Inhibitors of *Plasmodium falciparum* and *Plasmodium vivax* N-Myristoyltransferase.
- [92] M. D. Rackham, J. A. Brannigan, K. Rangachari, S. Meister, A. J. Wilkinson, A. A. Holder, R. J. Leatherbarrow, E. W. Tate, *J. Med. Chem.* **2014**, *57*, 2773–2788. Design and Synthesis of High Affinity Inhibitors of *Plasmodium falciparum* and *Plasmodium vivax* N-Myristoyltransferases Directed by Ligand Efficiency Dependent Lipophilicity (LELP).
- [93] N. Nirmalan, P. Wang, P. F. G. Sims, J. E. Hyde, *Mol. Microbiol.* **2002**, *46*, 179–190. Transcriptional Analysis of Genes Encoding Enzymes of the Folate Pathway in the Human Malaria Parasite *Plasmodium falciparum*.
- [94] N. Hagner, M. Joerger, *Cancer Manag. Res.* **2010**, *2*, 293–301. Cancer Chemotherapy: Targeting Folic Acid Synthesis.
- [95] M. Kalanon, G. I. McFadden, *Biochem. Soc. Trans.* **2010**, *38*, 775–782. Malaria, *Plasmodium falciparum* and Its Apicoplast.
- [96] G. I. McFadden, *Protozoa* **2011**, *248*, 641–650. The Apicoplast.
- [97] G. G. van Dooren, B. Striepen, *Annu. Rev. Microbiol.* **2013**, *67*, 271–289. The Algal Past and Parasite Present of the Apicoplast.
- [98] M. Witschel, M. Rottmann, M. Kaiser, R. Brun, *PLoS Negl. Trop. Dis.* **2012**, *6*, e1805. Agrochemicals against Malaria, Sleeping Sickness, Leishmaniasis and Chagas Disease.
- [99] M. G. Corral, J. Leroux, K. A. Stubbs, J. S. Mylne, *Sci. Rep.* **2017**, *7*, 45871. Herbicidal Properties of Antimalarial Drugs.
- [100] T. Efferth, *Semin. Cancer Biol.* **2017**. DOI: 10.1016/j.semcancer.2017.02.009. From Ancient Herb to Modern Drug: *Artemisia annua* and Artemisinin for Cancer Therapy.

- [101] M. B. Cassera, Y. Zhang, K. Z. Hazleton, V. L. Schramm, *Curr. Top. Med. Chem.* **2011**, *11*, 2103–2115. Purine and Pyrimidine Pathways as Targets in *Plasmodium falciparum*.
- [102] M. A. Phillips in *Neglected Diseases and Drug Discovery* (Eds.: M. J. Palmer, T. N. C. Wells), RCS Publishing, Cambridge, **2012**, pp. 65–87. Antimalarial Agents Targeting Nucleotide Synthesis and Electron Transport: Insight from Structural Biology.
- [103] J. E. Salcedo-Sora, S. A. Ward, *Mol. Biochem. Parasitol.* **2013**, *188*, 51–62. The Folate Metabolic Network of Falciparum Malaria.
- [104] D. R. Knighton, C.-C. Kan, E. Howland, C. A. Janson, Z. Hostomska, K. M. Welsh, D. A. Matthews, *Nat. Struct. Mol. Biol.* **1994**, *1*, 186–194. Structure of and Kinetic Channelling in Bifunctional Dihydrofolate Reductase-Thymidylate Synthase.
- [105] J. Yuvaniyama, P. Chitnumsub, S. Kamchonwongpaisan, J. Vanichtanankul, W. Sirawaraporn, P. Taylor, M. D. Walkinshaw, Y. Yuthavong, *Nat. Struct. Biol.* **2003**, *10*, 357–365. Insights into Antifolate Resistance from Malarial DHFR-TS Structures.
- [106] V. Schirch, D. M. E. Szebenyi, *Curr. Opin. Chem. Biol.* **2005**, *9*, 482–487. Serine Hydroxymethyltransferase Revisited.
- [107] W. Pornthanakasem, D. Kongkasuriyachai, C. Uthaipibull, Y. Yuthavong, U. Leartsakulpanich, *Malar. J.* **2012**, *11*, 387. *Plasmodium* Serine Hydroxymethyltransferase: Indispensability and Display of Distinct Localization.
- [108] S. Maenpuen, K. Sopitthummakhun, Y. Yuthavong, P. Chaiyen, U. Leartsakulpanich, *Mol. Biochem. Parasitol.* **2009**, *168*, 63–73. Characterization of *Plasmodium falciparum* Serine Hydroxymethyltransferase—A Potential Antimalarial Target.
- [109] K. Sopitthummakhun, S. Maenpuen, Y. Yuthavong, U. Leartsakulpanich, P. Chaiyen, *FEBS J.* **2009**, *276*, 4023–4036. Serine Hydroxymethyltransferase from *Plasmodium vivax* Is Different in Substrate Specificity from Its Homologues.
- [110] P. Chitnumsub, W. Ittarat, A. Jaruwat, K. Noytanom, W. Amornwatcharapong, W. Pornthanakasem, P. Chaiyen, Y. Yuthavong, U. Leartsakulpanich, *Acta Crystallogr.* **2014**, *D70*, 1517–1527. The Structure of *Plasmodium falciparum* Serine Hydroxymethyltransferase Reveals a Novel Redox Switch That Regulates Its Activities.
- [111] S. B. Renwick, K. Snell, U. Baumann, *Structure* **1998**, *6*, 1105–1116. The Crystal Structure of Human Cytosolic Serine Hydroxymethyltransferase: A Target for Cancer Chemotherapy.

- [112] C. K. T. Pang, J. H. Hunter, R. Gujjar, R. Podutoori, J. Bowman, D. G. Mudeppa, P. K. Rathod, *Mol. Biochem. Parasitol.* **2009**, *168*, 74–83. Catalytic and Ligand-Binding Characteristics of *Plasmodium falciparum* Serine Hydroxymethyltransferase.
- [113] P. Chitnumsub, A. Jaruwat, P. Riangrunroj, W. Ittarat, K. Noytanom, W. Oonant, J. Vanichthanankul, P. Chuankhayan, S. Maenpuen, C.-J. Chen, P. Chaiyen, Y. Yuthavong, U. Leartsakulpanich, *Acta Crystallogr.* **2014**, *D70*, 3177–3186. Structures of *Plasmodium vivax* Serine Hydroxymethyltransferase: Implications for Ligand-Binding Specificity and Functional Control.
- [114] V. Trivedi, A. Gupta, V. R. Jala, P. Saravanan, G. S. J. Rao, N. A. Rao, H. S. Savithri, H. S. Subramanya, *J. Biol. Chem.* **2002**, *277*, 17161–17169. Crystal Structure of Binary and Ternary Complexes of Serine Hydroxymethyltransferase from *Bacillus stearothermophilus*: Insights into the Catalytic Mechanism.
- [115] K. Sopitthummakhun, C. Thongpanchang, T. Vilaivan, Y. Yuthavong, P. Chaiyen, U. Leartsakulpanich, *Malar. J.* **2012**, *11*, 194. *Plasmodium* Serine Hydroxymethyltransferase as a Potential Anti-Malarial Target: Inhibition Studies Using Improved Methods for Enzyme Production and Assay.
- [116] M. C. Witschel, M. Rottmann, A. Schwab, U. Leartsakulpanich, P. Chitnumsub, M. Seet, S. Tonazzi, G. Schwertz, F. Stelzer, T. Mietzner, C. McNamara, F. Thater, C. Freymond, A. Jaruwat, C. Pinthong, P. Riangrunroj, M. Oufir, M. Hamburger, P. Mäser, L. M. Sanz-Alonso, S. Charman, S. Wittlin, Y. Yuthavong, P. Chaiyen, F. Diederich, *J. Med. Chem.* **2015**, *58*, 3117–3130. Inhibitors of Plasmodial Serine Hydroxymethyltransferase (SHMT): Cocrystal Structures of Pyrazolopyrans with Potent Blood- and Liver-Stage Activities.
- [117] G. Schwertz, M. C. Witschel, M. Rottmann, R. Bonnert, U. Leartsakulpanich, P. Chitnumsub, A. Jaruwat, W. Ittarat, A. Schäfer, R. A. Aponte, S. A. Charman, K. L. White, A. Kundu, S. Sadhukhan, M. Lloyd, G. M. Freiberg, M. Srikumaran, M. Siggel, A. Zwyssig, P. Chaiyen, F. Diederich, *J. Med. Chem.* **2017**, *60*, 4840–4860. Antimalarial Inhibitors Targeting Serine Hydroxymethyltransferase (SHMT) with in Vivo Efficacy and Analysis of Their Binding Mode Based on X-Ray Cocrystal Structures.
- [118] M. J. Gardner and 44 co-authors, *Nature* **2002**, *419*, 498–511. Genome Sequence of the Human Malaria Parasite *Plasmodium falciparum*.
- [119] The Arabidopsis Genome Initiative, *Nature* **2000**, *408*, 796–815. Analysis of the Genome Sequence of the Flowering Plant *Arabidopsis thaliana*.

- [120] J. K. Schjoerring, G. Mäck, K. H. Nielsen, S. Husted, A. Suzuki, S. Driscoll, R. Boldt, H. Bauwe, *Plant J.* **2006**, *45*, 71–82. Antisense Reduction of Serine Hydroxymethyltransferase Results in Diurnal Displacement of NH_4^+ Assimilation in Leaves of *Solanum tuberosum*.
- [121] M. Witschel, F. Stelzer, J. Hutzler, T. Qu, T. Mietzner, K. Kreuz, K. Grossmann, R. Aponte, H. W. Höffken, F. Calo, T. Ehrhardt, A. Simon, L. P. Rapado, WO 2013/182472 A1, **2013**. Pyrazolopyrans Having Herbicidal and Pharmaceutical Properties.
- [122] M. C. Witschel, **2011**. BASF Internal Report.
- [123] B. R. Beno, K.-S. Yeung, M. D. Bartberger, L. D. Pennington, N. A. Meanwell, *J. Med. Chem.* **2015**, *58*, 4383–4438. A Survey of the Role of Noncovalent Sulfur Interactions in Drug Design.
- [124] A. Lange, M. Günther, F. M. Büttner, M. O. Zimmermann, J. Heidrich, S. Hennig, S. Zahn, C. Schall, A. Sievers-Engler, F. Ansideri, P. Koch, M. Laemmerhofer, T. Stehle, S. A. Laufer, F. M. Boeckler, *J. Am. Chem. Soc.* **2015**, *137*, 14640–14652. Targeting the Gatekeeper MET146 of C-Jun N-Terminal Kinase 3 Induces a Bivalent Halogen/Chalcogen Bond.
- [125] P. R. Gerber, K. Müller, *J. Comput.-Aided Mol. Des.* **1995**, *9*, 251–268. MAB, a Generally Applicable Molecular Force Field for Structure Modelling in Medicinal Chemistry.
- [126] N. A. Meanwell, *J. Med. Chem.* **2011**, *54*, 2529–2591. Synopsis of Some Recent Tactical Application of Bioisosteres in Drug Design.
- [127] M. I. Javed, M. Brewer, *Org. Lett.* **2007**, *9*, 1789–1792. Diazo Preparation via Dehydrogenation of Hydrazones with “Activated” DMSO.
- [128] S. Kotha, K. Lahari, D. Kashinath, *Tetrahedron* **2002**, *58*, 9633–9695. Recent Applications of the Suzuki–Miyaura Cross-Coupling Reaction in Organic Synthesis.
- [129] G. Jones, *Org. React.* **1967**, *15*, 204–599. Knoevenagel Condensation.
- [130] G. Vasuki, K. Kumaravel, *Tetrahedron Lett.* **2008**, *49*, 5636–5638. Rapid Four-Component Reactions in Water: Synthesis of Pyranopyrazoles.
- [131] S. Gogoi, C.-G. Zhao, *Tetrahedron Lett.* **2009**, *50*, 2252–2255. Organocatalyzed Enantioselective Synthesis of 6-Amino-5-cyanodihydropyrano[2,3-*c*]pyrazoles.
- [132] C. G. Fortuna, C. Bonaccorso, A. Bulbarelli, G. Caltabiano, L. Rizzi, L. Goracci, G. Musumarra, A. Pace, A. Palumbo Piccionello, A. Guarcello, P. Pierro, C. E. A.

- Cocuzza, R. Musumeci, *Eur. J. Med. Chem.* **2013**, *65*, 533–545. New Linezolid-like 1,2,4-Oxadiazoles Active against Gram-positive Multiresistant Pathogens.
- [133] C. P. Hencken, L. Jones-Brando, C. Bordón, R. Stohler, B. T. Mott, R. Yolken, G. H. Posner, L. E. Woodard, *J. Med. Chem.* **2010**, *53*, 3594–3601. Thiazole, Oxadiazole, and Carboxamide Derivatives of Artemisinin Are Highly Selective and Potent Inhibitors of *Toxoplasma gondii*.
- [134] B. A. Robichaud, K. G. Liu, *Tetrahedron Lett.* **2011**, *52*, 6935–6938. Titanium Isopropoxide/Pyridine Mediated Knoevenagel Reactions.
- [135] J. Thierry, C. Yue, P. Potier, *Tetrahedron Lett.* **1998**, *39*, 1557–1560. 2-Phenyl Isopropyl and t-Butyl Trichloroacetimidates: Useful Reagents for Ester Preparation of N-Protected Amino Acids under Neutral Conditions.
- [136] A. Armstrong, I. Brackenridge, R. F. W. Jackson, J. M. Kirk, *Tetrahedron Lett.* **1988**, *29*, 2483–2486. A New Method for the Preparation of Tertiary Butyl Ethers and Esters.
- [137] K. A. Brameld, B. Kuhn, D. C. Reuter, M. Stahl, *J. Chem. Inf. Model.* **2008**, *48*, 1–24. Small Molecule Conformational Preferences Derived from Crystal Structure Data. A Medicinal Chemistry Focused Analysis.
- [138] L. M. Salonen, M. Ellermann, F. Diederich, *Angew. Chem. Int. Ed.* **2011**, *50*, 4808–4842; *Angew. Chem.* **2011**, *123*, 4908–4944. Aromatic Rings in Chemical and Biological Recognition: Energetics and Structures.
- [139] M. B. Jiménez-Díaz, T. Mulet, S. Viera, V. Gómez, H. Garuti, J. Ibáñez, A. Alvarez-Doval, L. D. Shultz, A. Martínez, D. Gargallo-Viola, I. Angulo-Barturen, *Antimicrob. Agents Chemother.* **2009**, *53*, 4533–4536. Improved Murine Model of Malaria Using *Plasmodium falciparum* Competent Strains and Non-Myelodepleted NOD-*scid* *IL2R γ ^{null}* Mice Engrafted with Human Erythrocytes.
- [140] L. M. Sanz, B. Crespo, C. De-Cózar, X. C. Ding, J. L. Llergo, J. N. Burrows, J. F. García-Bustos, F.-J. Gamo, *PloS one* **2012**, *7*, e30949. *P. falciparum* *In Vitro* Killing Rates Allow to Discriminate between Different Antimalarial Mode-of-Action.
- [141] A. R. Muci, S. L. Buchwald, *Top. Curr. Chem.* **2002**, *219*, 131–209. Practical Palladium Catalysts for C–N and C–O Bond Formation.
- [142] K. W. Anderson, R. E. Tundel, T. Ikawa, R. A. Altman, S. L. Buchwald, *Angew. Chem. Int. Ed.* **2006**, *45*, 6523–6527; *Angew. Chem.* **2006**, *118*, 6673–6677. Monodentate Phosphines Provide Highly Active Catalysts for Pd-Catalyzed C–N Bond-Forming Reactions of Heteroaromatic Halides/Amines and (H)N-Heterocycles.

- [143] O. S. Tee, M. Paventi, *J. Am. Chem. Soc.* **1982**, *104*, 4142–4146. Kinetics and Mechanism of Bromination of 2-Pyridinone and Related Derivatives in Aqueous Solution.
- [144] M. A. J. Duncton, M. Angels Estiarte, D. Tan, C. Kaub, D. J. R. O’Mahony, R. J. Johnson, M. Cox, W. T. Edwards, M. Wan, J. Kincaid, M. G. Kelly, *Org. Lett.* **2008**, *10*, 3259–3262. Preparation of Aryloxetanes and Arylazetidines by Use of an Alkyl–Aryl Suzuki Coupling.
- [145] F. González-Bobes, G. C. Fu, *J. Am. Chem. Soc.* **2006**, *128*, 5360–5361. Amino Alcohols as Ligands for Nickel-Catalyzed Suzuki Reactions of Unactivated Alkyl Halides, Including Secondary Alkyl Chlorides, with Arylboronic Acids.
- [146] D. Haas, J. M. Hammann, R. Greiner, P. Knochel, *ACS Catal.* **2016**, *6*, 1540–1552. Recent Developments in Negishi Cross-Coupling Reactions.
- [147] Y.-L. Li, W. Yao, A. P. Combs, E. W. Yue, S. Mei, W. Zhu, J. Glenn, T. P. Maduskuie, R. B. Sparks, B. Douty, WO 2013/033569 A1, **2013**. Preparation of Heterocyclamines as PI3K Inhibitors.
- [148] E. H. Kerns, L. Di in *Drug-Like Properties: Concepts, Structure Design and Methods from ADME to Toxicity Optimization*, Elsevier, San Diego, **2008**, pp. 209–214. hERG Blocking
- [149] C. E. Pollard, N. Abi Gerges, M. H. Bridgland-Taylor, A. Easter, T. G. Hammond, J.-P. Valentin, *Br. J. Pharmacol.* **2010**, *159*, 12–21. An Introduction to QT Interval Prolongation and Non-Clinical Approaches to Assessing and Reducing Risk.
- [150] G. Schwertz, M. S. Frei, M. C. Witschel, M. Rottmann, U. Leartsakulpanich, P. Chitnumsub, A. Jaruwat, W. Ittarat, A. Schäfer, R. A. Aponte, N. Trapp, K. Mark, P. Chaiyen, F. Diederich, *Chem. Eur. J.* **2017**, *23*, 14345–14357. Conformational Aspects in the Design of Inhibitors for Serine Hydroxymethyltransferase (SHMT): Biphenyl, Aryl Sulfonamide, and Aryl Sulfone Motifs.
- [151] J. A. Feng, I. Aliagas, P. Bergeron, J. M. Blaney, E. K. Bradley, M. F. T. Koehler, M.-L. Lee, D. F. Ortwine, V. Tsui, J. Wu, A. Gobbi, *J. Comput.-Aided Mol. Des.* **2015**, *29*, 511–523. An Integrated Suite of Modeling Tools That Empower Scientists in Structure- and Property-Based Drug Design.
- [152] A. Hillisch, N. Heinrich, H. Wild, *ChemMedChem* **2015**, *10*, 1958–1962. Computational Chemistry in the Pharmaceutical Industry: From Childhood to Adolescence.

- [153] B. Kuhn, M. Tichý, L. Wang, S. Robinson, R. E. Martin, A. Kuglstatter, J. Benz, M. Giroud, T. Schirmeister, R. Abel, F. Diederich, J. Hert, *J. Med. Chem.* **2017**, *60*, 2485–2497. Prospective Evaluation of Free Energy Calculations for the Prioritization of Cathepsin L Inhibitors.
- [154] C. Lerner, A. Ruf, V. Gramlich, B. Masjost, G. Zürcher, R. Jakob-Roetne, E. Borroni, F. Diederich, *Angew. Chem. Int. Ed.* **2001**, *40*, 4040–4042; *Angew. Chem.* **2001**, *113*, 4164–4166. X-Ray Crystal Structure of a Bisubstrate Inhibitor Bound to the Enzyme Catechol-*O*-methyltransferase: A Dramatic Effect of Inhibitor Preorganization on Binding Affinity.
- [155] M. Giroud, J. Ivkovic, M. Martignoni, M. Fleuti, N. Trapp, W. Haap, A. Kuglstatter, J. Benz, B. Kuhn, T. Schirmeister, F. Diederich, *ChemMedChem* **2017**, *12*, 257–270. Inhibition of the Cysteine Protease Human Cathepsin L by Triazine Nitriles: Amide···heteroarene π -Stacking Interactions and Chalcogen Bonding in the S3 Pocket.
- [156] J. Boström, P.-O. Norrby, T. Liljefors, *J. Comput.-Aided Mol. Des.* **1998**, *12*, 383–396. Conformational Energy Penalties of Protein-Bound Ligands.
- [157] R. Taylor, *Acta Crystallogr.* **2002**, *D58*, 879–888. Life-Science Applications of the Cambridge Structural Database.
- [158] F. H. Allen, R. Taylor, *Chem. Soc. Rev.* **2004**, *33*, 463–475. Research Applications of the Cambridge Structural Database (CSD).
- [159] G. M. Battle, G. M. Ferrence, F. H. Allen, *J. Appl. Cryst.* **2010**, *43*, 1208–1223. Applications of the Cambridge Structural Database in Chemical Education.
- [160] E. Pidcock, J. A. Chisholm, P. A. Wood, P. T. A. Galek, L. Fábíán, O. Korb, A. J. Cruz-Cabeza, J. W. Liebeschuetz, C. R. Groom, F. H. Allen in *Supramolecular Chemistry: From Molecule to Nanomaterials*, John Wiley & Sons, Ltd, **2012**, pp. 1–20. The Cambridge Structural Database System and Its Applications in Supramolecular Chemistry and Materials Design.
- [161] CCDC Website database. Available via the following link: <http://www.ccdc.cam.ac.uk/solutions/csd-system/components/csd/>, accessed on April 25, **2017**.
- [162] C. R. Groom, F. H. Allen, *Angew. Chem. Int. Ed.* **2014**, *53*, 662–671; *Angew. Chem.* **2014**, *126*, 675–684. The Cambridge Structural Database in Retrospect and Prospect.
- [163] H. M. Berman, J. Westbrook, Z. Feng, G. Gilliland, T. N. Bhat, H. Weissig, I. N. Shindyalov, P. E. Bourne, *Nucleic Acids Res.* **2000**, *28*, 235–242. The Protein Data Bank.

- [164] H. Berman, K. Henrick, H. Nakamura, *Nat. Struct. Biol.* **2003**, *10*, 980. Announcing the Worldwide Protein Data Bank.
- [165] S. J. Cottrell, T. S. G. Olsson, R. Taylor, J. C. Cole, J. W. Liebeschuetz, *J. Chem. Inf. Model.* **2012**, *52*, 956–962. Validating and Understanding Ring Conformations Using Small Molecule Crystallographic Data.
- [166] B. M. Hudson, E. Nguyen, D. J. Tantillo, *Org. Biomol. Chem.* **2016**, *14*, 3975–3980. The Influence of Intramolecular Sulfur–Lone Pair Interactions on Small-Molecule Drug Design and Receptor Binding.
- [167] CSD search: CSD Version 5.38, February 2017, containing about 875 000 entries. All searches were performed with Conquest 1.19 for structures with R-factor < 10% (no error, no partial disorder), excluding polymeric, powder, or metalorganic compounds. PDB search: searches were performed using Relibase+ V3.2.0. All searches were limited to resolution of protein crystal structures ≤ 2.5 Å.
- [168] C. P. Brock, R. P. Minton, *J. Am. Chem. Soc.* **1989**, *111*, 4586–4593. Systematic Effects of Crystal-Packing Forces: Biphenyl Fragments with H Atoms in All Four Ortho Positions.
- [169] M. J. Frisch and 73 co-authors, *Gaussian 09*, Revision A.02, Gaussian Inc., Wallingford CT, **2016**.
- [170] E. H. Kerns, L. Di in *Drug-Like Properties: Concepts, Structure Design and Methods from ADME to Toxicity Optimization*, Elsevier, San Diego, **2008**, pp. 86–99. Drug Permeation
- [171] K. Sugano, M. Kansy, P. Artursson, A. Avdeef, S. Bendels, L. Di, G. F. Ecker, B. Faller, H. Fischer, G. Gerebtzoff, H. Lennernaes, F. Senner, *Nat. Rev. Drug Discov.* **2010**, *9*, 597–614. Coexistence of Passive and Carrier-Mediated Processes in Drug Transport.
- [172] N. Noinaj, S. K. Buchanan, *Curr. Opin. Struct. Biol.* **2014**, *27*, 8–15. Structural Insights into the Transport of Small Molecules across Membranes.
- [173] R. E. Martin, R. I. Henry, J. L. Abbey, J. D. Clements, K. Kirk, *Genome Biol.* **2005**, *6*, R26. The 'Permeome' of the Malaria Parasite: An Overview of the Membrane Transport Proteins of *Plasmodium falciparum*.
- [174] S. G. Valderramos, D. A. Fidock, *Trends Pharmacol. Sci.* **2006**, *27*, 594–601. Transporters Involved in Resistance to Antimalarial Drugs.
- [175] A. B. S. Sidhu, D. Verdier-Pinard, D. A. Fidock, *Science* **2002**, *298*, 210–213. Chloroquine Resistance in *Plasmodium falciparum* Malaria Parasites Conferred by pfcrt Mutations.

- [176] A. Ecker, A. M. Lehane, J. Clain, D. A. Fidock, *Trends Parasitol.* **2012**, *28*, 504–514. PfCRT and Its Role in Antimalarial Drug Resistance.
- [177] Y. Lai, L. Xing, G. I. Poda, Y. Hu, *Drug Metab. Dispos.* **2007**, *35*, 937–945. Structure-Activity Relationships for Interaction with Multidrug Resistance Protein 2 (ABCC2/MRP2): The Role of Torsion Angle for a Series of Biphenyl-Substituted Heterocycles.
- [178] S. E. Wheeler, K. N. Houk, *J. Am. Chem. Soc.* **2008**, *130*, 10854–10855. Substituent Effects in the Benzene Dimer are Due to Direct Interactions of the Substituents with the Unsubstituted Benzene.
- [179] S. E. Wheeler, *J. Am. Chem. Soc.* **2011**, *133*, 10262–10274. Local Nature of Substituent Effects in Stacking Interactions.
- [180] S. E. Wheeler, *Acc. Chem. Res.* **2013**, *46*, 1029–1038. Understanding Substituent Effects in Noncovalent Interactions Involving Aromatic Rings.
- [181] R. M. Parrish, C. D. Sherrill, *J. Am. Chem. Soc.* **2014**, *136*, 17386–17389. Quantum-Mechanical Evaluation of π - π versus Substituent- π Interactions in π Stacking: Direct Evidence for the Wheeler–Houk Picture.
- [182] M. Harder, M. A. Carnero Corrales, N. Trapp, B. Kuhn, F. Diederich, *Chem. Eur. J.* **2015**, *21*, 8455–8463. Rebek Imide Platforms as Model Systems for the Investigation of Weak Intermolecular Interactions.
- [183] L.-J. Riwar, N. Trapp, B. Kuhn, F. Diederich, *Angew. Chem. Int. Ed.* **2017**, *56*, 11252–11257; *Angew. Chem.* **2017**, *129*, 11405–11410. Substituent Effects in Parallel-Displaced π - π Stacking Interactions: Distance Matters.
- [184] A. C. Flick, H. X. Ding, C. A. Leverett, R. E. Kyne, Jr., K. K.-C. Liu, S. J. Fink, C. J. O'Donnell, *Bioorg. Med. Chem.* **2016**, *24*, 1937–1980. Synthetic Approaches to the 2014 New Drugs.
- [185] A. C. Flick, H. X. Ding, C. A. Leverett, R. E. Kyne Jr., K. K.-C. Liu, S. J. Fink, C. J. O'Donnell, *J. Med. Chem.* **2017**, *60*, 6480–6615. Synthetic Approaches to the New Drugs Approved During 2015.
- [186] S. Senger, M. A. Convery, C. Chan, N. S. Watson, *Bioorg. Med. Chem. Lett.* **2006**, *16*, 5731–5735. Arylsulfonamides: A Study of the Relationship between Activity and Conformational Preferences for a Series of Factor Xa Inhibitors.

- [187] S. Senger, C. Chan, M. A. Convery, J. A. Hubbard, G. P. Shah, N. S. Watson, R. J. Young, *Bioorg. Med. Chem. Lett.* **2007**, *17*, 2931–2934. Sulfonamide-Related Conformational Effects and Their Importance in Structure-Based Design.
- [188] R. L. Beddoes, L. Dalton, J. A. Joule, O. S. Mills, J. D. Street, C. I. F. Watt, *J. Chem. Soc. Perkin. T. 2* **1986**, 787-797. The Geometry at Nitrogen in *N*-Phenylsulphonyl-pyrroles and -indoles. The Geometry of Sulphonamides.
- [189] G. L. Warren, T. D. Do, B. P. Kelley, A. Nicholls, S. D. Warren, *Drug Discovery Today* **2012**, *17*, 1270–1281. Essential Considerations for Using Protein–Ligand Structures in Drug Discovery.
- [190] J. B. Nicholas, R. Vance, E. Martin, B. J. Burke, A. J. Hopfinger, *J. Phys. Chem.* **1991**, *95*, 9803–9811. A Molecular Mechanics Valence Force Field for Sulfonamides Derived by ab Initio Methods.
- [191] G. Liang, J. P. Bays, J. P. Bowen, *J. Mol. Struct.: THEOCHEM* **1997**, *401*, 165–179. Ab Initio Calculations and Molecular Mechanics (MM3) Force Field Development for Sulfonamide and its Alkyl Derivatives.
- [192] T. C. Higgs, A. Parkin, S. Parsons, P. A. Tasker, *Acta Crystallogr.* **2002**, *E58*, o523-o525. *N*-Methylmethanesulfonamide at 150 K.
- [193] C. Aciro, S. K. Bagal, J. W. Harvey, L. H. Jones, C. E. Mowbray, R. M. Owen, Y. A. Sabnis, R. I. Storer, S. K. Yeap, WO 2010/131146 A1, **2010**. Preparation of Cyclobutenedione Derivatives for Treatment of Diseases Mediated by Activation of the CXCR-2 Receptor.
- [194] P. K. Sasmal, S. Ahmed, A. Tehim, V. Pradkar, P. M. M. Dattatreya, N. J., WO 2013/088256 A1, **2013**. Preparation of Substituted Heterocyclic Compounds as Tropomyosin Receptor Kinase α (TrkA) Inhibitors.
- [195] J. B. Aggen, P. Dozzo, A. A. Goldblum, D. J. Hildebrandt, T. R. Kane, M. J. Gliedt, M. S. Linsell, WO 2011/044538 A1, **2011**. Preparation of Antibacterial Aminoglycoside Analogs.
- [196] A. D. Brown, J. Bryans, M. E. Bunnage, P. Glossop, C. Lane, S. Mantell, R. A. Lewthwaite, EP 1460064 A1, **2004**. Preparation and in Vitro Activity of Novel Indole-2-Carboxamide β 2-Adrenoreceptor Agonists.
- [197] R. H. Green, A. J. Brown, H. E. Connor, A. J. Eatherton, G. M. P. Giblin, K. S. Jandu, R. G. Knowles, W. L. Mitchell, A. Naylor, C. T. O’Shaughnessy, G. Palombi, D. A. Rawlings, B. P. Slingsby, C. J. Tralau-Stewart, A. R. Whittington, R. A. Williamson,

- WO 2005/074939 A1, **2005**. Preparation of Aminopyri(mi)dinecarboxamide CB2 Modulators for Use in Combination with PDE4 Inhibitors for Treating Pain, Immune, Inflammatory and Rheumatic Diseases.
- [198] G. M. Dubowchik, J. A. Michne, D. Zuev, *Bioorg. Med. Chem. Lett.* **2004**, *14*, 3147–3149. An Efficient Sequence for the Preparation of Small Secondary Amine Hydrochloride Salts for Focused Library Generation without Need for Distillation or Chromatographic Purification.
- [199] J. Daun, S. Fields, S. Kobayashi, US 2004/0186127 A1, **2004**. Preparation of Deazapurines for Use in Pharmaceutical Compositions for the Treatment of Reperfusion Injuries, Osteoporosis and/or Bone Metastasis.
- [200] C. Bissantz, B. Kuhn, M. Stahl, *J. Med. Chem.* **2010**, *53*, 5061–5084. A Medicinal Chemist's Guide to Molecular Interactions.
- [201] N. Sagawa, T. Shikata, *Phys. Chem. Chem. Phys.* **2014**, *16*, 13262–13270. Are All Polar Molecules Hydrophilic? Hydration Numbers of Nitro Compounds and Nitriles in Aqueous Solution.
- [202] A. Bondi, *J. Phys. Chem.* **1964**, *68*, 441–451. van der Waals Volumes and Radii.
- [203] ACD/Labs Version 12.01, Advanced Chemistry Development, Toronto **2009**.
- [204] D. A. Smith, B. C. Jones, D. K. Walter, *Med. Res. Rev.* **1996**, *16*, 243–266. Design of Drugs Involving the Concepts and Theories of Drug Metabolism and Pharmacokinetics.
- [205] E. H. Kerns, L. Di in *Drug-Like Properties: Concepts, Structure Design and Methods from ADME to Toxicity Optimization*, Elsevier, San Diego, **2008**, pp. 187–196. Plasma Protein Binding
- [206] K. Mortelmans, E. Zeiger, *Mutat. Res., Fundam. Mol. Mech. Mutagen.* **2000**, *455*, 29–60. The Ames *Salmonella*/Microsome Mutagenicity Assay.
- [207] R. Paulini, K. Müller, F. Diederich, *Angew. Chem. Int. Ed.* **2005**, *44*, 1788–1805; *Angew. Chem.* **2005**, *117*, 1820–1839. Orthogonal Multipolar Interactions in Structural Chemistry and Biology.
- [208] K. Müller, C. Faeh, F. Diederich, *Science* **2007**, *317*, 1881–1886. Fluorine in Pharmaceuticals: Looking Beyond Intuition.
- [209] E. Persch, O. Dumele, F. Diederich, *Angew. Chem. Int. Ed.* **2015**, *54*, 3290–3327; *Angew. Chem.* **2015**, *127*, 3341–3382. Molecular Recognition in Chemical and Biological Systems.
- [210] M. R. Bauer, R. N. Jones, M. G. J. Baud, R. Wilcken, F. M. Boeckler, A. R. Fersht, A. C. Joerger, J. Spencer, *ACS Chem. Biol.* **2016**, *11*, 2265–2274. Harnessing Fluorine–

- Sulfur Contacts and Multipolar Interactions for the Design of p53 Mutant Y220C Rescue Drugs.
- [211] S. G. Krimmer, M. Betz, A. Heine, G. Klebe, *ChemMedChem* **2014**, *9*, 833–846. Methyl, Ethyl, Propyl, Butyl: Futile But Not for Water, as the Correlation of Structure and Thermodynamic Signature Shows in a Congeneric Series of Thermolysin Inhibitors.
- [212] M. Betz, T. Wulsdorf, S. G. Krimmer, G. Klebe, *J. Chem. Inf. Model.* **2016**, *56*, 223–233. Impact of Surface Water Layers on Protein–Ligand Binding: How Well Are Experimental Data Reproduced by Molecular Dynamics Simulations in a Thermolysin Test Case?
- [213] S. G. Krimmer, J. Cramer, M. Betz, V. Fridh, R. Karlsson, A. Heine, G. Klebe, *J. Med. Chem.* **2016**, *59*, 10530–10548. Rational Design of Thermodynamic and Kinetic Binding Profiles by Optimizing Surface Water Networks Coating Protein-Bound Ligands.
- [214] M. Marani, A. Paone, A. Fiascarelli, A. Macone, M. Gargano, S. Rinaldo, G. Giardina, V. Pontecorvi, D. Koes, L. McDermott, T. Yang, A. Paiardini, R. Contestabile, F. Cutruzzolà, *Oncotarget* **2015**, *7*, 4570–4583. A Pyrazolopyran Derivative Preferentially Inhibits the Activity of Human Cytosolic Serine Hydroxymethyltransferase and Induces Cell Death in Lung Cancer Cells.
- [215] G. S. Singh, Z. Y. Desta, *Chem. Rev.* **2012**, *112*, 6104–6155. Isatins as Privileged Molecules in Design and Synthesis of Spiro-Fused Cyclic Frameworks.
- [216] A. Leoni, A. Locatelli, R. Morigi, M. Rambaldi, *Expert Opin. Ther. Pat.* **2016**, *26*, 149–173. 2-Indolinone a Versatile Scaffold for Treatment of Cancer: A Patent Review (2008–2014).
- [217] G. J. Roth, A. Heckel, F. Colbatzky, S. Handschuh, J. Kley, T. Lehmann-Lintz, R. Lotz, U. Tontsch-Grunt, R. Walter, F. Hilberg, *J. Med. Chem.* **2009**, *52*, 4466–4480. Design, Synthesis, and Evaluation of Indolinones as Triple Angiokinase Inhibitors and the Discovery of a Highly Specific 6-Methoxycarbonyl-Substituted Indolinone (BIBF 1120).
- [218] T. P. Cho, S. Y. Dong, F. Jun, F. J. Hong, Y. J. Liang, X. Lu, P. J. Hua, L. Y. Li, Z. Lei, H. Bing, Z. Ying, L. F. Qiong, F. B. Bei, L. L. Guang, G. A. Shen, S. G. Hong, S. W. Hong, M. X. Tai, *J. Med. Chem.* **2010**, *53*, 8140–8149. Novel Potent Orally Active Multitargeted Receptor Tyrosine Kinase Inhibitors: Synthesis, Structure–Activity Relationships, and Antitumor Activities of 2-Indolinone Derivatives.

- [219] G. J. Roth, R. Binder, F. Colbatzky, C. Dallinger, R. Schlenker-Herceg, F. Hilberg, S.-L. Wollin, R. Kaiser, *J. Med. Chem.* **2015**, *58*, 1053–1063. Nintedanib: From Discovery to the Clinic.
- [220] C. V. Galliford, K. A. Scheidt, *Angew. Chem. Int. Ed.* **2007**, *46*, 8748–8758; *Angew. Chem.* **2007**, *119*, 8902–8912. Pyrrolidinyl-Spirooxindole Natural Products as Inspirations for the Development of Potential Therapeutic Agents.
- [221] J. R. Reyes, J. Xu, K. Kobayashi, V. Bhat, V. H. Rawal, *Angew. Chem. Int. Ed.* **2017**, *56*, 9962–9966; *Angew. Chem.* **2017**, *129*, 10094–10098. Total Synthesis of (–)-*N*-Methylwelwitindolinone B Isothiocyanate.
- [222] M. Arthuis, R. Pontikis, G. G. Chabot, J. Seguin, L. Quentin, S. Bourg, L. Morin-Allory, J.-C. Florent, *ChemMedChem* **2011**, *6*, 1693–1705. Synthesis and Structure–Activity Relationships of Constrained Heterocyclic Analogues of Combretastatin A4.
- [223] A. Huang, A. Moretto, K. Janz, M. Lowe, P. W. Bedard, S. Tam, L. Di, V. Clerin, N. Sushkova, B. Tchernychev, D. H. H. Tsao, J. C. Keith Jr., G. D. Shaw, R. G. Schaub, Q. Wang, N. Kaila, *J. Med. Chem.* **2010**, *53*, 6003–6017. Discovery of 2-[1-(4-Chlorophenyl)cyclopropyl]-3-hydroxy-8-(trifluoromethyl)quinoline-4-carboxylic Acid (PSI-421), a P-Selectin Inhibitor with Improved Pharmacokinetic Properties and Oral Efficacy in Models of Vascular Injury.
- [224] C. H. Wang, A. R. White, S. N. Schwartz, S. Alluri, T. M. Cattabiani, L. K. Zhang, T. M. Chan, A. V. Buevich, A. K. Ganguly, *Tetrahedron* **2012**, *68*, 9750–9762. Novel Synthesis and Functionalization of *ortho*–*ortho* Disubstituted Biphenyls and a Highly Condensed Novel Heterocycle Using Radical Cyclization Reaction.
- [225] H. M. Al-Matar, K. D. Khalil, A. Y. Adam, M. H. Elnagdi, *Molecules* **2010**, *15*, 6619–6629. Green One Pot Solvent-Free Synthesis of Pyrano[2,3-*c*]-Pyrazoles and Pyrazolo[1,5-*a*]Pyrimidines.
- [226] H. Mecadon, M. R. Rohman, M. Rajbangshi, B. Myrboh, *Tetrahedron Lett.* **2011**, *52*, 2523–2525. γ -Alumina as a Recyclable Catalyst for the Four-Component Synthesis of 6-Amino-4-alkyl/aryl-3-methyl-2,4-dihydropyrano[2,3-*c*]pyrazole-5-carbonitriles in Aqueous Medium.
- [227] T. T. Talele, *J. Med. Chem.* **2017**. DOI: 10.1021/acs.jmedchem.7b00315. Natural-Products-Inspired Use of the *gem*-Dimethyl Group in Medicinal Chemistry.

- [228] S. Matsumoto, D. Samata, M. Akazome, K. Ogura, *Tetrahedron Lett.* **2009**, *50*, 111–114. Synthesis and Physical Properties of Various Organic Dyes Derived from a Single Core Skeleton, 1,2-Dihydroindol-3-one.
- [229] A. Makoto, L. D. Arnold, J. Dinges, R. W. Dixon, S. W. Djuric, A. M. Ericsson, K. Fischer, A. F. Gasielki, V. J. Gracias, J. H. Holms, M. R. Michaelides, M. A. Muckey, P. Rafferty, D. H. Steinman, C. K. Wada, Z. Xia, I. Akritopoulou-zanze, H. Q. Zhang, WO 2005/095387 A1, **2005**. Preparation of Tricyclic Pyrazole Kinase Inhibitors.
- [230] R. Frank, G. Bahrenberg, T. Christoph, K. Schiene, J. De Vry, N. Damann, S. Frommann, B. Lesch, J. Lee, Y.-S. Kim, M.-S. Kim, WO 2010/127855 A1, **2010**. Preparation of Substituted Aromatic Carboxamide and Urea Derivatives as Vanilloid Receptor Ligands for the Treatment of Pain.
- [231] Y. Wang, M. Dai, H. Hatoum-Mokdad, Z. Hong, H. C. E. Kluender, G. H. Ladouceur, T. Li, D. B. Lowe, E. S. Mull, T. E. Shelekhin, R. A. Smith, W. C. Wong, WO 2004/094376 A1, **2004**. Preparation of Hydroxamic Acids Useful in the Treatment of Hyper-Proliferative Disorders.
- [232] D. L. Musso, G. F. Orr, F. R. Cochran, J. L. Kelley, J. L. Selph, G. C. Rigdon, B. R. Cooper, M. L. Jones, *J. Med. Chem.* **2003**, *46*, 409–416. Indanylidene. 2. Design and Synthesis of (*E*)-2-(4-Chloro-6-fluoro-1-indanylidene)-*N*-methylacetamide, a Potent Antiinflammatory and Analgesic Agent without Centrally Acting Muscle Relaxant Activity.
- [233] T. T. Talele, *J. Med. Chem.* **2016**, *59*, 8712–8756. The "Cyclopropyl Fragment" Is a Versatile Player That Frequently Appears in Preclinical/Clinical Drug Molecules.
- [234] O. G. Kulinkovich, S. V. Sviridov, D. A. Vasilevski, *Synthesis* **1991**, 234. Titanium(IV) Isopropoxide-Catalyzed Formation of 1-Substituted Cyclopropanols in the Reaction of Ethylmagnesium Bromide with Methyl Alkanecarboxylates.
- [235] R. Appel, *Angew. Chem. Int. Ed.* **1975**, *14*, 801–811. Tertiary Phosphane/Tetrachloromethane, a Versatile Reagent for Chlorination, Dehydration, and P–N Linkage.
- [236] A. de Meijere, S. I. Kozhuskov, T. Späth, *Org. Synth.* **2002**, *78*, 142. Bicyclopropylidene.
- [237] A. Mai, S. Massa, D. Rotili, S. Simeoni, R. Ragno, G. Botta, A. Nebbioso, M. Miceli, L. Altucci, G. Brosch, *J. Med. Chem.* **2006**, *49*, 6046–6056. Synthesis and Biological Properties of Novel, Uracil-Containing Histone Deacetylase Inhibitors.

- [238] F. Carraro, A. Naldini, A. Pucci, G. A. Locatelli, G. Maga, S. Schenone, O. Bruno, A. Ranise, F. Bondavalli, C. Brullo, P. Fossa, G. Menozzi, L. Mosti, M. Modugno, C. Tintori, F. Manetti, M. Botta, *J. Med. Chem.* **2006**, *49*, 1549–1561. Pyrazolo[3,4-*d*]pyrimidines as Potent Antiproliferative and Proapoptotic Agents toward A431 and 8701-BC Cells in Culture Via Inhibition of c-Src Phosphorylation.
- [239] S. K. Zahn, G. Böhmelt, A. Mantoulidis, U. Reiser, M. Treu, U. Gürtler, A. Schoop, F. Solca, U. Tontsch-Grunt, R. Brückner, C. Reither, L. Herfurth, O. Krämer, H. Stadtmüller, H. Engelhardt, WO 2007/003596 A1, **2007**. Preparation of 2,4-Diaminopyrimidines as Aurora-B Kinase Inhibitors for the Treatment of Abnormal Cell Proliferation.
- [240] A. F. Kluge, R. C. Petter, R. W. Tester, L. Qiao, D. Niu, W. F. Westlin, J. Singh, H. Mazdiyasi, WO 2009/158571 A1, **2009**. Preparation of Heteroaryl Compounds Protein Kinase Inhibitors.
- [241] F. Marchetti, C. Cano, N. J. Curtin, B. T. Golding, R. J. Griffin, K. Haggerty, D. R. Newell, R. J. Parsons, S. L. Payne, L. Z. Wang, I. R. Hardcastle, *Org. Biomol. Chem.* **2010**, *8*, 2397–2407. Synthesis and Biological Evaluation of 5-Substituted *O*⁴-Alkylpyrimidines as CDK2 Inhibitors.
- [242] C. Baker-Glenn, D. J. Burdick, M. Chambers, B. K. Chan, H. Chen, A. Estrada, J. L. Gunzner, D. Shore, Z. K. Sweeney, S. Wang, G. Zhao, WO 2011/151360 A1, **2011**. Aminopyrimidine Derivatives as LRRK2 Modulators and Their Preparation and Use for the Treatment of Parkinson's Disease.
- [243] D. T. Cohen, S. L. Buchwald, *Org. Lett.* **2015**, *17*, 202–205. Mild Palladium-Catalyzed Cyanation of (Hetero)Aryl Halides and Triflates in Aqueous Media.
- [244] B. M. Moore II, S. Gurley, S. Mustafa, WO 2011/022694 A1, **2011**. Preparation of Furanopyrimidine Derivatives as Cannabinoid Receptor Ligands.
- [245] P. A. Brough, X. Barril, J. Borgognoni, P. Chene, N. G. M. Davies, B. Davis, M. J. Drysdale, B. Dymock, S. A. Eccles, C. Garcia-Echeverria, C. Fromont, A. Hayes, R. E. Hubbard, A. M. Jordan, M. R. Jensen, A. Massey, A. Merrett, A. Padfield, R. Parsons, T. Radimerski, F. I. Raynaud, A. Robertson, S. D. Roughley, J. Schoepfer, H. Simmonite, S. Y. Sharp, A. Surgenor, M. Valenti, S. Walls, P. Webb, M. Wood, P. Workman, L. Wright, *J. Med. Chem.* **2009**, *52*, 4794–4809. Combining Hit Identification Strategies: Fragment-Based and in Silico Approaches to Orally Active 2-Aminothieno[2,3-*d*]pyrimidine Inhibitors of the Hsp90 Molecular Chaperone.

- [246] R. L. Summerfield, D. M. Daigle, S. Mayer, D. Mallik, D. W. Hughes, S. G. Jackson, M. Sulek, M. G. Organ, E. D. Brown, M. S. Junop, *J. Med. Chem.* **2006**, *49*, 6977–6986. A 2.13 Å Structure of *E. coli* Dihydrofolate Reductase Bound to a Novel Competitive Inhibitor Reveals a New Binding Surface Involving the M20 Loop Region.
- [247] C. Courme, N. Gresh, C. Lenoir, M. Vidal, C. Garbay, J.-C. Florent, E. Bertounesque, *Heterocycles* **2010**, *81*, 867–882. Synthesis of Bis-Aryl Phosphates Based on Triazine Scaffold.
- [248] I. Lalezari, H. Golgolab, *J. Chem. Eng. Data* **1971**, *16*, 117. Improved Synthesis of Arylguanamines. Reaction of Aromatic Nitriles with Dicyandiamide in Presence of Sodium Ethoxide.
- [249] R. Deans, G. Cooke, V. M. Rotello, *J. Org. Chem.* **1997**, *62*, 836–839. Model Systems for Flavoenzyme Activity. Regulation of Flavin Recognition via Modulation of Receptor Hydrogen-Bond Donor–Acceptor Properties.
- [250] C. P. Spears, A. H. Shahinian, R. G. Moran, C. Heidelberger, T. H. Corbett, *Cancer Res.* **1982**, *42*, 450–456. In Vivo Kinetics of Thymidylate Synthetase Inhibition in 5-Fluorouracil-sensitive and -resistant Murine Colon Adenocarcinomas.
- [251] F. Daidone, R. Florio, S. Rinaldo, R. Contestabile, M. L. di Salvo, F. Cutruzzolà, F. Bossa, A. Paiardini, *Eur. J. Med. Chem.* **2011**, *46*, 1616–1621. *In Silico* and *in Vitro* Validation of Serine Hydroxymethyltransferase as a Chemotherapeutic Target of the Antifolate Drug Pemetrexed.
- [252] A. Paiardini, A. Fiascarelli, S. Rinaldo, F. Daidone, G. Giardina, D. R. Koes, A. Parroni, G. Montini, M. Marani, A. Paone, L. A. McDermott, R. Contestabile, F. Cutruzzolà, *ChemMedChem* **2015**, *10*, 490–497. Screening and *in Vitro* Testing of Antifolate Inhibitors of Human Cytosolic Serine Hydroxymethyltransferase.
- [253] T. A. Garrow, A. A. Brenner, V. M. Whitehead, X.-N. Chen, R. G. Duncan, J. R. Korenberg, B. Shane, *J. Biol. Chem.* **1993**, *268*, 11910–11916. Cloning of Human cDNAs Encoding Mitochondrial and Cytosolic Serine Hydroxymethyltransferases and Chromosomal Localization.
- [254] S. Bernhardt, M. Bayerlová, M. Vetter, A. Wachter, D. Mitra, V. Hanf, T. Lantzsch, C. Uleer, S. Peschel, J. John, J. Buchmann, E. Weigert, K.-F. Bürrig, C. Thomssen, U. Korf, T. Beissbarth, S. Wiemann, E. J. Kantelhardt, *Breast Cancer Res.* **2017**, *19*:112. Proteomic Profiling of Breast Cancer Metabolism Identifies SHMT2 and ASCT2 as Prognostic Factors.

- [255] D. Kim, B. P. Fiske, K. Birsoy, E. Freinkman, K. Kami, R. L. Possemato, Y. Chudnovsky, M. E. Pacold, W. W. Chen, J. R. Cantor, L. M. Shelton, D. Y. Gui, M. Kwon, S. H. Ramkisson, K. L. Ligon, S. W. Kang, M. Snuderl, M. G. Vander Heiden, D. M. Sabatini, *Nature* **2015**, *520*, 363–367. SHMT2 Drives Glioma Cell Survival in Ischaemia but Imposes a Dependence on Glycine Clearance.
- [256] G. Giardina, P. Brunotti, A. Fiascarelli, A. Cicalini, M. G. S. Costa, A. M. Buckle, M. L. di Salvo, A. Giorgi, M. Marani, A. Paone, S. Rinaldo, A. Paiardini, R. Contestabile, F. Cutruzzolà, *FEBS J.* **2015**, *282*, 1225–1241. How Pyridoxal 5'-Phosphate Differentially Regulates Human Cytosolic and Mitochondrial Serine Hydroxymethyltransferase Oligomeric State.
- [257] C. Pinthong, S. Maenpuen, W. Amornwatcharapong, Y. Yuthavong, U. Leartsakulpanich, P. Chaiyen, *FEBS J.* **2014**, *281*, 2570–2583. Distinct Biochemical Properties of Human Serine Hydroxymethyltransferase Compared with the *Plasmodium* Enzyme: Implications for Selective Inhibition.
- [258] A. N. Lane, T. W.-M. Fan, *Nucleic Acids Res.* **2015**, *43*, 2466–2485. Regulation of Mammalian Nucleotide Metabolism and Biosynthesis.
- [259] E. A. Rayl, B. A. Moroson, G. P. Beardsley, *J. Biol. Chem.* **1996**, *271*, 2225–2233. The Human *purH* Gene Product, 5-Aminoimidazole-4-carboxamide Ribonucleotide Formyltransferase/IMP Cyclohydrolase: Cloning, Sequencing, Expression, Purification, Kinetic Analysis, and Domain Mapping.
- [260] C.-G. Cheong, D. W. Wolan, S. E. Greasley, P. A. Horton, G. P. Beardsley, I. A. Wilson, *J. Biol. Chem.* **2004**, *279*, 18034–18045. Crystal Structures of Human Bifunctional Enzyme Aminoimidazole-4-carboxamide Ribonucleotide Transformylase/IMP Cyclohydrolase in Complex with Potent Sulfonyl-containing Antifolates.
- [261] C. J. Allegra, J. C. Drake, J. Jolivet, B. A. Chabner, *Proc. Natl. Acad. Sci. U. S. A.* **1985**, *82*, 4881–4885. Inhibition of Phosphoribosylaminoimidazolecarboxamide Transformylase by Methotrexate and Dihydrofolic Acid Polyglutamates.
- [262] T. H. Marsilje, M. A. Labroli, M. P. Hedrick, Q. Jin, J. Desharnais, S. J. Baker, L. T. Gooljarsingh, J. Ramcharan, A. Tavassoli, Y. Zhang, I. A. Wilson, G. P. Beardsley, S. J. Benkovic, D. L. Boger, *Bioorg. Med. Chem.* **2002**, *10*, 2739–2749. 10-Formyl-5,10-dideaza-acyclic-5,6,7,8-tetrahydrofolic Acid (10-Formyl-DDACTHF): A Potent Cytotoxic Agent Acting by Selective Inhibition of Human GAR Tfase and the De Novo Purine Biosynthetic Pathway.

- [263] J. Desharnais, I. Hwang, Y. Zhang, A. Tavassoli, J. Baboval, S. J. Benkovic, I. A. Wilson, D. L. Boger, *Bioorg. Med. Chem.* **2003**, *11*, 4511–4521. Design, Synthesis and Biological Evaluation of 10-CF₃CO-DDACTHF Analogues and Derivatives as Inhibitors of GAR Tfase and the De Novo Purine Biosynthetic Pathway.
- [264] S. B. Rothbart, A. C. Racanelli, R. G. Moran, *Cancer Res.* **2010**, *70*, 10299–10309. Pemetrexed Indirectly Activates the Metabolic Kinase AMPK in Human Carcinomas.
- [265] D. J. Asby, F. Cuda, M. Beyaert, F. D. Houghton, F. R. Cagampang, A. Tavassoli, *Chem. Biol.* **2015**, *22*, 838–848. AMPK Activation via Modulation of De Novo Purine Biosynthesis with an Inhibitor of ATIC Homodimerization.
- [266] C. Jose, E. Hébert-Chatelain, N. Bellance, A. Larendra, M. Su, K. Nouette-Gaulain, R. Rossignol, *Biochim. Biophys. Acta, Bioenerg.* **2011**, *1807*, 707–718. AICAR Inhibits Cancer Cell Growth and Triggers Cell-type Distinct Effects on OXPHOS Biogenesis, Oxidative Stress and Akt Activation.
- [267] J. E. Sullivan, F. Carey, D. Carling, R. K. Beri, *Biochem. Biophys. Res. Commun.* **1994**, *200*, 1551-1556. Characterization of 5'-AMP-Activated Protein Kinase in Human Liver Using Specific Peptide Substrates and the Effects of 5'-AMP Analogues on Enzyme Activity.
- [268] Y. Sun, K. E. Connors, D.-Q. Yang, *Mol. Cell. Biochem.* **2007**, *306*, 239–245. AICAR Induces Phosphorylation of AMPK in an ATM-Dependent, LKB1-Independent Manner.
- [269] J. Cheng, T. Huang, Y. Li, Y. Guo, Y. Zhu, Q. Wang, X. Tan, W. Chen, Y. Zhang, W. Cheng, T. Yamamoto, X. Jing, J. Huang, *PloS one* **2014**, *9*, e93256. AMP-Activated Protein Kinase Suppresses the *in Vitro* and *in Vivo* Proliferation of Hepatocellular Carcinoma.
- [270] M. Jain, R. Nilsson, S. Sharma, N. Madhusudhan, T. Kitami, A. L. Souza, R. Kafri, M. W. Kirschner, C. B. Clish, V. K. Mootha, *Science* **2012**, *336*, 1040–1044. Metabolite Profiling Identifies a Key Role for Glycine in Rapid Cancer Cell Proliferation.
- [271] I. Amelio, F. Cutruzzolá, A. Antonov, M. Agostini, G. Melino, *Trends Biochem. Sci.* **2014**, *39*, 191–198. Serine and Glycine Metabolism in Cancer.
- [272] D. J. Montefusco, B. Newcomb, J. L. Gandy, S. E. Brice, N. Matmati, L. A. Cowart, Y. A. Hannun, *J. Biol. Chem.* **2012**, *287*, 9280–9289. Sphingoid Bases and the Serine Catabolic Enzyme *CHAI* Define a Novel Feedforward/Feedback Mechanism in the Response to Serine Availability.

- [273] T. J. de Koning, K. Snell, M. Duran, R. Berger, B.-T. Poll-The, R. Surtees, *Biochem. J.* **2003**, *371*, 653–661. L-Serine in Disease and Development.
- [274] J. D. Rabinowitz, H. Kim, G. S. Ducker, J. M. Ghergurovich, WO 2016/145252 A1, **2016**. SHMT Inhibitors.
- [275] B. R. Blank, J. Gut, P. J. Rosenthal, A. R. Renslo, *J. Med. Chem.* **2017**, *60*, 6400–6407. Enantioselective Synthesis and in Vivo Evaluation of Regioisomeric Analogues of the Antimalarial Arterolane.
- [276] K. Griesbaum, X. Liu, A. Kassiaris, M. Scherer, *Liebigs Ann./Recueil* **1997**, 1381–1390. Ozonolyses of *O*-Alkylated Ketoximes in the Presence of Carbonyl Groups: A Facile Access to Ozonides.
- [277] T. Persson, J. Nielsen, *Org. Lett.* **2006**, *8*, 3219–3222. Synthesis of *N*-Methoxy-*N*-methyl- β -enaminoketoesters: New Synthetic Precursors for the Regioselective Synthesis of Heterocyclic Compounds.
- [278] C. S. Marvel, F. E. Smith, *J. Am. Chem. Soc.* **1923**, *45*, 2696–2698. Identification of Amines.
- [279] Y. Hayashi, J. Katada, T. Harada, A. Tachiki, K. Iijima, Y. Takiguchi, M. Muramatsu, H. Miyazaki, T. Asari, T. Okazaki, Y. Sato, E. Yasuda, M. Yano, I. Uno, I. Ojima, *J. Med. Chem.* **1998**, *41*, 2345–2360. GPIIb/IIIa Integrin Antagonists with the New Conformational Restriction Unit, Trisubstituted β -Amino Acid Derivatives, and a Substituted Benzamidine Structure.
- [280] C. Koradin, M. Kordes, R. Le Vezouet, D. L. Culbertson, D. D. Anspaugh, WO 2008/017649 A1, **2008**. Preparation of Substituted Azolin-2-yl-amino Compounds for Combating Arthropod Pests or Nematodes.
- [281] A. Minidis, F. Rahm, J. Viklund, WO 2013/054108 A1, **2013**. Preparation of Mono-fluoro Spiro Compounds as β -Secretase Inhibitors for Treating Amyloid β -related Pathologies.
- [282] A. Mai, M. Artico, R. Ragno, G. Sbardella, S. Massa, C. Musiu, M. Mura, F. Marturana, A. Cadeddu, G. Maga, P. La Colla, *Bioorg. Med. Chem.* **2005**, *13*, 2065–2077. 5-Alkyl-2-alkylamino-6-(2,6-difluorophenylalkyl)-3,4-dihydropyrimidin-4(3*H*)-ones, a New Series of Potent, Broad-Spectrum Non-Nucleoside Reverse Transcriptase Inhibitors Belonging to the DABO Family.
- [283] W. Trager, J. B. Jensen, *Science* **1976**, *193*, 673–675. Human Malaria Parasites in Continuous Culture.

- [284] A. Dorn, R. Stoffel, H. Matile, A. Bubendorf, R. G. Ridley, *Nature* **1995**, *374*, 269–271. Malarial Haemozoin/ β -Haematin Supports Haem Polymerization in the Absence of Protein.
- [285] W. Huber, J. C. Koella, *Acta Trop.* **1993**, *55*, 257–261. A Comparison of Three Methods of Estimating EC₅₀ in Studies of Drug Resistance of Malaria Parasites.
- [286] R. S. Obach, *Drug Metab. Dispos.* **1999**, *27*, 1350–1359. Prediction of Human Clearance of Twenty-Nine Drugs from Hepatic Microsomal Intrinsic Clearance Data: An Examination of in Vitro Half-Life Approach and Nonspecific Binding to Microsomes.
- [287] T. R. Bridal, M. Margulis, X. Wang, M. Donio, S. Sorota, *Assay Drug Dev. Technol.* **2010**, *8*, 755–765. Comparison of Human *Ether-à-go-go* Related Gene Screening Assays Based on Ionworks Quattro and Thallium Flux.
- [288] D. Nakai, K. Kumamoto, C. Sakikawa, T. Kosaka, T. Tokui, *J. Pharm. Sci.* **2004**, *93*, 847–854. Evaluation of the Protein Binding Ratio of Drugs by a Micro-Scale Ultracentrifugation Method.
- [289] F. Lombardo, M. Y. Shalaeva, K. A. Tupper, F. Gao, *J. Med. Chem.* **2001**, *44*, 2490–2497. ElogD_{oct}: A Tool for Lipophilicity Determination in Drug Discovery. 2. Basic and Neutral Compounds.
- [290] A. J. McCoy, R. W. Grosse-Kunstleve, P. D. Adams, M. D. Winn, L. C. Storoni, R. J. Read, *J. Appl. Cryst.* **2007**, *40*, 658–674. Phaser Crystallographic Software.
- [291] P. Emsley, B. Lohkamp, W. G. Scott, K. Cowtan, *Acta Crystallogr.* **2010**, *D66*, 486–501. Features and Development of *Coot*.
- [292] G. N. Murshudov, P. Skubák, A. A. Lebedev, N. S. Pannu, R. A. Steiner, R. A. Nicholls, M. D. Winn, F. Long, A. A. Vagin, *Acta Crystallogr.* **2011**, *D67*, 355–367. *REFMAC5* for the Refinement of Macromolecular Crystal Structures.
- [293] Hyperchem(TM) Professional 7.51, Hypercube, Inc., 1115 NW 4th Street, Gainesville, Florida 32601, USA.
- [294] Centre for Integrative Bioinformatics VU, *PRALINE*, accessible via the following link: <http://www.ibi.vu.nl/programs/pralinewww/>
- [295] G. M. Sheldrick, *SADABS. Program for Empirical Absorption Correction of Area Detector Data*. University of Göttingen: Göttingen, Germany, **1996**.
- [296] G. Sheldrick, *Acta Crystallogr.* **2008**, *A64*, 112–122. A Short History of *SHELX*.

- [297] G. Sheldrick, *Acta Crystallogr.* **2015**, *A71*, 3–8. *SHELXT* – Integrated Space-Group and Crystal-Structure Determination.
- [298] L. Palatinus, G. Chapuis, *J. Appl. Crystallogr.* **2007**, *40*, 786–790. *SUPERFLIP* – A Computer Program for the Solution of Crystal Structures by Charge Flipping in Arbitrary Dimensions.
- [299] L. Palatinus, S. J. Prathapa, S. van Smaalen, *J. Appl. Crystallogr.* **2012**, *45*, 575–580. *EDMA*: A Computer Program for Topological Analysis of Discrete Electron Densities.
- [300] G. Sheldrick, *Acta Crystallogr.* **2015**, *C71*, 3–8. Crystal Structure Refinement with *SHELXL*.
- [301] O. V. Dolomanov, L. J. Bourhis, R. J. Gildea, J. A. K. Howard, H. Puschmann, *J. Appl. Crystallogr.* **2009**, *42*, 339–341. *OLEX2*: A Complete Structure Solution, Refinement and Analysis Program.

Curriculum Vitae

1989 Born on December 5th in Mulhouse, France

Education

- Nov 2013–present PhD Student in the Group of Prof. Dr. François Diederich, ETH Zurich, Zurich, Switzerland.
- Sep 2012–Sep 2013 Master Degree in “Molecular and Supramolecular Chemistry”, University of Strasbourg, Strasbourg, France.
- Sep 2009–Sep 2013 European School of Chemistry, Polymers, and Material Sciences (ECPM), Strasbourg, France.
- Sep 2007–Jun 2009 Higher National Diploma in Chemistry (Graduated with Honors) University Institute of Technology (IUT), Illkirch-Graffenstaden, France.

Work experiences

- Nov 2013–present PhD Thesis in the Group of Prof. Dr. François Diederich, ETH Zurich, Zurich, Switzerland.
- Apr–Sep 2013 Master Thesis in the Group of Prof. Dr. Françoise Colobert and Dr. Frédéric Leroux, UMR 7509 UDS/CNRS, Strasbourg, France.
- Feb–Jul 2012 Training Period at Sanofi-Aventis, Vitry-sur-Seine, France.
Worked as Master/Grad Student Trainee in the Oncology Department.
Advisor: Dr. Yann Foricher
- Jul–Dec 2011 Training period at Novartis NIBR/GDC, Basel, Switzerland
Worked as Master/Grad Student Trainee in the Autoimmunity, Transplantation and Inflammatory Diseases Department.
Advisor: Dr. Daniela Angst
- Jul–Aug 2010 Training Period at Biowind, Schiltigheim, France.
Worked as a Trainee Engineer in the R&D Department.
Advisor: Dr. Jérôme Tarantot
- Apr–Jul 2009 Training Period at Prestwick Chemical, Illkirch, France
Worked as a Trainee Chemical Technician.
Advisor: Dr. Muriel Joubert

Zurich, October 2017

Geoffrey Schwertz